UNIVERSITY OF CALIFORNIA

Santa Barbara

Expanding the Frontiers of f-Element Coordination Chemistry: New Routes to Lanthanide Ligand Multiple Bonds, High Valent Lanthanides, and *Trans/Cis* Isomerization and Functionalization of the Uranyl Ion

A dissertation submitted in partial satisfaction of the

requirements for the degree Doctor of Philosophy

in Chemistry

by

Mikiyas K. Assefa

Committee in charge:

Professor Trevor W. Hayton, Chair

Professor Gabriel Menard

Professor Peter C. Ford

Professor Horia Metiu

September 2020

The dissertation of Mikiyas K. Assefa is approved.

_____

Professor Gabriel Menard

_____

Professor Peter C. Ford

_____

Professor Horia Metiu

_____

Professor Trevor W. Hayton, Committee Chair

August 2020

Expanding the Frontiers of f-Element Coordination Chemistry: New Routes to Lanthanide Ligand Multiple Bonds, High Valent Lanthanides, and *Trans/Cis* Isomerization and Functionalization of the Uranyl Ion

Mikiyas K. Assefa

Dedicated to Ato Kurabachew Assefa

Acknowledgements

I would first like to extend my most heartfelt gratitude towards my high school chemistry teacher Ato Tsehaye Sebhatu Yohannes for sparking my interest in chemistry and inspiring me to pursue a PhD. He has taught me well, and I will cherish his lessons throughout my professional career. I would, of course, also like to thank my research advisor Prof. Trevor Hayton for accepting me into his group and teaching me how to become a successful synthetic chemist. He has been a continuous source of support and guidance throughout my graduate tenure, and I appreciate all the effort he put into making sure I succeeded. In addition, thanks to my PhD committee members Prof. Gab Menard, Prof. Peter Ford, and my ping-pong partner Prof. Horia Metiu for advice and mentorship throughout graduate school.

Big thanks to Hayton group alumni Dr. Ellie Owens, Dr. Danil Smiles and Ed Paul for training me on the glovebox and Schlenk line, and Dr. Nate Hartmann and Dr. Andrew Cook for training on fixing vacuum pumps. Big thanks also to current Hayton group members, especially Selena Staun and Gregg Kent, for taking extra care of the space that we shared over the years. In addition, special thanks to my good friend and the Department's X-ray crystallographer Dr. Guang Wu, for entertaining me with educational and humorous conversations during stressful days in the lab.

Finally, I would like to thank my family and friends both here in the U.S. and abroad in my home country Ethiopia for always checking in on me and my well-being throughout my educational journey. I am especially indebted to my aunt Muluemebet Teferi and my dearest friend Rediet Tilahun. Undoubtedly, the support of family and friends near and far has played paramount role in all of my accomplishments.

For financial support, I would like to thank the National Science Foundation (CHE 1361654 and CHE 1764345) and the U.S. Department of Energy, Office of Basic Energy Sciences, Chemical Sciences, Biosciences, and Geosciences Division (DE-SC-0001861). This research made use of the 400 MHz NMR Spectrometer of the UCSB Chemistry Department, an NIH SIG (1S10OD012077-01A1), and a 500 MHz NMR Spectrometer under the NSF Major Research Instrumentation (MRI) Award 1920299. Additionally, this study made use of the MRL Shared Experimental Facilities at the University of California at Santa Barbara, supported by the NSF MRSEC program under Award DMR 1720256; a member of the NSF-funded Materials Research Facilities Network.

Vita of Mikiyas K. Assefa

August 2020

Education:

Doctor of Philosophy: Chemistry

University of California Santa Barbara (September 2020 Expected)

Advisor – Prof. Trevor W. Hayton

Dissertation: "Expanding the Frontiers of f-Element Coordination Chemistry: New Routes to Lanthanide Ligand Multiple Bonds, High Valent Lanthanides, and *Trans/Cis* Isomerization and Functionalization of the Uranyl Ion"

Bachelor of Arts (ACS certified) *Summa Cum Laude*: Chemistry and Physics

Berea College (July 2015)

Professional Employment:

- Graduate Student Researcher - UC Santa Barbara, Dept. of Chemistry (7/15 - Present)
- Research Assistant - University of Georgia, Dept. of Chemistry (5/14 - 8/14)
- Research Assistant - Ohio State University, Dept. of Chemistry (5/13 - 8/13)
- Research Mentor - UC Santa Barbara, Summer Sessions (6/18 - 8/18, 6/19 - 8/19)
- Graduate Teaching Assistant - UC Santa Barbara, Dept. of Chemistry (09/15 - 12/18)
- Undergraduate Teaching Assistant - Berea College, Dept. of Chemistry (09/13 - 12/14)

Refereed Publications:

- Assefa, M.K.; Hayton T.W. Bis(1,2-dimethoxyethane)tetrachlorouranium(IV). *Inorg. Synt.* **2020**, *Accepted Manuscript*.
- Assefa, M.K.; Wu, G.; Hayton, T.W. Uranyl Oxo Silylation Promoted by Silsesquioxane Coordination. *J. Am. Chem. Soc*. **2020**, *142*, 8738-8747.
- Assefa, M.K.; Sergentu, D-C.; Seaman, L.A.; Wu, G.; Autschbach, J.; Hayton, T.W. Synthesis, Characterization, and Electrochemistry of the Homoleptic f Element Ketimide Complexes, $[Li]_2[M(N=C^tBuPh)_6]$ (M = Ce, Th). *Inorg. Chem.* **2019**, *58*, 12654-12661.
- Assefa, M.K.; Pedrick, E.A.; Wakefield, M.E.; Wu, G.; Hayton, T.W. Oxidation of the 14-Membered Macrocycle Dibenzotetramethyltetraaza[14]annulene upon Ligation to the Uranyl Ion. *Inorg. Chem.* **2018**, *57*, 8317-8324.

- Assefa, M.K.; Wu, G; Hayton, T.W. Synthesis of a Terminal Ce(IV) Oxo Complex by Photolysis of a Ce(III) Nitrate Complex. *Chem. Sci.* **2017**, *8*, 7873-7878.
- Pedrick, E.A.; Assefa, M.K.; Wakefield, M.E.; Wu, G.; Hayton, T.W. Uranyl Coordination by the 14-Membered Macrocycle Dibenzotetramethyltetraaza[14]annulene. *Inorg. Chem.* **2017**, *56*, 6638-6644.
- Assefa, M.K.; Devera, J.L.; Brathwaite, A.D.; Mosley, J.D.; Duncan, M.A. Vibrational Scaling Factors for Transition Metal Carbonyls. *Chem. Phys. Lett*. **2015**, *640,* 175-179.

Awards:

- Phillip Chase Mabe Memorial Fellowship, UC Santa Barbara (2020)
- Graduate Division Dissertation Fellowship, UC Santa Barbara (2019)
- J. Stanton King Science Award, Berea College (2015)
- Thomas Beebe Organic Chemistry Award, Berea College (2014)

Major Field: Synthetic Inorganic Chemistry

Studies in Organometallic Lanthanide and Actinide Chemistry with Professor Trevor W. Hayton

Abstract

Expanding the Frontiers of f-Element Coordination Chemistry: New Routes to Lanthanide Ligand Multiple Bonds, High Valent Lanthanides, and *Trans/Cis* Isomerization and Functionalization of the Uranyl Ion

by

Mikiyas K. Assefa

Reaction of $[Ce(NR_2)_3]$ (R = $SiMe_3$) with $LiNO_3$ in THF, in the presence of 2,2,2-cryptand, results in the formation of the Ce(III) "ate" complex, [Li(2,2,2-cryptand)][Ce(κ^2-O_2NO)$(NR_2)_3$] in 38% yield. Photolysis of this complex at 380 nm affords [Li(2,2,2-cryptand)][Ce(O)$(NR_2)_3$] in 33% isolated yield after reaction workup. This complex is the first reported example of a Ce(IV) oxo complex where the oxo ligand is not supported by hydrogen bonding or alkali metal coordination. Also formed during photolysis are $[Li(2,2,2\text{-cryptand})]_2[(\mu_3\text{-O})\{Ce(\mu\text{-O})(NR_2)_2\}_3]$ and [Li(2,2,2-cryptand)][Ce($OSiMe_3$)$(NR_2)_3$], whose identities were confirmed by X-ray crystallography. The latter complex can also be prepared independently via reaction of $[Ce(NR_2)_3]$ with $LiOSiMe_3$ in THF, in the presence of 2,2,2-cryptand. When synthesized in this fashion, it can be isolated in 47% yield.

Reaction of $[Ce(NO_3)_3(THF)_4]$ with 6 equiv of Li(N=C^{t}BuPh), followed by addition of 0.5 equiv of I_2, affords the homoleptic Ce(IV) ketimide, $[Li]_2[Ce(N{=}C^tBuPh)_6]$, which can be isolated in 44% yield after workup. Similarly, reaction of $[ThCl_4(DME)_2]$ with 6 equiv of Li(N=C^{t}BuPh) in THF affords the isostructural Th(IV) ketimide, $[Li]_2[Th(N{=}C^tBuPh)_6]$, which can be isolated in 53% yield after workup. Both complexes were fully characterized, including analysis by X-ray crystallography, allowing for a detailed structural and

spectroscopic comparison. The electronic structures of both complexes were also explored with density functional theory (DFT) calculations. Additionally, the redox chemistry of $[Li]_2[Ce(N{=}C^tBuPh)_6]$, was probed by cyclic voltammetry, which revealed a highly cathodic Ce(IV)/Ce(III) reduction potential, providing evidence for the ability of the ketimide ligand to stabilize high oxidation states of the lanthanides.

Reaction of anhydrous $CeCl_3$ with 2 equiv of $[Li(Et_2O)]_2$[1,8-DMC] (1,8-DMC = 1,8-dimethyl-1,4,8,11-tetraazacyclotetradecane) in THF at 65 °C for 2 d affords [Li][Ce(1,8-DMC)$_2$] as yellow blocks in 75% yield, after crystallization from a concentrated Et_2O solution. Similarly, reaction of anhydrous $PrCl_3$ with 2 equiv of $[Li(Et_2O)]_2$[1,8-DMC] in THF at 65 °C for 2 d affords [Li][Pr(1,8-DMC)$_2$] as pale blue blocks in 63% yield. Both complexes were fully characterized, including analysis by X-ray crystallography, UV-Vis/NIR spectroscopy and cyclic voltammetry. Oxidation of [Li][Ce(1,8-DMC)$_2$] with 0.5 equiv of I_2 in THF affords the Ce(IV) bis-cyclam complex [Ce(1,8-DMC)$_2$] as purple plates in 34% yield. In contrast, reaction of [Li][Pr(1,8-DMC)$_2$] with 0.5 equiv of I_2 or 1 equiv of AgOTf in Et_2O or THF only results in isolation of [Li(py)(1,8-DMC^{H2})][X] (X = I, OTf). No praseodymium containing material could be isolated from these reactions. Interestingly, reaction of [Li][Pr(1,8-DMC)$_2$] with 0.5 equiv of I_2, in the presence of 1 equiv of 2,2,2-cryptand, results in formation of the Pr(III) iodocyclam complex [Pr(1,8-DMC)(2,2,2-crypt)(I)], which was characterized by X-ray crystallography. Both attempts at oxidizing the Pr(III) center in [Li][Pr(1,8-DMC)$_2$] are believed to result in either direct ligand protonation or ligand oxidation followed by hydrogen atom abstraction from solvent.

Reaction of Li_2(tmtaa) (tmtaaH_2 = dibenzotetramethyltetraaza[14]annulene) with 1 equiv of $[UO_2Cl_2(THF)_3]$, in an attempt to form *cis*-$[UO_2$(tmtaa)], affords the bis(uranyl) complex,

$[Li(THF)_3][Li(THF)_2][(UO_2Cl_2)_2(tmtaa)]$, as a red-brown crystalline solid in modest yield. This complex can be synthesized rationally by reaction of $Li_2(tmtaa)$ with 2 equiv of $[UO_2Cl_2(THF)_3]$. Under these conditions, it can be isolated in 44% yield. In contrast to the $Li_2(tmtaa)$ reaction, addition of $[K(DME)]_2[tmtaa]$ to 1 equiv of $[UO_2Cl_2(THF)_3]$ results in formation of the $2e^-$ oxidation products of $(tmtaa)^{2-}$. Specifically, three isomers of $C_{22}H_{22}N_4$ were isolated as a mixture of orange crystals in 41% combined yield. All three isomers were characterized by X-ray crystallography. We hypothesize that these ligand oxidation products are formed upon decomposition of the unobserved cis uranyl intermediate, *cis*-$[UO_2(tmtaa)]$, which undergoes a facile intramolecular redox reaction.

Reaction of $[UO_2(N(SiMe_3)_2)_2(THF)_2]$ with 1 equiv of $Cy_7Si_7O_9(OH)_3$ in THF affords $[U(OSiMe_3)_3(Cy_7Si_7O_{12})]$ as orange plates in 24% isolated yield. We propose that the formation of this complex proceeds through a transient uranyl silsesquioxide intermediate, $[\{Cy_7Si_7O_{11}(OH)\}UO_2]$, which undergoes rapid oxo silylation by $HN(SiMe_3)_2$, followed by silyloxy ligand scrambling, to form $[U(OSiMe_3)_3(Cy_7Si_7O_{12})]$ and the U(VI) bis(silsesquioxane) complex, $[U(Cy_7Si_7O_{12})_2]$, among other products. The formation of $[U(Cy_7Si_7O_{12})_2]$ was confirmed by its independent synthesis and comparison of its $^{29}Si\{^1H\}$ NMR spectrum with that of the *in situ* reaction mixture. In contrast to the reaction in THF, the reaction of $[UO_2(N(SiMe_3)_2)_2(THF)_2]$ with $Cy_7Si_7O_9(OH)_3$ in hexanes, followed by recrystallization from Et_2O/MeCN, results in formation of the uranyl cluster, $[(UO_2)_3(Cy_7Si_7O_{12})_2(Et_2O)(MeCN)_2]$, as yellow rods in 42% isolated yield. Overall, the conversion of $[UO_2(N(SiMe_3)_2)_2(THF)_2]$ to $[U(OSiMe_3)_3(Cy_7Si_7O_{12})]$ and $[U(Cy_7Si_7O_{12})_2]$ is likely promoted by the strong electron donor ability of the silsesquioxane ligand, and suggests

that the actinide coordination chemistry of mineral surface mimics, such as silsesquioxane, is a fruitful arena for the discovery of new reactivity.

Table of Contents

List of Figures

List of Schemes

List of Tables

List of Abbreviations

°	degree
°C	degree Celsius
ε	extinction coefficient
Δ	difference
δ	chemical shift, ppm
η^n	hapticity of order n
κ^n	denticity of order n
μ	micro or denotes bridging atom
ν	stretching frequency, cm^{-1}
χ_M	Molar Magnetic Susceptibility
Å	angstrom, 10^{-10} m
acac	acetylacetonate
An	Actinide
av.	average
BDE	bond dissociation energy
bpdc	2,2'-bipyridine-6,6'-dicarboxylic acid
$(Bpin)_2$	Bis(pinacolato)diboron
br	broad
Bu	butyl
calcd.	calculated
$^{13}C\{^1H\}$	Carbon-13 proton decoupled
ca.	circa
CCD	charge-coupled-device
chp	6-chloro-2-hydroxypyridinate
COSY	Homonuclear Correlation Spectroscopy
cot	1,3,5,7-cyclooctatetraene
Cp'	$1,2,4\text{-}^tBu_3C_5H_2$
Cp^*	$\eta^5\text{-}C_5Me_5$
Cp	$\eta^5\text{-}C_5H_5$

cm^{-1}	wavenumber
12-crown-4	1,4,7,10-tetraoxacyclododecane
18-crown-6	1,4,7,10,13,16-hexaoxacyclooctadecane
2,2,2-cryptand	4,7,13,16,21,24-hexaoxa-1,10-diazabicyclo[8.8.8]hexacosane
CSM	Continuous Shape Measure
CV	cyclic voltammetry
Cy	Cyclohexyl
cyclam	1,4,8,11-tetraazacyclotetradecane
d	doublet *or* day(s)
d_n	deuterated in *n* positions
DFT	Density Functional Theory
Dipp	2,6-diisopropylphenyl
DME	1,2-dimethoxyethane
DMF	Dimethylformamide
DMSO	Dimethylsulfoxide
DOTA	1,4,7,10-tetraazacyclododecane-N,N′,N″,N‴-tetraacetic acid
$E_{1/2}$	average wave potential, $(E_{p,a} + E_{p,c})/2$
$E_{p,a}$	anodic half-wave potential
$E_{p,c}$	cathodic half-wave potential
e^-	electron
eq	equation
emu	electromagnetic unit
EPR	Electron Paramagnetic Resonance
equiv	equivalent
Et	ethyl
Et_2O	diethyl ether
Fc	ferrocene
g	gram(s)
GOF	goodness of fit
^1H	Hydrogen-1
h	hour(s)

H_2(1,8-DMC),	1,8-dimethyl-1,4,8,11-tetraazacyclotetradecane
H_2NTClPP	5,10,15,20-tetrakis[(4-*tert*-butyl)phenyl]porphyri
H_2TBPP	5,10,15,20-tetrakis(4-chlorophenyl)porphyrin
$^{H}N_4$	2,11-diaza[3,3(2,6) pyridinophane
HOMO	Highest Occupied Molecular Orbital
HYSCORE	Hyperfine Sub-level Correlation Spectroscopy
Hz	Hertz
$i_{p,a}$	anodic half-wave current
$i_{p,c}$	cathodic half-wave current
^{i}Pr	isopropyl
IR	infrared
ITI	Inverse Trans Influence
J	NMR coupling constant
J	Joule
K	Kelvin
K_f	Formation Constant
L	liter *or* ligand
LED	Light Emitting Diode
^{7}Li{^{1}H}	Lithium-7 proton decoupled
Ln	lanthanide
M	Molar *or* Mega
m	meter *or* multiplet *or* medium
m	meta
Me	methyl
MeCN	Acetonitrile
$^{Me}N_4$	*N*,*N*-dimethyl-2,11-diaza[3,3(2,6) pyridinophane
min	minute(s)
mL	milliliter(s)
mmol	millimole(s)
MO	Molecular Orbital
mol	mole(s)

NBO	natural bond order
^{n}Bu	n-butyl
NHE	Normal Hydrogen Electrode
NIR	near infrared
NLMO	Natural Localized Molecular Orbital
NMR	nuclear magnetic resonance
Np	neopentoxide
o	ortho
OEP	octaethylporphyrin
omtaaH_2	dibenzooctamethyltetraazaannulene
ORTEP	Oak Ridge Thermal Ellipsoid Program
OTf	trifluoromethylsulfonate
p	para
Ph	phenyl
phen	phenanthroline
pip	piperidine
Pn*	Permethylpentalene
ppm	parts per million
py	pyridine
q	quartet
QTAIM	Quantum Theory of Atoms-in-Molecules
redox	reduction-oxidation
RT	room temperature
s	singlet *or* strong *or* second(s)
sh	shoulder
^{29}Si{^{1}H}	Silicon-29 proton decoupled
SQUID	Superconducting Quantum Interference Device
T	Tesla
t	triplet
^{t}Bu	*tert*-butyl
THF	tetrahydrofuran

TIP	Temperature Independent Paramagnetism
TMEDA	*N,N,N',N'*-tetramethylethylenediamine
TMP	2,2,6,6-tetramethylpiperidinate
tmtaaH_2	dibenzotetramethyltetraaza[14]annulene
tol	toluene
trop	tropolonate
UV	ultraviolet
V	Volt
vis	visible
vs	very strong *or* versus
vw	very weak
w	weak
WBI	Wiberg Bond Index
WFT	Multi-configurational Wavefunction Theory
XAS	X-ray Absorption Spectroscopy
XPS	X-ray Photoelectron Spectroscopy

Chapter 1. Introduction

1.1 Covalency in Lanthanide-Ligand Bonding

In contrast to their transition metal analogues, lanthanide ligand bonding interactions were traditionally thought to be predominantly ionic due to the energy mismatch between the 4f and 5d valence orbitals of highly electropositive lanthanides and the frontier orbitals of highly electronegative co-ligands that are commonly employed in such systems.[1–3] The 4f orbitals also have limited radial extension which renders them core-like, and prevents interactions with ligand-based orbitals. The earliest reports of lanthanide covalency were theoretical studies that found that the electrostatic model of ligand field theory did not adequately represent the electronic structure and thermodynamic properties of some lanthanide compounds.[4–6] These studies instead suggested that a covalent model that involved metal-based orbitals would be more appropriate. Indeed, it was suggested that covalent bonding may be necessary to account for the thermochemical atomization energies of the lanthanide trihalides[5] and the dissociation energies of gas phase lanthanide chalcogenides.[6]

Some of the earliest experimental evidence for lanthanide covalency appeared from an X-ray photoelectron spectroscopy study of σ and π-bonded organogadolinium compounds.[7] This study surprisingly found the presence of electron "shakeup" satellite peaks in the XPS spectra of the series [Cp_xGdR_y] (R = Cl, CH_3, C≡CPh; x = 0, 1, 2, 3; y = 0, 1, 2, 3). These peaks were believed to be a result of the transition of a valence band electron into an empty 4f orbital. As such, their presence was indicative of orbital overlap between Gd 4f orbitals and the appropriate σ and π bonding orbitals on the ligands. Further support for lanthanide covalency emerged from electronic absorption spectroscopy studies of selected lanthanide complexes.[8,9] The shielding of the 4f orbitals was originally thought to virtually eliminate any ligand field effects on the energies and intensities of the f-f transitions of lanthanide compounds. However,

these studies found a notable correlation between ligand basicity and the oscillator strengths, band energies and sensitivities of the f-f transitions in the absorption spectra of a series of lanthanide chelates and trihalides. This correlation was believed to be due to accompanying variations in the degree of metal ligand bond covalency. Covalent effects in lanthanide ligand bonding were also observed in studies of complexation of lanthanide β-diketonates by a series of nitrogen donor bases in $CDCl_3$.[10] These reactions were analyzed by empirically derived parameters originally developed by Drago *et al*. (E_B and C_B) to correlate the complexation free energies with the electrostatic (E_B) and covalent (C_B) components of the metal ligand interactions.[11] This analysis obtained a linear fit for $\log\beta_1$ and C_B with good correlation (R^2 = 0.996), while no correlation was found using E_B (R^2 = 0.34). These results were also rationalized by enhanced covalency in the Ln-N_{base} interactions.

Since these seminal studies, the advent of more sophisticated computational and spectroscopic techniques has allowed for a more rigorous analysis of the extent of covalency in lanthanides. For example, Denning and coworkers have presented quantitative evidence for 4f covalency in [$YbCp_3$] using pulsed EPR experiments and DFT calculations.[12] Specifically, it was suggested that the electronic ground state of [$YbCp_3$] can be represented by an admixture of an ionic configuration Yb(III):$4f^{13}(Cp_3)$ and a charge transfer configuration Yb(II):$4f^{14}(Cp_3)^{-1}$. The relative weight of the latter configuration (c_1^2) – a measure for covalency – was determined to be significant through various methods. For instance, HYSCORE experiments on [$YbCp_3$] revealed augmentation of the spin density on the cyclopentadienyl carbon atoms, a direct effect of the aforementioned charge transfer configuration. This effect was quantified by a c_1^2 value of 0.126 ± 0.009. Conversely, a reduction in spin density on the Yb center was determined from analysis of ^{171}Yb hyperfine

interactions, which was quantified by a corresponding c_1^2 value of 0.17 ± 0.03. DFT calculations performed to evaluate the electronic structure of [$YbCp_3$] were also consistent with 4f orbital covalency. Indeed, the MO diagram obtained for [$YbCp_3$] in C_{3h} symmetry revealed overlap between the a'(f_{3c}) orbitals on the Yb and the a' HOMO centered on the Cp ligands, which is representative of a charge-transfer electronic configuration (Figure 1.1). This type of covalency in [$YbCp_3$] was attributed to the energy near-degeneracy of the Yb 4f orbitals and the Cp-π orbitals that manifests as a result of the strong donor ability of Cp ligand and the relatively less negative reduction potential of [$YbCp_3$] (-1.92 V vs Fc/Fc^+).[13]

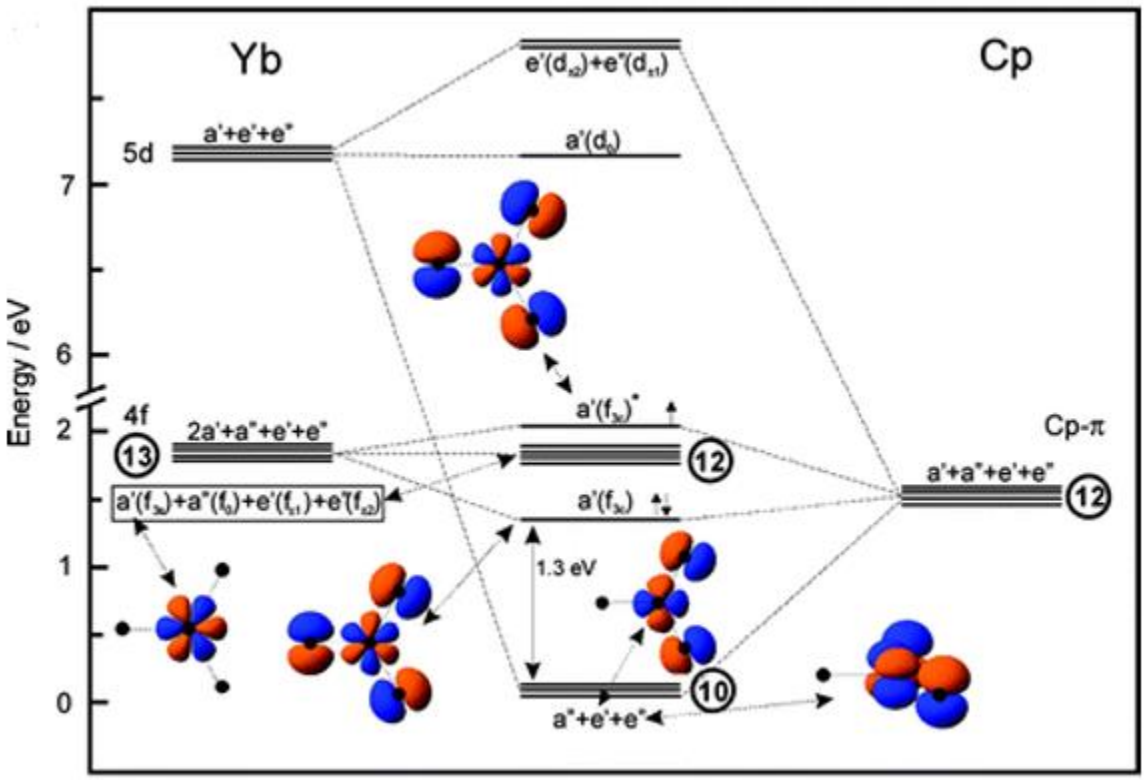

Figure 1.1. Schematic of the MO diagram for [$YbCp_3$] (taken from Ref[12])

Quantitative evidence for lanthanide ligand orbital mixing has also emerged from X-ray Absorption Spectroscopy studies in recent years. For example, L_3-edge XAS was used to

quantify Ln 4f and O 2p mixing in the tetravalent lanthanide oxides CeO_2, PrO_2 and TbO_2.[14–16] The ground states of these compounds can be described by superposition of $4f^n5d^0$ and $4f^{n+1}\underline{L}5d^0$ configurations, where $\underline{L}$ represents an O 2p hole resulting from O2p→4f charge transfer. Accordingly, the L_3-edge XAS spectra of all three lanthanide oxides exhibited a doublet feature, consistent with the two-configuration description (Figure 1.2). The relative weight of the charge transfer configuration can be determined from the ratio of the respective peak areas, and provides a direct measure for Ln 4f and O2p orbital mixing. Measured in this manner, the amount of covalent character in the Ln-O bonds of CeO_2, PrO_2 and TbO_2 was determined to be 28, 32 and 21 %, respectively.[14] The relatively high degree of covalency in these tetravalent lanthanide oxides was ascribed to the substantial multiple bond character in the Ln-O interactions.

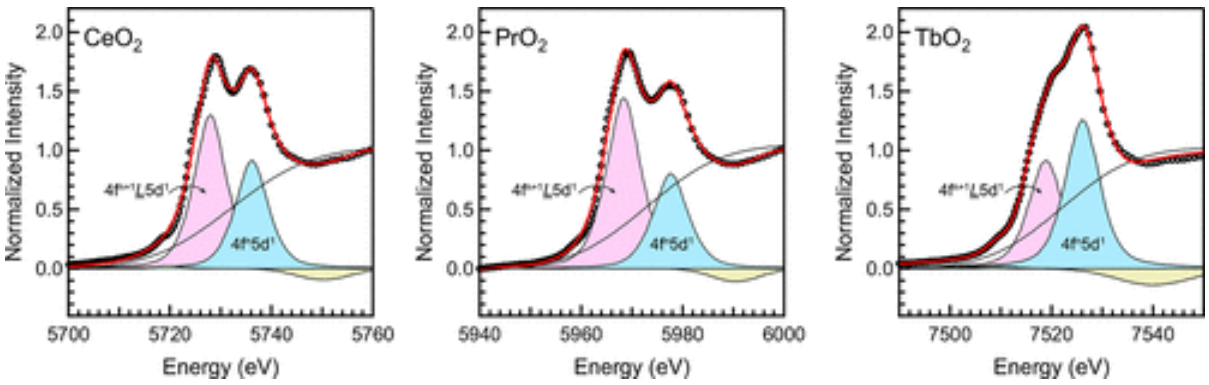

Figure 1.2. Ln L_3-edge XAS spectra for CeO_2, PrO_2 and TbO_2 (taken from Ref[14])

X-ray Absorption Spectroscopy studies have also revealed that the extent of covalency in lanthanides can be heavily dependent on the Ln oxidation state. Kozimor and co-workers have utilized ligand K-edge XAS to excellently depict this dependence.[17] This technique can be used to quantify the intensity of bound-state transitions between ligand 1s orbitals and metal-based unoccupied orbitals with partial ligand p character. Since the 1s orbitals are localized on the

ligand, the intensities of these transitions are primarily governed by the amount of ligand p character in the final state, which in turn serves as a measure of lanthanide ligand orbital mixing. Interestingly, Kozimor *et al*. found the Cl K-edge XAS spectra for the octahedral hexachlorocerate anions $[CeCl_6]^{2-}$ (formally Ce^{IV}) and $[CeCl_6]^{3-}$ (formally Ce^{III}) to be quite different. The spectrum for $[CeCl_6]^{2-}$ exhibited a pre-edge feature at low energy that arises from transitions into t_1u and t_2u symmetric Ce 4f orbitals with partial Cl 3p character, while no such transition was observed for $[CeCl_6]^{3-}$ (Figure 1.3). The amount of Cl 3p character in the unoccupied 4f orbitals of $[CeCl_6]^{2-}$ was determined to be 9.9(9)% using the corresponding pre-edge peak intensity.[17] The "turning on" of such f orbital mixing for $[CeCl_6]^{2-}$ was rationalized by the energy near-degeneracy of Ce 4f and Cl 3p orbitals that is promoted by the higher Ce oxidation state.

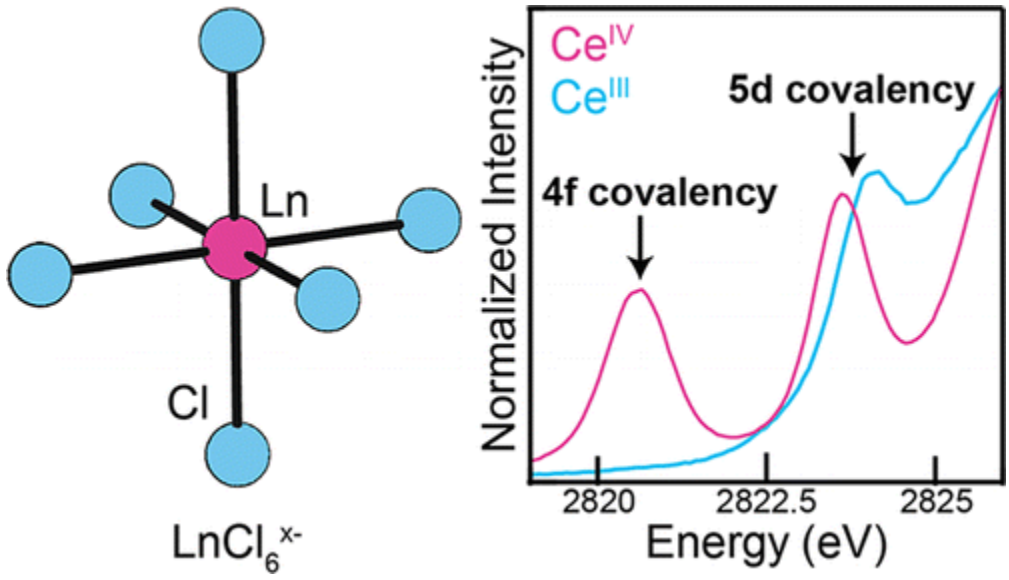

Figure 1.3. Cl K-edge XAS spectra for $[CeCl_6]^{2-}$and $[CeCl_6]^{3-}$ (taken from Ref[17])

1.2 Lanthanide-Ligand Multiple Bonds

The concepts of covalency and metal-ligand multiple bonding in the lanthanides are closely tied to one another. For example, Clark and co-workers have shown that the metallocene Ce(IV) complexes Cp_2CeZ (Z = O, NH, CH^-) exhibit rather covalent Ce-Z interactions that also possess significant multiple bond character.[18] Indeed, DFT calculations revealed the Ce-Z bonds in all cases to be composed of one σ and two π interactions, suggestive of a triple bond (Figure 1.4). The atomic orbital compositions in these interactions reached up to 39.4% for Ce 5d and 31.8% for Ce 4f orbitals. In addition, both NBO and Mulliken charge analyses found the effective charge on the cerium to be only slightly higher than +2 for all three compounds, which is substantially reduced from the theoretical ionic value of +4. These results allude to the significant covalent character in the Ce-Z bonds that arises due to an efficient charge transfer from the Z ligand to the Ce center. This charge transfer presumably results in a simultaneous rise in energy and spatial expansion of the cerium 4f orbitals. The better energy match and greater overlap between Ce 4f and Z donor orbitals subsequently allows for a stronger Ce-Z interaction.

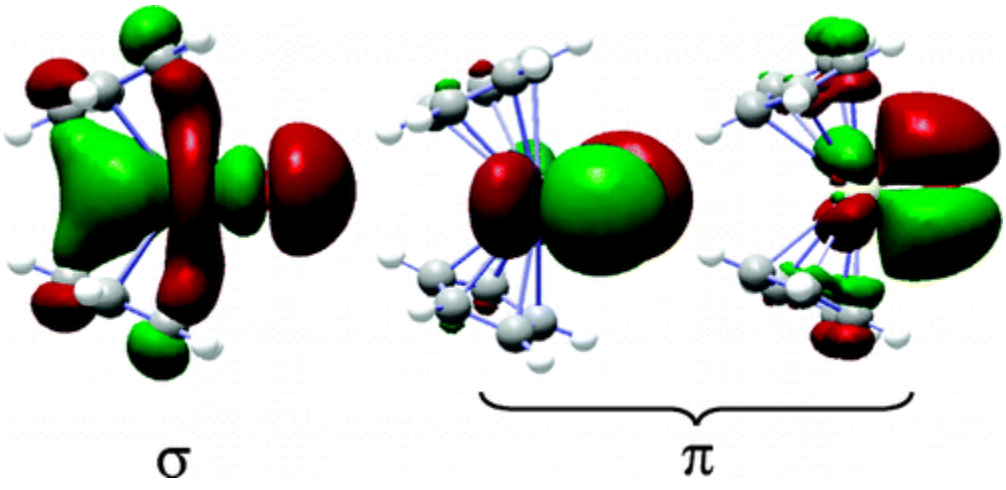

Figure 1.4. σ and π NLMOs for $[Cp_2CeCH]^-$ (taken from Ref[18])

The likelihood of prevalence of covalent character in lanthanide ligand multiple bonds makes them attractive synthetic targets for deeper evaluation of the role of the 4f orbitals in lanthanide ligand bonding. However, the propensity of lanthanides to achieve high coordination numbers and the strong nucleophilicity of the multiply bonded functional group often result in oligomerization, which breaks the lanthanide ligand π bonds. For example, Lappert and co-workers have demonstrated that reaction of $Ce(NR_2)_3$ (R = $SiMe_3$) with O_2 in hexanes at -27 °C affords $[(R_2N)_2Ce(\mu\text{-}O)]_2$, which is formed via dimerization of unsaturated and nucleophilic $[(R_2N)_2Ce{=}O)]$ units (Scheme 1.1).[19] Likewise, reaction of the bulkier cerium amide $Ce(NR'_2)_3$ (R' = $NC(Me)_2(CH_2)_3CMe_2$) with O_2 in toluene at -27 °C affords tetrameric $[(R'_2N)_2Ce(\mu\text{-}O)]_4$ via a similar mechanism.[19] The Ce-O distances in these cyclocer(IV)oxanes were consistent with Ce-O single bonds, indicating the absence of any π bonding.

Scheme 1.1. Products of oligomerization of $[(R_2N)_2Ce{=}O)]$ and $[(R'_2N)_2Ce{=}O)]$[19]

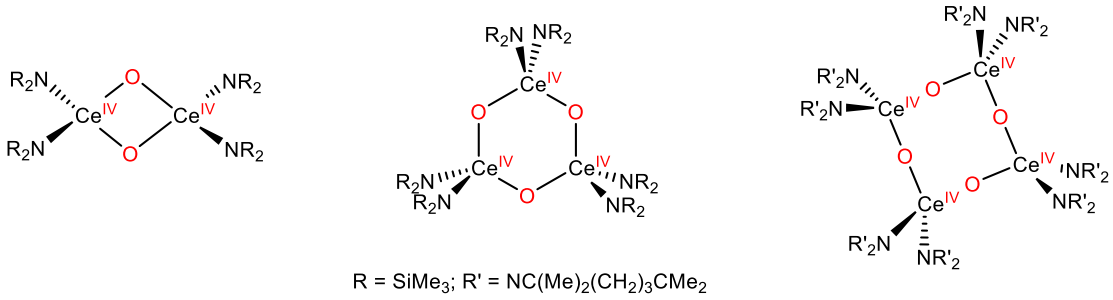

R = $SiMe_3$; R' = $NC(Me)_2(CH_2)_3CMe_2$

Despite the aforementioned unsuccessful attempts in synthesizing lanthanide complexes containing metal-ligand multiple bonds, the past ten years has seen significant progress towards this end. These successes were made possible by careful choices of reaction conditions and supporting co-ligands. For example, addition of stochiometric amounts of MNR_2 (M = Na, K; R = $SiMe_3$) to the aforementioned reaction of $Ce(NR_2)_3$ with O_2 in hexanes at -27 °C affords the alkali capped Ce(IV) oxos $[M]_2[Ce(\mu\text{-}O)(NR_2)_3]_2$ (**I**) in modest yields (Scheme 1.2).[19] In

this reaction, the introduction of MNR_2 saturates the coordination sphere of the cerium in the $[(R_2N)_2Ce{=}O)]$ units, which prevents their oligomerization to cycloceroxanes. Significant progress has also been made towards the use of tailored supporting ligands to stabilize Ce=O multiple bonds. For example, Leung and co-workers recently reported the synthesis of a Ce(IV) oxo complex ligated by the tripodal Kläui ligand, $[(L_{OEt})_2Ce(O)(H_2O)]\cdot MeC(O)NH_2$ (**II**, L_{OEt} = $CpCo\{P(O)(OEt)_2\}_3$, Scheme 1.2).[20] Additionally, Hayton and co-workers reported the synthesis of the cerium(IV) oxo complex supported by the TREN ligand, [Li(12-crown-4)][$(NN'_3)Ce(O)$] (**III**, NN'_3 = $N(CH_2CH_2NR)_3$, R = Si^tBuMe_2), which was synthesized by thermal decomposition of a Ce(III) nitrate precursor [Li(12-crown-4)][$(NN'_3)Ce(\kappa^2\text{-}O_2NO)$].[21] More recently, Schelter and co-workers reported the synthesis of a Ce(IV) oxo supported by the tripodal TriNOx ligand, $[(TriNOx)\{Ce(O)\}Rb]_4$ (**IV**).[22] Examples of lanthanide complexes bearing Ln=C and Ln=N multiple bonds have also appeared in the literature in recent years. For example, Liddle and co-workers recently reported the synthesis of the first Ce(IV) carbene complex, $[Ce(BIMP^{TMS})(ODipp)_2]$ (Dipp = 2,6-diisopropylphenyl), employing an NCN-type pincer ligand.[23] In addition, Anwander and co-workers have recently described the synthesis of the first terminal lanthanide imido complex, $[(Tp^{tBu,Me})Lu{=}N(3,5\text{-}(CF_3)_2C_6H_3)(DMAP)]$, via Lewis base-induced methane elimination.[24] Similarly, Schelter and co-workers reported the synthesis of a series of Ce(IV) imido complexes, $[ML_n][Ce{=}N(3,5\text{-}(CF_3)_2C_6H_3)(TriNOx)]$ (TriNOx = $N(o\text{-}CH_2C_6H_4N(^tBu)O)_3$; ML_n = Li(THF)(Et_2O), Li(TMEDA), $K(DME)_2$, $Rb(DME)_2$, $Cs(DME)_2$), which were formed via deprotonation of their anilide precursors.[22] This series of cerium imidos exhibited interesting reactivity (see below), which included Si-O and C-O activation.

Scheme 1.2. Selected complexes bearing lanthanide-oxygen multiple bonds[19–22]

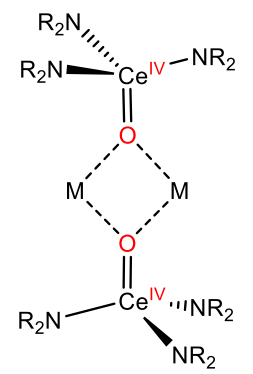

M = Na, K; R = $SiMe_3$

I

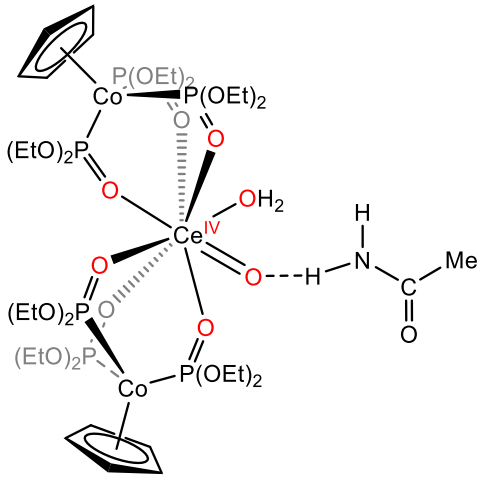

II

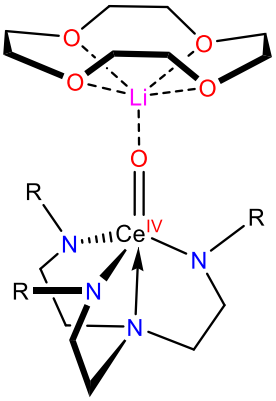

R = Si^tBuMe_2

III

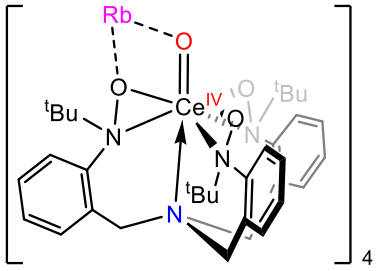

IV

The metal ligand multiple bonds in the aforementioned lanthanide complexes have been shown to exhibit appreciable covalent character according to DFT analyses. For example, NBO analysis of the Ce-C bond in [Ce($BIMP^{TMS}$)$(ODipp)_2$] found one σ interaction with 13% cerium character and one π interaction with 12% cerium character, suggestive of a two-fold multiple bond.[23] Even more surprising was the dominant 4f (as opposed to 5d) character of the cerium component in the σ and π interactions (76 and 80%, respectively). Efficient ligand electron density transfer to cerium was also demonstrated by the calculated atomic charges of

+1.91 and -1.47 for the cerium and carbon atoms, respectively. Similar type of covalency was observed in the series of Ce(IV) imido complexes, $[ML_n][Ce{=}N(3,5\text{-}(CF_3)_2C_6H_3)(TriNOx)]$. In particular, NBO analysis also found two bonding Ce-N interactions featuring σ and π symmetry with corresponding Ce atomic orbital compositions of 10-14% and 17-20%, respectively.[22] A slightly different bonding picture was observed for the Ce(IV) oxo [Li(12-crown-4)][(NN′$_3$)Ce(O)], where NBO analysis finds the Ce-O interaction to be a σ + 2π triple bond with an average cerium atomic orbital composition of ~15%.[21] Quantum theory of atoms-in-molecules (QTAIM) analysis also revealed the M-O bond order in this complex to be greater than that in the analogous Th(IV) oxo complex, suggestive a stronger covalent character in the Ce-O bond.[21]

Scheme 1.3. Reactivity of lanthanide-ligand multiple bonds[20,22]

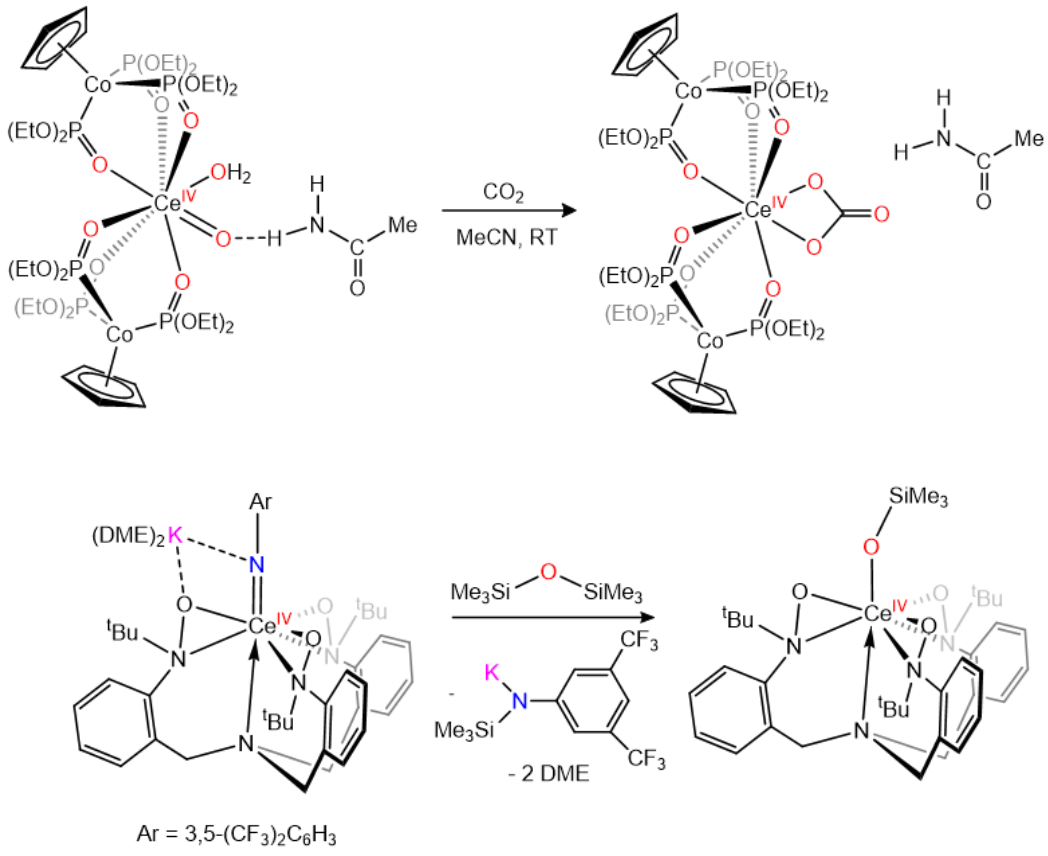

The lanthanide complexes mentioned above have found interesting applications in mediating difficult transformations such as small molecule activation. For example, Leung's Ce(IV) oxo complex $[(L_{OEt})_2Ce(O)(H_2O)]\cdot MeC(O)NH_2$ reacts with CO_2 and CO at room tempetaure to form the cerium carbonates $[(L_{OEt})_2Ce(CO_3)]\cdot$and $[(L_{OEt})_2Ce(\mu\text{-}CO_3)Ce(H_2O)(L_{OEt})_2]$, respectively (Scheme 1.3).[20] Additionally, Schelter's Ce(IV) imido $[K(DME)_2][Ce{=}N(3,5\text{-}(CF_3)_2C_6H_3)(TriNOx)]$ is capable of cleaving the strong Si-O bond in hexamethyldisilyloxane to generate the Ce(IV) silyloxide $[Ce(OSiMe_3)(TriNOx)]$ and $[K][N(SiMe_3)(3,5\text{-}(CF_3)_2C_6H_3)]$.[22] Similarly, reaction of $[Rb(DME)_2][Ce{=}N(3,5\text{-}(CF_3)_2C_6H_3)(TriNOx)]$ with benzophenone results in C-O cleavage to form the Ce(IV) oxo $[(TriNOx)\{Ce(O)\}Rb]_4$ and $[Ph_2C{=}N(3,5\text{-}(CF_3)_2C_6H_3)]$.[22] This reaction represented the first transformation of a Ce=N double bond to a Ce=O double bond. Overall, these reactivity studies reflect the rather strong nucleophilic character of the metal ligand multiple bonds in these rare lanthanide complexes.

1.3 High Valent Lanthanides

Generally, a greater degree of covalency in the lanthanides is expected with increasing lanthanide oxidation state.[14,17,25–29] This, however, poses a problem from a synthetic perspective, as all lanthanides have strong preference for trivalent oxidation state in solution. The paucity of higher oxidation states in the lanthanides can be explained by their ionization energy profile and their Ln(III/IV) redox potentials. In particular, the 4th ionization energies of all lanthanides are greater than the sum of their 1st, 2nd and 3rd ionization energies.[30] Similarly, the Ln(III/IV) redox potentials of all lanthanides exceed +3.1 V except for cerium, which has a Ce(III/IV) redox potential of 1.7 V in aqueous solutions.[31] This redox potential can be significantly lowered in non-aqueous systems by ligation to strong σ and π donor ligands and

can reach up to E_{pc} = -2.08 V vs NHE.[29,32] The unique stability of tetravalent cerium can be explained by its closed shell noble gas electronic configuration. Accordingly, the solution chemistry of Ce(IV) has seen significant progress, while that of the remaining lanthanide series is virtually non-existent. Indeed, tetravalent lanthanides other than Ce(IV) have historically only been encountered in solid-state fluoride and oxide materials containing Tb(IV), Pr(IV), Nd(IV) and Dy(IV).[14,27,28,33–38] Inspired by this scarcity, and the opportunity to further probe covalency and unravel new redox chemistry, access to tetravalent oxidation states in the later lanthanides has gained significant research interest in recent years. The most attention has been given to stabilizing Tb(IV), Pr(IV), Nd(IV) and Dy(IV) complexes in solution, as these ions have the lowest fourth ionization energies[30] and the lowest Ln(IV/III) reduction potentials[31] amongst the lanthanide series. These efforts have recently culminated in isolation and full characterization of the first examples of molecular Tb(IV) and Pr(IV) complexes that are stable both in solution and in the solid state,[29,39–42] as well as the gas phase and solid noble-gas matrix observation of a Pr(V) ion.[43]

According to its Ln(IV/III) redox potential (3.1 V vs NHE),[31] Tb(IV) is the next most readily accessible tetravalent ion after Ce(IV). However, until recently, examples of tetravalent terbium were confined to those (electro)chemically generated *in-situ* in alkaline carbonate and tetrametaphosphate solutions,[44,45] and those observed in a handful solid state metal oxides and fluorides.[14,27,28,33,36,38,46] Few attempts to generate Tb(IV) from molecular Tb(III) carbene, nitroxide and alkyl precursors have also been unsuccessful, resulting in either cation exchange or ligand oxidation.[47–49] Nonetheless, the first example of a molecular Tb(IV) complex that is stable in solution was reported by Mazzanti and coworkers in 2019.[39] In this report, the $4f^7$ Tb(IV) complex [Tb(OSi(O^{t}Bu)$_3$)$_3$(κ^2-OSi(O^{t}Bu)$_3$)] was prepared by oxidation of the Tb(III)

analogue [KTb(O(Si(O^{t}Bu)$_3$)$_4$] with [N(C$_6$H$_4$Br)$_3$][SbCl$_6$] in MeCN or THF (Scheme 1.4). This material was characterized by various techniques which unambiguously confirmed the tetravalent oxidation state of the terbium center. For example, the UV-Vis spectrum of [Tb(OSi(O^{t}Bu)$_3$)$_3$(κ^2-OSi(O^{t}Bu)$_3$)] in toluene revealed a broad absorption at 371 nm (ε = 4200 M^{-1}cm^{-1}), similar to that observed for (electro)chemically generated aqueous carbonate and tetrametaphosphate solutions of Tb(IV) (365 nm).[44,45] In addition, the X-band EPR spectrum of [Tb(OSi(O^{t}Bu)$_3$)$_3$(κ^2-OSi(O^{t}Bu)$_3$)] at 20 K exhibited strong features at g = 8.9, g = 7.7 and g = 5.0, which were consistent with those reported for fluoride phosphate glasses and silicates containing Tb(IV).[50,51] Similar strong features were also observed in the EPR spectrum of the isoelectronic 4f^7 Gd(III) silyloxide [KGd(O(Si(O^{t}Bu)$_3$)$_4$]. Furthermore, temperature-dependent magnetic susceptibility measurements on [Tb(OSi(O^{t}Bu)$_3$)$_3$(κ^2-OSi(O^{t}Bu)$_3$)] revealed a χ_MT value of 7.77 emu·K/mol, which is nearly identical to the 7.78 emu·K/mol obtained for [KGd(O(Si(O^{t}Bu)$_3$)$_4$]. This value is also in agreement with the χ_MT value predicted for a 4f^7 ion by first approximation *LS* coupling (7.88 emu·K/mol). Finally, cyclic voltammetry experiments on [Tb(OSi(O^{t}Bu)$_3$)$_3$(κ^2-OSi(O^{t}Bu)$_3$)] revealed an irreversible reduction feature at E_{pc} = 0.10 V vs NHE and a related oxidation feature at E_{pa} = 1.65 V vs NHE. The potential for the oxidation feature is consistent with that applied to generate Tb(IV) ions in alkaline carbonate solutions (1.3 V vs NHE).[45] This potential is also similar to that reported for Ce(IV) in aqueous solutions (1.7 V vs NHE), and is significantly lower than the standard reduction potential for Tb(IV) (3.1 V vs NHE).[31] These data combined indicate strong stabilization of the +4 state in [Tb(OSi(O^{t}Bu)$_3$)$_3$(κ^2-OSi(O^{t}Bu)$_3$)], likely due to the strongly donating nature of the silyloxide ligand.

Scheme 1.4. Synthesis of $[Tb(OSi(O^tBu)_3)_3(\kappa^2\text{-}OSi(O^tBu)_3)]$[39]

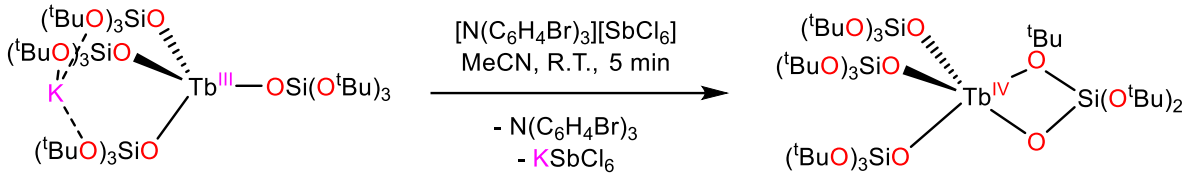

Also in 2019, La Pierre *et al*. independently reported another molecular Tb(IV) complex that is stable both in solution and the solid state by making use of an imidophosphorane ligand incorporating a bulky chelating diamide group.[40] Ligands of this type had previously been shown to significantly stabilize tetravalent oxidation states in the lanthanides by promoting strong covalent character in the metal ligand bonds through both symmetry and energy allowed orbital mixing.[25] Accordingly, La Pierre *et al*. showed that the Tb(III) imidophosphorane $[K(Et_2O)][Tb(NP(1,2\text{-bis-}^tBu\text{-diamidoethane})(NEt_2))_4]$ can be rapidly oxidized (<10 min) with AgI at room temperature to afford the corresponding S_4 symmetric Tb(IV) imidophosphorane $[Tb(NP(1,2\text{-bis-}^tBu\text{-diamidoethane})(NEt_2))_4]$ in good yield (Scheme 1.5).[40] Previous attempts by Mazzanti and co-workers to synthesize $[Tb(OSi(O^tBu)_3)_3(\kappa^2\text{-}OSi(O^tBu)_3)]$ by oxidation of $[KTb(O(Si(O^tBu)_3)_4]$ with AgI had resulted in no reaction.[39] The facile oxidation of Tb(III) by the mild oxidant AgI in La Pierre's case was ascribed to the unique electronic and steric effects of the imidophosphorane ligand framework. Specifically, the incorporated chelating diamide group enforces planarity at the chelating amide nitrogen atoms which aligns their lone pairs with the σ* orbital of the P-N_{imide} bond, rendering the ligand more σ basic. Additionally, the chelating diamide sterically enforces a zwitterionic resonance structure which increases the π basic character of the ligand. Ultimately, both of these effects result in minimal structural reorganization during oxidation of the Tb(III) imidophosphorane precursor, thus requiring only mild reaction conditions for the synthesis of $[Tb(NP(1,2\text{-bis-}^tBu\text{-diamidoethane})(NEt_2))_4]$.

Scheme 1.5. Synthesis of [Tb(NP(1,2-bis-^{t}Bu-diamidoethane)(NEt$_2$))$_4$][40]

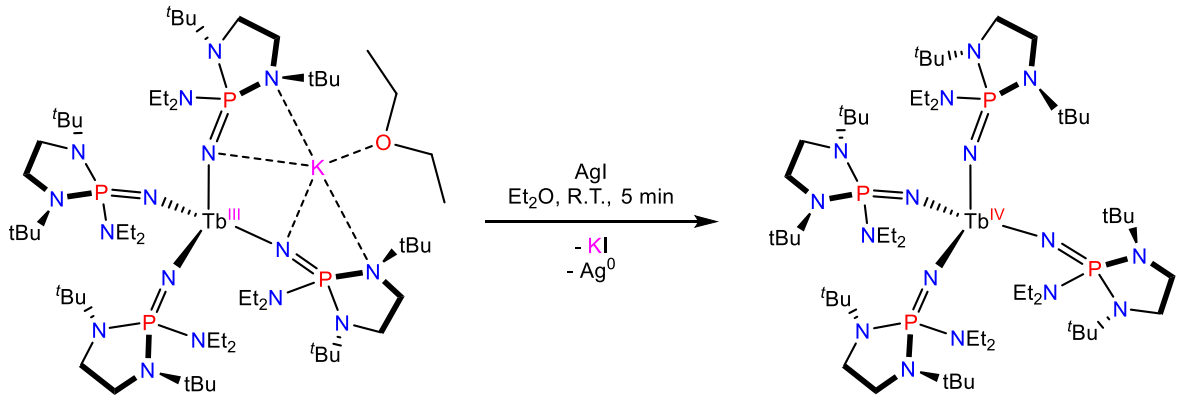

The significant stability of La Pierre's Tb(IV) imidophosphorane complex allowed for direct confirmation of the terbium oxidation state via L_3-edge X-ray Absorption Spectroscopy. Particularly, the L_3-edge XAS spectrum of [Tb(NP(1,2-bis-^{t}Bu-diamidoethane)(NEt$_2$))$_4$] exhibited a double-peak white line structure that is diagnostic of those obtained for other formally Ln(IV) complexes (Figure 1.5).[14,17,27,28] This feature corresponds to transitions arising from $4f^n5d^0$ and $4f^{n+1}\underline{L}5d^0$ configurations, where $\underline{L}$ represents a hole on the ligand. Fitting of the spectrum with Voigt and step-like functions allowed estimation of the relative amount of the $4f^{n+1}\underline{L}5d^0$ character in the ground state via a weighted ratio of the area under the two peaks. This analysis gave a value of 0.39(4) for the charge-transfer configuration component, which is similar to the 0.42(3) observed for TbO_2.[14] The L_3-edge XAS feature energies for the aforementioned Tb(IV) and Tb(III) imidophosphorane complexes also support the assignment of their respective terbium oxidation states. In particular, the inflection point and the two peak maxima of the doublet feature for [Tb(NP(1,2-bis-^{t}Bu-diamidoethane)(NEt$_2$))$_4$] were shifted to higher energy when compared to the feature observed for [K(Et$_2$O)][Tb(NP(1,2-bis-^{t}Bu-diamidoethane)(NEt$_2$))$_4$], consistent with the higher Z_{eff} for Tb(IV) vs Tb(III). Overall, the comparison of the L_3-edge XAS spectra for [Tb(NP(1,2-bis-^{t}Bu-diamidoethane)(NEt$_2$))$_4$] with

those of [K(Et_2O)][Tb(NP(1,2-bis-^{t}Bu-diamidoethane)(NEt_2))$_4$] and other formally Ln(IV) complexes unambiguously confirm the tetravalent oxidation state of the Tb in [Tb(NP(1,2-bis-^{t}Bu-diamidoethane)(NEt_2))$_4$].

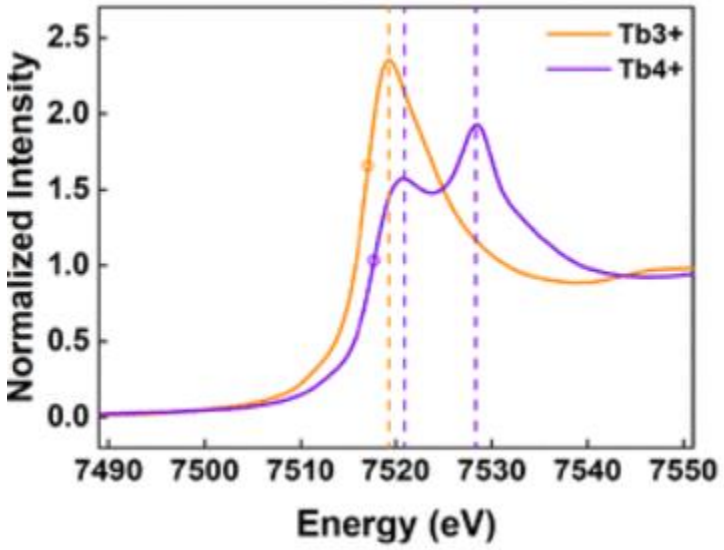

Figure 1.5. Terbium L_3-edge XAS spectra for[K(Et_2O)][Tb(NP(1,2-bis-^{t}Bu-diamidoethane)(NEt_2))$_4$] (orange) and [Tb(NP(1,2-bis-^{t}Bu-diamidoethane)(NEt_2))$_4$] (purple) (taken from Ref[40]).

La Pierre's Tb(IV) imidophosphorane complex was also characterized by electronic absorption spectroscopy, magnetic susceptibility studies and Natural Bond Orbital (NBO) analysis. The UV-Vis-NIR spectrum of [Tb(NP(1,2-bis-^{t}Bu-diamidoethane)(NEt_2))$_4$] in benzene exhibited a broad absorption at 575 nm (ε = 3700 $M^{-1}cm^{-1}$) that is assignable to a Ligand to Ligand Charge Transfer (LLCT) with an appreciable Ligand to Metal Charge Transfer (LMCT) contribution, according to Natural Transition Orbital (NTO) analysis. This feature is redshifted when compared to that observed for Mazzanti's Tb(IV) silyloxide complex [Tb(OSi(O^{t}Bu)$_3$)$_3$(κ^2-OSi(O^{t}Bu)$_3$)] (371 nm, ε = 4200 $M^{-1}cm^{-1}$),[39] which likely reflects the lower ionization potential of N2p orbitals vs O2p orbitals. Variable temperature dc

magnetic susceptibility measurements on [Tb(NP(1,2-bis-^{t}Bu-diamidoethane)(NEt$_2$))$_4$] revealed a room temperature χ_MT value of 8.55 emu·K/mol, which is comparable to the theoretical value for a $^8S_{7/2}$ ion (7.94 emu·K/mol). Finally, NBO analysis on [Tb(NP(1,2-bis-^{t}Bu-diamidoethane)(NEt$_2$))$_4$] found four Tb-N σ and eight Tb-N π bonding interactions with 8.31 and 5.69 % Tb contributions, respectively. The ligand to metal donation was found to be lower in [K(Et$_2$O)][Tb(NP(1,2-bis-^{t}Bu-diamidoethane)(NEt$_2$))$_4$], which also has four Tb-N σ and eight Tb-N π bonding interactions, but with smaller Tb contributions of 5.23 and 2.24% , respectively. The Tb components in all cases were predominantly 5d and 4f in character. All in all, the NBO results support the greater degree of covalency in tetravalent lanthanide-ligand bonds over their trivalent counterparts.

Scheme 1.6. Synthesis of [Pr(OSiPh$_3$)$_4$(MeCN)$_2$][42]

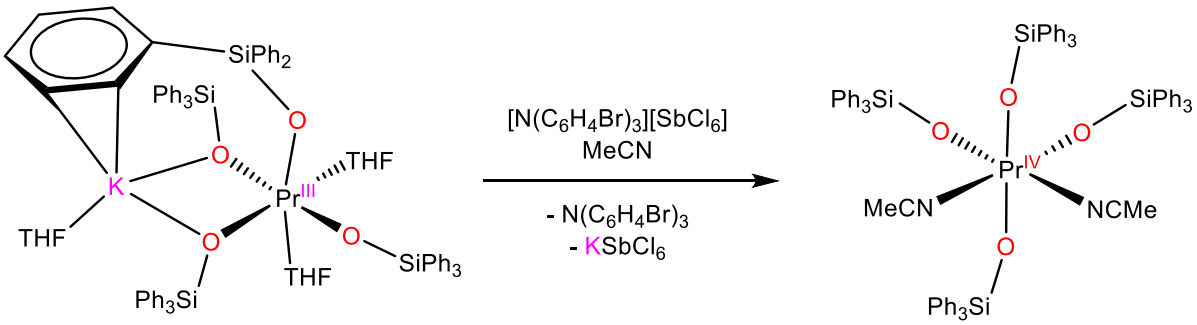

Pr(IV) is the next most easily accessible tetravalent lanthanide ion after Tb(IV), with a Ln(IV/III) reduction potential of 3.2 vs NHE.[31] Until recently, however, Pr(IV) was only observed in extended solid state fluoride and oxide materials,[14,27,33,35,36,52,53] and (electro)chemically generated *in-situ* in alkaline carbonate solutions.[45] There have also been attempts to prepare molecular Pr(IV) complexes by oxidation of a Pr(III) carbene precursor, which only resulted in cation exchange.[48] Nonetheless, Mazzanti and coworkers recently isolated and fully characterized the first example of a molecular Pr(IV) complex

$[Pr(OSiPh_3)_4(MeCN)_2]$.[42] This material was prepared by oxidation of the Pr(III) precursor $[KPr(OSiPh_3)_4(THF)_3]$ with $[N(C_6H_4Br)_3][SbCl_6]$ in MeCN or THF (Scheme 1.6). An isomorphous Tb(IV) analogue, $[Tb(OSiPh_3)_4(MeCN)_2]$, can also be prepared in a similar manner by oxidation of $[KTb(OSiPh_3)_4(THF)]$ with $[N(C_6H_4Br)_3][SbCl_6]$ or $[N(C_6H_4Br)_3][OTf]$ in MeCN.[41] The Ln(IV) ions in both complexes are ligated by two MeCN solvent molecules, suggesting that saturation of the coordination sphere at the Ln center is not a requirement for stabilizing the +4 state. However, the isolation of the Pr(IV) silyloxide complex proved challenging, and required thorough drying of the reaction mixture *in vacuo* followed by addition of fresh solvent prior to workup. In line with these observations, the Pr(IV) silyloxide was much less stable in solution when compared to its Tb(IV) analogue. For example, THF-d_8 solutions of $[Pr(OSiPh_3)_4(MeCN)_2]$ exhibited 30% decomposition after standing at room temperature for 3 h,[42] whereas $[Tb(OSiPh_3)_4(MeCN)_2]$ was found to be stable for several days in THF solutions.[41] $[Pr(OSiPh_3)_3(THF)_3]$.was the only identifiable decomposition product observed in the former monitoring experiment.

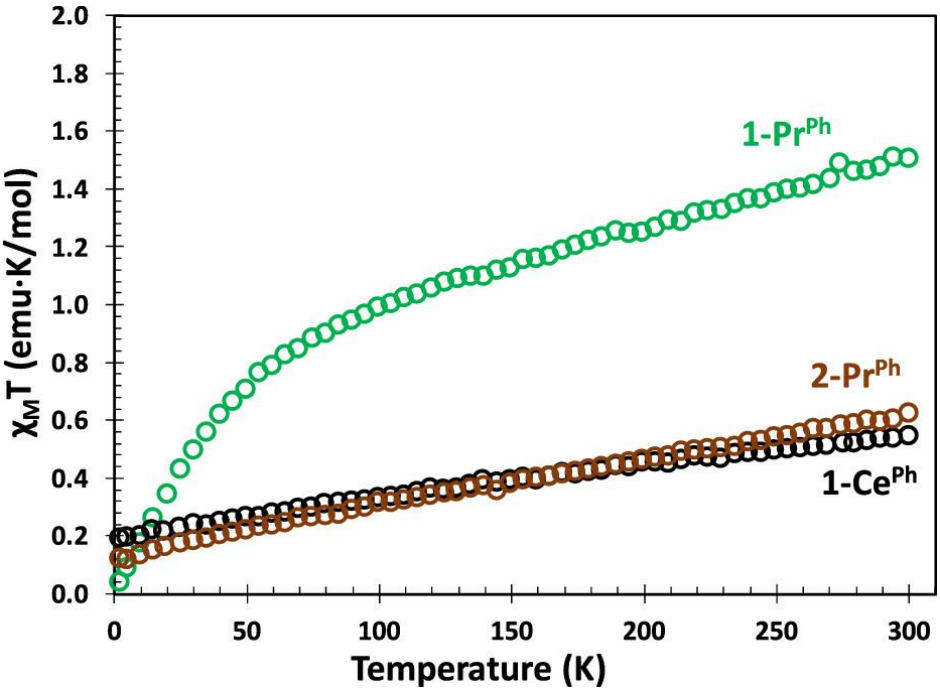

Figure 1.6. Variable-temperature magnetic susceptibility data for $[KCe(O(SiOPh_3)_4(THF)_3]$ (black), $[KPr(OSiPh_3)_4(THF)_3]$ (green), and $[Pr(OSiPh_3)_4(MeCN)_2]$ (brown) collected at 1T (taken from Ref[42]).

The +4 oxidation state of the Pr center in $[Pr(OSiPh_3)_4(MeCN)_2]$ was confirmed via a suite of characterization techniques. For example, the UV-Vis spectrum of $[Pr(OSiPh_3)_4(MeCN)_2]$ in THF exhibited a broad absorption maximum at 363 nm (ε = 3800 $M^{-1}cm^{-1}$), which is comparable to that reported for electrochemically generated solutions of Pr(IV) in alkaline carbonate media (283 nm, $\varepsilon > 1000$ $M^{-1}cm^{-1}$).[45] Additionally, the $\chi_M T$ vs T data measured for $[Pr(OSiPh_3)_4(MeCN)_2]$ matched with those measured for the isoelectronic $4f^1$ Ce(III) ion in $[KCe(O(SiOPh_3)_4(THF)_3]$ between 300 and 2 K (Figure 1.6). The room temperature $\chi_M T$ value for $[Pr(OSiPh_3)_4(MeCN)_2]$ (0.622 emu·K/mol) was also comparable to that obtained for $[KCe(O(SiOPh_3)_4(THF)_3]$ (0.544 emu·K/mol). In addition, these values are in agreement with the theoretical $\chi_M T$ value calculated for a $4f^1$ complex (0.8 emu·K/mol), but much lower than

the experimental (1.5 emu·K/mol) and theoretical (1.6 emu·K/mol) $\chi_M T$ values obtained for the $4f^2$ Pr(III) ion in $[KPr(OSiPh_3)_4(THF)_3]$. The electrochemical properties of $[Pr(OSiPh_3)_4(MeCN)_2]$ were also probed by cyclic voltammetry, which revealed a metal based reduction feature at E_{pc} = -0.38 V vs Fc/Fc^+ and a related oxidation feature at E_{pa} = 0.67 vs Fc/Fc^+ with a peak separation of ΔE = 1.05 V.[42] The oxidation feature appears at a potential 0.18 V more positive than that of $[Tb(OSiPh_3)_4(MeCN)_2]$ (Epa = 0.49 V vs Fc/Fc^+),[41] which is consistent with the difference between their respective standard Ln(IV/III) reduction potentials (0.1 V).[31] Finally, DFT calculations on $[KPr(OSiPh_3)_4(THF)_3]$ and $[Pr(OSiPh_3)_4(MeCN)_2]$ found unpaired spin densities of 2.03 and 1.1, respectively, which are consistent with $4f^2$ Pr(III) and $4f^1$ Pr(IV) complexes. Both spin densities were found to be located at the Pr center, ruling out the possibility of ligand radical character in the complexes (Figure 1.7). Curiously, NBO analysis on $[Pr(OSiPh_3)_4(MeCN)_2]$ found a Pr-O Wiberg bond index (WBI) of 0.85,[42] which is higher than the Tb-O WBIs for $[Tb(OSiPh_3)_4(MeCN)_2]$ (0.60-0.65),[41] suggesting a more covalent M-O bond for Pr(IV) vs Tb(IV). This WBI is also higher than those calculated for $[KPr(OSiPh_3)_4(THF)_3]$ (0.41-0.52),[42] consistent with a greater degree of covalency with increasing oxidation state. On the whole, all the characterization data mentioned above conclusively confirm the Pr^{4+} oxidation state in $[Pr(OSiPh_3)_4(MeCN)_2]$.

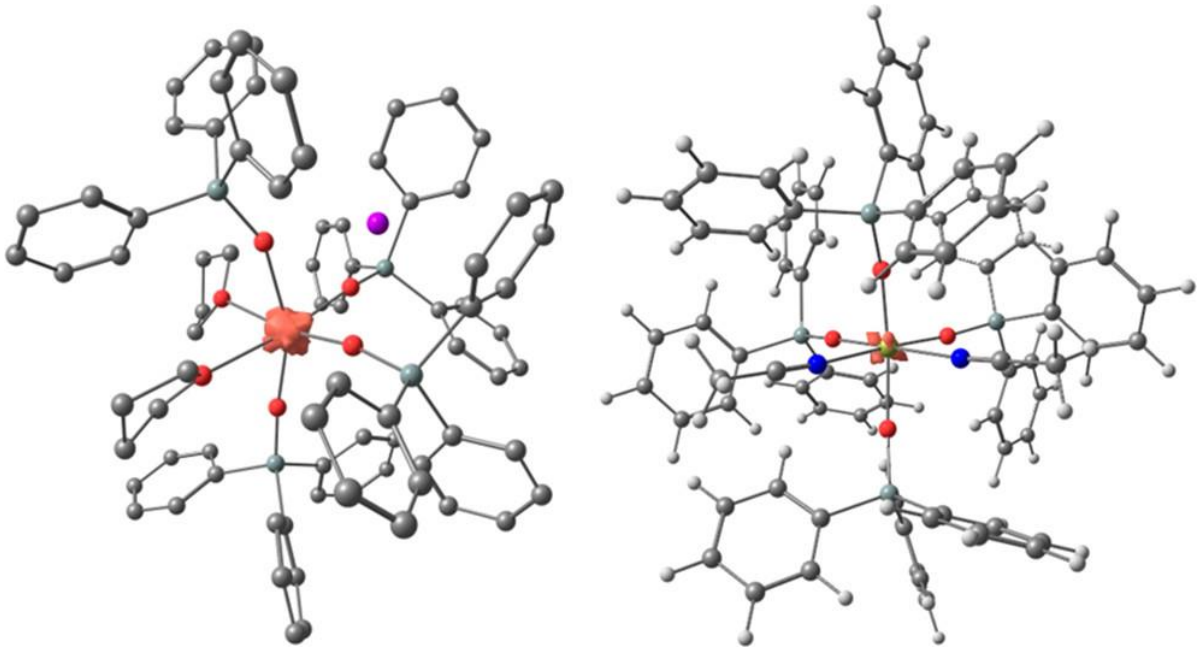

Figure 1.7. Unpaired spin density plot for [KPr(OSiPh$_3$)$_4$(THF)$_3$] (left) and [Pr(OSiPh$_3$)$_4$(MeCN)$_2$] (right) (taken form Ref[42]).

Remarkably, pentavalent praseodymium has also been observed in the gas phase and in solid noble-gas matrices, which represents the highest oxidation state reported for a lanthanide ion. For example, Li and co-workers have used combined gas-phase infrared photodissociation spectroscopy, matrix-isolated infrared absorption spectroscopy and ab initio multiconfigurational wavefunction theory (WFT) studies to identify a +5 oxidation state for the Pr in (η^2-O$_2$)PrO$_2$ and PrO$_2^+$.[43] Specifically, the IR spectra for PrO$_2^+$ in the gas phase and solid argon-matrix experiments exhibited a single peak at 918 and 907 cm^{-1}, respectively, assignable to the antisymmetric OPrO stretch. These absorptions matched those calculated for PrO$_2^+$ in the singlet Pr(V) state using WFT methods. The WFT analysis also found that the Pr center in PrO$_2^+$ has an (f^0d^0) ground state electronic configuration, consistent with a Pr(V) oxidation state. In addition, NBO analysis on PrO$_2^+$ revealed a σ + 2π Pr-O triple bond, consistent with the calculated Pr-O mayor bond order of 2.10. The σ bonds consisted of 38.4%

Pr character with a 5d/4f contribution of 48:50, while the π bonds consisted of 18.2% Pr character with a 5d/4f contribution of 50:49. The significant covalent character in the Pr-O bonds is believed to impart stability to the +5 state by partially compensating the high fifth ionization energy of Pr(V).

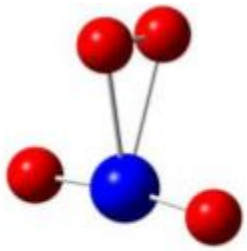

$(\eta^2\text{-}O_2)PrO_2$, C_{2v}, $^2A_2$

Figure 1.8. DFT optimized structure of $(\eta^2\text{-}O_2)PrO_2$ (taken from Ref[43])

On the other hand, the argon-matrix IR spectrum for $(\eta^2\text{-}O_2)PrO_2$ exhibited three absorptions at 1141.6, 827.0, and 695.3 cm^{-1} assignable to the O-O stretch, the antisymmetric and symmetric OPrO stretches, respectively. Notably, the observed O-O stretch fell within the range expected for a superoxide,[54,55] while the band position of the antisymmetric OPrO stretch suggested that the two oxygen atoms in the PrO_2 fragment of $(\eta^2\text{-}O_2)PrO_2$ are $(O)^{2-}$. These data suggest $(\eta^2\text{-}O_2)PrO_2$ can be described as the neutral praseodymium dioxide/superoxide complex $[(Pr^{+V}O_2)^+(O_2)^-]$, which was further corroborated by WFT studies. Specifically, geometry optimizations found the lowest-energy structure to be the side-on bound C_{2v} symmetric $(\eta^2\text{-}O_2)PrO_2$ in a doublet ground state (Figure 1.8), consistent with the spectroscopic data. The calculated vibrational frequencies for this structure also matched the experimental values. Additionally, bonding analysis found the unpaired spin density to be located on the π_u* MO of the $\eta^2\text{-}O_2$ ligand with a $Pr(f^0d^0)$ metal center, consistent with the dioxide/superoxide

description mentioned above. Moreover, WFT calculations found no significant multiconfigurational character for both PrO_2^+ and $(\eta^2\text{-}O_2)PrO_2$, which makes the assignment of the Pr(V) oxidation state less vague. Interestingly, attempts to prepare analogous pentavalent lanthanide oxides using Tb, Nd and Dy, under the same conditions, were unsuccessful. The unique ability of Pr to form a +5 ion was attributed to its lowest fifth ionization energy and its lowest sum of first to fifth ionization energies amongst the lanthanide series.[43]

1.4. Trans/Cis Isomerization of the Uranyl Ion

Compared to the lanthanides, actinide elements are expected to exhibit a greater degree of covalency due the diffuse nature of their 5f valence orbitals that allows for a more optimal spatial overlap with ligand frontier orbitals.[2,56] Most research on actinide coordination chemistry has focused on uranium due to its relatively low radiotoxicity, its stable naturally-occurring isotopes and its versatile redox chemistry that is akin to that of the transition metals.[57] Indeed, uranium exists a wide range of common oxidations states including the +3,+4,+5 and +6 states, although few examples of molecular U(II) complexes have recently appeared in the literature.[58–63] The +6 oxidation state is the most stable in solution, and the most common form of uranium in this oxidation state is the uranyl ion $[UO_2]^{2+}$.[57,64] This fragment is exceptionally stable in both solution and the solid state, and exists exclusively as the trans isomer. It also exhibits high solubility in aqueous solutions and accounts for >95% of spent nuclear fuel.[65] As such, it poses a significant health hazard as a ground water contaminant in densely populated areas where uranium mining and nuclear power plants are prevalent. The high thermodynamic stability of this ion is reflected in its large U-O bond dissociation enthalpy (604 kJ/mol),[66] which 72 kJ/mol greater than the BDE for C-O bond in carbon dioxide (532 kJ/mol).[67] The U-O bond in uranyl is also kinetically inert; experiments on the rate of isotopic oxygen exchange

of uranyl with water in 1M perchloric acid solution at room temperature find half-lives greater than 30,000 h.[68] The exceptional thermodynamic and kinetic stability of the uranyl ion is attributed to the strong covalent character in the U-O bonds, which renders them resistant to substitution or functionalization.[57] However, effective strategies of nuclear waste remediation and nuclear fuel reprocessing will require novel methods for facile manipulation of the uranyl ion, which has incited interest in deeper investigation of its electronic structure and reactivity.

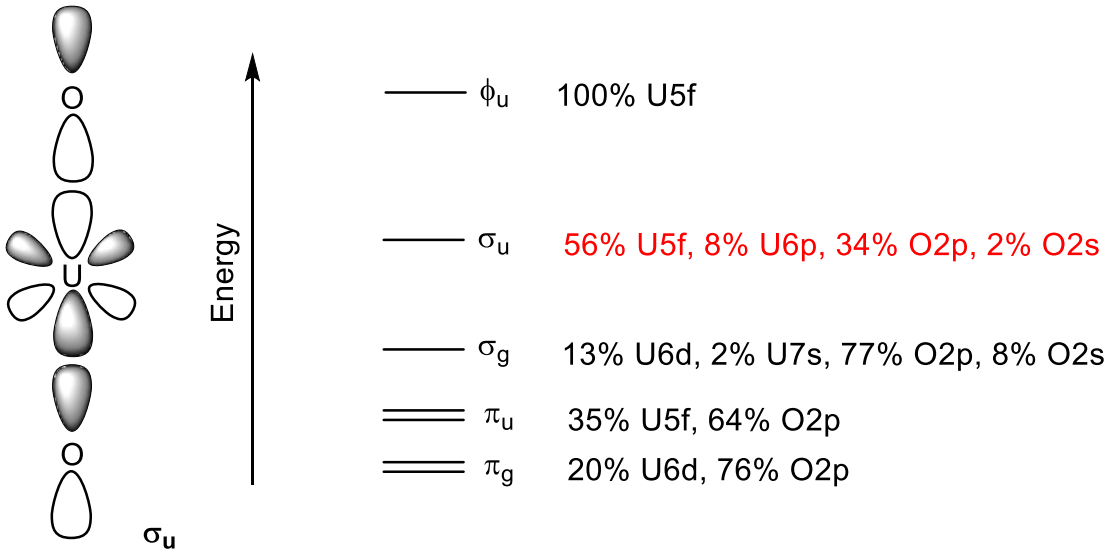

Figure 1.9. Schematic of the MO diagram for the uranyl ion[69]

The electronic structure of the uranyl has seen much debate, especially with respect to the ordering of its frontier orbitals.[57,66,69–80] There is a general consensus that the frontier orbitals consist of mostly oxygen based σ_u, σ_g, π_u, and π_g orbitals, but the relative energies of these MOs have been controversial. Some theoretical calculations using Kohn-Sham DFT methods have suggested an energetic ordering of $\pi_g < \pi_u < \sigma_g << \sigma_u$ (Figure 1.9).[69] Notably, the atomic orbital compositions of these MOs were used to rationalize the exclusively trans geometry observed for the O-U-O fragment in uranyl. Specifically, the σ_u HOMO was calculated to have 56% U5f, 8% U6p, 34% O2p, 2% O2s atomic orbital compositions which explains the strong

covalent nature of the U-O bonds. The involvement of 6p orbitals in the U-O bonding was unexpected, but optimal mixing/overlap of these "pseudo-core" orbitals with U5f and O2p valence orbitals can only occur in a trans geometry, resulting in a linear O-U-O angle that rarely deviates past 170°. This analysis is consistent with the geometry observed for the uranyl ion experimentally. Indeed, approximately 93% of all the uranyl structures deposited on the Cambridge Structural Database feature O-U-O angles greater than 175°.[81] It is important to note, however, that O-U-O bending is likely to have a profound effect on the electronic structure, reactivity and covalency of the U-O bonds in uranyl, thus providing an opportunity to uncover new methods of uranyl manipulation, and gain unique insights into actinide covalency and 5f-orbital participation in bonding. Inspired by these promises, there have been several efforts directed towards stabilizing the as-yet-unknown cis isomer of the uranyl ion, which have culminated in isolation of uranyl complexes with O-U-O angles as low as *ca.*161°.[82,83]

Scheme 1.7. *Trans/cis* isomerization of the uranyl ion[84,85]

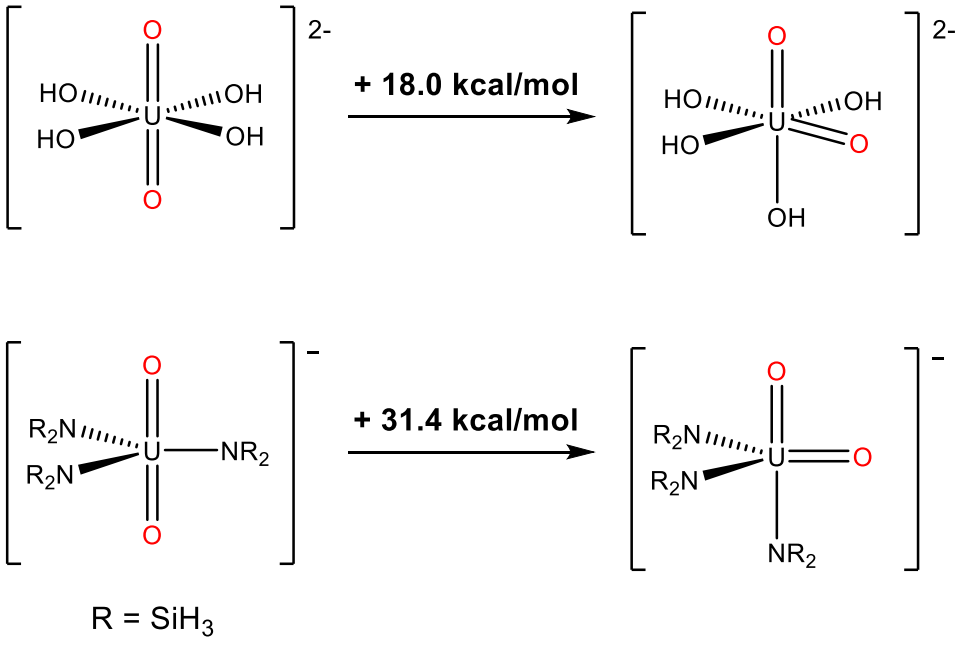

There have been several theoretical studies performed to evaluate the thermodynamic favorability of a trans to cis isomerization in uranyl.[75,76,84–87] In all cases, the cis isomer was found to be less stable than the trans isomer. For example, the cis isomer of $[UO_2(OH)_4]^{2-}$ was found to be 18.0 kcal/mol higher in energy than the trans isomer (Scheme 1.7).[84] Similarly, the cis isomer of $[UO_2(NR_2)_3]^-$ (R = SiH_3) was calculated to be 31.4 kcal/mol higher in energy than the trans isomer.[85] Both studies reveal that the energy penalty for a trans/cis isomerization could be greatly affected by the type of equatorial co-ligands, with those that are strongly donating resulting in a lower penalty. This result is consistent with previous reports that find that strongly donating equatorial ligands weaken the U-O bonds in uranyl, particularly by disrupting its π bonding framework.[88–90] Additionally, the calculated values for the differences in energy between the cis and trans isomers suggest the cis isomers could be represented as local minima on the respective complexes' potential energy landscape. As such, these results suggest that stable cis uranyl complexes could be isolable by careful choice of equatorial co-ligands and reaction conditions. In practice, however, O_{yl}-U-O_{yl} bending of significant magnitude has been hard to implement. Interestingly, adsorption of UO_2^{2+} onto a variety of mineral surfaces is predicted to cause greater O_{yl}-U-O_{yl} bending than that found in any homogeneous coordination complex.[91–94] For example, the adsorption of uranyl onto alumina or gibbsite is predicted to result in O_{yl}-U-O_{yl} angles of ca. 149° and 144°, respectively.[91,94] In both cases, O_{yl}-U-O_{yl} bending is likely caused by the close approach of the two oxo ligands to the mineral surface upon coordination of uranyl. To my knowledge, these are the smallest O_{yl}-U-O_{yl} angles predicted for any uranyl-containing species. However, O_{yl}-U-O_{yl} bending upon uranyl adsorption has not been confirmed experimentally.

Scheme 1.8. Synthesis of $[UO_2(OTf)_2(^{H}N_4)]$ and $[UO_2(OTf)(THF)(^{Me}N_4)][OTf]$[82]

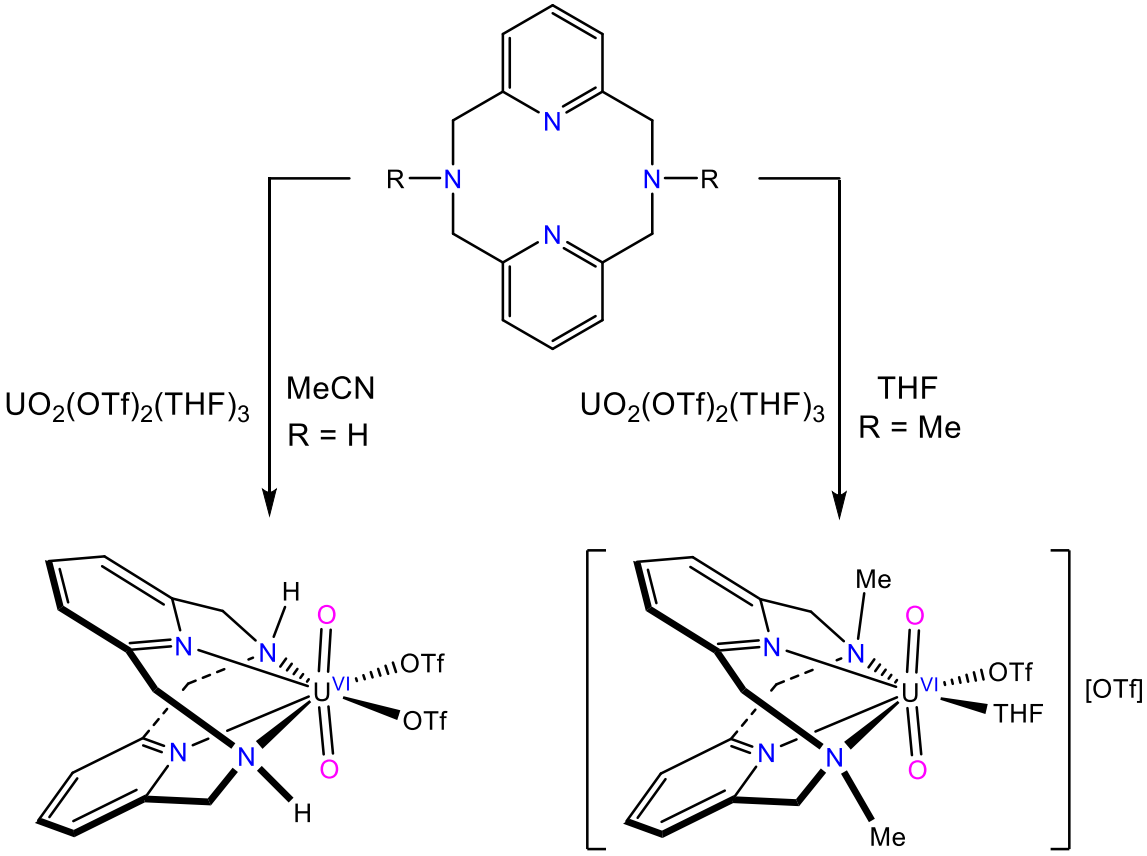

In 2016, Hayton and coworkers synthesized a series uranyl complexes that exhibited the lowest O-U-O angles reported to date by making use of a 12-membered macrocycle.[82] These attempts to prepare a cis uranyl complex were inspired by the observation that the uranyl ion cannot fit into the binding pocket of 16- or less-membered macrocycles.[95] As such, coordination of these macrocycles to uranyl would result in a substantial steric clash with the two O_{yl} oxo ligands that could potentially enforce a cis dioxo stereochemistry. Thus, reactions of the 12-membered macrocycles 2,11-diaza[3,3(2,6) pyridinophane ($^{H}N_4$) and *N*,*N*-dimethyl-2,11-diaza[3,3(2,6) pyridinophane ($^{Me}N_4$) with 1 equiv of $[UO_2(OTf)_2(THF)_3]$ in MeCN and THF, respectively, afforded the bent uranyl complexes $[UO_2(OTf)_2(^{H}N_4)]$ and $[UO_2(OTf)(THF)(^{Me}N_4)][OTf]$ in good yields (Scheme 1.8). These complexes exhibited O-U-

O angles of 162.8(3) and 161.7(5) °, respectively, which are the smallest angles reported at that time. The manifestation of these bent geometries was rationalized by the steric repulsion between the oxo ligands of the uranyl fragment and the macrocycle backbone, which is a consequence of the small binding pocket of the 12-membered macrocycles. The coordination to the poorly donating $[OTf]^-$ co-ligand also likely plays a role by strengthening the U-N interactions when compared to those in analogous Cl^- coordinated uranyl pyridinophanes. Ultimately, however, these complexes cannot be described as containing cis uranyl, as the O-U-O distortions are too small. Indeed, the U-N bonds in $[UO_2(OTf)_2(^{H}N_4)]$ and $[UO_2(OTf)(THF)(^{Me}N_4)][OTf]$ (2.580(7) – 2.635(7) Å and 2.63(1) – 2.73(1) Å, respectively) are still considered weak, likely due to the neutral charge on the macrocycles. Additionally, the N_{pyr}-U-N_{pyr} angles (59.4(2) and 57.8(3)°, respectively) are relatively acute, which reveal that both $^{H}N_4$ and $^{Me}N_4$ are rather flexible. This flexibility in turn limits the steric pressure applied onto the uranyl oxo ligands, resulting in small O-U-O angle deformations. However, while unsuccessful in enforcing a trans to cis isomerization of uranyl, these results provide proof-of-concept that anionic ≤16-membered macrocycles with greater rigidity could potentially be employed to isolate an authentic cis uranyl complex.

Scheme 1.9. Synthesis of $[UO_2Cl_2(phen)_2]$[83]

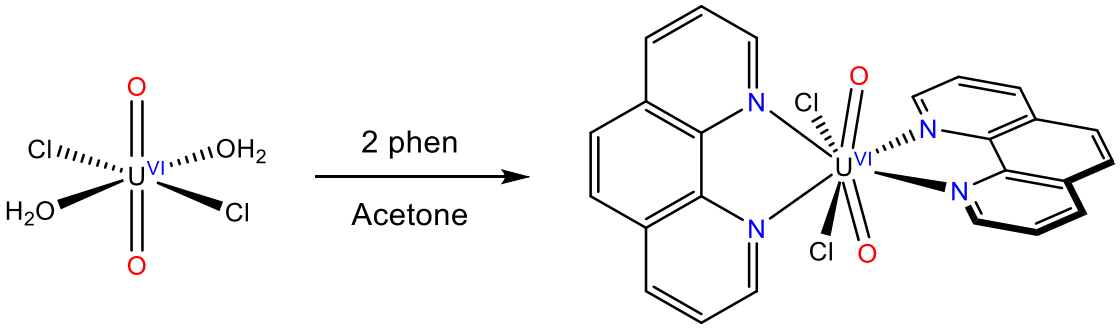

In 2017, Ikeda-Ohno et al. reported another uranyl complex featuring a bent uranyl unit by making use of a simple commercially available ligand.[83] In this report, $UO_2Cl_2 \cdot nH_2O$ was treated with 2 equiv of phenanthroline in acetone to afford $[UO_2Cl_2(phen)_2]$, the first uranyl phenanthroline complex with a U:phen ratio of 1:2 (Scheme 1.9). This complex exhibited an unusual dodecadeltahedron geometry that consists of a $\{UO_2Cl_2\}$ unit coordinated by two mutually perpendicular phenanthroline ligands. This unique geometry results in a bent O-U-O angle of 161.8(1)°, which is comparable to that reported for $[UO_2(OTf)(THF)(^{Me}N_4)][OTf]$ by Hayton and co-workers (161.7(5)°).[82] The preference for a dodecadeltahedron geometry in $[UO_2Cl_2(phen)_2]$ was attributed to intermolecular π-π stacking interactions between adjacent phenanthroline molecules that sandwich the uranium atoms in between. This preferred geometry also results in weak but distinct interactions between uranyl oxygen/chlorine atoms and nearby hydrogens atoms on the phenanthroline molecules that further reinforce O-U-O bending. Notably, DFT calculations revealed that the U-O bond weakens upon formation of $[UO_2Cl_2(phen)_2]$, a likely consequence of O-U-O bending. In particular, the Mayer bond order of the U-O bond in $[UO_2Cl_2(phen)_2]$ (2.3385) was calculated to be lower than that for free linear uranyl (2.4943). Similarly, the ν_3 asymmetric U-O stretching frequency for this complex (933.14 cm^{-1}) was also calculated to be lower than that for free linear uranyl (1097.88 cm^{-1}). Overall, these results suggest that extended π-π networking interactions could potentially be harnessed to enforce a trans/cis isomerization in uranyl.

1.5. Uranyl Oxo Activation

As mentioned above, O_{yl}-U-O_{yl} bending appears to be a promising strategy for uranyl manipulation and functionalization. For example, it has been shown that O_{yl}-U-O_{yl} bending renders the U^{6+} center easier to reduce. In particular, Andersen and co-workers have shown

that reaction of Cp'_2UCl_2 (Cp' = 1,2,4-^{t}Bu$_3$C$_5$H$_2$) with KC_8 and pyridine-*N*-oxide affords the U(V) oxo cluster $Cp'_4(bipy)_3U_6O_{13}$, along with Cp'H and $(Cp')_2$.[96] This reaction likely proceeds through a cis uranyl intermediate *cis*-Cp'_2UO_2, which undergoes rapid homolytic Cp'-U cleavage. A similarly putative *cis*-$Cp^*_2UO_2$ intermediate has been proposed for the reaction between $Cp^*_2UI(THF)$ and pyridine-*N*-oxide in the presence of KC_8, which resulted in isolation of a Cp^*_2 dimer and reduced uranium oxides.[97] In both instances, bending of the O_{yl}-U-O_{yl} fragment likely weakens the U-O bonds, rendering the uranium center a much stronger oxidant. This phenomenon has potential implications in remediation of nuclear waste, where routes to facile reduction of uranyl are being sought for solubility-based separations.[98,99] In addition, it is possible that O_{yl}-U-O_{yl} bending may also render the uranyl oxo ligands more susceptible to exchange or functionalization. For example, Gibson and co-workers observed that the 12-crown-4 ligated peroxo-bridged uranyl(VI) dimer, $[(12\text{-crown-4})UO_2(\mu\text{-}O_2)UO_2(12\text{-crown-4})]^{2+}$ converts to the oxo-bridged U(V) dimer, $[(12\text{-crown-4})UO(\mu\text{-}O)_2UO(12\text{-crown-4})]^{2+}$, upon loss of O_2 in the gas phase.[100] In this case, it is notable that the peroxo-bridged precursor is predicted to feature an O_{yl}-U-O_{yl} angle of 154°, presumably because of the steric constraints imposed by coordination of the small 12-crown-4 macrocycle to the UO_2^{2+} ion.

Scheme 1.10. Uranyl oxo activation via ligation to polydentate chelating agents[101]

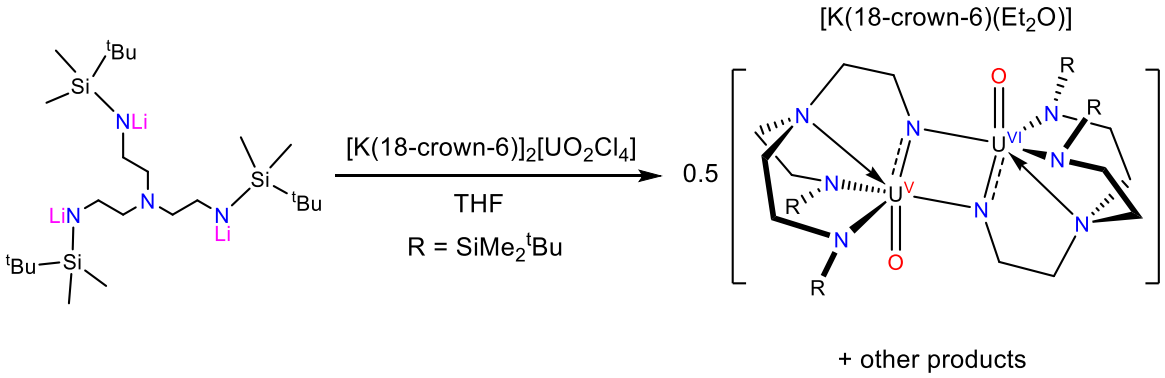

Coordination of uranyl to polydentate chelating agents has also been shown to effect uranyl activation. For example, Clark and co-workers have shown that ligation of the triamidoamine TREN tripod $Li_3NN'_3$ (NN'_3 = $N(CH_2CH_2NR)_3$, R = Si^tBuMe_2) to $[K(18\text{-crown-6})]_2[UO_2Cl_4]$ results in formation of the mixed-valent uranium (V/VI) oxo-imido dimer $[K(18\text{-crown-6})(Et_2O)_2][UO(\mu_2\text{-}NCH_2CH_2NN'_2)]_2$ in moderate yield (Scheme 1.10).[101] This complex is generated via formal loss of a uranyl oxo ligand, elimination of a silyl group from an amido nitrogen and $1e^-$ reduction. While the exact mechanism for the formation of this complex is unknown, it is possible that the observed ligand decomposition and O_{yl} cleavage are a consequence of the instability of a putative cis uranyl intermediate. Indeed, it is reasonable to envision that κ^3 coordination of $Li_3NN'_3$ to trans uranyl would enforce a cis dioxo stereochemistry. If true, this hypothesis suggests that O-U-O bending could be utilized to effect uranyl oxo activation via U-O bond cleavage.

Scheme 1.11. Uranyl oxo activation via coordination to Lewis acids[102]

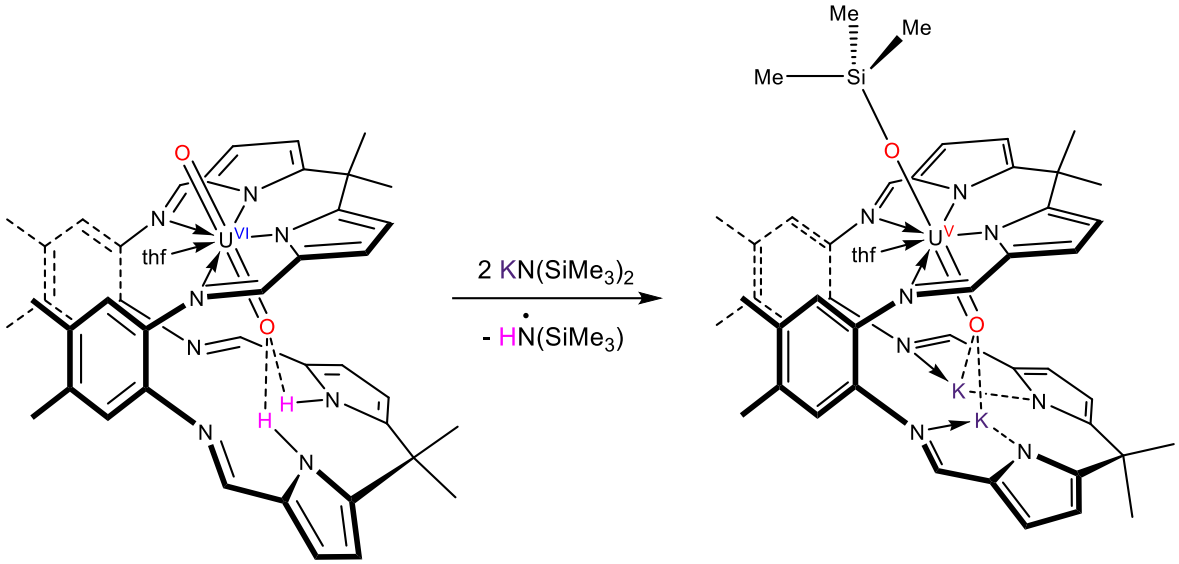

Another mode of uranyl oxo activation is via coordination to strong Lewis acids. For example, deprotonation of the uranyl pyrrole-imine complex $[U^{VI}O_2(THF)(H_2L)]$ (L= a polypyrrolic macrocycle) with 2 equiv $KN(SiMe_3)_2$ results in elimination of $HN(SiMe_3)_2$ and coordination of the *endo* O_{yl} ligand to both potassium cations (Scheme 1.11).[102] These *endo* O_{yl}→K dative interactions substantially polarize the *exo* U-O bond, resulting in silylation of the *exo* O_{yl} ligand by the eliminated $HN(SiMe_3)_2$. This result was surprising, as $HN(SiMe_3)_2$ is generally considered to be a weak electrophile. However, the unique Pac-Man topology of the polypyrrolic macrocycle sterically enforces sufficiently strong *endo* O_{yl}→K interactions that activate the *exo* U-O bond towards silylation by $HN(SiMe_3)_2$. Concurrent addition of FeI_2 to the reaction mixture affords the stable U(V) silyloxide $[U^{V}O(OSiMe_3)(THF)(Fe_2I_2L)]$, which features asymmetrically lengthened U-O bonds. This reaction was termed "reductive silylation" of uranyl and was the first reported method of controlled uranyl oxo functionalization. Several variants of "reductive silylation" have since appeared in the literature, framing this strategy as a general method of uranyl oxo activation.[103–113] A similar

reductive functionalization of uranyl using silyl sources can be achieved to afford non-uranyl U(IV) complexes.[103,105,109,110,114–116] For example, addition of excess Me_3SiX (X = Cl, Br, I) to $UO_2I_2(THF)_3$ or $UO_2(OTf)_2$ in MeCN results complete deoxygenation of uranyl to afford the U(IV) tetrahalides $UX_4(MeCN)_4$ in good yields.[103] This type of activation is driven by the formation of strong Si-O bonds which likely eliminates $Me_3SiOSiMe_3$ as a byproduct. Other types of electrophiles can also functionalize uranyl oxo ligands in a similar manner, which include $(Bpin)_2$,[117] $[Cp_2TiCl]_2$,[118] and $[Sm\{N(SiMe_3)_2\}_2]$.[104,119]

Scheme 1.12. Previous example of uranyl oxo ligand scrambling[120]

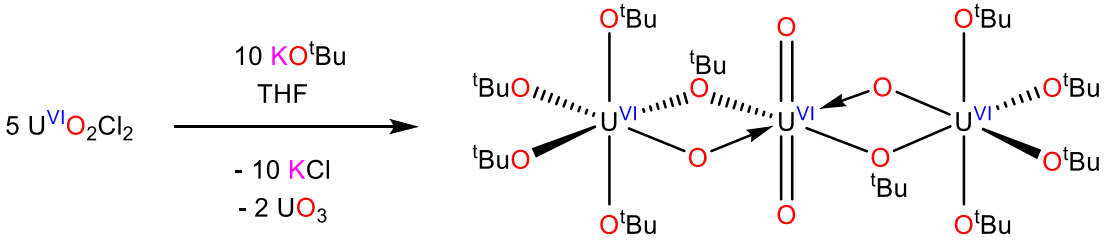

Finally, uranyl oxo activation can also be achieved via ligation to strongly donating equatorial co-ligands. While it is known that strongly donating equatorial co-ligands weaken the uranyl U-O bonds, and even induce dative interactions with electrophiles,[88,121] strongly donating co-ligands can also activate uranyl via oxo ligand scrambling.[122] Indeed, while coordination of aryloxides to uranyl has been shown to promote $O_{yl}\rightarrow M$ dative interactions,[121] coordination to the more strongly donating alkoxides is known to result in oxo/alkoxide scrambling.[88,120,123,124] For example, reaction of UO_2Cl_2 with 2 equiv of KO^tBu in THF results in isolation of $[UO_2][U(\mu\text{-}O)(\mu\text{-}O^tBu)(O^tBu)_4]_2$ in modest yield (Scheme 1.12).[120] The formation of this complex proceeds via initial generation of $UO_2(O^tBu)_2$, followed by a formal exchange of an $(O)^{2-}$ ligand with two $(O^tBu)^-$ ligands to form the coordinatively unsaturated intermediate $UO(O^tBu)_4$. Two equivalents of $UO(O^tBu)_4$ then rapidly get trapped by another

molecule of $UO_2(O^tBu)_2$, forming the final product $[UO_2][U(\mu\text{-}O)(\mu\text{-}O^tBu)(O^tBu)_4]_2$. Notably, an insoluble precipitate is formed during the reaction that is attributable to $UO_3(THF)_x$, the expected byproduct of oxo/alkoxide substitution in $UO_2(O^tBu)_2$. In this example, it was suggested that the strongly σ-donating nature of the tert-butoxide equatorial co-ligands renders the normally strong and covalent U-O bonds in uranyl easier to cleave, thereby lowering the kinetic barrier for oxo/alkoxide exchange. Coordinative unsaturation also seems to play a significant role, as addition of $OPPh_3$ during the course of the reaction results in isolation of $UO_2(O^tBu)_2(OPPh_3)_2$ instead of the oxo/tert-butoxide scrambling product. Consistent with this hypothesis, use of more sterically demanding alkoxides such as $KOCHPh_2$ and $KOCH(^tBu)Ph$ results in no oxo/alkoxide ligand exchange, but instead affords the uranyl alkoxides $UO_2(OCHPh_2)_2(THF)_2$ and $UO_2\{OCH(^tBu)Ph\}_2(THF)_2$ in modest yields.[124] Oxo ligand scrambling is also observed in the reaction of KONp (Np = $CH_2{}^tBu$) with $[UO_2Cl_2(THF)_2]_2$, which results in the formation of the homoleptic U(VI) alkoxide $[U(ONp)_6]$.[124] This complex is presumably formed via successive oxo/neopentoxide redistribution events that also liberate UO_3 as a byproduct. Given the greater steric profile of KONp vs KO^tBu, the complete deoxygenation of uranyl in this case may be due to the greater σ-donating ability of neopentoxide vs tert-butoxide. Overall, these results confirm the premise that strongly donating equatorial co-ligands increase the Lewis basicity of the O_{yl} ligands in uranyl, rendering them prone to further reactivity.

1.6. General Remarks

This dissertation is divided into six chapters and covers three main areas of research: 1) stabilization of terminal lanthanide-ligand multiple bonds, 2) stabilization of tetravalent lanthanide ions in solution, and 3) *trans*/*cis* isomerization and functionalization of the uranyl

ion. The work described herein attempts to expand our limited understanding of the fundamental bonding interactions, covalent character and redox chemistry of the f elements, providing the avenue for potential discovery of new applications in nuclear waste treatment and redox catalysis.

Chapter 2 describes the synthesis of the first terminal lanthanide oxo complex that is not supported by alkali metal interactions or hydrogen bonding. This complex was generated via photolysis of a Ce(III) nitrate precursor, which results in photochemical cleavage of its nitrate co-ligand. Also formed during photolysis are a Ce(IV) oxo cluster and a Ce(III) silyloxide complex. All three products were characterized by X-ray crystallography, and the mechanism of their formation was thoroughly investigated using ^{1}H and ^{7}Li{^{1}H} NMR spectroscopies and cyclic voltammetry.

Chapter 3 details the synthesis and characterization of the first homoleptic cerium and thorium ketimide complexes. A detailed comparative spectroscopic and structural study of these two complexes was performed using X-ray crystallography, UV-Vis spectroscopy, and DFT calculations. In addition, the ability of the ketimide ligand to stabilize high oxidation states in the lanthanides was explored using cyclic voltammetry.

Chapter 4 explores the ability of a dimethyl-substituted cyclam ligand to stabilize the tetravalent oxidation state in praseodymium. Model studies were first performed with cerium, which found that the cyclam ligand allows easy oxidation of Ce(III) with mild oxidants. Both the Ce(III) and Ce(IV) cyclam complexes were fully characterized. Parallel studies on oxidation of a Pr(III) cyclam complex are then detailed, and the results explained using cyclic voltammetry, ^{1}H NMR spectroscopy and previously reported DFT calculations. Finally, the

suitability of the cyclam ligand for facilitating the *trans*/*cis* isomerization of the uranyl ion is investigated in an appendix.

Chapter 5 describes my attempts to generate an unprecedented cis-uranyl complex using an anionic 14-membered macrocycle. These attempts resulted in isolation of a trans uranyl complex with an unusual 2:1 metal to ligand ratio, and observation of products of $2e^-$ oxidation of the 14-membered macrocycle. The mechanism for the generation of these products is investigated, and explained in terms of the redox properties and electronic structure of the putative cis-uranyl intermediate.

Chapter 6 investigates the ligation of the tripodal silsesquioxane ligand to trans uranyl, which results in generation of a U(VI) tris(silyloxide) via an unprecedented oxo silylation reaction. Mechanistic studies on this unusual transformation were performed using $^{29}Si\{^1H\}$ NMR spectroscopy and X-ray photoelectron spectroscopy, which identified a new non-reductive pathway for uranyl oxo silylation. This new mode of uranyl activation could potentially be exploited for the development of new strategies for the treatment of nuclear waste. Additionally, this work demonstrates that the actinide coordination chemistry of mineral surface mimics, such as silsesquioxane, is a fruitful arena for the discovery of new reactivity.

1.7 References

(1) Ji, W.-X.; Xu, W.; Schwarz, W. H. E.; Wang, S.-G. Ionic Bonding of Lanthanides, as Influenced by d- and f-Atomic Orbitals, by Core–Shells and by Relativity. *J. Comput. Chem.* **2015**, *36* (7), 449–458.

(2) Choppin, G. R. Comparative Solution Chemistry of the 4f and 5f Elements. *J. Alloys Compd.* **1995**, *223* (2), 174–179.

(3) Choppin, G. R. Covalency in F-Element Bonds. *J. Alloys Compd.* **2002**, *344* (1), 55–59.

(4) Jo/rgensen, C. K.; Pappalardo, R.; Schmidtke, H. Do the ``Ligand Field'' Parameters in Lanthanides Represent Weak Covalent Bonding? *J. Chem. Phys.* **1963**, *39* (6), 1422–1430.

(5) Myers, C. E. Case for Covalent Bonding in Lanthanide Trihalides. *Inorg. Chem.* **1975**, *14* (1), 199–201.

(6) Bergman, C.; Coppens, P.; Drowart, J.; Smoes, S. Mass Spectrometric Determination of the Dissociation Energies of the Gaseous Rare Earth Monoselenides and Monotellurides. *Trans. Faraday Soc.* **1970**, *66* (0), 800–808.

(7) Dubois, R.; Carver, J. C.; Tsutsui, M. THE X-RAY PHOTOELECTRON SPECTRA OF SIGMA AND Pi BONDED ORGANOGADOLINIUM COMPOUNDS: A SEARCH FOR 4f ORBITAL COVALENCY. *J. Coord. Chem.* **1977**, *7* (1), 31–34.

(8) Henrie, D. E.; Choppin, G. R. Environmental Effects on f–f Transitions. II. "Hypersensitivity" in Some Complexes of Trivalent Neodymium. *J. Chem. Phys.* **1968**, *49* (2), 477–481.

(9) Katzin, L. I.; Barnett, M. L. Spectral Evidence on Rare Earth Covalent Binding[1a]. *J. Phys. Chem.* **1964**, *68* (12), 3779–3785.

(10) Choppin, G. R.; Yao, K. Ligand Basicities from Reactions with $Nd[(CF_3CO)_2CH]_3 \cdot THF$. *Inorganica Chim. Acta* **1988**, *147* (1), 131–133.

(11) Drago, R. S. Quantitative Evaluation and Prediction of Donor-Acceptor Interactions. *Struct. Bond.* **1973**, *15*, 73.

(12) Denning, R. G.; Harmer, J.; Green, J. C.; Irwin, M. Covalency in the 4f Shell of Tris-Cyclopentadienyl Ytterbium ($YbCp_3$)-A Spectroscopic Evaluation. *J. Am. Chem. Soc.* **2011**, *133* (50), 20644.

(13) Bond, A. M.; Deacon, G. B.; Newnham, R. H. Organolanthanoids. 9. Electrochemical Reduction of Tris(Cyclopentadienyl)Samarium(III), -Ytterbium(III), and -Europium(III) Compounds in Tetrahydrofuran. *Organometallics* **1986**, *5* (11), 2312–2316.

(14) Minasian, S. G.; Batista, E. R.; Booth, C. H.; Clark, D. L.; Keith, J. M.; Kozimor, S. A.; Lukens, W. W.; Martin, R. L.; Shuh, D. K.; Stieber, S. C. E.; Tylisczcak, T.; Wen, X. D. Quantitative Evidence for Lanthanide-Oxygen Orbital Mixing in CeO_2, PrO_2, and TbO_2. *J. Am. Chem. Soc.* **2017**, *139*, 18052.

(15) Bianconi, A.; Marcelli, A.; Dexpert, H.; Karnatak, R.; Kotani, A.; Jo, T.; Petiau, J. Specific Intermediate-Valence State of Insulating 4f Compounds Detected by L_3 X-Ray Absorption. *Phys. Rev. B* **1987**, *35* (2), 806–812.

(16) Dexpert, H.; Karnatak, R. C.; Esteva, J.-M.; Connerade, J. P.; Gasgnier, M.; Caro, P. E.; Albert, L. X-Ray Absorption Studies of CeO_2, PrO_2, and TbO_2. II. Rare-Earth Valence State by L_{III} Absorption Edges. *Phys. Rev. B* **1987**, *36* (3), 1750–1753.

(17) Loble, M. W.; Keith, J. M.; Altman, A. B.; Stieber, S. C.; Batista, E. R.; Boland, K. S.; Conradson, S. D.; Clark, D. L.; Lezama Pacheco, J.; Kozimor, S. A.; Martin, R. L.; Minasian, S. G.; Olson, A. C.; Scott, B. L.; Shuh, D. K.; Tyliszczak, T.; Wilkerson, M. P.; Zehnder, R. A. Covalency in Lanthanides. An X-Ray Absorption Spectroscopy and Density Functional Theory Study of $LnCl_6^{(x-)}$ (x = 3, 2). *J. Am. Chem. Soc.* **2015**, *137* (7), 2506–2523.

(18) Clark, D. L.; Gordon, J. C.; Hay, P. J.; Poli, R. Existence and Stability of Lanthanide−Main Group Element Multiple Bonds. New Paradigms in the Bonding of the 4f Elements. A DFT Study of Cp_2CeZ (Z = F^+, O, NH, CH^-, CH_2) and the Ligand Adduct $Cp_2Ce(CH_2)(NH_3)$. *Organometallics* **2005**, *24* (23), 5747–5758.

(19) Coles, M. P.; Hitchcock, P. B.; Khvostov, A. V; Lappert, M. F.; Li, Z.; Protchenko, A. V. Crystalline Amidocerium(Iv) Oxides and a Side-on Bridging Dioxygen Complex. *Dalt. Trans.* **2010**, *39* (29), 6780–6788.

(20) So, Y.-M.; Wang, G.-C.; Li, Y.; Sung, H. H. Y.; Williams, I. D.; Lin, Z.; Leung, W.-H. A Tetravalent Cerium Complex Containing a Ce=O Bond. *Angew. Chemie Int. Ed.* **2014**, *53* (6), 1626–1629.

(21) Damon, P. L.; Wu, G.; Kaltsoyannis, N.; Hayton, T. W. Formation of a Ce(IV) Oxo Complex via Inner Sphere Nitrate Reduction. *J. Am. Chem. Soc.* **2016**, *138* (39), 12743–12746.

(22) Solola, L. A.; Zabula, A. V; Dorfner, W. L.; Manor, B. C.; Carroll, P. J.; Schelter, E. J. Cerium(IV) Imido Complexes: Structural, Computational, and Reactivity Studies. *J. Am. Chem. Soc.* **2017**, *139* (6), 2435–2442.

(23) Gregson, M.; Lu, E.; McMaster, J.; Lewis, W.; Blake, A. J.; Liddle, S. T. A Cerium(IV)–Carbon Multiple Bond. *Angew. Chemie Int. Ed.* **2013**, *52* (49), 13016–13019.

(24) Schädle, D.; Meermann-Zimmermann, M.; Schädle, C.; Maichle-Mössmer, C.; Anwander, R. Rare-Earth Metal Complexes with Terminal Imido Ligands. *Eur. J. Inorg. Chem.* **2015**, *2015* (8), 1334–1339.

(25) Rice, N. T.; Su, J.; Gompa, T. P.; Russo, D. R.; Telser, J.; Palatinus, L.; Bacsa, J.; Yang, P.; Batista, E. R.; La Pierre, H. S. Homoleptic Imidophosphorane Stabilization of Tetravalent Cerium. *Inorg. Chem.* **2019**, *58* (8), 5289–5304.

(26) Baker, J. M.; Chadwick, J. R.; Garton, G.; Hurrell, J. P.; Bleaney, B. E.p.r. and Endor of Tb^{4+} in Thoria. *Proc. R. Soc. London. Ser. A. Math. Phys. Sci.* **1965**, *286* (1406), 352–365.

(27) Hu, Z.; Kaindl, G.; Müller, B. G. Core-Level Spectroscopy of the Tetravalent Lanthanide Compounds M_3LnF_7 (with M=Cs, Rb; Ln=Ce, Pr, Nd, Tb, Dy). *J. Alloys Compd.* **1997**, *246* (1), 177–185.

(28) Hu, Z.; Cho, E.-J.; Kaindl, G.; Müller, B. G. Valency and 4f Covalency of Cs_2RbTbF_7. *Phys. Rev. B* **1995**, *51* (12), 7514–7520.

(29) Rice, N. T.; Popov, I. A.; Russo, D. R.; Gompa, T. P.; Ramanathan, A.; Bacsa, J.; Batista, E. R.; Yang, P.; La Pierre, H. S. Comparison of Tetravalent Cerium and Terbium Ions in a Conserved, Homoleptic Imidophosphorane Ligand Field. *Chem. Sci.* **2020**, *11* (24), 6149–6159.

(30) Lang, P. F.; Smith, B. C. Ionization Energies of Lanthanides. *J. Chem. Educ.* **2010**, *87* (8), 875–881.

(31) Nugent, L. J.; Baybarz, R. D.; Burnett, J. L.; Ryan, J. L. Electron-Transfer and f → d Absorption Bands of Some Lanthanide and Actinide Complexes and the Standard (III–IV) Oxidation Potentials for Each Member of the Lanthanide and Actinide Series. *J. Inorg. Nucl. Chem.* **1971**, *33* (8), 2503–2530.

(32) Piro, N. A.; Robinson, J. R.; Walsh, P. J.; Schelter, E. J. The Electrochemical Behavior of Cerium(III/IV) Complexes: Thermodynamics, Kinetics and Applications in Synthesis. *Coord. Chem. Rev.* **2014**, *260*, 21.

(33) Mazej, Z. Room Temperature Syntheses of Lanthanoid Tetrafluorides (LnF_4, Ln = Ce, Pr, Tb). *J. Fluor. Chem.* **2002**, *118* (1), 127–129.

(34) Varga, L. P.; Asprey, L. B. Free Ion $4f^n$ Levels of the Tetravalent Lanthanides. Fluorescence and Absorption Spectra of Cesium Dysprosium (IV) Heptafluoride. *J. Chem. Phys.* **1968**, *48* (1), 139–146.

(35) Schulz, A.; Liebman, J. F. Paradoxes and Paradigms: High Oxidation States and Neighboring Rows in the Periodic Table—Lanthanides, Actinides, Exotica and Explosives. *Struct. Chem.* **2008**, *19* (4), 633–635.

(36) Tramšek, M.; Benkič, P.; Turičnik, A.; Tavčar, G.; Žemva, B. Coordination Compounds with XeF_2, AsF_3 and HF as Ligands to Metal Ions: A Review of Reaction Systematics, Raman Spectra and Metal, Fluoro-Ligand Polyhedra. *J. Fluor. Chem.* **2002**, *114* (2), 143–148.

(37) Varga, L. P.; Asprey, L. B. Electronic Spectra of Weak-Field Fluoride Complexes of Tetravalent Neodymium. *J. Chem. Phys.* **1968**, *49* (10), 4674–4679.

(38) Hoppe, R.; Rödder, K.-M. Komplexe Fluoride Seltener Erden: Cs_3TbF_7. *Zeitschrift für Anorg. und Allg. Chemie* **1961**, *312* (5-6), 277–281.

(39) Palumbo, C. T.; Zivkovic, I.; Scopelliti, R.; Mazzanti, M. Molecular Complex of Tb in the +4 Oxidation State. *J. Am. Chem. Soc.* **2019**, *141* (25), 9827–9831.

(40) Rice, N. T.; Popov, I. A.; Russo, D. R.; Bacsa, J.; Batista, E. R.; Yang, P.; Telser, J.; La Pierre, H. S. Design, Isolation, and Spectroscopic Analysis of a Tetravalent Terbium Complex. *J. Am. Chem. Soc.* **2019**, *141*, 13222.

(41) Willauer, A. R.; Palumbo, C. T.; Scopelliti, R.; Zivkovic, I.; Douair, I.; Maron, L.; Mazzanti, M. Stabilization of the Oxidation State + IV in Siloxide-Supported Terbium Compounds. *Angew. Chem., Int. Ed.* **2020**, *59*, 3549.

(42) Willauer, A. R.; Palumbo, C. T.; Fadaei-Tirani, F.; Zivkovic, I.; Douair, I.; Maron, L.; Mazzanti, M. Accessing the +IV Oxidation State in Molecular Complexes of Praseodymium. *J. Am. Chem. Soc.* **2020**, *142* (12), 5538–5542.

(43) Zhang, Q.; Hu, S.-X.; Qu, H.; Su, J.; Wang, G.; Lu, J.-B.; Chen, M.; Zhou, M.; Li, J. Pentavalent Lanthanide Compounds: Formation and Characterization of Praseodymium(V) Oxides. *Angew. Chemie Int. Ed.* **2016**, *55* (24), 6896–6900.

(44) Li, X.; Dong, W.; Qi, Y.; Wang, D.; Yang, R. Studies on the Stabilization of Terbium(IV) in Aqueous Tetrametaphosphate Solution. *Polyhedron* **1991**, *10* (13), 1479–1483.

(45) Hobart, D. E.; Samhoun, K.; Young, J. P.; Norvell, V. E.; Mamantov, G.; Peterson, J. R. Stabilization of Praseodymium(Iv) and Terbium(Iv) in Aqueous Carbonate Solution. *Inorg. Nucl. Chem. Lett.* **1980**, *16*, 321.

(46) Hinatsu, Y.; Doi, Y. Crystal Structures and Magnetic Properties of Alkali-Metal Lanthanide Oxides A_2LnO_3 (A=Li, Na; Ln=Ce, Pr, Tb). *J. Alloys Compd.* **2006**, *418* (1), 155–160.

(47) Kim, J. E.; Bogart, J. A.; Carroll, P. J.; Schelter, E. J. Rare Earth Metal Complexes of Bidentate Nitroxide Ligands: Synthesis and Electrochemistry. *Inorg. Chem.* **2016**, *55*, 775.

(48) Gregson, M.; Lu, E.; Mills, D. P.; Tuna, F.; McInnes, E. J. L.; Hennig, C.; Scheinost, A. C.; McMaster, J.; Lewis, W.; Blake, A. J.; Kerridge, A.; Liddle, S. T. The Inverse-Trans-Influence in Tetravalent Lanthanide and Actinide Bis(Carbene) Complexes. *Nat. Commun.* **2017**, *8* (1), 14137.

(49) Noh, W.; Girolami, G. S. X-Ray Crystal Structure of the Tetra(Tert-Butyl)Erbate Anion and Attempts to Prepare Tetravalent Organolanthanide Complexes. *Polyhedron* **2007**,

26, 3865.

(50) Hansen, S.; Mosel, B. D.; Müller-Warmuth, W.; Fielding, P. E. EPR Studies of Tb^{4+} in Single Crystals of Zircon and Scheelite Structure Silicates and Germanates. *Zeitschrift für Naturforsch. A* **1996**, *51* (8), 885–894.

(51) Ebendorff-Heidepriem, H.; Ehrt, D. Electron Spin Resonance Spectra of Eu^{2+} and Tb^{4+} Ions in Glasses. *J. Phys. Condens. Matter* **1999**, *11* (39), 7627–7634.

(52) Hinatsu, Y. Magnetic Susceptibility and Electron Paramagnetic Resonance Spectrum of Tetravalent Praseodymium Ions in $BaPrO_3$. *J. Solid State Chem.* **1993**, *102* (2), 362–367.

(53) Hinatsu, Y.; Itoh, M.; Edelstein, N. Structure and Magnetic Properties of Tetravalent Praseodymium Perovskite $SrPrO_3$. *J. Solid State Chem.* **1997**, *132*, 337.

(54) Cramer, C. J.; Tolman, W. B.; Theopold, K. H.; Rheingold, A. L. Variable Character of O—O and M—O Bonding in Side-on (η^2) 1:1 Metal Complexes of O_2. *Proc. Natl. Acad. Sci.* **2003**, *100* (7), 3635 LP – 3640.

(55) Gong, Y.; Zhou, M.; Andrews, L. Spectroscopic and Theoretical Studies of Transition Metal Oxides and Dioxygen Complexes. *Chem. Rev.* **2009**, *109* (12), 6765–6808.

(56) Katz, J. J. *The Chemistry of the Actinide and Transactinide Elements (Volumes 1-5)*; Springer Science & Business Media, 2007; Vol. 1.

(57) Denning, R. G. Electronic Structure and Bonding in Actinyl Ions. *Struct. Bond. (Berlin, Ger.)* **1992**, *79*, 215.

(58) MacDonald, M. R.; Fieser, M. E.; Bates, J. E.; Ziller, J. W.; Furche, F.; Evans, W. J. Identification of the + 2 Oxidation State for Uranium in a Crystalline Molecular Complex, [K(2.2.2-Cryptand)][$(C_5H_4SiMe_3)_3U$]. *J. Am. Chem. Soc.* **2013**, *135*, 13310.

(59) La Pierre, H. S.; Scheurer, A.; Heinemann, F. W.; Hieringer, W.; Meyer, K. Synthesis and Characterization of a Uranium(II) Monoarene Complex Supported by δ Backbonding. *Angew. Chem., Int. Ed.* **2014**, *53*, 7158.

(60) Windorff, C. J.; MacDonald, M. R.; Meihaus, K. R.; Ziller, J. W.; Long, J. R.; Evans, W. J. Expanding the Chemistry of Molecular U^{2+} Complexes: Synthesis, Characterization, and Reactivity of the $\{[C_5H_3(SiMe_3)_2]_3U\}^-$ Anion. *Chem. – A Eur. J.* **2016**, *22* (2), 772–782.

(61) Huh, D. N.; Ziller, J. W.; Evans, W. J. Chelate-Free Synthesis of the U(II) Complex, $[(C_5H_3(SiMe_3)_2)_3U]^{1-}$, Using Li and Cs Reductants and Comparative Studies of La(II) and Ce(II) Analogs. *Inorg. Chem.* **2018**, *57* (18), 11809–11814.

(62) Billow, B. S.; Livesay, B. N.; Mokhtarzadeh, C. C.; McCracken, J.; Shores, M. P.; Boncella, J. M.; Odom, A. L. Synthesis and Characterization of a Neutral U(II) Arene

Sandwich Complex. *J. Am. Chem. Soc.* **2018**, *140* (50), 17369–17373.

(63) Guo, F.-S.; Tsoureas, N.; Huang, G.-Z.; Tong, M.-L.; Mansikkamäki, A.; Layfield, R. A. Isolation of a Perfectly Linear Uranium(II) Metallocene. *Angew. Chemie Int. Ed.* **2020**, *59* (6), 2299–2303.

(64) Kaltsoyannis, N.; Scott, P. *The f Elements*; 1999.

(65) *GAO-12-70 NUCLEAR FUEL CYCLE OPTIONS*; 2011.

(66) Denning, R. G. Electronic Structure and Bonding in Actinyl Ions and Their Analogs. *J. Phys. Chem. A* **2007**, *111* (20), 4125–4143.

(67) Gibson, J. K.; Haire, R. G.; Santos, M.; Marçalo, J.; Pires de Matos, A. Oxidation Studies of Dipositive Actinide Ions, An^{2+} (An = Th, U, Np, Pu, Am) in the Gas Phase: Synthesis and Characterization of the Isolated Uranyl, Neptunyl, and Plutonyl Ions UO_2^{2+}(g), NpO_2^{2+}(g), and PuO_2^{2+}(g). *J. Phys. Chem. A* **2005**, *109* (12), 2768–2781.

(68) Gordon, G.; Taube, H. The Exchange Reaction between Uranyl Ion and Water in Perchloric Acid Solution. *J. Inorg. Nucl. Chem.* **1961**, *19* (1), 189–191.

(69) Kaltsoyannis, N. Computational Study of Analogues of the Uranyl Ion Containing the −NUN− Unit: Density Functional Theory Calculations on UO_2^{2+}, UON^{+}, UN_2, $UO(NPH_3)^{3+}$, $U(NPH_3)_2^{4+}$, $[UCl_4\{NPR_3\}_2]$ (R = H, Me), and $[UOCl_4\{NP(C_6H_5)_3\}]^{-}$. *Inorg. Chem.* **2000**, *39* (26), 6009–6017.

(70) de Jong, W. A.; Visscher, L.; Nieuwpoort, W. C. On the Bonding and the Electric Field Gradient of the Uranyl Ion. *J. Mol. Struct. THEOCHEM* **1998**, *458* (1), 41–52.

(71) Dekock, R. L.; Baerends, E. J.; Boerrigter, P. M.; Snijders, J. G. On the Nature of the First Excited States of the Uranyl Ion. *Chem. Phys. Lett.* **1984**, *105* (3), 308–316.

(72) Pyykko, P.; Laaksonen, L. Relativistically Parameterized Extended Hueckel Calculations. 8. Double-.Zeta. Parameters for the Actinoids Thorium, Protactinium, Uranium, Neptunium, Plutonium, and Americium and an Application on Uranyl. *J. Phys. Chem.* **1984**, *88* (21), 4892–4895.

(73) Jørgensen, C. K. Can the Highest Occupied Molecular Orbital of the Uranyl Ion Be Essentially 5f? *Chem. Phys. Lett.* **1982**, *89* (6), 455–458.

(74) Tatsumi, K.; Hoffmann, R. Bent Cis d^0 MoO_2^{2+} vs. Linear Trans d^0f^0 UO_2^{2+}: A Significant Role for Nonvalence 6p Orbitals in Uranyl. *Inorg. Chem.* **1980**, *19*, 2656.

(75) Wadt, W. R. Why Uranyl Ion(2+) Is Linear and Isoelectronic Thorium Dioxide Is Bent. *J. Am. Chem. Soc.* **1981**, *103* (20), 6053–6057.

(76) Dyall, K. G. Bonding and Bending in the Actinyls. *Mol. Phys.* **1999**, *96* (4), 511–518.

(77) Cornehl, H. H.; Heinemann, C.; Marçalo, J.; de Matos, A. P.; Schwarz, H. The "Bare" Uranyl(2+) Ion, UO_2^{2+}. *Angew. Chemie Int. Ed. English* **1996**, *35* (8), 891–894.

(78) Pepper, M.; Bursten, B. E. The Electronic Structure of Actinide-Containing Molecules: A Challenge to Applied Quantum Chemistry. *Chem. Rev.* **1991**, *91* (5), 719–741.

(79) Pyykkoe, P.; Li, J.; Runeberg, N. Quasirelativistic Pseudopotential Study of Species Isoelectronic to Uranyl and the Equatorial Coordination of Uranyl. *J. Phys. Chem.* **1994**, *98* (18), 4809–4813.

(80) Zhang, Z.; Pitzer, R. M. Application of Relativistic Quantum Chemistry to the Electronic Energy Levels of the Uranyl Ion. *J. Phys. Chem. A* **1999**, *103* (34), 6880–6886.

(81) Hayton, T. W. Understanding the Origins of O_{Yl}–U–O_{Yl} Bending in the Uranyl (UO_2^{2+}) Ion. *Dalt. Trans.* **2018**, *47* (4), 1003–1009.

(82) Pedrick, E. A.; Schultz, J. W.; Wu, G.; Mirica, L. M.; Hayton, T. W. Perturbation of the O–U–O Angle in Uranyl by Coordination to a 12-Membered Macrocycle. *Inorg. Chem.* **2016**, *55* (11), 5693–5701.

(83) Schöne, S.; Radoske, T.; März, J.; Stumpf, T.; Patzschke, M.; Ikeda-Ohno, A. $[UO_2Cl_2(Phen)_2]$, a Simple Uranium(VI) Compound with a Significantly Bent Uranyl Unit (Phen=1,10-Phenanthroline). *Chem. – A Eur. J.* **2017**, *23* (55), 13574–13578.

(84) Schreckenbach, G.; Hay, P. J.; Martin, R. L. Theoretical Study of Stable Trans and Cis Isomers in $[UO_2(OH)_4]^{2-}$ Using Relativistic Density Functional Theory. *Inorg. Chem.* **1998**, *37* (17), 4442–4451.

(85) Mullane, K. C.; Lewis, A. J.; Yin, H.; Carroll, P. J.; Schelter, E. J. Anomalous One-Electron Processes in the Chemistry of Uranium Nitrogen Multiple Bonds. *Inorg. Chem.* **2014**, *53* (17), 9129–9139.

(86) Silver, M. A.; Dorfner, W. L.; Cary, S. K.; Cross, J. N.; Lin, J.; Schelter, E. J.; Albrecht-Schmitt, T. E. Why Is Uranyl Formohydroxamate Red? *Inorg. Chem.* **2015**, *54* (11), 5280–5284.

(87) Bühl, M.; Schreckenbach, G. Oxygen Exchange in Uranyl Hydroxide via Two "Nonclassical" Ions. *Inorg. Chem.* **2010**, *49* (8), 3821–3827.

(88) Fortier, S.; Hayton, T. W. Oxo Ligand Functionalization in the Uranyl Ion (UO_2^{2+}). *Coord. Chem. Rev.* **2010**, *254* (3), 197–214.

(89) Clark, D. L.; Conradson, S. D.; Donohoe, R. J.; Keogh, D. W.; Morris, D. E.; Palmer, P. D.; Rogers, R. D.; Tait, C. D. Chemical Speciation of the Uranyl Ion under Highly Alkaline Conditions. Synthesis, Structures, and Oxo Ligand Exchange Dynamics. *Inorg. Chem.* **1999**, *38* (7), 1456–1466.

(90) McGlynn, S. P.; Smith, J. K.; Neely, W. C. Electronic Structure, Spectra, and Magnetic Properties of Oxycations. III. Ligation Effects on the Infrared Spectrum of the Uranyl Ion. *J. Chem. Phys.* **1961**, *35* (1), 105–116.

(91) Moskaleva, L. V; Nasluzov, V. A.; Rösch, N. Modeling Adsorption of the Uranyl Dication on the Hydroxylated α-Al_2O_3(0001) Surface in an Aqueous Medium. Density Functional Study. *Langmuir* **2006**, *22* (5), 2141–2145.

(92) Pan, Q.-J.; Odoh, S. O.; Asaduzzaman, A. M.; Schreckenbach, G. Adsorption of Uranyl Species onto the Rutile (110) Surface: A Periodic DFT Study. *Chem. – A Eur. J.* **2012**, *18* (5), 1458–1466.

(93) Geckeis, H.; Lützenkirchen, J.; Polly, R.; Rabung, T.; Schmidt, M. Mineral–Water Interface Reactions of Actinides. *Chem. Rev.* **2013**, *113* (2), 1016–1062.

(94) Hattori, T.; Saito, T.; Ishida, K.; Scheinost, A. C.; Tsuneda, T.; Nagasaki, S.; Tanaka, S. The Structure of Monomeric and Dimeric Uranyl Adsorption Complexes on Gibbsite: A Combined DFT and EXAFS Study. *Geochim. Cosmochim. Acta* **2009**, *73* (20), 5975–5988.

(95) Sessler, J. L.; Vivian, A. E.; Seidel, D.; Burrell, A. K.; Hoehner, M.; Mody, T. D.; Gebauer, A.; Weghorn, S. J.; Lynch, V. Actinide Expanded Porphyrin Complexes. *Coord. Chem. Rev.* **2001**, *216–217*, 411–434.

(96) Duval, P. B.; Burns, C. J.; Clark, D. L.; Morris, D. E.; Scott, B. L.; Thompson, J. D.; Werkema, E. L.; Jia, L.; Andersen, R. A. Synthesis and Structural Characterization of the First Uranium Cluster Containing an Isopolyoxometalate Core. *Angew. Chemie Int. Ed.* **2001**, *40* (18), 3357–3361.

(97) Cantat, T.; Graves, C. R.; Scott, B. L.; Kiplinger, J. L. Challenging the Metallocene Dominance in Actinide Chemistry with a Soft PNP Pincer Ligand: New Uranium Structures and Reactivity Patterns. *Angew. Chem. Int. Ed.* **2009**, *48* (xx), 3681–3684.

(98) Williams, K. H.; Bargar, J. R.; Lloyd, J. R.; Lovley, D. R. Bioremediation of Uranium-Contaminated Groundwater: A Systems Approach to Subsurface Biogeochemistry. *Curr. Opin. Biotechnol.* **2013**, *24* (3), 489–497.

(99) Noubactep, C.; Meinrath, G.; Dietrich, P.; Merkel, B. Mitigating Uranium in Groundwater: Prospects and Limitations. *Environ. Sci. Technol.* **2003**, *37* (18), 4304–4308.

(100) Hu, S.-X.; Jian, J.; Li, J.; Gibson, J. K. Destruction of the Uranyl Moiety in a U(V) "Cation–Cation" Interaction. *Inorg. Chem.* **2019**, *58* (15), 10148–10159.

(101) Duval, P. B.; Burns, C. J.; Buschmann, W. E.; Clark, D. L.; Morris, D. E.; Scott, B. L. Reaction of the Uranyl(VI) Ion (UO_2^{2+}) with a Triamidoamine Ligand: Preparation and Structural Characterization of a Mixed-Valent Uranium(V/VI) Oxo-Imido Dimer. *Inorg. Chem.* **2001**, *40*, 5491.

(102) Arnold, P. L.; Patel, D.; Wilson, C.; Love, J. B. Reduction and Selective Oxo Group Silylation of the Uranyl Dication. *Nature* **2008**, *451*, 315.

(103) Berthet, J.-C.; Siffredi, G.; Thuéry, P.; Ephritikhine, M. Controlled Chemical Reduction of Uranyl Salts into $UX_4(MeCN)_4$ (X = Cl, Br, I) with Me_3SiX Reagents. *Eur. J. Inorg. Chem.* **2007**, *2007* (25), 4017–4020.

(104) Arnold, P. L.; Hollis, E.; Nichol, G. S.; Love, J. B.; Griveau, J.-C.; Caciuffo, R.; Magnani, N.; Maron, L.; Castro, L.; Yahia, A.; Odoh, S. O.; Schreckenbach, G. Oxo-Functionalization and Reduction of the Uranyl Ion through Lanthanide-Element Bond Homolysis: Synthetic, Structural, and Bonding Analysis of a Series of Singly Reduced Uranyl–Rare Earth 5f1-4fn Complexes. *J. Am. Chem. Soc.* **2013**, *135* (10), 3841–3854.

(105) Pedrick, E. A.; Wu, G.; Hayton, T. W. Oxo Ligand Substitution in a Cationic Uranyl Complex: Synergistic Interaction of an Electrophile and a Reductant. *Inorg. Chem.* **2015**, *54* (14), 7038–7044.

(106) Arnold, P. L.; Jones, G. M.; Odoh, S. O.; Schreckenbach, G.; Magnani, N.; Love, J. B. Strongly Coupled Binuclear Uranium–Oxo Complexes from Uranyl Oxo Rearrangement and Reductive Silylation. *Nat. Chem.* **2012**, *4*, 221.

(107) Pedrick, E. A.; Wu, G.; Kaltsoyannis, N.; Hayton, T. W. Reductive Silylation of a Uranyl Dibenzoylmethanate Complex: An Example of Controlled Uranyl Oxo Ligand Cleavage. *Chem. Sci.* **2014**, *5*, 3204–3213.

(108) Pedrick, E. A.; Wu, G.; Hayton, T. W. Reductive Silylation of the Uranyl Ion with Ph_3SiOTf. *Inorg. Chem.* **2014**, *53* (23), 12237–12239.

(109) Kiernicki, J. J.; Cladis, D. P.; Fanwick, P. E.; Zeller, M.; Bart, S. C. Synthesis, Characterization, and Stoichiometric U–O Bond Scission in Uranyl Species Supported by Pyridine(Diimine) Ligand Radicals. *J. Am. Chem. Soc.* **2015**, *137* (34), 11115–11125.

(110) Brown, J. L.; Mokhtarzadeh, C. C.; Lever, J. M.; Wu, G.; Hayton, T. W. Facile Reduction of a Uranyl(VI) β-Ketoiminate Complex to U(IV) Upon Oxo Silylation. *Inorg. Chem.* **2011**, *50* (11), 5105–5112.

(111) Arnold, P. L.; Pecharman, A.-F.; Hollis, E.; Yahia, A.; Maron, L.; Parsons, S.; Love, J. B. Uranyl Oxo Activation and Functionalization by Metal Cation Coordination. *Nat. Chem.* **2010**, *2* (12), 1056–1061.

(112) Schnaars, D. D.; Wu, G.; Hayton, T. W. Borane-Mediated Silylation of a Metal–Oxo Ligand. *Inorg. Chem.* **2011**, *50* (11), 4695–4697.

(113) Schnaars, D. D.; Wu, G.; Hayton, T. W. Silylation of the Uranyl Ion Using $B(C_6F_5)_3$-Activated Et_3SiH. *Inorg. Chem.* **2011**, *50* (19), 9642–9649.

(114) Kiernicki, J. J.; Zeller, M.; Bart, S. C. Facile Reductive Silylation of UO_2^{2+} to

Uranium(IV) Chloride. *Angew. Chemie Int. Ed.* **2017**, *56* (4), 1097–1100.

(115) Kiernicki, J. J.; Harwood, J. S.; Fanwick, P. E.; Bart, S. C. Reductive Silylation of Cp*UO_2(^{Mes}PDI^{Me}) Promoted by Lewis Bases. *Dalt. Trans.* **2016**, *45* (7), 3111–3119.

(116) Coughlin, E.; Bart, S. C. Reductive Silylation of Uranyl Mediated by Iminosemiquinone Ligands. *Polyhedron* **2019**, *170*, 783–787.

(117) Faizova, R.; Fadaei-Tirani, F.; Bernier-Latmani, R.; Mazzanti, M. Ligand-Supported Facile Conversion of Uranyl(VI) into Uranium(IV) in Organic and Aqueous Media. *Angew. Chemie Int. Ed.* **2020**, *59* (17), 6756–6759.

(118) Zegke, M.; Zhang, X.; Pidchenko, I.; Hlina, J. A.; Lord, R. M.; Purkis, J.; Nichol, G. S.; Magnani, N.; Schreckenbach, G.; Vitova, T.; Love, J. B.; Arnold, P. L. Differential Uranyl(v) Oxo-Group Bonding between the Uranium and Metal Cations from Groups 1, 2, 4, and 12; a High Energy Resolution X-Ray Absorption, Computational, and Synthetic Study. *Chem. Sci.* **2019**, *10* (42), 9740–9751.

(119) Arnold, P. L.; Hollis, E.; White, F. J.; Magnani, N.; Caciuffo, R.; Love, J. B. Single-Electron Uranyl Reduction by a Rare-Earth Cation. *Angew. Chemie Int. Ed.* **2011**, *50* (4), 887–890.

(120) Burns, C. J.; Sattelberger, A. P. Uranium(VI) Oxo-Alkoxide Cluster Synthesis via Ligand Redistribution. *Inorg. Chem.* **1988**, *27* (21), 3692–3693.

(121) Barnhart, D. M.; Burns, C. J.; Sauer, N. N.; Watkin, J. G. Synthesis of Neutral and Anionic Uranyl Aryloxide Complexes from Uranyl Amide Precursors: X-Ray Crystal Structures of UO_2(O-2,6-i-$Pr_2C_6H_3$)$_2$(Py)$_3$ and [Na(THF)$_3$]$_2$[UO_2(O-2,6-$Me_2C_6H_3$)$_4$]. *Inorg. Chem.* **1995**, *34*, 4079–4084.

(122) Bradley, D.; Mehrotra, R. C.; Rothwell, I.; Singh, A. *Alkoxo and Aryloxo Derivatives of Metals*; Elsevier, 2001.

(123) Bradley, D. C.; Chatterjee, A. K.; Chatterjee, A. K. Sexavalent Compounds of Uranium—I Uranyl Alkoxides and Uranium Hexa-Alkoxides. *J. Inorg. Nucl. Chem.* **1959**, *12*, 71.

(124) Wilkerson, M. P.; Burns, C. J.; Dewey, H. J.; Martin, J. M.; Morris, D. E.; Paine, R. T.; Scott, B. L. Basicity of Uranyl Oxo Ligands upon Coordination of Alkoxides. *Inorg. Chem.* **2000**, *39* (23), 5277–5285.

Chapter 2. Synthesis of a Terminal Ce(IV) Oxo Complex by Photolysis of a Ce(III) Nitrate Complex

Portions of this work were published in:

Assefa, M.K.; Wu, G; Hayton, T.W. *Chem. Sci.* **2017**, *8*, 7873-7878.

2.1 Introduction

Given their highly reactive nature, all cerium oxo complexes isolated thus far have utilized external non-covalent interactions to instill stability to the Ce=O functional group. For example, the Ce=O bond in the first reported cerium oxo complex $[(L_{OEt})_2Ce(O)(H_2O)]\cdot MeC(O)NH_2$ (L_{OEt} = $CpCo\{P(O)(OEt)_2\}_3$) is stabilized by hydrogen bonding to an acetamide solvent molecule.[1] Similarly, the oxo ligands in the subsequently reported cerium oxos [Li(12-crown-4)][$(NN'_3)Ce(O)$] (NN'_3 = $N(CH_2CH_2NR)_3$, R = Si^tBuMe_2), and $[(TriNOx)\{Ce(O)\}Rb]_4$, are stabilized by their interactions with a capping alkali metal counterion.[2-3] The prevalence of these non-covalent interactions can be rationalized by the poor overlap of the metal f and d orbitals with oxygen 2p orbitals, which results in weak π bonds within the Ce=O fragment, concomitant with considerable oxo nucleophilicty.[4-7] Indeed, controlling this nucleophilic character has been one of the key challenges to synthesizing a terminal lanthanide oxo complex.[1]

The unique redox chemistry of the lanthanides also poses a barrier for the synthesis of lanthanide oxo complexes. In particular, cerium redox chemistry is dominated by the Ce(III/IV) redox couple, and thus formation of a Ce(IV) oxo complex from a Ce(III) precursor essentially mandates a $1e^-$ O-atom transfer process. However, traditional O-atom transfer reagents, such as N_2O, pyridine-*N*-oxide, and peroxyacids, are $2e^-$ oxidants.[8] Gratifyingly, nitrate has been previously demonstrated to act as a $1e^-$ O-atom transfer reagent. For example, in the recent synthesis of [Li(12-crown-4)][$(NN'_3)Ce(O)$] by Hayton *et al.*, the oxo ligand was formed via thermal reduction of a nitrate ligand, via a formal $1e^-$ O-atom transfer (Scheme 2.1). Several other examples demonstrating the use of nitrate as a $1e^-$ O-atom source have emerged in recent years,[9-12] suggesting that $[NO_3]^-$ could be a valuable reagent for the generation of f-

element oxo complexes. This mode of reactivity can also be promoted with light. For example, Berry and co-workers demonstrated that photolysis of $Ru_2(chp)_4(NO_3)$ (chp = 6-chloro-2-hydroxypyridinate) generated a metal oxo with concomitant release of NO_2.[9] Similarly, Suslick and co-workers reported that photolysis of $Mn(TPP)(NO_3)$ also resulted in metal oxo generation and release of NO_2.[11] However, it should be noted that in both of these examples the resulting metal oxo was unstable and not isolated.

Scheme 2.1. Synthesis of [Li(12-crown-4)][(NN′$_3$)Ce(O)] (scheme adopted from Ref 2)

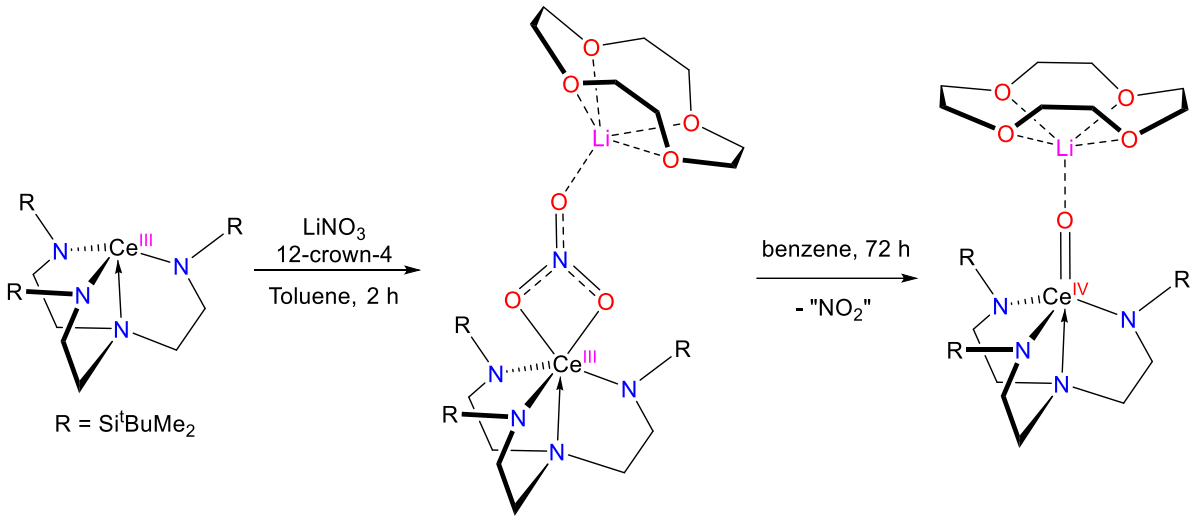

Drawing on these results, I endeavored to further develop of the use of $[NO_3]^-$ as an O-atom source for the synthesis of f-element oxo complexes. Building upon the method employed for the synthesis of [Li(12-crown-4)][(NN′$_3$)Ce(O)] - which features a partially encapsulated Li cation coordinated to the Ce=O fragment - a stronger lithium ion-encapsulating reagent that facilitates the generation of an outer-sphere alkali counterion was sought for the synthesis of a terminal Ce(IV) oxo complex lacking non-covalent Li-oxo interactions. Conveniently, Mauro *et al.* have previously reported that $[Li(2,2,2\text{-cryptand})]^+$ exhibits a formation constant (K_f) value that is three orders of magnitude higher than that for $[Li(12\text{-crown-4})]^+$ in MeCN

solutions at 25 °C,[13-14] suggesting that 2,2,2-cryptand may be used for full encapsulation of Li cations. Herein I describe the utility 2,2,2-cryptand for the generation of the first terminal Ce(IV) oxo complex via photochemical cleavage of nitrate in a Ce(III) "ate" precursor.

2.2 Results and Discussion

2.2.1 Synthesis and Characterization of [Li(2,2,2-cryptand)][Ce(κ^2-O_2NO)(NR_2)$_3$] (2.1)

Synthesis of the Ce(III) nitrate precursor was attempted by reaction of [Ce(NR_2)$_3$] (R = $SiMe_3$) with $LiNO_3$ in THF, in the presence of 2,2,2-cryptand, which resulted in the formation of the Ce(III) "ate" complex, [Li(2,2,2-cryptand)][Ce(κ^2-O_2NO)(NR_2)$_3$] (**2.1**) (eq 2.1). This material can be isolated as a yellow crystalline solid in 38% yield after crystallization from a concentrated Et_2O solution layered with hexanes. The ^{1}H NMR spectrum of **2.1** in py-d_5 displays a broad singlet at -1.32 ppm, assignable to the $SiMe_3$ environment, and three resonances at 2.48, 3.45 and 3.51 ppm, assignable to the cryptand moiety. The chemical shift of the methyl resonance, along with its broad appearance, support the presence of a paramagnetic Ce(III) center in this complex. Similarly, the ^{7}Li{^{1}H} NMR spectrum reveals a broad resonance at -1.08 ppm, indicative of a single lithium environment.

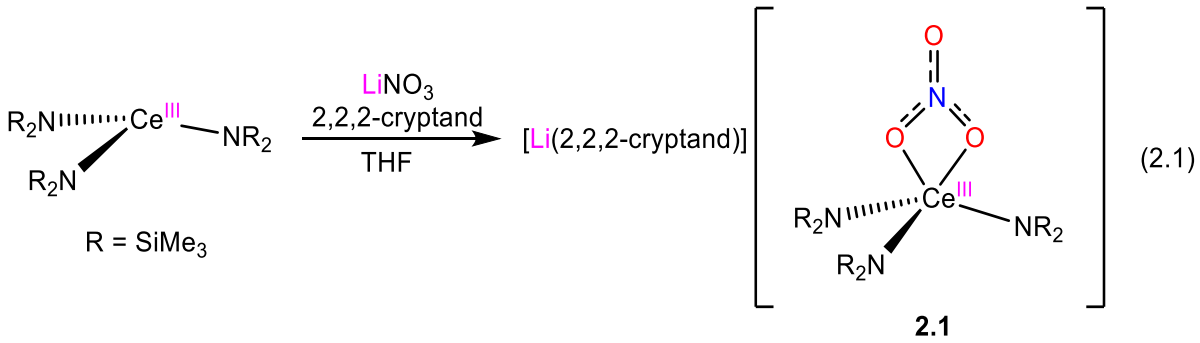

Complex **2.1** crystallizes in the monoclinic space group $P2_1/c$ and its solid-state molecular structure is shown in Figure 2.1. The structure of **2.1** reveals a pentacoordinate Ce(III) center that contains a κ^2 nitrate ligand and three monoanionic $N(SiMe_3)_2$ co-ligands within its coordination sphere. Notably, the Ce-O distances in **2.1** (2.653(2) and 2.562(2) Å) are shorter than those observed for the cerium(III) nitrate TREN complex [Li(12-crown-4)][$(NN'_3)Ce(NO_3)$] (2.724(6) and 2.745(6) Å),[2] likely because of the bulkier TREN ligand in the latter and the absence of Li-O interactions in the former. However, the Ce-N distances in **2.1** (2.367(2)-2.398(2) Å) are comparable to those reported for other Ce(III) amido complexes such as $Ce(TMP)_3(THF)$ (TMP = 2,2,6,6-tetramethylpiperidinato) (2.346(2)-2.374(2) Å) and [Li(THF)][$Ce(NCy_2)_4$] (2.320(2)–2.330(2) Å).[15-16] The structure of **2.1** also features an outer-sphere $[Li(2,2,2\text{-cryptand})]^+$ counter-ion, wherein five of the eight donor atoms in the cryptand moiety are bound to the lithium; two nitrogen atoms and one oxygen atom remain uncoordinated. Similar binding modes have been observed in other $[Li(2,2,2\text{-cryptand})]^+$ complexes.[17-20]

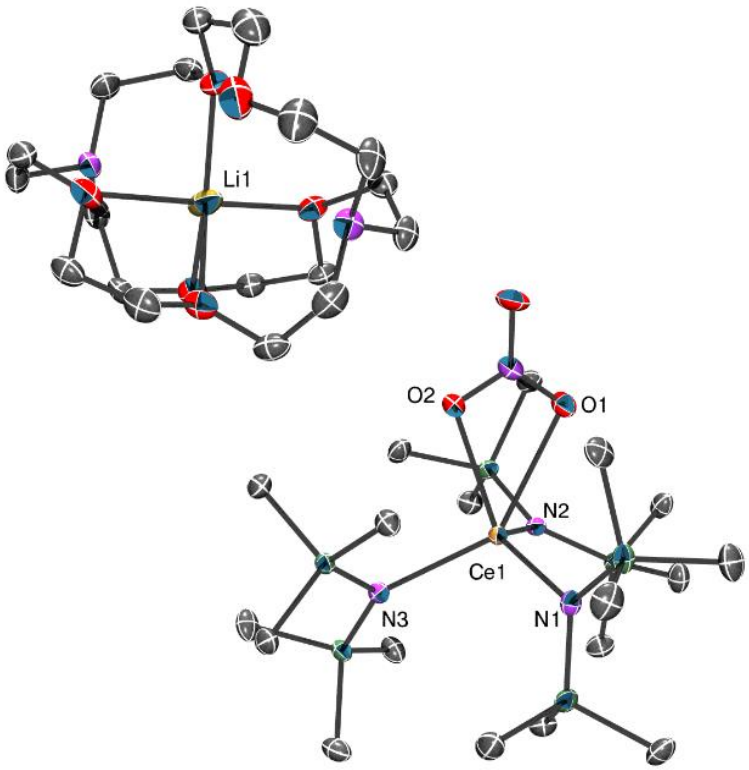

Figure 2.1. ORTEP diagram of **2.1** shown with 50% probability ellipsoids. Hydrogen atoms are omitted for clarity. Selected bond distances (Å) and angles (°): Ce1-O1 = 2.653(2), Ce1-O2 = 2.562(2), Ce1-N1 = 2.385(3), Ce1-N2 = 2.367(2), Ce1-N3 = 2.398(2), N2-Ce1-N1 = 121.01(8), N2-Ce1-N3 = 112.82(8), N1-Ce1-N3 = 101.96(9).

2.2.2 Thermal and Photochemical Reactivity of 2.1

With complex **2.1** in hand, I explored its thermal and photochemical reactivity for the generation of a terminal Ce(IV) oxo complex. Thus, a py-d_5 solution of **2.1** was stored at room temperature in the absence of light and monitored by ^{1}H NMR spectroscopy. Interestingly, the ^{1}H NMR spectrum revealed that ~80% of this sample still consisted of complex **2.1** after 24 h. The remaining components of the mixture are revealed by resonances at 0.69, 0.20, and -0.58 ppm (Figure A2.9), and were later identified as belonging to [Li(2,2,2-

cryptand)][Ce(O)(NR_2)$_3$] (**2.2**), [Li(2,2,2-cryptand)]$_2$[(μ_3-O){Ce(μ-O)(NR_2)$_2$}$_3$] (**2.3**), and [Li(2,2,2-cryptand)][Ce($OSiMe_3$)(NR_2)$_3$] (**2.4**), respectively (*vide infra*). These three complexes were present in a relative ratio of 2:27:1. This result stands in stark contrast to that observed for [Li(12-crown-4)][(NN′$_3$)Ce(NO_3)], which is completely consumed upon standing at room temperature for 72 h. Thus, the relatively high thermal stability of **2.1** suggests that formation of a terminal Ce(IV) oxo complex through thermal activation of the nitrate co-ligand in **2.1** is not synthetically viable.

Given the relatively high thermal stability of **2.1**, I sought a photolytic route to activate its nitrate co-ligand. Gratifyingly, Schelter and co-workers have previously reported that photolysis of [Ce(NR_2)$_3$] resulted in formation of a relatively long-lived excited state,[21] that is strongly reducing and elicits reduction of $PhCH_2Cl$ to bibenzyl.[22] Drawing inspiration from their results, I recorded the UV-vis spectrum of **2.1**, which revealed two absorptions at 380 nm (ε = 200 $M^{-1}\cdot cm^{-1}$) and 336 nm (ε = 140 $M^{-1}\cdot cm^{-1}$) (Figure 2.2). The former transition is assignable to a metal-based 4f$\rightarrow$5d_z^2 transition, while the latter is assignable to a 4f$\rightarrow$5$d_{xz/yz}$ transition, by analogy with the assignments reported for [Ce(NR_2)$_3$]. For comparison, the corresponding transitions for [Ce(NR_2)$_3$] occur at 413 nm and 341 nm, respectively.[22] The ca. 30 nm blue shift observed for the 4f$\rightarrow$5d_z^2 transition in **2.1** is likely due to the presence of the additional nitrate co-ligand, as well as its overall negative charge.

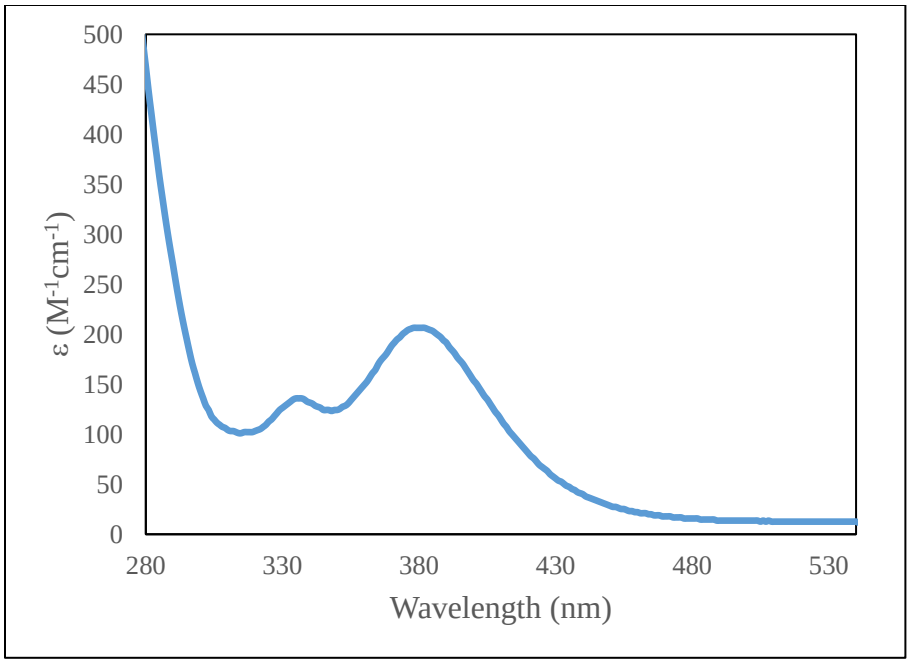

Figure 2.2. UV-Vis spectrum of **2.1** in Et_2O (0.95 mM).

Given the similar optical properties of **2.1** and [$Ce(NR_2)_3$], I hypothesized that photolysis of **2.1** would induce reduction of the nitrate ligand to afford a terminal Ce(IV) oxo complex. Thus, a 2:1 tol-d_8/py-d_5 solution of **2.1** in a J-Young NMR tube was exposed to 380 nm LED light for 6 h at -5 °C (Figure 2.3). A ^{1}H NMR spectrum of this sample revealed an approximately 80% consumption of **2.1**, as evidenced by integration of its $SiMe_3$ resonance relative to the NCH_2 resonance of the 2,2,2-cryptand moiety. In addition, the appearance of a sharp singlet at 0.80 ppm, and broad singlets at 0.28, -0.21, and -0.43 ppm was observed (Figure A2.8). I have assigned the sharp singlet at 0.80 ppm to the terminal Ce(IV) oxo complex [Li(2,2,2-cryptand)][$Ce(O)(NR_2)_3$] (**2.2**), while I have tentatively assigned the resonance at 0.28 ppm to the Ce(IV) oxo cluster [Li(2,2,2-cryptand)]$_2$[(μ_3-O){Ce(μ-O)$(NR_2)_2$}$_3$] (**2.3**). In addition, the resonances at -0.21 and -0.43 ppm, which integrate to 9 and 54 protons, respectively, are assignable to the Ce(III) silyloxide [Li(2,2,2-

cryptand)][Ce(OSiMe$_3$)(NR$_2$)$_3$] (**2.4**). After 6 h of photolysis, these three species were present in an approximately 11:2.5:1 ratio, according to NMR spectroscopy. Interestingly, large scale photolysis reactions, as well as photolyses for longer times resulted in decreased yields of **2.2**. The use of the 2:1 tol-d_8/py-d_5 solvent system was also critical to maximize the amount of **2.2** formed in the reaction mixture. For example, photolyses performed in neat py-d_5 resulted in formation of complexes **2.2** and **2.3** in nearly equal amounts, suggesting that complex **2.3** is likely the thermodynamic sink of the reaction. Moreover, photolyses performed in neat tol-d_8 proved impractical because of the low solubility of complex **2.1** in that solvent. Finally, photolyses conducted in NMR tubes resulted in the most efficient consumption of **2.1**, likely due to their high surface-to-volume ratio (which made photolysis more efficient).

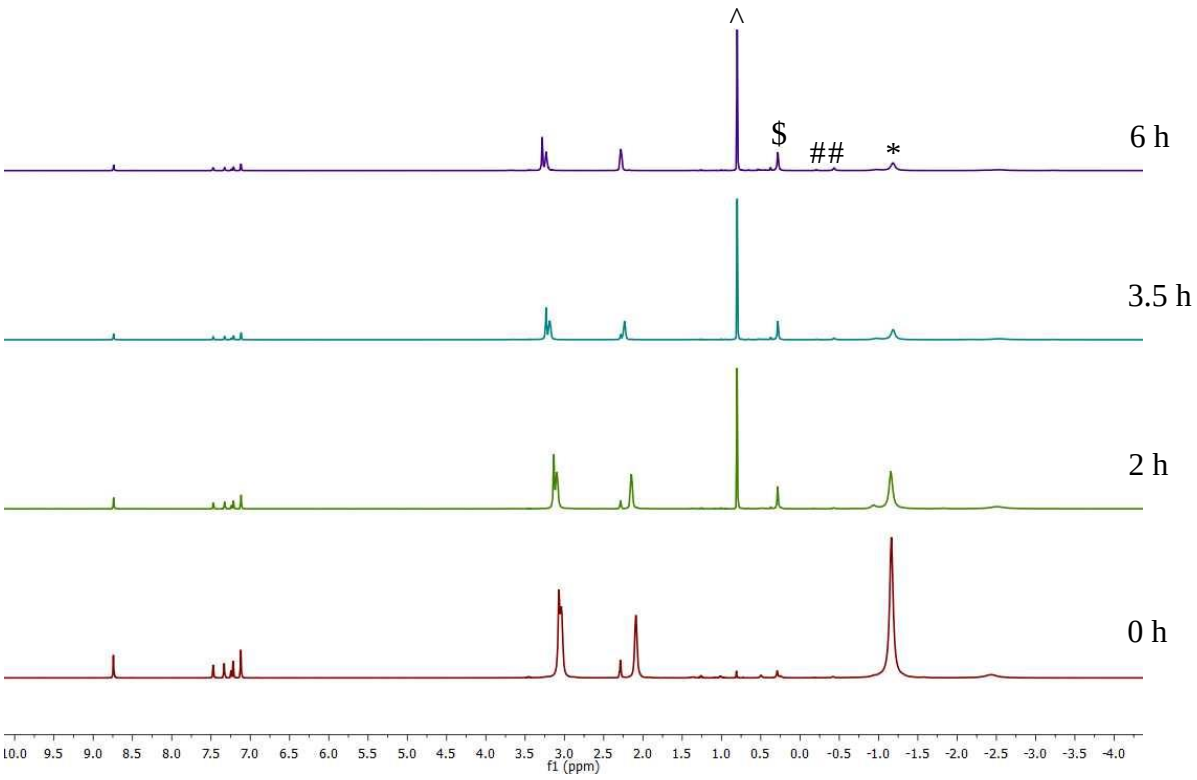

Figure 2.3. ^{1}H NMR spectrum of the photolysis of **2.1** in 2:1 tol-d_8/py-d_5. * indicates the presence of **2.1**. ^ indicates the presence of **2.2**. $ indicates the presence of **2.3**. # indicates the presence of **2.4**.

As mentioned above, work-up of small-scale photolysis reactions afforded complex **2.2** as yellow plates in the highest isolated yield (33%). However, pure samples of complex **2.2** can be isolated in bulk by photolyses of multiple small-scale reactions that were combined during work-up. When synthesized via this fashion, complex **2.2** can be isolated in 18% yield. In one instance, I obtained small amounts of pale yellow crystals and colorless plates during crystallization, which were subsequently identified as **2.3** and **2.4**, respectively, by X-ray crystallography.

Scheme 2.2. Synthesis of complexes **2.2**, **2.3**, and **2.4** via photolysis of **2.1**.

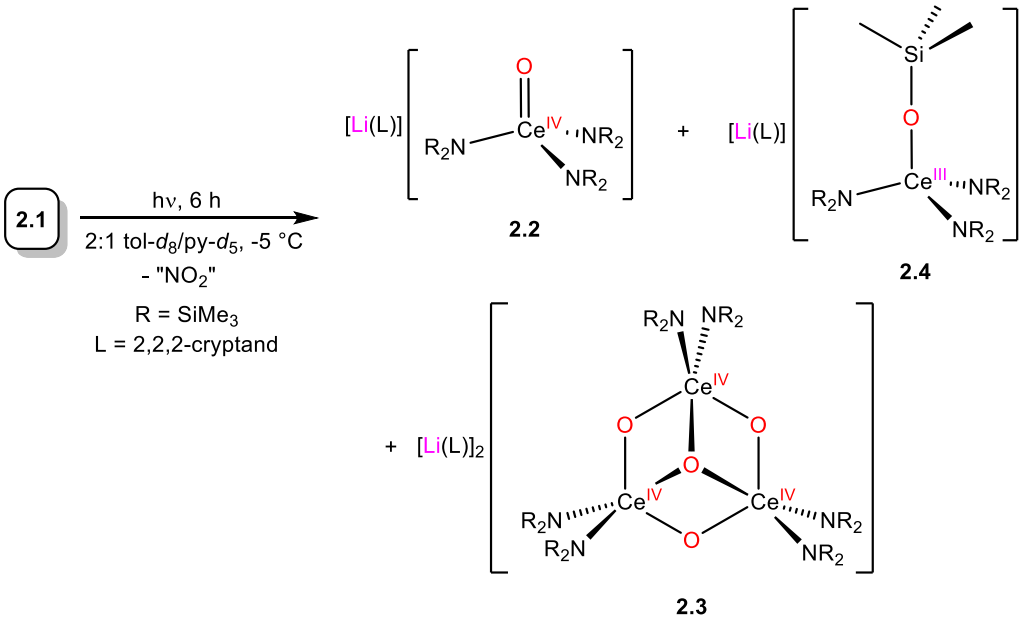

2.2.3 Structural and Spectroscopic Characterization of [Li(2,2,2-cryptand)][Ce(O)(NR_2)$_3$] (2.2), [Li(2,2,2-cryptand)]$_2$[(μ_3-O){Ce(μ-O)(NR_2)$_2$}$_3$] (2.3) and [Li(2,2,2-cryptand)][Ce($OSiMe_3$)(NR_2)$_3$] (2.4)

Complex **2.2** crystallizes in the monoclinic space group $P2_1/c$ (Figure 2.4). The solid-state molecular structure of **2.2** reveals a pseudo-tetrahedral cerium center featuring a terminal, non-bridging Ce=O linkage. The Li counter-ion in **2.2** is fully encapsulated by the 2,2,2-cryptand moiety, prohibiting any Li-oxo interaction, and rendering **2.2** a separated cation-anion pair. In particular, six of the eight donor atoms in the cryptand moiety are bound to the lithium ion; one nitrogen atom and one oxygen atom remain uncoordinated. Importantly, the Ce-O bond length in **2.2** (1.840(7) Å) is the shortest reported to date, indicating formal Ce=O multiple bond character. For example, the Ce-O distances observed for [Li(12-crown-4)][(NN'_3)Ce(O)] (1.902(2) Å), [(TriNOx){Ce(O)}Rb]$_4$ (1.887(4)–1.902(4) Å), and [M]$_2$[Ce(μ-O)(NR_2)$_3$]$_2$ (M = Na, K; R = $SiMe_3$), (1.908(3) Å),[2-4] are somewhat longer, likely due to the presence of alkali metal-oxo interactions in their structures.[2-3] Consistent with this hypothesis, the potassium analogue of complex **2.2**, [K(18-crown-6)][Ce(O)(NR_2)$_3$], which also features an alkali metal-oxo interaction, was previously calculated to exhibit a slightly longer Ce-O distance at 1.904 Å.[2] Interestingly, the Ce-O distance in **2.2** is very similar to that observed for hydrogen-bond stabilized [(L_{OEt})$_2$Ce(O)(H_2O)]·$MeC(O)NH_2$ (1.857(3) Å),[1] suggesting that the hydrogen bonding interaction in its structure does not substantially disrupt the Ce=O bond. For further comparison, the Ce-N distances in **2.2** (2.353(8)-2.397(8) Å) are slightly longer than those reported for other Ce(IV) amides. For example, the Ce-N distances in Ce(NCy_2)$_4$ range from 2.238(5) to 2.247(6) Å, while those of [Ce(X)(NR_2)$_3$] (X = Cl, Br) are 2.217(3) and 2.219(7) Å, respectively.[16, 23-24] This lengthening may be a consequence of the strongly donating nature

of the oxo ligand, along with the complex's overall negative charge. In line with this observation, [Li(12-crown-4)][(NN′$_3$)Ce(O)] also features longer than expected Ce-N distances.[2]

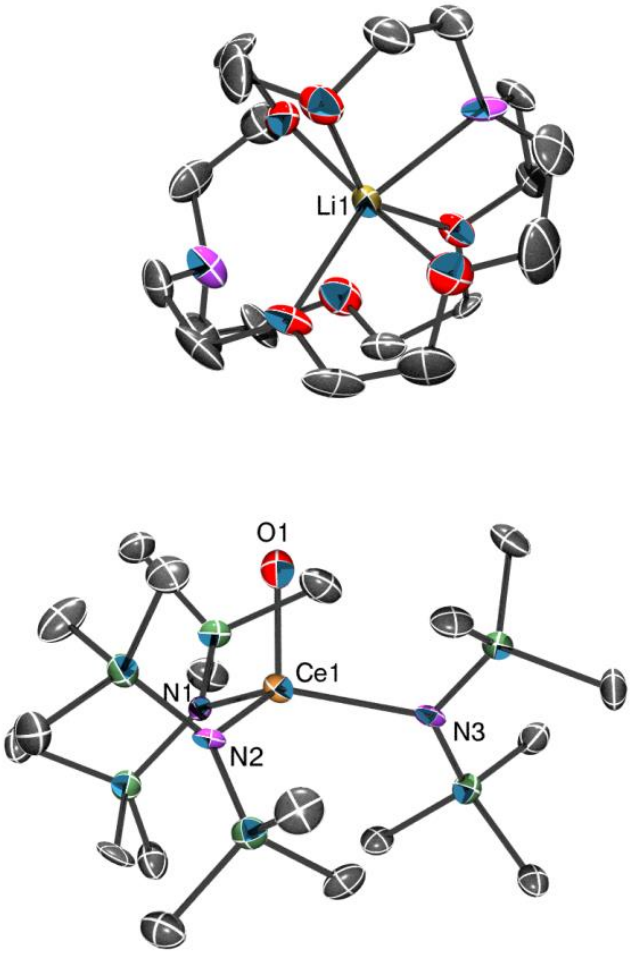

Figure 2.4. ORTEP diagram of **2.2** shown with 50% probability ellipsoids. Hydrogen atoms are omitted for clarity. Selected bond distances (Å) and angles (°): Ce1-O1 = 1.840(7), Ce1-N1 = 2.397(8), Ce1-N2 = 2.353(8), Ce1-N3 = 2.383(8), N2-Ce1-N1 = 116.4(3), N3-Ce1-N1 = 113.4(3), N2-Ce1-N3 = 116.8(3), O1-Ce1-N1 = 103.9(3), O1-Ce1-N2 = 101.7(3), O1-Ce1-N3 = 101.5(3).

Complex **2.2** is soluble in toluene, Et_2O, benzene, and pyridine, but decomposes in THF, acetonitrile, and dichloromethane (forming $HN(SiMe_3)_2$ as the only identifiable product). It also features moderate thermally sensitivity in 2:1 tol-d_8/py-d_5, according to ^{1}H NMR spectroscopy. For example, a solution of **2.2** in 2:1 tol-d_8/py-d_5 stored at room temperature for 4 d decomposes to a mixture of **2.3**, **2.4**, and $LiN(SiMe_3)_2$ (along with other unidentified products) with about 70% conversion, according to integration of the $SiMe_3$ resonance of **2.2** relative to the CHD_2 resonance of tol-d_8 (Figure A2.10). Under these conditions, complexes **2.3** and **2.4** are present in an approximately 3:1 ratio. Finally, the UV-Vis spectrum of **2.2** in Et_2O features a broad absorption at 306 ($\varepsilon = 830\ M^{-1}\cdot cm^{-1}$), which is significantly blue-shifted when compared to that of **2.1**. This blueshift alludes to the relative photochemical stability of **2.2** to the photolysis reaction conditions. Unfortunately, the Raman spectrum of **2.2** did not exhibit obvious features that could definitively be assigned to the Ce=O stretch.

The ^{1}H NMR spectrum of **2.2** in py-d_5 features a sharp singlet at 0.69 ppm integrating to 54 protons that is assignable to the $SiMe_3$ environment. This spectrum also features resonances at 2.56, 3.52, and 3.59 ppm, each integrating to 12 protons, that are assignable to the cryptand moiety. The chemical shift of its $SiMe_3$ resonance is nearly identical to that assigned to this complex in the spectrum of the crude reaction mixture (Figure A2.8). Additionally, the ^{7}Li{^{1}H} NMR spectrum of **2.2** features a broad singlet centered at -1.00 ppm. This chemical shift is in the range previously reported for the Li[2,2,2-cryptand]$^+$ ion.[25-26]

Complex **2.3** crystallizes in triclinic space group P-1 (Figure 2.5), as the Et_2O solvate **2.3**·Et_2O. Its structure consists of a partial cubane Ce_3O_4 core, wherein each Ce center is ligated by two $N(SiMe_3)_2$ co-ligands. Additionally, the structure of **2.3** exhibits two outer-sphere [Li(2,2,2-cryptand)] cations, confirming the tetravalent oxidation state of each cerium atom.

The Ce-O(μ_2-oxo) distances observed for **2.3** (2.071(7) - 2.133(7) Å) are comparable to those reported for the structurally related Ce(IV) oxo cluster, [{(μ-O)Ce(NR_2)$_2$}$_3$].[4] The Ce-O(μ_3-oxo) distances observed in **2.3** are expectedly longer (2.289(7) - 2.310(7) Å), but are similar to those reported for other [Ce_3(μ_3-oxo)] clusters.[27-28] I can rule out the presence of a hydroxo ligand in **2.3** on the basis of its structural data. In particular, the Ce-O distances of μ_2- or μ_3-hydroxo ligands are anticipated to be substantially longer than the Ce-O distances observed for **2.3**.[29-30] Finally, as in **2.2**, the Ce-N distances in **2.3** (2.366(8)-2.415(9) Å) are somewhat longer than those typically reported for Ce(IV) amides.[16, 23-24] Unfortunately, multiple attempts to isolate pure samples of **2.3** in bulk have been unsuccessful, which prevented its complete characterization.

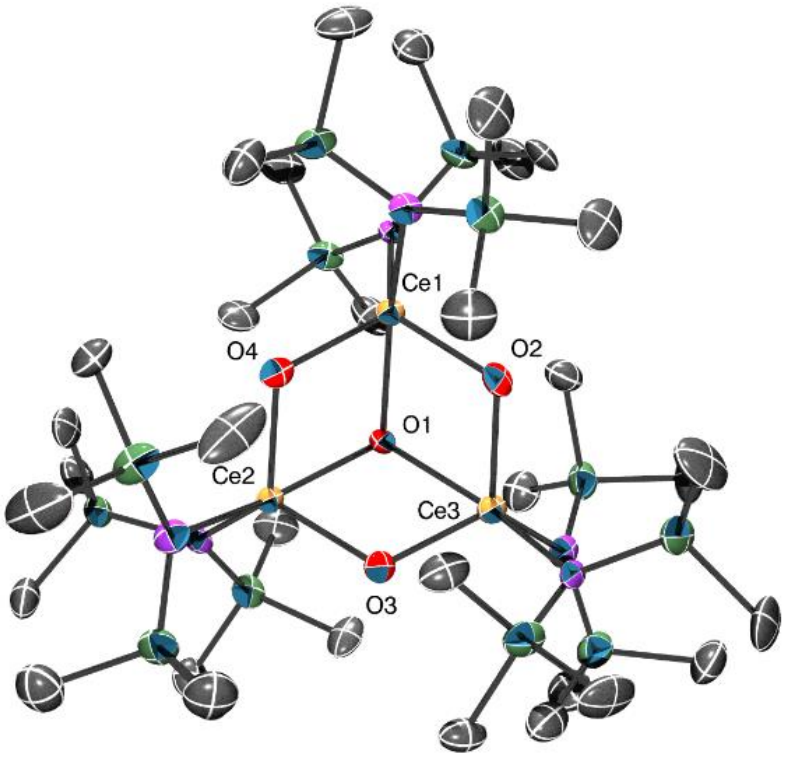

Figure 2.5. ORTEP diagram of **2.3** shown with 50% probability ellipsoids. Hydrogen atoms, diethyl ether solvate and two [Li(2,2,2-crpytand)] counter-ions are omitted for clarity. Selected

bond distances (Å) and angles (°): Ce1-O1 = 2.294(7), Ce1-O2 = 2.078(7), Ce1-O4 = 2.133(7), Ce2-O1 = 2.310(7), Ce2-O3 = 2.109(7), Ce2-O4 = 2.071(7), Ce3-O1 = 2.289(7), Ce3-O2 = 2.130(7), Ce3-O3 = 2.100(7), Ce1-N1 = 2.391(8), Ce1-N2 = 2.366(8), Ce2-N5 = 2.389(8), Ce2-N6 = 2.380(9), Ce3-N3 = 2.386(9), Ce3-N4 = 2.415(9), Ce3-O1-Ce1 = 99.8(3), Ce3-O1-Ce2 = 99.6(3), Ce1-O1-Ce2 = 99.5(3).

Complex **2.4** crystallizes in the monoclinic space group $P2_1/n$ and its solid-state molecular structure is shown in Figure 2.6. The structure of **2.4** consists of a pseudo-tetrahedral Ce(III) center ligated by one silyloxide and three silylamide co-ligands, along with an outer-sphere $[Li(2,2,2\text{-cryptand})]^+$ moiety. The Ce-O bond length in **2.4** (2.214(3) Å) is significantly longer than that found in **2.2** (1.840(7) Å), further supporting the presence of Ce=O multiple bond character in **2.2**. However, this distance is similar to the average $Ce\text{-}O_{SiPh3}$ distance in $Ce(OSiPh_3)_3(THF)_3$ (2.22 Å).[31] Additionally, complex **2.4** exhibits an average Ce-N distance (2.41 Å) that is comparable to that observed for **2.1** (2.38 Å), consistent with its anticipated Ce(III) oxidation state. Finally, the Ce-O-Si bond angle (178.9(2)°) in **2.4** indicates some extent of π bonding within this unit, and is similar to that observed for $Ce(OSiPh_3)_3(THF)_3$ (av. 174°)[31] and $[(NN'_3)Ce(OSiMe_2{}^tBu)]$ (167.2(2)°).[2]

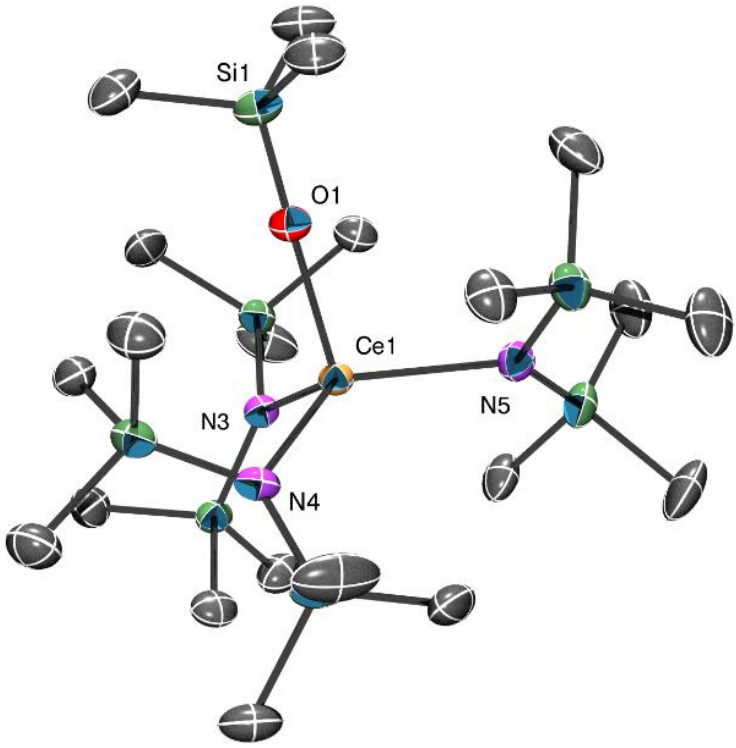

Figure 2.6. ORTEP diagram of **2.4** shown with 50% probability ellipsoids. Hydrogen atoms and [Li(2,2,2-cryptand)] counterion are omitted for clarity. Selected bond distances (Å) and angles (°): Ce1-O1 = 2.214(3), Ce1-N3 = 2.430(4), Ce1-N4 = 2.396(4), Ce1-N5 = 2.413(4), O1-Si1 = 1.607(4), N4-Ce1-N3 = 109.97(13), N4-Ce1-N5 = 117.68(14), N5-Ce1-N3 = 117.42(13), Si1-O1-Ce1 = 178.9(2).

Gratifyingly, the formulation of **2.4** was further confirmed by its independent synthesis and full characterization. Complex **2.4** can be prepared separately via reaction of $[Ce(NR_2)_3]$ with $LiOSiMe_3$ in THF, in the presence of 2,2,2-cryptand (eq 2.2). Synthesized via this route, **2.4** can be isolated as a white solid in 47% yield after work-up.

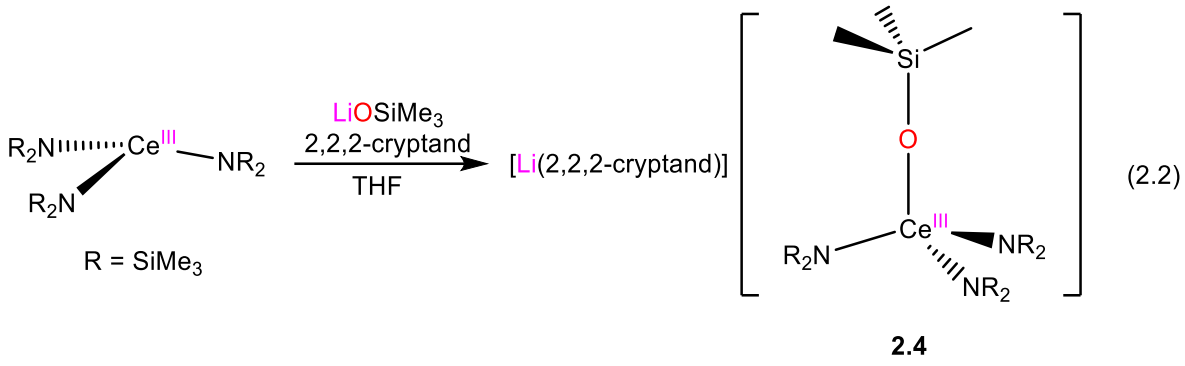

(2.2)

2.4

The ^{1}H NMR spectrum of **2.4** in py-d_5 features two broad singlets at -0.37 and -0.59 ppm, integrating to 9 and 54 protons, respectively. These resonances are assignable to the $OSiMe_3$ and $N(SiMe_3)_2$ methyl environments, respectively. Importantly, these resonances are nearly identical to those assigned to this complex in the spectrum of crude reaction mixture (Figure A2.8). Also observed in the ^{1}H NMR spectrum of **2.4** are resonances at 2.56, 3.52 and 3.60 ppm, each integrating to 12 protons, which are assignable to the cryptand moiety. Finally, its ^{7}Li{^{1}H} NMR spectrum consists of a single resonance at -0.97 ppm.

2.2.4 Mechanistic Considerations for the Formation of 2.2, 2.3 and 2.4

To explain the mechanism of formation of **2.2**, **2.3**, and **2.4**, I propose that photolysis of **2.1** first generates **2.2** and NO_2, via homolytic cleavage of the N-O bond in its nitrate co-ligand (Scheme 2.3). However, **2.2** is thermally unstable and decomposes via (1) ligand scrambling and oligomerization to form **2.3**; and, (2) abstraction of a trimethylsilyl cation to form a transient Ce(IV) silyloxide, $[Ce^{IV}(OSiMe_3)(NR_2)_3]$, followed by 1e$^-$ reduction to form **2.4**. Alternatively, this ligand cannibalization pathway could proceed via direct $\cdot SiMe_3$ abstraction by **2.2** to form **2.4**. To support these hypotheses, I note that complex **2.2** is thermally unstable in 2:1 tol-d_8/py-d_5, and slowly decomposes to form a mixture of **2.3** and **2.4** in a 3:1 relative ratio (Figure A2.10). This ratio is essentially identical to that observed for the two species in

the *in situ* ^{1}H NMR spectrum of photolysis (Figure A2.8), suggesting that their formation is likely a direct result of thermal decomposition of **2.2**. Additionally, there is a minor resonance at 0.53 ppm in the ^{1}H NMR spectrum of the photolysis reaction mixture (Figure A2.8) that is assignable to $LiN(SiMe_3)_2$ – a compound also formed during thermal decomposition of **2.2** (Figure A2.10). Its presence is consistent with the proposed conversion of **2.2** to **2.3** via ligand scrambling and loss of $LiN(SiMe_3)_2$. Finally, Hayton and co-workers have previously demonstrated that the Ce(IV) silyloxide, $[(NN'_3)Ce(OSi^tBuMe_2)]$, was formed as a minor by-product during the conversion of $[Li(12\text{-crown-4})][(NN'_3)Ce(\kappa^2\text{-}O_2NO)]$ to the Ce(IV) oxo, $[Li(12\text{-crown-4})][(NN'_3)Ce(O)]$,[2] presumably via a similar adventitious $[SiR_3]^+$ abstraction.

Scheme 2.3. Proposed mechanism for formation of complexes **2.2**, **2.3**, and **2.4**.

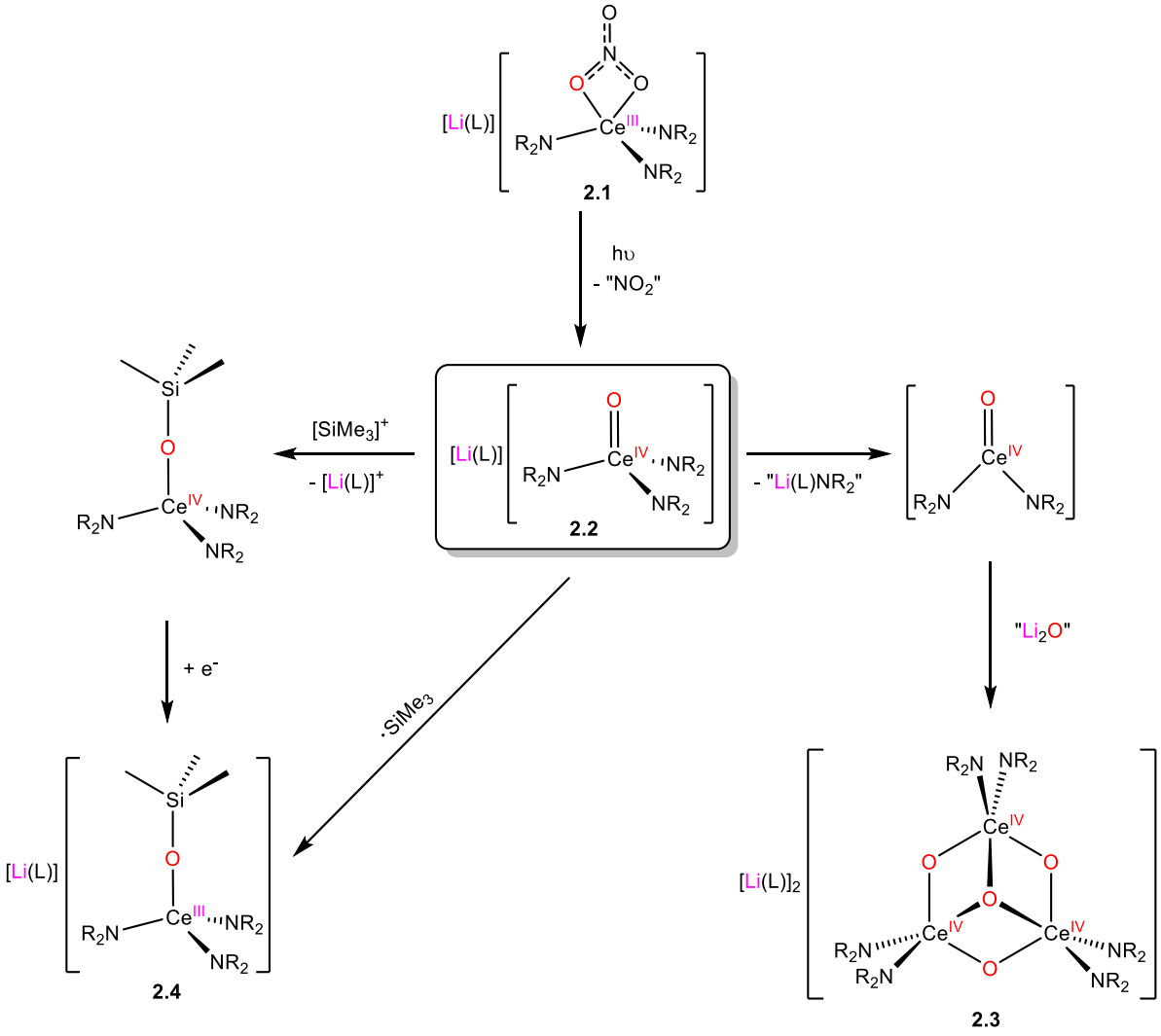

2.2.5 Electrochemistry of 2.4

To determine which ligand cannibalization pathway is operative for the formation of **2.4**, I investigated its electrochemistry by cyclic voltammetry. The cyclic voltammogram of **2.4** in THF features a redox feature centered at -0.53 V at 200 mV/s (vs Fc/Fc^+, Figure 2.7) assignable to the Ce(III/IV) couple. The large difference between the potentials of the anodic and cathodic peaks of this feature (0.72 V at 200 mV/s) is suggestive of an *ECE*-type mechanism. Notably, the potential of this feature is comparable to those previously reported for cerium complexes

with similar ligand frameworks, including [Ce(F)$(NR_2)_3$] (-0.56 V), [Ce(Cl)$(NR_2)_3$] (-0.30 V) and [Ce(Br)$(NR_2)_3$] (-0.31 V),[32-34]. However, its electrochemical irreversibility suggests that the proposed [$Ce^{IV}(OSiMe_3)(NR_2)_3$] intermediate is rather unstable. Therefore, complex **2.4** may not be formed via a straightforward $1e^-$ reduction of a [$Ce^{IV}(OSiMe_3)(NR_2)_3$] intermediate. Instead, the cyclic voltammetry data may be evidence for a concerted $\cdot SiMe_3$ abstraction by **2.2** to form **2.4**. A similar $\cdot SiMe_3$ abstraction by the uranyl fragment has been reported by Arnold and co-workers.[35-37]

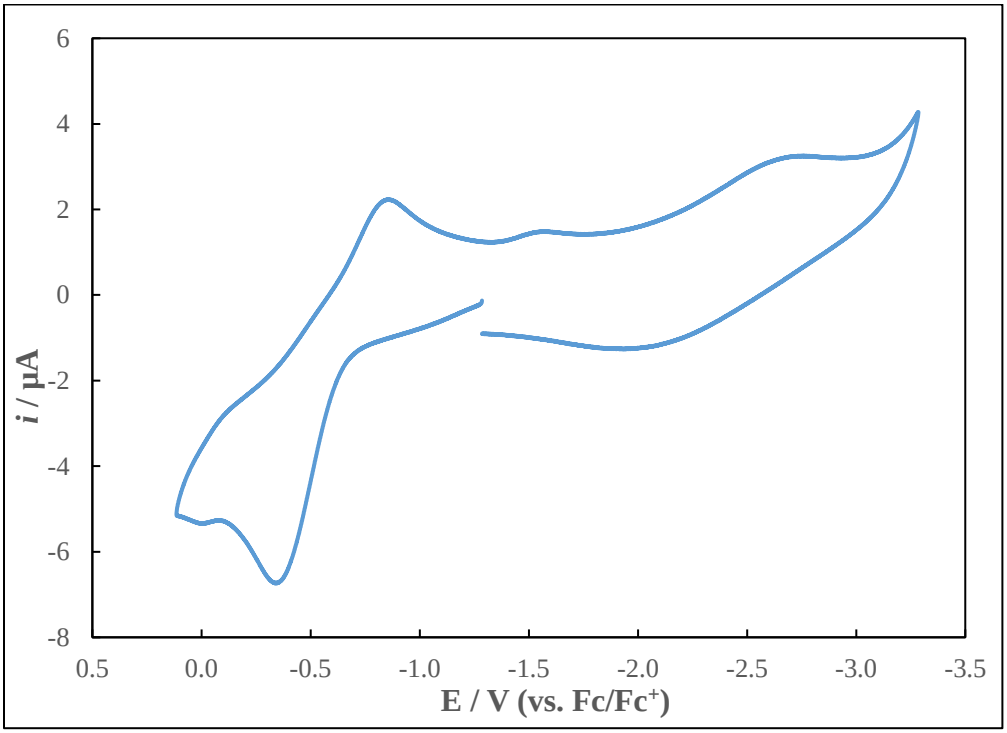

Figure 2.7. Cyclic voltammogram of complex **2.4** (200 mV/s scan rate, vs. Fc/Fc^+). Measured in THF with 0.1 M [NBu_4][PF_6] as the supporting electrolyte.

2.3 Summary

In summary, I report the synthesis of the first lanthanide oxo complex where the oxo ligand is not supported by hydrogen bonding or alkali metal coordination, namely, [Li(2,2,2-

cryptand)][Ce(O)(NR_2)$_3$] (**2.2**). This complex was generated by photochemical cleavage of a nitrate co-ligand in the Ce(III) nitrate precursor [Li(2,2,2-cryptand)][Ce(κ^2-O_2NO)(NR_2)$_3$] (**2.1**). Notably, use of the 2,2,2-cryptand reagent was paramount to generate a non-bridging Ce=O linkage by full encapsulation of the Li counterion in **2.2**. Also formed in the photolysis reaction are the Ce(IV) oxo cluster, [Li(2,2,2-cryptand)]$_2$[(μ_3-O){Ce(μ-O)(NR_2)$_2$}$_3$] (**2.3**), and the Ce(III) silyloxide complex, [Li(2,2,2-cryptand)][Ce($OSiMe_3$)(NR_2)$_3$] (**2.4**), which I believe to be products of thermal decomposition of **2.2** after its initial generation in the reaction mixture. Overall, this work further highlights the utility of $[NO_3]^-$ reduction for the generation of lanthanide oxo complexes. Additionally, I have shown that cerium oxo formation via this method can proceed via both thermal and photochemical routes. Future work will involve attempts to synthesize a Ln(III) oxo complex via $1e^-$ O-atom transfer from $[NO_3]^-$. This is anticipated to be a greater challenge because the lower Ln oxidation state results in reduced Ln-O bond covalency.[38]

2.4 Experimental

2.4.1 General Procedures. All reactions and subsequent manipulations were performed under anaerobic and anhydrous conditions in the glovebox or on the Schlenk line, under an atmosphere of dinitrogen. Hexanes, diethyl ether (Et_2O), and tetrahydrofuran (THF) were dried by passage over activated molecular sieves using a Vacuum Atmospheres solvent purification system. Isooctane was dried over activated 3Å molecular sieves for 24 h, degassed by bubbling dry N_2 into the solvent for 30 min, cannula transferred into a new vessel, and again dried over 3Å molecular sieves for 24 h prior to use. Pyridine-d_5 and toluene-d_8 were dried over activated 3 Å molecular sieves for 24 h prior to use. Ce(NO_3)$_3$(THF)$_4$ was prepared by the reported literature procedure.[39] Lumcrissy 12V flexible LED Lightstrips, emitting at 380 nm, were used

for photolyses. All other reagents were purchased from commercial suppliers and used as received.

^{1}H, $^{13}C\{^{1}H\}$, and $^{7}Li\{^{1}H\}$ NMR spectra were recorded on an Agilent Technologies 400 MHz 400-MR DD2 or Varian UNITY INOVA 500 spectrometer. ^{1}H and $^{13}C\{^{1}H\}$ NMR spectra were referenced to external $SiMe_4$ using residual protio solvent resonances as internal standards. $^{7}Li\{^{1}H\}$ NMR spectra were referenced indirectly to the ^{1}H chemical shift of $SiMe_4$ at 0 ppm, according to IUPAC standard.[40-41] IR spectra were recorded on a Nicolet 6700 FT-IR spectrometer. Electronic absorption spectra were recorded on a Shimadzu UV3600 UV-NIR Spectrometer. Elemental analyses were performed by the Microanalytical Laboratory at University of California (Berkeley, CA).

Raman Spectroscopy. Raman spectra were recorded on a LabRam Aramis microRaman system (Horiba Jobin Yvon) equipped with 1200 grooves/mm holographic gratings and a Peltier-cooled CCD camera. The 633 nm output of a Melles Griot He-Ne laser was used to excite the sample, and spectra were collected in a back scattering geometry using a confocal Raman Microscope (high stability BX40) equipped with Olympus objectives (MPlan 50x). Sample preparation was performed inside the glovebox: Pure crystalline solid samples were placed between a glass microscope slide and coverslip, sealed with a bead of silicone grease, and removed from the glovebox for spectral acquisition.

Cyclic Voltammetry Measurements. CV experiments were performed with a CH Instruments 600c Potentiostat, and the data were processed using CHI software (version 6.29). All experiments were performed in a glove box using a 20 mL glass vial as the cell. The working electrode consisted of a platinum disk embedded in glass (2 mm diameter), the counter

electrode and the reference electrode were both platinum wires. Solutions employed for CV studies were typically 1 mM in analyte, and 0.1 M in $[NBu_4][PF_6]$. All potentials are reported versus the $[Cp_2Fe]^{0/+}$ couple.

2.4.2 Synthesis of $LiOSiMe_3$: To a stirring, colorless solution of $LiN(SiMe_3)_2$ (453.0 mg, 2.707 mmol) in hexanes (3 mL) was added dropwise a solution of $HOSiMe_3$ (0.30 mL, 240 mg, 2.7 mmol) in hexanes (1 mL). The resulting colorless reaction mixture was stirred for 30 min at room temperature. Subsequent concentration of this solution to ca. 1 mL and storage at -25 °C for 24 h resulted in deposition of white crystals of $LiOSiMe_3$, which were isolated by decanting off the supernatant (172.5 mg, 66% yield). ^{1}H NMR (C_6D_6, 25 °C, 400 MHz): δ 0.19 (s, SiCH_3). ^{7}Li{^{1}H} NMR (C_6D_6, 25 °C, 155 MHz): δ 0.65 (s). The ^{1}H NMR spectrum of this material is in good agreement with the previously reported spectrum for this compound.[42]

2.4.3 Synthesis of $Ce(N(SiMe_3)_2)_3$: The synthesis of $Ce(N(SiMe_3)_2)_3$ was modified from a literature procedure.[43] To a stirring, colorless solution of $Ce(NO_3)_3(THF)_4$ (428.2 mg, 0.696 mmol) in THF (4 mL) was added a pale yellow solution of $LiN(SiMe_3)_2$ (350.1 mg, 2.092 mmol) in hexanes (3 mL). Upon addition, the solution immediately turned yellow. The reaction mixture was stirred for 5 h at room temperature, which resulted in the deposition of a very fine white precipitate. The volatiles were then removed *in vacuo,* and the resulting solid was triturated with hexanes (1 mL) to yield a yellow powder. The solid was then extracted into hexanes (5 mL) and filtered through a Celite column supported on glass wool (0.5 cm × 2 cm). The pale orange filtrate was concentrated to ca. 2 mL, and subsequent storage of this solution at -25 °C for 24 h resulted in the deposition of a mixture of yellow needles and yellow-orange powder. The crude product was collected by decanting off the supernatant. The solid was redissolved in hexanes (4 mL), and the resulting solution was filtered through a Celite column

supported on glass wool (0.5 cm × 2 cm). The volume of the filtrate was then reduced to ca. 3 mL and the solution was stored at -25 °C for 24 h, resulting in deposition of bright yellow needles (110.7 mg). A second crop of crystals was obtained by further concentration of the supernatant, followed by storage of the concentrated solution at -25 °C for 24 h (Total: 182.4 mg, 42 % yield). ^{1}H NMR (C_6D_6, 25 °C, 400 MHz): δ -3.43 (br s, CH_3). The ^{1}H NMR spectrum of this material is in good agreement with the previously reported spectrum for this complex.[9]

2.4.4 Synthesis of [Li(2,2,2-cryptand)][Ce(κ^2-O_2NO)(NR_2)$_3$] (2.1): To an orange solution of Ce(N($SiMe_3$)$_2$)$_3$ (177.1 mg, 0.286 mmol) in THF (1 mL) was added $LiNO_3$ (20.0 mg, 0.289 mmol). This resulted in immediate formation of a yellow-orange solution. After stirring for 20 min, a colorless solution of 2,2,2-cryptand (102.0 mg, 0.270 mmol, 0.95 eq) in THF (1 mL) was added dropwise, which resulted in an immediate color change to yellow. The solution was stirred for a further 20 min. The volatiles were then removed *in vacuo*, which yielded a yellow oil. The oil was triturated with hexanes (1 mL) and the resulting yellow solid was then extracted into Et_2O (2 mL) and filtered through a Celite column supported on glass wool (0.5 cm × 2 cm). The filtrate was then concentrated to ca. 1 mL and layered with hexanes (1 mL). Storage of this solution at -25 °C for 24 h resulted in deposition of a mixture of yellow crystals and white powder**.** The crude solid was collected by decanting off the solvent and was then redissolved in Et_2O (2 mL). The resulting yellow solution was filtered through a Celite column supported on glass wool (0.5 cm × 2 cm). The yellow filtrate was then concentrated to ca. 1 mL and layered with hexanes (1 mL). Storage of this solution at -25 °C for 24 h resulted in deposition of yellow plates, which were isolated by decanting off the supernatant (110.5 mg, 38 % yield). Anal. Calcd for $C_{36}H_{90}CeLiN_6O_9Si_6$: C, 40.53; H, 8.50; N, 7.88. Found: C, 40.37; H, 8.73; N, 8.00. ^{1}H NMR (py-d_5, 25 °C, 400 MHz): δ -1.32 (br s, 54H, NSiCH_3), 2.48 (s, 12H,

NCH_2), 3.45 (s, 12H, OCH_2CH_2N), 3.51 (s, 12H, OCH_2CH_2O). ^{7}Li{^{1}H} NMR (py-d_5, 25 °C, 155 MHz): δ -1.08 (s). UV-Vis/NIR (Et_2O, 0.95 mM, 25 °C, L·mol^{-1}·cm^{-1}): 336 (ε = 140), 380 (ε = 200). IR (KBr pellet, cm^{-1}): 2951 (s), 2889 (s), 2819 (m), 1919 (vw), 1637 (w), 1491 (s), 1446 (s), 1385 (m), 1356 (s), 1286 (s), 1242 (vs), 1184 (m), 1130 (m), 1093 (vs), 1009 (m), 985 (vs), 931 (s), 866 (s), 829 (vs), 769 (s), 754 (m), 685 (w), 665 (s), 598 (s), 563 (vw), 515 (vw). Raman (neat solid, cm^{-1}): 1479 (m), 1441 (m), 1406 (m), 1294 (m), 1259 (m), 1168 (vw), 1132 (m), 1096 (w), 1072 (m), 1043 (s), 917 (br m), 855 (m), 825 (w), 742 (w), 678 (m), 571 (vs), 562 (s), 440 (br w), 347 (w).

2.4.5 Small Scale Synthesis of [Li(2,2,2-cryptand)][Ce(O)(NR$_2$)$_3$] (2.2): Yellow crystals of **2.1** (40.0 mg, 0.037 mmol) were dissolved in a 2:1 mixture of tol-d_8 and py-d_5 (1 mL total volume) resulting in formation of a clear yellow solution. This solution was transferred to an NMR tube equipped with a J-Young valve, brought out of the glovebox, cooled to -5 °C in a salt water/dry ice bath, and photolysed for 6 h using a flexible LED lightstrip that emitted at 380 nm. The temperature of the bath was kept at ca. -5 °C by periodically adding small pieces of dry ice. The color of the solution gradually changed from yellow to yellow-orange over the course of the photolysis. A ^{1}H NMR spectrum was then recorded. Integration of the $SiMe_3$ resonance assigned to complex **2.1**, relative to the NCH_2 resonance of the 2,2,2-cryptand moiety, revealed approximately 80 % consumption of **2.1**. ^{1}H NMR (2:1 tol-d_8/py-d_5, 25 °C, 400 MHz): δ -1.18 (br s, 54H, NSiCH_3, complex **2.1**), -0.43 (s, 54H, NSiCH_3, complex **2.4**), -0.21 (s, 9H, OSiCH_3, complex **2.4**), 0.28 (br s, 108H, NSiCH_3, complex **2.3**), 0.80 (s, 54H, NSiCH_3, complex **2.2**), 2.28 (t, 12H, J_{HH} = 4 Hz, NCH_2), 3.23 (t, 12H, J_{HH} = 4 Hz, OCH_2CH_2N), 3.28 (s, 12H, OCH_2CH_2O). The sample was then returned to glovebox and the volatiles were removed in vacuo. The resulting oil was triturated with Et_2O (2 × 1 mL) to yield

an orange-brown solid. The solid was then extracted into Et_2O (2 mL) and filtered through a Celite column supported on glass wool (0.5 cm × 2 cm), resulting in generation of a yellow filtrate and leaving a plug of orange-brown solid on the Celite. The filtrate was transferred to a 4 mL scintillation vial, which was then placed inside a 20 mL scintillation vial. Isooctane (1 mL) was added to the outer vial. Storage of the two-vial system at -25 °C for 72 h resulted in the deposition of yellow plates, which were isolated by decanting off the supernatant (12.6 mg, 33 % yield). In one instance, storage of the two-vial system at -25 °C for 5 d resulted in deposition of **2.2**, along with the deposition of small amounts of pale-yellow plates and colorless plates, which were subsequently identified as **2.3** and **2.4**, respectively, by X-ray crystallography. Anal. Calcd for $C_{36}H_{90}CeLiN_5O_7Si_6$: C, 42.36; H, 8.89; N, 6.86. Found: C, 42.12; H, 8.77; N, 6.86. ^{1}H NMR (py-d_5, 25 °C, 500 MHz): δ 0.69 (s, 54H, NSiCH_3), 2.56 (t, 12H, J_{HH} = 6 Hz, NCH_2), 3.52 (t, 12H, J_{HH} = 5 Hz, OCH_2CH$_2$N), 3.59 (s, 12H, OCH_2CH_2O). ^{13}C NMR (py-d_5, 25 °C, 125 MHz): δ 6.39 (SiCH$_3$), 54.4 (NCH$_2$), 69.3 (overlapping signals for OCH$_2$CH$_2$N and OCH$_2$$CH_2$O). ^{7}Li{^{1}H} NMR (py-d_5, 25 °C, 155 MHz): δ -1.00 (s). UV-Vis/NIR (Et_2O, 0.79 mM, 25 °C, L·mol^{-1}·cm^{-1}): 306 (ε = 830). IR (KBr pellet, cm^{-1}): 2943 (vs), 2885 (vs), 2821 (s), 2112 (vw), 1900 (vw), 1594 (vw), 1456 (m), 1358 (s), 1300 (m), 1238 (vs), 1157 (w), 1130 (s), 1095 (vs), 995 (vs), 933 (s), 866 (vs), 825 (vs), 768 (s), 752 (s), 685 (s), 663 (s), 594 (s), 561 (vw). Raman (neat solid, cm^{-1}): 1479 (s), 1464 (s), 1445 (s), 1372 (w), 1294 (m), 1266 (m), 1176 (w), 1108 (s), 1068 (w), 1039 (m), 983 (vw), 917 (m), 888 (w), 830 (m), 737 (s), 418 (br vs), 312 (vw).

2.4.6 Larger Scale Synthesis of [Li(2,2,2-cryptand)][Ce(O)(NR$_2$)$_3$] (2.2): Yellow crystals of **2.1** (264.6 mg, 0.248 mmol) were dissolved in a 2:1 mixture of tol-d_8 and py-d_5 (5 mL total volume) resulting in formation of a clear yellow solution. This solution was then divided into

five portions and each portion was transferred to an NMR tube equipped with a J-Young valve. The samples were brought out of the glovebox, cooled to -5 °C in a salt water/dry ice bath, and photolysed for 7 h using a flexible LED lightstrip that emitted at 380 nm. The temperature of the bath was kept at ca. -5 °C by periodically adding small pieces of dry ice. The color of the solution gradually changed from yellow to yellow-orange over the course of the photolysis. A ^{1}H NMR spectrum of one of these samples was then recorded. Integration of the $SiMe_3$ resonance assigned to complex **2.1**, relative to the NCH_2 resonance of the 2,2,2-cryptand moiety, reveals approximately 77 % consumption of **2.1**.^{1}H NMR (2:1 tol-d_8/py-d_5, 25 °C, 400 MHz): δ -1.12 (br s, 54H, NSiCH_3, complex **2.1**), -0.42 (s, 54H, NSiCH_3, complex **2.4**), -0.12 (s, 9H, OSiCH_3, complex **2.4**), 0.29 (br s, 108H, NSiCH_3, complex **2.3**), 0.81 (s, 54H, NSiCH_3, complex **2.2**), 2.37 (t, 12H, J_{HH} = 4 Hz, NCH_2), 3.32 (t, 12H, J_{HH} = 4 Hz, OCH_2CH$_2$N), 3.38 (s, 12H, OCH_2CH_2O). The five tubes were returned to the glovebox and combined into a single 20 mL scintillation vial. The volatiles were then removed under reduced pressure and the resulting oil was triturated with Et_2O (2 × 1 mL) to yield an orange-brown solid. The solid was extracted into Et_2O (4 mL) and filtered through a Celite column supported on glass wool (0.5 cm × 2 cm), resulting in generation of a yellow filtrate and leaving a plug of orange-brown solid on the Celite. The filtrate was concentrated to ca. 2 mL and transferred to a 4 mL scintillation vial, which was then placed inside a 20 mL scintillation vial. Isooctane (1 mL) was added to the outer vial. Storage of the two-vial system at -25 °C for 72 h resulted in the deposition of yellow plates, which were isolated by decanting off the supernatant (45.5 mg, 18

% yield). This material was identical to that prepared via the small scale synthesis (described above), according to ^{1}H NMR spectroscopy.

2.4.7 Synthesis of [Li(2,2,2-cryptand)][Ce(OSiMe$_3$)(NR$_2$)$_3$] (2.4): To a stirring, orange solution of Ce(N(SiMe$_3$)$_2$)$_3$ (100.1 mg, 0.161 mmol) in THF (3 mL) was added LiOSiMe$_3$ (15.0 mg, 0.156 mmol) as a solid, which resulted in an immediate color change to pale yellow. After stirring for 45 min, 2,2,2-cryptand (56.2 mg, 0.149 mmol) was added to the pale yellow solution. The solution was then stirred for a further 15 min. The volatiles were removed *in vacuo* and the resulting white solid was triturated with hexanes (2 × 2 mL). The solid was then extracted into Et$_2$O (3 mL) and filtered through a Celite column supported on glass wool (0.5 cm × 2 cm). The resulting pale yellow filtrate was concentrated to ca. 2 mL and layered with hexanes (1 mL). Storage of this solution at -25 °C for 24 h resulted in deposition of colorless crystals, which were isolated by decanting off the supernatant (76.8 mg, 47 % yield). Anal. Calcd for $C_{39}H_{99}CeLiN_5O_7Si_7$: C, 42.82; H, 9.12; N, 6.40. Found: C, 42.69; H, 9.09; N, 6.44. ^{1}H NMR (py-d_5, 25 °C, 400 MHz): δ -0.59 (br s, 54H, NSiCH_3), -0.37 (s, 9H, OSiCH_3), 2.56 (s, 12H, NCH_2), 3.52 (s, 12H, OCH_2CH$_2$N), 3.60 (s, 12H, OCH_2CH_2O). ^{7}Li{^{1}H} NMR (py-d_5, 25 °C, 155 MHz): δ -0.97 (s). UV-Vis/NIR (Et$_2$O, 0.68 mM, 25 °C, L·mol^{-1}·cm^{-1}): 276 (ε = 780), 330 (ε = 630), 347 (ε = 740). IR (KBr pellet, cm^{-1}): 2945 (s), 2889 (s), 2845 (m), 1917 (vw), 1618 (w), 1471 (w), 1456 (m), 1377 (w), 1358 (m), 1304 (m), 1238 (vs), 1182 (w), 1117 (w), 1097 (s), 1003 (vs), 964 (vs), 933 (m), 870 (s), 830 (vs), 768 (m), 750 (m), 687 (w), 663 (m), 609 (w), 592 (m), 517 (vw). Raman (neat solid, cm^{-1}): 1481 (m), 1450 (m), 1408 (w),

1378 (vw), 1292 (w), 1265 (w), 1174 (vw), 1110 (m), 1070 (w), 1038 (w), 981 (vw), 915 (w), 887 (w), 833 (m), 741 (m), 673 (m), 622 (m), 566 (vs), 418 (br m) 347 (br m).

2.4.8 X-ray Crystallography. Data for **2.1** – **2.4** were collected on a Bruker KAPPA APEX II diffractometer equipped with an APEX II CCD detector using a TRIUMPH monochromater with a Mo Kα X-ray source (α = 0.71073 Å). The crystals of **2.1** – **2.4** were mounted on a cryoloop under Paratone-N oil, and all data were collected at 100(2) K using an Oxford nitrogen gas cryostream system. X-ray data for **2.1**, **2.2**, **2.3** and **2.4** were collected utilizing frame exposures of 5, 60, 10 and 5 seconds, respectively. Data collection and cell parameter determination were conducted using the SMART program.[44] Integration of the data frames and final cell parameter refinement were performed using SAINT software.[45] Absorption corrections of the data were carried out using the multi-scan method SADABS.[46] Subsequent calculations were carried out using SHELXTL.[47] Structure determination was done using direct or Patterson methods and difference Fourier techniques. All hydrogen atom positions were idealized, and rode on the atom of attachment. Structure solution, refinement, graphics, and creation of publication materials were performed using SHELXTL.[47] Complexes **2.1** – **2.4** have been deposited in the Cambridge Structural Database (**2.1**: CCDC 1569781; **2.2**: CCDC 1569782; **2.3**: CCDC 1569783; **2.4**: CCDC 1569784).

One 2,2,2-cryptand moiety in complex **2.3** exhibited positional disorder. Disordered carbon atoms were modelled over two positions with 50% occupancy. Hydrogen atoms were not assigned to disordered carbon atoms and disordered carbon atoms were refined isotropically.

Table 2.1. Crystallographic details for complexes **2.1** and **2.2**.

	2.1	**2.2**
Formula	$C_{36}H_{90}CeLiN_6O_9Si_6$	$C_{36}H_{90}CeLiN_5O_7Si_6$
Crystal Habit, Color	Plate, Yellow	Plate, Yellow
Crystal Size (mm)	0.30 × 0.25 × 0.10	0.10 × 0.10 × 0.05
MW (g/mol)	1066.73	1020.72
crystal system	Monoclinic	Monoclinic
space group	$P2_1/c$	$P2_1/c$
a (Å)	11.3890(6)	16.2803(14)
b (Å)	34.790(2)	15.8306(16)
c (Å)	14.0047(8)	22.128(2)
α (°)	90	90.00
β (°)	92.144(3)	109.570(5)
γ (°)	90	90.00
V ($Å^3$)	5545.0(5)	5373.7(9)
Z	4	4
T (K)	100(2)	100(2)
λ (Å)	0.71073	0.71073
GOF	1.107	0.981
Density (calcd) (Mg/m^3)	1.278	1.262
Absorption coefficient (mm^{-1})	0.999	1.024
F_{000}	2260	2168
Total no Reflections	30623	20203
Unique Reflections	11256	8631
Final R indices*	$R_1 = 0.0391$	$R_1 = 0.0780$
	$wR_2 = 0.0768$	$wR_2 = 0.1493$
Largest Diff. peak and hole ($e^- A^{-3}$)	1.383, -0.730	2.609, -0.922

* For [$I > 2\sigma(I)$]

Table 2.2. Crystallographic details for complexes **2.3** and **2.4**.

	2.3·Et_2O	**2.4**
Formula	$C_{76}H_{172}Ce_3Li_2N_{10}O_{17}Si_{12}$	$C_{39}H_{99}CeLiN_5O_7Si_7$
Crystal Habit, Color	Plate, Yellow	Plate, Colorless
Crystal Size (mm)	0.20 × 0.10 × 0.05	0.15 × 0.15 × 0.05
MW (g/mol)	2269.55	1093.92
crystal system	Triclinic	Monoclinic
space group	P-1	$P2_1/n$
a (Å)	15.060(2)	19.3389(7)
b (Å)	15.339(3)	15.0467(5)
c (Å)	25.158(4)	21.7679(8)
α (°)	89.555(5)	90.00
β (°)	89.167(5)	107.901(2)
γ (°)	84.713(5)	90.00
V ($Å^3$)	5786.2(16)	6027.5(4)
Z	2	4
T (K)	100(2)	100(2)
λ (Å)	0.71073	0.71073
GOF	0.983	1.076
Density (calcd) (Mg/m^3)	1.303	1.205
Absorption coefficient (mm^{-1})	1.340	0.936
F_{000}	2364	2332
Total no Reflections	41741	33086
Unique Reflections	19719	10257
Final R indices*	R_1 = 0.0733	R_1 = 0.0469
	wR_2 = 0.1434	wR_2 = 0.1176
Largest Diff. peak and hole ($e^- A^{-3}$)	1.887, -1.029	1.199, -0.607

* For [I > 2σ(I)]

2.5 Appendix

2.5.1 NMR Spectra

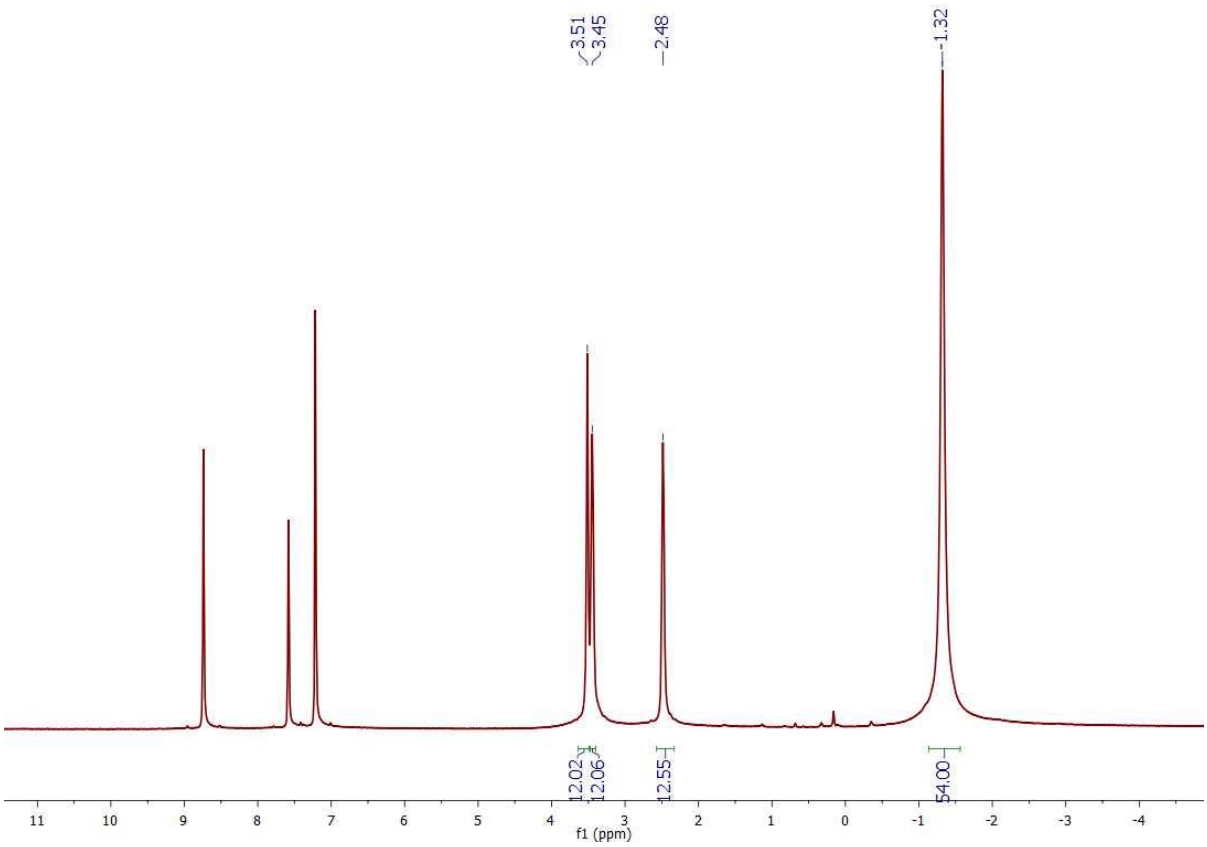

Figure A2.1. ^{1}H NMR spectrum of [Li(2,2,2-cryptand)][Ce(κ^2-O_2NO)(NR_2)$_3$] (**2.1**) in py-d_5.

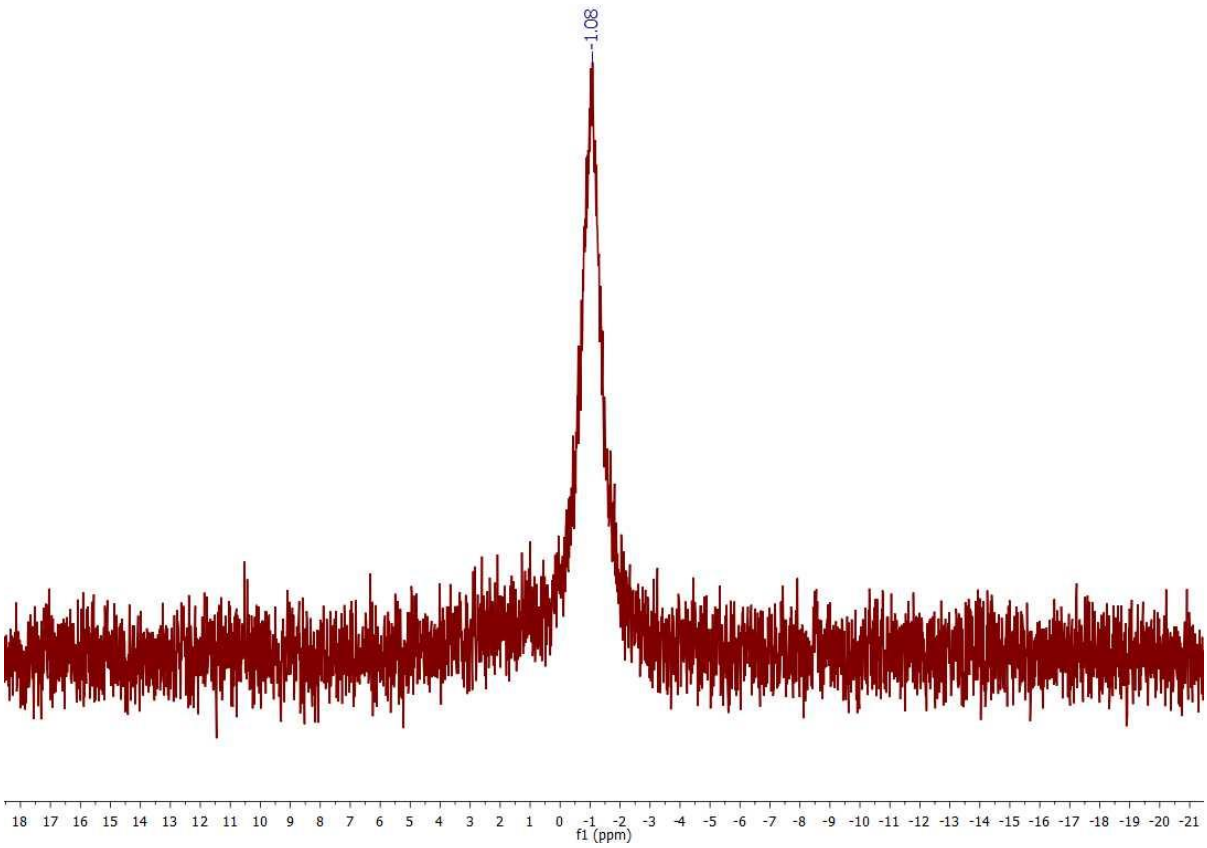

Figure A2.2. $^{7}Li\{^{1}H\}$ NMR spectrum of [Li(2,2,2-cryptand)][Ce(κ^2-O_2NO)(NR_2)$_3$] (**2.1**) in py-d_5.

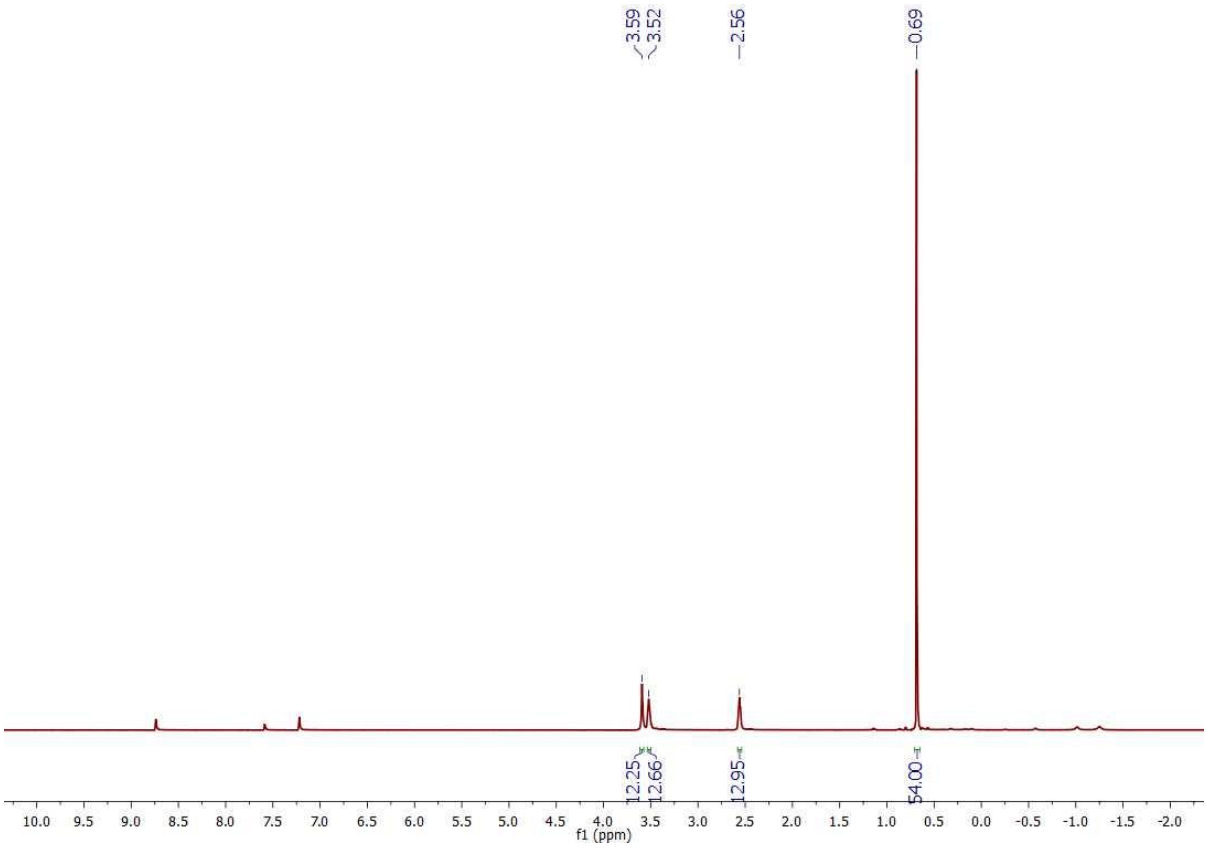

Figure A2.3. ^{1}H NMR spectrum of [Li(2,2,2-cryptand)][Ce(O)(NR_2)$_3$] (**2.2**) in py-d_5.

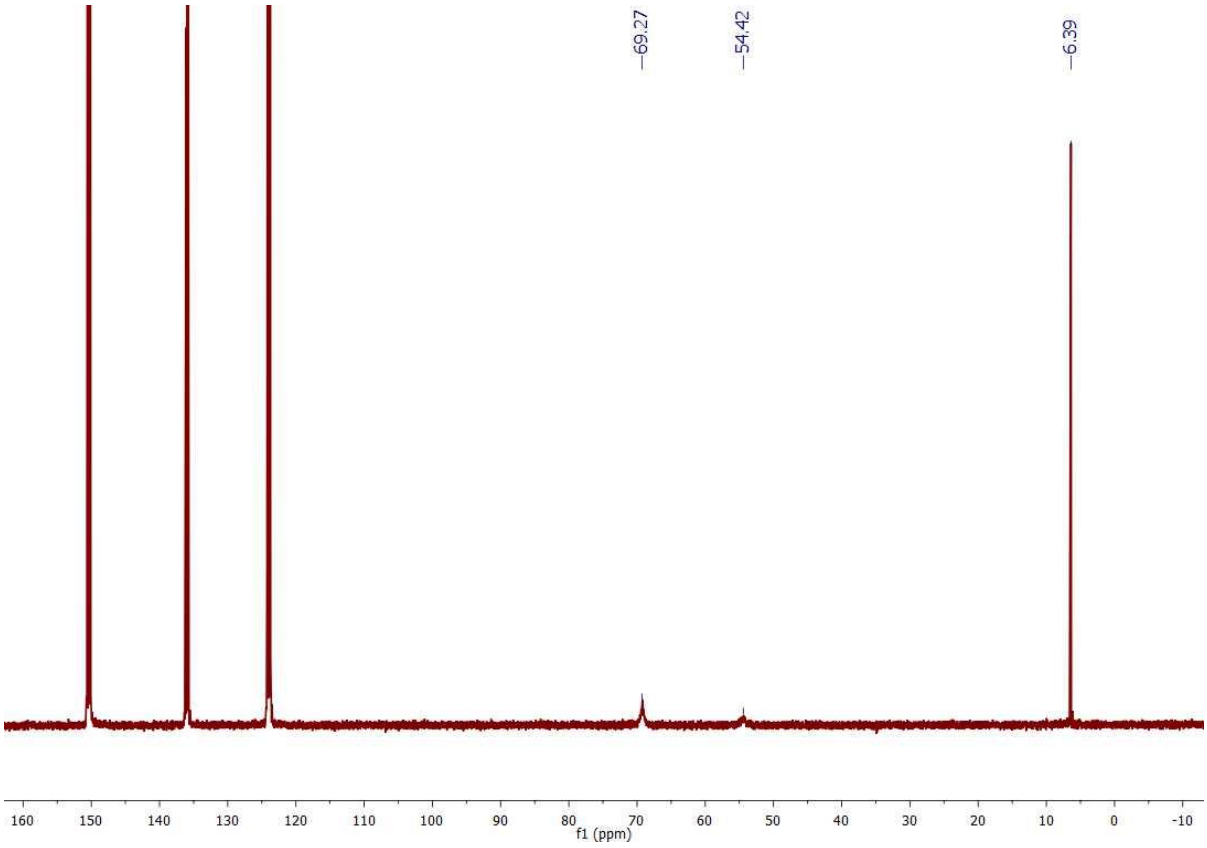

Figure A2.4. $^{13}C\{^{1}H\}$ NMR spectrum of [Li(2,2,2-cryptand)][Ce(O)$(NR_2)_3$] (**2.2**) in py-d_5.

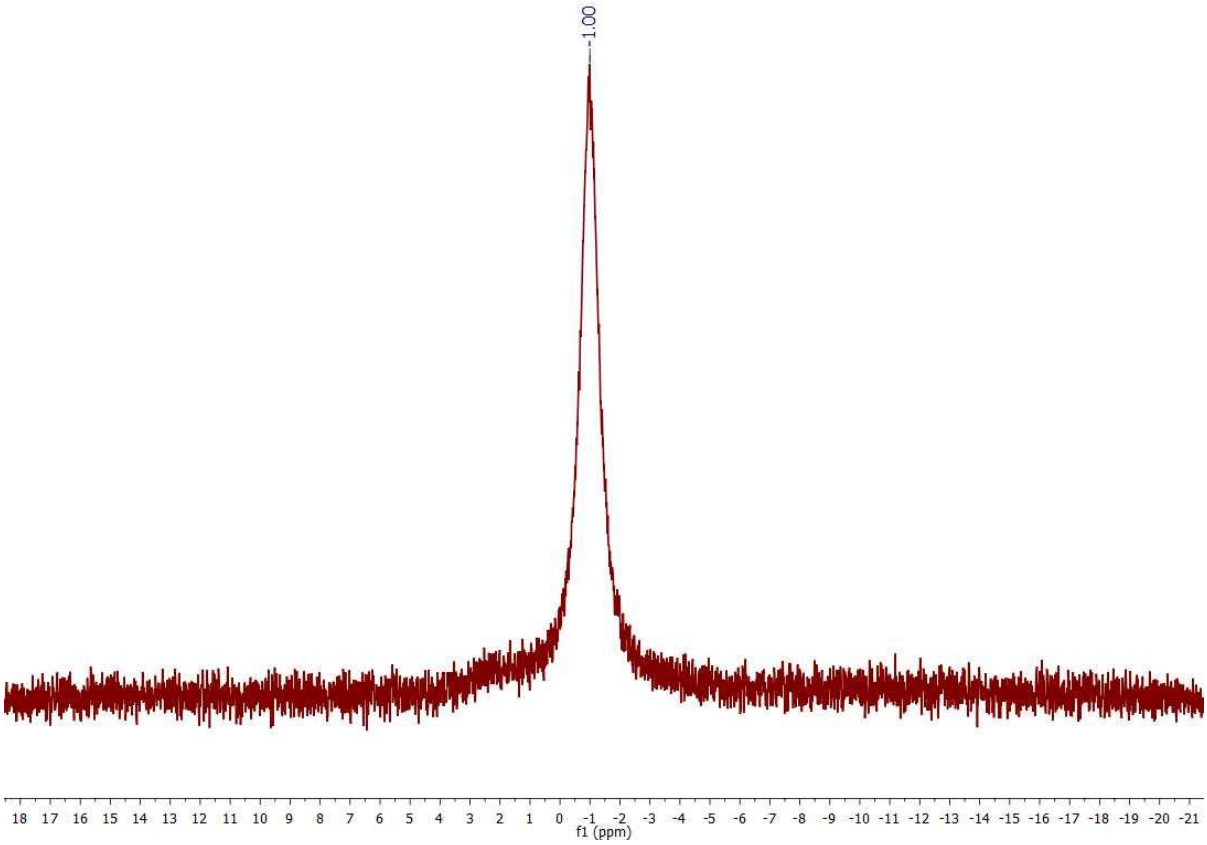

Figure A2.5. $^{7}Li\{^{1}H\}$ NMR spectrum of [Li(2,2,2-cryptand)][Ce(O)$(NR_2)_3$] (**2.2**) in py-d_5.

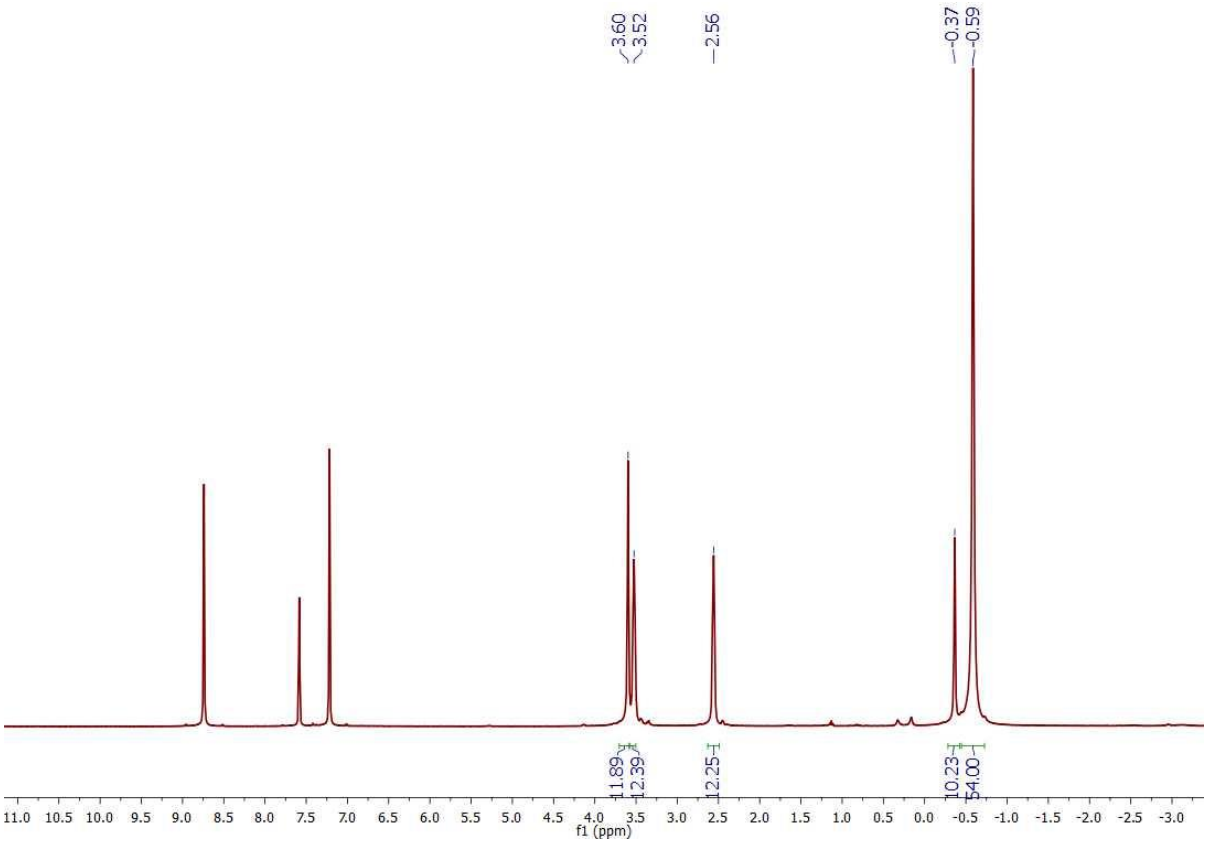

Figure A2.6. ^{1}H NMR spectrum of [Li(2,2,2-cryptand)][Ce(OSiMe$_3$)(NR$_2$)$_3$] (**2.4**) in py-d_5.

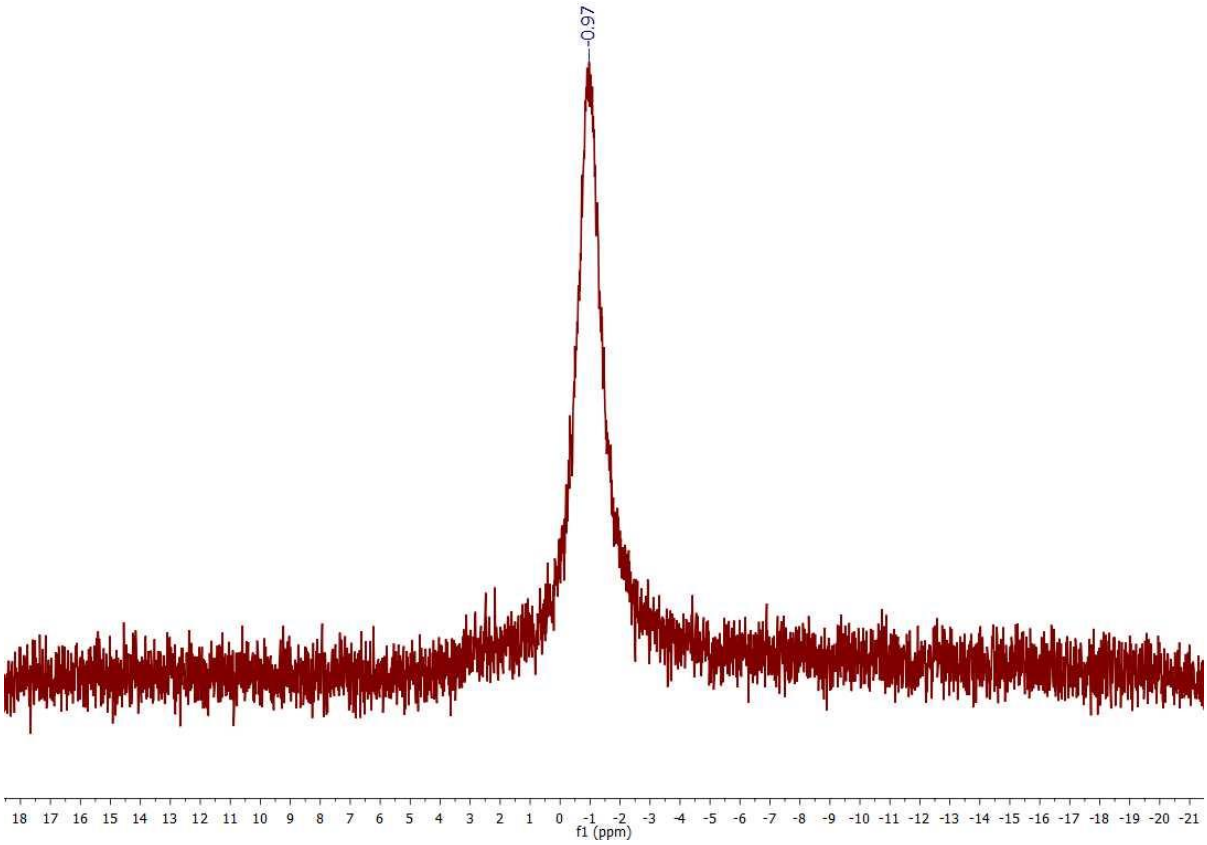

Figure A2.7. $^{7}Li\{^{1}H\}$ NMR spectrum of [Li(2,2,2-cryptand)][Ce($OSiMe_3$)(NR_2)$_3$] (**2.4**) in py-d_5.

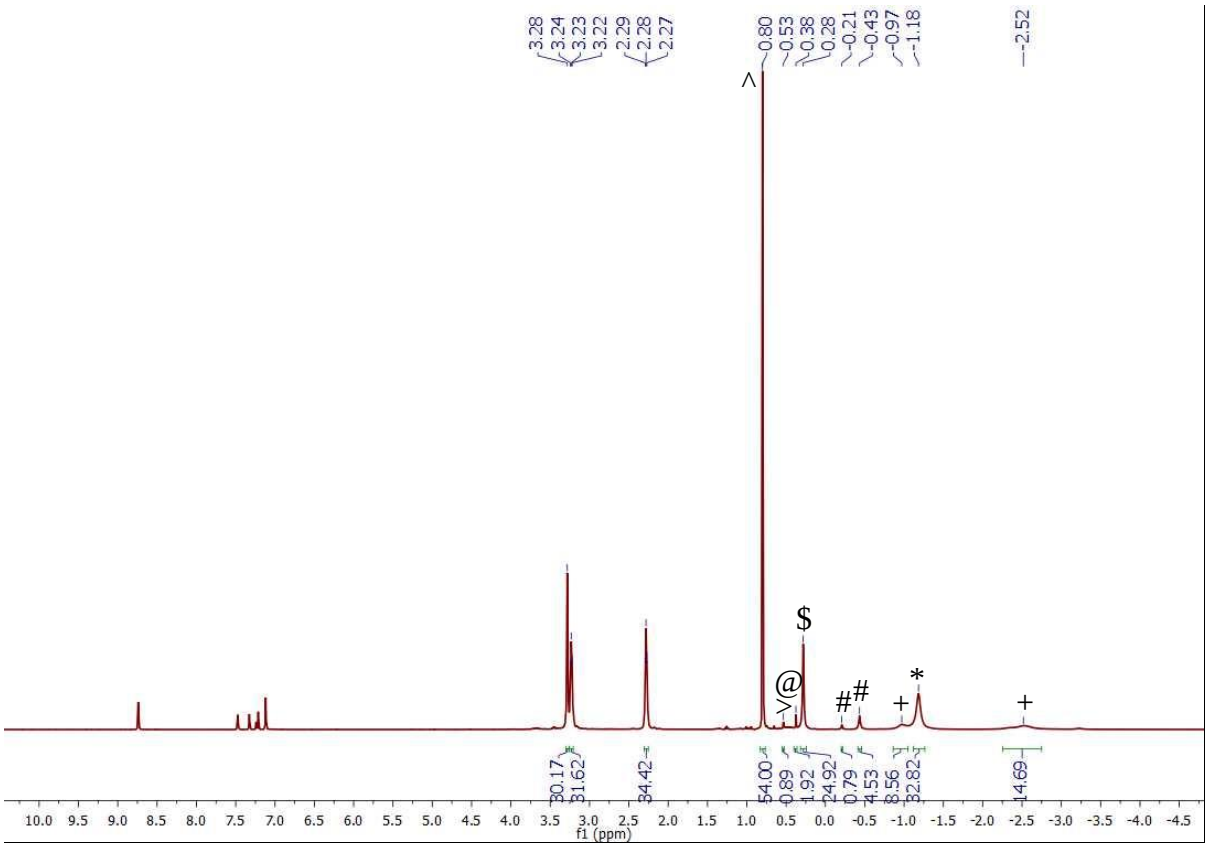

Figure A2.8. ^{1}H NMR spectrum of the photolysis of **2.1** after 6 h in 2:1 tol-d_8/py-d_5. Integration of the $SiMe_3$ resonance assigned to complex **2.1**, relative to the NCH_2 resonance of the 2,2,2-cryptand moiety, reveals approximately 80 % consumption of **2.1**. * indicates the presence of **2.1**. ^ indicates the presence of **2.2**. $ indicates the presence of **2.3**. # indicates the presence of **2.4**. > indicates the presence of $LiN(SiMe_3)_2$. @ indicates a resonance tentatively assigned to $HN(SiMe_3)_2$. + indicates the presence of unidentified products.

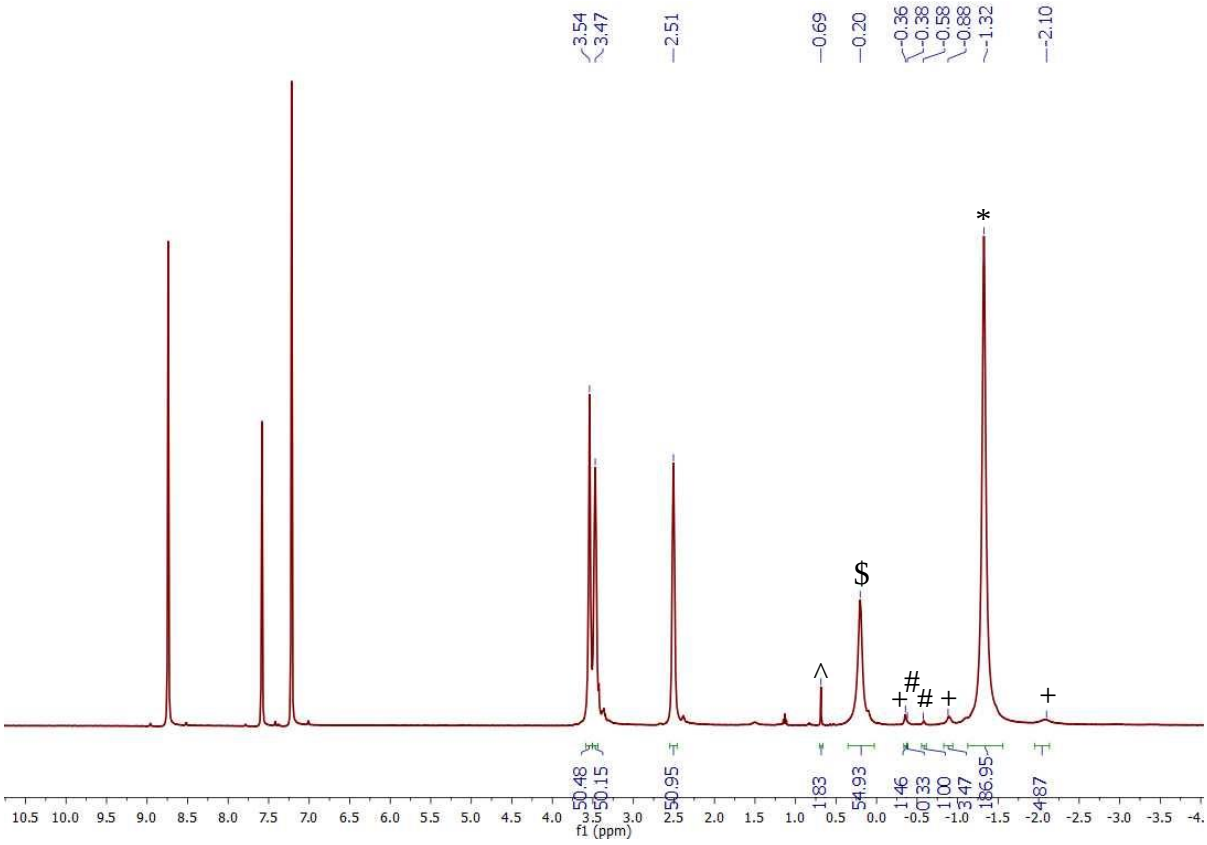

Figure A2.9. ^{1}H NMR spectrum of **2.1** in py-d_5 after standing at room temperature for 24 h. **Experimental details:** Yellow crystals of **2.1** (13.5 mg, 0.013 mmol) were dissolved in py-d_5 (0.75 mL), and the resulting yellow solution was transferred to an NMR tube equipped with a J-Young valve, and stored at room temperature in the absence of light for 24 h. Integration of the $SiMe_3$ resonance assigned to complex **2.1**, relative to the NCH_2 resonance of 2,2,2-cryptand moiety, suggests that approximately 80% of complex **2.1** remains unreacted. * indicates the presence of **2.1**. ^ indicates the presence of **2.2**. $ indicates the presence of **2.3**. # indicates the presence of **2.4**. + indicates presence of unidentified products.

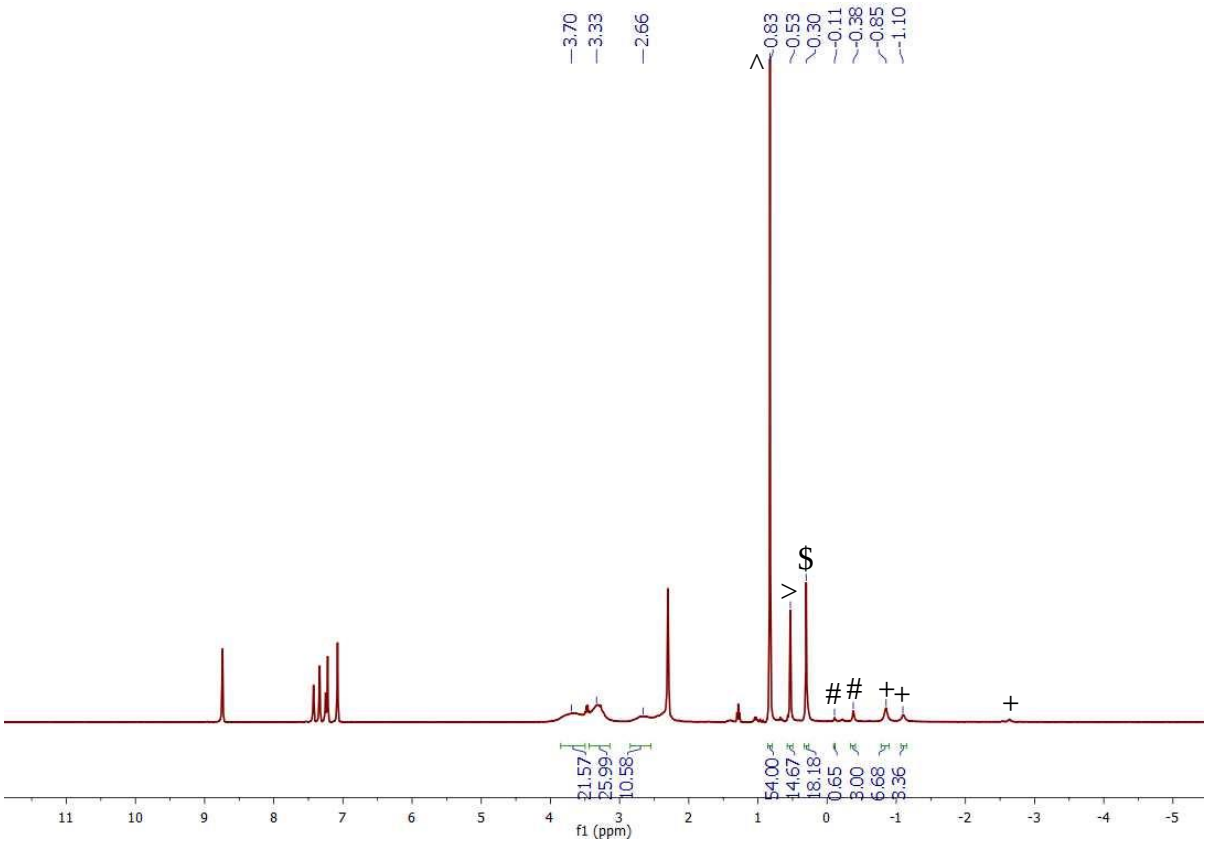

Figure A2.10. ^{1}H NMR spectrum of **2.2** in 2:1 tol-d_8/py-d_5 after standing at room temperature for 4d. **Experimental Details:** Yellow crystals of **2.2** (7.0 mg, 0.007 mmol) were dissolved in 2:1 tol-d_8/py-d_5 (total volume: 0.75 mL) and the resulting yellow solution was transferred to an NMR tube equipped with a J-Young valve and stored at room temperature in the absence of light for 4 d. Integration of the $SiMe_3$ resonance assigned to complex **2.2**, relative to the CHD_2 resonance of tol-d_8, reveals approximately 70% consumption of complex **2.2**. ^ indicates the presence of **2.2**. $ indicates the presence of **2.3**. # indicates the presence of **2.4**. > indicates the presence of $LiN(SiMe_3)_2$. + indicates presence of unidentified products.

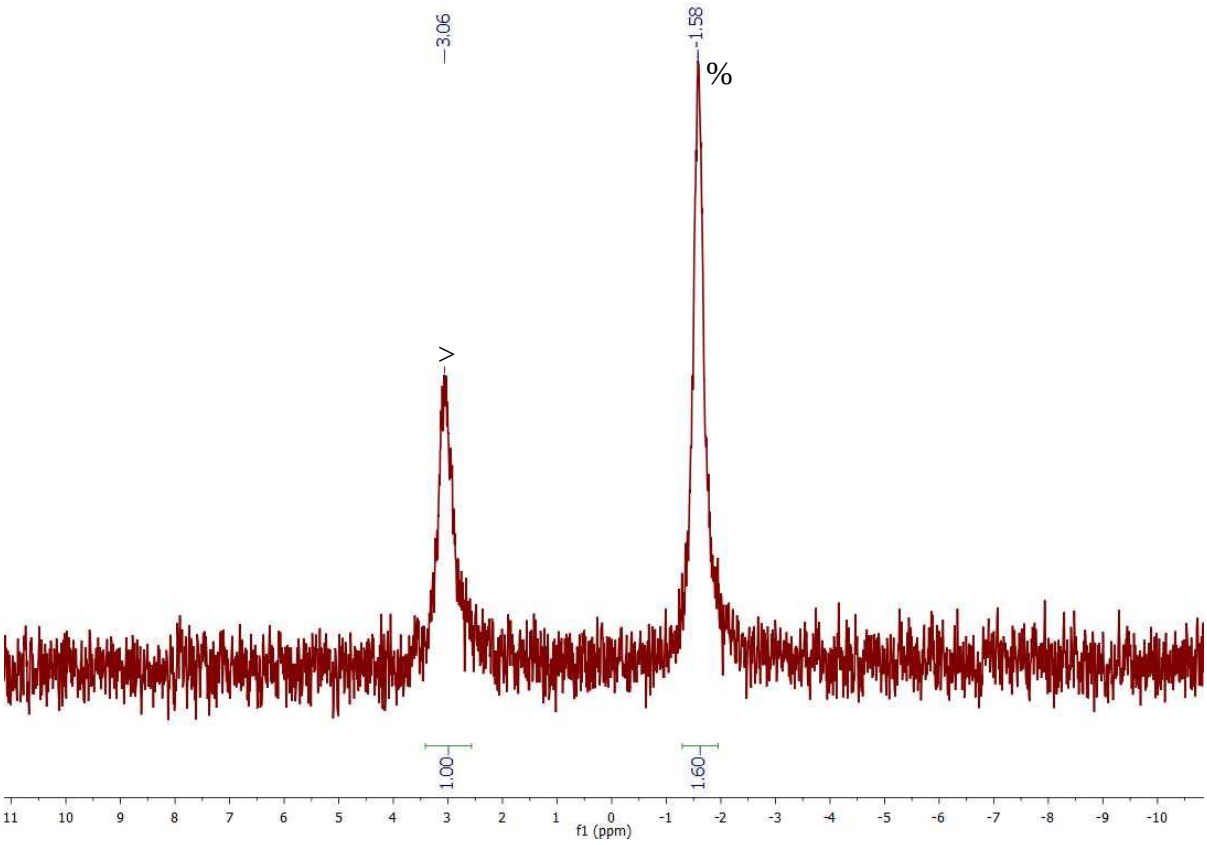

Figure A2.11. $^{7}Li\{^{1}H\}$ NMR spectrum of **2.2** in 2:1 tol-d_8/py-d_5 after standing at room temperature for 4d. > indicates the presence of $LiN(SiMe_3)_2$. % indicates overlapping resonances assignable to complexes **2.2**, **2.3** and **2.4**. **Experimental Details:** See Figure A2.10 caption.

2.5.2 UV-Vis Spectra

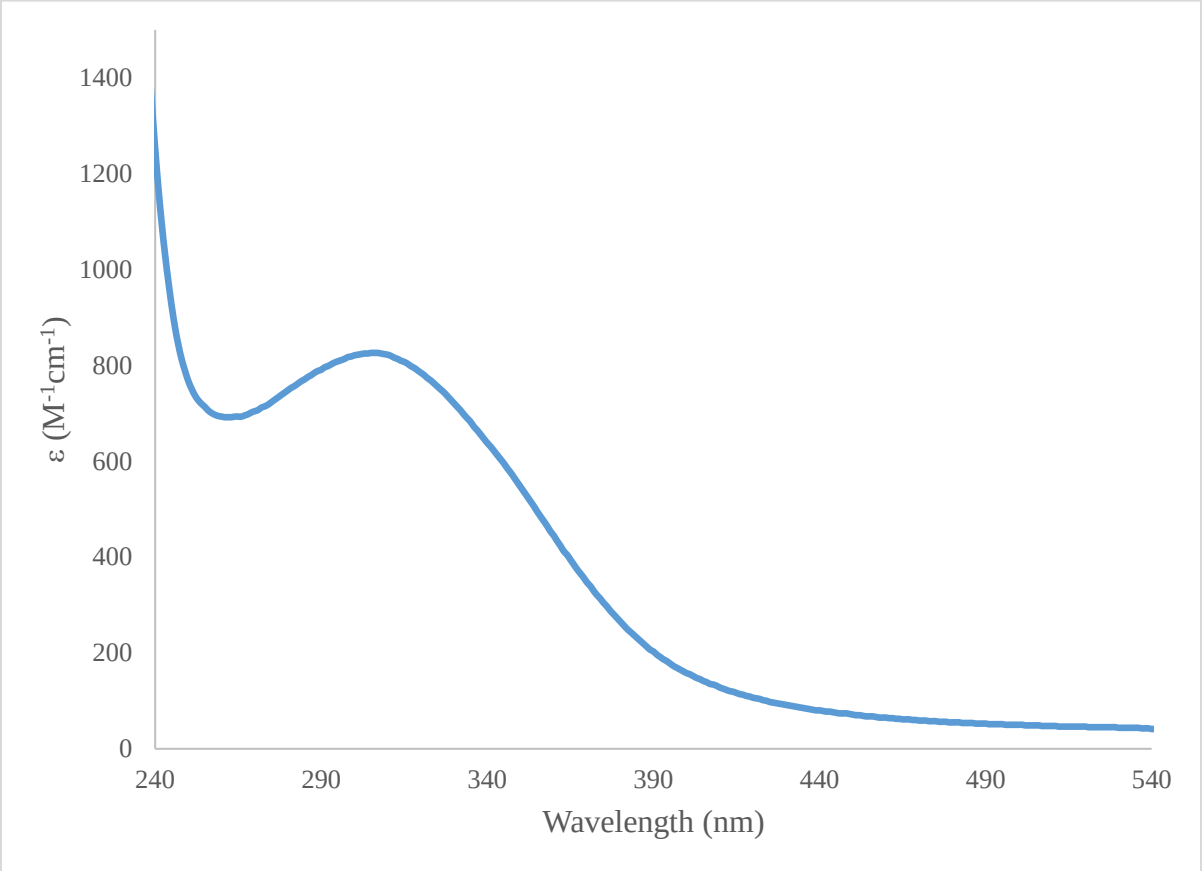

Figure A2.12. UV-Vis spectrum of **2.2** in Et_2O (0.79 mM).

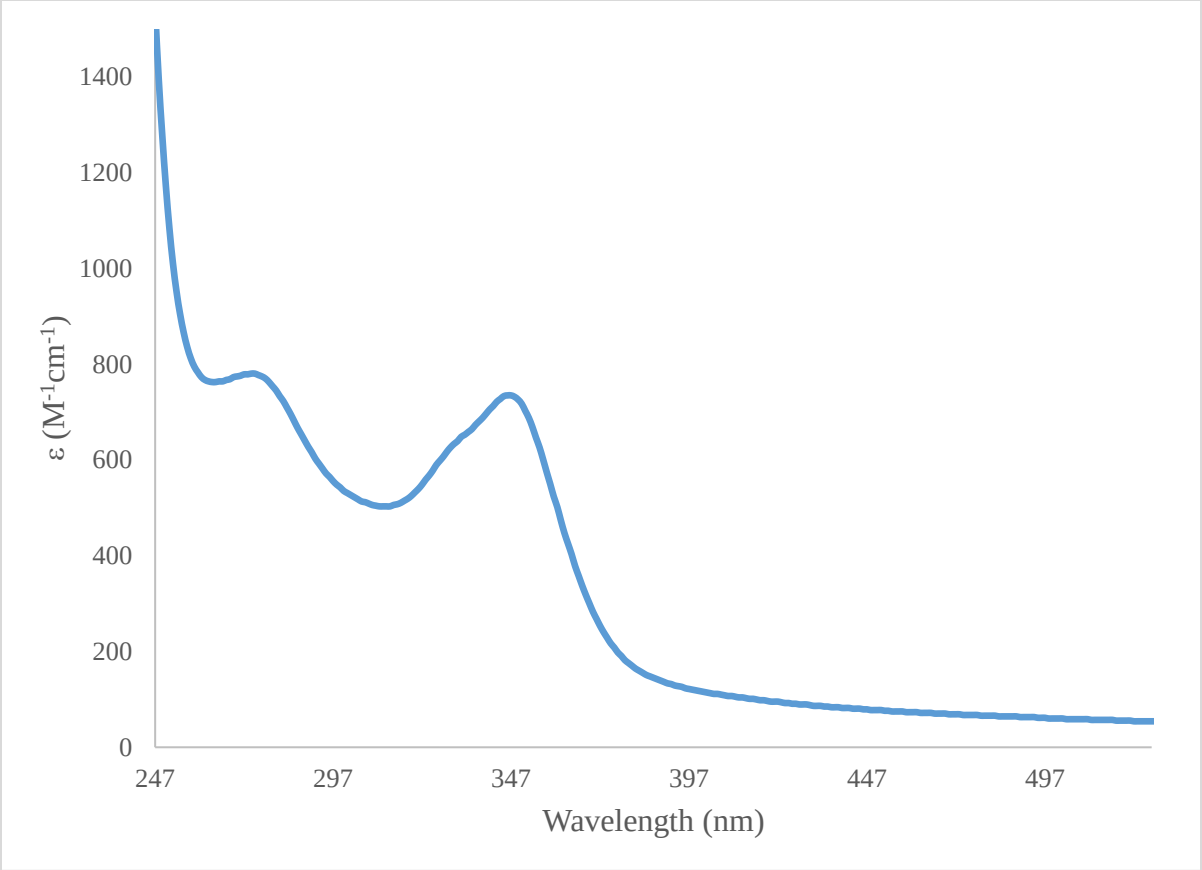

Figure A2.13. UV-Vis spectrum of **2.4** in Et_2O (0.68 mM).

2.5.3 Cyclic Voltammetry

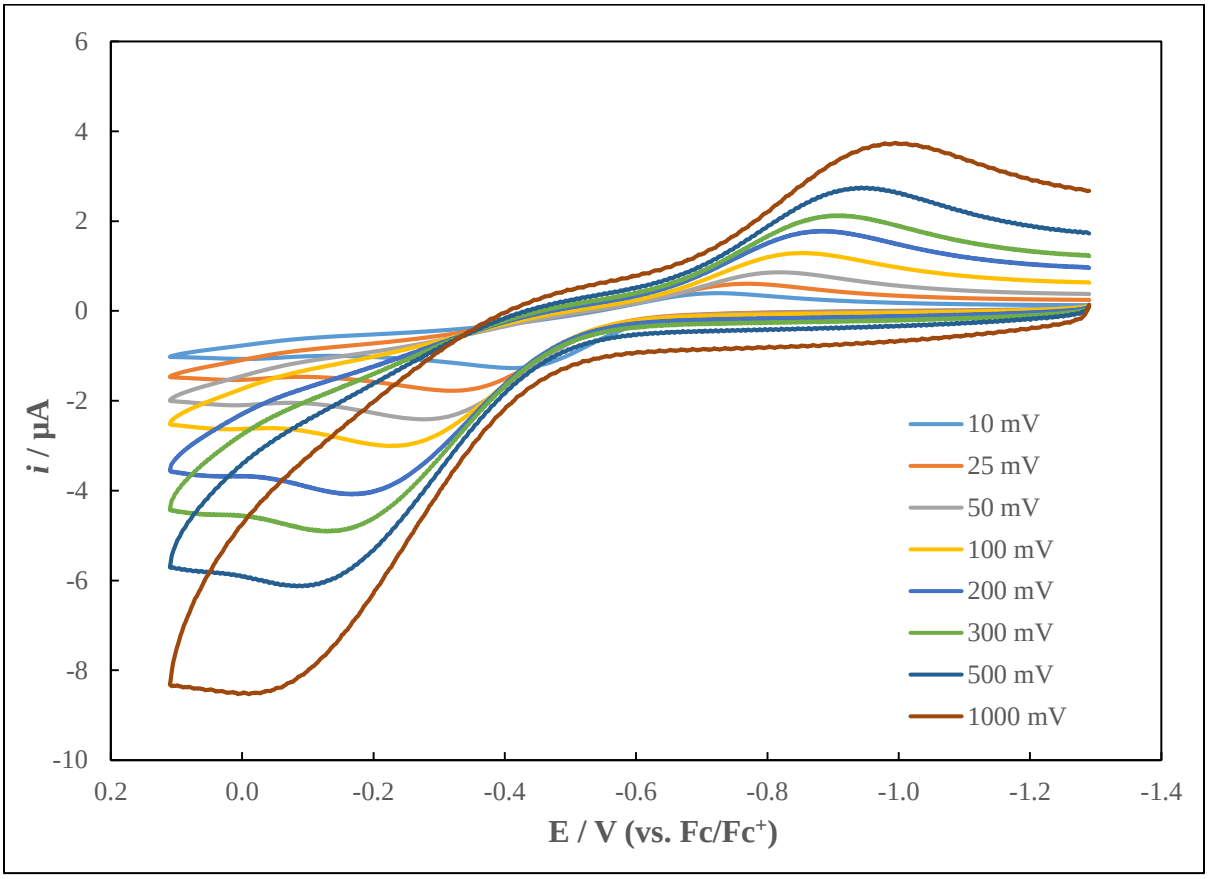

Figure A2.14. Partial cyclic voltammogram of the Ce(III)/Ce(IV) redox feature of complex **2.4** measured in THF with 0.1 M $[NBu_4][PF_6]$ as the supporting electrolyte (vs. Fc/Fc^+).

Table A2.1. Electrochemical parameters for [Li(2,2,2-cryptand)][Ce(OSiMe$_3$)(NR$_2$)$_3$] (**2.4**) in THF (vs. Fc/Fc$^+$, [NBu$_4$][PF$_6$] as the supporting electrolyte).

Oxidation Feature	Scan Rate, V/s	$E_{p,a}$, V	$E_{p,c}$, V	$E_{1/2}$, V	ΔE_p, V	$i_{p,a}/i_{p,c}$
	0.010	-0.412	-0.726	-0.57	0.314	2.5
	0.025	-0.318	-0.769	-0.54	0.451	3.7
	0.050	-0.276	-0.824	-0.55	0.548	4.2
	0.100	-0.225	-0.860	-0.54	0.635	4.4
	0.200	-0.166	-0.883	-0.53	0.717	3.9
	0.300	-0.125	-0.914	-0.52	0.789	3.4
	0.500	-0.083	-0.944	-0.51	0.861	3.3
	1.000	-0.011	-0.995	-0.50	0.984	4.2

2.5.4 IR Spectra

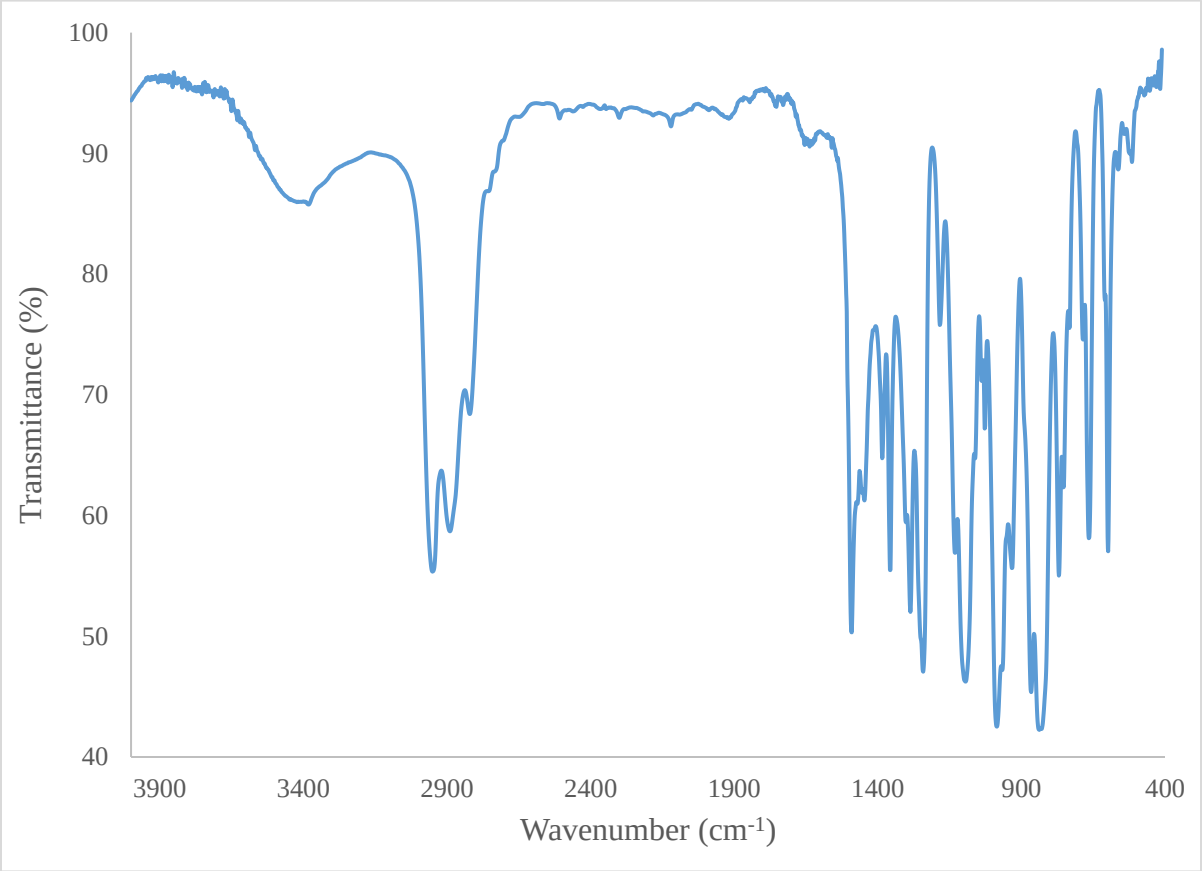

Figure A2.15. IR spectrum of **2.1** as a KBr pellet.

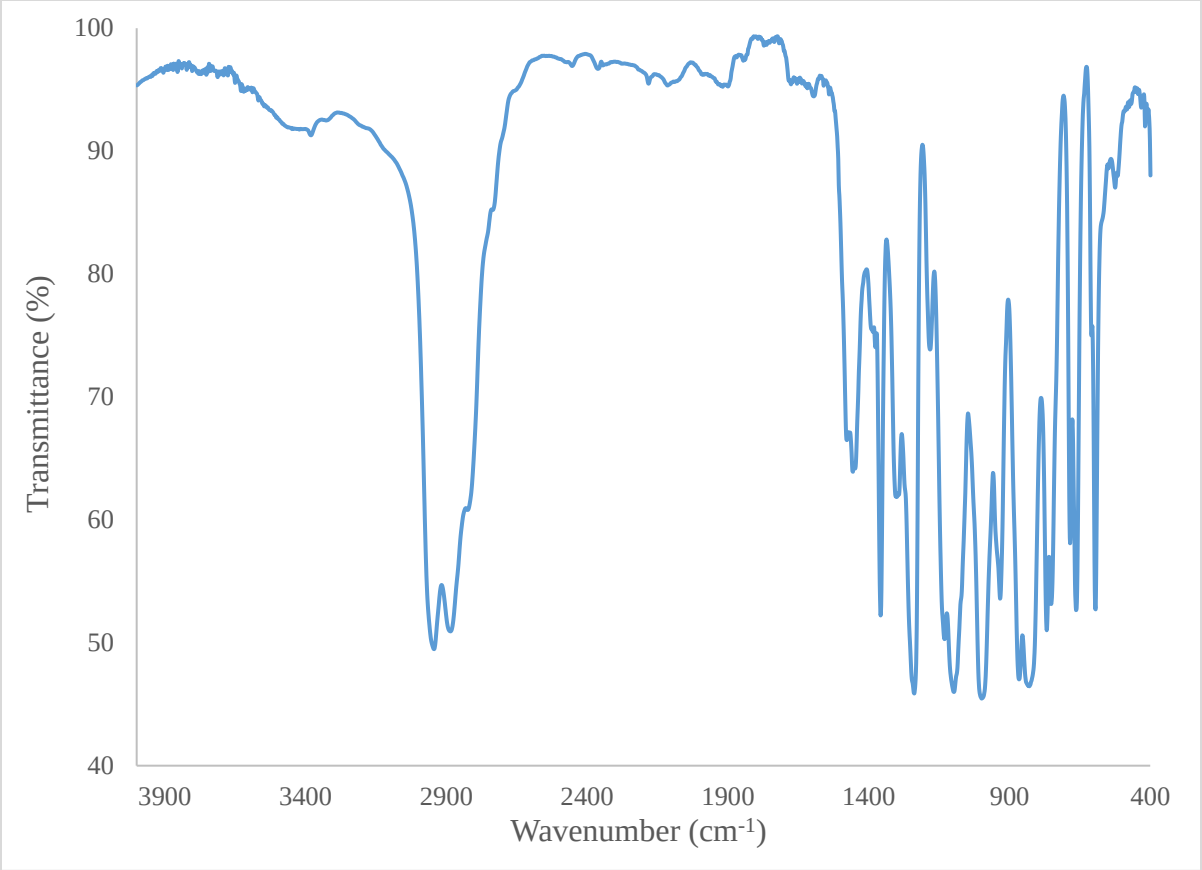

Figure A2.16. IR spectrum of **2.2** as a KBr pellet.

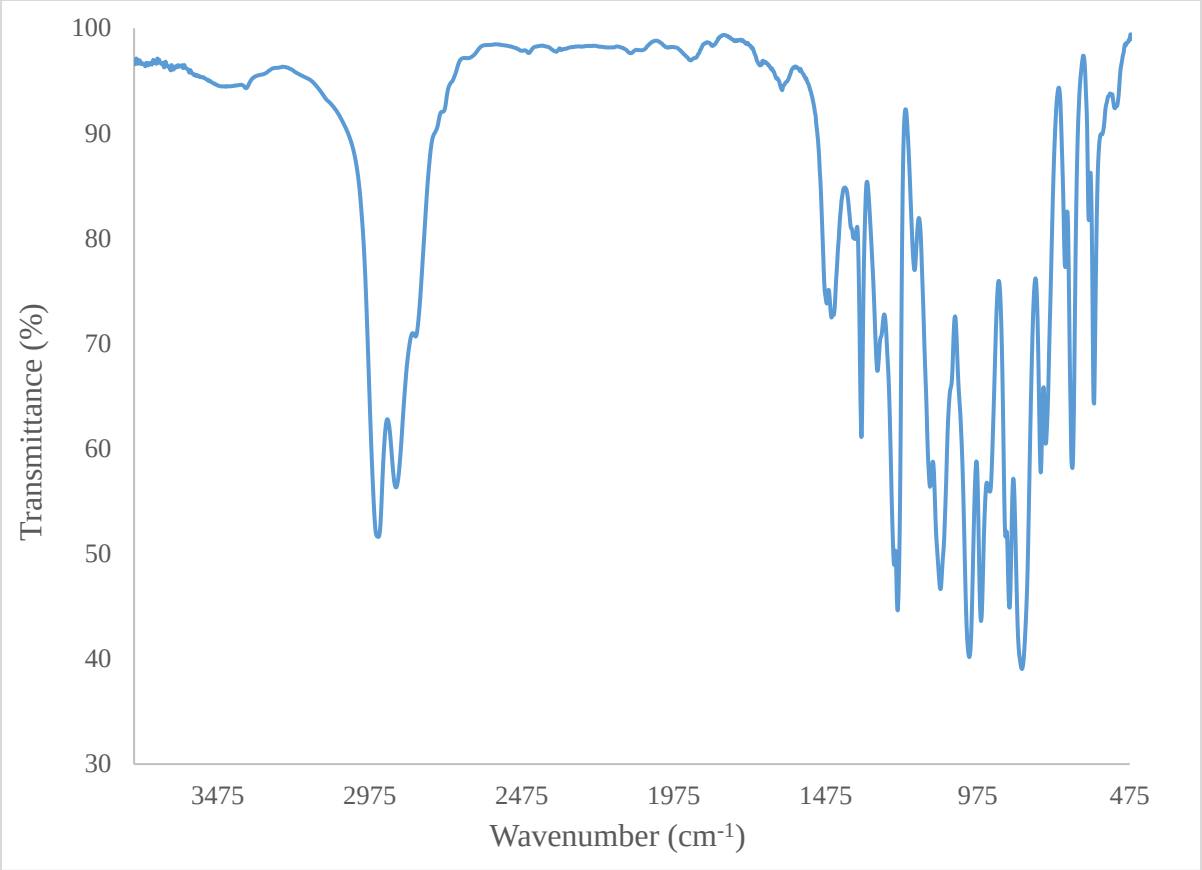

Figure A2.17. IR spectrum of **2.4** as a KBr pellet.

2.5.5 Raman Spectra

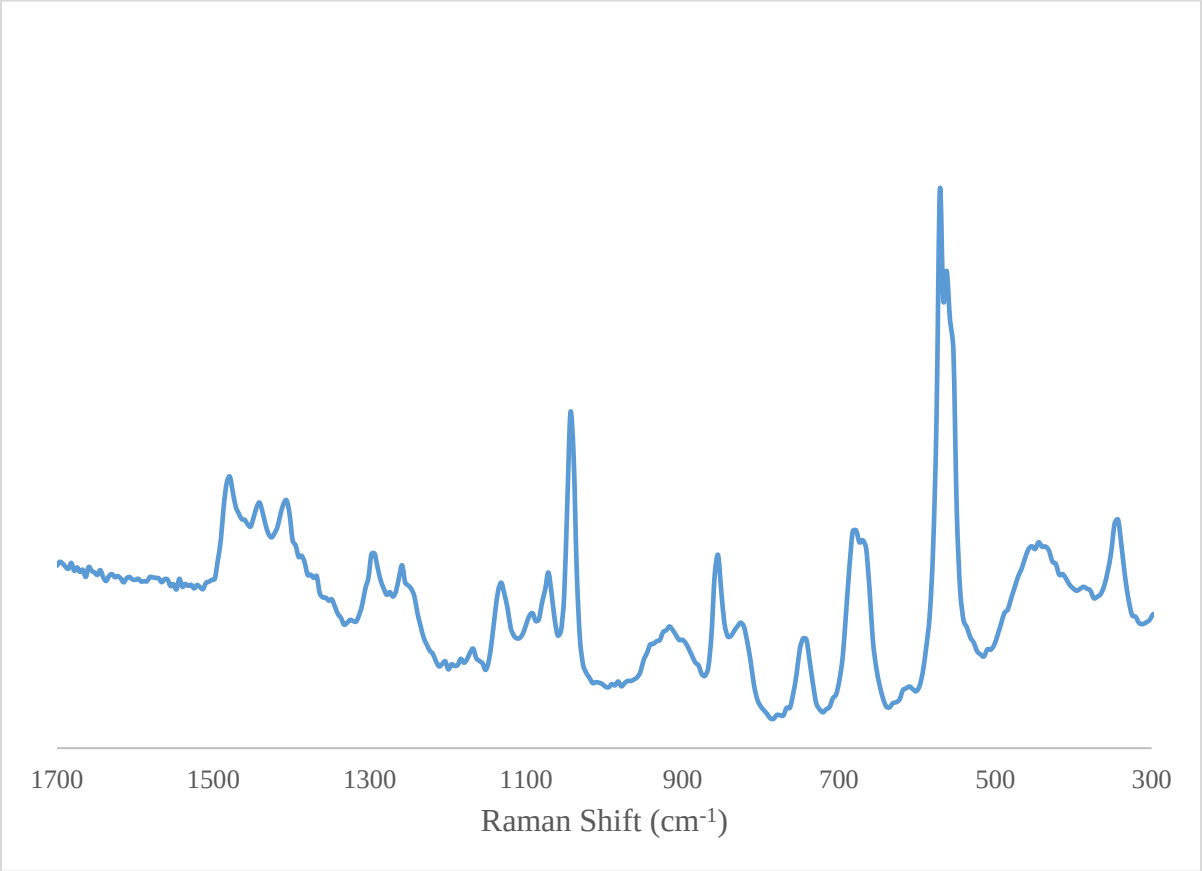

Figure A2.18. Partial Raman spectrum of **2.1**.

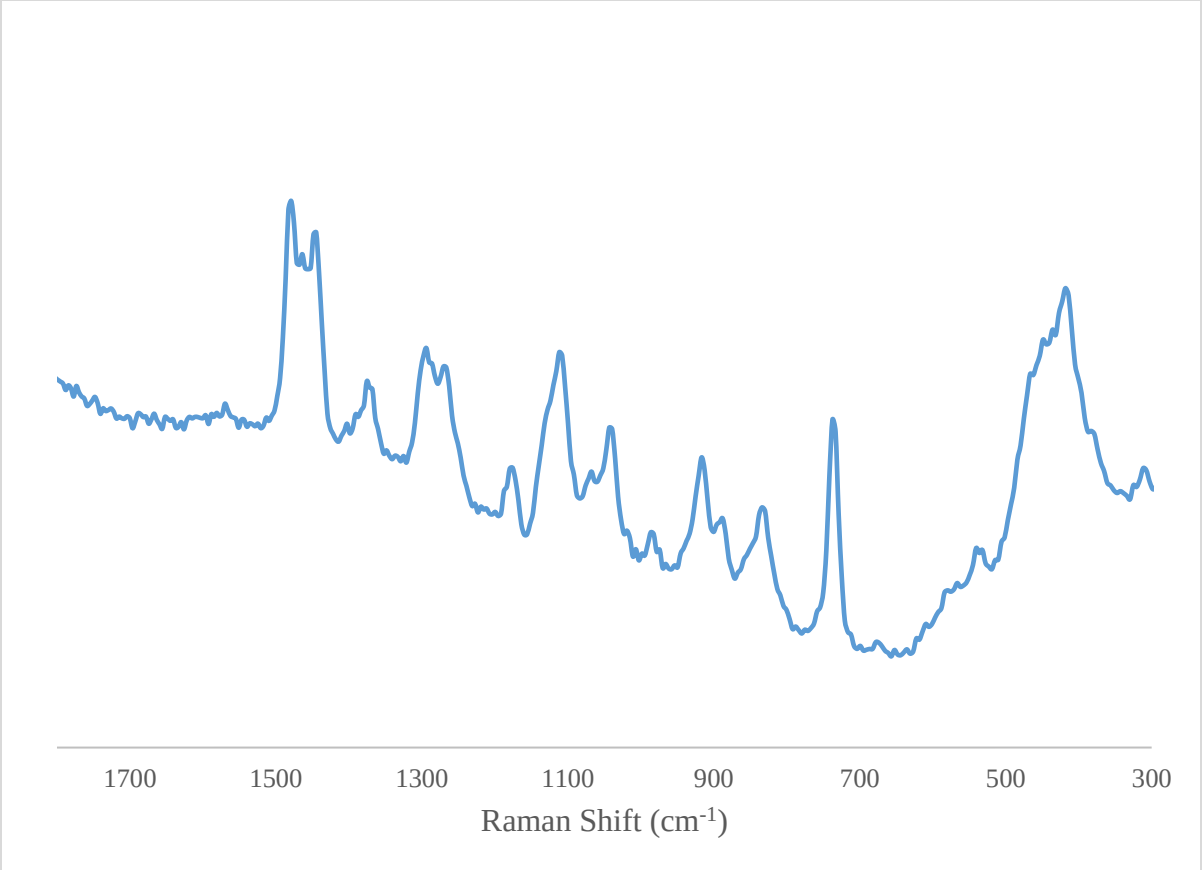

Figure A2.19. Partial Raman spectrum of **2.2**.

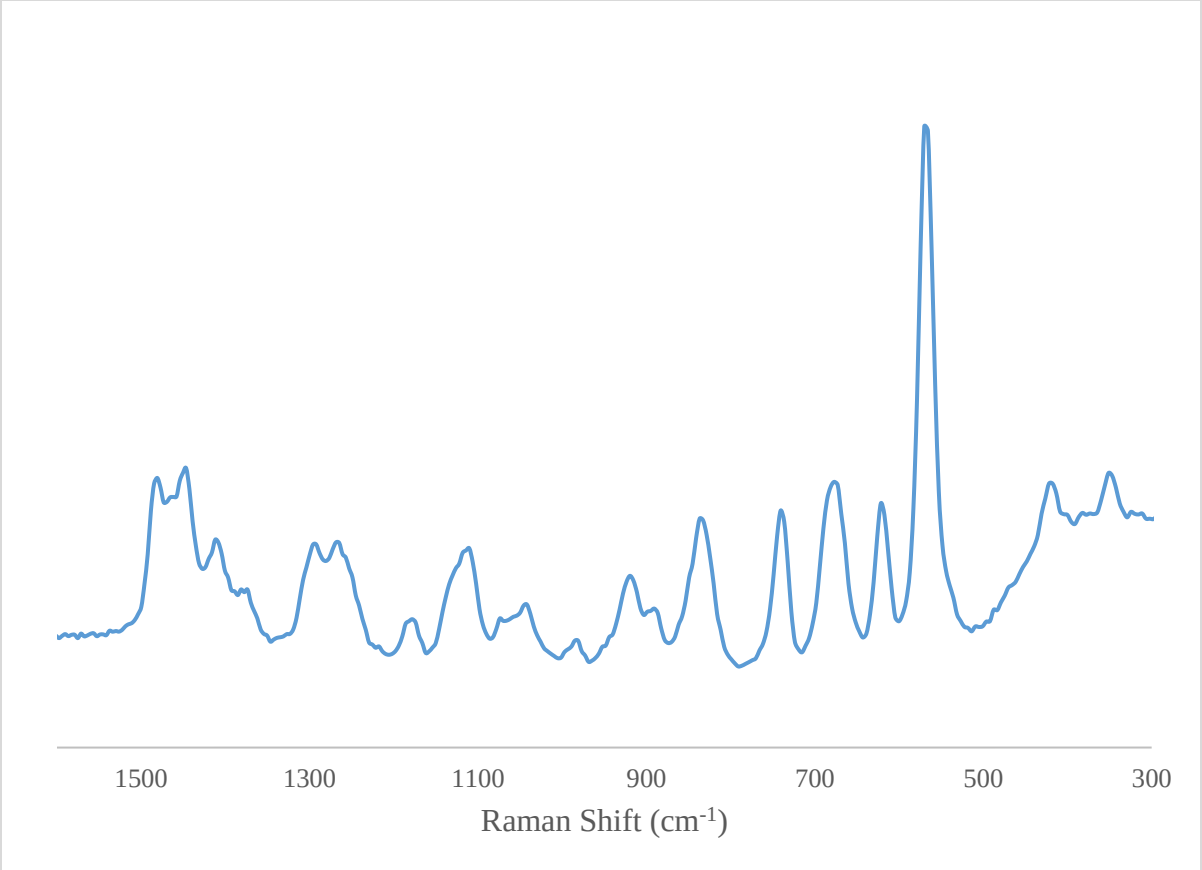

Figure A2.20. Partial Raman spectrum of **2.4**.

2.6 References

1. So, Y.-M.; Wang, G.-C.; Li, Y.; Sung, H. H. Y.; Williams, I. D.; Lin, Z.; Leung, W.-H., A Tetravalent Cerium Complex Containing a Ce=O Bond. *Angew. Chem. Int. Ed.* **2014,** *53* (6), 1626-1629.

2. Damon, P. L.; Wu, G.; Kaltsoyannis, N.; Hayton, T. W., Formation of a Ce(IV) Oxo Complex via Inner Sphere Nitrate Reduction. *J. Am. Chem. Soc.* **2016,** *138* (39), 12743-12746.

3. Solola, L. A.; Zabula, A. V.; Dorfner, W. L.; Manor, B. C.; Carroll, P. J.; Schelter, E. J., Cerium(IV) Imido Complexes: Structural, Computational, and Reactivity Studies. *J. Am. Chem. Soc.* **2017,** *139* (6), 2435-2442.

4. Coles, M. P.; Hitchcock, P. B.; Khvostov, A. V.; Lappert, M. F.; Li, Z.; Protchenko, A. V., Crystalline amidocerium(iv) oxides and a side-on bridging dioxygen complex. *Dalton Trans.* **2010,** *39* (29), 6780-6788.

5. Hong, J.; Zhang, L.; Yu, X.; Li, M.; Zhang, Z.; Zheng, P.; Nishiura, M.; Hou, Z.; Zhou, X., Syntheses, Structures, and Reactivities of Homometallic Rare-Earth-Metal Multimethyl Methylidene and Oxo Complexes. *Chem. Eur. J.* **2011,** *17* (7), 2130-2137.

6. Scott, J.; Fan, H.; Wicker, B. F.; Fout, A. R.; Baik, M.-H.; Mindiola, D. J., Lewis Acid Stabilized Methylidene and Oxoscandium Complexes. *J. Am. Chem. Soc.* **2008,** *130* (44), 14438-14439.

7. Summerscales, O. T.; Gordon, J. C., Complexes containing multiple bonding interactions between lanthanoid elements and main-group fragments. *RSC Adv.* **2013,** *3* (19), 6682-6692.

8. Holm, R. H., Metal-centered oxygen atom transfer reactions. *Chem. Rev.* **1987,** *87* (6), 1401-1449.

9. Corcos, A. R.; Pap, J. S.; Yang, T.; Berry, J. F., A Synthetic Oxygen Atom Transfer Photocycle from a Diruthenium Oxyanion Complex. *J. Am. Chem. Soc.* **2016,** *138* (31), 10032-10040.

10. Radford, R. J.; Lim, M. D.; Silva, R. S. D.; Ford, P. C., Photochemical cleavage of nitrate ion coordinated to a Cr(III) porphyrin. *J. Coord. Chem.* **2010,** *63* (14-16), 2743-2749.

11. Suslick, K. S.; Watson, R. A., Photochemical reduction of nitrate and nitrite by manganese and iron porphyrins. *Inorg. Chem.* **1991,** *30* (5), 912-919.

12. Taylor, R. D.; Todd, P. G.; Chasteen, N. D.; Spence, J. T., Reduction of nitrate by monomeric molybdenum(V) complexes in dimethylformamide. *Inorg. Chem.* **1979,** *18* (1), 44-48.

13. D'Aprano, A.; Salomon, M.; Mauro, V., Solvent effects on complexation of crown ethers with $LiClO_4$, $NaClO_4$ and $KClO_4$ in methanol and acetonitrile. *J. Solution Chem.* **1995,** *24* (7), 685-702.

14. D'Aprano, A.; Sesta, B.; Mauro, V.; Salomon, M., Complexation of Li^+, Na^+ and K^+ Ions by [222], [222D], [221], [221D] Cryptands in Acetonitrile at 25 °C: Conductometric Determination of the True Thermodynamic Formation Constants. *J. Incl. Phenom. Macrocycl. Chem.* **1999,** *35* (3), 451-465.

15. Hitchcock, P. B.; Huang, Q.-G.; Lappert, M. F.; Wei, X.-H., Lanthanide metal amides revisited; the use of the 2,2,6,6-tetramethylpiperidinato (TMP) ligand. *J. Mater. Chem.* **2004,** *14* (21), 3266-3273.

16. Hitchcock, P. B.; Lappert, M. F.; Protchenko, A. V., Facile formation of a homoleptic Ce(iv) amide *via* aerobic oxidation. *ChemComm* **2006,** (33), 3546-3548.

17. Chekhlov, A. N., Crystal Structure of (2.2.2-Cryptand)lithium Perchlorate. *Russ. J. Coord. Chem.* **2003,** *29* (12), 828-832.

18. Dillon, R. E. A.; Stern, C. L.; Shriver, D. F., Structural comparisons of fast ion conductors consisting of $Li[(CF_3SO_2)_2N]$ complexes with cryptands or crown ether. *Solid State Ion.* **2000,** *133* (3), 247-255.

19. Moores, A.; Ricard, L.; Le Floch, P.; Mézailles, N., First X-ray Crystal Study and DFT Calculations of Anionic λ^4-Phosphinines. *Organometallics* **2003,** *22* (9), 1960-1966.

20. Rudd, P. A.; Planas, N.; Bill, E.; Gagliardi, L.; Lu, C. C., Dinitrogen Activation at Iron and Cobalt Metallalumatranes. *Eur. J. Inorg. Chem.* **2013,** *2013* (22-23), 3898-3906.

21. Yin, H.; Carroll, P. J.; Manor, B. C.; Anna, J. M.; Schelter, E. J., Cerium Photosensitizers: Structure-Function Relationships and Applications in Photocatalytic Aryl Coupling Reactions. *J. Am. Chem. Soc.* **2016,** *138* (18), 5984-93.

22. Yin, H.; Carroll, P. J.; Anna, J. M.; Schelter, E. J., Luminescent Ce(III) Complexes as Stoichiometric and Catalytic Photoreductants for Halogen Atom Abstraction Reactions. *J. Am. Chem. Soc.* **2015,** *137* (29), 9234-9237.

23. Eisenstein, O.; Hitchcock, P. B.; Hulkes, A. G.; Lappert, M. F.; Maron, L., Cerium masquerading as a Group 4 element: synthesis, structure and computational characterisation of $[CeCl\{N(SiMe_3)_2\}_3]$. *ChemComm* **2001,** (17), 1560-1561.

24. Hitchcock, P. B.; Hulkes, A. G.; Lappert, M. F., Oxidation in Nonclassical Organolanthanide Chemistry: Synthesis, Characterization, and X-ray Crystal Structures of Cerium(III) and -(IV) Amides. *Inorg. Chem.* **2004,** *43* (3), 1031-1038.

25. Pasgreta, E.; Puchta, R.; Galle, M.; van Eikema Hommes, N.; Zahl, A.; van Eldik, R., Ligand Exchange Processes on Solvated Lithium Cations. II. Complexation by Cryptands in γ-Butyrolactone as Solvent. *J. Incl. Phenom. Macro.* **2007,** *58* (1), 81-88.

26. Rhinebarger, R. R.; Popov, A. I., Lithium-7 NMR studies of macrobicyclic complexes in ambient temperature molten salts. *Polyhedron* **1988,** *7* (15), 1341-1347.

27. Aspinall, H. C.; Bacsa, J.; Jones, A. C.; Wrench, J. S.; Black, K.; Chalker, P. R.; King, P. J.; Marshall, P.; Werner, M.; Davies, H. O.; Odedra, R., Ce(IV) Complexes with Donor-Functionalized Alkoxide Ligands: Improved Precursors for Chemical Vapor Deposition of CeO_2. *Inorg. Chem.* **2011,** *50* (22), 11644-11652.

28. Schläfer, J.; Stucky, S.; Tyrra, W.; Mathur, S., Heterobi- and Trimetallic Cerium(IV) tert-Butoxides with Mono-, Di-, and Trivalent Metals (M = K(I), Ge(II), Sn(II), Pb(II), Al(III), Fe(III)). *Inorg. Chem.* **2013,** *52* (7), 4002-4010.

29. Lehn, J.-S. M.; Hoffman, D. M., (μ_3-Hydroxo)-(μ_3-oxo)-tris(μ_2-2,3-dimethyl-2-butoxo)-hexakis(2,3-dimethyl-2-butoxy)-tri-cerium In *CCDC 272487: Experimental Crystal Structure Determination*, 2014.

30. Natrajan, L.; Pécaut, J.; Mazzanti, M.; LeBrun, C., Controlled Hydrolysis of Lanthanide Complexes of the N-Donor Tripod Tris(2-pyridylmethyl)amine versus Bisligand Complex Formation. *Inorg. Chem.* **2005,** *44* (13), 4756-4765.

31. Gradeff, P. S.; Yunlu, K.; Deming, T. J.; Olofson, J. M.; Doedens, R. J.; Evans, W. J., Synthesis of yttrium and lanthanide silyloxy complexes from anhydrous nitrate and oxo alkoxide precursors and the x-ray crystal structure of $[Ce(OSiPh_3)_3(THF)_3](THF)$. *Inorg. Chem.* **1990,** *29* (3), 420-424.

32. Robinson, J. R.; Carroll, P. J.; Walsh, P. J.; Schelter, E. J., The Impact of Ligand Reorganization on Cerium(III) Oxidation Chemistry. *Angew. Chem. Int. Ed.* **2012,** *51* (40), 10159-10163.

33. Williams, U. J.; Carroll, P. J.; Schelter, E. J., Synthesis and Analysis of a Family of Cerium(IV) Halide and Pseudohalide Compounds. *Inorg. Chem.* **2014,** *53* (12), 6338-6345.

34. Williams, U. J.; Robinson, J. R.; Lewis, A. J.; Carroll, P. J.; Walsh, P. J.; Schelter, E. J., Synthesis, Bonding, and Reactivity of a Cerium(IV) Fluoride Complex. *Inorg. Chem.* **2014,** *53* (1), 27-29.

35. Arnold, P. L.; Patel, D.; Wilson, C.; Love, J. B., Reduction and selective oxo group silylation of the uranyl dication. *Nature* **2008,** *451* (7176), 315-317.

36. Yahia, A.; Arnold, P. L.; Love, J. B.; Maron, L., A DFT study of the single electron reduction and silylation of the U-O bond of the uranyl dication in a macrocyclic environment. *ChemComm* **2009,** (17), 2402-2404.

37. Yahia, A.; Arnold, P. L.; Love, J. B.; Maron, L., The Effect of the Equatorial Environment on Oxo-Group Silylation of the Uranyl Dication: A Computational Study. *Chem. Eur. J.* **2010,** *16* (16), 4881-4888.

38. Löble, M. W.; Keith, J. M.; Altman, A. B.; Stieber, S. C. E.; Batista, E. R.; Boland, K. S.; Conradson, S. D.; Clark, D. L.; Lezama Pacheco, J.; Kozimor, S. A.; Martin, R. L.; Minasian, S. G.; Olson, A. C.; Scott, B. L.; Shuh, D. K.; Tyliszczak, T.; Wilkerson, M. P.; Zehnder, R. A., Covalency in Lanthanides. An X-ray Absorption Spectroscopy and Density Functional Theory Study of $LnCl_6^{x-}$ (x = 3, 2). *J. Am. Chem. Soc.* **2015,** *137* (7), 2506-2523.

39. Niemeyer, M., 1,2-Dimethoxyethan- und Tetrahydrofuran-Komplexe der Seltenerdmetallnitrate. *Z. Anorg. Allg. Chem.* **2006,** *632* (8-9), 1449-1456.

40. Harris, R. K.; Becker, E. D.; Menezes, S. M. C. d.; Goodfellow, R.; Granger, P., NMR nomenclature. Nuclear spin properties and conventions for chemical shifts (IUPAC Recommendations 2001). *Pure Appl. Chem.* **2001,** *73* (11), 1795-1818.

41. Harris, R. K.; Becker, E. D.; Menezes, S. M. C. d.; Granger, P.; Hoffman, R. E.; Zilm, K. W., Further conventions for NMR shielding and chemical shifts (IUPAC Recommendations 2008). *Pure Appl. Chem.* **2008,** *80* (1), 59-84.

42. Kern, B.; Vitze, H.; Bolte, M.; Wagner, M.; Lerner, H.-W., Kristallstruktur des Lithium-Trimethylsilanolats $[Li_7(OSiMe_3)_7(THF)]$. *Z. Anorg. Allg. Chem.* **2008,** *634* (11), 1830-1832.

43. Hitchcock, P. B.; Hulkes, A. G.; Lappert, M. F.; Li, Z., Cerium(iii) dialkyl dithiocarbamates from $[Ce\{N(SiMe_3)_2\}_3]$ and tetraalkylthiuram disulfides, and $[Ce(\kappa^2\text{-}S_2CNEt_2)_4]$ from the Ce^{III} precursor; Tb^{III} and Nd^{III} analogues. *Dalton Trans.* **2004,** (1), 129-136.

44. *SMART Apex II*, 2.1; Bruker AXS Inc.: Madison, WI, 2005.

45. *SAINT Software User's Guide*, 7.34a; Bruker AXS Inc.: Madison, WI, 2005.

46. Sheldrick, G. M. *SADABS*, University of Gottingen: Germany, 2005.

47. *SHELXTL PC*, 6.12; Bruker AXS Inc.: Madison, WI, 2005.

Chapter 3. Synthesis, Characterization and Electrochemistry of the Homoleptic f Element Ketimide Complexes $[Li]_2[M(N{=}C^tBuPh)_6]$ (M = Ce, Th)

Portions of this work were published in:

Assefa, M.K.; Sergentu, D-C.; Seaman, L.A.; Wu, G.; Autschbach, J.; Hayton, T.W. *Inorg. Chem.* **2019**, *58*, 12654-12661.

http://pubs.acs.org/articlesonrequest/AOR-Jen9W3AKnCkCKhGyC7Ax

3.1 Introduction

The chemistry of high-valent lanthanide ions has remained enigmatic.[1-7] Indeed, cerium is the only lanthanide element that can easily form stable molecular +4 complexes, which has paved the way for extensive study of its redox properties, both in solid-state and solution.[8-16] This redox chemistry is relevant to both fundamental and applied research.[17-33] For example, multi-configurational ground states have recently been revealed in several molecular and solid-state Ce(IV) materials.[25, 29-37] Moreover, X-ray absorption spectroscopy and density functional theory studies on tetravalent cerium have revealed considerable covalency and f orbital participation in Ce(IV)-L bonding.[24-29, 38] In addition, the Ce(IV/III) redox couple has proved instrumental for separation of cerium from mineral ores and in the mechanism of action of several ceria-supported catalysts.[8, 10, 23, 39, 40] Despite these successes, there still are only a handful of ligands that are capable of stabilizing high oxidation states in the lanthanides, especially in non-aqueous environments. Examples include nitroxide,[9] tetraazaannulene,[41] imidophosphorane,[14, 42] atrane,[16] binolate,[43] silyloxide,[44] and methanediide.[27, 45, 46]

The ketimide ligand ($R_2C{=}N^-$) is considered to be strongly electron donating, and thus, is predicted to stabilize high oxidation states in otherwise oxidizing metal centers. For instance, Hayton and co-workers have previously utilized this ligand to synthesize the tetravalent transition metal ketimides, $M(N{=}C^tBu_2)_4$ (M = Mn, Fe, Co, V, Nb, Ta), in moderate to good yields.[47-50] Similarly, Hoffman and co-workers have reported the synthesis of the analogous group VI ketimides, $M(N{=}C^tBu_2)_4$ (M = Cr, Mo, W).[51] DFT calculations and ligand field analyses on these complexes have found that the ketimide ligand is a strong σ- and π-donor, as well as a strong π-acceptor.[47, 48, 51, 52] Drawing on these results, the extent to which this ligand can stabilize high oxidation states in the lanthanides, specifically in cerium, is explored herein.

While the synthesis and redox chemistry of high-valent actinide ketimides has recently been explored,[53-55] that of the lanthanide analogues is unknown. In this work, the synthesis and computational and electrochemical analysis of a homoleptic cerium(IV) ketimide and its isostructural thorium(IV) analogue is described.

Scheme 3.1. σ and π bonding of the ketimide ligand (Scheme adopted from Ref[47]).

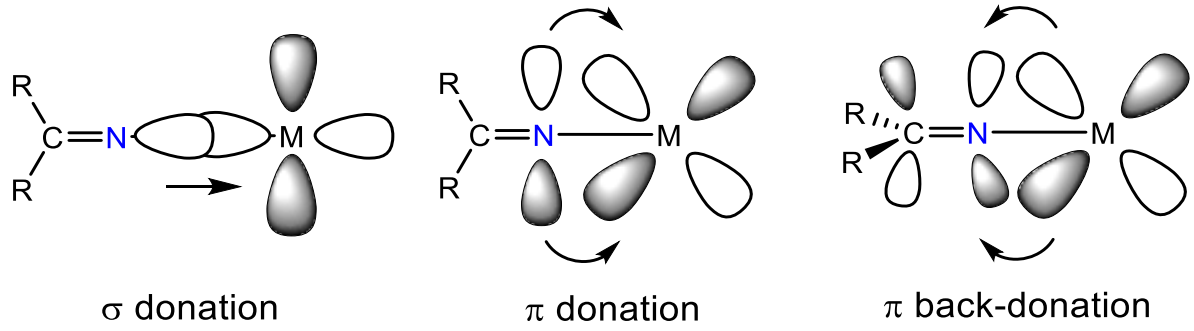

3.2 Results and Discussion

3.2.1 Synthesis and Characterization of $[Li]_2[Ce(N{=}C^tBuPh)_6]$ (3.1)

Reaction of $[Ce(NO_3)_3(THF)_4]$ with 6 equiv of $Li(N{=}C^tBuPh)$ in THF, followed by addition of 0.5 equiv of I_2, results in the formation of a deep purple solution. Work-up of this solution results in isolation of $[Li]_2[Ce(N{=}C^tBuPh)_6]$ (**3.1**), as purple plates in 44% yield (Scheme 3.2). Intriguingly, **3.1** is also formed in small quantities during the reaction of $Li(N{=}C^tBuPh)$ with $[Ce(NO_3)_3(THF)_4]$, in the absence of I_2, according to a ^1H NMR spectrum of an aliquot of the reaction mixture. The oxidation to Ce(IV) under these conditions can likely be attributed to the redox activity of the nitrate co-ligand in the $[Ce(NO_3)_3(THF)_4]$ starting material, which has been shown to oxidize Ce(III) under certain conditions.[56]

Complex **3.1** is readily soluble in diethyl ether (Et_2O), toluene, and THF, but only sparingly soluble in non-polar aliphatic solvents, such as hexanes. Its IR spectrum exhibits two strong absorptions at 1624 and 1637 cm^{-1} assignable to the C=N stretches of the ketimide ligand. Additionally, its ^1H NMR spectrum in C_6D_6 features a sharp singlet at 1.36 ppm, integrating to 54 protons, which is attributable to the *tert*-butyl protons of the ketimide ligand. This spectrum also features two multiplets at 6.62 and 6.99 ppm that integrate to 12 and 18 protons, respectively, which are assignable to the *ortho* and overlapping *meta*/*para* protons of the ketimide phenyl rings. The $^{13}C\{^1H\}$ NMR spectrum of **3.1** in C_6D_6 exhibits a resonance at 175.08 ppm assignable to the ketimide C=N environment. This chemical shift is nearly identical to that observed for the C=N resonance in the octahedral U(VI) ketimide complex [U(N=C^{t}BuPh)$_6$] (180.40 ppm).[55] Finally, the $^7Li\{^1H\}$ NMR spectrum of **3.1** in C_6D_6 features a single resonance at 0.06 ppm. Likewise, the $^7Li\{^1H\}$ NMR spectrum of **3.1** in toluene-d_8 features a single resonance at -0.02 ppm (Figure A3.5). Curiously, though, the $^7Li\{^1H\}$ NMR spectrum of **3.1** in THF-d_8 features broad resonances at 1.94, 1.75, and 0.65 ppm (Figure A3.7). The resonances at 1.94 and 1.75 ppm are assignable to free Li(N=C^{t}BuPh) (Figure A3.16),[57] suggesting that dissociation of one equiv of Li(N=C^{t}BuPh) from **3.1** occurs in this solvent, resulting in formation of [Li][Ce(N=C^{t}BuPh)$_5$] (**3.1'**). Consistent with this hypothesis, the $^7Li\{^1H\}$ signals assignable to Li(N=C^{t}BuPh) and **3.1'** are present in a 1:1 ratio. No evidence for the dissociation of Li(N=C^{t}BuPh) from **3.1** is observed in C_6D_6 or toluene-d_8, suggesting that the strong donor ability of THF facilitates formation of the lithium ketimide salt. Finally, complex **3.1** features moderate thermal stability: a solution of **3.1** in C_6D_6 exhibits about 20% decomposition after 2 d at room temperature, according to ^1H NMR spectroscopy. The

principal decomposition product appears to be a Ce(III) complex on the basis of the paramagnetically-shifted resonances observed in the ^{1}H NMR spectrum.

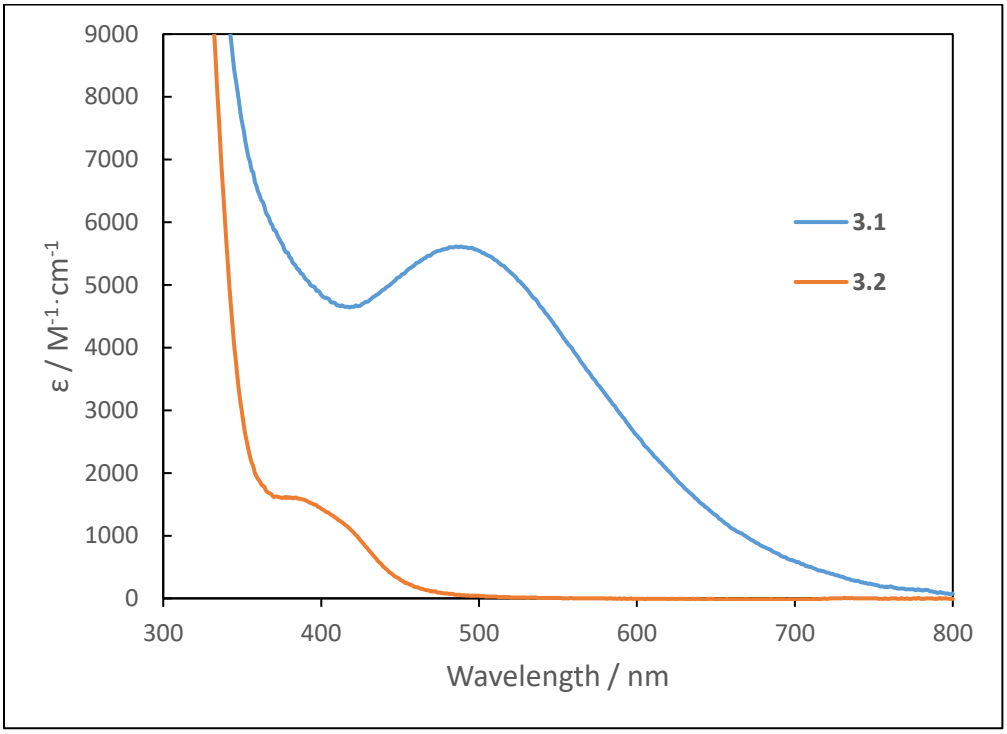

Figure 3.1. UV-Vis spectra of **3.1** (0.089 mM) and **3.2** (0.13 mM) in toluene.

The UV-Vis spectrum of **3.1** in toluene exhibits a strong, broad absorption at 485 nm (ε = 5600 $M^{-1}\cdot cm^{-1}$), which is assignable to a ligand-to-metal charge transfer (Figure 3.1, also see discussion below). It is quite common for Ce(IV) complexes to be deeply colored. For example, $[Ce(trop)_4]$[31] and $[Ce(\eta^8\text{-}Pn^*)_2]$[30] feature intense and broad LMCT absorptions at 450 and 530 nm, respectively. $[Ce(cot)_2]$, $[Ce(tmtaa)_2]$, and $[Ce(BIPM^{TMS})_2]$ are also deeply colored.[34, 46, 58, 59]

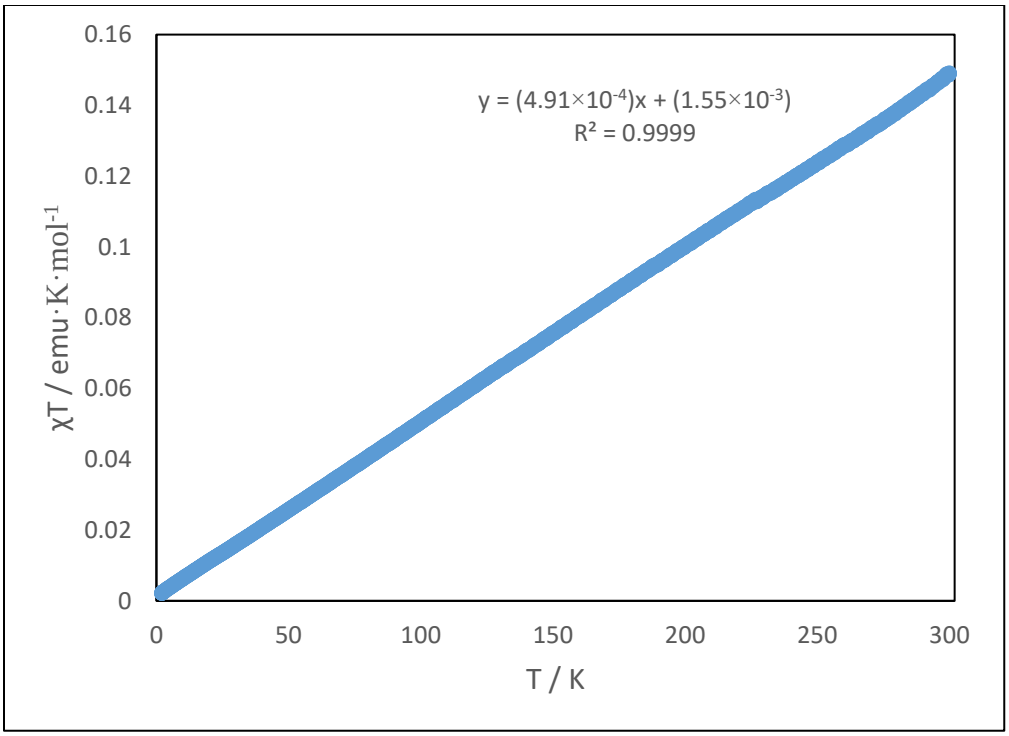

Figure 3.2. Variable-temperature magnetic susceptibility (χT) data for **3.1** collected at 1 Tesla.

The solid-state magnetic susceptibility of **3.1** was also measured using SQUID magnetometry. Significantly, this measurement reveals temperature independent paramagnetism for **3.1**. The value of χ_{TIP}, extracted from the temperature dependent χT data), is 4.91×10^{-4} emu/mol, which is comparable to the χ_{TIP} values reported for $Ce(tmtaa)_2$ (2.33×10^{-4} emu/mol), $Ce(cot)_2$ (1.4×10^{-4} emu/mol), and $Ce(acac)_4$ (2.1×10^{-4} emu/mol).[31, 35] The observation of TIP in Ce(IV) complexes has been interpreted as evidence of multi-configurational character.[31] However, it could also simply indicate field-induced mixing of a closed shell singlet ground state with a low lying triplet excited state, as is known for some U(VI) complexes and d^0 transition metal oxo anions.[60-62]

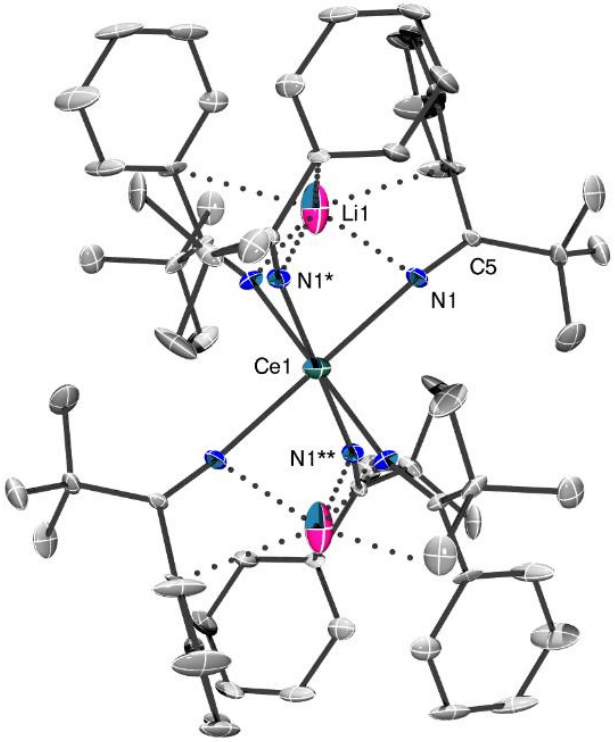

Figure 3.3. Solid-State Molecular Structure of **3.1**. Hydrogen atoms omitted for clarity.

Crystals of **3.1** suitable for an X-ray diffraction analysis were grown from a dilute pentane solution stored at -25 °C. Complex **3.1** crystallizes in the rhombohedral space group R-3, and its solid-state molecular structure is shown in Figure 3.3. A selection of metrical parameters can be found in Table 3.1. In the solid state, **3.1** adopts a distorted octahedral geometry (e.g., N1-Ce1-N1* = 81.8(2)° and N1-Ce1-N1** = 98.2(2)°) about the Ce center, which is ligated by six crystallographically equivalent ketimide ligands. The C=N bond distance in **3.1** (1.256(8) Å) is similar to that observed in the U(V) ketimide, [Li][U(N=C^{t}BuPh)$_6$] (1.260(3) Å),[55] and other homoleptic transition metal ketimides (1.25 – 1.27 Å).[47-51] The Ce-N bond length (2.338(5) Å) is longer than those reported for the homoleptic Ce(IV) phosphoiminato complex [Ce(NP(pip)$_3$)$_4$] (av. 2.20(2) Å),[14] and the Ce(IV) amides [Ce(N^{i}Pr$_2$)$_4$] (2.225(1) and 2.223(1) Å),[63] [Ce(NCy$_2$)$_4$] (2.238(5) – 2.247(6) Å),[64] and [Ce(N(SiHMe$_2$)$_2$)$_4$] (2.2378(11) –

2.2574(11) Å),[65] likely due to the higher coordination number in **3.1**, as well as the dianionic charge at the Ce center. This distance is also considerably longer than the U-N distance in the structurally similar U(V) ketimide complex [Li][U(N=C^{t}BuPh)$_6$] (2.217(2) Å),[55] consistent with the larger ionic radius of Ce(IV). The structure of **3.1** also features two Li cations within the secondary coordination sphere. These ions are supported by dative interactions with three nitrogen atoms and the ipso carbons of three phenyl rings. The Li-N distance (2.138(19) Å) is shorter than that in [Li][U(N=C^{t}BuPh)$_6$] (2.265(16) Å), which features a Li ion with an identical binding mode.[55] Finally, the Ce-N-C angle (165.9(5)°) is slightly smaller than the U-N-C angle in [Li][U(N=C^{t}BuPh)$_6$] (176.9(2)°),[55] which may be a consequence of the longer M-N bond lengths in **3.1**.

Scheme 3.2. Synthesis of complexes **3.1** and **3.2**

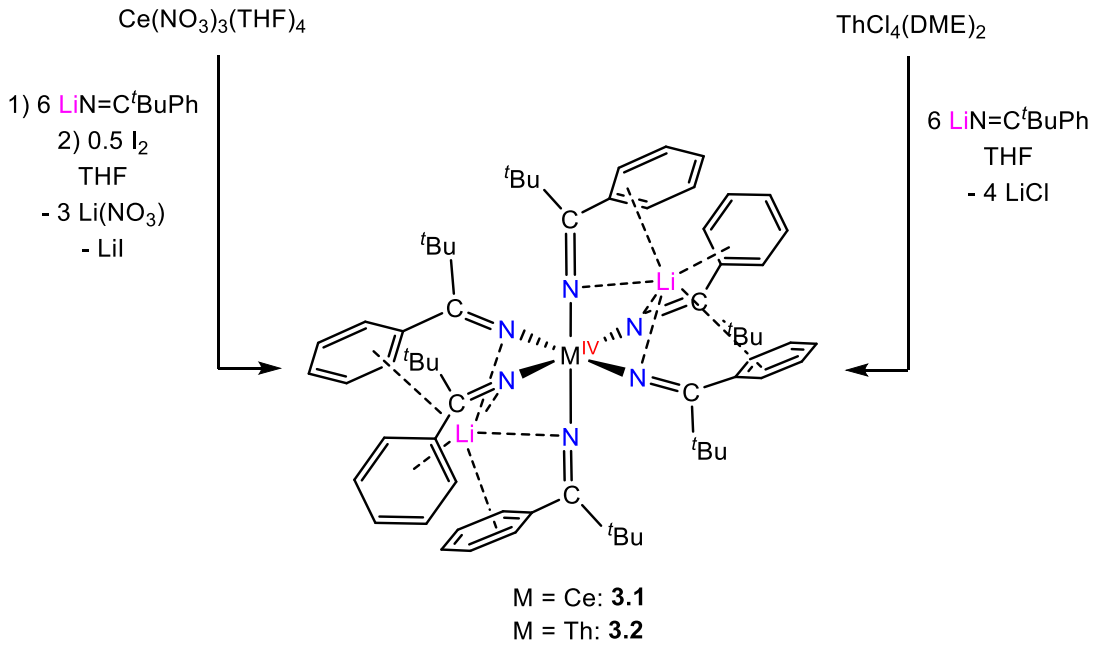

3.2.2 Synthesis and Characterization of $[Li]_2[Th(N=C^tBuPh)_6]$ (3.2)

To better contextualize the cerium results, the synthesis of the analogous thorium(IV) ketimide complex, $[Li]_2[Th(N=C^tBuPh)_6]$ (**3.2**) was attempted. Complex **3.2** was prepared by reaction of $[ThCl_4(DME)_2]$ with 6 equiv of $Li(N=C^tBuPh)$ in THF (Scheme 3.2). Workup of the reaction mixture followed by recrystallization from a concentrated THF/hexanes solution afforded **3.2** as yellow blocks in 53% yield. Curiously, reaction of UCl_4 with 6 equiv of $Li(N=C^tBuPh)$ only resulted in formation of the 5-coordinate ketimide complex, $[Li(THF)_2][U(N=C^tBuPh)_5]$, a difference that likely reflects the smaller ionic radius of U(IV).[55]

Complex **3.2** is soluble Et_2O, toluene, and THF, but features limited solubility in pentanes or hexanes. Its UV-Vis spectrum in toluene is missing the obvious ligand-to-metal charge transfer band that was observed for **3.1** (Figure 3.1); however, the NMR spectral data of **3.2** are very similar to those of **3.1**. Specifically, its ^1H NMR spectrum in C_6D_6 features a singlet at 1.27 ppm, which is assignable to the 54 *tert*-butyl protons of the ketimide ligand, while multiplets at 6.67 and 7.00 ppm correspond to the *ortho* and overlapping *meta*/*para* phenyl protons of the ketimide ligand, respectively. In addition, the C=N resonance in the $^{13}C\{^1H\}$ NMR spectrum of **3.2** (178.73 ppm) is observed at a similar chemical shift to that of **3.1**. Lastly, its $^7Li\{^1H\}$ NMR spectra in C_6D_6 or toluene-d_8 feature single resonances at 0.53 ppm and 0.47 ppm, respectively (Figures A3.10 and A3.12).

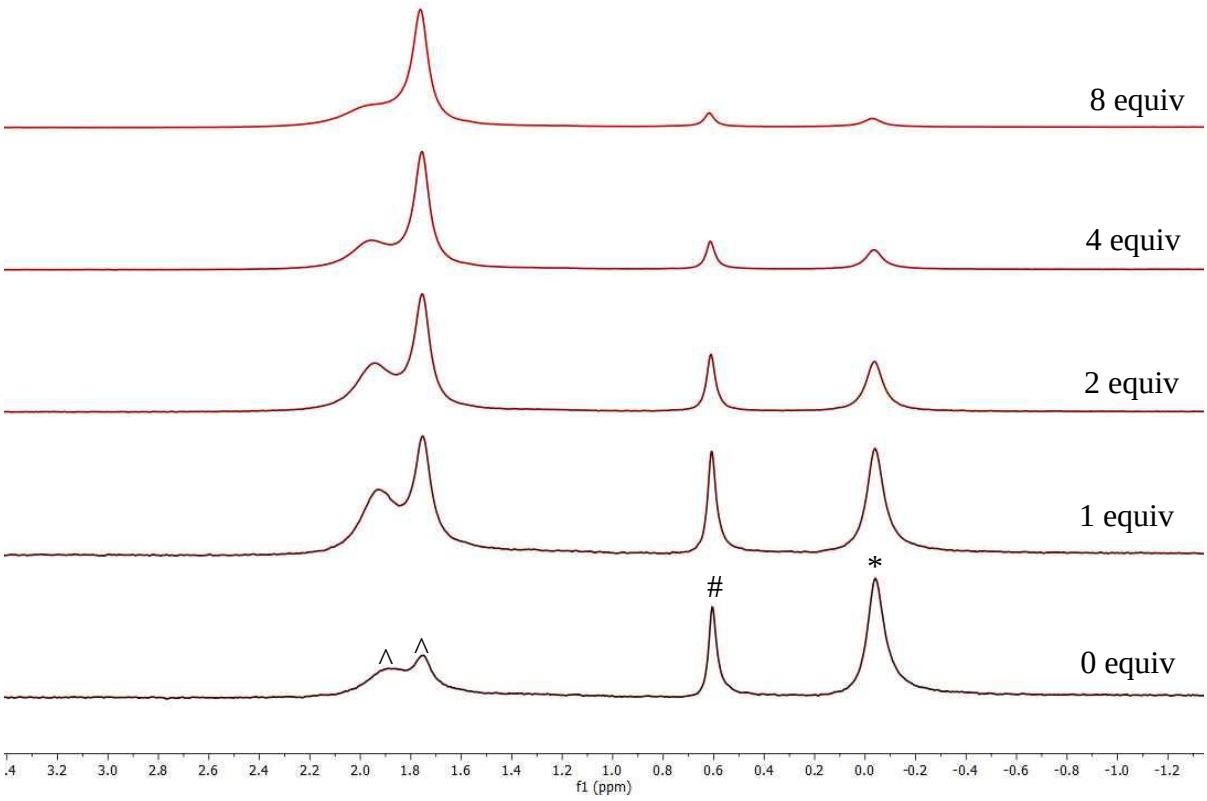

Figure 3.4. ^{7}Li{^{1}H} NMR spectra of the titration of **3.2** with Li(N=C^{t}BuPh) in THF-d_8. The resonance marked with * is assignable to [Li][Th(N=C^{t}BuPh)$_5$] (**3.2'**), the resonance marked with # is assignable to **3.2**, and the resonances marked with ^ are assignable to Li(N=C^{t}BuPh). **Experimental Details:** See details for Figure A3.21.

Interestingly, complex **3.2** also displays evidence of Li(N=C^{t}BuPh) dissociation in THF-d_8. Specifically, its ^{7}Li{^{1}H} NMR spectrum in this solvent features resonances at 1.90, 1.75, 0.61, and 0.04 ppm (Figure A3.14). The resonances at 1.90 and 1.75 ppm are assignable to Li(N=C^{t}BuPh), while the resonances at 0.61 ppm and 0.04 ppm are assignable to **3.2** and [Li][Th(N=C^{t}BuPh)$_5$] (**3.2'**), respectively. These two Th complexes are present in a 1:5.5 ratio. As expected, addition of Li(N=C^{t}BuPh) to this sample results in an increase in the relative amount of **3.2**, and after addition of 8 equiv, **3.2** and **3.2'** are present in a 1:2 ratio (Figure

A3.23). In contrast to the results collected for **3.2**, there was no evidence for the formation of **3.1** upon addition of excess Li(N=C^{t}BuPh) to THF-d_8 solutions of **3.1'** (Figure A3.19). This difference can be rationalized by the larger ionic radius of Th^{4+},[66] which allows this ion to better accommodate the high charge associated with six strongly donating ketimide ligands.

Table 3.1. Selected Bond Lengths (Å) and Angles (°) for Complexes **3.1** and **3.2**

	3.1	**3.2**
M-N	2.338(5)	2.376(2)
C-N	1.256(8)	1.257(2)
Li1-N1	2.138(19)	2.166(4)
Li1-C$_{ipso}$	2.918(11)	2.908(2)
M-N1-C5	165.9(5)	166.24(14)
N1-M-N1*	81.8(2)	79.78(6)
N1-M-N1**	98.2(2)	100.22(6)

Storage of a concentrated toluene solution of **3.2** at -25 °C for 24 h afforded crystals suitable for X-ray analysis. As expected, complexes **3.1** and **3.2** are isostructural (Table 3.3). Additionally, the Th center in **3.2** possesses a distorted octahedral geometry (e.g., N1-Th1-N1* = 79.78(6)° and N1-Th1-N1** = 100.22(6)°). The Th-N distance (2.376(2) Å) is slightly longer than the Ce-N distance in **3.1** (2.338(5) Å) (Table 1), but significantly longer than the U-N distance in the closely related U(V) ketimide, [Li][U(N=C^{t}BuPh)$_6$] (2.217(2) Å),[55] in accord with their different ionic radii.[66] This distance is also considerably longer than those reported for the Th(IV) bis(ketimido) complex [Cp*$_2$Th(N=CPh$_2$)$_2$] (2.259(4) and 2.265(5) Å),[67] which may be due to the dianionic charge at the Th center, as well as the Li coordination to the ketimide N atoms. The lithium cations are hexa-coordinate and possess an octahedral geometry, with similar Li-N (2.166(4) Å) and Li-C$_{ipso}$ (2.908(2) Å) distances to those observed

for **3.1**. The C=N bond length (1.257(2) Å) is also identical to that in **3.1** (1.256(8) Å). Lastly, the Th-N-C angle in **3.2** (166.24(14)°) is essentially identical to the Ce-N-C angle in **3.1** (165.9(5)°), but more acute than the U-N-C angle in [Li][U(N=C^{t}BuPh)$_6$] (176.9(2)°).[55]

3.2.3 Electronic Structures of 3.1 and 3.2

In an effort to understand the electronic structures of **3.1** and **3.2**, a series of Kohn-Sham density functional theory (DFT) calculations with the TPSS functional[68] were performed by our collaborators Dr. Dumitru-Claudiu Sergentu and Prof. Jochen Autschbach at University at Buffalo, State University of New York, using the X-ray structural parameters of **3.1** and **3.2**. Figure 3.5 shows molecular orbital (MO) diagrams obtained for **3.1** and **3.2** with DFT. The frontier MOs for both complexes exhibit six N-2p lone pairs exhibiting σ-donation to the metal centers, which represents a ligand–metal orbital mixing that is stronger for **3.1** than for **3.2**. For instance, the Ce-4f contributions (weights) to the frontier HOMOs of **3.1** range from ~7% to 12% whereas the Th-5f contributions to the frontier HOMOs of **3.2** range from ~3% to 5%. Additionally, the natural localized molecular orbitals (NLMOs) suggest enhanced covalency for **3.1** as revealed by the admittedly nitrogen-polarized σ and π bonds, with about 10% density weight at Ce. The Ce 4f/5d character in the Ce-N bonds of **3.1** may explain its observed temperature-independent paramagnetism.[60] According to the NLMO analysis, there is greater 4f orbital participation in both the σ and π NLMOs of **3.1** than 5f orbital participation in the corresponding NLMOs of **3.2**. Similar results were recently observed for series of isostructural cerium and thorium imido complexes.[69] Moreover, Ce(IV)-L bonds involving significant

donation into the Ce-4f orbitals have been described previously.[27, 45, 70, 71]

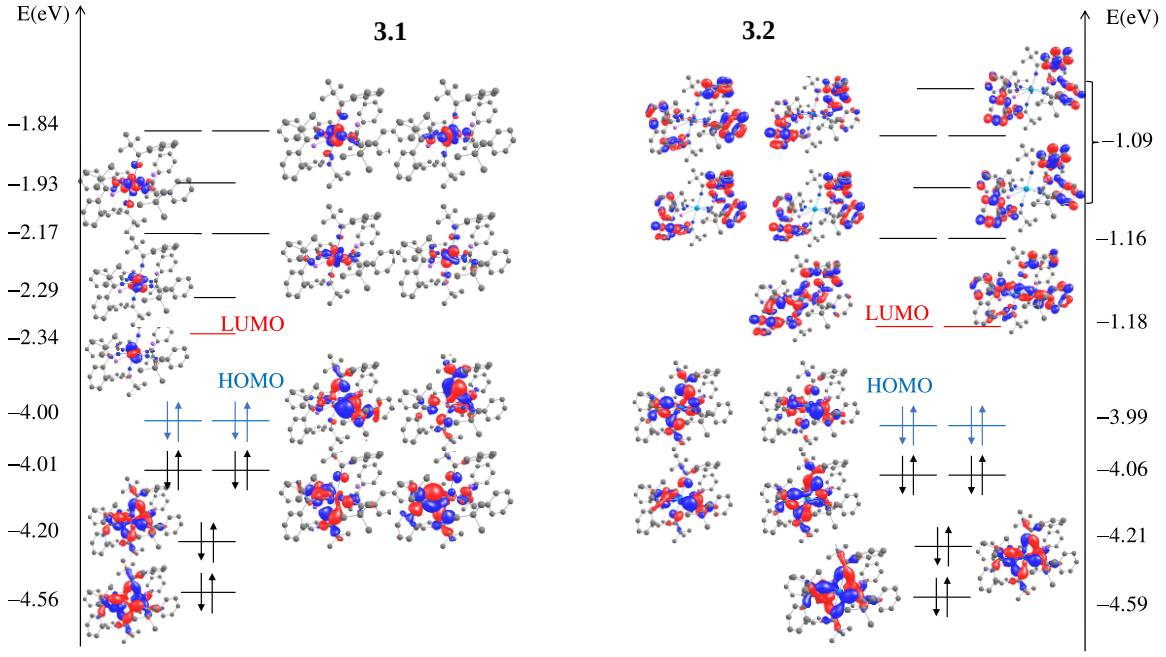

Figure 3.5. Molecular orbital (MO) diagrams obtained with all-electron scalar relativistic DFT for **3.1** (left) and **3.2** (right). Canonical MO isosurfaces at ±0.03 a.u. Taken from Ref[72].

3.2.4 Electrochemistry of 3.1 and 3.2

To better understand the donor ability of the ketimide ligand, the electrochemical properties of **3.1** and **3.2** were investigated by cyclic voltammetry. The cyclic voltammogram of **3.1** in THF at a scan rate of 200 mV/s exhibits an irreversible redox feature at $E_{p,c}$ = -2.16 V (vs. Fc/Fc^+, Figure 3.6), which is attributed to the Ce(IV/III) reduction of [Li][Ce(N=C^{t}BuPh)$_5$] (**3.1'**). This feature remains irreversible, even at scan rates of 2000 mV/s. This assignment was confirmed by comparison with the cyclic voltammogram recorded for complex **3.2**, which features no reduction features within the solvent window (Figure 3.6). The cyclic voltammograms of **3.1** and **3.2** also exhibit a complex series of irreversible oxidation features between -1.1 V and 0 V (vs. Fc/Fc^+), which is attributed to ligand oxidation events. Similar

ligand-based oxidation features were observed in the cyclic voltammogram of the related uranium ketimide, [U(N=C^{t}BuPh)$_6$],[55] as well as for Li(N=C^{t}BuPh) (Figure 3.6).

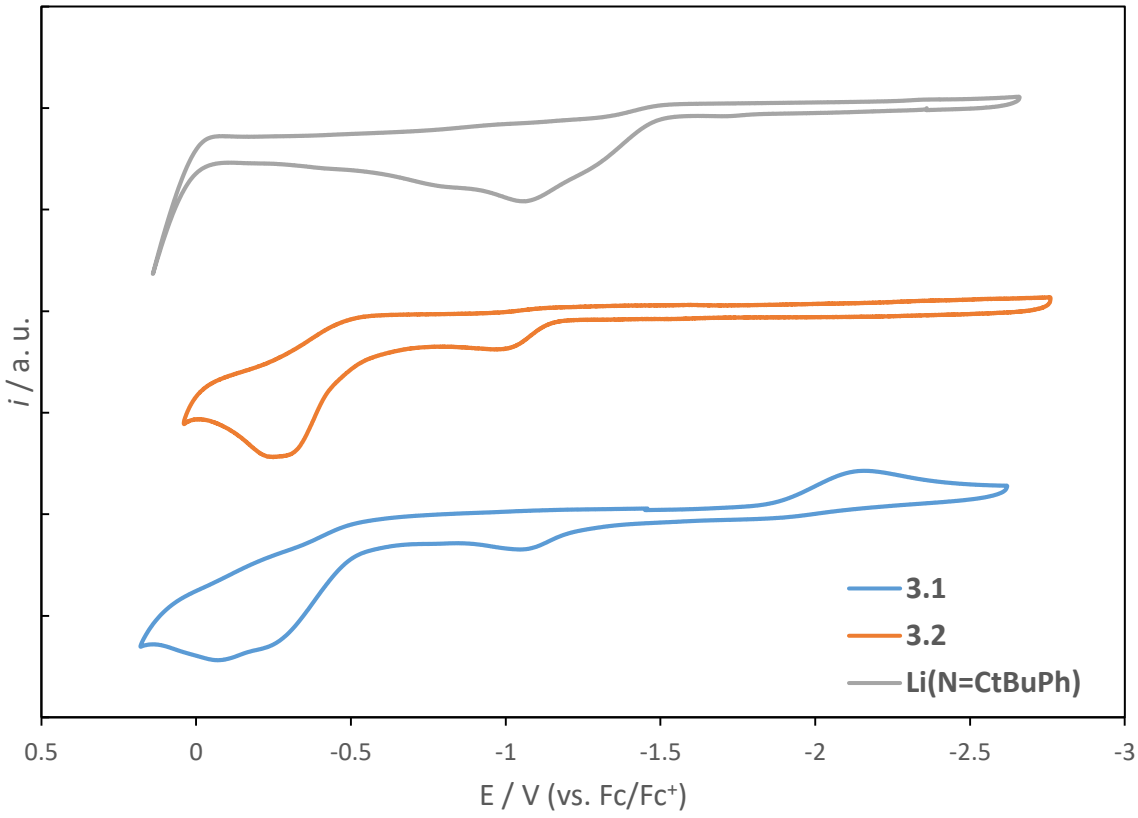

Figure 3.6. Cyclic voltammograms of **3.1**, **3.2** and Li(N=C^{t}BuPh) (200 mV/s scan rate, vs. Fc/Fc$^+$). Measured in THF with 0.1 M [NBu$_4$][BPh$_4$] as the supporting electrolyte.

The Ce(IV/III) redox feature observed for **3.1'** is amongst the lowest reported for this element (Table 3.2). For comparison, the cerium(III) tris(binolate) complex [Li(THF)]$_3$[(binolate)$_3$Ce(THF)] features an electrochemically irreversible Ce(IV/III) reduction feature at -1.09 V (vs. Fc/Fc$^+$),[43, 73] which is much more anodic than that observed for **3.1'**, suggesting that the ketimide ligand better stabilizes the Ce(IV) oxidation state than the binolate ligand. For further comparison, the Ce(IV/III) reduction features for the ferrocene-

bridged Schiff base complexes [Ce(L)(O^{t}Bu)$_2$] (LH_2 = 1,1'-di(2,4-bis-*tert*-butyl-salicylimino)ferrocene) and [Ce(L')(O^{t}Bu)$_2$] (L'H_2 = 1,1'-di(2-*tert*-butyl-salicyl-(bis-phenyl)-iminophosphorano)ferrocene) are at -2.07 and -2.39 V (vs. Fc/Fc^+), respectively.[42] These values are more in-line with the redox potential observed for **3.1'**. Similarly, the Ce(IV/III) reduction potential for [Ce(NP(pip)$_3$)$_4$] in THF was recently determined to be within the range of -2.30 to -2.47 V (vs. Fc/Fc^+).[14]

Table 3.2. Ce(IV/III) Redox Potentials for Selected Cerium Complexes

Complex	Potential (V)	Conditions
[Ce(acac)$_4$][58]	0.22 ± 0.02 vs. SHE	0.1 M $TBAPF_6$ in MeCN/acetone
[CeL]$^{4-}$, [29]	-0.454 vs. SHE	1 M KCl
[Li$_3$][(binolate)$_3$Ce][43]	-1.09 vs. Fc/Fc^+	0.1 M TPAB in THF
[Ce(BIPM^{TMS})$_2$][46]	-1.63 vs. Fc/Fc^+	0.1 M TPAB in THF
[Ce(omtaa)$_2$][41]	-1.7 vs. Fc/Fc^+	0.1 M TPAB in THF
[Ce(OSi(O^{t}Bu)$_3$)$_4$][44]	-1.72 vs. Fc/Fc^+	0.1 M $[NBu_4][B(C_6F_5)_4]$ in THF
{Ce(atrane)(OAr)}$_2$[16]	-1.86 vs. Fc/Fc^+	0.1 M TPAB in THF
[Ce(pyNO)$_4$][9]	-1.95 vs. Fc/Fc^+	0.1 M TPAB in DCM
[Ce(L')(O^{t}Bu)$_2$][42]	-2.07 vs. Fc/Fc^+	0.5 M TPAB in THF
3.1'	-2.16 vs. Fc/Fc^+	0.1 M $TBABPh_4$ in THF
[Ce(L")(O^{t}Bu)$_2$][42]	-2.39 vs. Fc/Fc^+	0.5 M TPAB in THF
[Ce(NP(pip)$_3$)$_4$][14]	-2.30 – -2.47 vs. Fc/Fc^+	-
[Ce(NP(pip)$_3$)$_4$]$^-$, [14]	-2.64 – -3.10 vs. Fc/Fc^+	-

TPAB = $[^nPr_4N][B(3,5\text{-}(CF_3)_2C_6H_3)_4]$, $TBAPF_6$ = $[NBu_4][PF_6]$, $TBABPh_4$ = $[NBu_4][BPh_4]$

3.3 Summary

This chapter details the preparation and structural characterization the first homoleptic cerium ketimide, $[Li]_2[Ce(N=C^tBuPh)_6]$ (**3.1**), along with the first homoleptic thorium ketimide, $[Li]_2[Th(N=C^tBuPh)_6]$ (**3.2**). DFT calculations on **3.1** and **3.2** reveal the presence of polarized σ and π Ce/Th-N bonding interactions with modest metal-ligand covalency, which is somewhat larger for **3.1** than for **3.2**. Additionally, an electrochemical analysis of **3.1** revealed one of the most cathodic Ce(IV)/Ce(III) reduction potentials yet recorded, due, in part, to the strongly donating nature of the ketimide ligand along with the anionic charge at the Ce center, and indicating considerable stabilization of the Ce(IV) state. The electrochemical findings suggest that, for cerium at least, the ketimide ligand is more strongly donating than alkoxide, but less donating than phosphiniminato. Going forward, the ability of the ketimide ligand to stabilize Pr^{4+} and Tb^{4+} will be examined. This goal seems all the more plausible given the recent isolation and crystallographic characterization of one Pr^{4+} [74] and three Tb^{4+} complexes.[44, 75, 76]

3.4 Acknowledgements

I would like to thank Dr. Dumitru-Claudiu Sergentu and Prof. Jochen Autschbach at University at Buffalo, State University of New York for performing DFT calculations. I also thank Dr. Lani Seaman for preliminary work in optimizing the synthesis of complexes **3.1** and **3.2**.

3.5 Experimental

3.5.1 General Procedures. All reactions and subsequent manipulations were performed under anaerobic and anhydrous conditions in the glovebox or on a Schlenk line, under an atmosphere

of dinitrogen. Hexanes, diethyl ether (Et_2O), and toluene were dried by passage over activated molecular sieves using a Vacuum Atmospheres solvent purification system. Tetrahydrofuran (THF) was distilled over Na/benzophenone and stored over activated 3 Å molecular sieves for 24 h prior to use. C_6D_6 was dried over activated 3 Å molecular sieves for 24 h prior to use. $[Ce(NO_3)_3(THF)_4]$,[77] $[ThCl_4(DME)_2]$,[78] and $Li(N=C^tBuPh)$[79] were prepared according to the reported literature procedures. All other reagents were purchased from commercial suppliers and used as received.

^1H, $^{13}C\{^1H\}$, and $^7Li\{^1H\}$ NMR spectra were recorded on an Agilent Technologies 400 MHz 400-MR DD2. ^1H and $^{13}C\{^1H\}$ NMR spectra were referenced to external $SiMe_4$ using residual protio solvent resonances as internal standards. $^7Li\{^1H\}$ NMR spectra were referenced indirectly with the ^1H chemical shift of $SiMe_4$ at 0 ppm, according to IUPAC standard.[80, 81] IR spectra were recorded on a Nicolet 6700 FT-IR spectrometer. Electronic absorption spectra were recorded on a Shimadzu UV3600 UV-NIR Spectrometer. Elemental analyses were performed by the Microanalytical Laboratory at University of California (Berkeley, CA).

Cyclic Voltammetry Measurements. CV experiments were performed with a CH Instruments 600c Potentiostat, and the data were processed using CHI software (version 6.29). All experiments were performed in a glove box using a 20 mL glass vial as the cell. The working electrode was glassy carbon (3 mm diameter), the counter electrode was a platinum wire, and the reference electrode was a silver wire electroplated with silver chloride. Solutions employed for CV studies were typically 1 mM in analyte and 0.1 M in $[NBu_4][BPh_4]$. All potentials are reported versus the $[Cp_2Fe]^{0/+}$ couple using Cp_2Co (-1.31 V vs Fc/Fc^+) as an internal standard.

Magnetic Susceptibility. Magnetic measurements were made using a 7 T Quantum Design MPMS 3 SQUID magnetometer. All loading equipment, including quartz wool and quartz tubes, were oven-dried at 120 °C for several days prior to use. Complex **3.1** (32.7 mg, 0.029 mmol) was sandwiched between high purity quartz wool (32.6 mg total) in a 5 mm quartz tube that was flame-sealed at one end, and tightly packed to a length of ~2 cm. Latex gloves were worn over glovebox gloves during sample loading, and contact with quartz wool was minimized to prevent contamination. A vacuum adaptor was attached to the open end of the quartz tube, and the sample was subsequently flame-sealed under static vacuum. The susceptibility data were corrected for diamagnetic contributions of the ligands using Pascal constants.[82] No correction was applied to account for the contribution of the quartz tube or quartz wool to the overall sample susceptibility.

3.5.2 Synthesis of $[Li]_2[Ce(N{=}C^tBuPh)_6]$ (3.1): To a stirring, colorless solution of $[Ce(NO_3)_3(THF)_4]$ (152.0 mg, 0.247 mmol) in THF (1 mL) was added a yellow solution of $Li(N{=}C^tBuPh)$ (247.7 mg, 1.483 mmol) in THF (1 mL). This addition resulted in an immediate color change to deep red-brown. The mixture was allowed to stir for 90 min at room temperature, whereupon an orange solution of I_2 (31.0 mg, 0.122 mmol) in THF (1 mL) was added dropwise. This addition resulted in an immediate color change to deep purple. The resulting purple mixture was then stirred for a further 15 min. The volatiles were removed *in vacuo* and the resulting purple oil was triturated with pentane (3 × 2 mL) to yield a purple powder. The powder was washed with pentane (4 mL) and the dark brown washings were discarded. The remaining residue was then extracted into Et_2O (6 mL) and filtered through a Celite column supported on glass wool (0.5 cm × 2 cm) to yield a purple filtrate. The filtrate was concentrated to ~2 mL and subsequently stored at -25 °C for 24 h, which resulted in

deposition of purple plates. The crystals were then washed with pentane (3 × 2 mL) and dried *in vacuo* (68.8 mg). Concentration of the supernatant, followed by layering with equal volume of hexanes, and subsequent storage of this solution at -25 °C for 24 h, resulted in deposition of a second crop of purple plates. These crystals were also washed with pentane (3 × 2 mL) and subsequently dried *in vacuo* (Total: 122.0 mg, 44% yield). Anal. Calcd for $C_{66}H_{84}CeLi_2N_6$: C, 71.07; H, 7.59; N, 7.53. Found: C, 70.73; H, 7.64; N, 7.59. ^{1}H NMR (C_6D_6, 25 °C, 400 MHz): δ 1.36 (s, 54H, CC*H*$_3$), 6.62 (m, 12H, *o*-aryl C*H*), 6.99 (m, 18H, overlapping peaks for *m*- and *p*- aryl C*H*). ^{1}H NMR (Tol-*d*$_8$, 25 °C, 400 MHz): δ 1.32 (s, 54H, CC*H*$_3$), 6.56 (m, 12H, *o*-aryl C*H*), 6.98 (m, 18H, overlapping peaks for *m*- and *p*- aryl C*H*). ^{1}H NMR (THF-*d*$_8$, 25 °C, 400 MHz): δ 1.00 (s, 9H, CC*H*$_3$, Li(N=C^{t}BuPh)), 1.06 (s, 45H, CC*H*$_3$, [Li][Ce(N=C^{t}BuPh)$_5$]), 7.02 (m, 12H, *o*-aryl C*H*), 7.12 (m, 18H, overlapping peaks for *m*- and *p*- aryl C*H*). ^{13}C{^{1}H} NMR (C_6D_6, 25 °C, 100 MHz): δ 29.15 (C*C*H$_3$), 45.37 (*C*CH$_3$), 125.84 (*p*-aryl *C*H), 126.16 (*o*-aryl *C*H), 128.90 (*m*-aryl *C*H), 149.40 (*ipso*-aryl *C*), 175.08 (N*C*). ^{7}Li{^{1}H} NMR (C_6D_6, 25 °C, 155 MHz): δ 0.06 (s, 2Li). ^{7}Li{^{1}H} NMR (Tol-*d*$_8$, 25 °C, 155 MHz): δ -0.02 (s, 2Li). ^{7}Li{^{1}H} NMR (THF-*d*$_8$, 25 °C, 155 MHz): δ 0.65 (s, [Li][Ce(N=C^{t}BuPh)$_5$]), 1.75 (s, Li(N=C^{t}BuPh)), 1.94 (s, Li(N=C^{t}BuPh)). UV-Vis (Toluene, 0.089 mM, 25 °C, $M^{-1}\cdot cm^{-1}$): 485 (ε = 5600). IR (KBr pellet, cm^{-1}): 3072 (vw), 3055 (vw), 2962 (m), 2899 (w), 2864 (w), 1637 (vs, ν_{CN}), 1624 (vs, ν_{CN}), 1473 (m), 1439 (w), 1385 (w), 1360 (m), 1259 (vw), 1198 (w), 1188 (m), 1074 (br, vw), 1070 (w), 1024 (w), 997 (vw), 943 (s), 904 (m), 773 (s), 708 (s), 687 (m), 615 (w), 563 (m), 436 (m).

3.5.3 Synthesis of [Li]$_2$[Th(N=C^{t}BuPh)$_6$] (3.2): To a stirring, colorless solution of [$ThCl_4(DME)_2$] (121.5 mg, 0.219 mmol) in THF (1 mL) was added a yellow solution of Li(N=C^{t}BuPh) (220.0 mg, 1.316 mmol) in THF (1 mL). The resulting yellow solution was

allowed to stir for 2 h at room temperature. The solvent was then removed *in vacuo* to yield a bright yellow solid, which was extracted into 3:1 hexanes/THF (4 mL) and filtered through a Celite column supported on glass wool (0.5 cm × 2 cm). The filtrate was concentrated to ~2 mL and subsequently stored at -25 °C for 72 h, which resulted in deposition of yellow blocks (139.2 mg, 53% yield). X-ray quality crystals were obtained from a concentrated toluene solution stored at -25 °C for 24 h. Anal. Calcd for $C_{66}H_{84}Li_2N_6Th$: C, 65.66; H, 7.01; N, 6.96. Found: C, 65.64; H, 6.85; N, 7.10. ^{1}H NMR (C_6D_6, 25 °C, 400 MHz): δ 1.27 (s, 54H, CC*H*$_3$), 6.67 (m, 12H, *o*-aryl C*H*), 7.00 (m, 18H, overlapping peaks for *m*- and *p*- aryl C*H*). ^{1}H NMR (Tol-*d*$_8$, 25 °C, 400 MHz): δ 1.24 (s, 54H, CC*H*$_3$), 6.63 (m, 12H, *o*-aryl C*H*), 6.98 (m, 18H, overlapping peaks for *m*- and *p*- aryl C*H*). ^{1}H NMR (THF-*d*$_8$, 25 °C, 400 MHz): δ 1.00 (s, 9H, CC*H*$_3$, Li(N=C^{t}BuPh)), 1.07 (s, 54H, CC*H*$_3$, **3.2**), 1.11 (s, 45H, CC*H*$_3$, [Li][Th(N=C^{t}BuPh)$_5$]), 6.98 (m, 12H, *o*-aryl C*H*, **3.2**), 7.04 (m, 10H, *o*-aryl C*H*, [Li][Th(N=C^{t}BuPh)$_5$]), 7.10 (m, 18H, overlapping peaks for *m*- and *p*- aryl C*H*). ^{13}C{^{1}H} NMR (C_6D_6, 25 °C, 100 MHz): δ 29.22 (C*C*H$_3$), 43.13 (*C*CH$_3$), 125.84 (*p*-aryl *C*H), 126.09 (*o*-aryl *C*H), 128.79 (*m*-aryl *C*H), 148.27 (*ipso*-aryl *C*), 178.73 (N*C*). ^{7}Li{^{1}H} NMR (C_6D_6, 25 °C, 155 MHz): δ 0.53 (s, 2Li). ^{7}Li{^{1}H} NMR (Tol-*d*$_8$, 25 °C, 155 MHz): δ 0.47 (s, 2Li). ^{7}Li{^{1}H} NMR (THF-*d*$_8$, 25 °C, 155 MHz): δ 0.04 (s, [Li][Th(N=C^{t}BuPh)$_5$]), 0.61 (s, 2Li, **3.2**), 1.75 (s, Li(N=C^{t}BuPh)), 1.90 (s, Li(N=C^{t}BuPh)). UV-Vis (Toluene, 0.13 mM, 25 °C, $M^{-1}\cdot cm^{-1}$): 385 (ε = 1595). IR (KBr pellet, cm^{-1}): 3072 (vw), 3057 (vw), 3012 (vw), 2962 (m), 2945 (sh m), 2895 (w), 2864 (w), 1643 (vs, ν_{CN}), 1626 (vs, ν_{CN}), 1475 (m), 1460 (w), 1439 (w), 1385 (w), 1360 (m), 1261 (vw), 1215 (w),

1198 (w), 1190 (m), 1070 (w), 1024 (w), 997 (vw), 945 (s), 904 (m), 773 (s), 704 (s), 687 (m), 617 (w), 565 (m), 438 (m).

3.5.4 Computational Details. A series of Kohn-Sham density functional theory (DFT) calculations were performed on the crystal structure of $[Li]_2[Ce(N=C^tBuPh)_6]$ (**3.1**) and $[Li]_2[Th(N=C^tBuPh)_6]$ (**3.2**) in order to assess the ground state metal-ligand bonding. Ground state DFT calculations with the TPSS meta-generalized gradient approximation[68] (meta-GGA) were performed with ORCA v4.1.2,[83, 84] using the SDD effective small-core potential[85-88] for Ce and Th along with def2-TZVP (Ce, N and C), Stuttgart RSC (Th), and def2-SVP (H) valence basis sets.[89, 90] These calculations used the RIJ approximation with very large RIJ basis sets generated with the AutoAux procedure (automatic construction of a general purpose auxiliary basis set).[91] Additionally, ground state DFT/TPSS calculations were performed with the Amsterdam Density Functional package (ADF, v2017)[92] using the all-electron scalar-relativistic zero-order regular approximation (ZORA) Hamiltonian[93] with triple-ζ doubly polarized (TZ2P) basis sets for all atoms. The extent of metal-ligand bonding was determined from the ORCA and ADF calculations via analyses of the natural localized molecular orbitals (NLMOs) generated with a locally modified version of NBO6.[94]

3.5.5 X-ray Crystallography. Data for **3.1** and **3.2** were collected on a Bruker KAPPA APEX II diffractometer equipped with an APEX II CCD detector using a TRIUMPH monochromater with a Mo Kα X-ray source (α = 0.71073 Å). The crystals of **3.1** and **3.2** were mounted on a cryoloop under Paratone-N oil, and all data were collected at 100(2) K using an Oxford nitrogen gas cryostream system. X-ray data for **3.1** and **3.2** were collected utilizing frame exposures of 15 and 5 s, respectively. Data collection and cell parameter determinations were conducted using the SMART program.[95] Integration of the data frames and final cell parameter

refinement were performed using SAINT software.[96] Absorption corrections of the data were carried out using the multi-scan method SADABS.[97] Subsequent calculations were carried out using SHELXTL.[98] Structure determination was done using direct or Patterson methods and difference Fourier techniques. All hydrogen atom positions were idealized, and rode on the atom of attachment. Structure solution, refinement, graphics, and creation of publication materials were performed using SHELXTL.[98]

Table 3.3. Crystallographic details for complexes **3.1** and **3.2**.

	3.1	**3.2**
Formula	$C_{66}H_{84}CeLi_2N_6$	$C_{66}H_{84}Li_2N_6Th$
Crystal Habit, Color	Plate, Purple	Diamond, Yellow
Crystal Size (mm)	0.20 × 0.15 × 0.10	0.15 × 0.10 × 0.05
MW (g/mol)	1115.39	1207.31
crystal system	Trigonal	Trigonal
space group	R-3	R-3
a (Å)	12.350(3)	12.1710(17)
b (Å)	12.350(3)	12.1710(17)
c (Å)	36.693(10)	37.279(5)
α (°)	90	90
β (°)	90	90
γ (°)	120	120
V ($Å^3$)	4847(3)	4782.5(15)
Z	3	3
T (K)	100(2)	100(2)
λ (Å)	0.71073	0.71073
GOF	1.293	1.044
Density (calcd) (Mg/m^3)	1.146	1.258
Absorption coefficient (mm^{-1})	0.745	2.380
F_{000}	1758	1854
Total no Reflections	3987	8244
Unique Reflections	2439	2656
Final R indices*	R_1 = 0.0846	R_1 = 0.0194
	wR_2 = 0.2501	wR_2 = 0.0423
Largest Diff. peak and hole ($e^- A^{-3}$)	1.229, -0.647	0.526, -0.320

* For [I > 2σ(I)]

3.6 Appendix

3.6.1 NMR Spectra

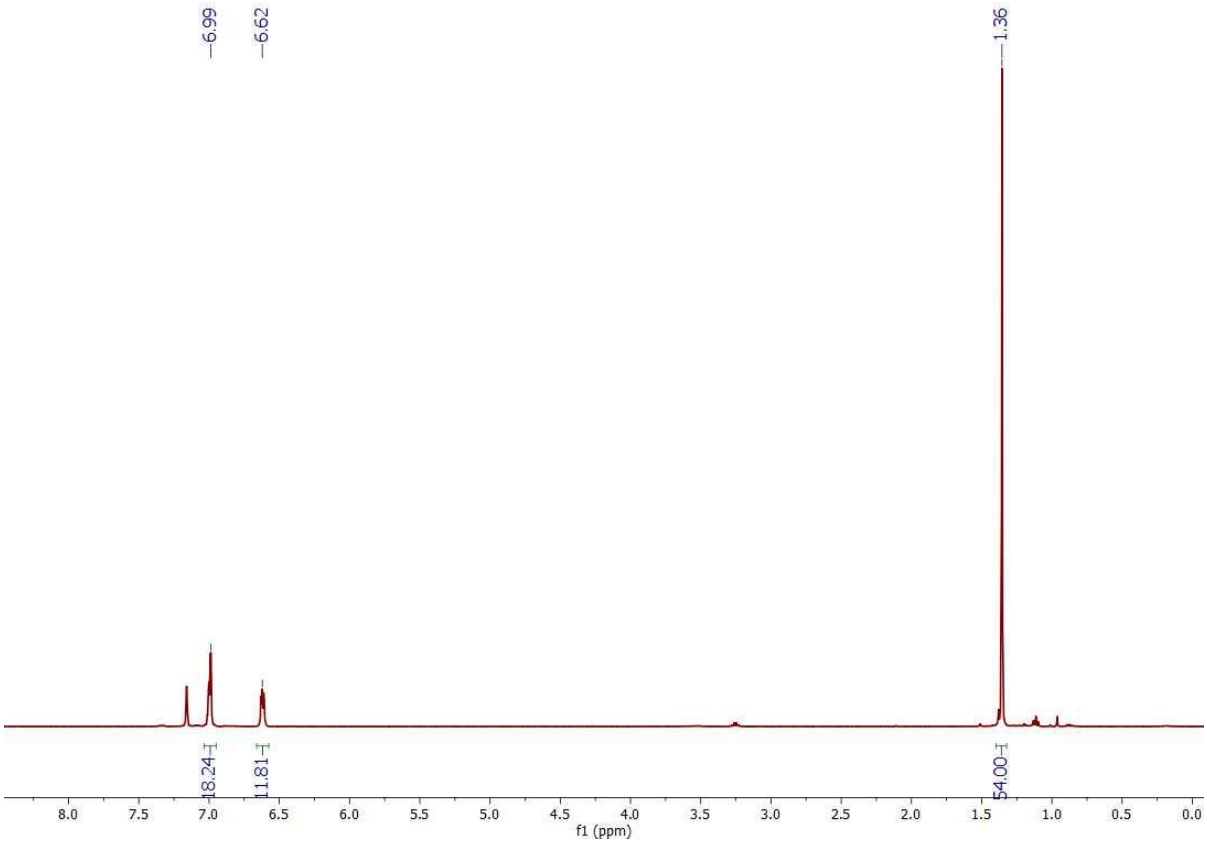

Figure A3.1. ^{1}H NMR spectrum of **3.1** in C_6D_6.

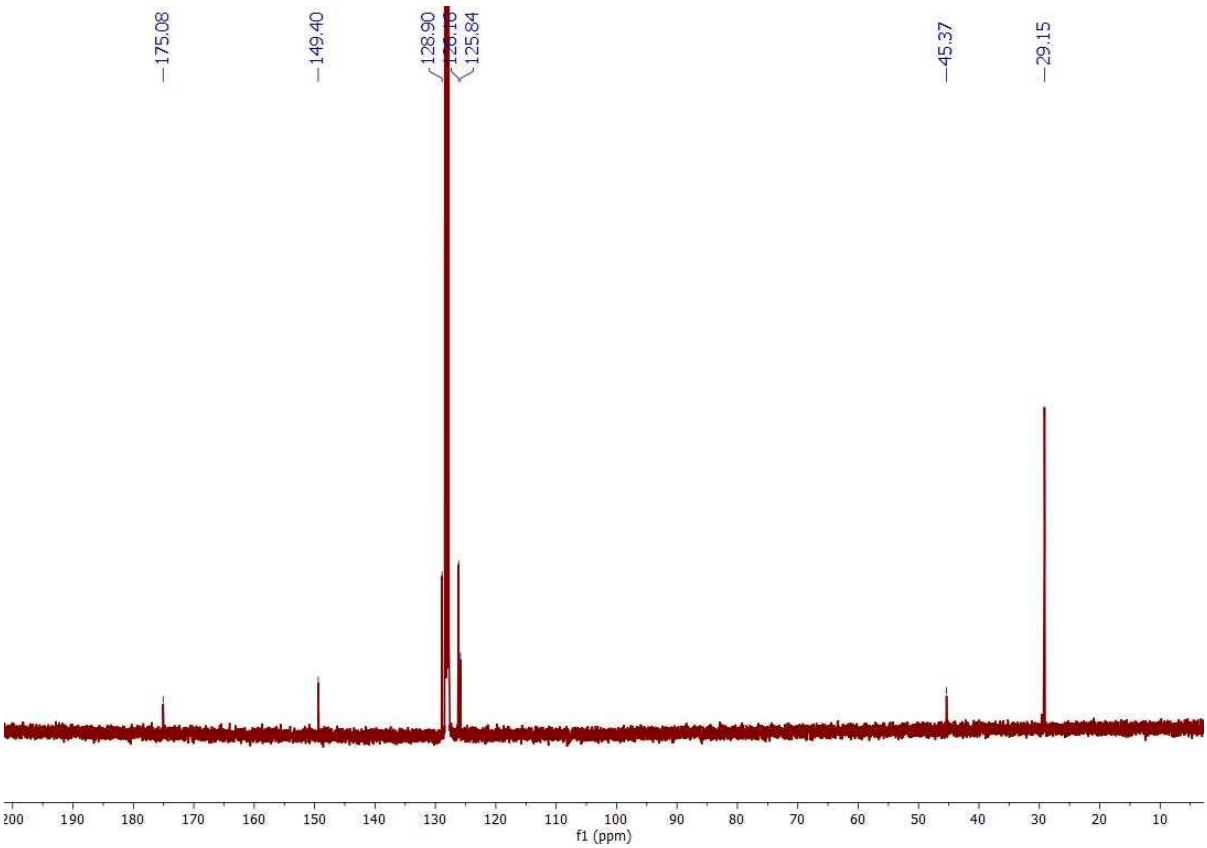

Figure A3.2. $^{13}C\{^{1}H\}$ NMR spectrum of **3.1** in C_6D_6.

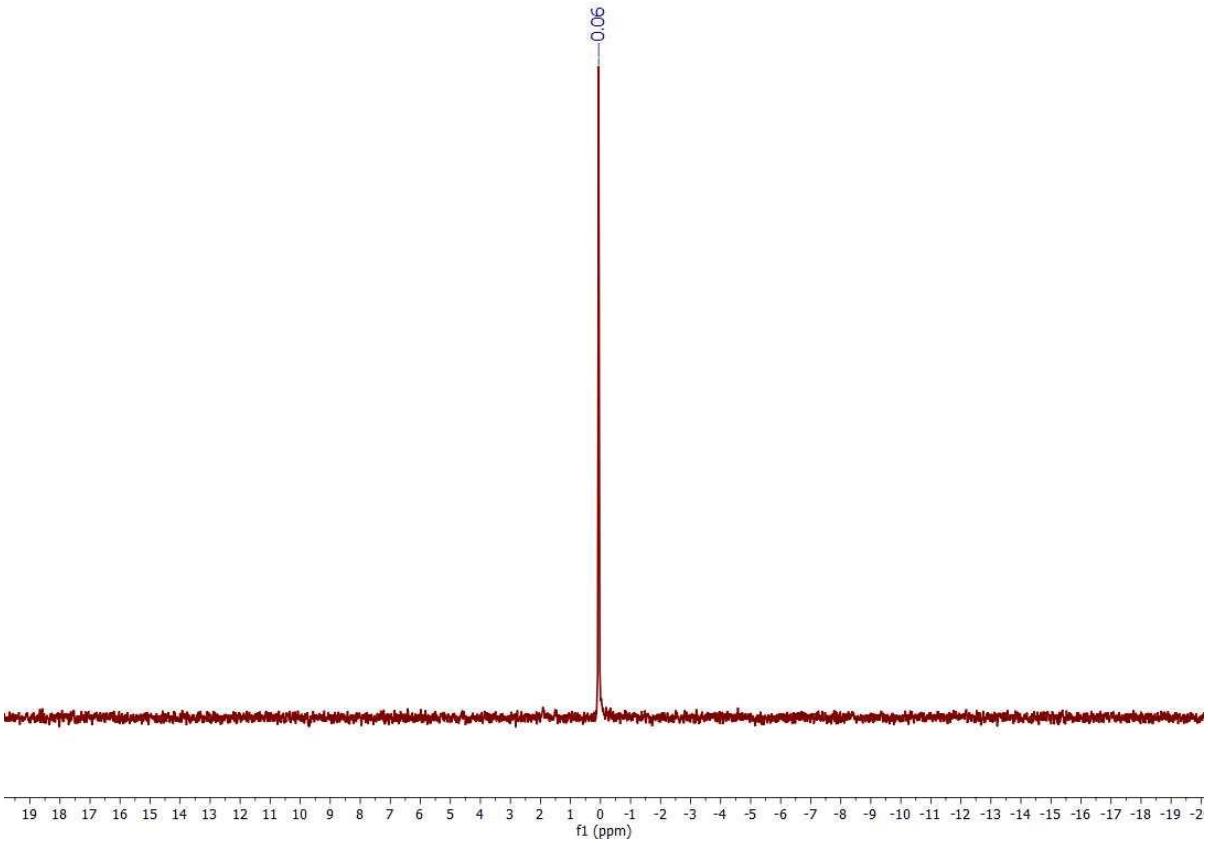

Figure A3.3. $^{7}Li\{^{1}H\}$ NMR spectrum of **3.1** in C_6D_6.

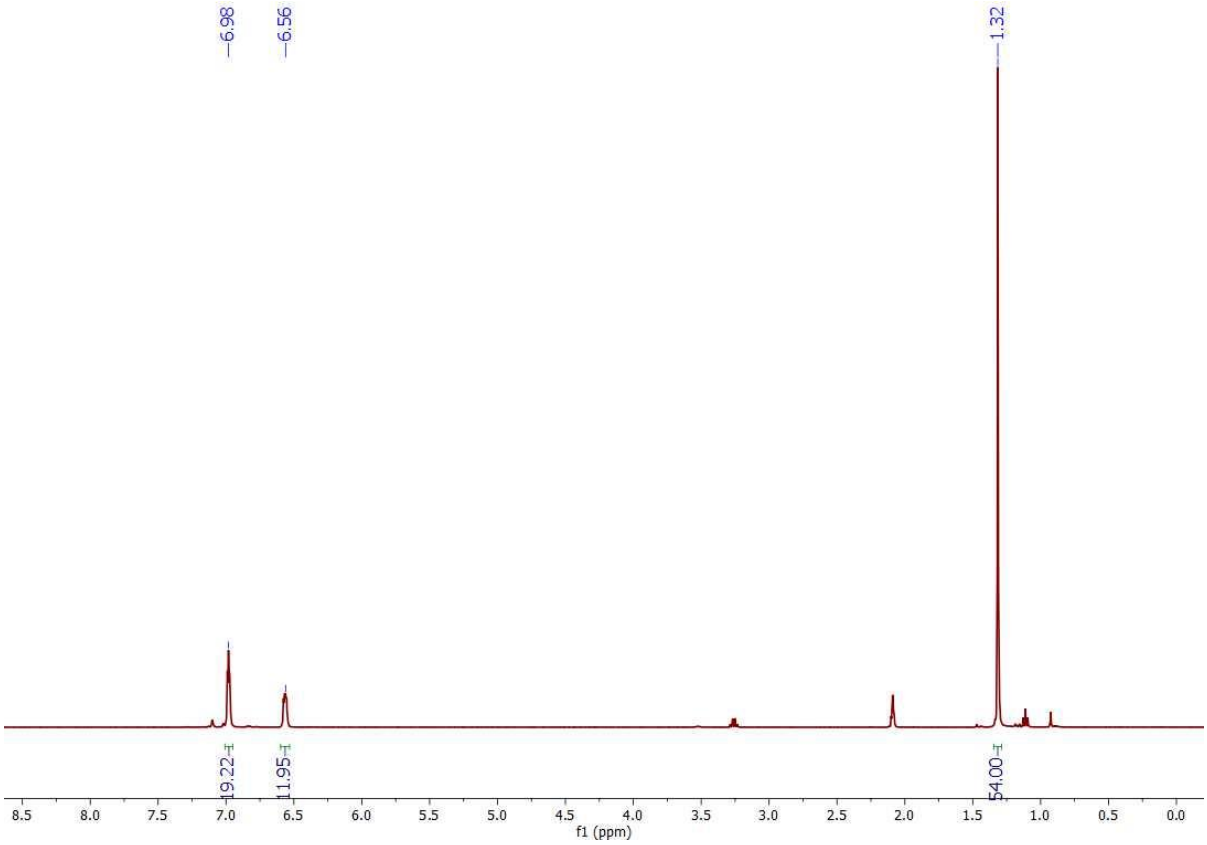

Figure A3.4. ^{1}H NMR spectrum of **3.1** in Tol-d_8.

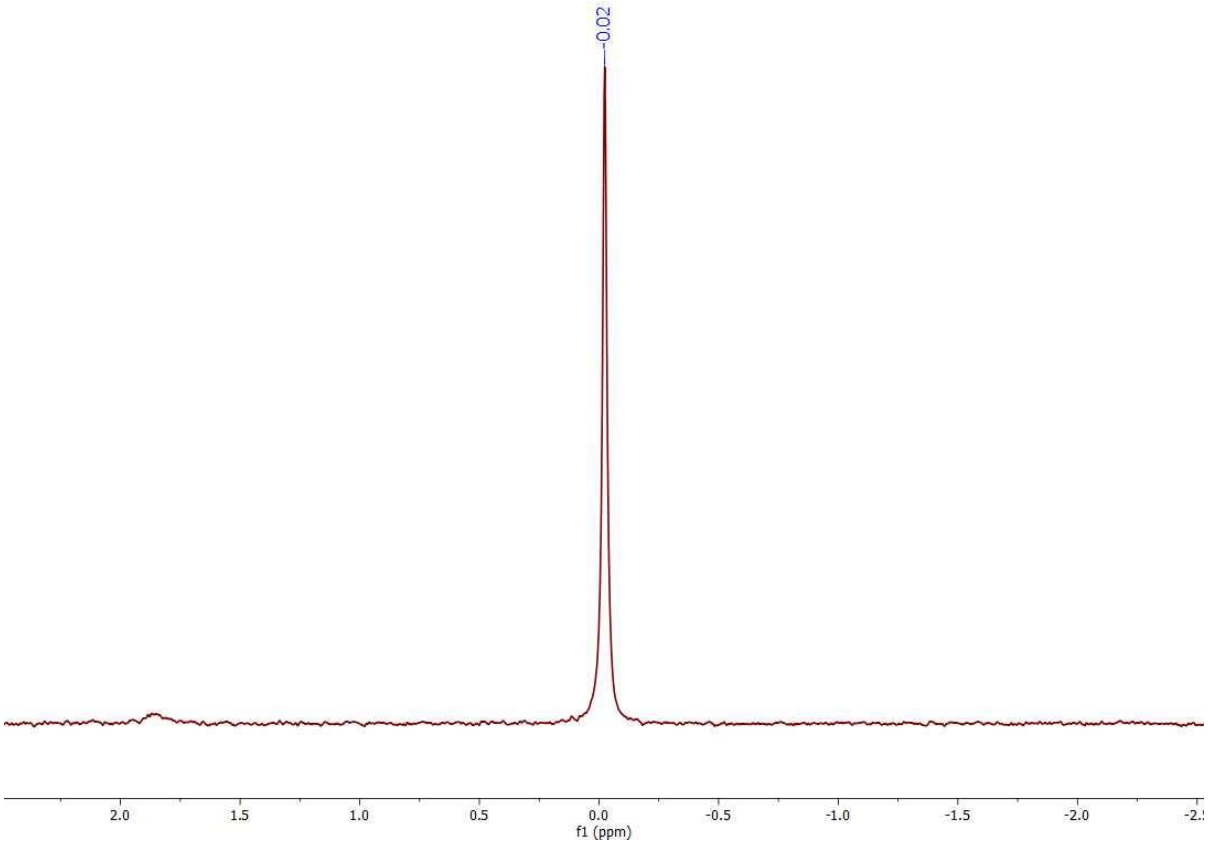

Figure A3.5. $^{7}Li\{^{1}H\}$ NMR spectrum of **3.1** in Tol-d_8.

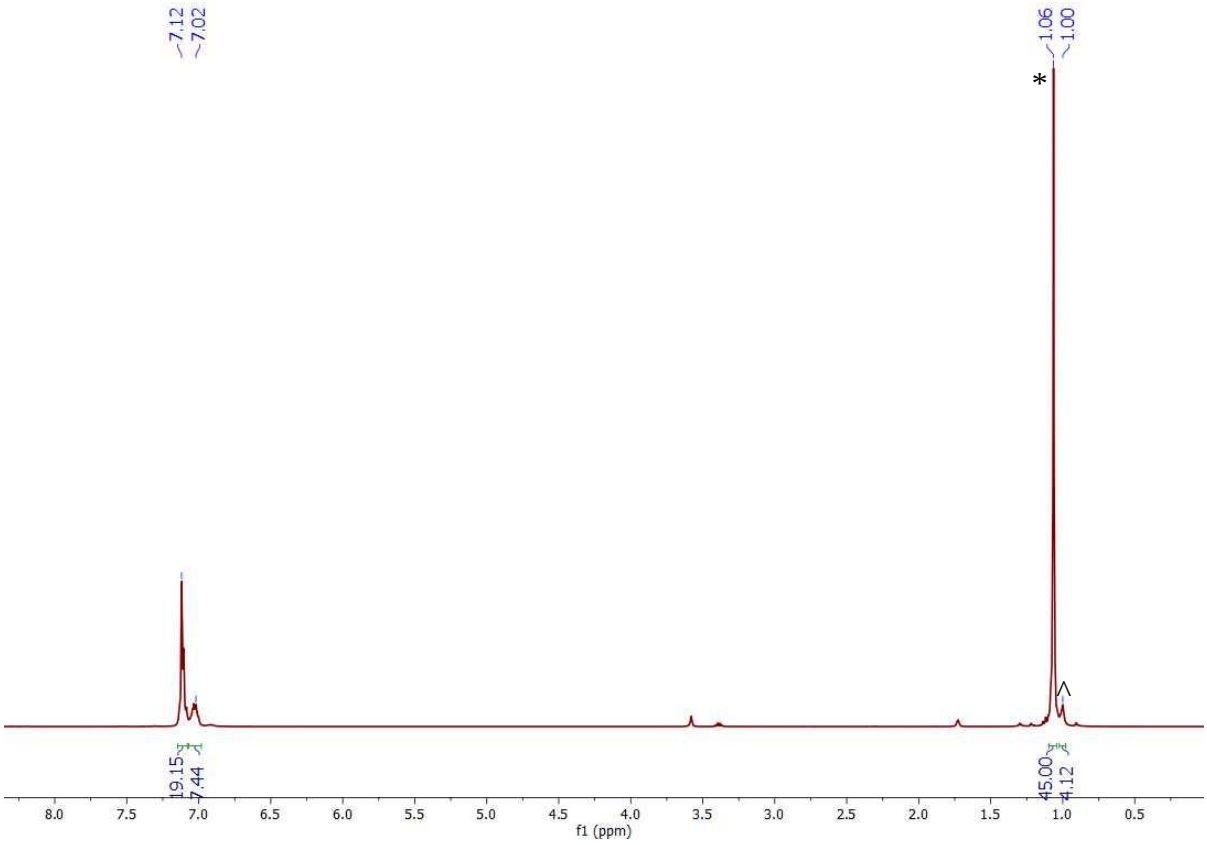

Figure A3.6. ^{1}H NMR spectrum of **3.1** in THF-d_8. The resonance marked with * is assignable to [Li][Ce(N=C^{t}BuPh)$_5$] (**3.1'**) and the resonance marked with ^ is assignable to Li(N=C^{t}BuPh).

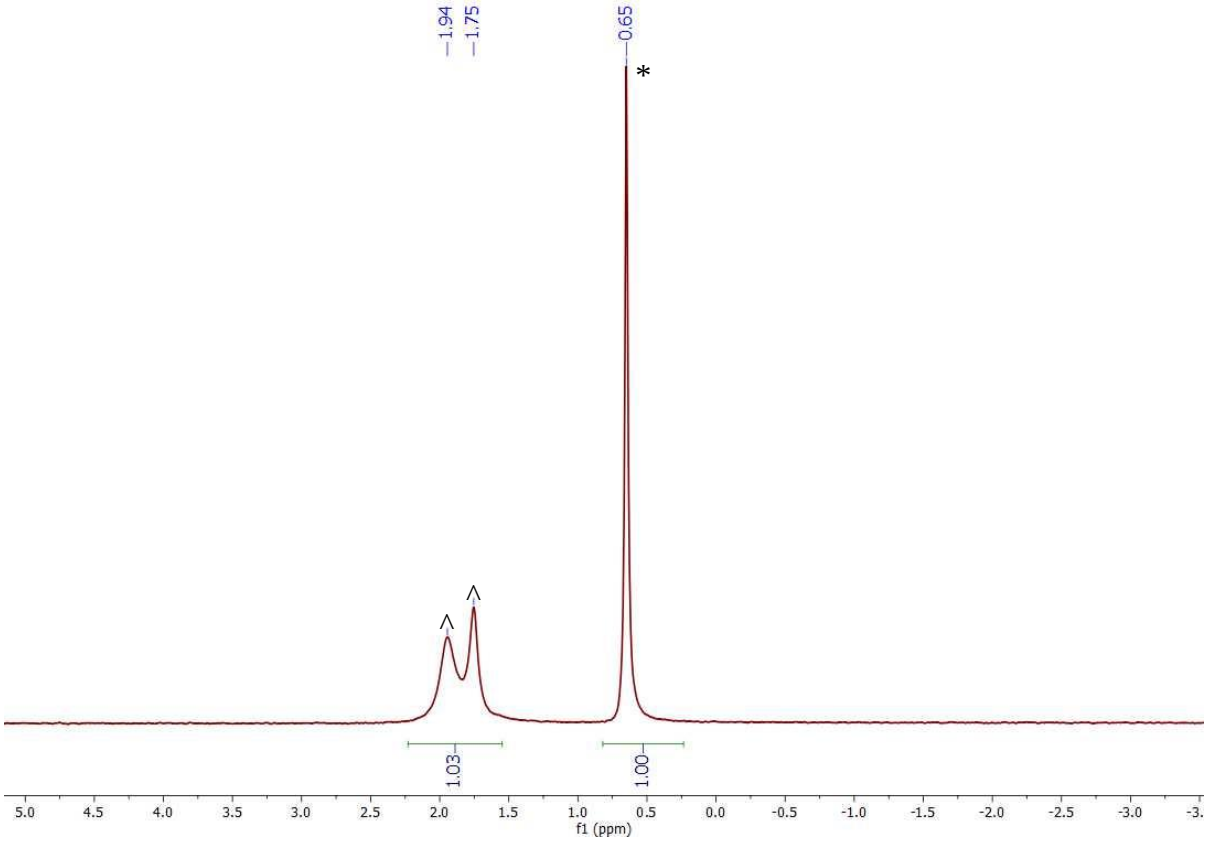

Figure A3.7. $^{7}Li\{^{1}H\}$ NMR spectrum of **3.1** in THF-d_8. The resonance marked with * is assignable to [Li][Ce(N=C^{t}BuPh)$_5$] (**3.1'**) and the resonances marked with ^ are assignable to Li(N=C^{t}BuPh).

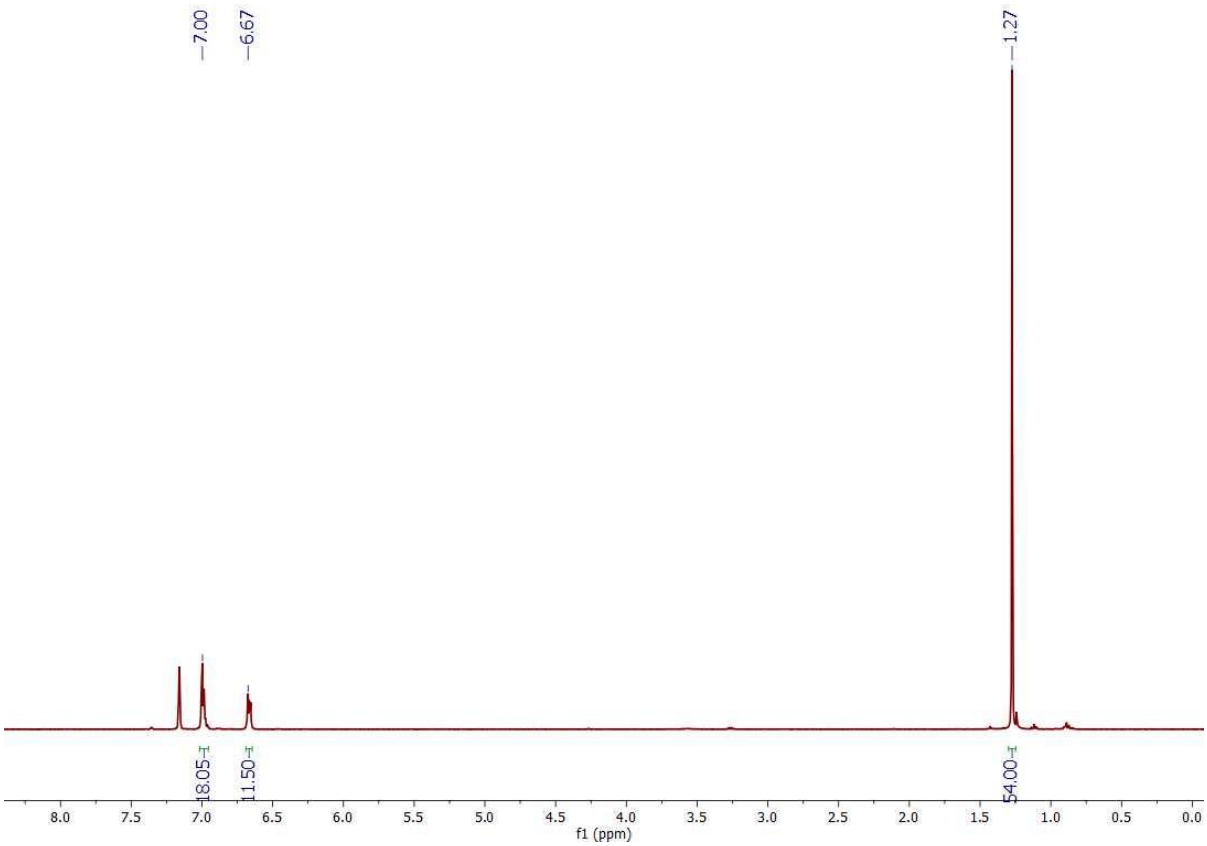

Figure A3.8. ^{1}H NMR spectrum of **3.2** in C_6D_6.

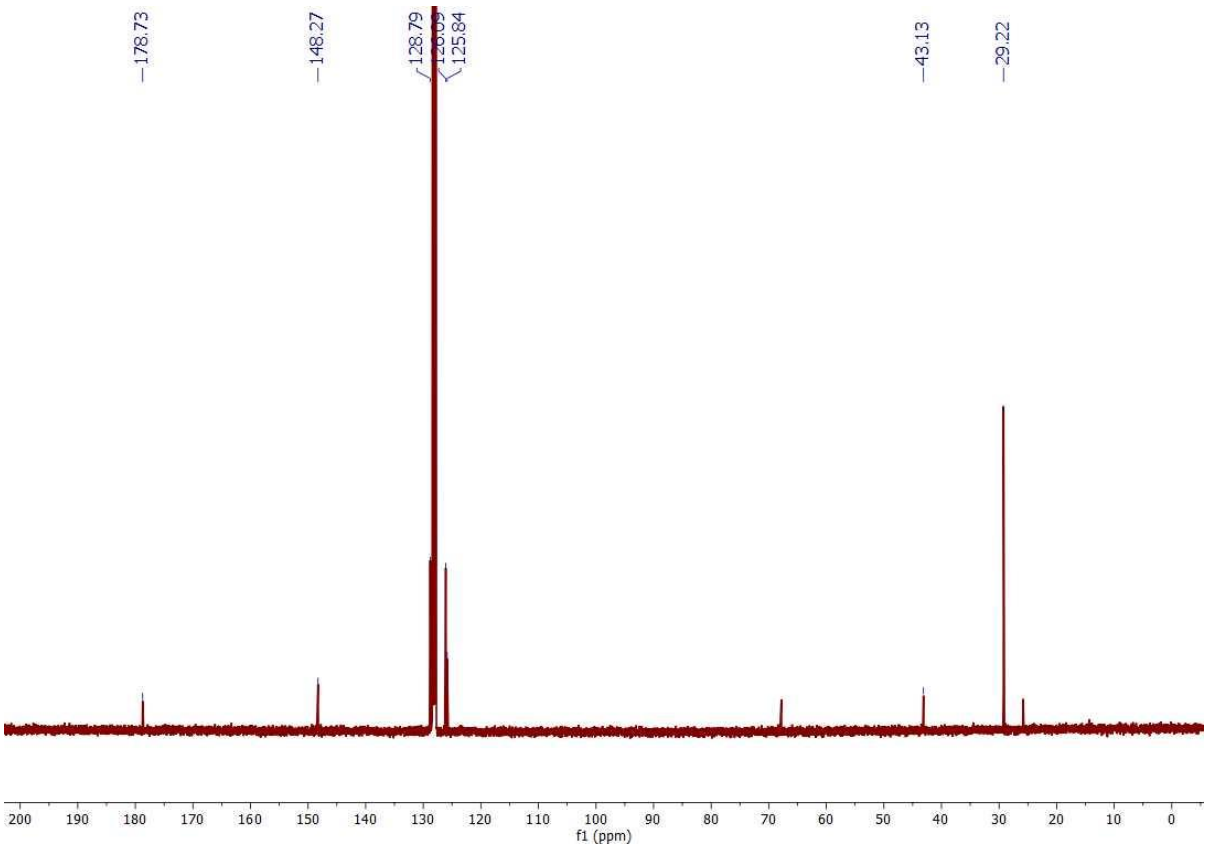

Figure A3.9. $^{13}C\{^{1}H\}$ NMR spectrum of **3.2** in C_6D_6.

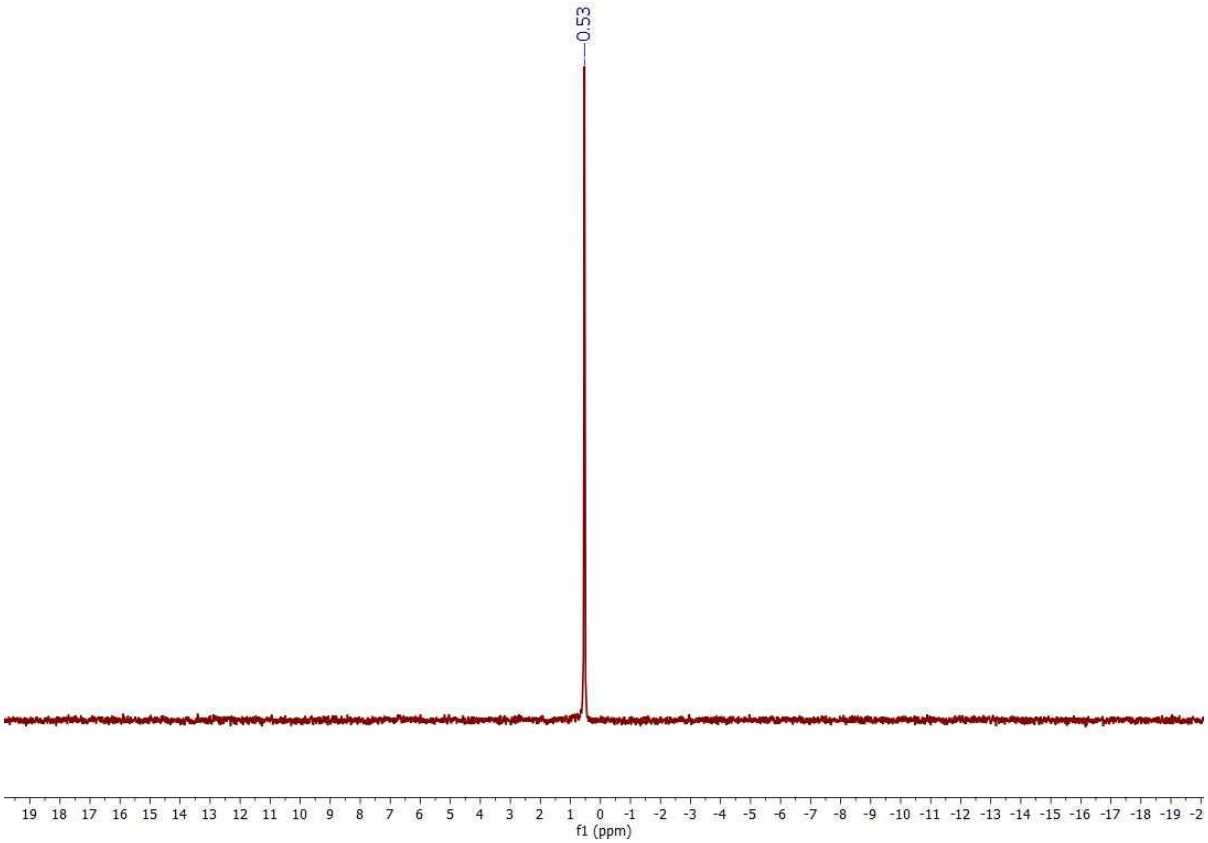

Figure A3.10. $^{7}Li\{^{1}H\}$ NMR spectrum of **3.2** in C_6D_6.

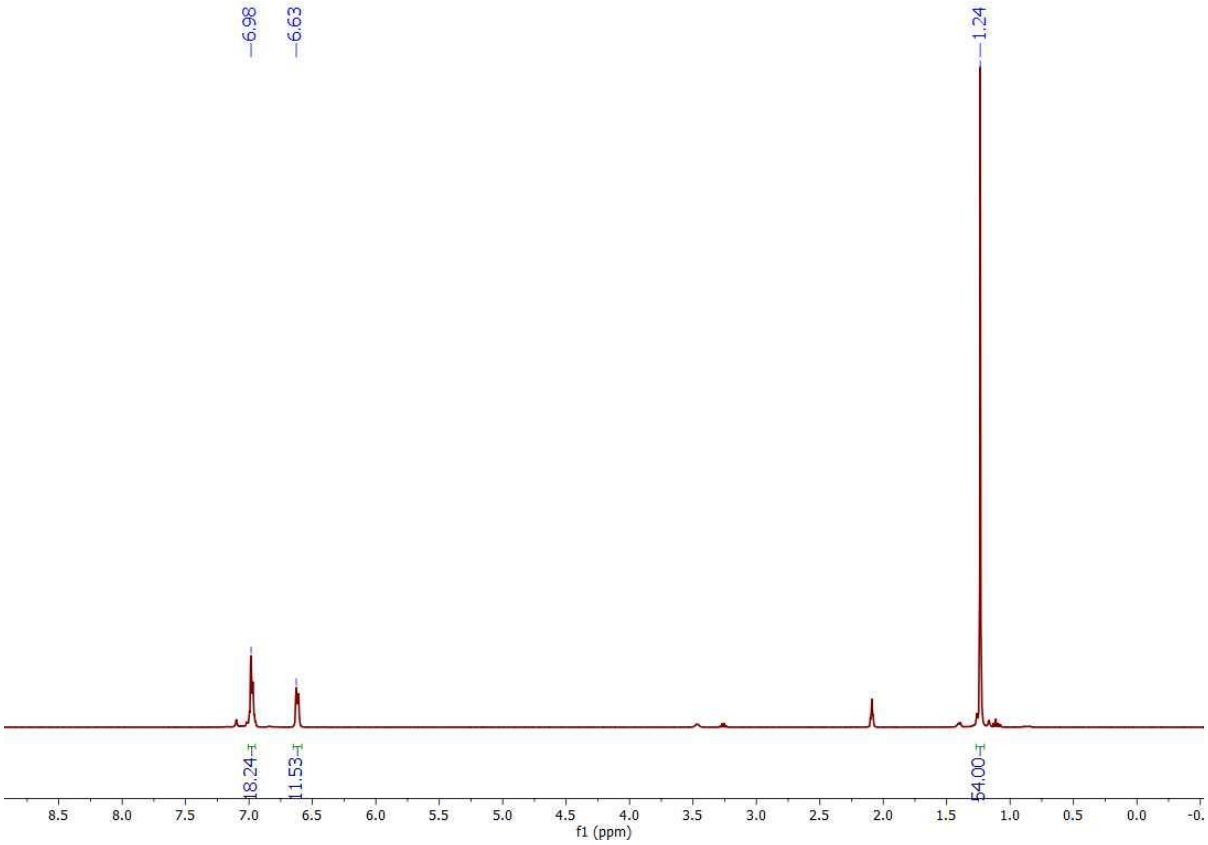

Figure A3.11. ^{1}H NMR spectrum of **3.2** in Tol-d_8.

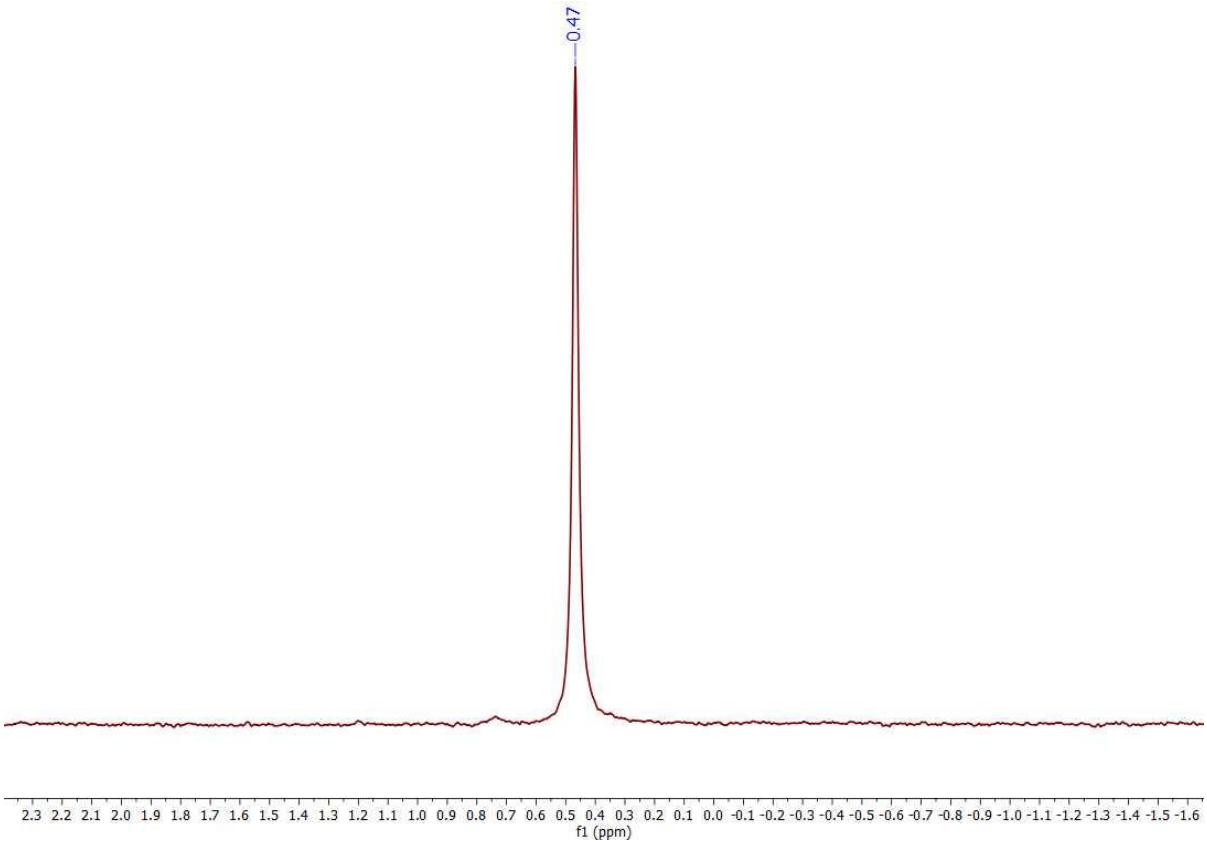

Figure A3.12. $^{7}Li\{^{1}H\}$ NMR spectrum of **3.2** in Tol-d_8.

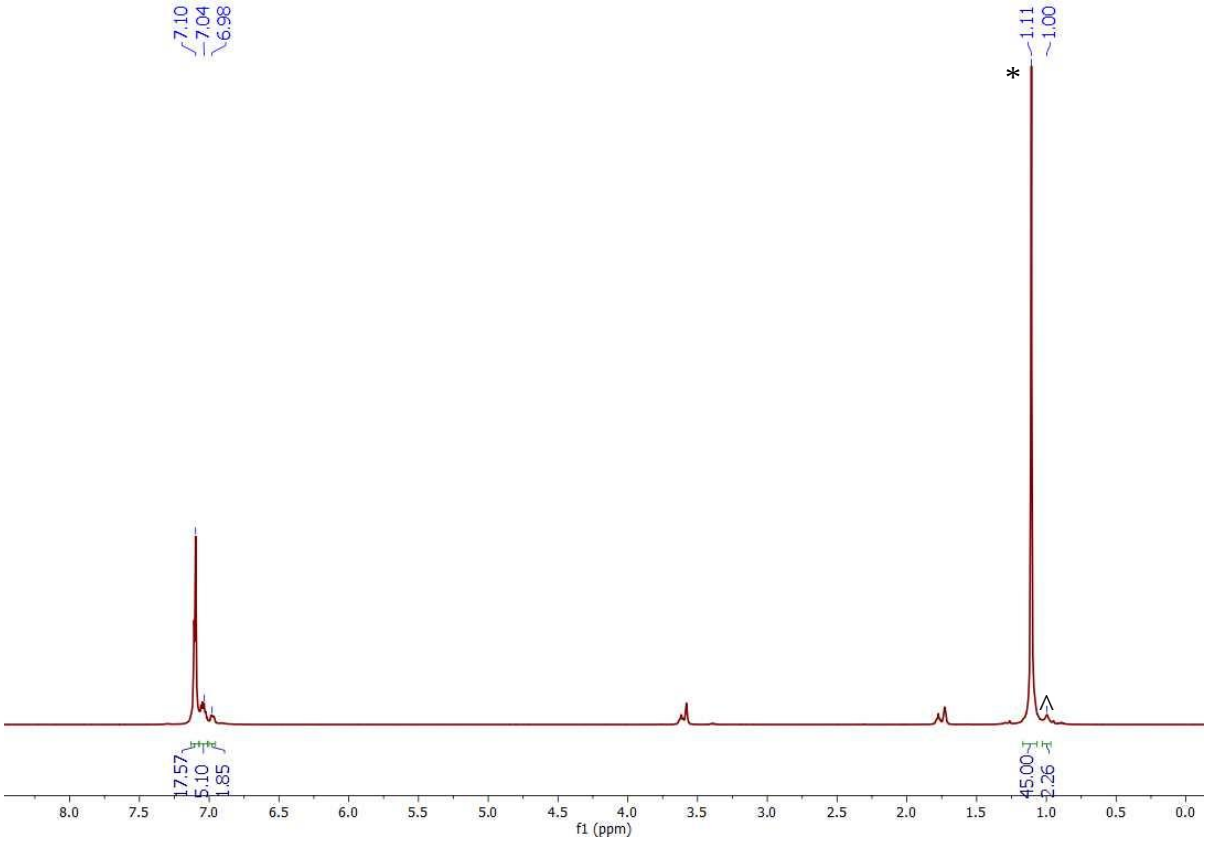

Figure A3.13. ^{1}H NMR spectrum of **3.2** in THF-d_8. Resonance marked with * is assignable to [Li][Th(N=C^{t}BuPh)$_5$] (**3.2'**) and resonance marked with ^ is assignable to Li(N=C^{t}BuPh).

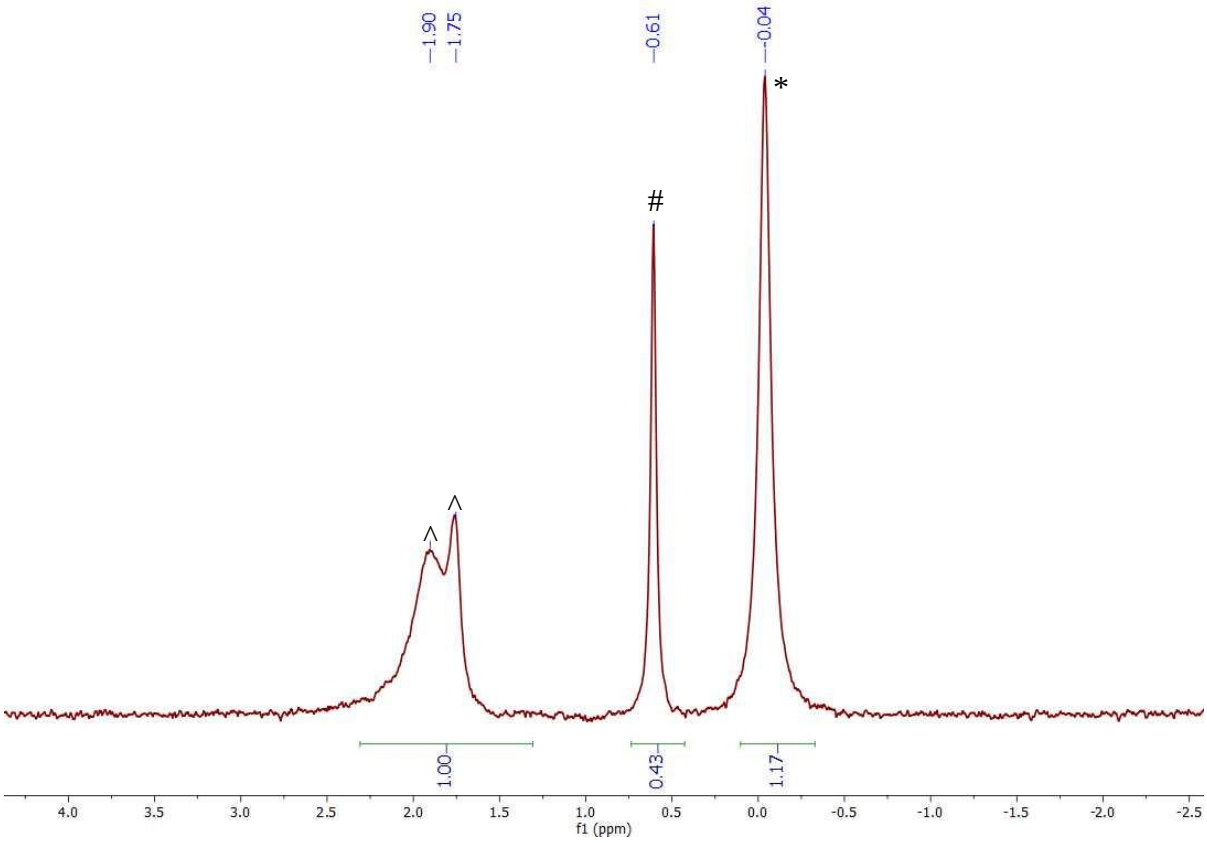

Figure A3.14. $^{7}Li\{^{1}H\}$ NMR spectrum of **3.2** in THF-d_8. Resonance marked with * is assignable to [Li][Th(N=C^{t}BuPh)$_5$] (**3.2'**), resonance marked with # is assignable to **3.2**, and resonances marked with ^ are assignable to Li(N=C^{t}BuPh).

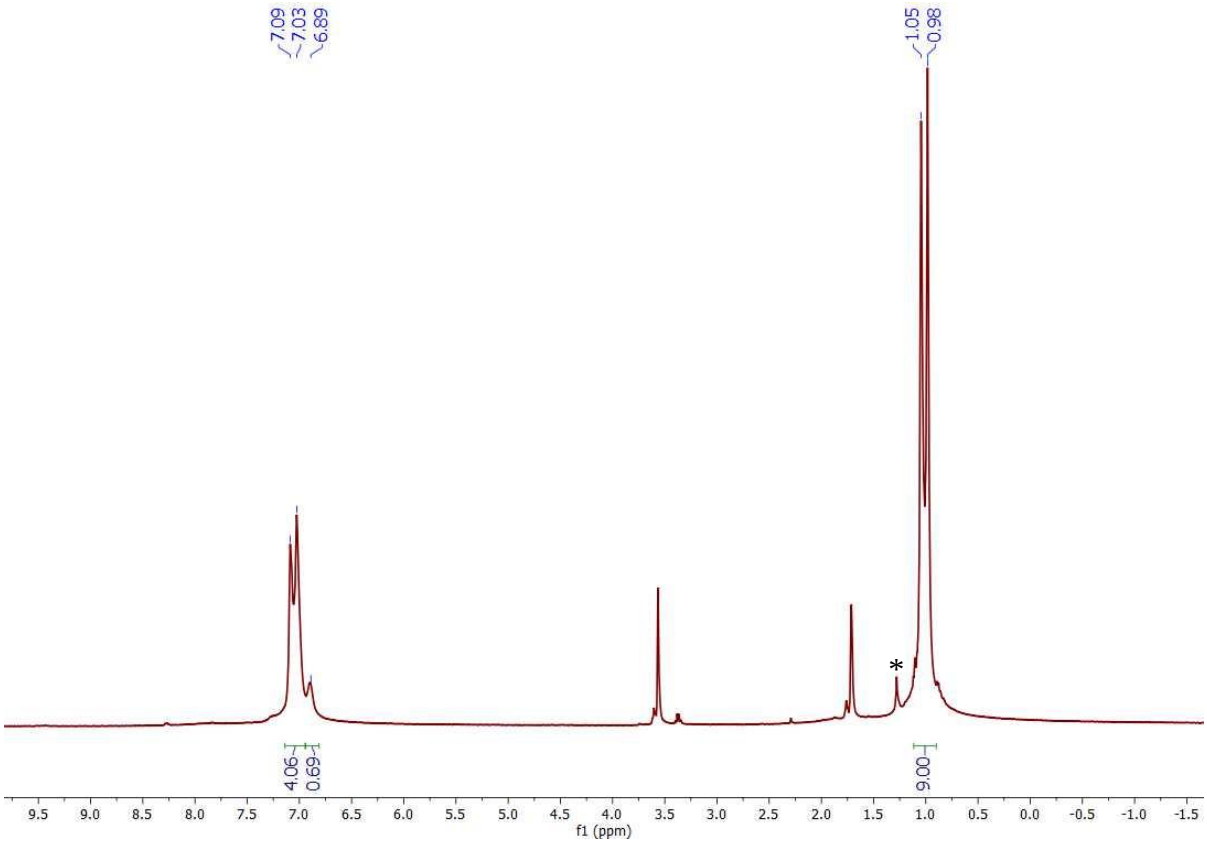

Figure A3.15. ^{1}H NMR spectrum of Li(N=C^{t}BuPh) in THF-d_8. Resonance marked with * is assignable to hexanes.

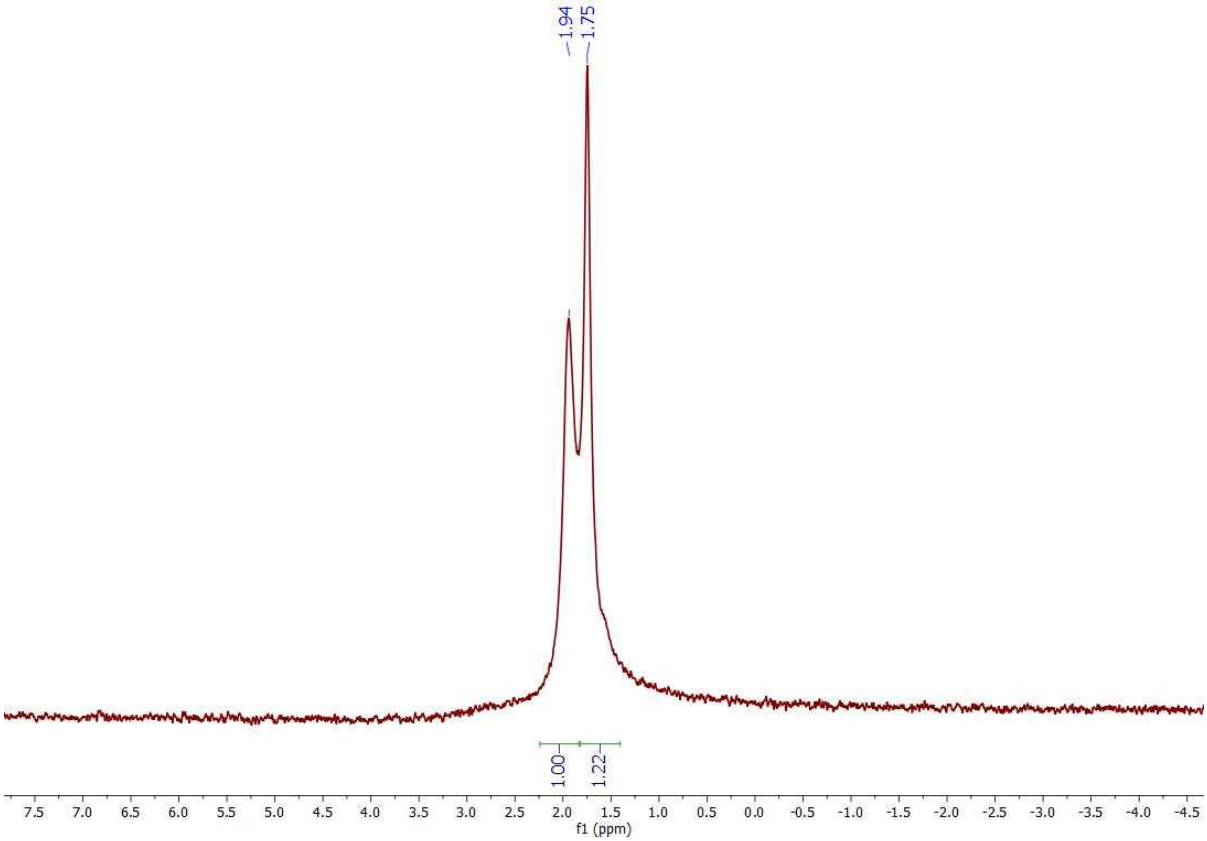

Figure A3.16. $^{7}Li\{^{1}H\}$ NMR spectrum of Li(N=C^{t}BuPh) in THF-d_8.

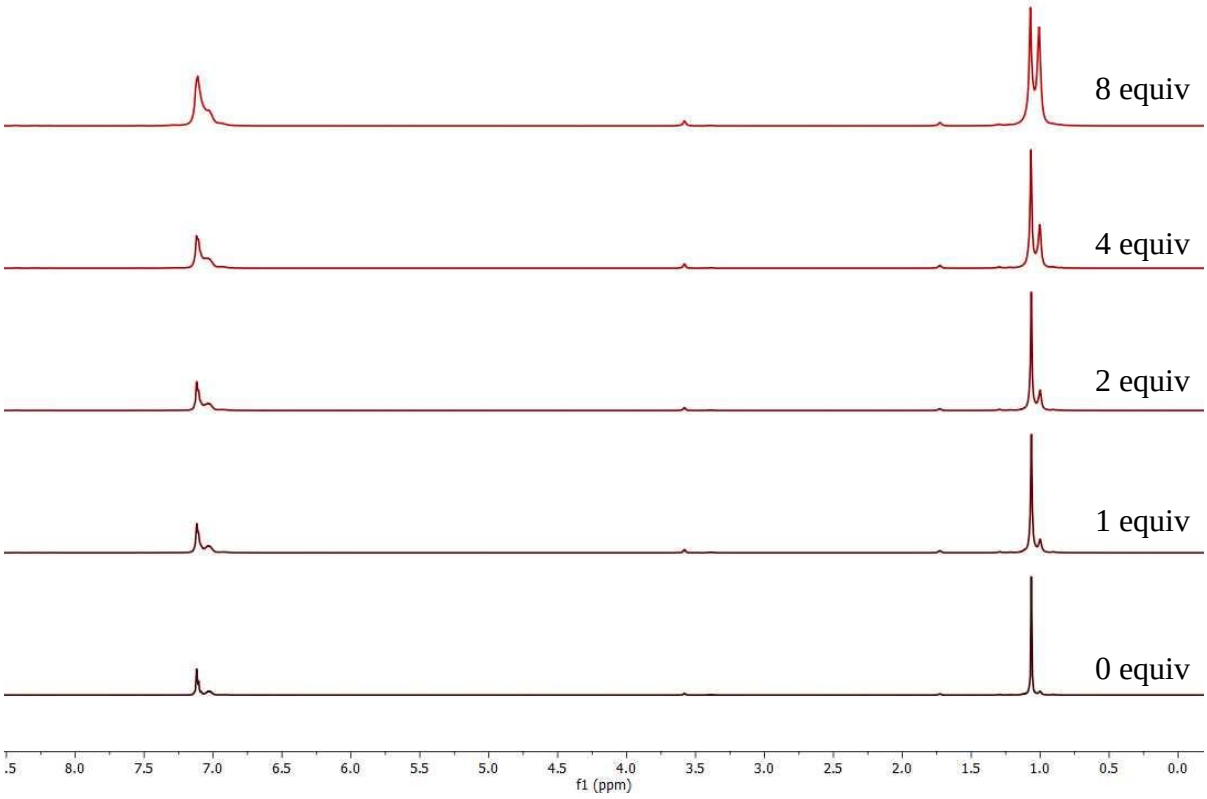

Figure A3.17. ^{1}H NMR spectra of the titration of **3.1** with Li(N=C^{t}BuPh) in THF-d_8. **Experimental Details:** Purple crystals of **3.1** (19.5 mg, 0.017 mmol) were dissolved in THF-d_8 (0.75 mL) yielding a deep purple solution. The mixture was transferred to a J. Young NMR tube equipped with a rotoflow Teflon valve, brought out of the glovebox, and ^{1}H and ^{7}Li{^{1}H} spectra were recorded. The sample was then brought back into the glove box and Li(N=C^{t}BuPh) was added as a solid (3.1 mg, 0.018 mmol, 1 equiv). No obvious color change was observed. The sample was brought out of the box and ^{1}H and ^{7}Li{^{1}H} spectra were re-recorded. This procedure was repeated three more times, bringing the total amount of Li(N=C^{t}BuPh) added to 8 equiv.

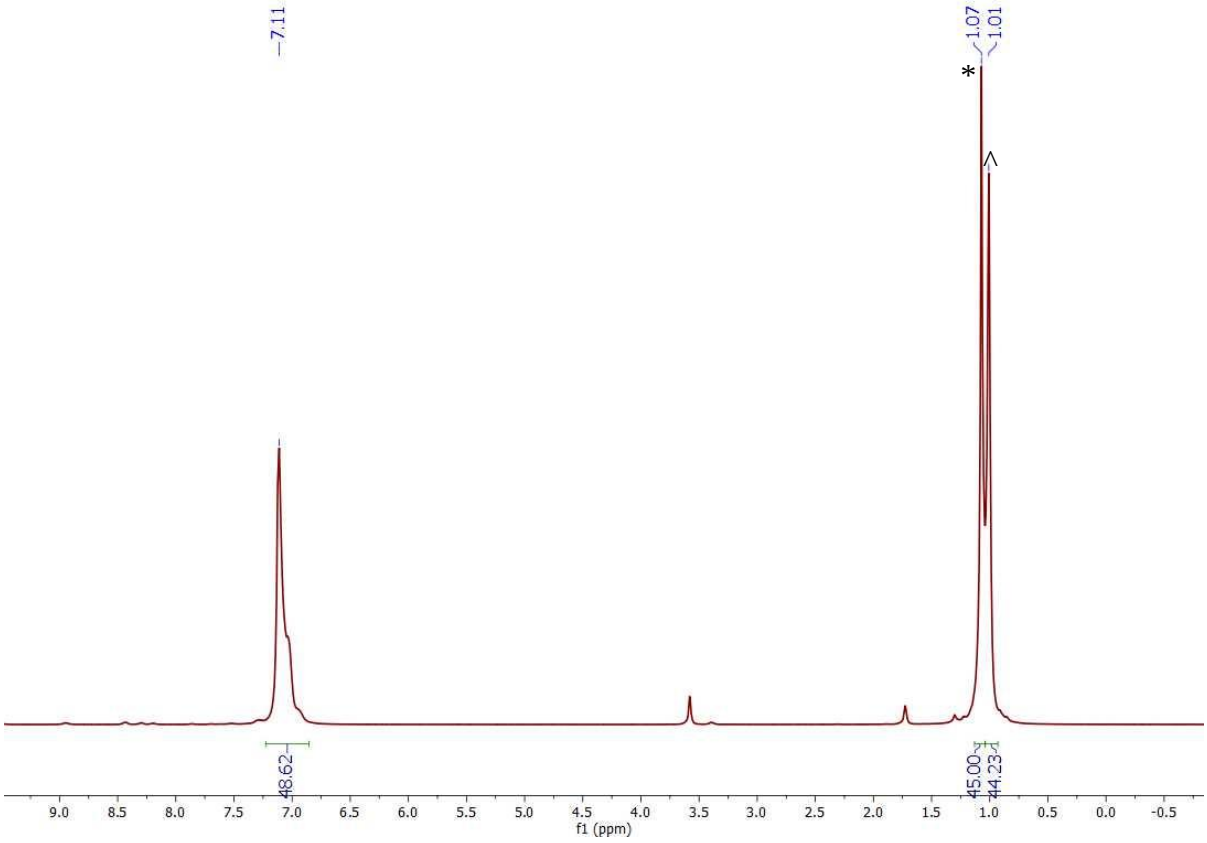

Figure A3.18. ^{1}H NMR spectrum of a mixture of **3.1** and 8 equiv of Li(N=CtBuPh) in THF-d_8. The resonance marked with * is assignable to [Li][Ce(N=C^{t}BuPh)$_5$] (**3.1'**) and the resonance marked with ^ is assignable to Li(N=C^{t}BuPh).

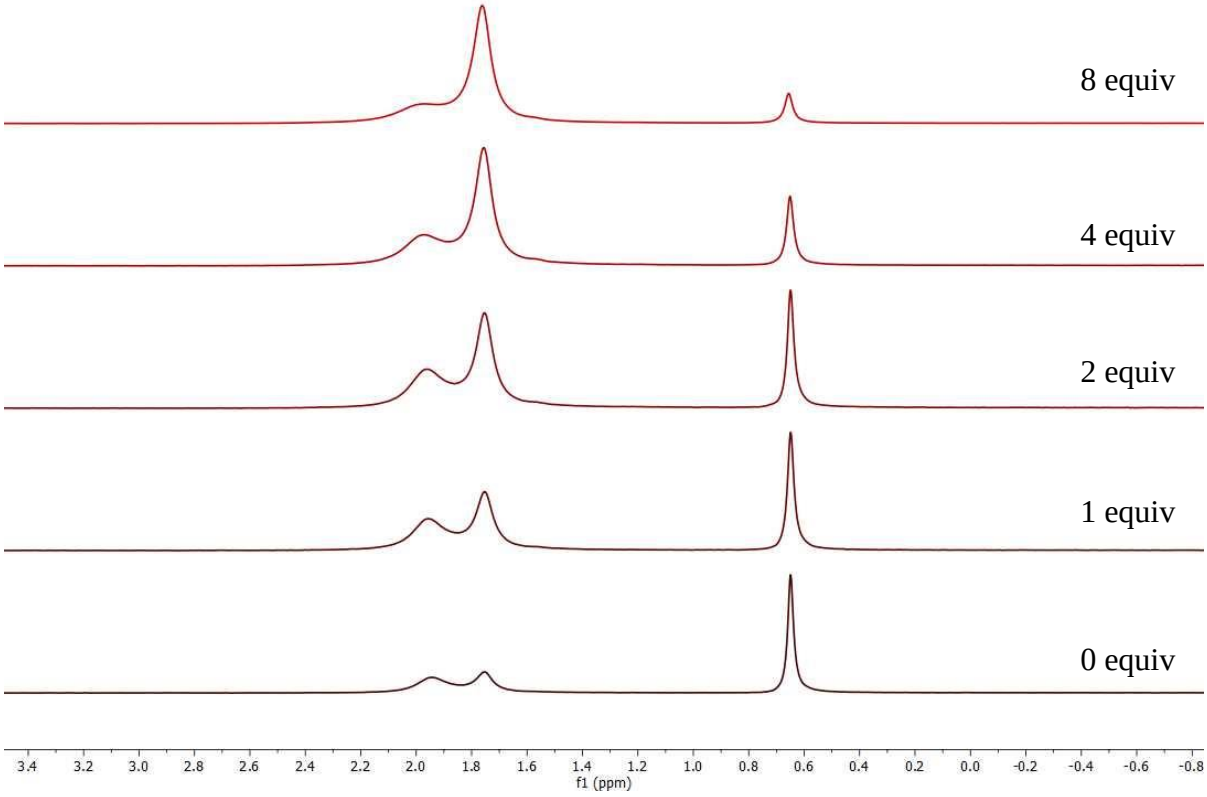

Figure A3.19. $^{7}Li\{^{1}H\}$ NMR spectra of the titration of **3.1** with Li(N=C^{t}BuPh) in THF-d_8.

Experimental Details: See details for Figure A3.17.

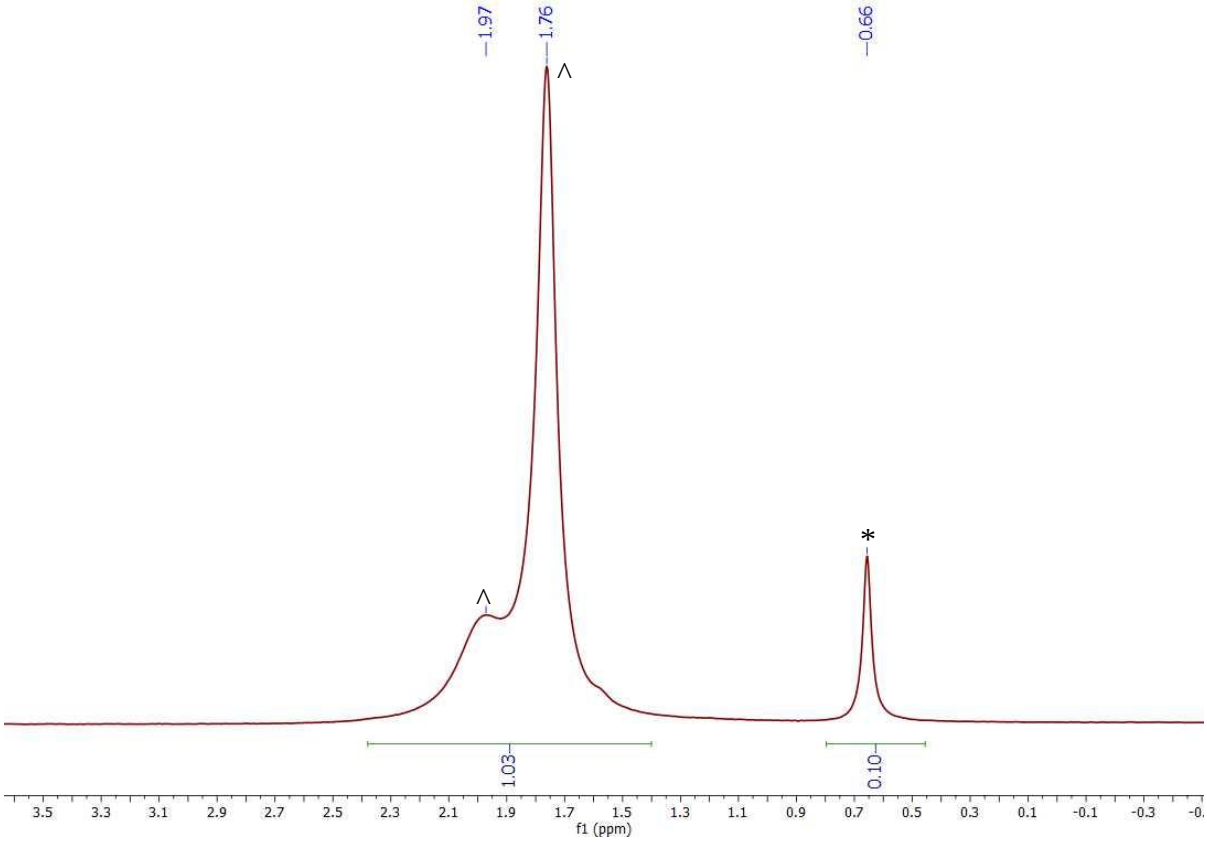

Figure A3.20. $^{7}Li\{^{1}H\}$ NMR spectrum of a mixture of **3.1** and 8 equiv of Li(N=C^{t}BuPh) in THF-d_8. The resonance marked with * is assignable to [Li][Ce(N=C^{t}BuPh)$_5$] (**3.1'**) and the resonances marked with ^ are assignable to Li(N=C^{t}BuPh).

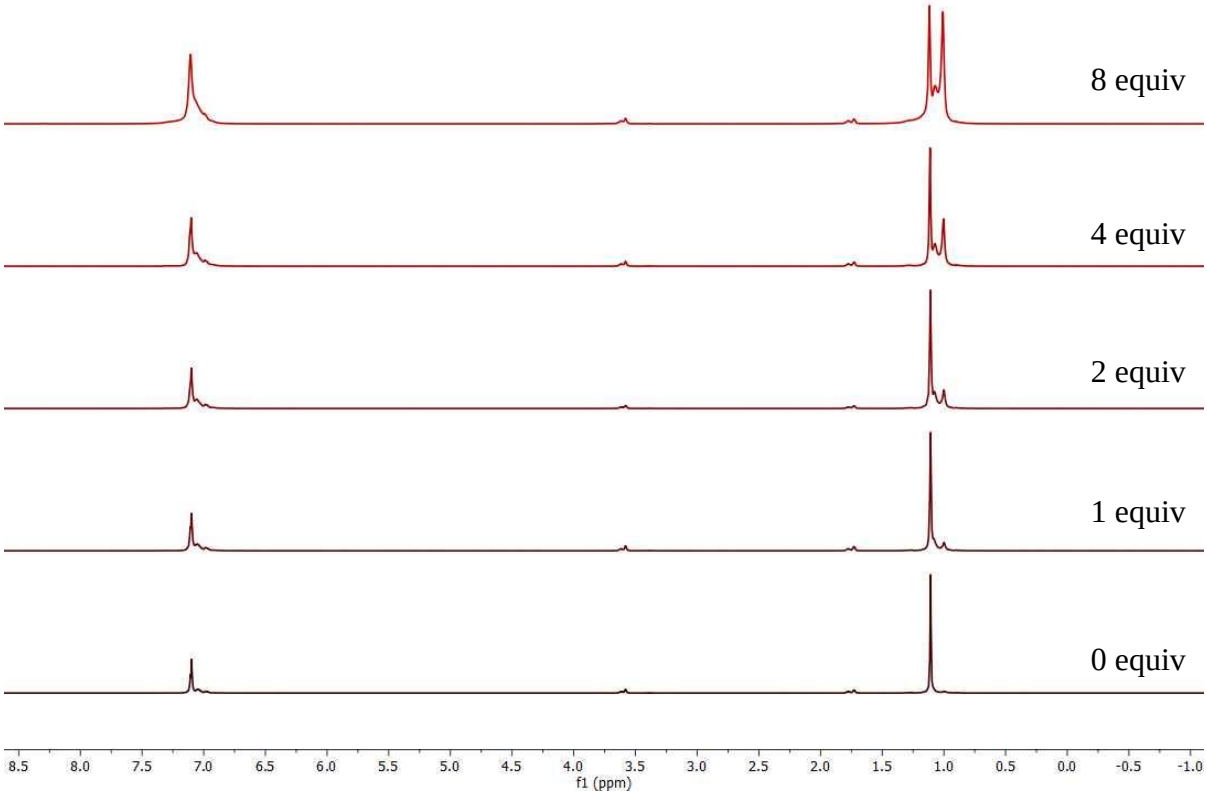

Figure A3.21. ^{1}H NMR spectra of the titration of **3.2** with Li(N=C^{t}BuPh) in THF-d_8. **Experimental Details:** Yellow crystals of **3.2** (21.2 mg, 0.018 mmol) were dissolved in THF-d_8 (0.75 mL) yielding a yellow solution. The mixture was transferred to a J. Young NMR tube equipped with a rotoflow Teflon valve, brought out of the glovebox, and ^{1}H and ^{7}Li{^{1}H} spectra were recorded. The sample was then brought back into the glove box and Li(N=C^{t}BuPh) was added as a solid (2.9 mg, 0.017 mmol, 1 equiv). No obvious color change was observed. The sample was brought out of the box and ^{1}H and ^{7}Li{^{1}H} spectra were re-recorded. This procedure was repeated three more times, bringing the total amount of Li(N=C^{t}BuPh) added to 8 equiv.

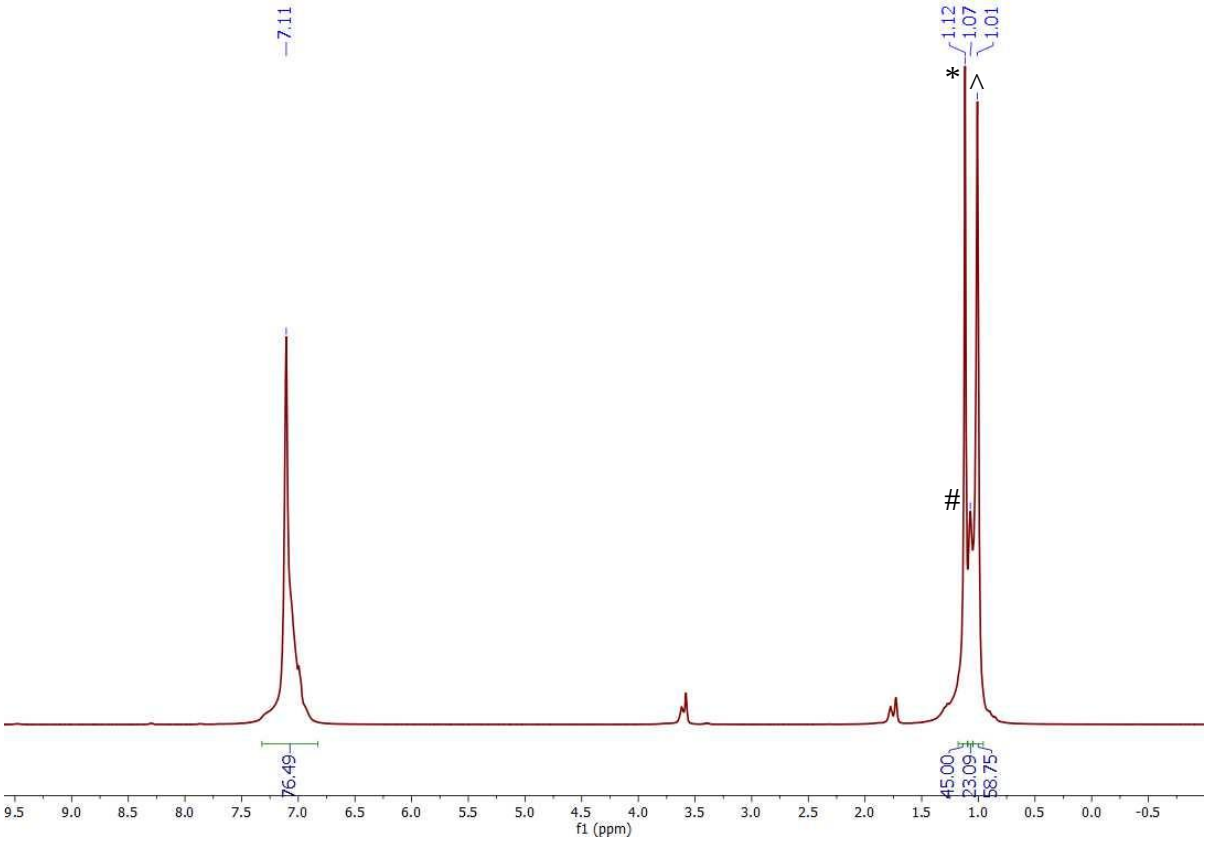

Figure A3.22. ^{1}H NMR spectrum of a mixture of **3.2** and 8 equiv of Li(N=C^{t}BuPh) in THF-d_8. The resonance marked with * is assignable to [Li][Th(N=C^{t}BuPh)$_5$] (**3.2'**), the resonance marked with # is assignable to **3.2**, and the resonance marked with ^ is assignable to Li(N=C^{t}BuPh).

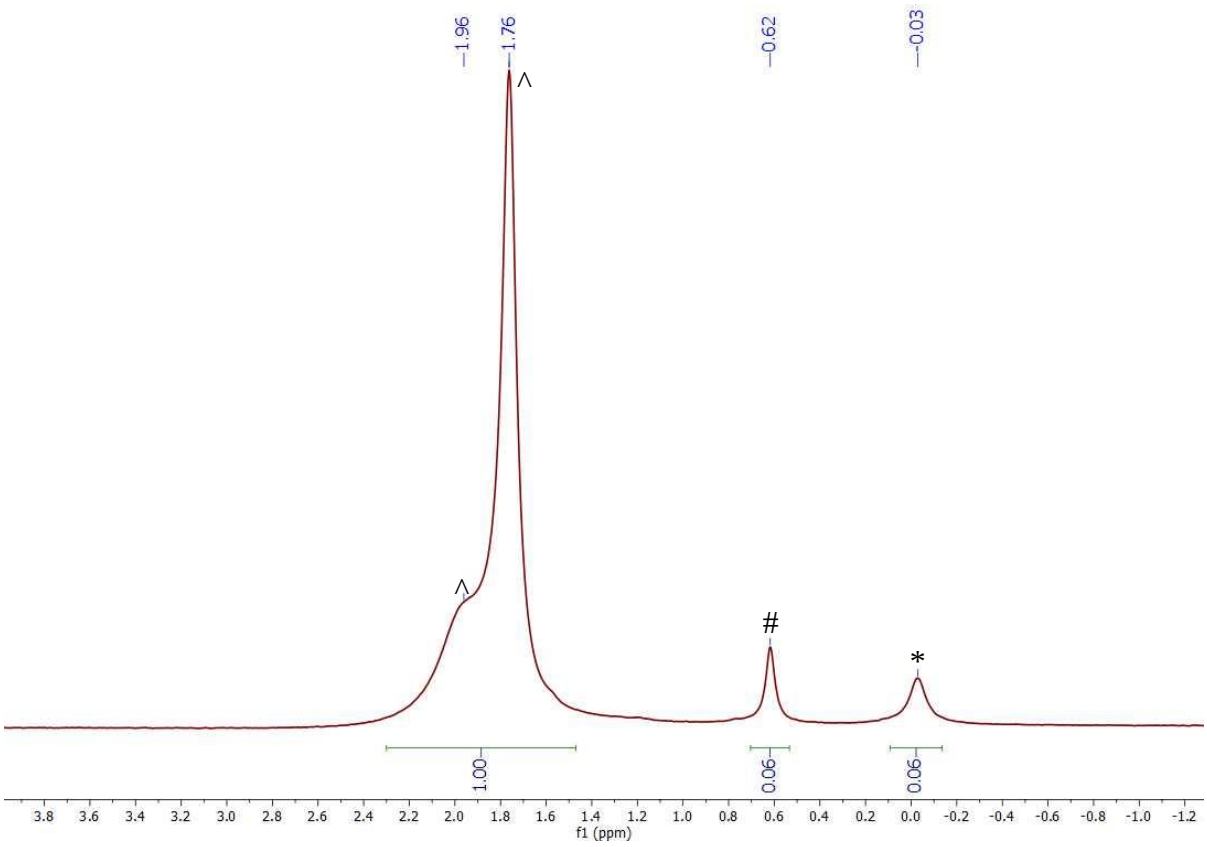

Figure A3.23. $^{7}Li\{^{1}H\}$ NMR spectrum of a mixture of **3.2** and 8 equiv of Li(N=C^{t}BuPh) in THF-d_8. The resonance marked with * is assignable to [Li][Th(N=C^{t}BuPh)$_5$] (**3.2'**), the resonance marked with # is assignable to **3.2**, and the resonances marked with ^ are assignable to Li(N=C^{t}BuPh).

3.6.2 IR Spectra

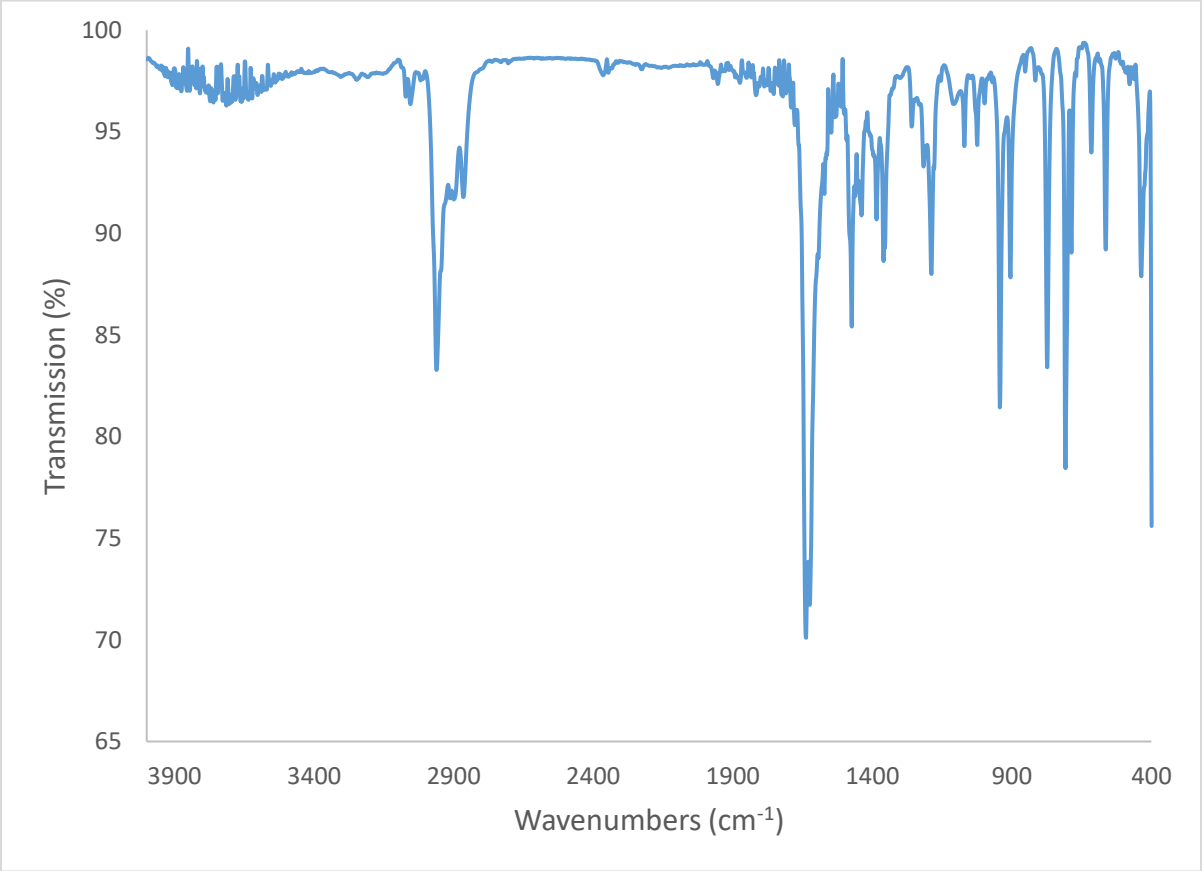

Figure A3.24. IR spectrum of **3.1** (KBr pellet).

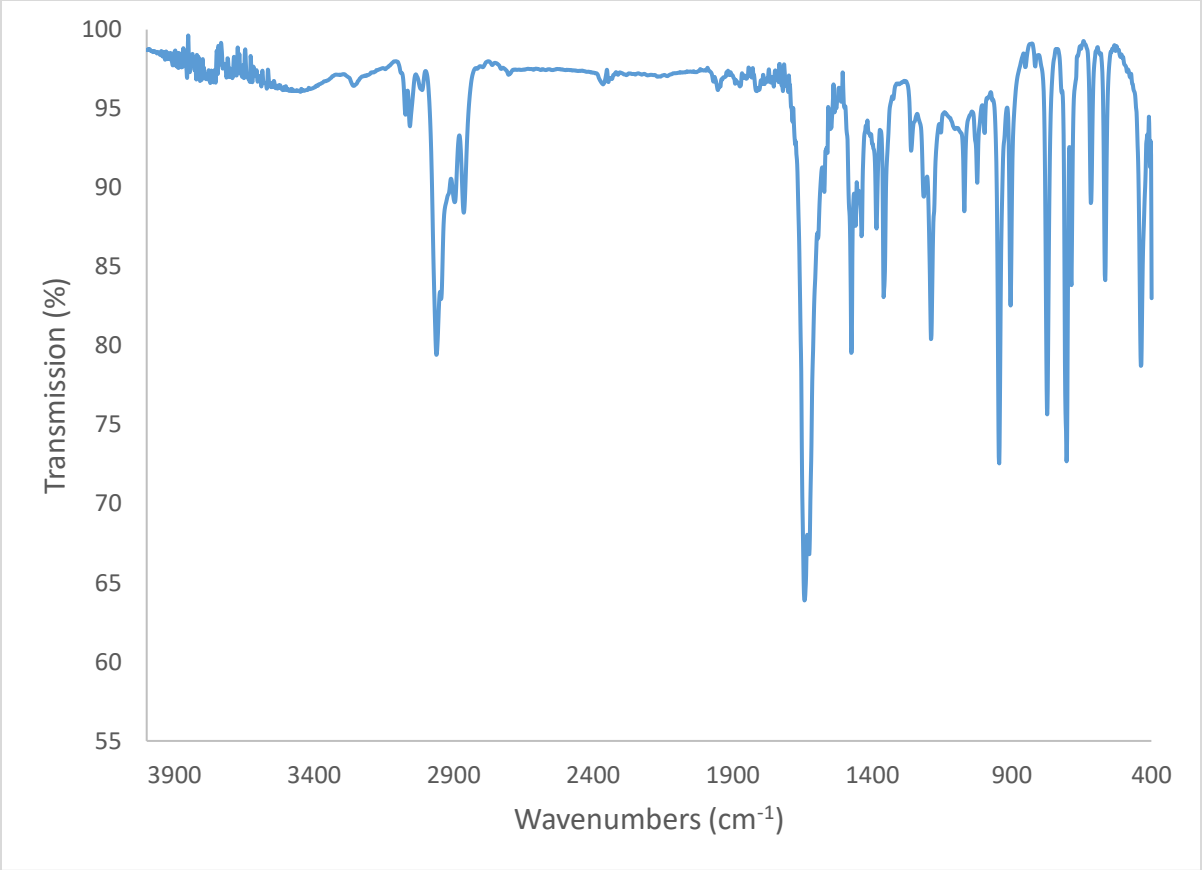

Figure A3.25. IR spectrum of **3.2** (KBr pellet).

3.6.3 Cyclic Voltammetry

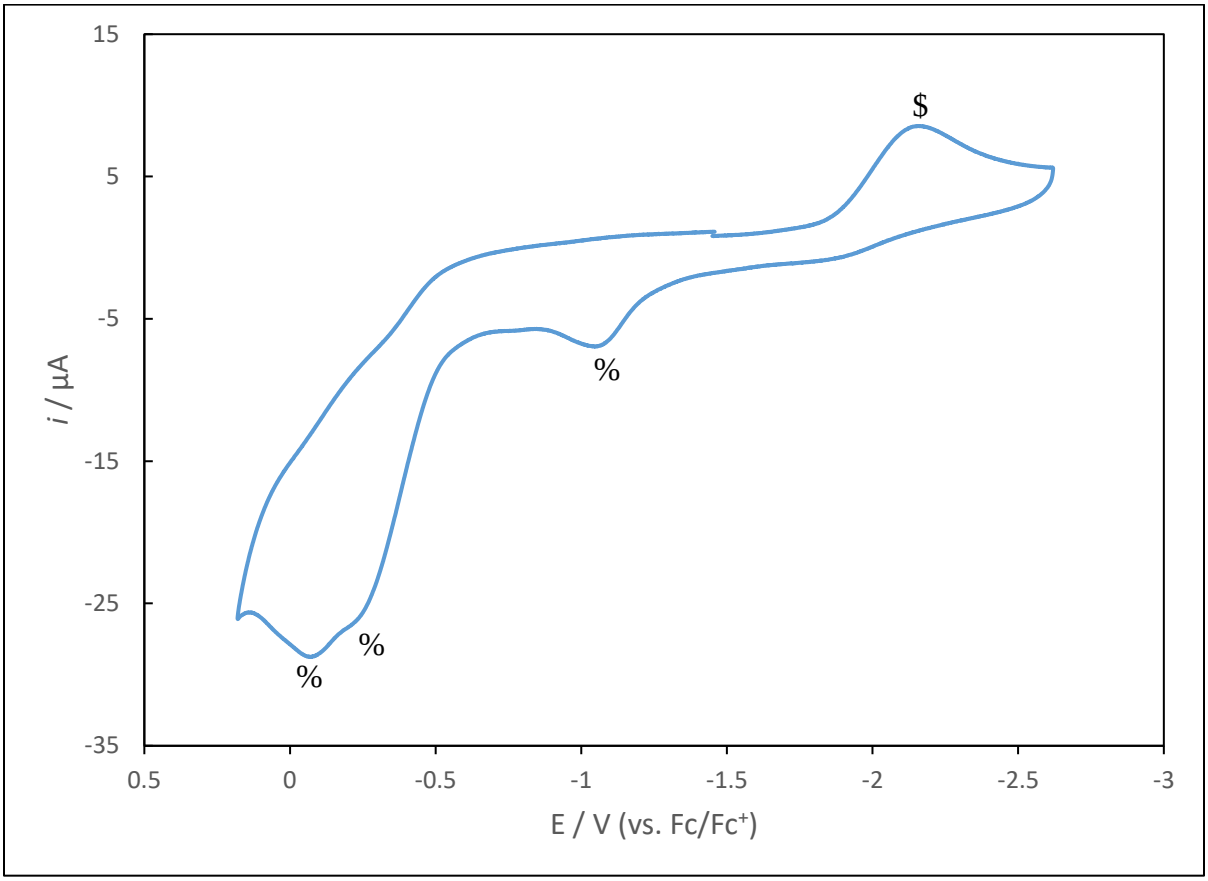

Figure A3.26. Cyclic voltammogram of complex **3.1** (200 mV/s scan rate, vs. Fc/Fc^{+}). Measured in THF with 0.1 M $[NBu_4][BPh_4]$ as the supporting electrolyte. $ is assignable to the irreversible Ce(IV/III) reduction, and % are assignable to irreversible ketimide ligand oxidation events.

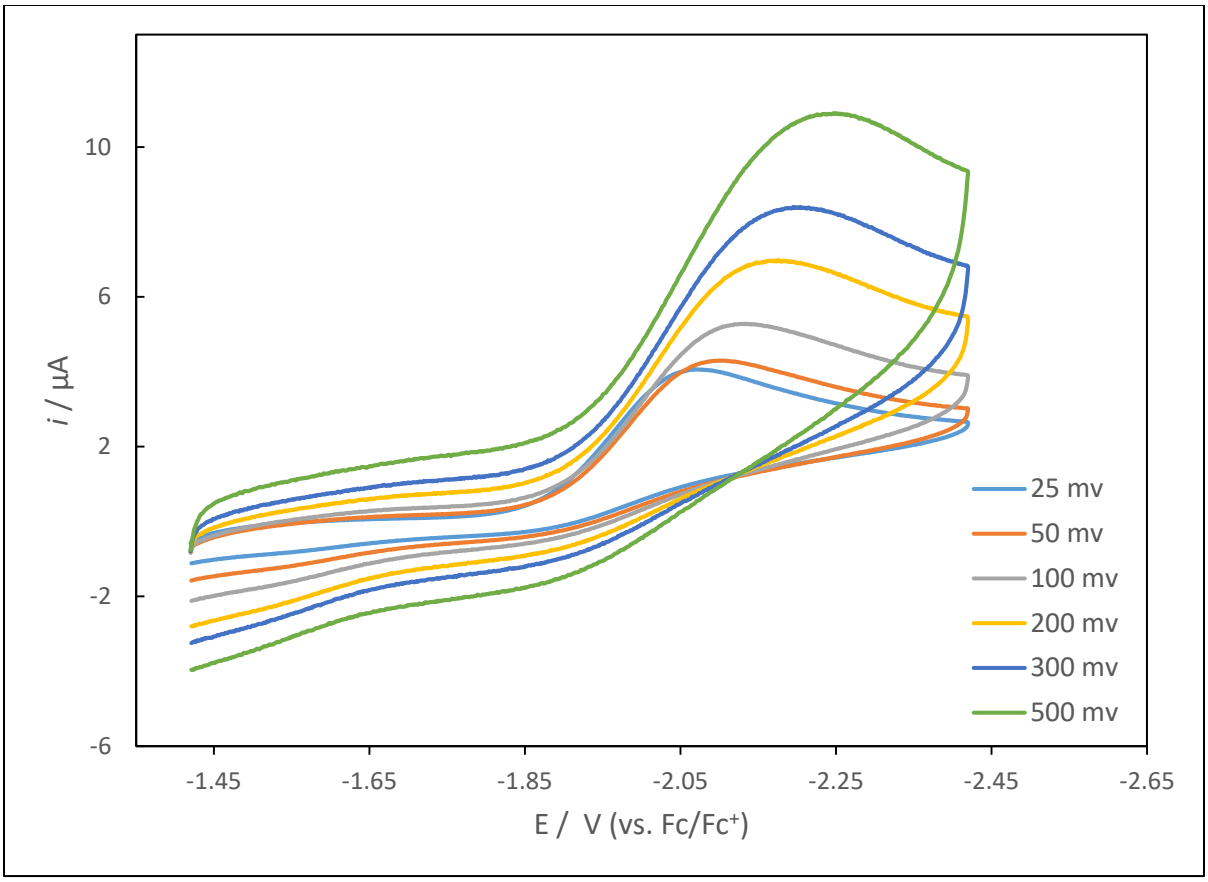

Figure A3.27. Cyclic voltammogram of the irreversible Ce(IV)/Ce(III) reduction event of complex **3.1** measured in THF with 0.1 M $[NBu_4][BPh_4]$ as the supporting electrolyte (vs. Fc/Fc^+).

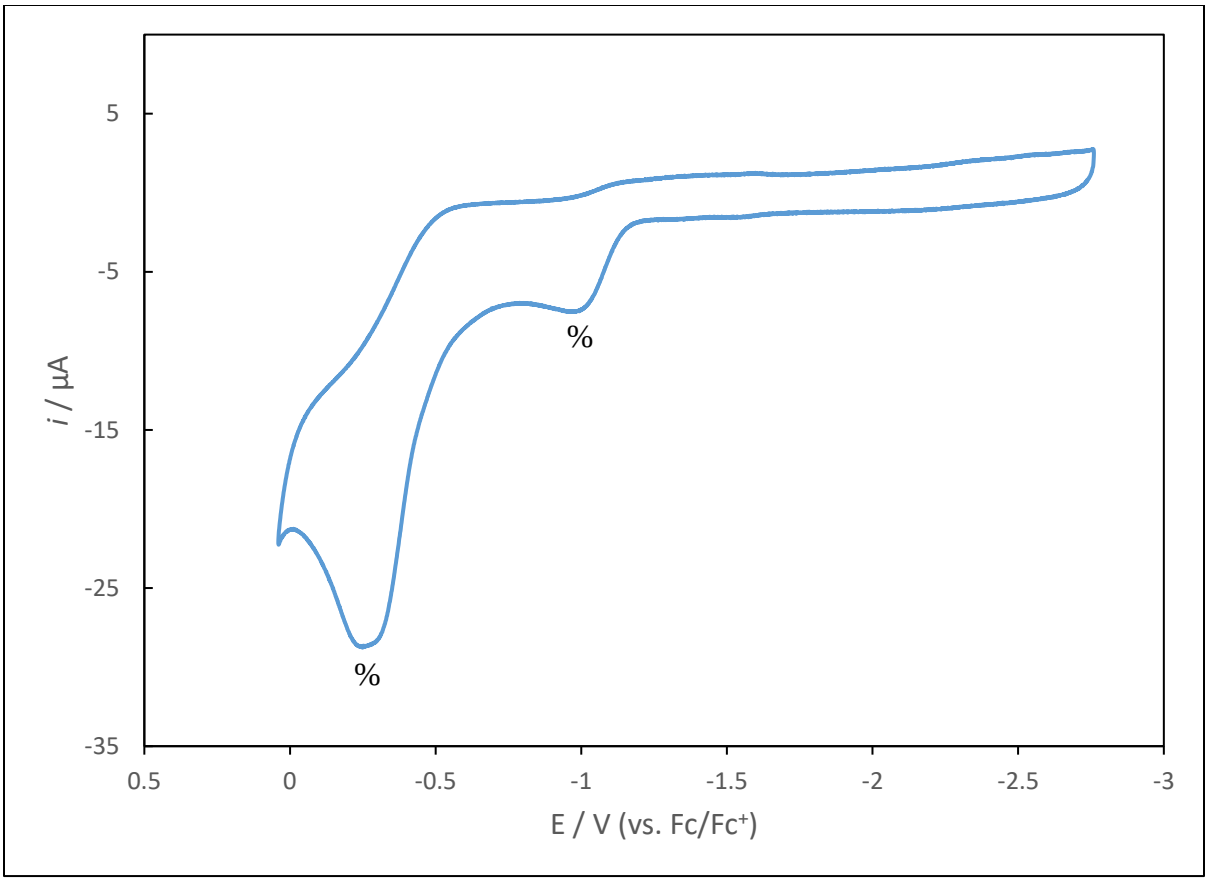

Figure A3.28. Cyclic voltammogram of complex **3.2** (200 mV/s scan rate, vs. Fc/Fc^{+}). Measured in THF with 0.1 M $[NBu_4][BPh_4]$ as the supporting electrolyte. % are assignable to irreversible ketimide ligand oxidation events.

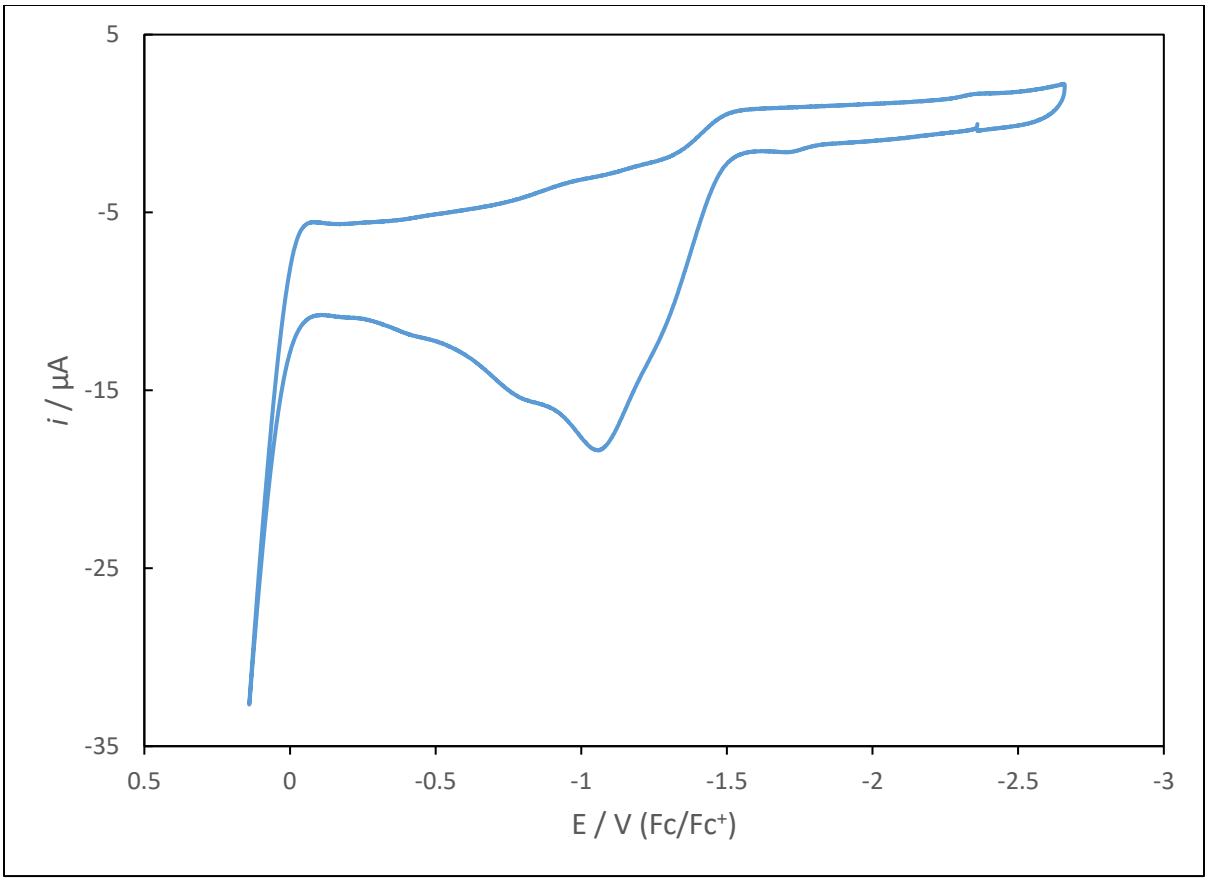

Figure A3.29. Cyclic voltammogram of Li(N=C^{t}BuPh) (200 mV/s scan rate, vs. Fc/Fc^{+}). Measured in THF with 0.1 M [NBu$_4$][BPh$_4$] as the supporting electrolyte.

Table A3.1. Electrochemical parameters for $[Li]_2[Ce(N=C^tBuPh)_6]$ (**3.1**) in THF (vs. Fc/Fc^+, $[NBu_4][BPh_4]$ as the supporting electrolyte)

Reduction Feature	Scan Rate, V/s	$E_{p,c}$, V
	0.025	-2.034
	0.050	-2.096
	0.100	-2.122
	0.200	-2.158
	0.300	-2.189
	0.500	-2.228

Oxidation Feature	Scan Rate, V/s	$E_{p,a}$, V
1	0.200	-0.082
2	0.200	-0.231
3	0.200	-1.067

Table A3.2. Electrochemical parameters for $[Li]_2[Th(N=C^tBuPh)_6]$ (**3.2**) in THF (vs. Fc/Fc^+, $[NBu_4][BPh_4]$ as the supporting electrolyte)

Oxidation Feature	Scan Rate, V/s	$E_{p,a}$, V
1	0.200	-0.261
2	0.200	-0.997

Table A3.3. Electrochemical parameters for $Li(N=C^tBuPh)$ in THF (vs. Fc/Fc^+, $[NBu_4][BPh_4]$ as the supporting electrolyte)

Oxidation Feature	Scan Rate, V/s	$E_{p,a}$, V
1	0.200	-0.807
2	0.200	-1.063

3.6.4 Magnetism

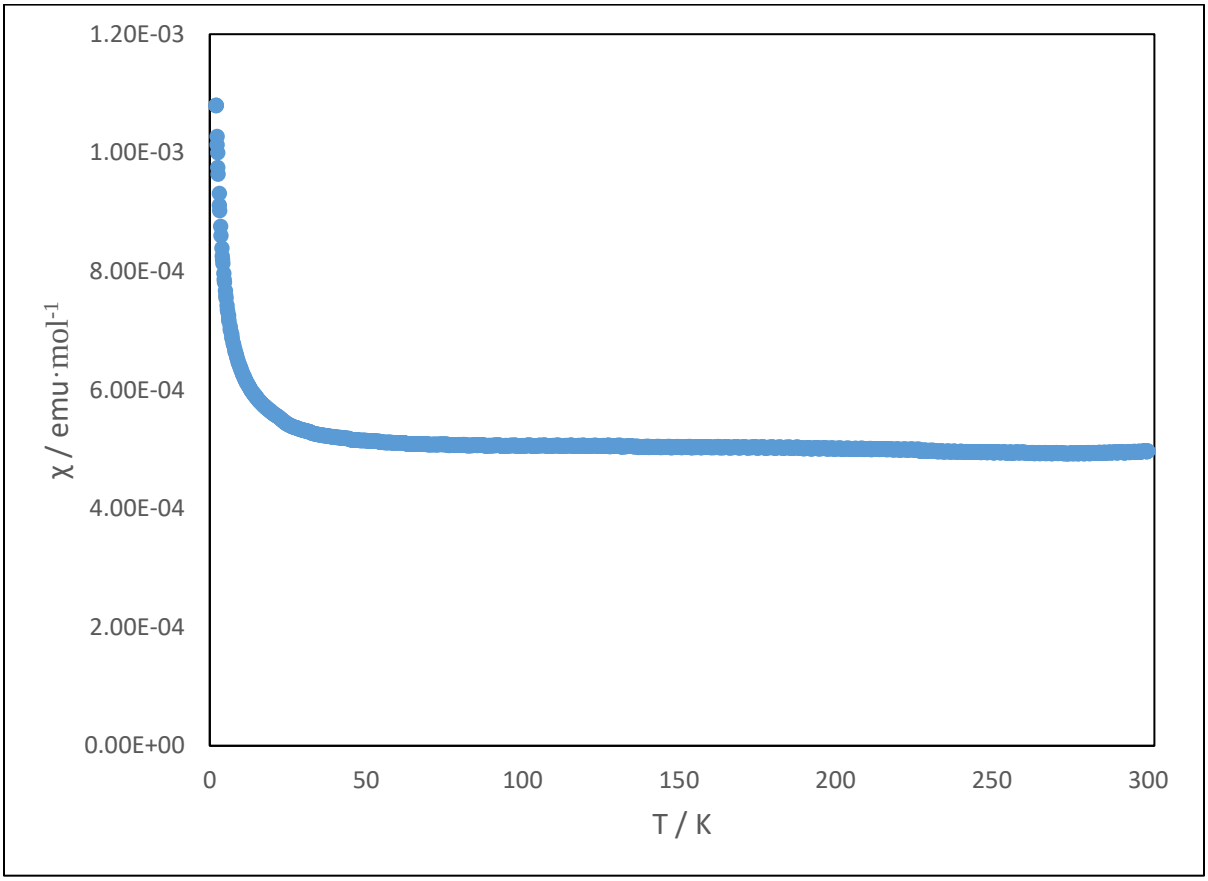

Figure A3.30. Variable-temperature magnetic susceptibility (χ) data for **3.1** collected at 1 Tesla.

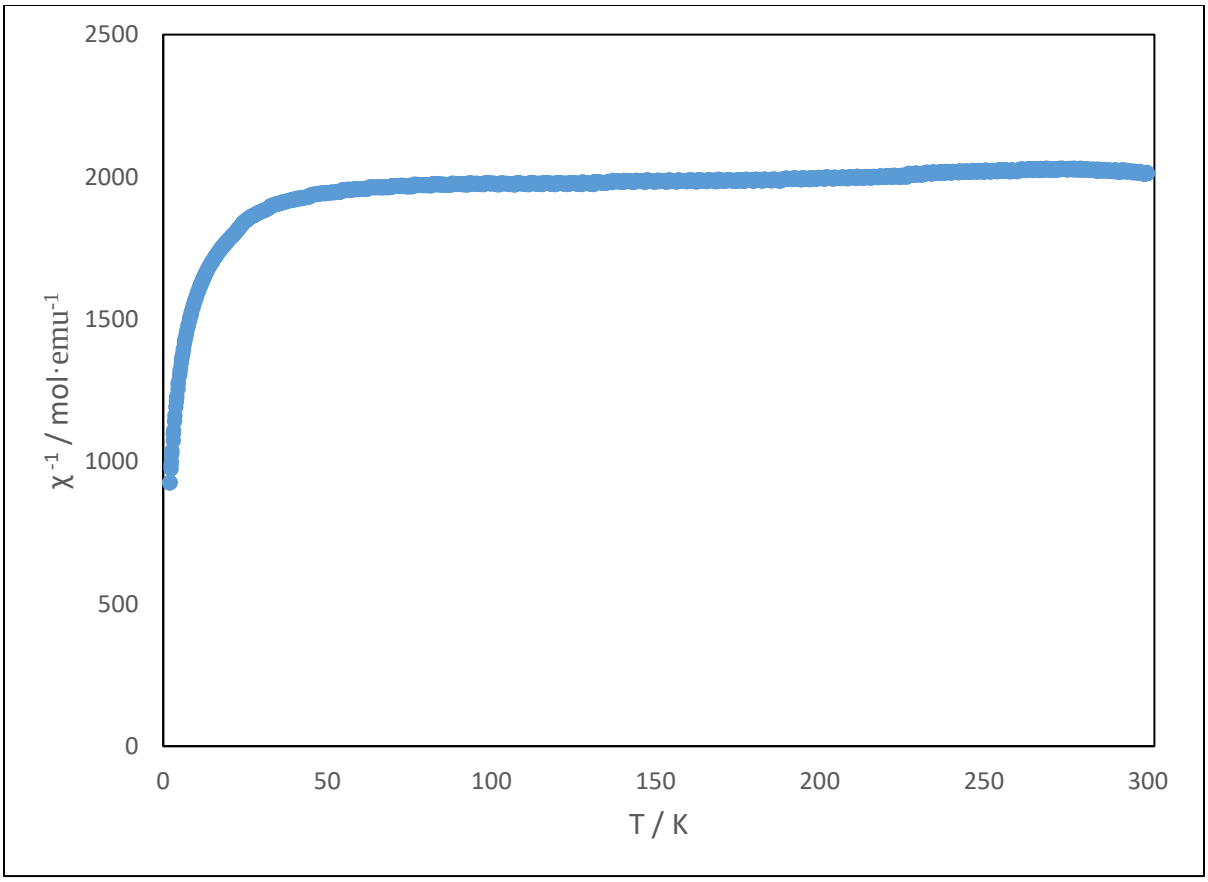

Figure A3.31. Variable-temperature magnetic susceptibility (1/χ) data for **3.1** collected at 1 Tesla.

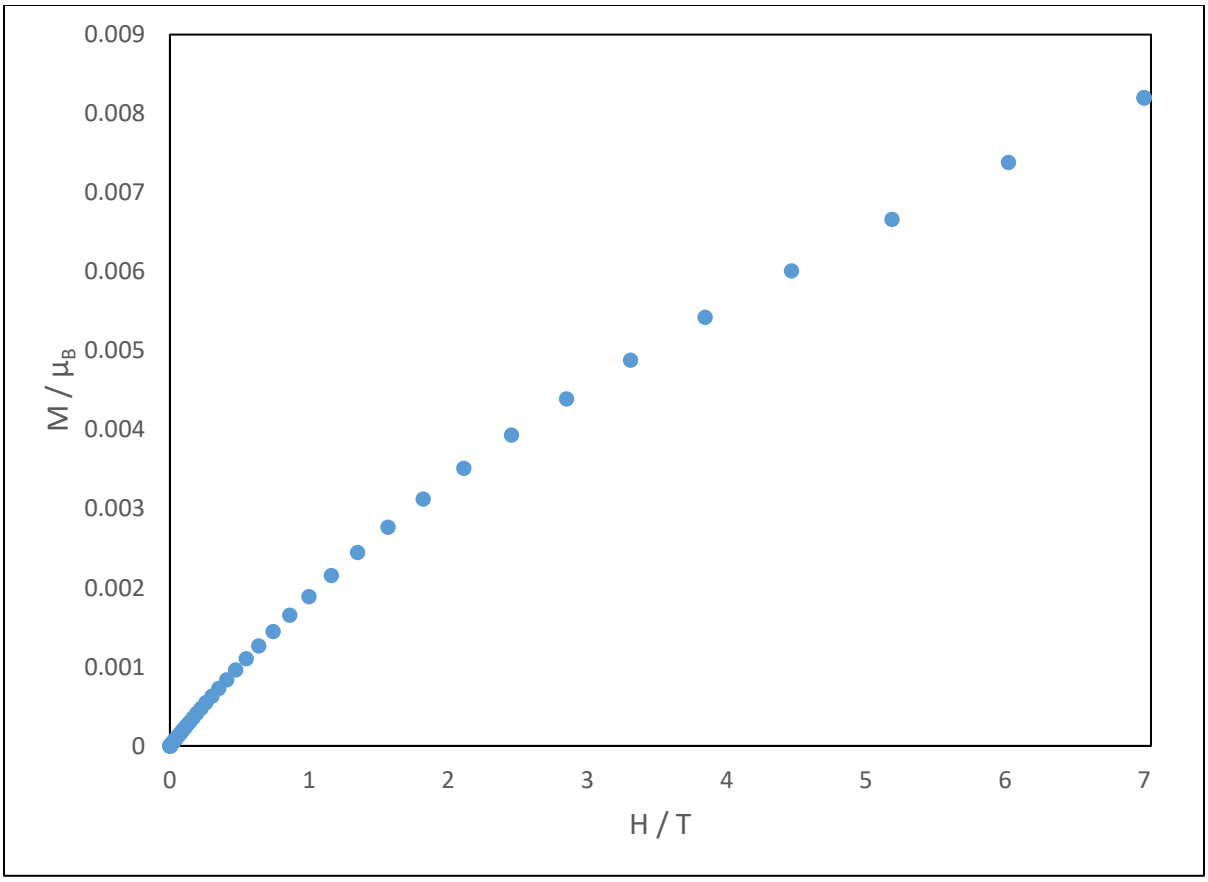

Figure A3.32. Variable-field data for **3.1** collected at 2 K.

3.6.5 Computational Details

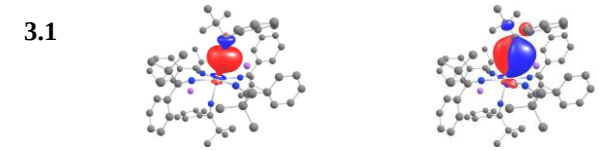

3.1	σ(Ce–N)	π (Ce–N)
GTO/SDD	87% N (54 s; 46 p) 11% Ce (14 s; 58 d; 28 f)	81% N (100 p) 10% Ce (47 d; 53 f)
STO/ZORA	89% N (54 s; 46 p) 9% Ce (14 s; 59 d; 27 f)	83% N (100 p) 9% Ce (47 d; 53 f)

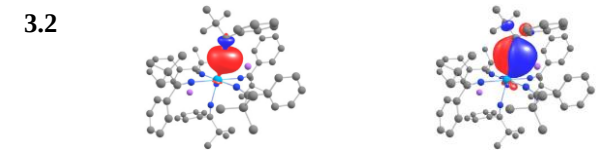

3.2	σ(Th–N)	π (Th–N)
GTO/SDD	89% N (57 s; 43 p) 9% Th (17 s; 2 p; 58 d; 23 f)	84% N (100 p) 7% Th (1 s; 64 d; 35 f)
STO/ZORA	88% N (56 s; 44 p) 10% Th (13 s; 50 d; 37 f)	84% N (100 p) 8% Th (56 d; 44 f)

Figure A3.33. Bonding Ce–N (one σ and one π) natural localized molecular orbitals (isosurface of ±0.03 a.u.) of **3.1** (top) and **3.2** (bottom), obtained with Gaussian type orbital (GTO) vs. Slater type orbital (STO) basis sets. The π NLMO has slight five-center character, i.e. there is a small delocalization tail toward adjacent C(butyl) and C(phenyl) centers. Only NLMO contributions from Ce and N centers are shown below the graphics. There are six equivalent such NLMO pairs corresponding to the six Ce-N interactions.

3.7 References

1. Anwander, R.; Dolg, M.; Edelmann, F. T. The difficult search for organocerium(iv) compounds. *Chem. Soc. Rev.* **2017,** 46, 6697-6709.

2. Avignant, D.; Largeau, E.; Gaumet, V.; Dugat, P.; El-Ghozzi, M. Recent progress in tetravalent terbium chemistry. *J. Alloy Compd.* **1998,** 275-277, 1-5.

3. El-Ghozzi, M.; Avignant, D. Crystal chemistry and magnetic structures of Tb(IV) fluorides. *J. Fluorine Chem.* **2001,** 107, 229-233.

4. Hobart, D. E.; Young, J. P.; Norvell, V. E.; Mamantov, G.; Peterson, J. R.; Samhoun, K. Stabilization of praseodymium(IV) and terbium(IV) in aqueous carbonate solution. *Inorg. Nucl. Chem. Lett.* **1980,** 16, 321-328.

5. Sroor, F. M.; Edelmann, F. T. In *Encycl. Inorg. Bioinorg. Chem.*; 2012; pp 1-14.

6. Eller, P. G.; Penneman, R. A. Stabilization of actinides and lanthanides in high oxidation states. *J. Less-Common Metals* **1987,** 127, 19-33.

7. Nugent, L. J.; Baybarz, R. D.; Burnett, J. L.; Ryan, J. L. Electron-transfer and f-d absorption bands of some lanthanide and actinide complexes and the standard (II-III) oxidation potential for each member of the lanthanide and actinide series. *J. Phys. Chem.* **1973,** 77, 1528-1539.

8. Beckers, J.; Rothenberg, G. Sustainable selective oxidations using ceria-based materials. *Green Chem.* **2010,** 12, 939-948.

9. Bogart, J. A.; Lewis, A. J.; Medling, S. A.; Piro, N. A.; Carroll, P. J.; Booth, C. H.; Schelter, E. J. Homoleptic Cerium(III) and Cerium(IV) Nitroxide Complexes: Significant Stabilization of the 4+ Oxidation State. *Inorg. Chem.* **2013,** 52, 11600-11607.

10. Gorte, R. J. Ceria in catalysis: From automotive applications to the water–gas shift reaction. *AIChE J.* **2010,** 56, 1126-1135.

11. Lammert, M.; Wharmby, M. T.; Smolders, S.; Bueken, B.; Lieb, A.; Lomachenko, K. A.; Vos, D. D.; Stock, N. Cerium-based metal organic frameworks with UiO-66 architecture: synthesis, properties and redox catalytic activity. *ChemComm* **2015,** 51, 12578-12581.

12. Levin, J. R.; Dorfner, W. L.; Dai, A. X.; Carroll, P. J.; Schelter, E. J. Density Functional Theory as a Predictive Tool for Cerium Redox Properties in Nonaqueous Solvents. *Inorg. Chem.* **2016,** 55, 12651-12659.

13. Piro, N. A.; Robinson, J. R.; Walsh, P. J.; Schelter, E. J. The electrochemical behavior of cerium(III/IV) complexes: Thermodynamics, kinetics and applications in synthesis. *Coord. Chem. Rev.* **2014,** 260, 21-36.

14. Rice, N. T.; Su, J.; Gompa, T. P.; Russo, D. R.; Telser, J.; Palatinus, L.; Bacsa, J.; Yang, P.; Batista, E. R.; La Pierre, H. S. Homoleptic Imidophosphorane Stabilization of Tetravalent Cerium. *Inorg. Chem.* **2019,** 58, 5289-5304.

15. So, Y.-M.; Leung, W.-H. Recent advances in the coordination chemistry of cerium(IV) complexes. *Coord. Chem. Rev.* **2017,** 340, 172-197.

16. Solola, L. A.; Cheisson, T.; Yang, Q.; Carroll, P. J.; Schelter, E. J. Exploration of the Solid- and Solution-State Structures and Electrochemical Properties of Ce^{IV}(atrane) Complexes. *Inorg. Chem.* **2018,** 57, 10543-10547.

17. Das, A. K. Kinetic and mechanistic aspects of metal ion catalysis in cerium(IV) oxidation. *Coord. Chem. Rev.* **2001,** 213, 307-325.

18. Molander, G. A. Application of lanthanide reagents in organic synthesis. *Chem. Rev.* **1992,** 92, 29-68.

19. Nair, V.; Balagopal, L.; Rajan, R.; Mathew, J. Recent Advances in Synthetic Transformations Mediated by Cerium(IV) Ammonium Nitrate. *Acc. Chem. Res.* **2004,** 37, 21-30.

20. Nair, V.; Deepthi, A. Cerium(IV) Ammonium Nitrate - A Versatile Single-Electron Oxidant. *Chem. Rev.* **2007,** 107, 1862-1891.

21. Sridharan, V.; Menéndez, J. C. Cerium(IV) Ammonium Nitrate as a Catalyst in Organic Synthesis. *Chem. Rev.* **2010,** 110, 3805-3849.

22. Binnemans, K. In *Handbook on the Physics and Chemistry of Rare Earths*; Gschneidner, K. A., Bunzli, J.-C. G., Pecharsky, V. K., Ed.; Elsevier: 2006; Vol. 36, pp 281-392.

23. Ellis, R. J.; Antonio, M. R. Redox Chemistry of Third Phases Formed in the Cerium/Nitric Acid/Malonamide-*n*-Dodecane Solvent Extraction System. *ChemPlusChem* **2012,** 77, 41-47.

24. Berryman, V. E. J.; Whalley, Z. J.; Shephard, J. J.; Ochiai, T.; Price, A. N.; Arnold, P. L.; Parsons, S.; Kaltsoyannis, N. Computational analysis of M–O covalency in $M(OC_6H_5)_4$ (M = Ti, Zr, Hf, Ce, Th, U). *Dalton Trans.* **2019,** 48, 2939-2947.

25. Bianconi, A.; Marcelli, A.; Tomellini, M.; Davoli, I. Determination of mixing of 4f-ligand orbitals in $Ce(SO_4)_2$ by XANES. Is $Ce(SO_4)_2$ a mixed valent insulating system? *J. Magn. Magn. Mater.* **1985,** 47-48, 209-211.

26. Clark, D. L.; Gordon, J. C.; Hay, P. J.; Poli, R. Existence and Stability of Lanthanide−Main Group Element Multiple Bonds. New Paradigms in the Bonding of the 4f Elements. A DFT Study of Cp_2CeZ (Z = F^+, O, NH, CH^-, CH_2) and the Ligand Adduct $Cp_2Ce(CH_2)(NH_3)$. *Organometallics* **2005,** 24, 5747-5758.

27. Gregson, M.; Lu, E.; Tuna, F.; McInnes, E. J. L.; Hennig, C.; Scheinost, A. C.; McMaster, J.; Lewis, W.; Blake, A. J.; Kerridge, A.; Liddle, S. T. Emergence of comparable covalency in

isostructural cerium(iv)– and uranium(iv)–carbon multiple bonds. *Chem. Sci.* **2016,** 7, 3286-3297.

28. Minasian, S. G.; Batista, E. R.; Booth, C. H.; Clark, D. L.; Keith, J. M.; Kozimor, S. A.; Lukens, W. W.; Martin, R. L.; Shuh, D. K.; Stieber, S. C. E.; Tylisczcak, T.; Wen, X.-d. Quantitative Evidence for Lanthanide-Oxygen Orbital Mixing in CeO_2, PrO_2, and TbO_2. *J. Am. Chem. Soc.* **2017,** 139, 18052-18064.

29. Pham, T. A.; Altman, A. B.; Stieber, S. C. E.; Booth, C. H.; Kozimor, S. A.; Lukens, W. W.; Olive, D. T.; Tyliszczak, T.; Wang, J.; Minasian, S. G.; Raymond, K. N. A Macrocyclic Chelator That Selectively Binds Ln^{4+} over Ln^{3+} by a Factor of 10^{29}. *Inorg. Chem.* **2016,** 55, 9989-10002.

30. Ashley, A.; Balazs, G.; Cowley, A.; Green, J.; Booth, C. H.; O'Hare, D. Bis(permethylpentalene)cerium – another ambiguity in lanthanide oxidation state. *ChemComm* **2007**, 1515-1517.

31. Halbach, R. L.; Nocton, G.; Booth, C. H.; Maron, L.; Andersen, R. A. Cerium Tetrakis(tropolonate) and Cerium Tetrakis(acetylacetonate) Are Not Diamagnetic but Temperature-Independent Paramagnets. *Inorg. Chem.* **2018,** 57, 7290-7298.

32. Hiroaki, I.; Masahiko, S. Mixed Valence State of Cerium in Bis(phthalocyaninato)cerium Complex. *Chem. Lett.* **1992,** 21, 147-150.

33. Mooßen, O.; Dolg, M. Assigning the Cerium Oxidation State for CH_2CeF_2 and $OCeF_2$ Based on Multireference Wave Function Analysis. *J. Phys. Chem. A* **2016,** 120, 3966-3974.

34. Streitwieser, A.; Kinsley, S. A.; Jenson, C. H.; Rigsbee, J. T. Synthesis and Properties of Di-π-[8]annulenecerium(IV), Cerocene. *Organometallics* **2004,** 23, 5169-5175.

35. Booth, C. H.; Walter, M. D.; Daniel, M.; Lukens, W. W.; Andersen, R. A. Self-Contained Kondo Effect in Single Molecules. *Phys. Rev. Lett.* **2005,** 95, 267202.

36. Mooßen, O.; Dolg, M. Two interpretations of the cerocene electronic ground state. *Chem. Phys. Lett.* **2014,** 594, 47-50.

37. Walter, M. D.; Booth, C. H.; Lukens, W. W.; Andersen, R. A. Cerocene Revisited: The Electronic Structure of and Interconversion Between $Ce_2(C_8H_8)_3$ and $Ce(C_8H_8)_2$. *Organometallics* **2009,** 28, 698-707.

38. Löble, M. W.; Keith, J. M.; Altman, A. B.; Stieber, S. C. E.; Batista, E. R.; Boland, K. S.; Conradson, S. D.; Clark, D. L.; Lezama Pacheco, J.; Kozimor, S. A.; Martin, R. L.; Minasian, S. G.; Olson, A. C.; Scott, B. L.; Shuh, D. K.; Tyliszczak, T.; Wilkerson, M. P.; Zehnder, R. A. Covalency in Lanthanides. An X-ray Absorption Spectroscopy and Density Functional Theory Study of $LnCl_6^{x-}$ (x = 3, 2). *J. Am. Chem. Soc.* **2015,** 137, 2506-2523.

39. Aneggi, E.; Boaro, M.; Leitenburg, C. d.; Dolcetti, G.; Trovarelli, A. Insights into the redox properties of ceria-based oxides and their implications in catalysis. *J. Alloy Compd.* **2006,** 408-412, 1096-1102.

40. Vivier, L.; Duprez, D. Ceria-Based Solid Catalysts for Organic Chemistry. *ChemSusChem* **2010,** 3, 654-678.

41. Williams, U. J.; Mahoney, B. D.; Lewis, A. J.; DeGregorio, P. T.; Carroll, P. J.; Schelter, E. J. Single Crystal to Single Crystal Transformation and Hydrogen-Atom Transfer upon Oxidation of a Cerium Coordination Compound. *Inorg. Chem.* **2013,** 52, 4142-4144.

42. Broderick, E. M.; Thuy-Boun, P. S.; Guo, N.; Vogel, C. S.; Sutter, J.; Miller, J. T.; Meyer, K.; Diaconescu, P. L. Synthesis and Characterization of Cerium and Yttrium Alkoxide Complexes Supported by Ferrocene-Based Chelating Ligands. *Inorg. Chem.* **2011,** 50, 2870-2877.

43. Robinson, J. R.; Carroll, P. J.; Walsh, P. J.; Schelter, E. J. The Impact of Ligand Reorganization on Cerium(III) Oxidation Chemistry. *Angew. Chem. Int. Ed.* **2012,** 51, 10159-10163.

44. Palumbo, C. T.; Zivkovic, I.; Scopelliti, R.; Mazzanti, M. Molecular Complex of Tb in the +4 Oxidation State. *J. Am. Chem. Soc.* **2019,** 141, 9827-9831.

45. Gregson, M.; Lu, E.; McMaster, J.; Lewis, W.; Blake, A. J.; Liddle, S. T. A Cerium(IV)–Carbon Multiple Bond. *Angew. Chem. Int. Ed.* **2013,** 52, 13016-13019.

46. Gregson, M.; Lu, E.; Mills, D. P.; Tuna, F.; McInnes, E. J. L.; Hennig, C.; Scheinost, A. C.; McMaster, J.; Lewis, W.; Blake, A. J.; Kerridge, A.; Liddle, S. T. The inverse-trans-influence in tetravalent lanthanide and actinide bis(carbene) complexes. *Nat. Commun.* **2017,** 8, 14137.

47. Damon, P. L.; Liss, C. J.; Lewis, R. A.; Morochnik, S.; Szpunar, D. E.; Telser, J.; Hayton, T. W. Quantifying the Electron Donor and Acceptor Abilities of the Ketimide Ligands in $M(N{=}C^tBu_2)_4$ (M = V, Nb, Ta). *Inorg. Chem.* **2015,** 54, 10081-10095.

48. Lewis, R. A.; George, S. P.; Chapovetsky, A.; Wu, G.; Figueroa, J. S.; Hayton, T. W. Synthesis of a cobalt(iv) ketimide with a squashed tetrahedral geometry. *ChemComm* **2013,** 49, 2888-2890.

49. Lewis, R. A.; Wu, G.; Hayton, T. W. Synthesis and Characterization of an Iron(IV) Ketimide Complex. *J. Am. Chem. Soc.* **2010,** 132, 12814-12816.

50. Lewis, R. A.; Wu, G.; Hayton, T. W. Stabilizing High-Valent Metal Ions with a Ketimide Ligand Set: Synthesis of $Mn(N{=}C^tBu_2)_4$. *Inorg. Chem.* **2011,** 50, 4660-4668.

51. Soriaga, R. A. D.; Nguyen, J. M.; Albright, T. A.; Hoffman, D. M. Diamagnetic Group 6 Tetrakis(di-tert-butylketimido)metal(IV) Complexes. *J. Am. Chem. Soc.* **2010,** 132, 18014-18016.

52. Lewis, R. A.; Smiles, D. E.; Darmon, J. M.; Stieber, S. C. E.; Wu, G.; Hayton, T. W. Reactivity and Mössbauer Spectroscopic Characterization of an Fe(IV) Ketimide Complex and Reinvestigation of an Fe(IV) Norbornyl Complex. *Inorg. Chem.* **2013,** 52, 8218-8227.

53. Graves, C. R.; Vaughn, A. E.; Schelter, E. J.; Scott, B. L.; Thompson, J. D.; Morris, D. E.; Kiplinger, J. L. Probing the Chemistry, Electronic Structure and Redox Energetics in Organometallic Pentavalent Uranium Complexes. *Inorg. Chem.* **2008,** 47, 11879-11891.

54. Kiplinger, J. L.; Morris, D. E.; Scott, B. L.; Burns, C. J. The First f-Element Ketimido Complex: Synthesis and Characterization of $(C_5Me_5)_2U(=NCPh_2)_2$. *Organometallics* **2002,** 21, 3073-3075.

55. Seaman, L. A.; Wu, G.; Edelstein, N.; Lukens, W. W.; Magnani, N.; Hayton, T. W. Probing the 5f Orbital Contribution to the Bonding in a U(V) Ketimide Complex. *J. Am. Chem. Soc.* **2012,** 134, 4931-4940.

56. Damon, P. L.; Wu, G.; Kaltsoyannis, N.; Hayton, T. W. Formation of a Ce(IV) Oxo Complex via Inner Sphere Nitrate Reduction. *J. Am. Chem. Soc.* **2016,** 138, 12743-12746.

57. The observation of two resonances for Li(N=CtBuPh) can be explained by invoking the presence of lithium ketimide clusters with different nuclearities. See: Reed, D.; Barr, D.; Mulvey, R. E.; Snaith, R. High-field lithium-7 nuclear magnetic resonance spectroscopic and cryoscopic relative molecular mass studies on solutions of amido- and imido-lithium compoundset al. J. Chem. Soc., Dalton Trans., 1986, 557-564.

58. Behrsing, T.; Bond, A. M.; Deacon, G. B.; Forsyth, C. M.; Forsyth, M.; Kamble, K. J.; Skelton, B. W.; White, A. H. Cerium acetylacetonates—new aspects, including the lamellar clathrate $[Ce(acac)_4]\cdot 10H_2O$. *Inorg. Chim. Acta* **2003,** 352, 229-237.

59. Walter, M. D.; Fandos, R.; Andersen, R. A. Synthesis and magnetic properties of cerium macrocyclic complexes with tetramethyldibenzotetraaza[14]annulene, $tmtaaH_2$. *New J. Chem.* **2006,** 30, 1065-1070.

60. Eisenstein, J. C.; Pryce, M. H. L. The electronic structure and magnetic properties of uranyl-like ions I. Uranyl and neptunyl. *Proc. R. Soc. Lond. A* **1955,** 229, 20-38.

61. Fowler, P. W.; Steiner, E. Temperature-independent paramagnetism in closed-shell oxanions of first-row transition metals. *J. Chem. Soc., Faraday Trans.* **1993,** 89, 1915-1924.

62. Mullane, K. C.; Hrobárik, P.; Cheisson, T.; Manor, B. C.; Carroll, P. J.; Schelter, E. J. ^{13}C NMR Shifts as an Indicator of U–C Bond Covalency in Uranium(VI) Acetylide Complexes: An Experimental and Computational Study. *Inorg. Chem.* **2019,** 58, 4152-4163.

63. Schneider, D.; Spallek, T.; Maichle-Mossmer, C.; Tornroos, K. W.; Anwander, R. Cerium tetrakis(diisopropylamide) - a useful precursor for cerium(iv) chemistry. *ChemComm* **2014,** 50, 14763-14766.

64. Hitchcock, P. B.; Lappert, M. F.; Protchenko, A. V. Facile formation of a homoleptic Ce(iv) amide via aerobic oxidation. *ChemComm* **2006**, 3546-3548.

65. Crozier, A. R.; Bienfait, A. M.; Maichle-Mössmer, C.; Törnroos, K. W.; Anwander, R. A homoleptic tetravalent cerium silylamide. *ChemComm* **2013,** 49, 87-89.

66. Shannon, R. D. Revised effective ionic radii and systematic studies of interatomic distances in halides and chalcogenides. *Acta Crystallogr. A* **1976,** 32, 751-767.

67. Jantunen, K. C.; Burns, C. J.; Castro-Rodriguez, I.; Da Re, R. E.; Golden, J. T.; Morris, D. E.; Scott, B. L.; Taw, F. L.; Kiplinger, J. L. Thorium(IV) and Uranium(IV) Ketimide Complexes Prepared by Nitrile Insertion into Actinide−Alkyl and −Aryl Bonds. *Organometallics* **2004,** 23, 4682-4692.

68. Tao, J.; Perdew, J. P.; Staroverov, V. N.; Scuseria, G. E. Climbing the Density Functional Ladder: Nonempirical Meta-Generalized Gradient Approximation Designed for Molecules and Solids. *Phys. Rev. Lett.* **2003,** 91, 146401.

69. Cheisson, T.; Kersey, K. D.; Mahieu, N.; McSkimming, A.; Gau, M. R.; Carroll, P. J.; Schelter, E. J. Multiple Bonding in Lanthanides and Actinides: Direct Comparison of Covalency in Thorium(IV)- and Cerium(IV)-Imido Complexes. *J. Am. Chem. Soc.* **2019,** 141, 9185-9190.

70. Duignan, T. J.; Autschbach, J. Impact of the Kohn–Sham Delocalization Error on the 4f Shell Localization and Population in Lanthanide Complexes. *J. Chem. Theory Comput.* **2016,** 12, 3109-3121.

71. Qiao, Y.; Sergentu, D.-C.; Yin, H.; Zabula, A. V.; Cheisson, T.; McSkimming, A.; Manor, B. C.; Carroll, P. J.; Anna, J. M.; Autschbach, J.; Schelter, E. J. Understanding and Controlling the Emission Brightness and Color of Molecular Cerium Luminophores. *J. Am. Chem. Soc.* **2018,** 140, 4588-4595.

72. Assefa, M. K.; Sergentu, D.-C.; Seaman, L. A.; Wu, G.; Autschbach, J.; Hayton, T. W. Synthesis, Characterization, and Electrochemistry of the Homoleptic f Element Ketimide Complexes $[Li]_2[M(N{=}C^tBuPh)_6]$ (M = Ce, Th). *Inorg. Chem.* **2019,** 58, 12654-12661.

73. Robinson, J. R.; Gordon, Z.; Booth, C. H.; Carroll, P. J.; Walsh, P. J.; Schelter, E. J. Tuning Reactivity and Electronic Properties through Ligand Reorganization within a Cerium Heterobimetallic Framework. *J. Am. Chem. Soc.* **2013,** 135, 19016-19024.

74. Willauer, A. R.; Palumbo, C. T.; Fadaei-Tirani, F.; Zivkovic, I.; Douair, I.; Maron, L.; Mazzanti, M. Accessing the +IV Oxidation State in Molecular Complexes of Praseodymium. *J. Am. Chem. Soc.* **2020,** 142, 5538-5542.

75. Rice, N. T.; Popov, I. A.; Russo, D. R.; Bacsa, J.; Batista, E. R.; Yang, P.; Telser, J.; La Pierre, H. S. Design, Isolation, and Spectroscopic Analysis of a Tetravalent Terbium Complex. *J. Am. Chem. Soc.* **2019,** 141, 13222-13233.

76. Willauer, A. R.; Palumbo, C. T.; Scopelliti, R.; Zivkovic, I.; Douair, I.; Maron, L.; Mazzanti, M. Stabilization of the Oxidation State +IV in Siloxide-Supported Terbium Compounds. *Angew. Chem. Int. Ed.* **2020,** 59, 3549-3553.

77. Niemeyer, M. 1,2-Dimethoxyethan- und Tetrahydrofuran-Komplexe der Seltenerdmetallnitrate. *Z. Anorg. Allg. Chem.* **2006,** 632, 1449-1456.

78. Cantat, T.; Scott, B. L.; Kiplinger, J. L. Convenient access to the anhydrous thorium tetrachloride complexes $ThCl_4(DME)_2$, $ThCl_4(1,4\text{-dioxane})_2$ and $ThCl_4(THF)_{3.5}$ using commercially available and inexpensive starting materials. *ChemComm* **2010,** 46, 919-921.

79. Armstrong, D. R.; Barr, D.; Snaith, R.; Clegg, W.; Mulvey, R. E.; Wade, K.; Reed, D. The ring-stacking principle in organolithium chemistry: its development through the isolation and crystal structures of hexameric iminolithium clusters $(RR'C{=}NLi)_6$(R′= Ph, R = Bu^t or Me_2N; R = R′= Me_2N or Bu^t). *J. Chem. Soc., Dalton Trans.* **1987**, 1071-1081.

80. Harris, R. K.; Becker, E. D.; Cabral De Menezes, S. M.; Goodfellow, R.; Granger, P. NMR Nomenclature. Nuclear Spin Properties and Conventions for Chemical Shifts. *Pure Appl. Chem.* **2001,** 73, 1795-1818.

81. Harris, R. K.; Becker, E. D.; Cabral De Menezes, S. M.; Granger, P.; Hoffman, R. E.; Zilm, K. W. Further Conventions for NMR Shielding and Chemical Shifts. *Pure Appl. Chem.* **2008,** 80, 59-84.

82. Bain, G. A.; Berry, J. F. Diamagnetic Corrections and Pascal's Constants. *J. Chem. Educ.* **2008,** 85, 532.

83. Neese, F. The ORCA program system. *Wiley Interdiscip. Rev. Comput. Mol. Sci.* **2012,** 2, 73-78.

84. Neese, F. Software update: the ORCA program system, version 4.0. *Wiley Interdiscip. Rev. Comput. Mol. Sci.* **2018,** 8, e1327.

85. Bergner, A.; Dolg, M.; Küchle, W.; Stoll, H.; Preuß, H. Ab initio energy-adjusted pseudopotentials for elements of groups 13–17. *Mol. Phys.* **1993,** 80, 1431-1441.

86. Dolg, M.; Stoll, H.; Preuss, H. Energy-adjusted ab initio pseudopotentials for the rare earth elements. *J. Chem. Phys.* **1989,** 90, 1730-1734.

87. Cao, X.; Dolg, M.; Stoll, H. Valence basis sets for relativistic energy-consistent small-core actinide pseudopotentials. *J. Chem. Phys.* **2003,** 118, 487-496.

88. Küchle, W.; Dolg, M.; Stoll, H.; Preuss, H. Energy-adjusted pseudopotentials for the actinides. Parameter sets and test calculations for thorium and thorium monoxide. *J. Chem. Phys.* **1994,** 100, 7535-7542.

89. Weigend, F.; Ahlrichs, R. Balanced basis sets of split valence, triple zeta valence and quadruple zeta valence quality for H to Rn: Design and assessment of accuracy. *Phys. Chem. Chem. Phys.* **2005,** 7, 3297-3305.

90. Schuchardt, K. L.; Didier, B. T.; Elsethagen, T.; Sun, L.; Gurumoorthi, V.; Chase, J.; Li, J.; Windus, T. L. Basis Set Exchange: A Community Database for Computational Sciences. *J. Chem. Inf. Model.* **2007,** 47, 1045-1052.

91. Stoychev, G. L.; Auer, A. A.; Neese, F. Automatic Generation of Auxiliary Basis Sets. *J. Chem. Theory Comput.* **2017,** 13, 554-562.

92. E.J. Baerends, T. Z., A.J. Atkins, J. Autschbach, O. Baseggio, D. Bashford, A. Bérces, F.M. Bickelhaupt, C. Bo, P.M. Boerrigter, L. Cavallo, C. Daul, D.P. Chong, D.V. Chulhai, L. Deng, R.M. Dickson, J.M. Dieterich, D.E. Ellis, M. van Faassen, L. Fan, T.H. Fischer, A. Förster, C. Fonseca Guerra, M. Franchini, A. Ghysels, A. Giammona, S.J.A. van Gisbergen, A. Goez, A.W. Götz, J.A. Groeneveld, O.V. Gritsenko, M. Grüning, S. Gusarov, F.E. Harris, P. van den Hoek, Z. Hu, C.R. Jacob, H. Jacobsen, L. Jensen, L. Joubert, J.W. Kaminski, G. van Kessel, C. König, F. Kootstra, A. Kovalenko, M.V. Krykunov, E. van Lenthe, D.A. McCormack, A. Michalak, M. Mitoraj, S.M. Morton, J. Neugebauer, V.P. Nicu, L. Noodleman, V.P. Osinga, S. Patchkovskii, M. Pavanello, C.A. Peeples, P.H.T. Philipsen, D. Post, C.C. Pye, H. Ramanantoanina, P. Ramos, W. Ravenek, J.I. Rodríguez, P. Ros, R. Rüger, P.R.T. Schipper, D. Schlüns, H. van Schoot, G. Schreckenbach, J.S. Seldenthuis, M. Seth, J.G. Snijders, M. Solà, M. Stener, M. Swart, D. Swerhone, V. Tognetti, G. te Velde, P. Vernooijs, L. Versluis, L. Visscher, O. Visser, F. Wang, T.A. Wesolowski, E.M. van Wezenbeek, G. Wiesenekker, S.K. Wolff, T.K. Woo, A.L. Yakovlev *Amsterdam Density Functional*, 2017; SCM, Theoretical Chemistry, Vrije Universiteit Amsterdam, The Netherlands, 2017.

93. Lenthe, E. v.; Baerends, E. J.; Snijders, J. G. Relativistic regular two-component Hamiltonians. *J. Chem. Phys.* **1993,** 99, 4597-4610.

94. Glendening, E. D.; Landis, C. R.; Weinhold, F. NBO 6.0: Natural bond orbital analysis program. *J. Comput. Chem.* **2013,** 34, 1429-1437.

95. *SMART Apex II*, Version 2.1; Bruker AXS Inc.: Madison, WI, 2005.

96. *SAINT Software User's Guide*, Version 7.34a; Bruker AXS Inc.: Madison, WI, 2005.

97. Sheldrick, G. M. *SADABS*, University of Gottingen, Germany: 2005.

98. *SHELXTL PC*, Version 6.12; Bruker AXS Inc.: Madison, WI, 2005.

Chapter 4. Synthesis, Characterization, and Redox Chemistry of the Family of Lanthanide Cyclam Complexes $[Li]_x[M(1,8\text{-DMC})_2]$ (1,8-DMC = 1,8-dimethyl-1,4,8,11-tetraazacyclotetradecane) (M = Ce, x = 0, 1; M = Pr, x=1)

4.1 Introduction

Despite recent advances in the past decade, the macrocyclic chemistry of the lanthanides is arguably an area of research still at its infancy. This chemistry is usually undertaken in aqueous systems, which has presented interesting opportunities to explore the applications of lanthanide chelates as contrasting agents for immunotherapy,[1–7] paramagnetic metal tags for biomolecular structure analysis,[8–12] and PARASHIFT probes for magnetic resonance imaging,[13–16] among others. However, the non-aqueous chemistry of these materials remains relatively unexplored. This chemistry is especially poised to expand our limited understanding of the fundamental bonding and redox chemistry of lanthanides, and thus could pave way for new applications in nuclear waste treatment and redox catalysis.

Particularly relevant for these applications is the expansion of the very limited oxidation states available to these metals, as nearly all lanthanides exist exclusively in the trivalent oxidation state in solution. The main exception is cerium(IV), which has a xenon noble gas electronic configuration, although three examples of terbium(IV)[17–19] and one example of praseodymium(IV)[20] are also known to be stable in solution to date (Chapter 1). In this regard, ligation of polydentate macrocyclic ligands to lanthanide ions could potentially provide access to these rare tetravalent oxidation states. For instance, the macrocyclic and chelate effects of such types of ligands could be employed to simultaneously minimize the reorganization energy associated with the oxidation of trivalent lanthanides, and also bolster the entropic favorability of such oxidations.[21–23] For example, Raymond and coworkers have previously utilized an octadentate terephthalamide macrocyclic ligand comprising hard catecholate donors for the extreme stabilization of tetravalent cerium relative to the trivalent congener, with a corresponding stability constant amongst the highest recorded for Ce(IV) ($\log\beta_{110} = 61(2)$).[21]

Cyclic voltammetry studies have also shown promising results that support this hypothesis. For example, the double-decker Ce(IV) complexes $Ce(OEP)_2$ (OEP = octaethylporphyrin)[24] and $Ce(omtaa)_2$ (omtaa = dibenzooctamethyltetraazaannulene)[25] were reported to exhibit very low Ce(IV/III) reduction potentials in their CV traces, indicating strong stabilization of the +4 state in the cerium. Presumably, this stabilization has some contribution stemming from the macrocyclic and chelate effects of OEP and omtaa, which could be used to stabilize even more oxidizing ions such as Tb(IV) and Pr(IV).

Scheme 4.1. Synthetic strategy for preparation of Ln(IV) complexes

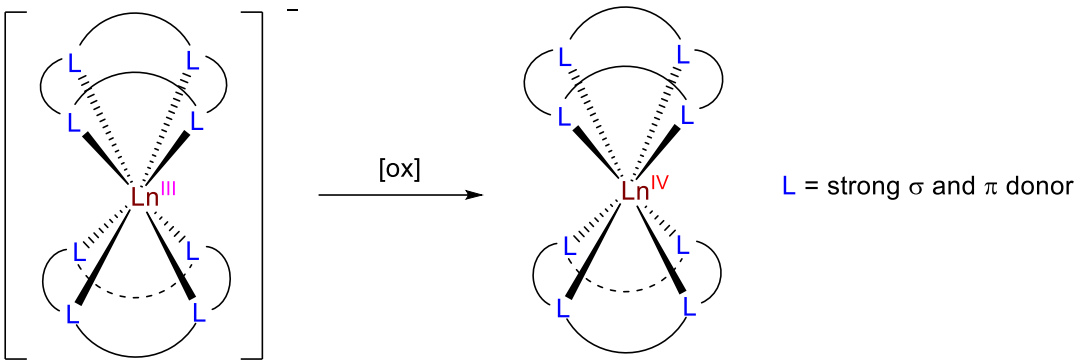

One macrocyclic ligand that could be used for this purpose is 1,4,8,11-tetraazacyclotetradecane (cyclam). The protio and methylated derivatives of this macrocycle have previously been utilized to (electro)chemically generate uncommon, high valent metal ions, such as Fe(VI),[26] Ag(III),[27] Cu(III)[28] and Ni(III).[29] Thus, I describe herein my attempts to investigate the viability of synthesizing a molecular Pr(IV) complex by oxidation of a suitable Pr(III) cyclam precursor. This investigation will be informed by analogous model studies using cerium. Generally, maximizing the coordination number at the metal center and ligation to strong σ and π donors are expected to lower the normally high oxidation potential of Pr(III) (Scheme 4.1). Utilization of anionic Pr(III) "ate" precursors should also facilitate

oxidation of the electron rich metal center to Pr(IV). Therefore, I sought to utilize the dianionic derivative of the cyclam ligand, {1,8-dimethyl-1,4,8,11-tetraazacyclotetradecane}$^{2-}$ (1,8-DMC), for the preparation of a Pr(III) "ate" bis-cyclam complex, which will then be treated with various 1e$^-$ oxidants. Complemented with benchmark studies using cerium, this chapter examines the suitability of the cyclam ligand for the stabilization of the +4 state in praseodymium.

4.2 Results and Discussion

4.2.1 Synthesis, Characterization and Electrochemistry of [Li][Ce(1,8-DMC)$_2$] (4.1)

Reaction of 1,8-dimethyl-1,4,8,11-tetraazacyclotetradecane, H_2(1,8-DMC), with 2 equiv of nBuLi in Et_2O/hexanes affords [Li(Et_2O)]$_2$[1,8-DMC] as pale yellow plates in 71% yield after workup. The ^{1}H NMR spectrum of [Li(Et_2O)]$_2$[1,8-DMC] in THF-d_8 exhibits a sharp singlet at 2.10 ppm integrating to six protons and ten multiplets between 1.54 and 3.22 ppm each integrating to two protons, that are assignable to the methyl and diastereotopic methylene environments of the cyclam ligand, respectively. This spectrum also exhibits a triplet at 1.11 ppm and a quartet at 3.38 ppm that are attributable to the two coordinated Et_2O solvent molecules. Finally, the ^{7}Li{^{1}H} spectrum of [Li(Et_2O)]$_2$[1,8-DMC] in THF-d_8 features a single resonance at -0.56 ppm.

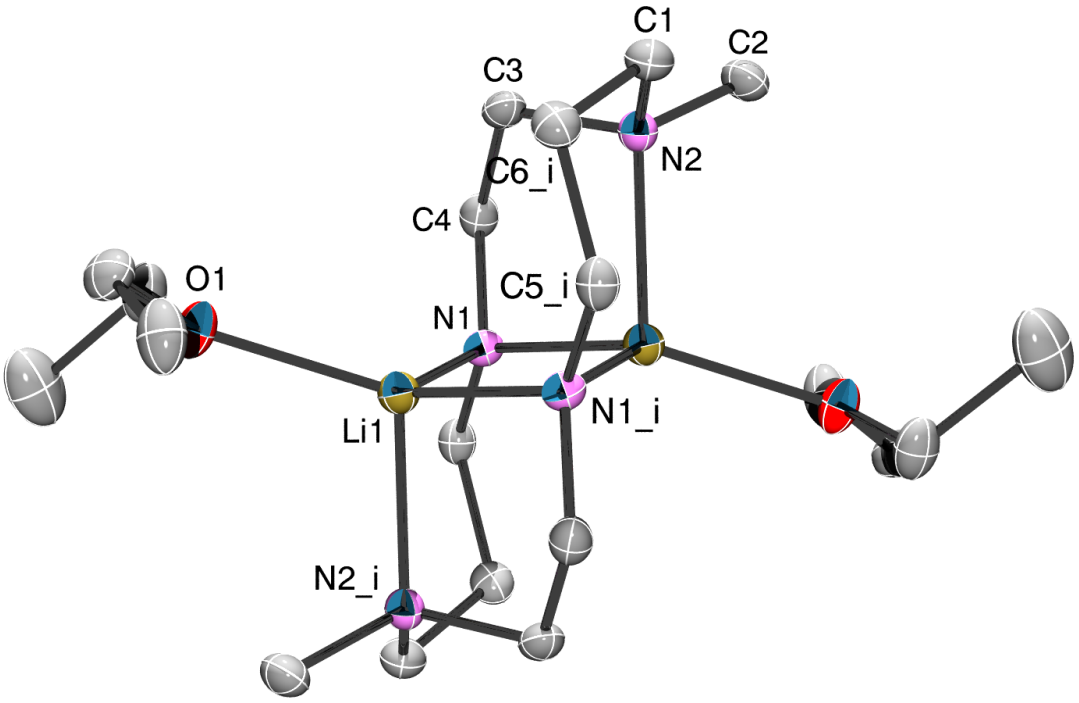

Figure 4.1. Solid-state molecular structure of $[Li(Et_2O)]_2$[1,8-DMC] shown with 50% probability ellipsoids. All hydrogen atoms have been omitted for clarity. Selected bond lengths (Å): Li1-N1 = 1.990(3), Li1-N2_i = 2.054(3), Li1-N1_i = 1.997(3), Li1-O1 = 2.004(3), N1-C4 = 1.438(2), C4-C3 = 1.522(2), C3-N2 = 1.478(2), N2-C2 = 1.461(2), N2-C1 = 1.472(2), C1-C6_i = 1.520(2), C6_i-C5_i = 1.522(2), C5_i-N1_i = 1.440(2).

$[Li(Et_2O)]_2$[1,8-DMC] crystallizes in the monoclinic $P2_1/n$ space group with half of the molecule in the asymmetric unit (Figure 4.1). The remaining half is symmetry related through a center of inversion. In the solid state, this compound exhibits a distorted cyclam dianion supporting two Li cations that each bind to both of its amide nitrogen atoms and one of its amine nitrogen atoms. Each Li cation also coordinates to an oxygen atom of an Et_2O molecule, resulting in an overall 4-coordinate geometry, The Li-N (1.990(3) and 2.054(3) Å) and Li-O (2.004(3) Å) distances are similar to previously reported Li-N[30–33] and Li-O(Et_2O)[34–36] dative interactions.

Reaction of anhydrous $CeCl_3$ with 2 equiv of $[Li(Et_2O)]_2$[1,8-DMC] (1,8-DMC = 1,8-dimethyl-1,4,8,11-tetraazacyclotetradecane) in THF at 65 °C for 2 d affords [Li][Ce(1,8-DMC)$_2$] (**4.1**) as yellow blocks in 75% yield, after crystallization from a concentrated Et_2O solution (eq 4.1). Complex **4.1** is soluble and stable in benzene, toluene, Et_2O and THF at room temperature, but decomposes in the presence of MeCN and CH_2Cl_2, forming H_2(1,8-DMC) as the only identifiable decomposition product. Its ^{1}H NMR spectrum in THF-d_8 exhibits 20 broad resonances between 64.13 and -60.41 ppm, assignable to the diastereotopic CH_2 protons on the cyclam ring (Figure 4.2). This spectrum also features two sharper resonances at 12.34 and -17.71 ppm, attributable to the two distinct methyl environments of the cyclam amino groups in C_2 symmetry.

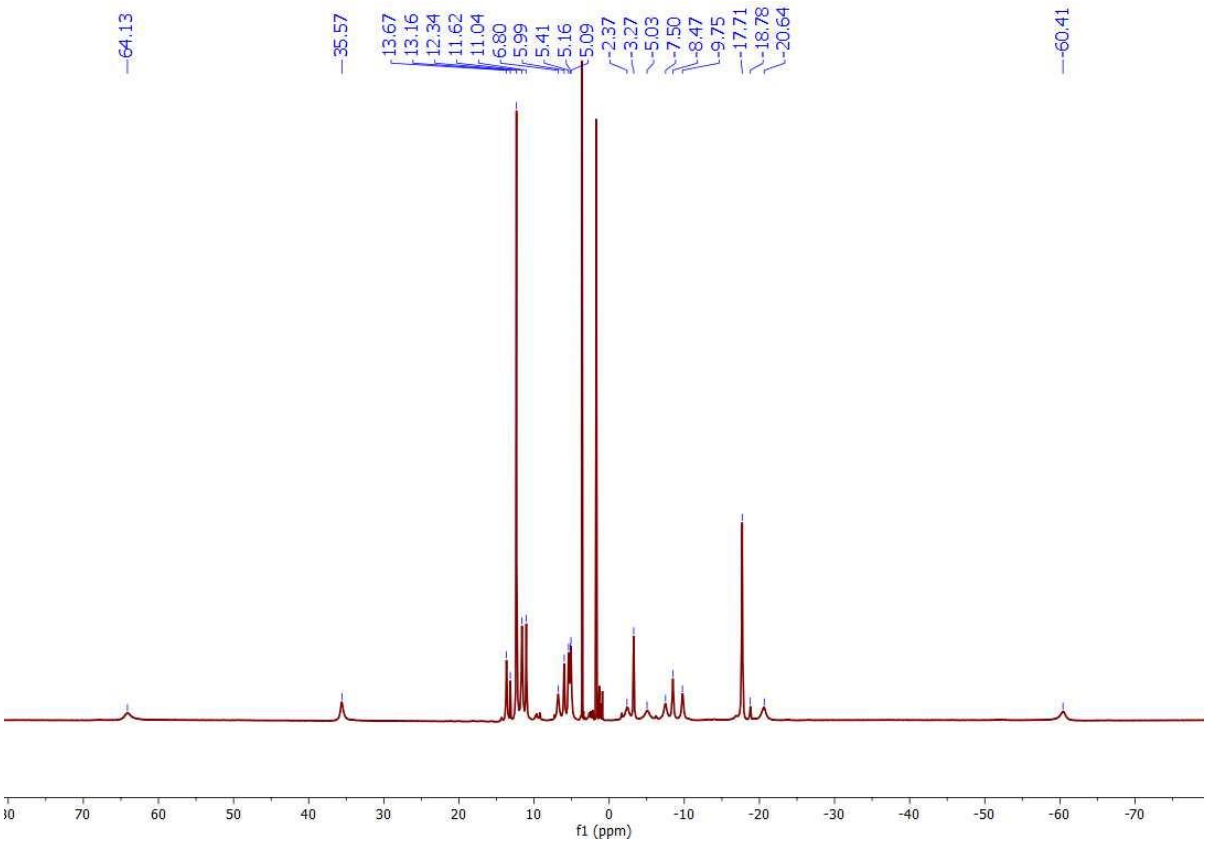

Figure 4.2. ^{1}H NMR spectrum of **4.1** in THF-d_8.

The UV-vis spectrum of **4.1** in THF reveals a well-defined feature at 464 nm (ε = 330 $M^{-1}\cdot cm^{-1}$), flanked by two broad absorptions at 365 nm (ε = 210 $M^{-1}\cdot cm^{-1}$) and 565 nm (ε = 95 $M^{-1}\cdot cm^{-1}$) (Figure 4.3). These values are comparable to those reported for the homoleptic Ce(III) amide [$Ce(N(SiMe_3)_2)_3$] (341 and 413 nm)[37] and the related $[Ce(DOTA)]^-$ (DOTA = 1,4,7,10-tetraazacyclododecane-N,N′,N″,N‴-tetraacetic acid) (317 nm).[38] The NIR spectrum of **4.1** in toluene also exhibits seven well-defined features between 1148 and 2024 nm (ε = 16 – 70 $M^{-1}\cdot cm^{-1}$) that are assignable to f-f transitions.

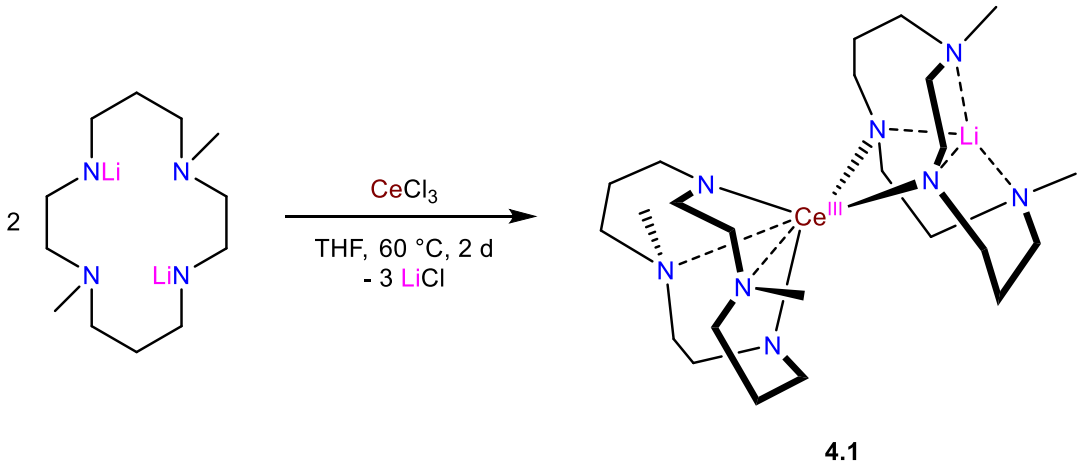

(4.1)

4.1

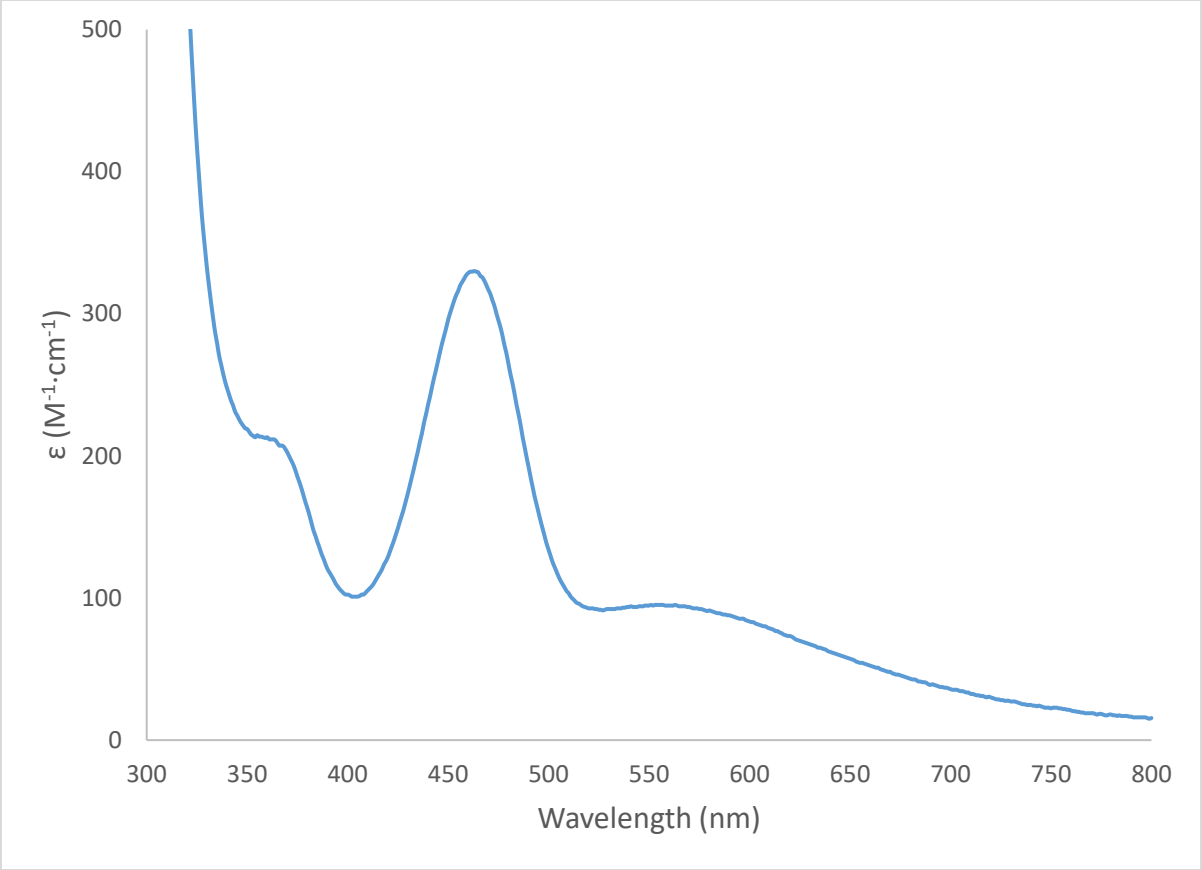

Figure 4.3. UV-Vis spectrum of **4.1** in THF (2.06 mM).

Crystals of **4.1** suitable for X-ray diffraction analysis were grown from a concentrated toluene solution stored at -25 °C for 24 h. Complex **4.1** crystallizes in the tetragonal $P4_3$ space group as the toluene solvate, **4.1**·C_7H_8 (Figure 4.4). Its solid-state molecular structure reveals a hexa-coordinate Ce center ligated by one κ^4 and one κ^2 cyclam macrocycle, resulting in a distorted trigonal prismatic geometry around the Ce center (CSM = 5.714).[39,40] The κ^2 macrocycle also supports an outer sphere Li cation within its binding pocket. This cation binds to both amino and both amido nitrogen atoms, generating a 4-coordinate geometry. Its presence in the structure confirms the trivalent oxidation state of the Ce center. The Ce-N(amide) bond distances (2.334(16) – 2.504(14) Å) are similar those reported for the monoanionic Ce(III) amide $[Na(THF)_4(Et_2O)][Ce(N(SiMe_3)_2)_4]$ (2.468(5) – 2.472(5) Å),[41] and

the structurally similar sandwich complexes [Ce(Htmtaa)(tmtaa)] (2.520(16) – 2.594(19) Å),[42] [Ce(Homtaa)(omtaa)] (2.5260(16) – 2.5690(16) Å)[25], [Li(THF)][Ce(tmtaa)$_2$] (2.474(5) and 2.484(4) Å),[30] and [Ce(HNTClPP)(TBPP)] (H_2NTClPP = 5,10,15,20-tetrakis[(4-*tert*-butyl)phenyl]porphyrin, H_2TBPP = 5,10,15,20-tetrakis(4-chlorophenyl)porphyrin) (av. 2.495 Å).[43] In contrast, the Ce-N(amine) distances (2.847(15) and 2.857(15) Å) are slightly longer than those reported for [Li(THF)][Ce(tmtaa)$_2$] (2.643(5) and 2.680(5) Å),[30] but comparable to those reported for the closely related Ce(III) DOTA complex Na[Ce(DOTA)(H_2O)]·$NaHCO_3$·7H_2O (2.70(1) – 2.77(1) Å),[44] and the Ce (III) hexaazacyclooctadecane complex [CeL^1][NO_3]$_3$·7H_2O (L^1 = Py$_2$[18]aneN$_6$) (2.743(8) and 2.799(8) Å).[45] Finally, the Li-N distances (1.942(16) – 2.021(18) Å) in **4.1** are comparable to previously reported Li-N dative interactions.[30–33]

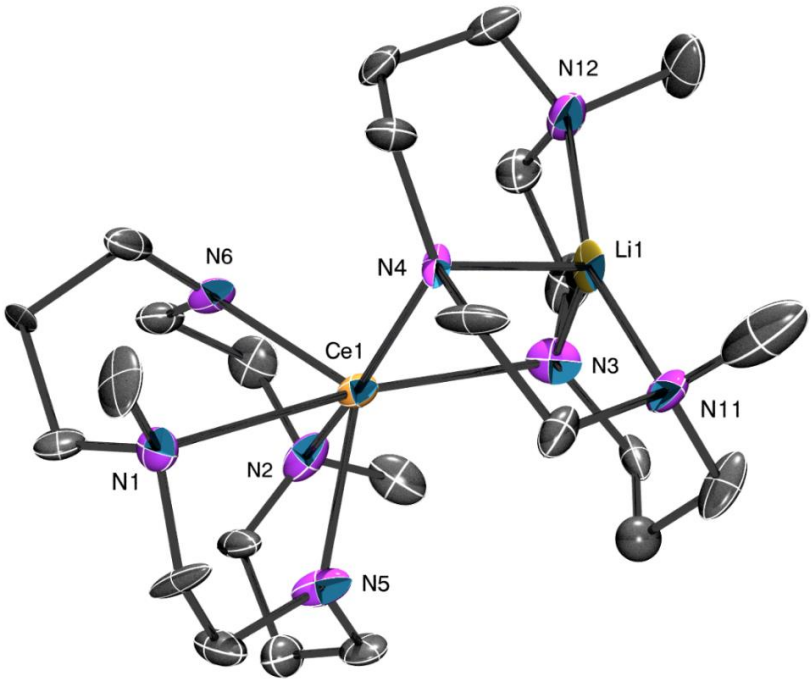

Figure 4.4. Solid-state molecular structure of **4.1**·C_7H_8 shown with 50% probability ellipsoids. All hydrogen atoms and a toluene solvate have been omitted for clarity. Selected bond lengths

(Å): Ce1-N1 = 2.847(15), Ce1-N2 = 2.857(15), Ce1-N3 = 2.504(14), Ce1-N4 = 2.503(14), Ce1-N5 = 2.334(16), Ce1-N6 = 2.347(16), Li1-N3 = 1.942(16), Li1-N4 = 1.943(16), Li1-N11 = 2.019(18), Li1-N12 = 2.021(18).

To investigate the stability of Ce^{4+} state within the cyclam ligand environment, I probed the electrochemical properties of **4.1** by cyclic voltammetry. The cyclic voltammogram of **4.1** in THF at 200 mV/s scan rate exhibits a reversible Ce(III)/Ce(IV) oxidation feature at -1.32 V vs Fc/Fc^+ (Figure 4.5). This value is amongst the lowest reported for a reversible Ce(III)/Ce(IV) redox processes measured by cyclic voltammetry. For comparison, Schelter and co-workers have previously reported a reversible metal-based reduction feature for $[Ce(omtaa)_2]$ at -1.7 V vs Fc/Fc^+.[25] The structurally related sandwich complex $Ce(OEP)_2$ also exhibits a low, reversible reduction feature at -1.06 V vs Fc/Fc^+.[24] Similarly, the Ce(IV) carbene complex $[Ce(BIPM^{TMS})_2]$ exhibits a quasi-reversible reduction feature at -1.63 V vs Fc/Fc^+.[46] More recently, Mazzanti and co-workers reported a highly reducing reduction potential for the electron rich Ce(IV) silyloxide $[Ce(O(Si(O^tBu)_3)_4]$ at -1.72 V vs Fc/Fc^+.[17] A similarly reducing reduction potential was also observed for the Ce(IV) ketimide $[Li]_2[Ce(N{=}C^tBuPh)_6]$ at -2.16 V vs Fc/Fc^+ (Chapter 3). Importantly, the highly cathodic value of the redox feature for **4.1**, along with its electrochemical reversibility, indicate strong stabilization of the +4 state of cerium within the cyclam ligand environment. In addition, these observations suggest that a neutral homoleptic Ce(IV) cyclam complex should be easily isolable, as is demonstrated below.

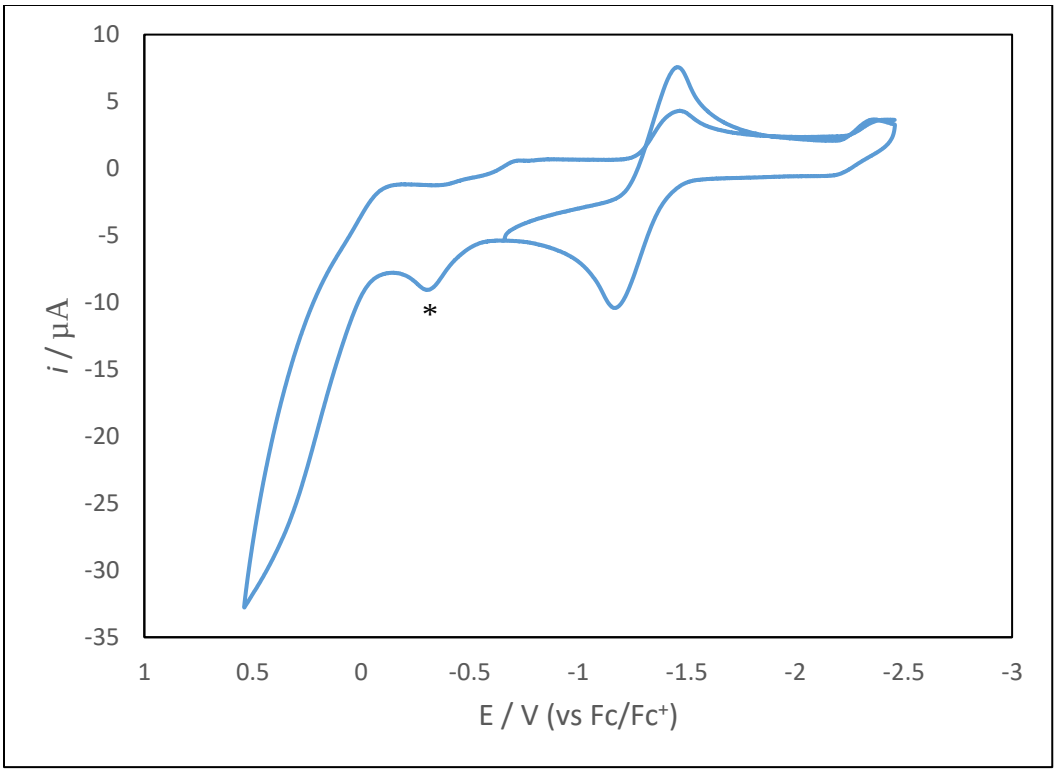

Figure 4.5. Cyclic voltammogram of **4.1** at 200 mV/sec, measured in THF using $[NBu_4][PF_6]$ as the supporting electrolyte. * indicates presences of a minor unidentified impurity.

4.2.2 Synthesis and Characterization of $[Ce(1,8\text{-}DMC)_2]$ (4.2)

On the basis of the electrochemical data collected for **4.1**, I_2 was chosen as a suitable oxidant for its $1e^-$ oxidation. Thus, reaction of **4.1** with 0.5 equiv of I_2 in THF results in formation of a deep purple solution, from which $[Ce(1,8\text{-}DMC)_2]$ (**4.2**) can be isolated as purple plates in 34% yield (eq 4.2). Complex **4.2** is readily soluble in Et_2O and THF, but only sparingly soluble in hexanes. Its ^1H NMR spectrum in C_6D_6 exhibits a sharp resonance at 2.39 ppm integrating to twelve protons that is assignable to the four equivalent methyl environments of the cyclam amino groups (Figure 4.6). This spectrum also features ten resonances between 1.44 and 4.99 ppm, each integrating to four protons, that are assignable to the diastereotopic CH_2

environments on the cyclam backbone. As expected, these resonances exhibit a complex splitting pattern, which necessitated the use of COSY NMR experiments to make specific assignments. Additionally, the number of signals in this spectrum are consistent with the S_4 symmetry observed for **4.2** in the solid state (see below). The $^{13}C\{^1H\}$ NMR spectrum of **4.2** in C_6D_6 exhibits five resonances at 44.28, 44.57, 49.71, 54.21, 62.93 ppm assignable to the CH_2 environments, and a resonance at 25.48 ppm assignable to the methyl environment of the cyclam ligand. The number of signals in this spectrum are also consistent with an S_4 symmetry for **4.2** in solution.

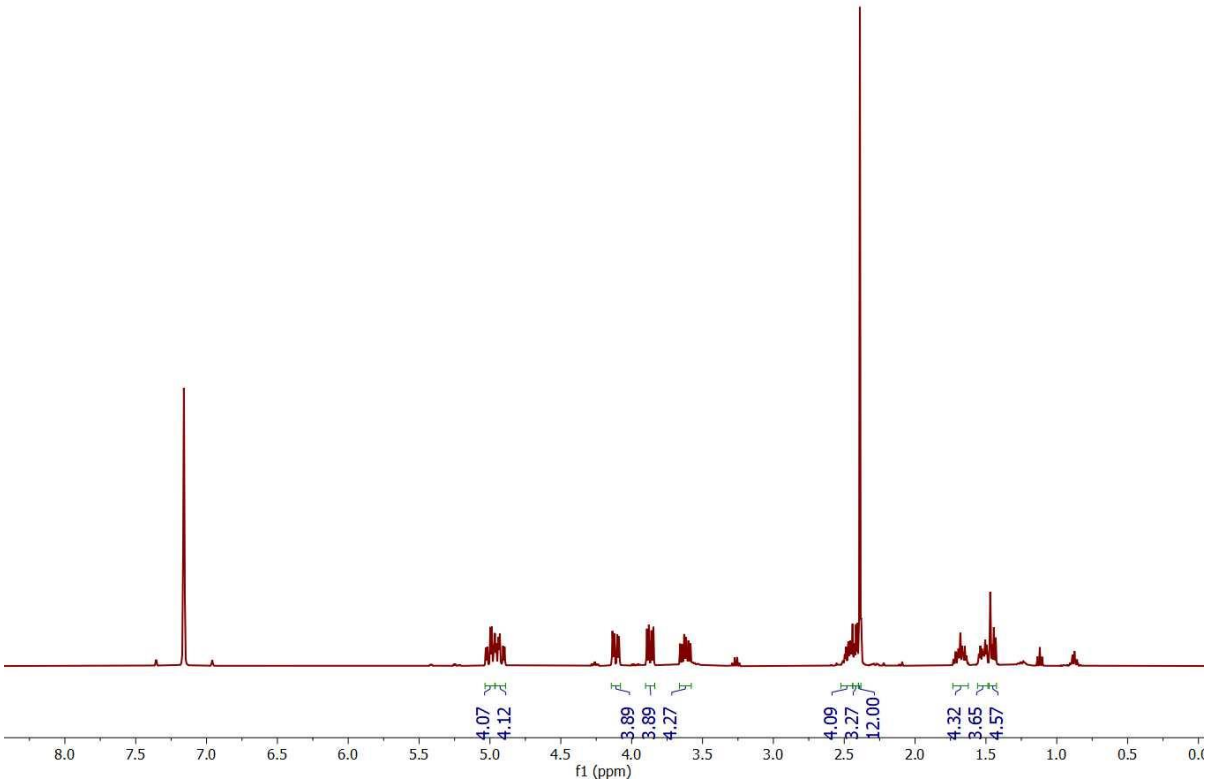

Figure 4.6. ^1H NMR spectrum of **4.2** in C_6D_6.

The UV-Vis spectrum of **4.2** in THF exhibits a broad, intense LMCT absorption at 561 nm (ε = 5914 $M^{-1}\cdot cm^{-1}$) (Figure 4.7). This value is slightly red-shifted when compared against

those reported for other deeply colored, homoleptic Ce(IV) complexes such as $Ce(trop)_4$ (450 nm, $\varepsilon = 2000\ M^{-1}\cdot cm^{-1}$),[47] $Ce(\eta^8\text{-}Pn^*)_2$ (530 nm, $\varepsilon = 17000\ M^{-1}\cdot cm^{-1}$),[48] $Ce(cot)_2$ (469 nm, $\varepsilon = 8000\ M^{-1}\cdot cm^{-1}$)[48] and $Ce(acac)_4$ (~400 nm, ε = ~3000 $M^{-1}\cdot cm^{-1}$).[49] Finally, **4.2** features moderate thermal stability according to ^1H NMR spectroscopy; monitoring of a C_6D_6 solution of **4.2** stored at room temperature for 2 d reveals ~20% decomposition. The sole decomposition product to be identified was H_2(1,8-DMC) on the basis of its diagnostic methyl resonance observed at 2.09 ppm.

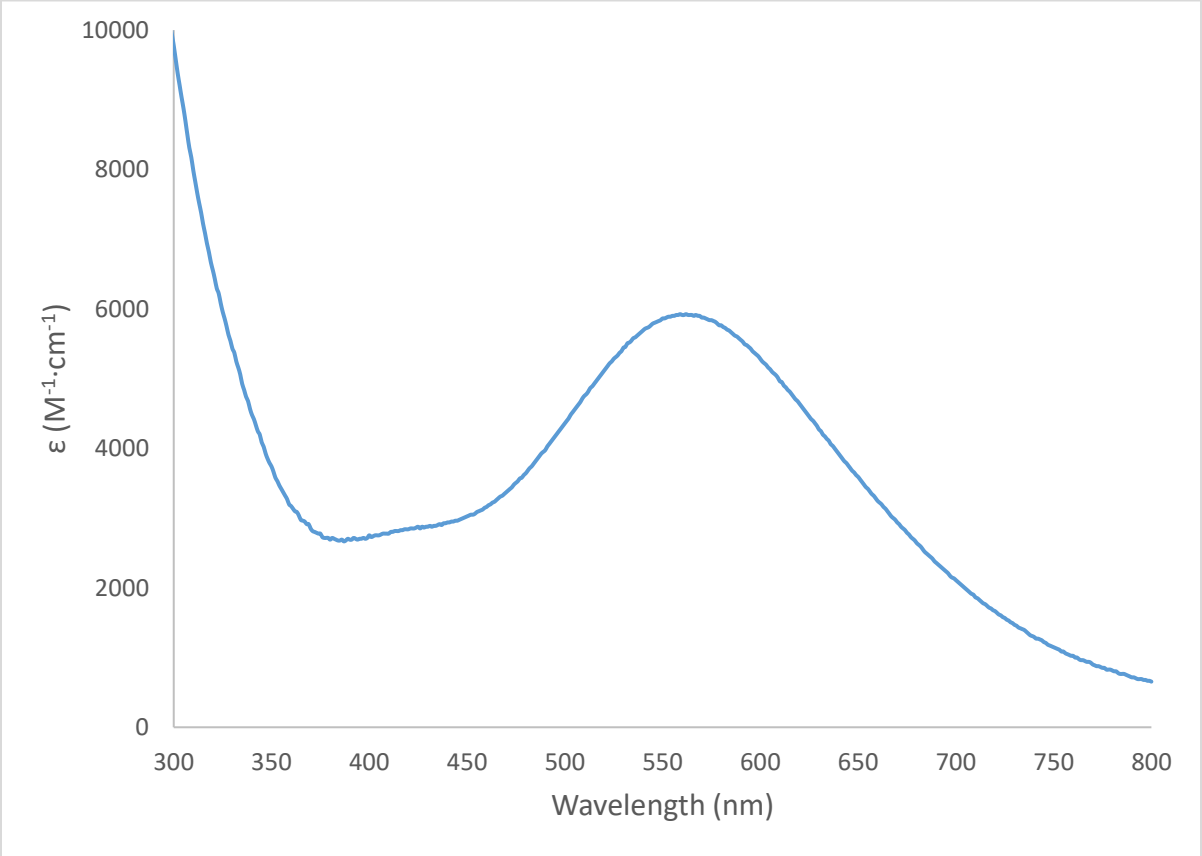

Figure 4.7. UV-Vis spectrum of **4.2** in THF (0.081 mM).

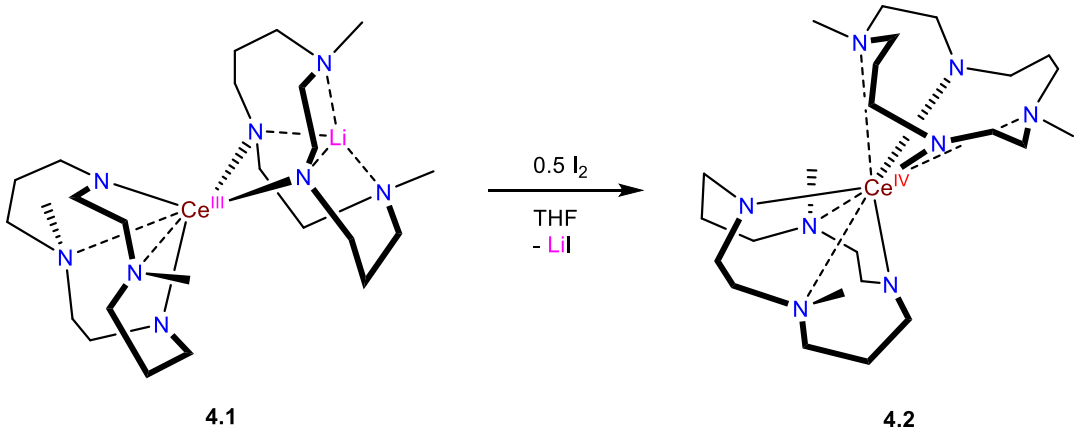

4.1 4.2 (4.2)

Complex **4.2** crystallizes in the triclinic *P*-1 space group with two molecules in the asymmetric unit (Figure 4.8). Due to the similar metrical parameters, the structure of only one independent molecule will be analyzed herein. The solid-state molecular structure of **4.2** reveals an eight-coordinate cerium center ligated by two κ^4 cyclam macrocycles in an overall triakis tetrahedron geometry (CSM = 1.100).[39,40] The cyclam macrocycles are rotated by 90° with respect to each other, resulting in an overall S_4 symmetry for **4.2** in the solid state. The Ce-N(amide) distances (2.280(7) – 2.295(7) Å) in **4.2** are shorter than those observed for **4.1** (2.334(16) – 2.504(14) Å) and $Ce(OEP)_2$ (av. 2.475(1) Å),[50] but similar to those reported for other homoleptic Ce(IV) amides such as $[Ce(N^iPr_2)_4]$ (2.225(1) and 2.223(1) Å),[51] $[Ce(NCy_2)_4]$ (2.238(5) – 2.247(6) Å),[52] and $[Ce(N(SiHMe_2)_2)_4]$ (2.2378(11) – 2.2574(11) Å).[53] Additionally, these distances are shorter than those reported for $[Ce(tmtaa)_2]$ (2.427(4) – 2.462(3) Å)[42] and $[Ce(omtaa)_2]$ (2.4367(15) – 2.4600(16) Å),[25] likely due to the delocalization within the β-diketiminate subunit of the tetraaza annulides in the latter complexes. Finally, the Ce-N(amine) distances (2.978(7) – 3.024(7) Å) in **4.2** are surprisingly longer than those in **4.1** (2.847(15) and 2.857(15) Å) and the Ce(IV) bipyridine complex $[Ce(bpdc)_2]\cdot H_2O$ (H_2bpdc = 2,2'-bipyridine-6,6'-dicarboxylic acid) (2.530(4) – 2.541(4) Å),[54] suggesting that the stronger

Ce-amide interactions in **4.2** are somewhat offset by weaker Ce-amine interactions, which may be due to the mismatch between the hard Ce(IV) ion and the soft amine donor.

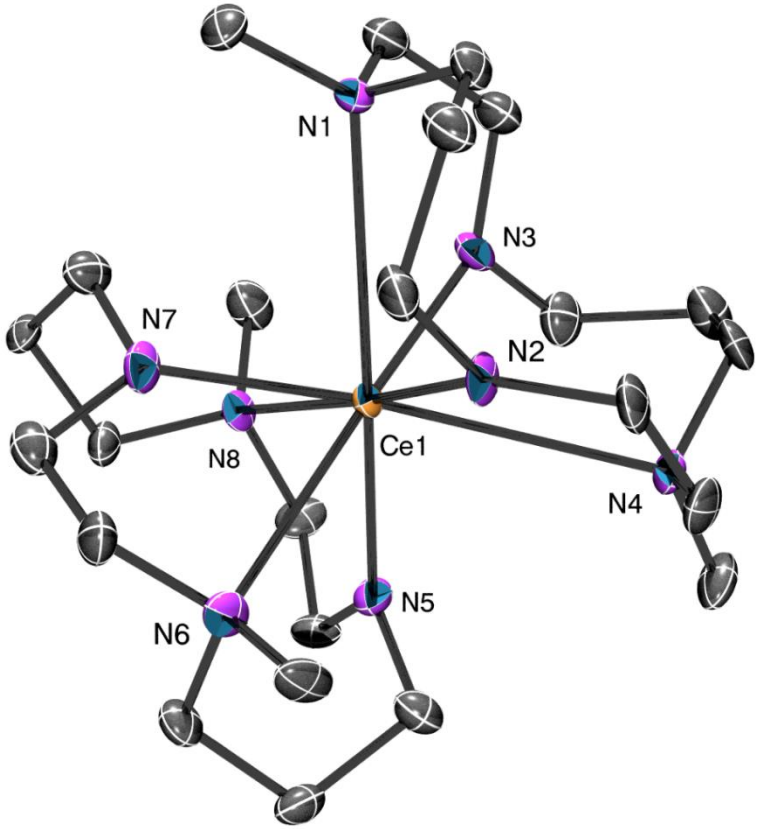

Figure 4.8. Solid-state molecular structure of **4.2** shown with 50% probability ellipsoids. All hydrogen atoms have been omitted for clarity. Selected bond lengths (Å): Ce1-N1 = 2.978(7), Ce1-N2 = 2.280(7), Ce1-N3 = 2.289(6), Ce1-N4 = 3.024(7), Ce1-N5 = 2.293(7), Ce1-N7 = 2.295(7), Ce1-N8 = 3.005(8).

4.2.3 Synthesis, Characterization and Electrochemistry of [Li][Pr(1,8-DMC)$_2$] (4.3)

Drawing inspiration from my cerium results, I sought to replicate the synthetic route for the preparation of a homoleptic Pr(IV) bis-cyclam complex. Thus, reaction of anhydrous $PrCl_3$ with 2 equiv of [Li(Et_2O)]$_2$[1,8-DMC] in THF at 65 °C for 2 d affords a pale blue solution

from which [Li][Pr(1,8-DMC)$_2$] (**4.3**) can be isolated as pale blue blocks in 63% yield (eq. 4.3). Complex **4.3** exhibits similar stability and solubility in organic solvents as **4.1**. Its ^{1}H NMR spectrum in THF-d_8 exhibits 20 broad resonances between 89.20 and -65.82 ppm, assignable to the diastereotopic CH_2 protons on the cyclam ring, as well as two resonances at 16.66 and -18.75 ppm, attributable to the two distinct methyl environments of the cyclam amino groups. As in **4.1**, the number of signals in this spectrum are consistent with C_2 symmetry for **4.3** in solution. Lastly, the UV-vis spectrum of **4.3** does not exhibit any obvious features, but its NIR spectrum in toluene reveals seven distinct f-f transitions between 1148 and 2022 nm with extinction coefficients ranging from 17 to 60 $M^{-1}\cdot cm^{-1}$.

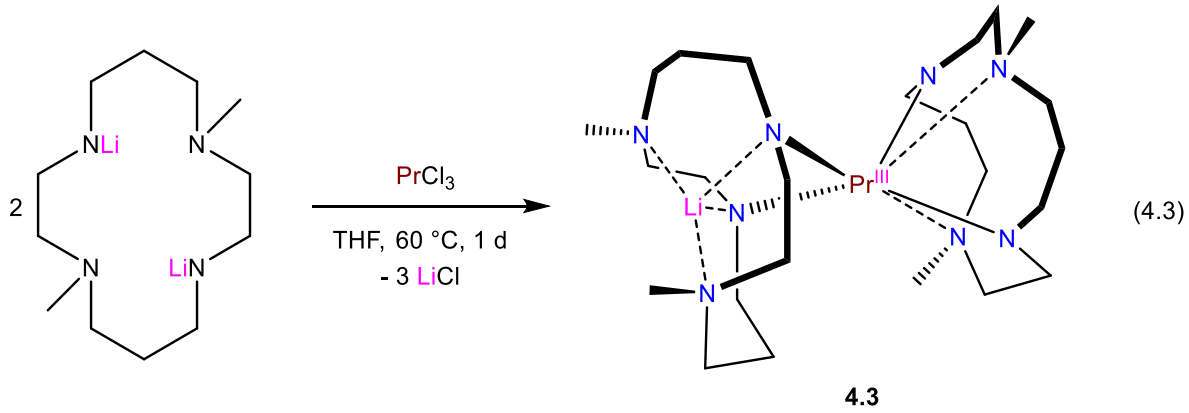

(4.3)

4.3

Storage of a concentrated Et_2O solution of **4.3** at -25 °C for 24 h affords crystals suitable for X-ray diffraction analysis. Complex **4.3** crystallizes in the monoclinic $P2_1/n$ space group and its solid-state structure is shown in Figure 4.9. Complex **4.3** is isostructural to its cerium analogue **4.1**, featuring a distorted trigonal prism geometry about the Pr center with a Continuous Shape Measure value of 6.183.[39,40] The κ^2 macrocycle also supports an outer sphere Li cation with Li-N interactions ranging from 1.985(7) to 2.003(7) Å. The Pr-N(amide) bond lengths (2.304(3) – 2.450(3) Å) are slightly shorter than the Ce-N(amide) distances in **4.1** (2.334(16) – 2.504(14) Å) and the Pr-N distances in the Pr(III) benzamidinate [Pr{4-

$MeOC_6H_4C(NSiMe_3)_2\}_3]$ (2.463(4) - 2.530(4) Å).[55] These distance are, however, within the range reported for the monoanionic Pr(III) amide $[K(THF)_6][Pr(N(SiMe_3)_2)_4]$ (2.423(8) – 2.431(8) Å).[41] The Pr-N(amine) distances (2.809(3) and 2.849(3) Å) are also shorter than the Ce-N(amine) distances in **4.1** (2.847(15) and 2.857(15) Å), but longer than previously reported Pr(III)-amine distances (2.587(5) – 2.745(3) Å).[44,56,57]

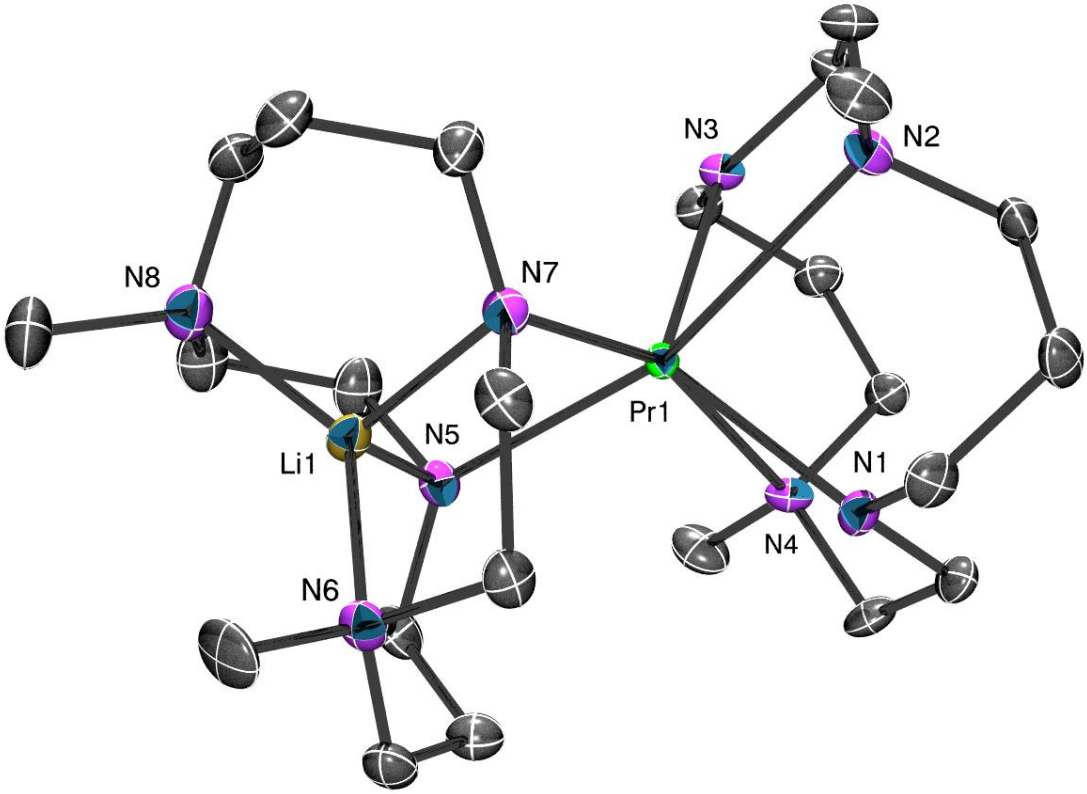

Figure 4.9. Solid-state molecular structure of **4.1** shown with 50% probability ellipsoids. All hydrogen atoms have been omitted for clarity. Selected bond lengths (Å): Pr1-N1 = 2.304(3), Pr1-N2 = 2.849(3), Pr1-N3 = 2.325(3), Pr1-N4 = 2.809(3), Pr1-N5 = 2.448(3), Pr1-N7 = 2.450(3), Li1-N8 = 1.985(7), Li1-N5 = 1.988(7), Li1-N6 = 1.995(7), Li1-N7 = 2.003(7).

To explore the possibility of its chemical oxidation, I probed the electrochemical properties of **4.3** by cyclic voltammetry. The cyclic voltammogram of **4.3** in THF at 200 mV/s scan rate

exhibits an irreversible oxidation feature at 0.92 V vs Fc/Fc^+ (Figure 4.10). This value is much more positive than those measured for Pr(III)/Pr(IV) redox processes using cyclic voltammetry. For example, the Pr(IV) and Tb(IV) silyloxide complexes $[M(OSiPh_3)_4(MeCN)_2]$ (M = Pr, Tb) exhibit irreversible, metal-based reduction features at E_{pc} = -0.38 and -0.96 V (vs Fc/Fc^+), with related oxidation features at E_{pa} = 0.67 and 0.49 V (vs Fc/Fc^+), respectively,[20] suggesting that this feature may be due to a ligand-based oxidation. In this regard, Hrobarik *et al*. have previously shown that electrochemical oxidation of $[Hg(cyclam)][BF_4]_2$ results in generation of a formally Hg(III) cyclam complex, which, however, exhibits significant ligand-based radical cation character, on the basis of DFT calculations.[58] Indeed, the Mulliken spin density analysis of $[Hg(cyclam)]^{3+}$,[59] found the bulk of the spin to be located on the cyclam nitrogen atoms, with a fraction of only less than one tenth on the metal center.[58] As such, these results point towards the possibility of redox noninnocence of the cyclam ligand, which is traditionally thought to be a redox inactive macrocycle. Thus, given the highly anodic oxidation potential observed for **4.3**, it is likely that the redox feature is ligand centered. To investigate ligand-based reactivity in **4.3**, its chemical oxidation was attempted using various oxidants.

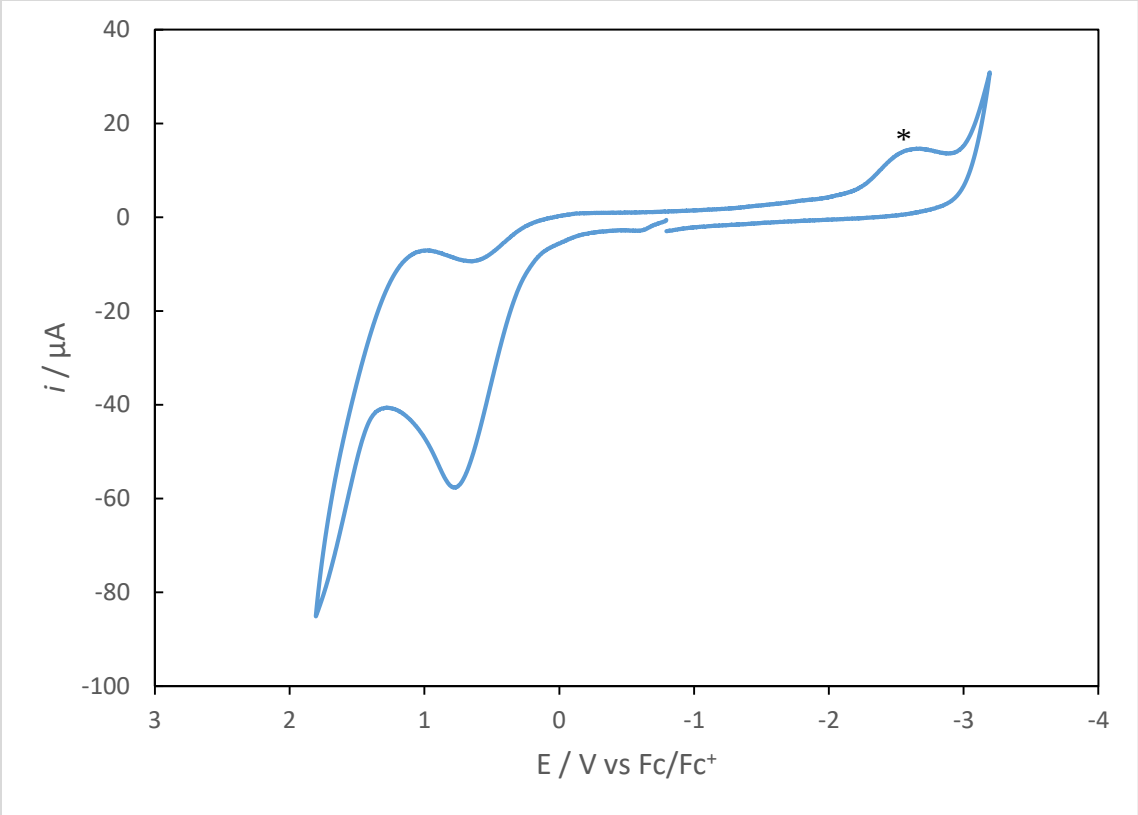

Figure 4.10. Cyclic voltammogram of **4.3** at 200 mV/sec, measured in THF using $[NBu_4][B(C_6F_5)_4]$ as the supporting electrolyte. * indicates presence of a minor unidentified impurity.

4.2.4 Synthesis and Characterization of [Pr(1,8-DMC)(2,2,2-crypt)(I)] (4.4)

Reaction of **4.3** with 0.5 equiv of I_2 or 1 equiv of AgOTf in Et_2O or THF results in formation of a yellow solution from which no praseodymium-containing species could be isolated. The products isolated from these reactions after workup were instead [Li(py)(1,8-DMC)][X] (X = I, OTf) (eq 4.4), whose formulations were confirmed by preliminary analyses of X-ray crystallographic structural data. Addition of excess equivalents of oxidants also resulted in similar reaction outcomes. While protonation of the cyclam ligand in [Li(py)(1,8-DMC)][X] could not be corroborated from the preliminary crystal structure, given the formation of I^- (and

Ag^0) and absence of any tractable Pr species, it is likely that ligand oxidation has occurred, forming an aminyl radical. This result is surprising given that I_2 should not be able to oxidize **4.3** on thermodynamic grounds, according to the aforementioned cyclic voltammetry studies. Nonetheless, there currently is not enough data to unambiguously confirm ligand-based reactivity in this reaction. Intriguingly, a ^{1}H NMR spectroscopy analysis of crystals of [Li(py)(1,8-DMC)][I] reveals overlapping resonances in the diamagnetic methyl and methylene regions, suggesting that any paramagnetic aminyl radical formed likely abstracts hydrogen atoms from the solvent to form diamagnetic [Li(py)(1,8-DMC^{H2})][I].

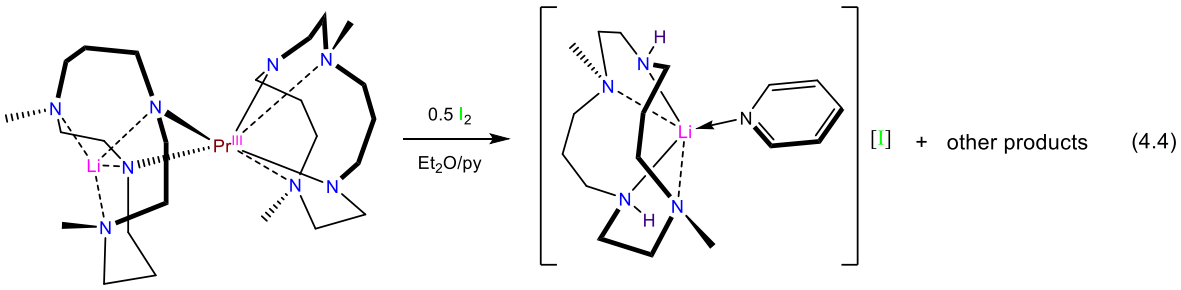

To engender a more electron rich metal center, and more easily oxidized, I added 2,2,2-cryptand to **4.3** prior to oxidation. Thus, addition of 0.5 equiv of I_2 to a mixture of **4.3** and 1 equiv of 2,2,2-cryptand, in THF, results in formation of a pale orange solution from which few X-ray quality single crystals of [Pr(1,8-DMC)(2,2,2-crypt)(I)] (**4.4**) could be isolated (eq 4.5). Due to the low yield, full characterization of this complex was not possible, but I have obtained a reliable crystal structure, which I discuss below.

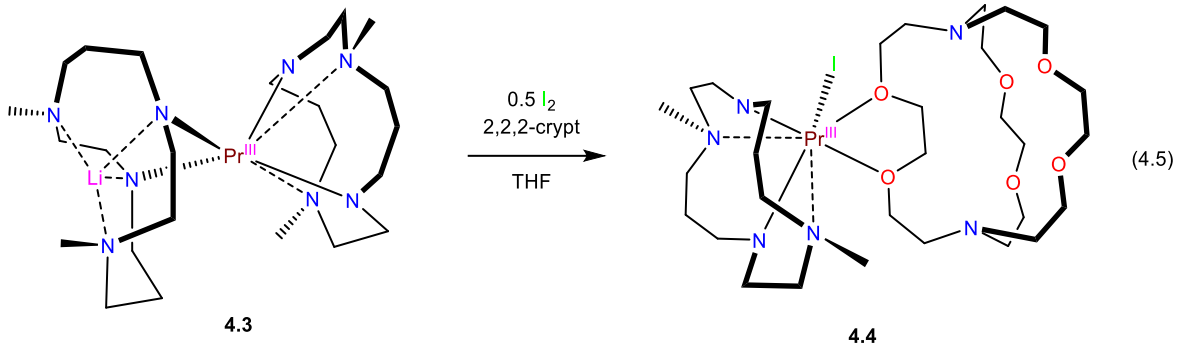

(4.5)

Complex **4.4** crystallizes in the triclinic *P*-1 space group as the THF solvate **4.4**·0.5THF (Figure 4.11). In the solid state, **4.4** exhibits a hepta-coordinate Pr center ligated by a κ^4 cyclam macrocycle, a κ^2 cryptand moiety and an iodide co-ligand, suggesting a trivalent oxidation state for the praseodymium. The 2,2,2-cryptand coordinates via two of its oxygen atoms with an average Pr-O distance of 2.616 Å. Ancillary binding of 2,2,2-cryptand to lanthanide(III) ions is extremely rare,[60–64] which highlights the challenges inherent in stabilizing Pr(IV). Notably, the Pr-N(amide) (2.266(5) and 2.296(6) Å) and Pr-N(amine) (2.766(6) and 2.829(6) Å) distances in **4.4** are comparable to those in **4.3** (2.304(3) – 2.450(3) Å and 2.809(3) and 2.849(3) Å, respectively), consistent with a Pr(III) oxidation state. The Pr-I distance in **4.4** (3.2052(7) Å) is also similar to the Pr(III)-I bond lengths in $[(NN^{TBS})Pr(THF)(\mu\text{-}I)]_2$ (NN^{TBS} = 1,1'-$Fc(NSiMe_2{}^tBu)_2$) (3.238(1) and 3.261(1) Å).[65]

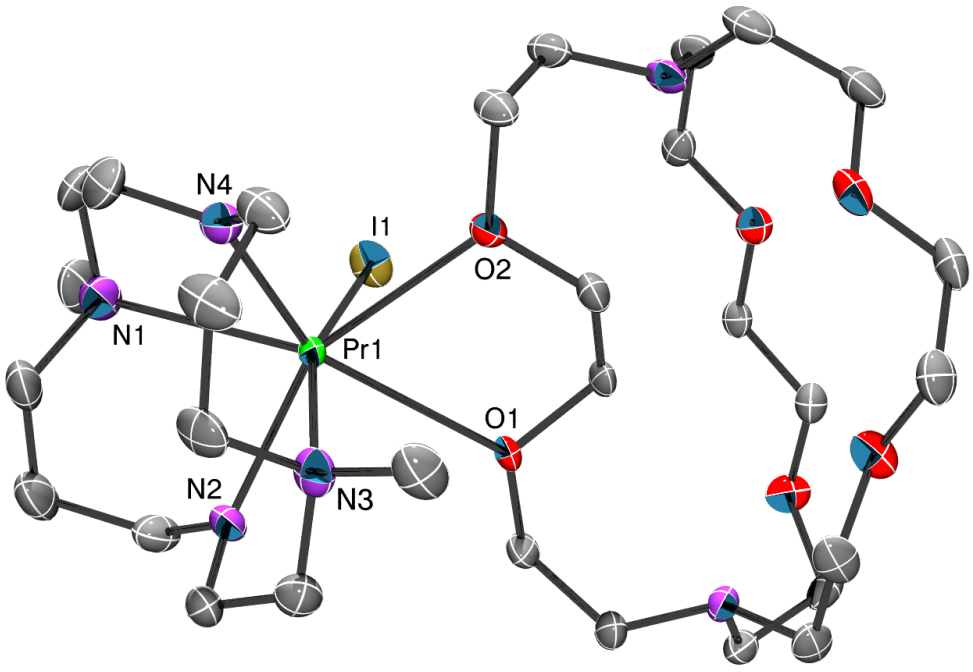

Figure 4.11. Solid-state molecular structure of **4.4**·0.5THF shown with 50% probability ellipsoids. All hydrogen atoms and a THF solvate have been omitted for clarity. Selected bond lengths (Å): Pr1-N1 = 2.766(6), Pr1-N2 = 2.266(5), Pr1-N3 = 2.829(6), Pr1-N4 = 2.296(6), Pr1-I1 = 3.2052(7), Pr1-O1 = 2.617(4), Pr1-O2 = 2.615(4).

The *in situ* ^{1}H NMR spectrum of the reaction between **4.3** and I_2, in the presence of 2,2,2-crpytand, reveals formation of both paramagnetic and diamagnetic products (Figure 4.12). In particular, the spectrum reveals a single broad methyl resonance at -61.58 ppm, and eight broad methylene resonances between -21.25 and 68.53 ppm that are tentatively assigned to the single cyclam environment of **4.4**. The two remaining methylene resonances for **4.4** are probably overlapping with the large diamagnetic signals in the region between 0 and 7 ppm. While it is possible that these diamagnetic resonances may be attributable to [Li(1,8-DMC^{H2})][I], the formation of this compound in this reaction has yet to be confirmed by X-ray crystallographic analysis of the remaining unidentified products present in the reaction mixture. Given these

spectroscopic data and the low yield of **4.4**, obvious uncertainties remain as to which species transfers an electron to I_2 to generate **4.4**.

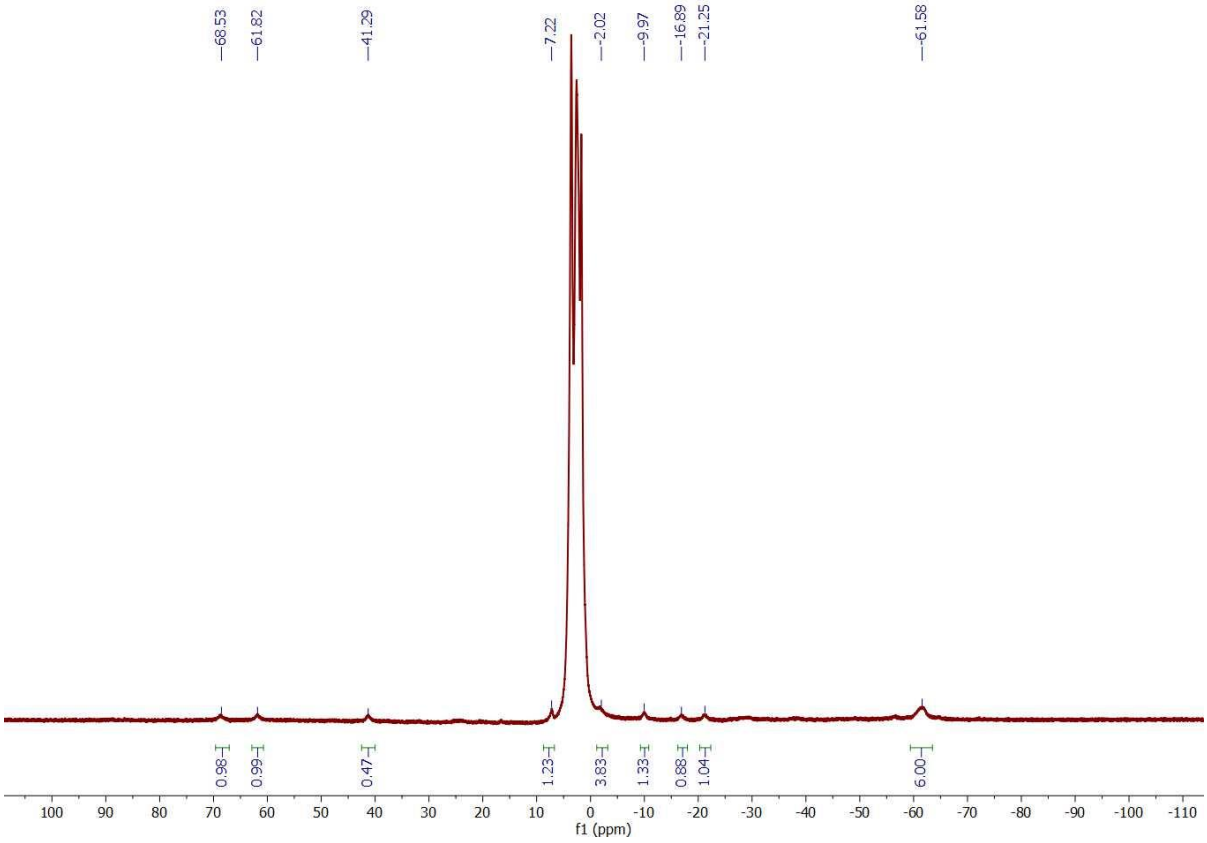

Figure 4.12. *In situ* ^{1}H NMR spectrum (in THF-d_8) of the reaction of **4.3** with I_2 in the presence of 2,2,2-cryptand.

4.3 Summary

This chapter describes the synthesis, structural and electrochemical characterization of the Ce(III) and Pr(III) bis-cyclam complexes [Li][Ce(1,8-DMC)$_2$] (**4.1**) and [Li][Pr(1,8-DMC)$_2$] (**4.3**). Both complexes were isostructural, exhibiting short M-N(amide) bond lengths and long M-N(amine) distances. Cyclic voltammetry studies revealed a highly cathodic oxidation potential for **4.1** and a highly anodic oxidation potential for **4.3**. Consistent with these findings,

oxidation of **4.1** with I_2 easily afforded a stable Ce(IV) cyclam complex [Ce(1,8-DMC)$_2$] (**4.2**) in moderate yield, while treatment of **4.3** with I_2 or AgOTf only resulted in isolation of [Li(py)(1,8-DMC^{H2})][X] (X = I, OTf). Interestingly, reaction of **4.3** with I_2 in the presence of 2,2,2-cryptand does not result in oxidation of the Pr(III) center, but instead affords the Pr(III) cryptate complex [Pr(1,8-DMC)(2,2,2-crypt)(I)] (**4.4**) in low yield. In both reactions of **4.3**, it is unclear what species is oxidized, but ^{1}H NMR spectroscopy suggests formation of diamagnetic [Li(py)(1,8-DMC^{H2})][X] as a major product. Its formation may occur by direct protonation, or by ligand oxidation followed by H-atom abstraction. The latter mechanism is consistent with the redox-noninnocence of the cyclam ligand originally put forward by Hrobarik *et al*. in 2008.[58] However, to definitely affirm ligand-based reactivity, the electrochemistry of [Li(Et$_2$O)]$_2$[1,8-DMC] needs to be investigated independently by cyclic voltammetry in future studies. Exploring the reactivity of [Li(Et$_2$O)]$_2$[1,8-DMC] with I_2 or AgOTf would also shed invaluable insight into the operative reaction mechanism. Additionally, independent synthesis of [Li(py)(1,8-DMC^{H2})][X] (X = I, OTf) by reactions of LiX with H$_2$(1,8-DMC), followed by detailed structural and NMR spectroscopic comparisons could confirm its formation in both oxidation reactions of **4.3**. Future work will also focus on utilizing macrocyclic ligands with stronger σ and π donors, as well as greater steric rigidity, to prepare highly elusive tetravalent lanthanide ions.

4.4 Experimental

4.4.1 General Procedures. All reactions and subsequent manipulations were performed under anaerobic and anhydrous conditions in the glovebox or on a Schlenk line, under an atmosphere of dinitrogen. Hexanes, diethyl ether (Et$_2$O), and toluene were dried by passage over activated molecular sieves using a Vacuum Atmospheres solvent purification system. Tetrahydrofuran

(THF) was distilled over Na/benzophenone and stored over activated 3 Å molecular sieves for 24 h prior to use. C_6D_6, pyridine-d_5 and THF-d_8 were dried over activated 3 Å molecular sieves for 24 h prior to use. All other reagents were purchased from commercial suppliers and used as received.

^1H, $^{13}C\{^1H\}$, and $^7Li\{^1H\}$ NMR spectra were recorded on an Agilent Technologies 400 MHz 400-MR DD2. ^1H and $^{13}C\{^1H\}$ NMR spectra were referenced to external $SiMe_4$ using residual protio solvent resonances as internal standards. $^7Li\{^1H\}$ NMR spectra were referenced indirectly with the ^1H chemical shift of $SiMe_4$ at 0 ppm, according to IUPAC standard.[66,67] IR spectra were recorded on a Nicolet 6700 FT-IR spectrometer. Electronic absorption spectra were recorded on a Shimadzu UV3600 UV-NIR Spectrometer. Elemental analyses were performed by the Microanalytical Laboratory at University of California (Berkeley, CA).

Cyclic Voltammetry Measurements. CV experiments were performed with a CH Instruments 600c Potentiostat, and the data were processed using CHI software (version 6.29). All experiments were performed in a glove box using a 20 mL glass vial as the cell. The working electrode was glassy carbon (2 mm diameter), the counter electrode was a platinum wire, and the reference electrode was a silver wire electroplated with silver chloride. Solutions employed for CV studies were typically 1 mM in analyte and 0.1 M in $[NBu_4][PF_6]$ (for **4.1**) or $[NBu_4][B(C_6F_5)_4]$ (for **4.3**). All potentials are reported versus the $[Cp_2Fe]^{0/+}$ couple.

4.4.2 Synthesis of $[Li(Et_2O)]_2$[1,8-DMC]: To a cold (-25 °C) stirring orange solution of 1,8-dimethylcyclam (2.0 mL, 8.3 mmol) in Et_2O (2 mL) was added dropwise a cold (-25 °C) pale yellow solution of n-BuLi in hexanes (6.6 mL, 16.5 mmol) diluted with Et_2O (2 mL). This addition resulted in an immediate color change to orange-brown concomitant with deposition

of a fine brown precipitate. The resulting mixture was allowed to stir for 15 min at room temperature, whereupon the solution was filtered over a Celite column supported on a medium porosity glass frit to yield a yellow orange filtrate. The filtrate was concentrated to 8 mL *in vacuo* and stored at -25 °C for 24 h which resulted in deposition of pale yellow plates. These crystals were isolated by decanting off the supernatant and dried under reduced pressure (1.6442 g). Concentration of the supernatant and subsequent storage at -25 °C for 24 h resulted in deposition of a second crop of crystals (Total yield: 2.2947 g, 71% yield. ^{1}H NMR (600 MHz, THF-d_8): δ 1.11 (t, J_{HH} = 6 Hz, 12H, OCH_2CH_3), 1.54 (d, J_{HH} = 18 Hz, 2H, $CH_2CH_2CH_2$), 1.76 (d, J_{HH} = 12 Hz, 2H, CH_2CH_2), 2.02 (q, J_{HH} = 12 Hz, 2H, $CH_2CH_2CH_2$), 2.10 (s, 6H, CH_3), 2.34 (d, J_{HH} = 12 Hz, 2H, $CH_2CH_2CH_2$), 2.56 (t, J_{HH} = 12 Hz, 2H, $CH_2CH_2CH_2$), 2.84 (d, J_{HH} = 12 Hz, 2H, CH_2CH_2), 3.07 (m, 2H, $CH_2CH_2CH_2$), 3.11 (t, J_{HH} = 12 Hz, 2H, $CH_2CH_2CH_2$), 3.15 (t, J_{HH} = 12 Hz, 2H, CH_2CH_2), 3.22 (td, J_{HH} (t) = 12 Hz, J_{HH} (d) = 3.5 Hz, 2H, CH_2CH_2), 3.38 (q, J_{HH} = 6 Hz, 8H, OCH_2CH_3), ^{7}Li{^{1}H} NMR (THF-d_8, 25 °C, 155 MHz): δ -0.56 (s, 2Li).

4.4.3 Synthesis of [Li][Ce(1,8-DMC)$_2$] (4.1): To a pale yellow solution of [Li(Et_2O)]$_2$[1,8-DMC] (598.3 mg, 1.540 mmol) in THF (7 mL) was added anhydrous $CeCl_3$ (190.1 mg, 0.771 mmol). The resulting mixture was transferred to a Schlenk flask equipped with a Roto-Kontes-Flow valve and stirred at 65 °C for 2 d, which resulted in dissolution of the $CeCl_3$ and formation of a golden yellow solution. The volatiles were removed *in vacuo*, and the resulting residue was extracted into Et_2O (5 mL) and filtered over a Celite column supported on glass wool to yield a yellow filtrate. Storage of this solution at -25 °C for 48 h resulted in deposition of bright yellow blocks, which were isolated by decanting off the supernatant (292.2 mg). Further concentration of the supernatant followed by storage at -25 °C for 48 h afforded an additional

crop of crystals (total yield: 348.9 mg, 75% yield). Anal. Calcd for $C_{24}H_{52}CeLiN_8$: C, 48.06; H, 8.74; N, 18.68. Found: C, 48.34; H, 8.60; N, 18.58. ^{1}H NMR (400 MHz, THF-d_8) δ -60.41 (s br, 2H, CH_2), -20.64 (s br, 2H, CH_2), -18.78 (s, 2H, CH_2), -17.71 (s, 6H, CH_3), -9.75 (s br, 2H, CH_2), -8.47 (s br, 2H, CH_2), -7.50 (s br, 2H, CH_2), -5.03 (s br, 2H, CH_2), -3.27 (s br, 2H, CH_2), -2.37 (s br, 2H, CH_2), 5.09, (s br, 2H, CH_2), 5.16 (s br, 2H, CH_2), 5.41 (s br, 2H, CH_2), 5.99 (s br, 2H, CH_2), 6.80 (s br, 2H, CH_2), 11.04 (s br, 2H, CH_2), 11.62 (s br, 2H, CH_2), 12.34 (s, 6H, CH_3), 13.16 (s, 2H, CH_2), 13.67 (s br, 2H, CH_2), 35.57 (s br, 2H, CH_2), 64.13 (s br, 2H, CH_2). UV-Vis (THF, 2.06 mM, 25 °C, $M^{-1}\cdot cm^{-1}$): 365 (ε = 210), 464 (ε = 330), 565 (ε = 95). NIR (Toluene, 8.3 mM, 25 °C, $M^{-1}\cdot cm^{-1}$): 1148 (ε = 59), 1194 (ε = 32), 1392 (ε = 33), 1442 (sh, ε = 22), 1486 (sh, ε = 16), 1878 (ε = 63), 2024 (ε = 70). IR (KBr pellet, cm^{-1}): 2941 (s), 2856 (sh s), 2816 (sh s), 2791 (s), 1664 (m), 1618 (m), 1460 (s), 1369 (sh vw), 1348 (w), 1298 (w), 1261 (vw), 1217 (vw), 1147 (sh m), 1134 (s), 1074 (sh m), 1045 (s), 962 (vw), 918 (vw), 864 (vw), 820 (sh vw), 814 (w), 795 (w), 744 (m), 586 (br m), 469 (vw), 434 (vw), 418 (vs).

4.4.4 Synthesis of [Ce(1,8-DMC)$_2$] (4.2): To a stirring yellow solution of **4.1** (313.1 mg, 0.522 mmol) in THF (2 mL) was added dropwise an orange solution of I_2 (66.2 mg, 0.261 mmol) in THF (1 mL). This addition resulted in an immediate color change to deep purple, whereupon the solution was allowed to stir for 30 min at room temperature. The volatiles were removed *in vacuo* and the resulting tacky solid was triturated with pentane (1 mL) to yield a purple powder. The powder was extracted into Et_2O (2 × 4 mL) and filtered over a Celite column supported on glass wool. The resulting purple filtrate was concentrated *in vacuo* to ~2 mL, and subsequently stored at -25 °C for 48 h which resulted in deposition of purple plates (105.4 mg, 34% yield). Anal. Calcd for $C_{24}H_{52}CeN_8$: C, 48.62; H, 8.84; N, 18.90. Found: C, 48.43; H, 8.55; N, 18.72. ^{1}H NMR (C_6D_6, 25 °C, 400 MHz): δ 1.44 (t, J_{HH} = 4 Hz, 4H, CH_2CH$_2$), 1.52

(dtt, J_{HH} (d) = 16 Hz, J_{HH} (t) = 4 Hz, 4H, $CH_2CH_2CH_2$), 1.68 (tt, J_{HH} (t) = 12 Hz, J_{HH} (t) = 8 Hz, 4H, $CH_2CH_2CH_2$), 2.39 (s, 12H, CH_3), 2.41 (q, J_{HH} = 4 Hz, 4H, CH_2CH_2), 2.46 (td, J_{HH} (t) = 12 Hz, J_{HH} (d) = 4 Hz, 4H, $CH_2CH_2CH_2$), 3.62 (td, J_{HH} (t) = 12 Hz, J_{HH} (d) = 6.7 Hz, 4H, CH_2CH_2), 3.87 (dd, J_{HH} (d) = 12 Hz, J_{HH} (d) = 4 Hz, 4H, CH_2CH_2), 4.11 (dd, J_{HH} (d) = 14Hz, J_{HH} (d) = 6 Hz, 4H, $CH_2CH_2CH_2$), 4.93 (td, J_{HH} (t) = 12 Hz, , J_{HH} (d) = 4 Hz, 4H, $CH_2CH_2CH_2$), 4.99 (td, J_{HH} (t) = 12 Hz, , J_{HH} (d) = 4 Hz, 4H, CH_2CH_2). $^{13}C\{^1H\}$ NMR (C_6D_6, 25 °C, 100 MHz): δ 25.48 (CH_3), 44.28 (CH_2), 44.57 (CH_2), 49.71 (CH_2), 54.21 (CH_2), 62.93 (CH_2). UV-Vis (THF, 0.081 mM, 25 °C, $M^{-1}\cdot cm^{-1}$): 561 (ε = 5914), IR (KBr pellet, cm^{-1}): 2962 (s), 2926 (s), 2858 (s), 2835 (s), 2789 (vs), 2758 (sh vs), 2671 (m), 1456 (s), 1446 (s), 1381 (m), 1348 (s), 1298 (m), 1284 (sh w), 1261 (vw), 1242 (m), 1217 (s), 1194 (w), 1161 (s), 1140 (s), 1078 (vs), 1055 (sh s), 1014 (vw), 964 (m), 926 (vw), 920 (m), 868 (s), 845 (m), 804 (m), 796 (sh w), 750 (w), 638 (w), 592 (w), 490 (w), 457 (m), 432 (vw), 422 (sh vw).

4.4.5 Synthesis of [Li][Pr(1,8-DMC)$_2$] (4.3): To a pale yellow solution of $[Li(Et_2O)]_2$[1,8-DMC] (730.4 mg, 1.880 mmol) in THF (7 mL) was added anhydrous $PrCl_3$ (232.4 mg, 0.940 mmol). The resulting mixture was transferred to a Schlenk flask equipped with a Roto-Kontes-Flow valve and stirred at 65 °C for 2 d, which resulted in dissolution of the $PrCl_3$ and formation of a pale blue solution. The volatiles were removed *in vacuo*, and the resulting solid was extracted into Et_2O (8 mL) and filtered over a Celite column supported on glass wool to yield a pale blue filtrate. Concentration of this solution and subsequent storage at -25 °C for 24 h resulted in deposition of pale blue blocks, which were isolated by decanting off the supernatant (357.1 mg, 63% yield). Anal. Calcd for $C_{24}H_{52}LiN_8Pr$: C, 48.00; H, 8.73; N, 18.66. Found: C, 48.20; H, 8.68; N, 18.34. ^1H NMR (THF-d_8, 25 °C, 400 MHz): δ -65.82 (s br, 2H, CH_2), -24.83 (s br, 2H, CH_2), -19.58 (s, 2H, CH_2), -18.75 (s, 6H, CH_3), -4.22 (s br, 2H, CH_2), -2.79 (s br,

2H, CH_2), -0.44 (s br, 2H, CH_2), 2.14 (s br, 2H, CH_2), 2.37 (s br, 2H, CH_2), 2.56 (s br, 2H, CH_2), 2.62, (s br, 2H, CH_2), 4.34 (s br, 2H, CH_2), 5.82 (s br, 2H, CH_2), 7.63 (s br, 2H, CH_2), 11.74 (s br, 2H, CH_2), 16.66 (s, 6H, CH_3), 16.80 (s br, 2H, CH_2), 17.64 (s br, 2H, CH_2), 20.27 (s, 2H, CH_2), 22.91 (s br, 2H, CH_2), 49.88 (s br, 2H, CH_2), 89.20 (s br, 2H, CH_2). UV-Vis NIR (Toluene, 10.3 mM, 25 °C, $M^{-1}\cdot cm^{-1}$): 1148 (ε = 48), 1194 (ε = 27), 1394 (ε = 30), 1442 (sh, ε = 20), 1488 (sh, ε = 17), 1880 (ε = 56), 2022 (ε = 60). IR (KBr pellet, cm^{-1}): 2941 (br s), 2792 (br sh, s), 2659 (br sh, s), 1670 (m), 1595 (m), 1464 (vs), 1416 (sh m), 1375 (w), 1350 (m), 1296 (w), 1261 (w), 1217 (vw), 1213 (m), 1184 (w), 1163 (m), 1134 (m), 1076 (w), 1053 (m), 1024 (w), 993 (w), 962 (m), 928 (m), 914 (w), 893 (vw), 877 (w), 864 (w), 850 (w), 816 (vw), 810 (m), 793 (w), 737 (m), 634 (m), 607 (m), 584 (m), 511 (w), 449 (vw), 447 (w), 420 (w), 402 (s).

4.4.6 Reaction of 4.3 with I_2: To a cold (-25 °C) pale blue solution of **4.3** (114.3 mg, 0.190 mmol) in Et_2O (5 mL) was added a cold (-25 °C) orange solution of I_2 (24.1 mg, 0.095 mmol) in Et_2O (1 mL). This addition resulted in an immediate color change to yellow, concomitant with deposition of copious amounts of yellow precipitate. The resulting mixture was allowed to stir for 5 min at room temperature, whereupon the solution was filtered over a Celite column supported on glass wool to yield a colorless filtrate and a large plug of yellow solid on the Celite. The plug was then dissolved into pyridine (1 mL) to yield a yellow filtrate. The filtrate was transferred into a 4 mL vial, which was placed inside a 20 mL vial. Diethyl ether (2 mL) was added to the outer vial. Storage of the two-vial system at -25 °C for 4 d resulted in deposition of yellow plates which were identified as [Li(py)(1,8-DMC)][I] by X-ray crystallography. The X-ray data, however, was incomplete, and thus structural details are not included herein. ^{1}H NMR (py-d_5, 25 °C, 400 MHz): δ 1.25 – 3.25 (m, 26H, overlapping peaks

for CH_3 and CH_2). ^{7}Li{^{1}H} NMR (py-d_5, 25 °C, 155 MHz): δ 0.92 (s, 1Li). Subsequent concentration of the supernatant and storage at -25 °C for several days only results in deposition of more [Li(py)(1,8-DMC)][I]. Crystals of [Li(1,8-DMC)][I] were also obtained, in small amounts, from the colorless Et_2O filtrate collected during workup, and no praseodymium containing species could be isolated from this fraction as well. Finally, reactions of **4.3** with 1 equiv of AgOTf using an identical procedure only results in isolation of [Li(py)(1,8-DMC)][OTf].

4.4.7 Synthesis of [Pr(1,8-DMC)(2,2,2-crypt)(I)] (4.4): To a cold (-25 °C) pale blue solution containing a mixture of **4.3** (49.4 mg, 0.082 mmol) and 2,2,2-cryptand (31.1mg, 0.083 mmol, 1 equiv) in THF (1 mL) was added a cold (-25 °C) orange solution of I_2 (10.4 mg, 0.041 mmol) in THF (1 mL). This addition resulted in formation of a cloudy orange solution along with deposition of a small amount of fine white precipitate. The mixture was allowed to stir for 5 min at room temperature, whereupon the solution was filtered over a Celite column supported on glass wool to yield a pale orange filtrate. The volatiles were removed from the filtrate *in vacuo* to yield a pale orange oil, which was triturated with pentane (2 × 1 mL). The resulting pale orange solid was extracted into Et_2O (2 mL) and filtered over a Celite column supported on glass wool to yield a pale yellow-orange filtrate and a plug of white solid on the Celite. The filtrate was then transferred into a 4 mL vial, which was placed inside a 20 mL vial. Hexanes (1 mL) was added to the outer vial. Storage of the two-vial system at -25 °C for 2 d resulted deposition of colorless plates of **4.4**. *In situ* ^{1}H NMR (THF-d_8, 25 °C, 400 MHz): δ -61.58 (br s, 6H, CH_3, **4.4**), -21.25 (br s, 2H, CH_2, **4.4**), -16.89 (br s, 2H, CH_2, **4.4**), -9.97 (br s, 2H, CH_2, **4.4**), -2.02 (br s, 2H, CH_2, **4.4**), 0.01 – 7.01 (br m, overlapping peaks for CH_3 and CH_2), 7.22 (br s, 2H, CH_2, **4.4**), 41.29 (br s, 2H, CH_2, **4.4**), 61.82 (br s, 2H, CH_2, **4.4**), 68.53 (br s, 2H,

C*H*$_2$, **4.4**). Two methylene resonances for **4.4** were not observed likely due to their overlap with the large diamagnetic signals between 0 and 7 ppm. *In situ* ^{7}Li{^{1}H} NMR (THF-d_8, 25 °C, 155 MHz): δ 0.42 (s, 1Li)

4.4.8 X-ray Crystallography. Data for [Li(Et$_2$O)]$_2$[1,8-DMC] and **4.1**-**4.4** were collected on a Bruker KAPPA APEX II diffractometer equipped with an APEX II CCD detector using a TRIUMPH monochromater with a Mo Kα X-ray source (α = 0.71073 Å). The crystals of [Li(Et$_2$O)]$_2$[1,8-DMC] and **4.1**-**4.4** were mounted on a cryoloop under Paratone-N oil before data collection. Data for [Li(Et$_2$O)]$_2$[1,8-DMC], **4.1**, **4.2**, **4.3** and **4.4** were collected at 100(2), 118(2), 100(2), 100(2) and 113(2) K, respectively, using an Oxford nitrogen gas cryostream system. X-ray data for [Li(Et$_2$O)]$_2$[1,8-DMC], **4.1**, **4.2**, **4.3** and **4.4** were collected utilizing frame exposures of 10, 2, 15, 5 and 2 s, respectively. Data collection and cell parameter determinations were conducted using the SMART program.[68] Integration of the data frames and final cell parameter refinement were performed using SAINT software.[69] Absorption corrections of the data were carried out using the multi-scan method SADABS.[70]Subsequent calculations were carried out using SHELXTL.[71] Structure determination was done using direct or Patterson methods and difference Fourier techniques. All hydrogen atom positions were idealized, and rode on the atom of attachment. Structure solution, refinement, graphics, and creation of publication materials were performed using SHELXTL.[71]

Both cyclam ligands and the toluene solvate in the structure of **4.1** exhibited positional disorder, which was addressed by constraining the affected atoms with the SADI and EADP commands. In addition, hydrogen atoms were not added to the carbon atoms of both cyclam rings and the toluene solvate. The THF solvate in the structure of **4.4** also exhibited positional disorder, which was addressed by constraining the affected atoms with the SADI command.

Additionally, the THF solvate was refined isotropically and no hydrogen atoms were added to its carbon atoms.

Table 4.1. Crystallographic details for $[Li(Et_2O)]_2[1,8\text{-DMC}]$, **4.1** and **4.2**.

	$[Li(Et_2O)]_2[1,8\text{-DMC}]$	**4.1·C_7H_8**	**4.2**
Formula	$C_{20}H_{46}Li_2N_4O_2$	$C_{31}H_{60}CeLiN_8$	$C_{24}H_{52}CeN_8$
Crystal Habit, Color	Plates, Yellow	Block, Yellow	Plate, Purple
Crystal Size (mm)	0.2 × 0.1 × 0.05	0.2 × 0.15 × 0.15	0.15 × 0.10 × 0.05
MW (g/mol)	388.49	691.93	592.85
crystal system	Monoclinic	Tetragonal	Triclinic
space group	$P2_1/n$	$P4_3$	P-1
a (Å)	8.9271(10)	10.877(3)	9.420(4)
b (Å)	12.9241(12)	10.877(3)	17.550(7)
c (Å)	10.3861(10)	29.035(9)	18.797(8)
α (°)	90	90	64.076(7)
β (°)	90.908(6)	90	81.839(8)
γ (°)	90	90	83.125(7)
V ($Å^3$)	1198.1(2)	3435(2)	2761(2)
Z	2	4	4
T (K)	100(2)	118(2)	100(2)
λ (Å)	0.71073	0.71073	0.71073
GOF	1.244	1.126	0.907
Density (calcd) (Mg/m^3)	1.077	1.338	1.426
Absorption coefficient (mm^{-1})	0.068	1.357	1.676
F_{000}	432	1452	1240
Total no Reflections	4257	22844	16895
Unique Reflections	2031	7035	11919
Final R indices*	$R_1 = 0.0469$	$R_1 = 0.0881$	$R_1 = 0.0649$
	$wR_2 = 0.0961$	$wR_2 = 0.2198$	$wR_2 = 0.1398$
Largest Diff. peak and hole ($e^- A^{-3}$)	0.195, -0.209	2.360, -1.346	1.719, -1.645

* For $[I > 2\sigma(I)]$

Table 4.2. Crystallographic details for complexes **4.3** and **4.4**.

	4.3	**4.4·0.5THF**
Formula	$C_{24}H_{52}LiN_8Pr$	$C_{32}H_{66}IN_6O_{6.5}Pr$
Crystal Habit, Color	Block, Blue	Plate, Colorless
Crystal Size (mm)	0.2 × 0.15 × 0.1	0.15 × 0.15 × 0.05
MW (g/mol)	600.58	906.71
crystal system	Monoclinic	Triclinic
space group	$P2_1/n$	P-1
a (Å)	10.0319(9)	10.127(2)
b (Å)	23.937(2))	12.352(3)
c (Å)	11.8650(11)	17.677(4)
α (°)	90	91.431(5)
β (°)	93.331(2)	105.550(6)
γ (°)	90	105.912(5)
V ($Å^3$)	2844.3(4)	2037.0(9))
Z	4	2
T (K)	100(2)	113(2)
λ (Å)	0.71073	0.71073
GOF	0.718	1.187
Density (calcd) (Mg/m^3)	1.402	1.478
Absorption coefficient (mm^{-1})	1.739	2.000
F_{000}	1256	928
Total no Reflections	13451	18243
Unique Reflections	6516	9867
Final R indices*	$R_1 = 0.0328$	$R_1 = 0.0574$
	$wR_2 = 0.0774$	$wR_2 = 0.1232$
Largest Diff. peak and hole ($e^- A^{-3}$)	0.841, -0.566	2.084, -2.692

* For [$I > 2\sigma(I)$]

4.5 Appendix

4.5.1 Synthesis and Characterization of $[Li]_2[UO_2(1,8\text{-DMC})_2]$ (4.5)

Given the anticipated rigidity of the macrocyclic ligand framework within 1,8-DMC, its suitability for the synthesis of a *cis*-uranyl cyclam complex was investigated. Thus, reaction of $[UO_2Cl_2(THF)_3]$ with 1 equiv of $[Li(Et_2O)]_2$[1,8-DMC] in THF results in formation of an orange-brown solution from which the 1:2 product $[Li]_2[UO_2(1,8\text{-DMC})_2]$ (**4.5**) can be isolated as orange plates in 22% yield (based on uranium) (eq A4.1). Complex **4.5** was structurally characterized by X-ray crystallography (Figure A4.1), which revealed a uranyl unit ligated by two κ^2 cyclam macrocycles that coordinate via both of their amide nitrogen atoms, resulting in an octahedral geometry about the uranium center. Each cyclam macrocycle also supports an outer-sphere Li cation within its binding pocket that binds to both its amide and amine nitrogen atoms. The uranyl fragment in **4.5** sits at a special position, resulting in a perfectly linear O-U-O angle and an overall D_{2h} symmetry for **4.5** in the solid state. In addition, the U-O_{yl} bond length (1.805(8) Å) in **4.5** is typical of the uranyl fragment (~1.78 Å), while the U-N distances (2.384(10) and 2.374(11) Å) are slightly longer than previously reported uranyl-amide bond distances.[33,72–77] The Li-N distances (1.94(2) – 2.02(2) Å) are also similar to previously reported Li-N dative interactions.[30–33]

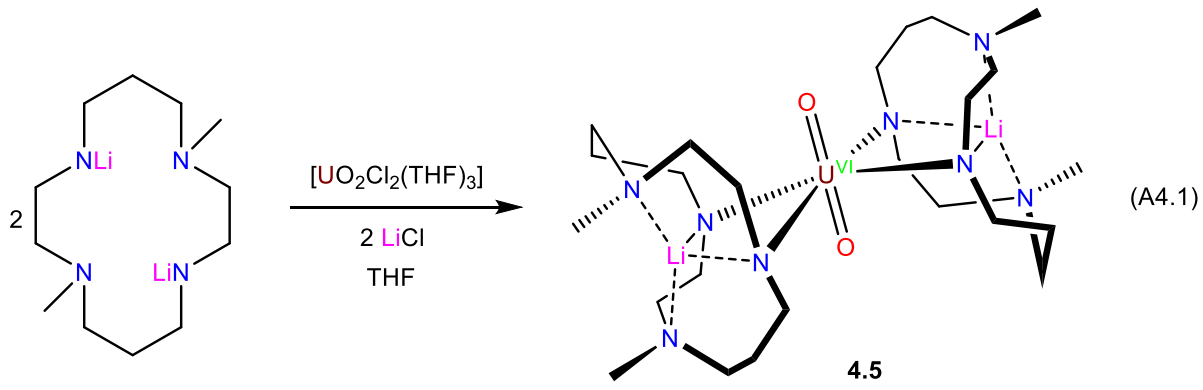

(A4.1)

The unwanted reaction stoichiometry observed in eq A4.1 is reminiscent of that detected in the reaction between $[K_3(DME)_2][Cy_7Si_7O_{12}]$ and $[UO_2Cl_2(THF)_3]$, in the presence of 2,2,2-cryptand, to form $[K(2,2,2\text{-cryptand})]_2[K_2UO_2(Cy_7Si_7O_{12})_2]$ (Chapter 6), as well the reaction between Li_2(tmtaa) and $[UO_2Cl_2(THF)_3]$ in THF to form $[Li(THF)_3][Li(THF)_2][(UO_2Cl_2)_2$(tmtaa)] (Chapter 5). These transformations were thought to be promoted by the presence of Lewis acidic alkali cations in the reaction mixtures. The Li cation in $[Li(Et_2O)]_2$[1,8-DMC] also likely plays a key role in the formation of **4.5**. Protonolysis of $[UO_2(NR_2)_2(THF)_2]$ (R = $SiMe_3$) with H_2(1,8-DMC), an alternative to salt metathesis, proved impractical due to the very weak acidity of H_2(1,8-DMC). All in all, these results suggest that the 1,8-dimethyl cyclam ligand is not suitable for facilitating the desired *trans*/*cis* isomerization of the uranyl ion.

Experimental Details: To a stirring yellow green solution of $[UO_2Cl_2(THF)_3]$ (84.1 mg, 0.151 mmol) in THF (1 mL) was added a pale yellow solution of $[Li(Et_2O)]_2$[1,8-DMC] (58.5 mg, 0.150 mmol, 1 equiv) in THF (1 mL). This addition resulted in an immediate color change to dark orange-brown. The resulting mixture was allowed to stir for 1 h at room temperature, whereupon the volatiles were removed *in vacuo* to yield a dark orange residue. The residue was extracted into Et_2O (2 mL) and filtered over a Celite column supported on glass wool to yield an orange filtrate. The filtrate was concentrated to ~1 mL and stored at -25 °C for 24 h, which resulted in deposition of orange plates of **4.5** (24.0 mg, 22% yield based on uranium). ^{1}H NMR (C_6D_6, 25 °C, 400 MHz): δ 1.46 (m, 4H, CH_2), 1.96 (s, 12H, CH_3), 2.19 (m, 4H, CH_2), 2.47 (m, 4H, CH_2), 3.45 (m, 4H, CH_2), 4.30 (m, 4H, CH_2), 4.56 (m, 4H, CH_2), 5.89 (m, 4H, CH_2), 5.99 (m, 4H, CH_2), 6.19 (t, J_{HH} = 12 Hz, 4H, CH_2), 6.32 (t, J_{HH} = 12 Hz, 4H, CH_2). ^{7}Li{^{1}H} NMR (C_6D_6, 25 °C, 400 MHz): δ 4.27 (s, 2Li).

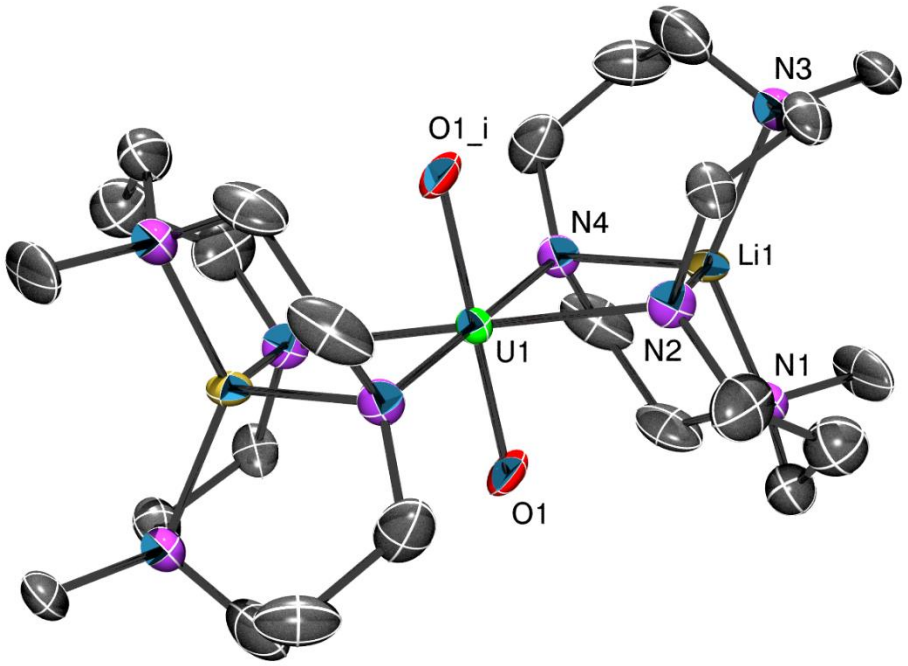

Figure A4.1. Solid-state molecular structure of **4.5** shown with 50% probability ellipsoids. All hydrogen atoms have been omitted for clarity. Selected bond lengths (Å) and angles (°): U1-O1 = 1.805(8), U1-N2 = 2.384(10), U1-N4 = 2.374(11), Li1-N1 = 1.98(2), Li1-N2 = 2.02(2), Li1-N3 = 1.94(2), Li1-N4 = 1.99(2), O1-U-O1_i = 180.0.

X-ray Crystallography. Data for **4.5** were collected on a Bruker KAPPA APEX II diffractometer equipped with an APEX II CCD detector using a TRIUMPH monochromater with a Mo Kα X-ray source (α = 0.71073 Å). The crystals of **4.5** were mounted on a cryoloop under Paratone-N oil, and data were collected at 100(2) K using an Oxford nitrogen gas cryostream system. X-ray data for **4.5** were collected utilizing frame exposures of 15 s. Data collection and cell parameter determinations were conducted using the SMART program.[68] Integration of the data frames and final cell parameter refinement were performed using SAINT software.[69] Absorption corrections of the data were carried out using the multi-scan method SADABS.[70]Subsequent calculations were carried out using SHELXTL.[71] Structure

determination was done using direct or Patterson methods and difference Fourier techniques. All hydrogen atom positions were idealized, and rode on the atom of attachment. Structure solution, refinement, graphics, and creation of publication materials were performed using SHELXTL.[71]

Complex **4.5** contains two cyclam nitrogen atoms and two cyclam carbon atoms in its asymmetric unit that exhibit positional disorder. This disorder was addressed by constraining the affected atoms with the EADP command.

Table A4.1. Crystallographic details for complexes **4.5**.

	4.5
Formula	$C_{24}H_{52}Li_2N_8O_2U$
Crystal Habit, Color	Plate, Orange
Crystal Size (mm)	0.2 × 0.15 × 0.05
MW (g/mol)	736.64
crystal system	Triclinic
space group	P-1
a (Å)	8.595(16)
b (Å)	8.848(15)
c (Å)	11.76(2)
α (°)	68.24(4)
β (°)	85.25(4)
γ (°)	62.08(4)
V ($Å^3$)	730(2)
Z	1
T (K)	100(2)
λ (Å)	0.71073
GOF	1.030
Density (calcd) (Mg/m^3)	1.677
Absorption coefficient (mm^{-1})	5.597
F_{000}	366
Total no Reflections	3022
Unique Reflections	2042
Final R indices*	$R_1 = 0.0560$ $wR_2 = 0.1253$
Largest Diff. peak and hole ($e^- A^{-3}$)	3.377, -2.296

* For [I > 2σ(I)]

4.5.2 NMR spectra

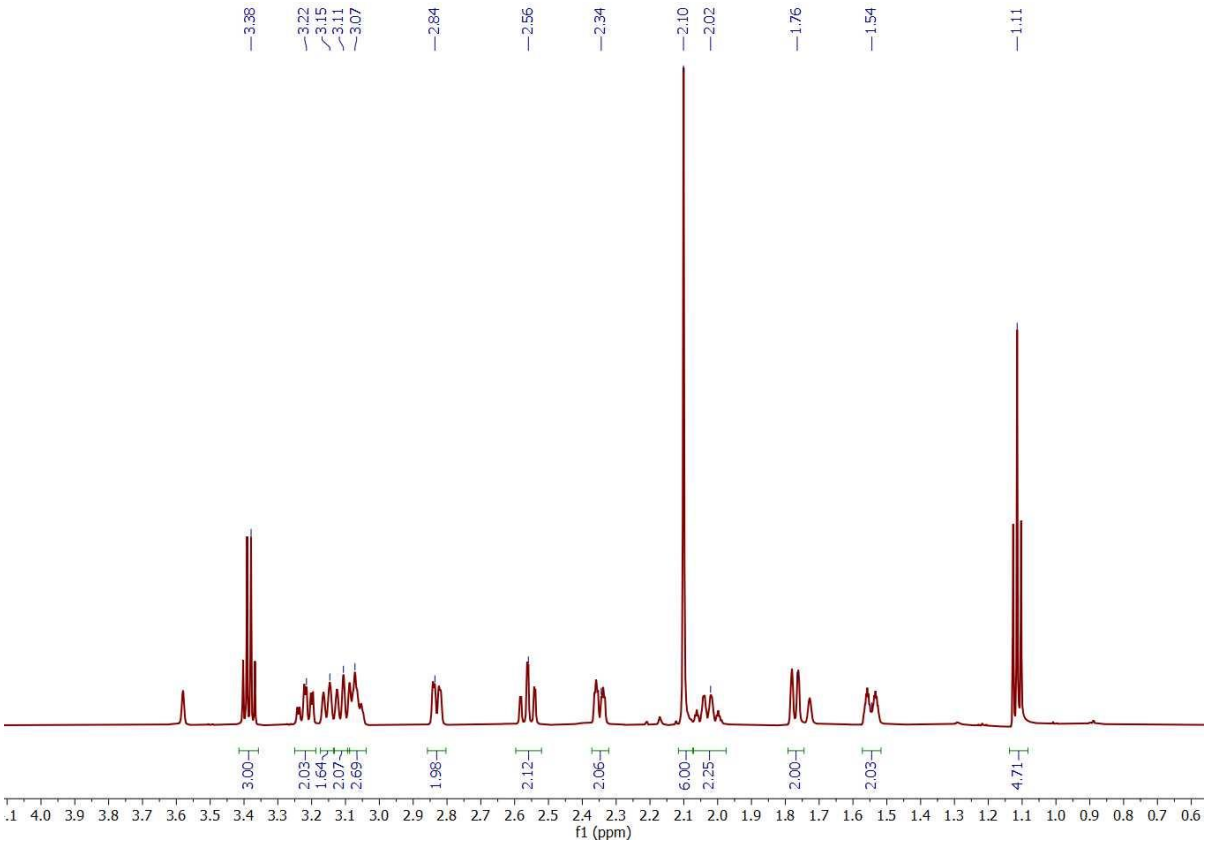

Figure A4.2. ^{1}H NMR spectrum of $[Li(Et_2O)]_2$[1,8-DMC] in THF-d_8.

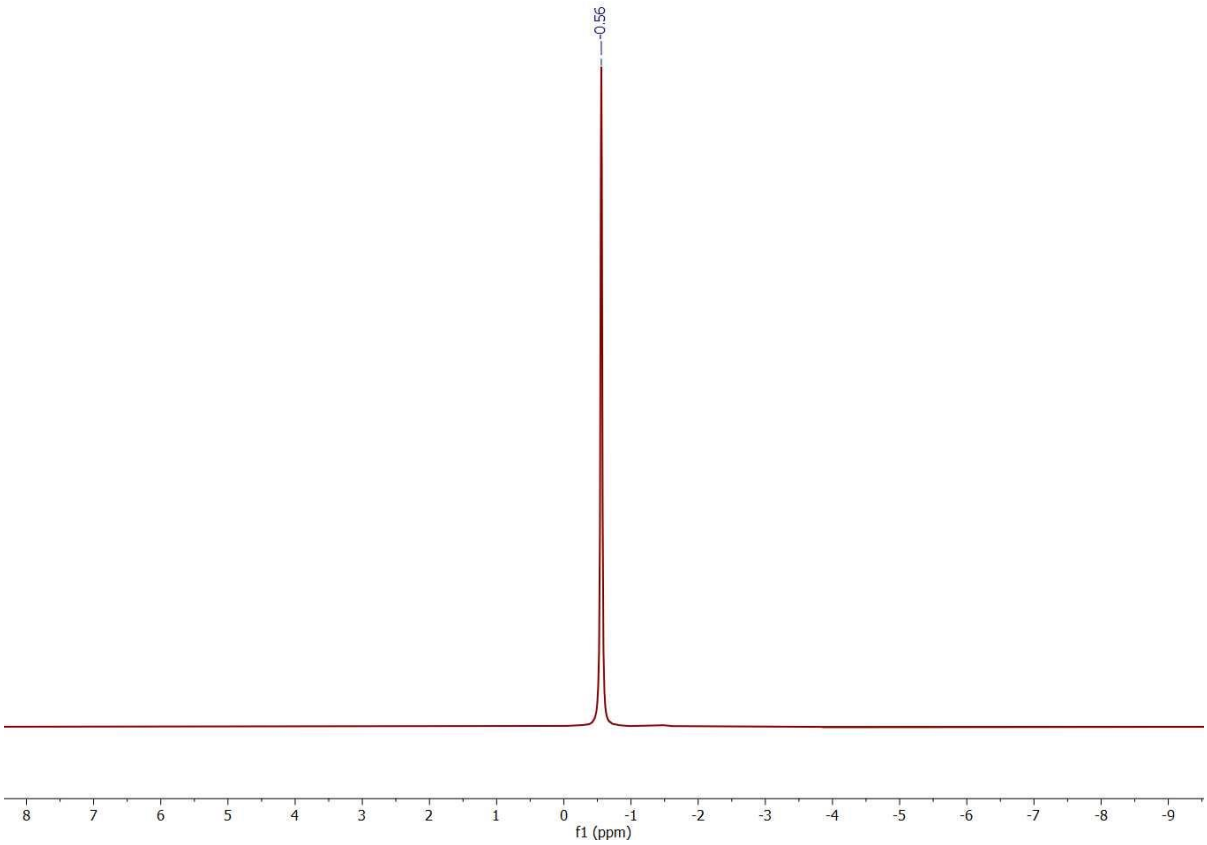

Figure A4.3. $^{7}Li\{^{1}H\}$ NMR spectrum of $[Li(Et_2O)]_2$[1,8-DMC] in THF-d_8.

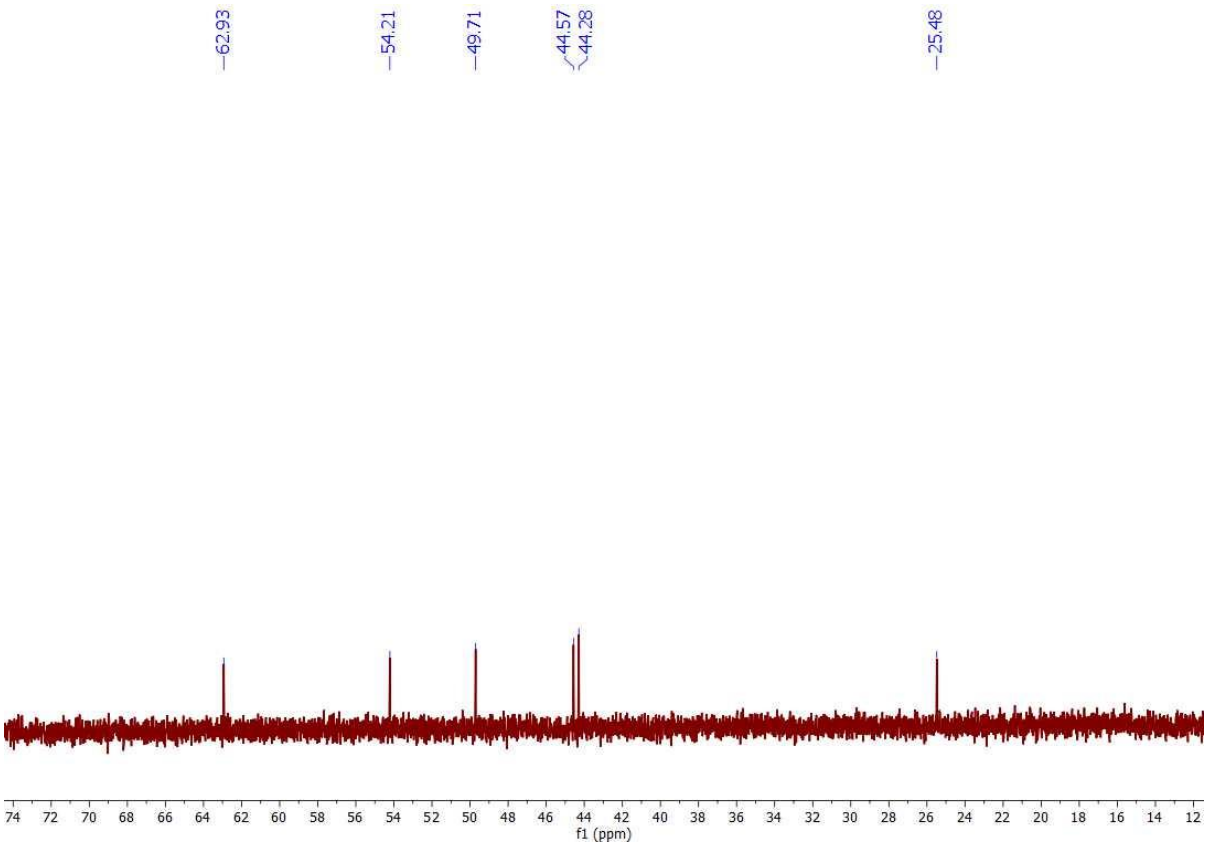

Figure A4.4. $^{13}C\{^{1}H\}$ NMR spectrum of **4.2** in C_6D_6.

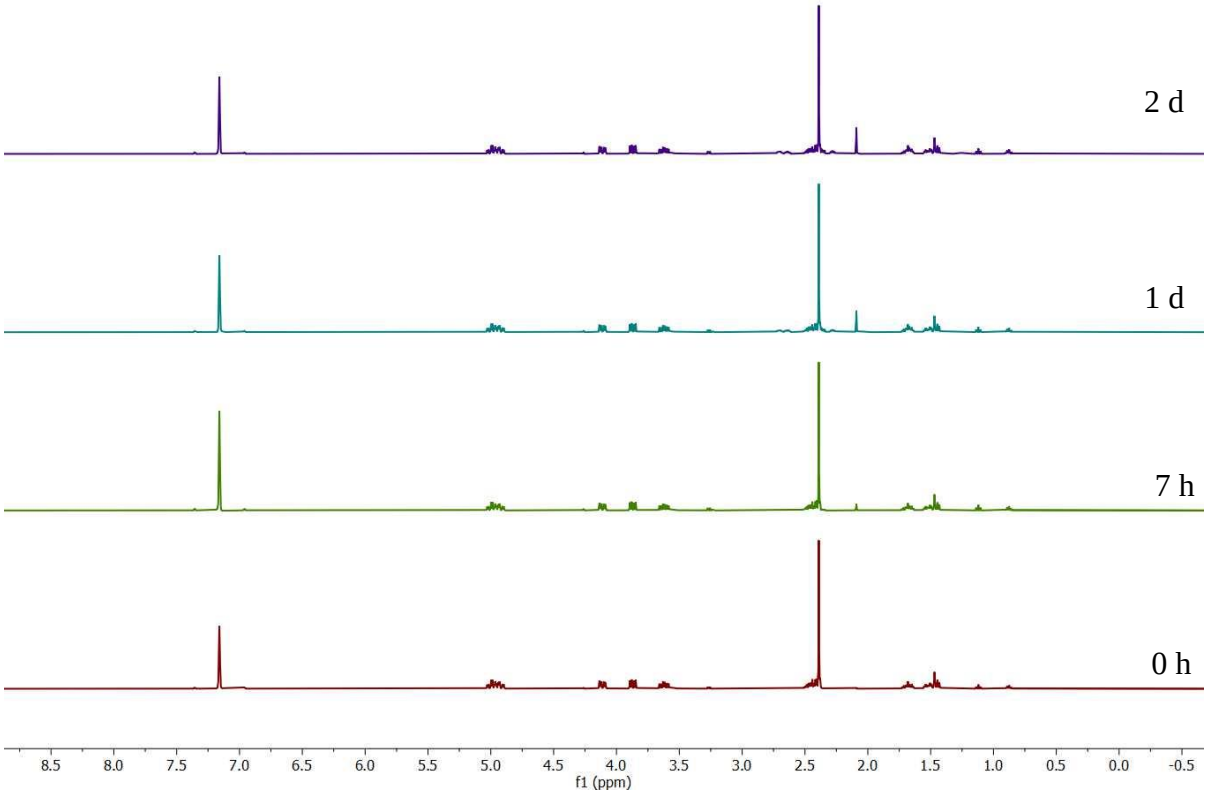

Figure A4.5. ^{1}H NMR spectrum (in C_6D_6) of the monitoring of the thermal stability of **4.2**.

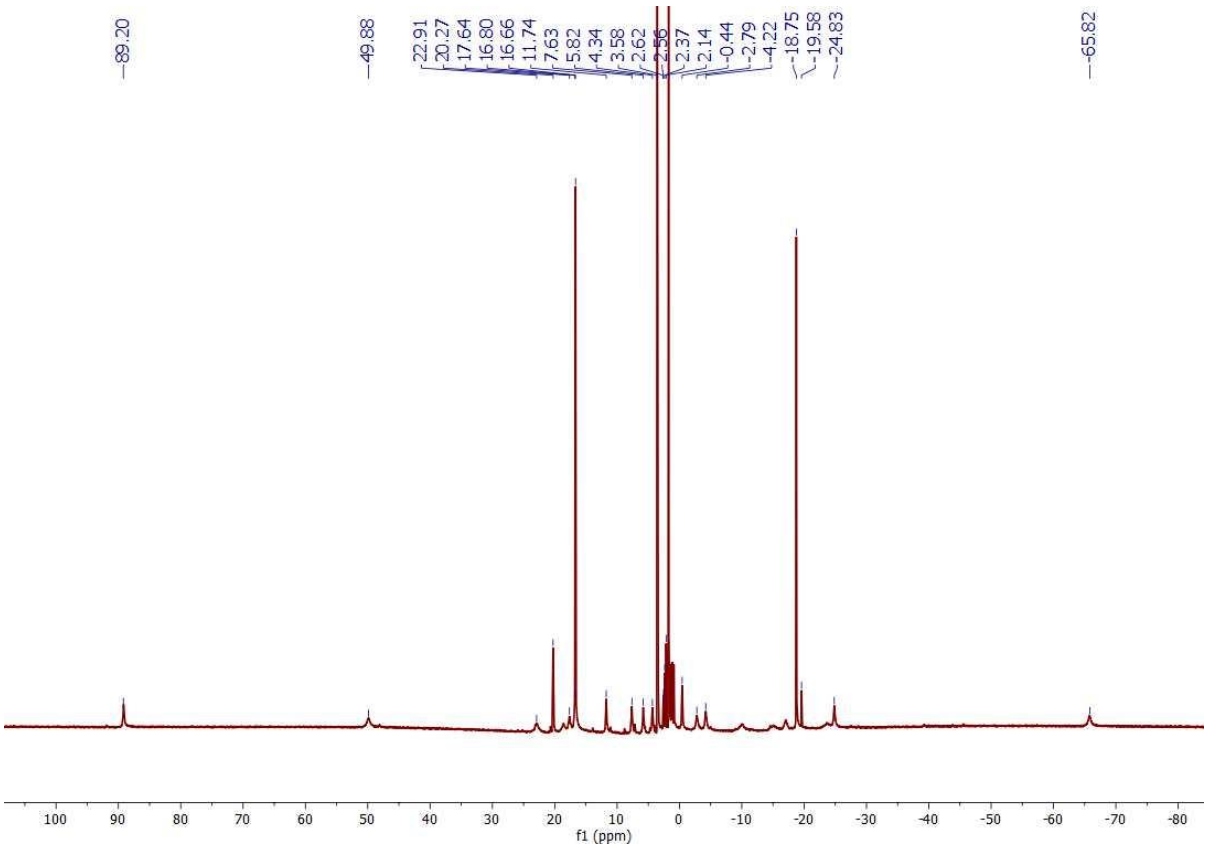

Figure A4.6. ^{1}H NMR spectrum of **4.3** in THF-d_8.

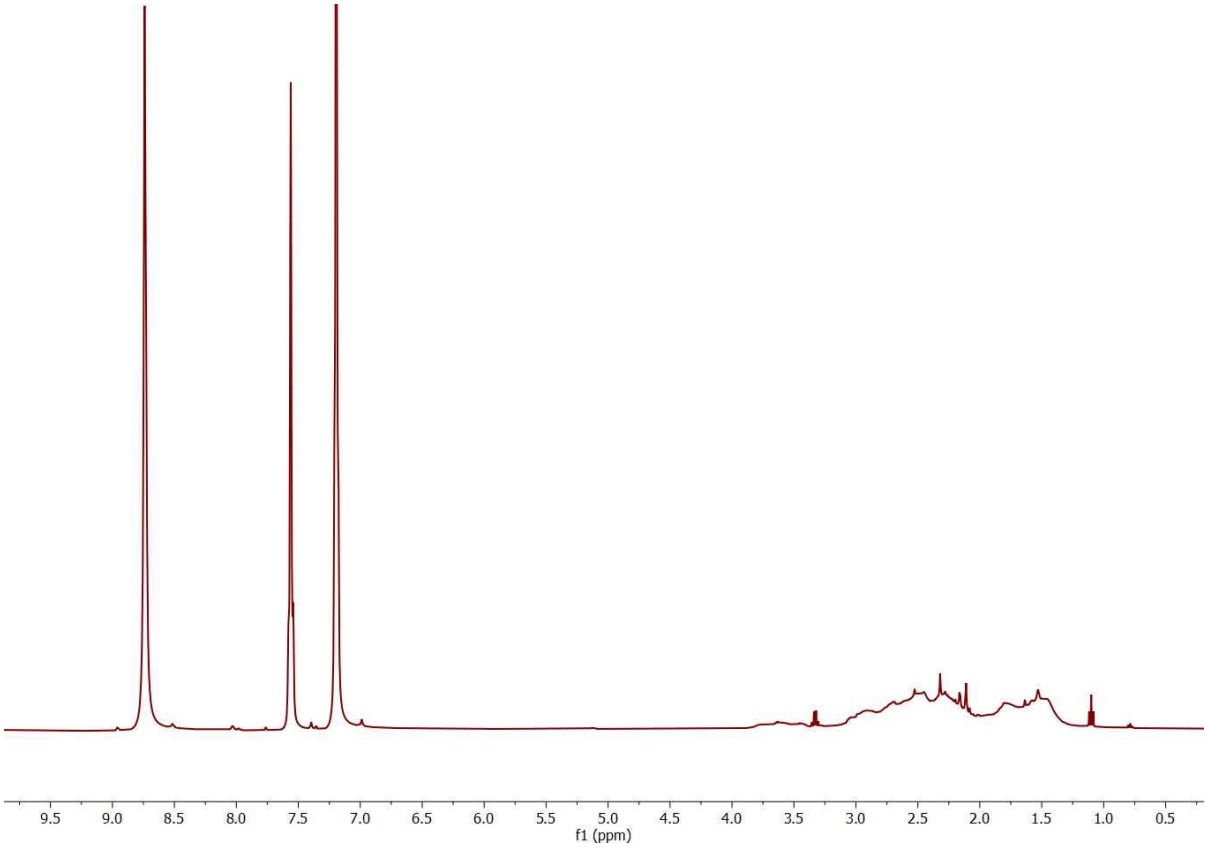

Figure A4.7. ^{1}H NMR spectrum of [Li(py)(1,8-DMC)][I] in py-d_5.

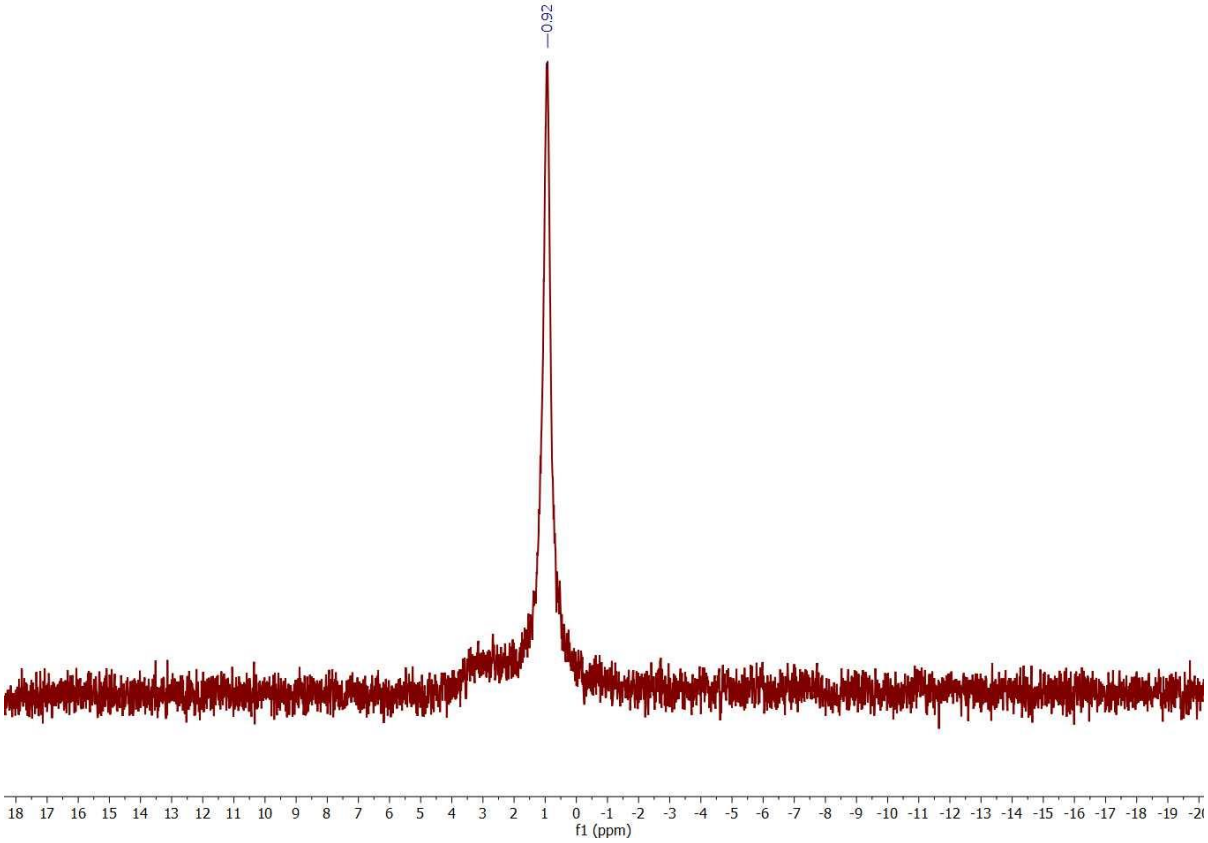

Figure A4.8. $^{7}Li\{^{1}H\}$ NMR spectrum of [Li(py)(1,8-DMC)][I] in py-d_5.

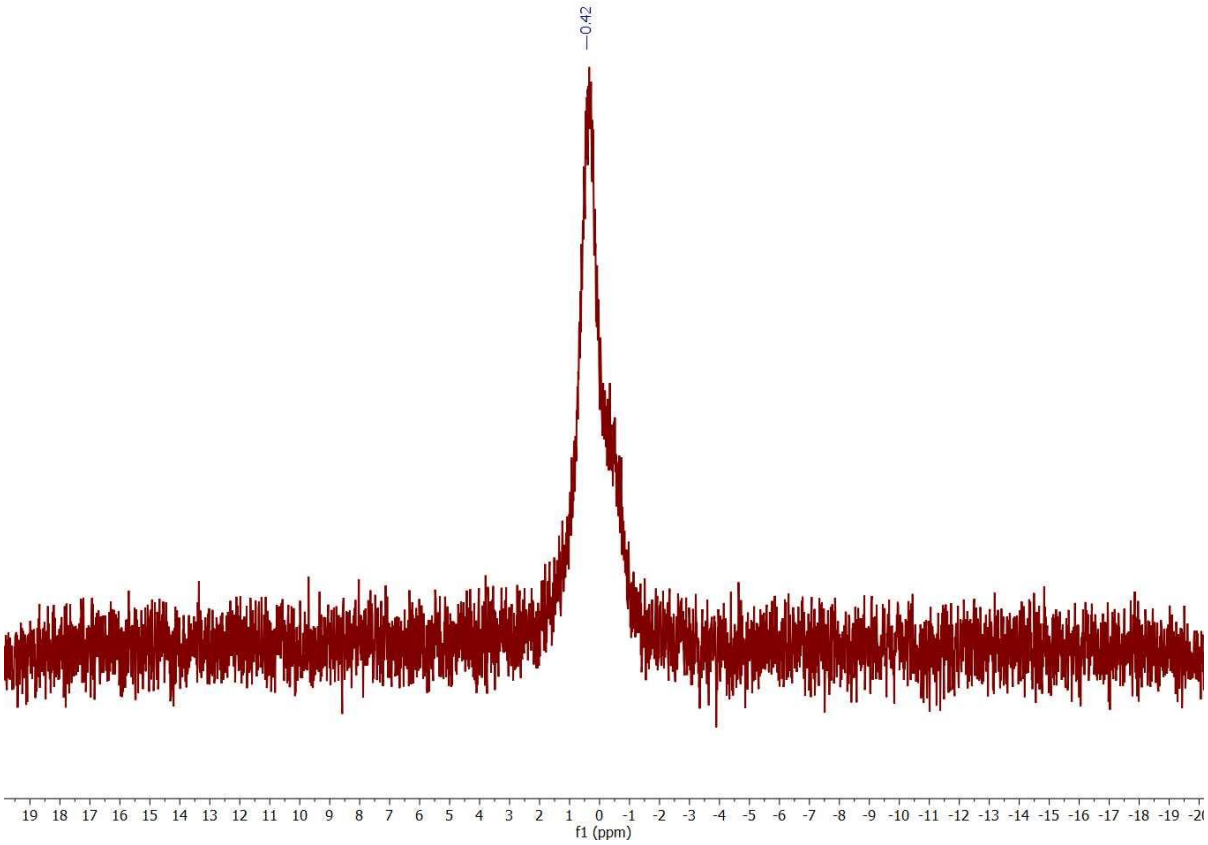

Figure A4.9. *In situ* $^{7}Li\{^{1}H\}$ NMR spectrum (in THF-d_8) of the reaction of **4.3** with I_2 in the presence of 2,2,2-cryptand.

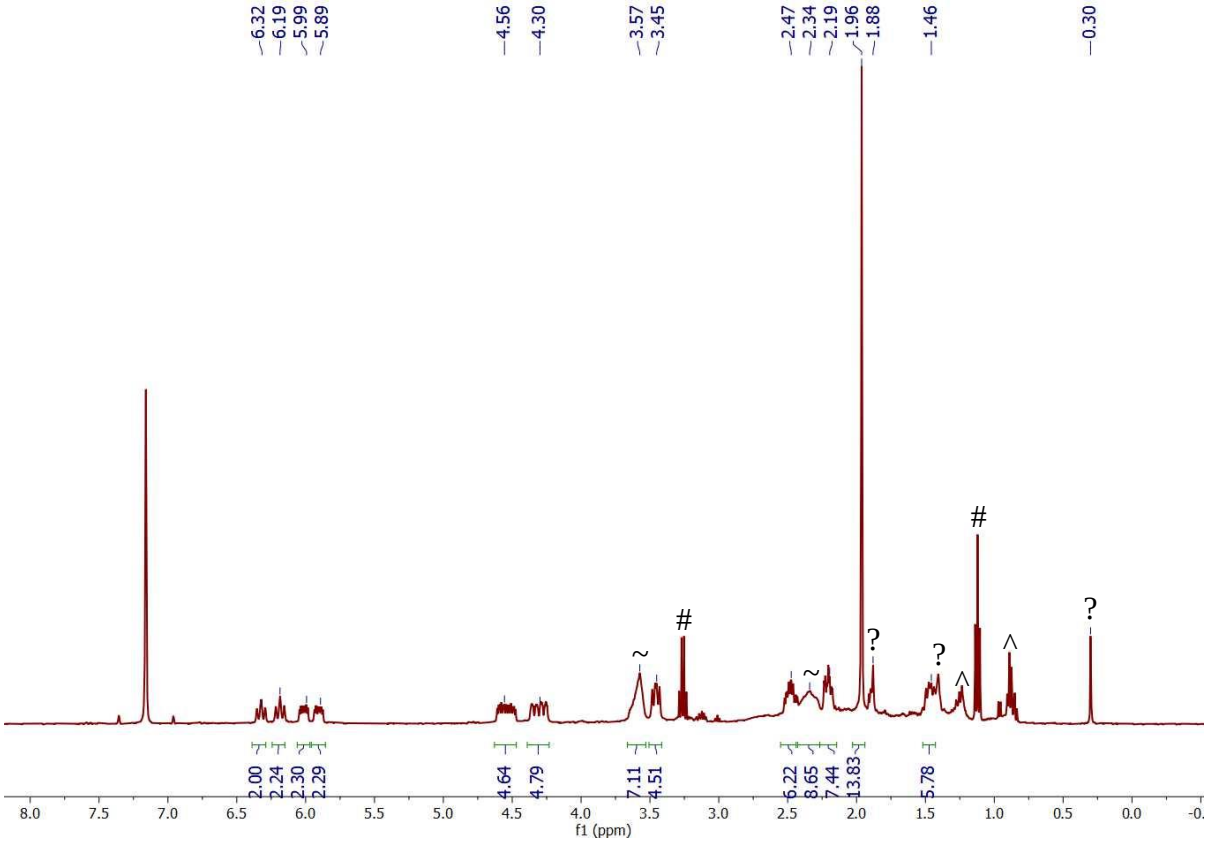

Figure A4.10. ^{1}H NMR spectrum of **4.5** in C_6D_6. ~ indicates resonances assignable to THF, # indicates resonances assignable to Et_2O, ^ indicates resonances assignable to hexanes, and ? indicates resonances assignable to minor unidentified impurities.

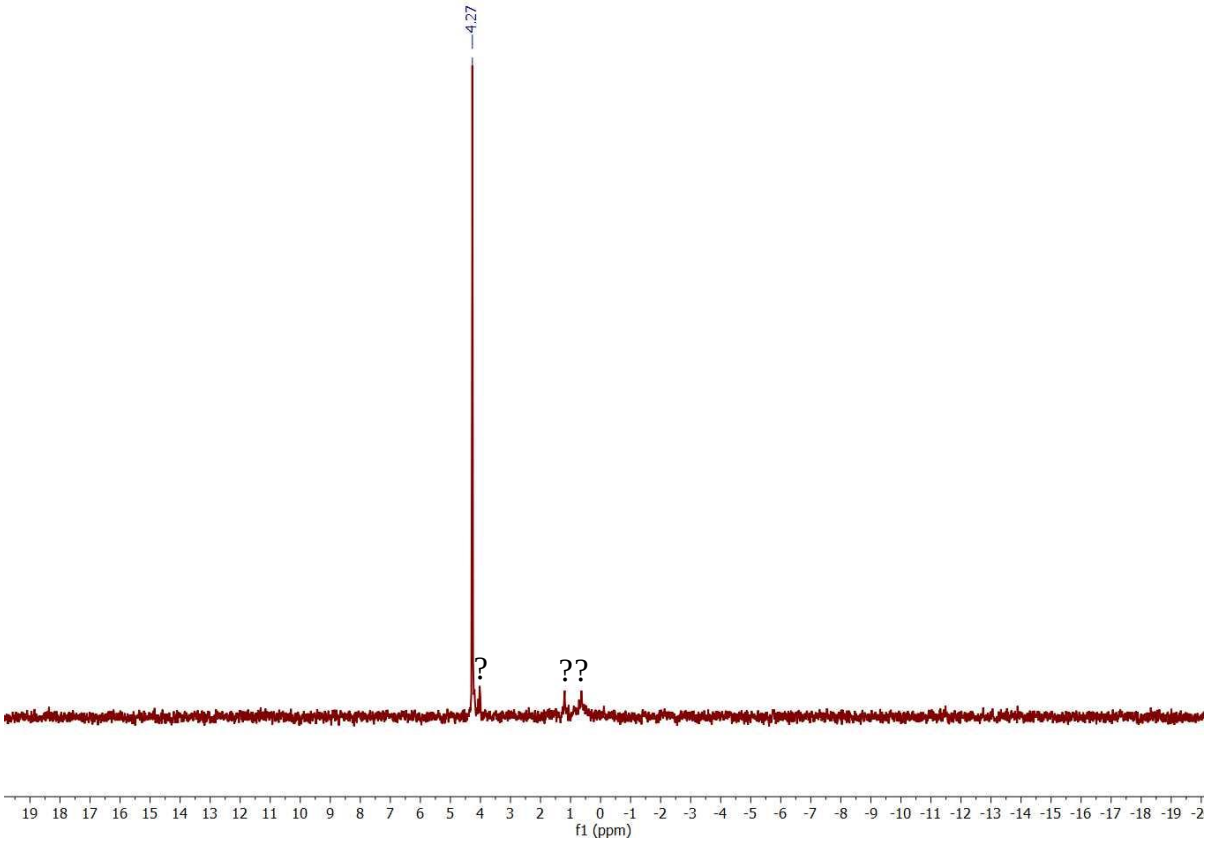

Figure A4.11. $^{7}Li\{^{1}H\}$ NMR spectrum of **4.5** in C_6D_6. ? indicates resonances assignable to minor unidentified impurities.

4.5.3 Cyclic Voltammetry

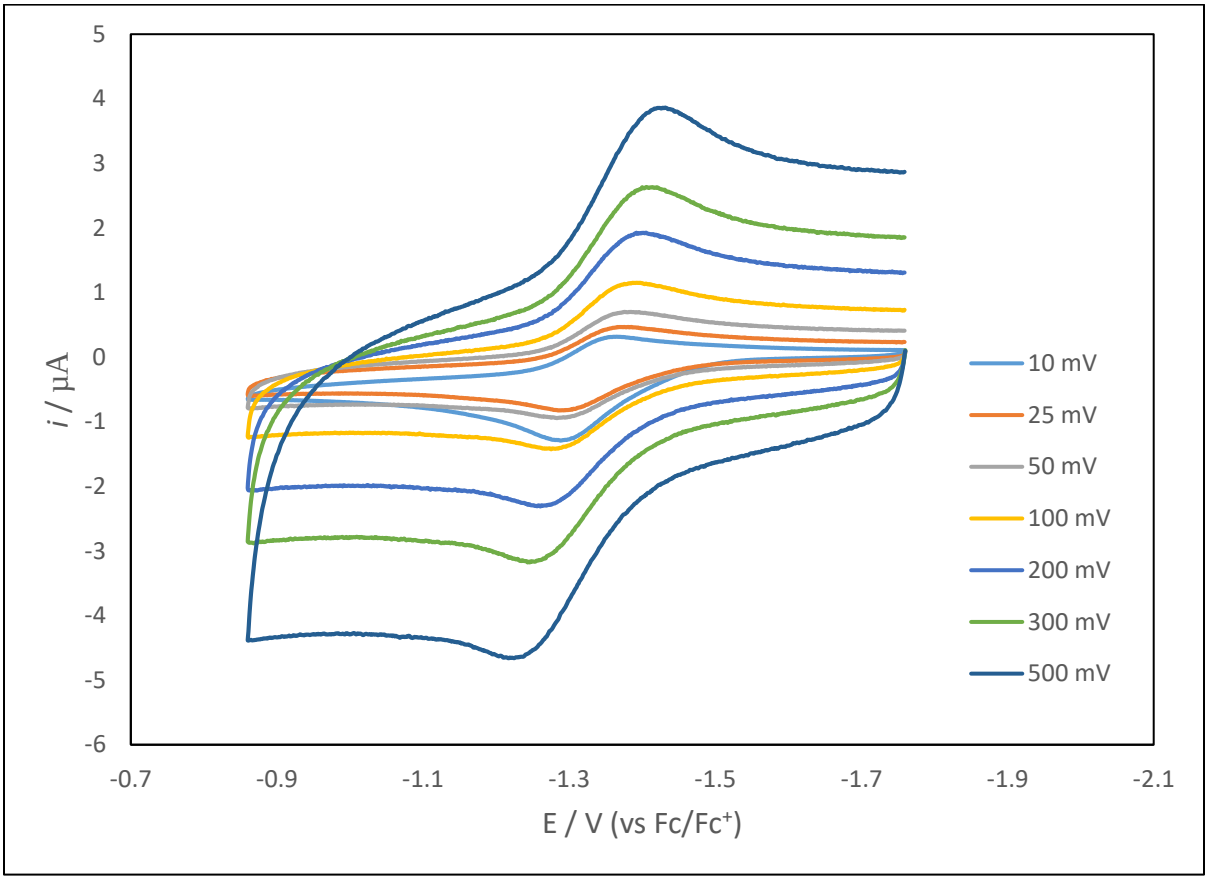

Figure A4.12. Partial cyclic voltammogram of the reversible Ce(III/IV) couple of **4.1** measured in THF with $[NBu_4][PF_6]$ as the supporting electrolyte.

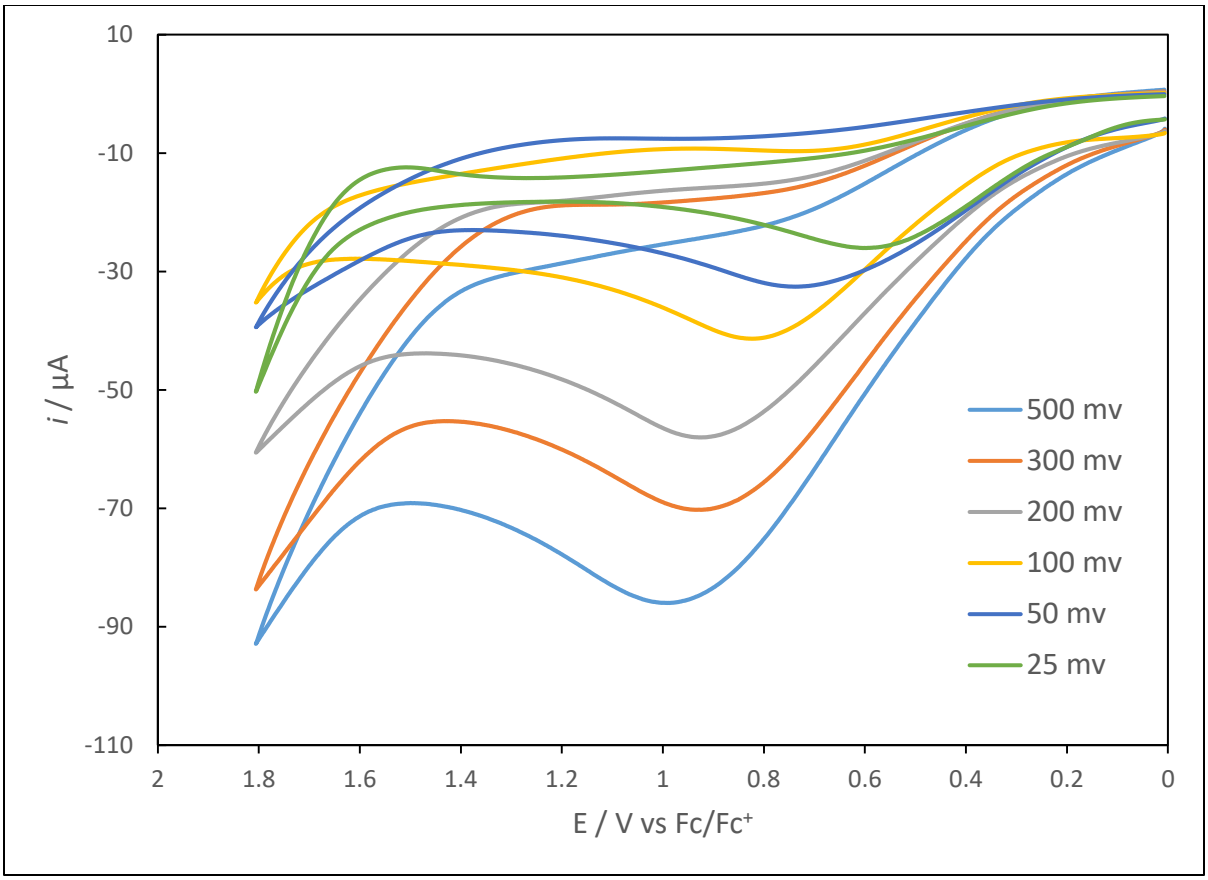

Figure A4.13. Partial cyclic voltammogram of the irreversible oxidation feature of **4.3** measured in THF with $[NBu_4][B(C_6F_5)_4]$ as the supporting electrolyte.

Table A4.2. Electrochemical parameters for [Li][Ce(1,8-DMC)$_2$] (**4.1**) in THF, (vs. Fc/Fc$^+$, [NBu$_4$][PF$_6$] as the supporting electrolyte).

Oxidation Feature	Scan Rate, V/s	$E_{p,a}$, V	$E_{p,c}$, V	$E_{1/2}$, V	ΔE_p, V	$i_{p,a}/i_{p,c}$
	0.010	-1.29	-1.36	-1.33	0.07	1.42
	0.025	-1.29	-1.37	-1.33	0.08	1.48
	0.050	-1.29	-1.38	-1.34	0.09	1.36
	0.100	-1.28	-1.38	-1.33	0.10	1.25
	0.200	-1.27	-1.40	-1.34	0.13	1.19
	0.300	-1.25	-1.41	-1.33	0.16	1.21
	0.500	-1.23	-1.42	-1.33	0.19	1.21

Table A4.3. Electrochemical parameters for [Li][Pr(1,8-DMC)$_2$] (**4.3**) in THF, (vs. Fc/Fc$^+$, [NBu$_4$][B(C$_6$F$_5$)$_4$] as the supporting electrolyte).

Oxidation Feature	Scan Rate, V/s	$E_{p,a}$, V
	0.025	0.586
	0.050	0.731
	0.100	0.821
	0.200	0.924
	0.300	0.917
	0.500	1.006

4.5.4 UV Vis/NIR Spectra

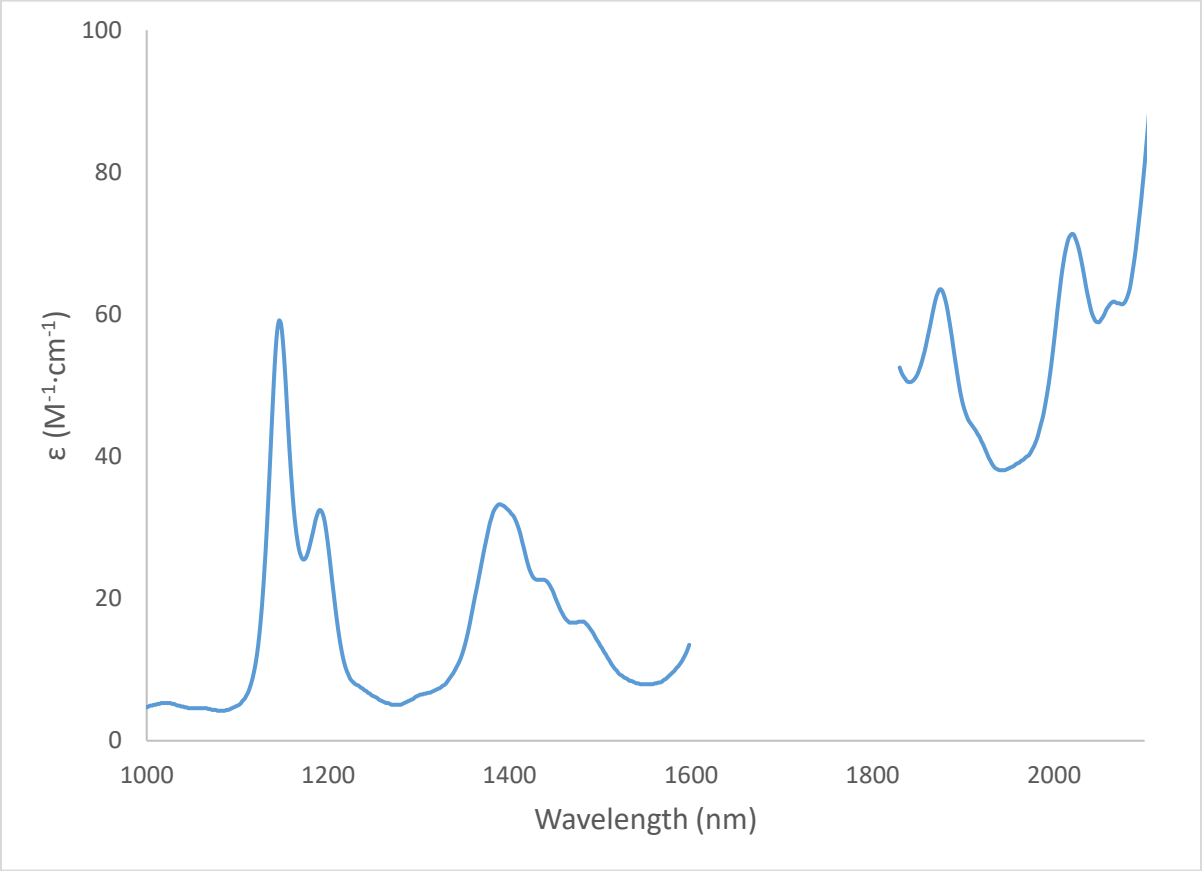

Figure A4.14. NIR spectrum of **4.1** in toluene (8.3 mM).

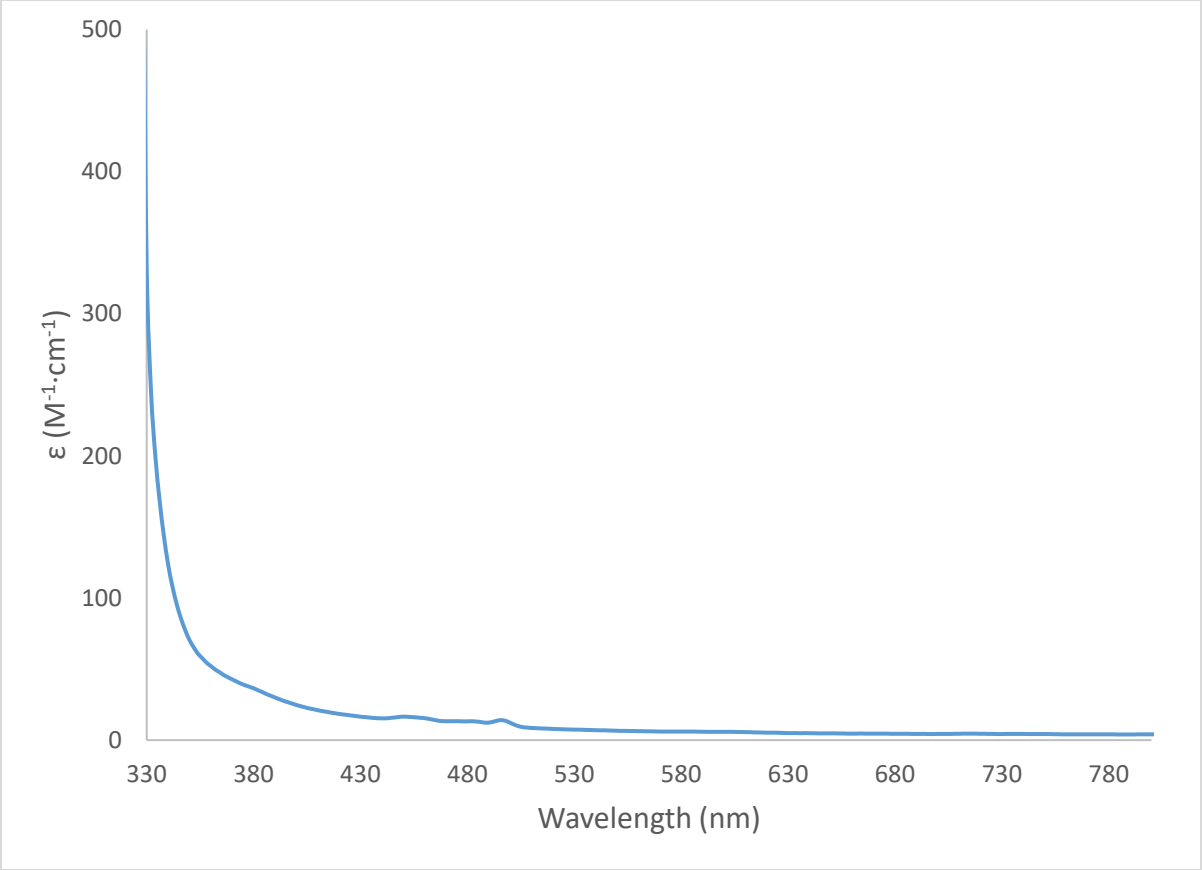

Figure A4.15. UV-Vis spectrum of **4.3** in toluene (10.3 mM).

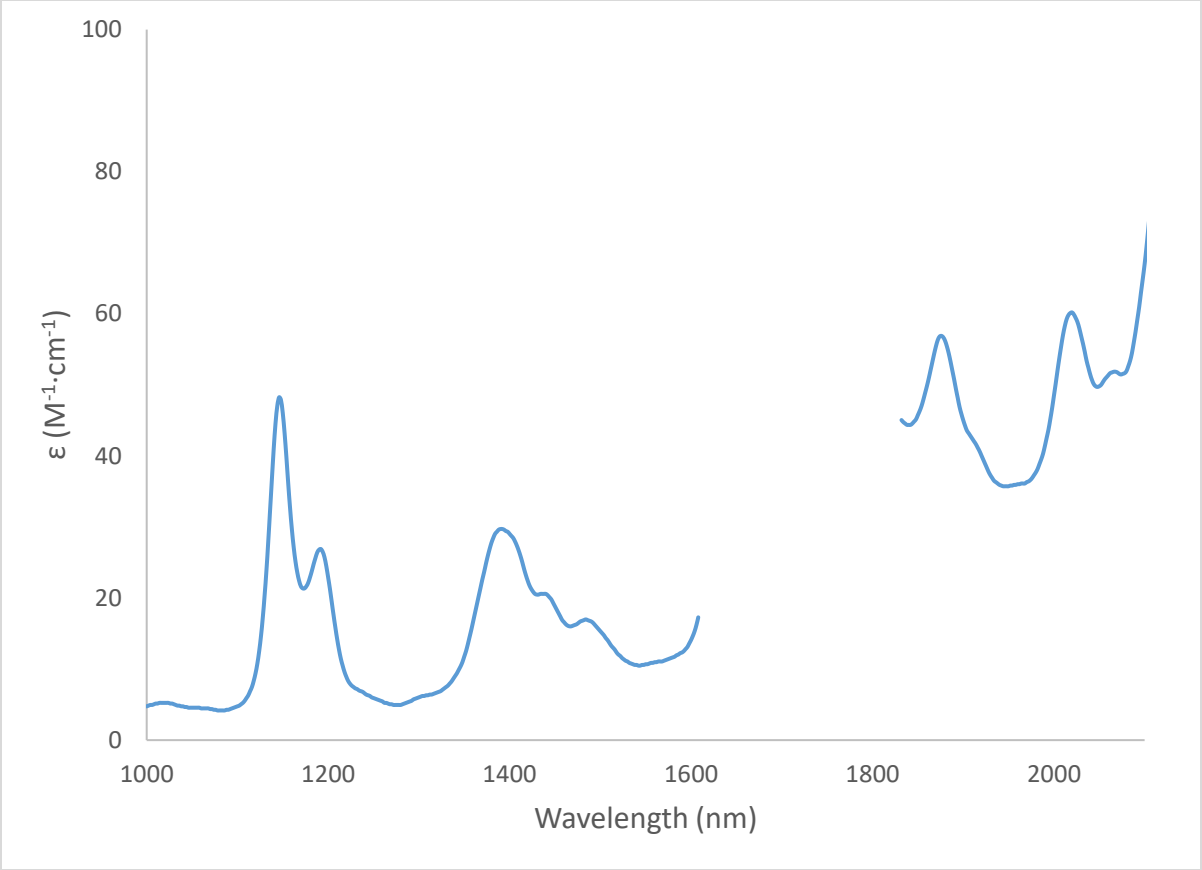

Figure A4.16. NIR spectrum of **4.3** in toluene (10.3 mM).

4.5.5 IR Spectra

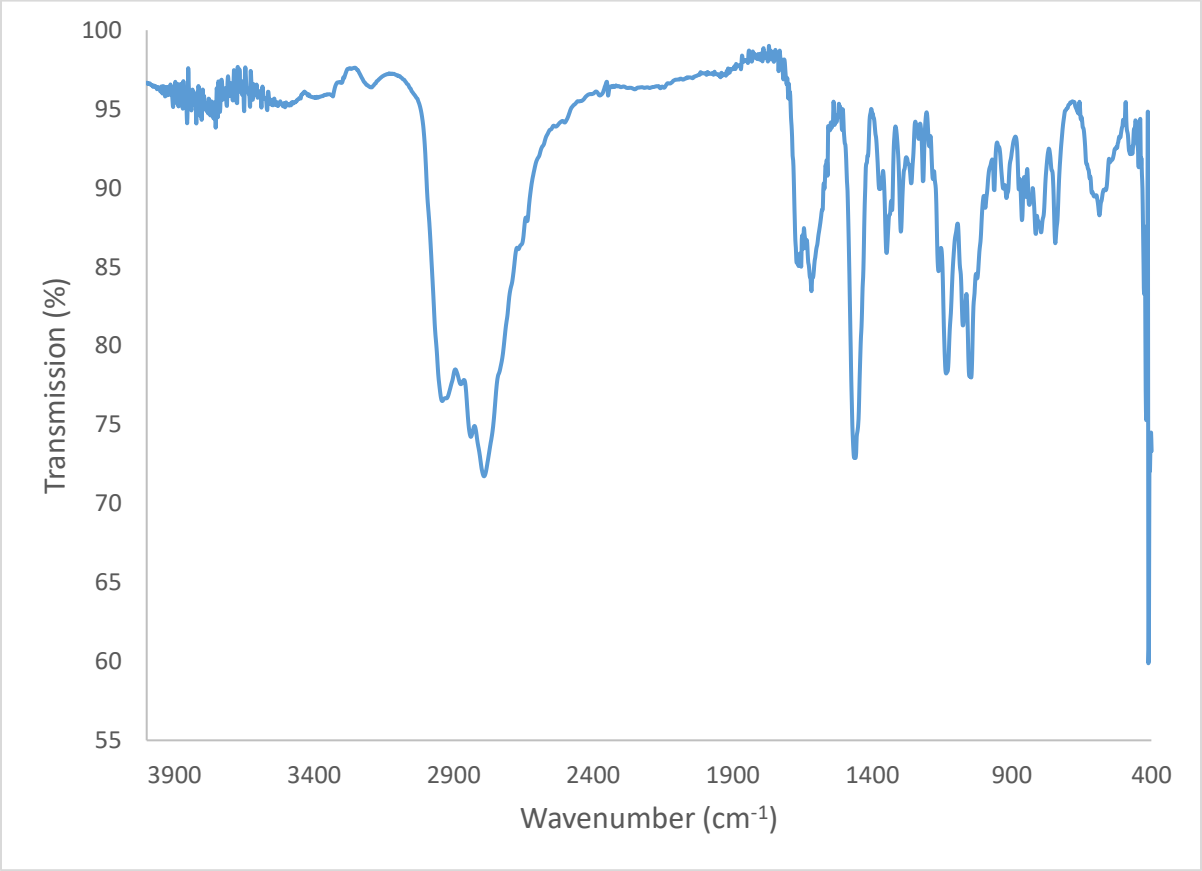

Figure A4.17. IR spectrum of **4.1** (KBr pellet).

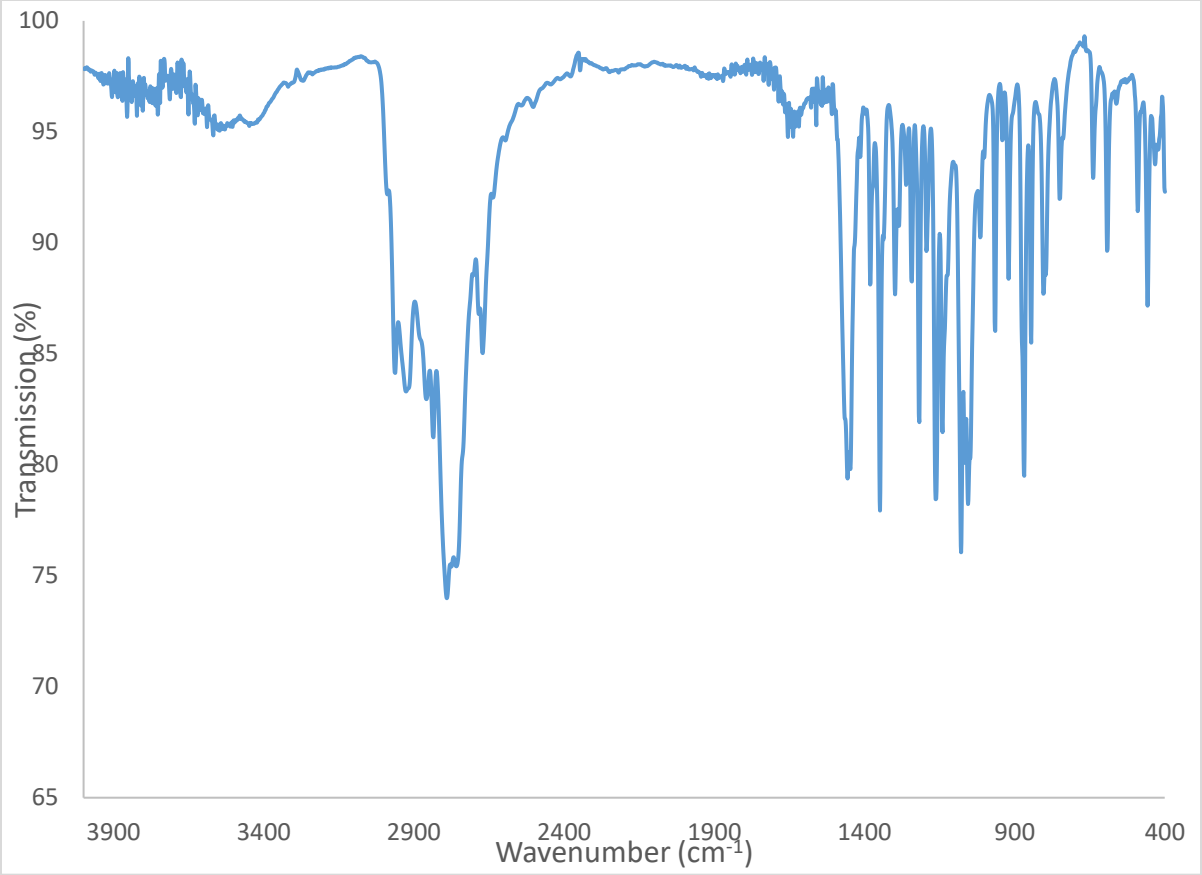

Figure A4.18. IR spectrum of **4.2** (KBr pellet).

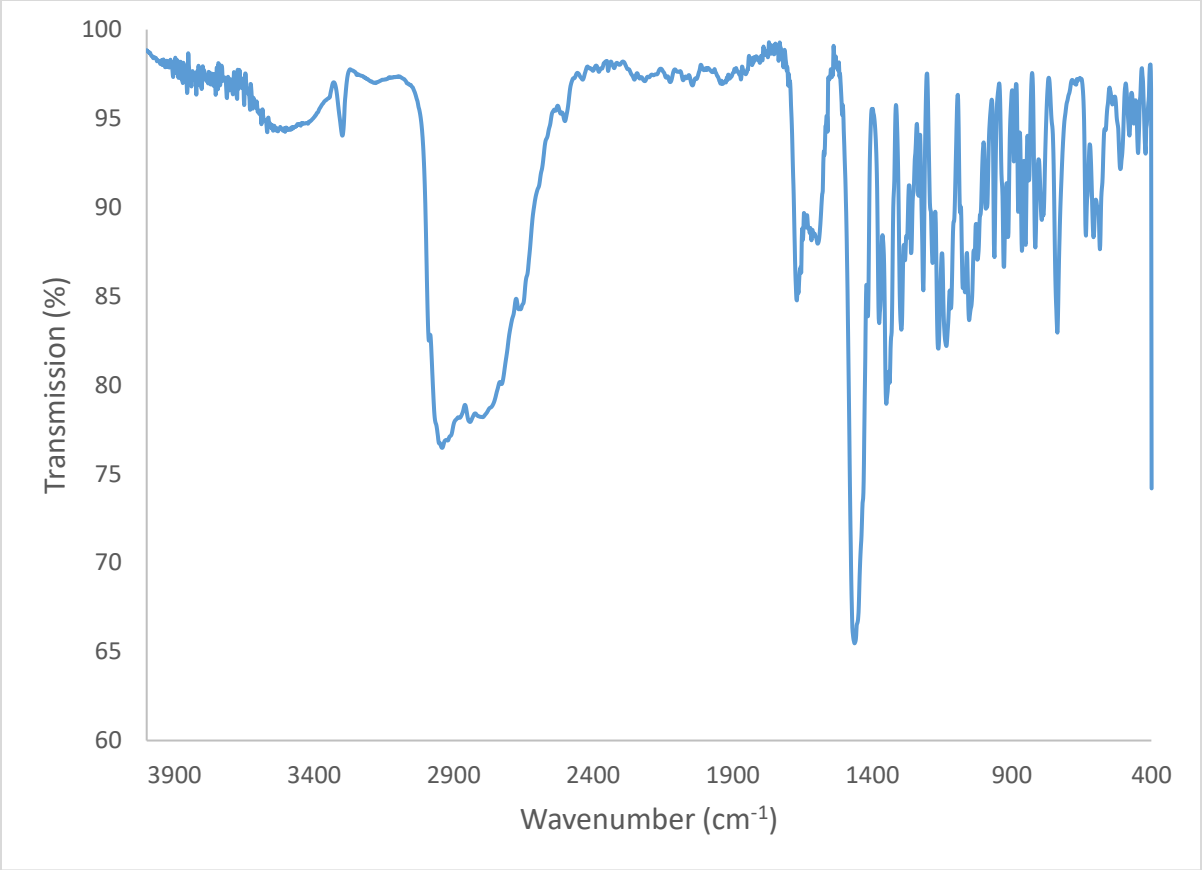

Figure A4.19. IR spectrum of **4.3** (KBr pellet).

4.6 References

(1) Bornhop, D. J.; Hubbard, D. S.; Houlne, M. P.; Adair, C.; Kiefer, G. E.; Pence, B. C.; Morgan, D. L. Fluorescent Tissue Site-Selective Lanthanide Chelate, Tb-PCTMB for Enhanced Imaging of Cancer. *Anal. Chem.* **1999**, *71* (14), 2607–2615.

(2) Bornhop, D. J.; Griffin, J. M. M.; Goebel, T. S.; Sudduth, M. R.; Bell, B.; Motamedi, M. Luminescent Lanthanide Chelate Contrast Agents and Detection of Lesions in the Hamster Oral Cancer Model. *Appl. Spectrosc.* **2003**, *57* (10), 1216–1222.

(3) Hubbard, D. S.; Houlne, M. P.; Kiefer, G.; Janssen, H. F.; Hacker, C.; Bornhop, D. J. Diagnostic Imaging Using Rare-Earth Chelates. *Lasers Med. Sci.* **1998**, *13* (1), 14–21.

(4) Houlne, M. P.; Hubbard, D. S.; Kiefer, G.; Bornhop, D. J. Imaging and Quantitation of a Tissue-Selective Lanthanide Chelate Using an Endoscopic Fluorometer. *J. Biomed. Opt.* **1998**, *3* (2), 145–153.

(5) Manning, H. C.; Goebel, T.; Marx, J. N.; Bornhop, D. J. Facile, Efficient Conjugation of a Trifunctional Lanthanide Chelate to a Peripheral Benzodiazepine Receptor Ligand. *Org. Lett.* **2002**, *4* (7), 1075–1078.

(6) Prata, M. I. M.; Santos, A. C.; Torres, S.; André, J. P.; Martins, J. A.; Neves, M.; García-Martín, M. L.; Rodrigues, T. B.; López-Larrubia, P.; Cerdán, S.; Geraldes, C. F. G. C. Targeting of Lanthanide(III) Chelates of DOTA-Type Glycoconjugates to the Hepatic Asyaloglycoprotein Receptor: Cell Internalization and Animal Imaging Studies. *Contrast Media Mol. Imaging* **2006**, *1* (6), 246–258.

(7) Caravan, P.; Ellison, J. J.; McMurry, T. J.; Lauffer, R. B. Gadolinium(III) Chelates as MRI Contrast Agents: Structure, Dynamics, and Applications. *Chem. Rev.* **1999**, *99* (9), 2293–2352.

(8) Müntener, T.; Kottelat, J.; Huber, A.; Häussinger, D. New Lanthanide Chelating Tags for PCS NMR Spectroscopy with Reduction Stable, Rigid Linkers for Fast and Irreversible Conjugation to Proteins. *Bioconjug. Chem.* **2018**, *29* (10), 3344–3351.

(9) Lee, M. D.; Dennis, M. L.; Swarbrick, J. D.; Graham, B. Enantiomeric Two-Armed Lanthanide-Binding Tags for Complementary Effects in Paramagnetic NMR Spectroscopy. *Chem. Commun.* **2016**, *52* (51), 7954–7957.

(10) Nitsche, C.; Otting, G. Pseudocontact Shifts in Biomolecular NMR Using Paramagnetic Metal Tags. *Prog. Nucl. Magn. Reson. Spectrosc.* **2017**, *98–99*, 20.

(11) Liu, W. M.; Overhand, M.; Ubbink, M. The Application of Paramagnetic Lanthanoid Ions in NMR Spectroscopy on Proteins. *Coord. Chem. Rev.* **2014**, *273–274*, 2.

(12) Müntener, T.; Häussinger, D.; Selenko, P.; Theillet, F. X. In-Cell Protein Structures from 2D NMR Experiments. *J. Phys. Chem. Lett.* **2016**, *7* (14), 2821.

(13) Finney, K.-L. N. A.; Harnden, A. C.; Rogers, N. J.; Senanayake, P. K.; Blamire, A. M.; O'Hogain, D.; Parker, D. Simultaneous Triple Imaging with Two PARASHIFT Probes: Encoding Anatomical, PH and Temperature Information Using Magnetic Resonance Shift Imaging. *Chem. – A Eur. J.* **2017**, *23* (33), 7976–7989.

(14) Senanayake, P. K.; Rogers, N. J.; Finney, K.-L. N. A.; Harvey, P.; Funk, A. M.; Wilson, J. I.; O'Hogain, D.; Maxwell, R.; Parker, D.; Blamire, A. M. A New Paramagnetically Shifted Imaging Probe for MRI. *Magn. Reson. Med.* **2017**, *77* (3), 1307–1317.

(15) Schmidt, R.; Nippe, N.; Strobel, K.; Masthoff, M.; Reifschneider, O.; Castelli, D. D.; Höltke, C.; Aime, S.; Karst, U.; Sunderkötter, C.; Bremer, C.; Faber, C. Highly Shifted Proton MR Imaging: Cell Tracking by Using Direct Detection of Paramagnetic Compounds. *Radiology* **2014**, *272* (3), 785–795.

(16) Harvey, P.; Blamire, A. M.; Wilson, J. I.; Finney, K.-L. N. A.; Funk, A. M.; Senanayake, P. K.; Parker, D. Moving the Goal Posts: Enhancing the Sensitivity of PARASHIFT Proton Magnetic Resonance Imaging and Spectroscopy. *Chem. Sci.* **2013**, *4* (11), 4251–4258.

(17) Palumbo, C. T.; Zivkovic, I.; Scopelliti, R.; Mazzanti, M. Molecular Complex of Tb in the +4 Oxidation State. *J. Am. Chem. Soc.* **2019**, *141* (25), 9827–9831.

(18) Willauer, A. R.; Palumbo, C. T.; Scopelliti, R.; Zivkovic, I.; Douair, I.; Maron, L.; Mazzanti, M. Stabilization of the Oxidation State + IV in Siloxide-Supported Terbium Compounds. *Angew. Chem., Int. Ed.* **2020**, *59*, 3549.

(19) Rice, N. T.; Popov, I. A.; Russo, D. R.; Bacsa, J.; Batista, E. R.; Yang, P.; Telser, J.; La Pierre, H. S. Design, Isolation, and Spectroscopic Analysis of a Tetravalent Terbium Complex. *J. Am. Chem. Soc.* **2019**, *141*, 13222.

(20) Willauer, A. R.; Palumbo, C. T.; Fadaei-Tirani, F.; Zivkovic, I.; Douair, I.; Maron, L.; Mazzanti, M. Accessing the +IV Oxidation State in Molecular Complexes of Praseodymium. *J. Am. Chem. Soc.* **2020**, *142* (12), 5538–5542.

(21) Pham, T. A.; Altman, A. B.; Stieber, S. C. E.; Booth, C. H.; Kozimor, S. A.; Lukens, W. W.; Olive, D. T.; Tyliszczak, T.; Wang, J.; Minasian, S. G.; Raymond, K. N. A Macrocyclic Chelator That Selectively Binds Ln^{4+} over Ln^{3+} by a Factor of 10^{29}. *Inorg. Chem.* **2016**, *55*, 9989.

(22) Deblonde, G. J.-P.; Sturzbecher-Hoehne, M.; Abergel, R. J. Solution Thermodynamic Stability of Complexes Formed with the Octadentate Hydroxypyridinonate Ligand 3,4,3-LI(1,2-HOPO): A Critical Feature for Efficient Chelation of Lanthanide(IV) and Actinide(IV) Ions. *Inorg. Chem.* **2013**, *52* (15), 8805–8811.

(23) Deblonde, G. J.-P.; Sturzbecher-Hoehne, M.; Rupert, P. B.; An, D. D.; Illy, M.-C.; Ralston, C. Y.; Brabec, J.; de Jong, W. A.; Strong, R. K.; Abergel, R. J. Chelation and Stabilization of Berkelium in Oxidation State +IV. *Nat. Chem.* **2017**, *9* (9), 843–849.

(24) Buchler, J. W.; De Cian, A.; Fischer, J.; Hammerschmitt, P.; Löffler, J.; Scharbert, B.; Weiss, R. Metal Complexes with Tetrapyrrole Ligands, LIV: Synthesis, Spectra, Structure, and Redox Properties of Cerium(IV) Bisporphyrinates with Identical and Different Porphyrin Rings in the Sandwich System. *Chem. Ber.* **1989**, *122* (12), 2219–2228.

(25) Williams, U. J.; Mahoney, B. D.; Lewis, A. J.; DeGregorio, P. T.; Carroll, P. J.; Schelter, E. J. Single Crystal to Single Crystal Transformation and Hydrogen-Atom Transfer upon Oxidation of a Cerium Coordination Compound. *Inorg. Chem.* **2013**, *52* (8), 4142–4144.

(26) Berry, J. F.; Bill, E.; Bothe, E.; George, S. D.; Mienert, B.; Neese, F.; Wieghardt, K. An Octahedral Coordination Complex of Iron(VI). *Science (80-.).* **2006**, *312* (5782), 1937 LP – 1941.

(27) Barefield, E. K.; Mocella, M. T. Complexes of Silver(II) and Silver(III) with Macrocyclic Tetraaza Ligands. *Inorg. Chem.* **1973**, *12* (12), 2829–2832.

(28) Maimon, E.; Zilbermann, I.; Cohen, H.; Meyerstein, D. Trivalent Copper Complexes with 1,4,8,11-Tetramethyl-1,4,8,11-Tetraazacyclotetradecane in Aqueous Solutions. A Pulse Radiolysis and Electrochemical Study. *J. Incl. Phenom. Macrocycl. Chem.* **2001**, *41* (1), 179–184.

(29) Zilbermann, I.; Golub, G.; Cohen, H.; Meyerstein, D. Kinetic Stabilization of Trivalent Nickel Complexes with Tertiary Tetraaza Macrocyclic Ligands in Aqueous Solution. *J. Chem. Soc. Dalt. Trans.* **1997**, No. 2, 141–144.

(30) Magull, J.; Simon, A. Zur Reaktion von Makrozyklen Mit Lanthanoiden. I. Die Struktur von [Li(Thf)][$(C_{22}H_{22}N_4)_2$Ce] · THF. *Zeitschrift für Anorg. und Allg. Chemie* **1992**, *615* (9), 77–80.

(31) Assefa, M. K.; Sergentu, D.-C.; Seaman, L. A.; Wu, G.; Autschbach, J.; Hayton, T. W. Synthesis, Characterization, and Electrochemistry of the Homoleptic f Element Ketimide Complexes $[Li]_2[M(N{=}C^tBuPh)_6]$ (M = Ce, Th). *Inorg. Chem.* **2019**, *58* (19).

(32) Seaman, L. A.; Wu, G.; Edelstein, N.; Lukens, W. W.; Magnani, N.; Hayton, T. W. Probing the 5f Orbital Contribution to the Bonding in a U(V) Ketimide Complex. *J. Am. Chem. Soc.* **2012**, *134* (10), 4931–4940.

(33) Seaman, L. A.; Schnaars, D. D.; Wu, G.; Hayton, T. W. Isolation of a Uranyl Amide by "Ate" Complex Formation. *Dalt. Trans.* **2010**, *39* (29), 6635–6637.

(34) Wei, X.-H.; Farwell, J. D.; Hitchcock, P. B.; Lappert, M. F. Synthesis and Structures of Some New Types of Lithium β-Diketiminates. *Dalt. Trans.* **2008**, No. 8, 1073–1080.

(35) Bartlett, R. A.; Chen, H.; Dias, H. V. R.; Olmstead, M. M.; Power, P. P. Synthesis and Spectroscopic and Structural Characterization of the Novel Lithium Borylamide Salts Trans-$[Li(Et_2O)NHBMes_2]_2$, a Dimer, and the Ion Pair $[Li(Et_2O)_3][Mes_2BNBMes_2]$

with a Linear Allene-like, $[R_2B = N = BR_2]^+$ Moiety. *J. Am. Chem. Soc.* **1988**, *110* (2), 446–449.

(36) Bartlett, R. A.; Olmstead, M. M.; Power, P. P.; Sigel, G. A. Synthesis and Spectroscopic and X-Ray Structural Studies of the Mesitylphosphines Ph_2Mes and $PHMes_2$ (Mes = 2,4,6-$Me_3C_6H_2$) and Their Lithium Salts $[Li(THF)_3PHMes]$ and $[\{Li(OEt_2)PMes_2\}_2]$. *Inorg. Chem.* **1987**, *26* (12), 1941–1946.

(37) Yin, H.; Carroll, P. J.; Anna, J. M.; Schelter, E. J. Luminescent Ce(III) Complexes as Stoichiometric and Catalytic Photoreductants for Halogen Atom Abstraction Reactions. *J. Am. Chem. Soc.* **2015**, *137* (29), 9234–9237.

(38) Toth, E.; Brucher, E.; Lazar, I.; Toth, I. Kinetics of Formation and Dissociation of Lanthanide(III)-DOTA Complexes. *Inorg. Chem.* **1994**, *33* (18), 4070–4076.

(39) Casanova, D.; Cirera, J.; Llunell, M.; Alemany, P.; Avnir, D.; Alvarez, S. Minimal Distortion Pathways in Polyhedral Rearrangements. *J. Am. Chem. Soc.* **2004**, *126* (6), 1755–1763.

(40) Pinsky, M.; Avnir, D. Continuous Symmetry Measures. 5. The Classical Polyhedra. *Inorg. Chem.* **1998**, *37* (21), 5575–5582.

(41) Evans, W. J.; Lee, D. S.; Rego, D. B.; Perotti, J. M.; Kozimor, S. A.; Moore, E. K.; Ziller, J. W. Expanding Dinitrogen Reduction Chemistry to Trivalent Lanthanides via the LnZ_3/Alkali Metal Reduction System: Evaluation of the Generality of Forming $Ln_2(\mu\text{-}\eta^2\text{:}\eta^2\text{-}N_2)$ Complexes via LnZ_3/K. *J. Am. Chem. Soc.* **2004**, *126* (44), 14574–14582.

(42) Walter, M. D.; Fandos, R.; Andersen, R. A. Synthesis and Magnetic Properties of Cerium Macrocyclic Complexes with Tetramethyldibenzotetraaza[14]Annulene, $TmtaaH_2$. *New J. Chem.* **2006**, *30* (7), 1065–1070.

(43) Zhang, Y.; Cao, W.; Wang, K.; Jiang, J. Constructing Bis(Porphyrinato) Rare Earth Double-Decker Complexes Involving N-Confused Porphyrin. *Dalt. Trans.* **2014**, *43* (24), 9152–9157.

(44) Benetollo, F.; Bombieri, G.; Calabi, L.; Aime, S.; Botta, M. Structural Variations Across the Lanthanide Series of Macrocyclic DOTA Complexes: Insights into the Design of Contrast Agents for Magnetic Resonance Imaging. *Inorg. Chem.* **2003**, *42* (1), 148–157.

(45) Lamelas, R.; Bastida, R.; Labisbal, E.; Macías, A.; Pereira, T.; Pérez-Lourido, P.; Valencia, L.; Vila, J. M.; Núñez, C. A New Series of Lanthanide Complexes with the Trans-Disubstituted Py_2[18]$AneN_6$ Macrocyclic Ligand: Synthesis, Structures and Properties. *Polyhedron* **2019**, *160*, 180–188.

(46) Gregson, M.; Lu, E.; Mills, D. P.; Tuna, F.; McInnes, E. J. L.; Hennig, C.; Scheinost, A. C.; McMaster, J.; Lewis, W.; Blake, A. J.; Kerridge, A.; Liddle, S. T. The Inverse-Trans-Influence in Tetravalent Lanthanide and Actinide Bis(Carbene) Complexes. *Nat.*

Commun. **2017**, *8* (1), 14137.

(47) Halbach, R. L.; Nocton, G.; Booth, C. H.; Maron, L.; Andersen, R. A. Cerium Tetrakis(Tropolonate) and Cerium Tetrakis(Acetylacetonate) Are Not Diamagnetic but Temperature-Independent Paramagnets. *Inorg. Chem.* **2018**, *57* (12), 7290–7298.

(48) Ashley, A.; Balazs, G.; Cowley, A.; Green, J.; Booth, C. H.; O'Hare, D. Bis(Permethylpentalene)Cerium – Another Ambiguity in Lanthanide Oxidation State. *Chem. Commun.* **2007**, No. 15, 1515–1517.

(49) Ciampolini, M.; Mani, F.; Nardi, N. Visible and Ultraviolet Spectra of Tetraethylammonium Tetrakis(β-Diketonato) Cerate(III) and Tetrakis(β-Diketonato)Cerium(IV) Complexes. *J. Chem. Soc. Dalt. Trans.* **1977**, No. 14, 1325–1328.

(50) Buchler, J. W.; De Cian, A.; Fischer, J.; Kihn-Botulinski, M.; Paulus, H.; Weiss, R. Metal Complexes with Tetrapyrrole Ligands. 40. Cerium(IV) Bis(Octaethylporphyrinate) and Dicerium(III) Tris(Octaethylporphyrinate): Parents of a New Family of Lanthanoid Double-Decker and Triple-Decker Molecules. *J. Am. Chem. Soc.* **1986**, *108* (13), 3652–3659.

(51) Schneider, D.; Spallek, T.; Maichle-Mossmer, C.; Tornroos, K. W.; Anwander, R. Cerium Tetrakis(Diisopropylamide) - a Useful Precursor for Cerium(Iv) Chemistry. *Chem. Commun.* **2014**, *50* (94), 14763–14766.

(52) Hitchcock, P. B.; Lappert, M. F.; Protchenko, A. V. Facile Formation of a Homoleptic Ce(Iv) Amide via Aerobic Oxidation. *Chem. Commun.* **2006**, No. 33, 3546–3548.

(53) Williams, U. J.; Schneider, D.; Dorfner, W. L.; Maichle-Mossmer, C.; Carroll, P. J.; Anwander, R.; Schelter, E. J. Variation of Electronic Transitions and Reduction Potentials of Cerium(Iv) Complexes. *Dalt. Trans.* **2014**, *43* (43), 16197–16206.

(54) Bai, F.; Xu, J.; Su, H.; Gu, X. Hydrogen Bond and π–π Interactions in a 3D Supramolecular Structure Containing 1D Helical Chains. *Zeitschrift für Anorg. und Allg. Chemie* **2012**, *638* (14), 2361–2364.

(55) Wedler, M.; Knösel, F.; Pieper, U.; Stalke, D.; Edelmann, F. T.; Amberger, H.-D. Sterische Cyclopentadienyl-Äquivalente in Der Chemie Der f-Elemente: Monomere, Homoleptische Lanthanid(III)-Tris[N,N′-Bis(Trimethylsilyl)-Benzamidinate]. *Chem. Ber.* **1992**, *125* (10), 2171–2181.

(56) Castro, G.; Regueiro-Figueroa, M.; Esteban-Gómez, D.; Bastida, R.; Macías, A.; Pérez-Lourido, P.; Platas-Iglesias, C.; Valencia, L. Exceptionally Inert Lanthanide(III) PARACEST MRI Contrast Agents Based on an 18-Membered Macrocyclic Platform. *Chem. – A Eur. J.* **2015**, *21* (51), 18662–18670.

(57) Jia, D.; Zhu, A.; Jin, Q.; Zhang, Y.; Jiang, W. Solvothermal Syntheses, and Characterization of $[Ln(En)_4(SbSe_4)]$ (Ln=Ce, Pr) and $[Ln(En)_4]SbSe_4 \cdot 0.5en$ (Ln=Eu,

Gd, Er, Tm, Yb): The Effect of Lanthanide Contraction on the Crystal Structures of Lanthanide Selenid. *J. Solid State Chem.* **2008**, *181* (9), 2370–2377.

(58) Hrobárik, P.; Kaupp, M.; Riedel, S. Is Allred's $[Hg(Cyclam)]^{3+}$ a True Mercury(III) Complex? *Angew. Chemie Int. Ed.* **2008**, *47* (45), 8631–8633.

(59) Deming, R. L.; Allred, A. L.; Dahl, A. R.; Herlinger, A. W.; Kestner, M. O. Tripositive Mercury. Low Temperature Electrochemical Oxidation of 1,4,8,11-Tetraazacyclotetradecanemercury(II) Tetrafluoroborate. *J. Am. Chem. Soc.* **1976**, *98* (14), 4132–4137.

(60) Mao, J.; Jin, Z. Synthesis and Structure Characterization of Lanthanum [2,2,2]Cryptates, $[LaCl[2,2,2](H_2O)]$ $Cl_2 \cdot H_2O$ and $[La(CF_3SO_3)[2,2,2](DMF)](CF_3SO_3)_2$. *Polyhedron* **1994**, *13* (2), 319–323.

(61) Yee, E. L.; Gansow, O. A.; Weaver, M. J. Electrochemical Studies of Europium and Ytterbium Cryptate Formation in Aqueous Solution. Effects of Varying the Metal Oxidation State upon Cryptate Thermodynamics and Kinetics. *J. Am. Chem. Soc.* **1980**, *102* (7), 2278–2285.

(62) Yang, G.; Liu, S.; Jin, Z. Coordination Chemistry and Structure Characterization of $C_{18}H_{36}O_6N_2Eu_2(NO_3)_6 \cdot H_2O$. *Inorganica Chim. Acta* **1987**, *131* (1), 125–128.

(63) Benetollo, F.; Bombieri, G.; Cassol, A.; De Paoli, G.; Legendziewicz, J. Coordination Chemistry of Lanthanides with Cryptands. An X-Ray and Spectroscopic Study of the Complex $Nd_2(NO_3)_6$ $[C_{18}H_{36}O_6N_2] \cdot H_2O$. *Inorganica Chim. Acta* **1985**, *110* (1), 7–13.

(64) Ciampolini, M.; Dapporto, P.; Nardi, N. Syntheses of Some Lanthanoid Complexes with 4,7,13,16,21,24-Hexaoxa-1,10-Diazabicyclo[8.8.8]Hexacosane. Crystal Structure of a Europium(III) Perchlorate Derivative. *J. Chem. Soc. Chem. Commun.* **1978**, No. 18, 788–789.

(65) Huang, W.; Brosmer, J. L.; Diaconescu, P. L. In Situ Synthesis of Lanthanide Complexes Supported by a Ferrocene Diamide Ligand: Extension to Redox-Active Lanthanide Ions. *New J. Chem.* **2015**, *39* (10), 7696–7702.

(66) Harris, R. K.; Becker, E. D.; Cabral De Menezes, S. M.; Granger, P.; Hoffman, R. E.; Zilm, K. W. Further Conventions for NMR Shielding and Chemical Shifts. *Pure Appl. Chem.* **2008**, *80* (1), 59–84.

(67) Harris, R. K.; Becker, E. D.; Cabral De Menezes, S. M.; Goodfellow, R.; Granger, P. NMR Nomenclature. Nuclear Spin Properties and Conventions for Chemical Shifts. *Pure Appl. Chem.* **2001**, *73* (11), 1795–1818.

(68) SMART Apex II. Version 2. Bruker AXS Inc.: Madison, WI 2005.

(69) SAINT Software User's Guide. Version 7. Bruker AXS Inc.: Madison, WI 2005.

(70) Sheldrick, G. M. SADABS. University of Gottingen, Germany 2005.

(71) SHELXTL PC. Version 6. Bruker AXS Inc.: Madison, WI 2005.

(72) Mungur, S. A.; Liddle, S. T.; Wilson, C.; Sarsfield, M. J.; Arnold, P. L. Bent Metal Carbene Geometries in Amido N-Heterocyclic Carbene Complexes. *Chem. Commun.* **2004**, *2*, 2738.

(73) Burns, C. J.; Clark, D. L.; Donohoe, R. J.; Duval, P. B.; Scott, B. L.; Tait, C. D. A Trigonal Bipyramidal Uranyl Amido Complex: Synthesis and Structural Characterization of $[Na(THF)_2][UO_2(N(SiMe_3)_2)_3]$. *Inorg. Chem.* **2000**, *39*, 5464.

(74) Vaughn, A. E.; Barnes, C. L.; Duval, P. B. X-Ray Crystal Structure of Trans-$UO_2(N(SiMe_3)_2)_2(THF)_2$: One in a Series of Uranyl(VI) Complexes Supported by Bis(Trimethylsilyl)Amido Ligands. *J. Chem. Crystallogr.* **2007**, *37*, 779.

(75) Pattenaude, S. A.; Coughlin, E. J.; Collins, T. S.; Zeller, M.; Bart, S. C. Expanding the Library of Uranyl Amide Derivatives: New Complexes Featuring the Tert-Butyldimethylsilylamide Ligand. *Inorg. Chem.* **2018**, *57* (8), 4543–4549.

(76) Cobb, P. J.; Moulding, D. J.; Ortu, F.; Randall, S.; Wooles, A. J.; Natrajan, L. S.; Liddle, S. T. Uranyl-Tri-Bis(Silyl)Amide Alkali Metal Contact and Separated Ion Pair Complexes. *Inorg. Chem.* **2018**, *57* (11), 6571–6583.

(77) Arnold, P. L.; Jones, G. M.; Odoh, S. O.; Schreckenbach, G.; Magnani, N.; Love, J. B. Strongly Coupled Binuclear Uranium–Oxo Complexes from Uranyl Oxo Rearrangement and Reductive Silylation. *Nat. Chem.* **2012**, *4*, 221

Chapter 5. Oxidation of the 14-Membered Macrocycle Dibenzotetramethyltetraaza[14]annulene upon Ligation to the Uranyl Ion

Portions of this work were published in:

Assefa, M.K.; Pedrick, E.A.; Wakefield, M.E.; Wu, G.; Hayton, T.W. *Inorg. Chem.* **2018**, *57*, 8317-8324.

http://pubs.acs.org/articlesonrequest/AOR-p96HYWZRuSfEfGg5nnqt

5.1 Introduction

The exceptional stability the ubiquitous uranyl ion (*trans*-UO_2^{2+}) is evidenced by its resistance to oxo functionalization and its low oxidation potential.[1, 2] For example, the standard U(VI)/U(V) redox potential for UO_2^{2+}(aq) is -0.35 V (vs. Fc/Fc^+),[3] and the coordination of anionic donor ligands only serves to lower this potential. Interestingly, disruption of the O=U=O bonding framework within uranyl has been shown to effect its U(VI)/U(V) and U(V)/U(IV) redox potentials.[4, 5] For example, Hayton and co-workers demonstrated that a 700 mV shift of the U(VI)/U(V) couple in $[UO_2(^{Ar}acnac)_2]$ ($^{Ar}acnac$ = Ar*N*C(Ph)CHC(Ph)*O*; Ar = 3,5-^{t}Bu$_2$C$_6$H$_3$) to more oxidizing potentials can be achieved by coordination of $B(C_6F_5)_3$ to one of the O_{yl} ligands.[6] Schelter and co-workers also demonstrated that coordination of potassium cations to the uranyl oxo ligands in $[K(toluene)]_2[UO_2(NPh(3,5\text{-}(CF_3)_2C_6H_3))_4]$ resulted in a similar shift of the U(VI)/U(V) couple to more oxidizing potentials when compared to that observed for the cation-anion separated pair $[K(16\text{-crown-}6)]_2[UO_2(NPh(3,5\text{-}(CF_3)_2C_6H_3))_4]$.[7] Both results can be interpreted as a consequence of a decrease in electron donation from the oxo ligands to the U^{6+} ion.

Scheme 5.1. Previous attempts to generate a *cis*-uranyl complex (Scheme 5.1a is adopted from Ref 8 and Scheme 5.1b is adopted from Ref 9)

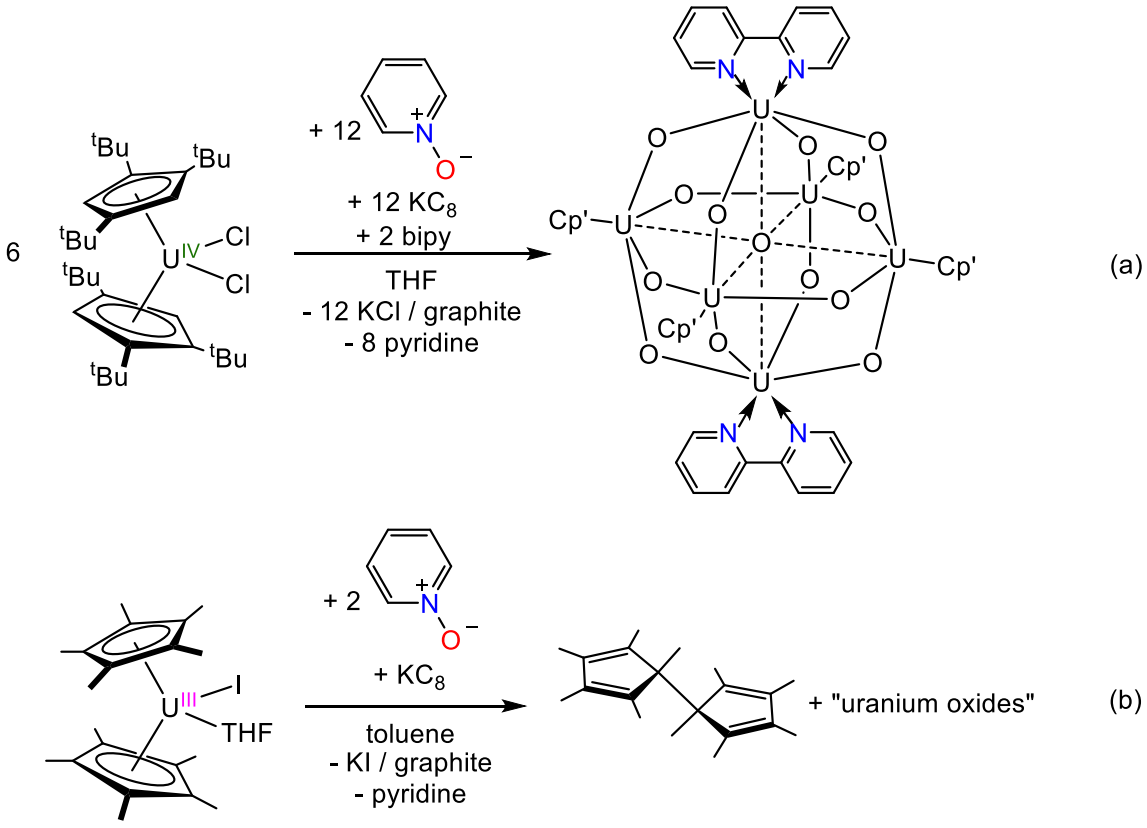

It is also possible that the U(VI)/U(V) redox potential in uranyl can be affected by a *trans*/*cis* isomerization. For example, reaction of Cp'$_2$UCl$_2$ (Cp' = 1,2,4-^{t}Bu$_3$C$_5$H$_2$) with KC$_8$ and pyridine-*N*-oxide, in THF, results in formation of the U(V) oxo cluster, Cp'$_4$(bipy)$_2$U$_6$O$_{13}$, the protonated ligand Cp'H, as well as the dimer (Cp')$_2$.[8] This result was rationalized by a mechanism that invokes the initial formation of a cis uranyl intermediate, *cis*-Cp'$_2$UO$_2$, which quickly decomposed via homolytic Cp'-U cleavage. A similarly putative *cis*-Cp*$_2$UO$_2$ intermediate has been predicted for the reaction between Cp*$_2$UI(THF) and pyridine-*N*-oxide in the presence of KC$_8$.[9] Therefore, it is likely that a *trans*/*cis* isomerization disrupts the O-U-O bonding framework in uranyl, which makes the U^{6+} center a stronger oxidant. Incidentally,

the successful synthesis of a stable *cis*-uranyl complex could provide unique insights into 5f orbital involvement in the U-O bonds[1] and the Inverse Trans Influence (ITI).[10-13]

Scheme 5.2. Perturbation of the O-U-O angle in uranyl by ligation to macrocyclic ligands (Scheme adopted from Ref 14)

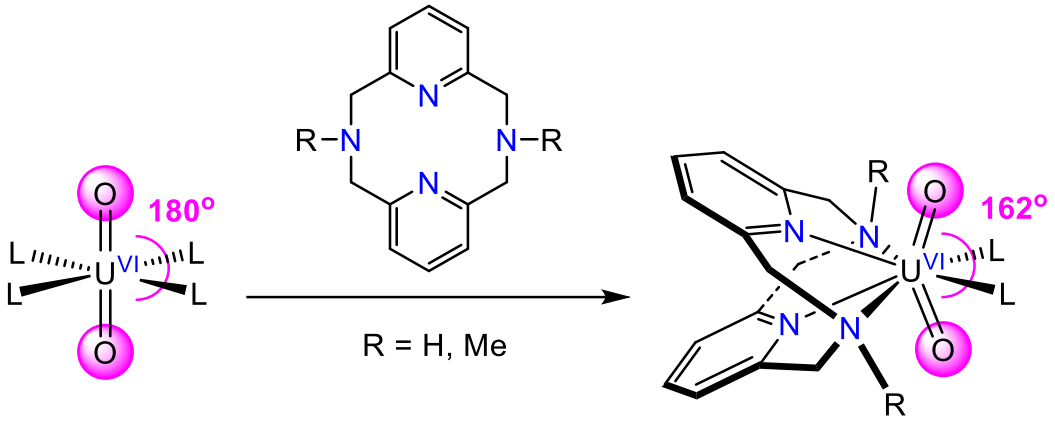

I have been exploring the coordination of macrocylic ligands to the uranyl ion in an effort to effect a *trans*/*cis* isomerization of the uranyl fragment. Hayton and co-workers recently reported that ligation of the neutral 12-membered macrocycles, $^{H}N_4$ ($^{H}N_4$ = 2,11-diaza[3,3](2,6) pyridinophane) and $^{Me}N_4$ ($^{Me}N_4$ = *N,N'*-dimethyl-2,11-diaza[3,3](2,6) pyridinophane), to *trans*-uranyl did, in fact, result in deformation of the O-U-O angle, most likely due to the steric pressure applied by the macrocycle backbone on the O-U-O fragment.[14] However, the changes were only small; the observed O-U-O angles in this series of complexes ranged from 162 - 168°. More recently, Hayton and co-workers attempted to synthesize *cis*-$[UO_2(tmtaa)]$ by reaction of the 14-membered macrocycle, $tmtaaH_2$ ($tmtaaH_2$ = dibenzotetramethyltetraaza[14]annulene), with $UO_2(N(SiMe_3)_2)_2(THF)_2$. This reaction resulted in clean formation of *trans*-$[UO_2(\kappa^2\text{-}tmtaaH)(N(SiMe_3)_2)(THF)]$,[15] which is the product of partial protonation of the bis(silylamide) starting material. Surprisingly,

thermolysis of this product did not drive the protonolysis to completion, revealing that $HN(SiMe_3)_2$ elimination does not provide sufficient driving force to cause the desired trans/cis oxo isomerization. Drawing on these results, I have turned my attention to the alkali metal salts of $(tmtaa)^{2-}$ on the assumption that MCl (M = Li, K) salt elimination would provide the requisite thermodynamic driving force for uranyl isomerization. In this regard, Arnold and co-workers recently reported that reaction of $M_2(tmtaa)$ (M = Li, K) with UX_4 afforded $[UX_2(tmtaa)]_n$ (X = Cl, n = 2; X = I, n = 1), demonstrating that κ^4 coordination of $(tmtaa)^{2-}$ to uranium was indeed possible.[16] Herein, I report my attempts to ligate $(tmtaa)^{2-}$ to the *trans*-uranyl ion in order to promote a *trans*/*cis* isomerization.

5.2 Results and Discussion

5.2.1 Synthesis and Characterization of $[Li(THF)_3][Li(THF)_2][(UO_2Cl_2)_2(tmtaa)]$ (5.1)

Addition of $Li_2(tmtaa)$ to 1 equiv of $[UO_2Cl_2(THF)_3]$ in THF resulted in formation of a deep brown solution, from which a few red-brown crystals of $[Li(THF)_3][Li(THF)_2][(UO_2Cl_2)_2(tmtaa)]$ (**5.1**) were isolated in modest yield (eq 5.1). Complex **5.1** features an unexpected M:L ratio of 2:1. It can be synthesized rationally by reaction of $Li_2(tmtaa)$ with 2 equiv of $[UO_2Cl_2(THF)_3]$. Under these conditions it can be isolated in 44% yield as an impure, red-brown solid. Complex **5.1** is insoluble in hexanes and Et_2O, but it is soluble in THF. It quickly decomposes in the presence of pyridine, dichloromethane, and acetonitrile. It is temperature sensitive in both solution and the solid-state, and attempts to purify the isolated material by recrystallization only led to further decomposition. While I have been unable to identify the products of decomposition, I surmise

that the temperature sensitivity of **5.1** is a consequence of a facile $(tmtaa)^{2-}$ oxidation reaction, as revealed by the reactivity of $K_2(tmtaa)$ with $[UO_2Cl_2(THF)_3]$ (see below).

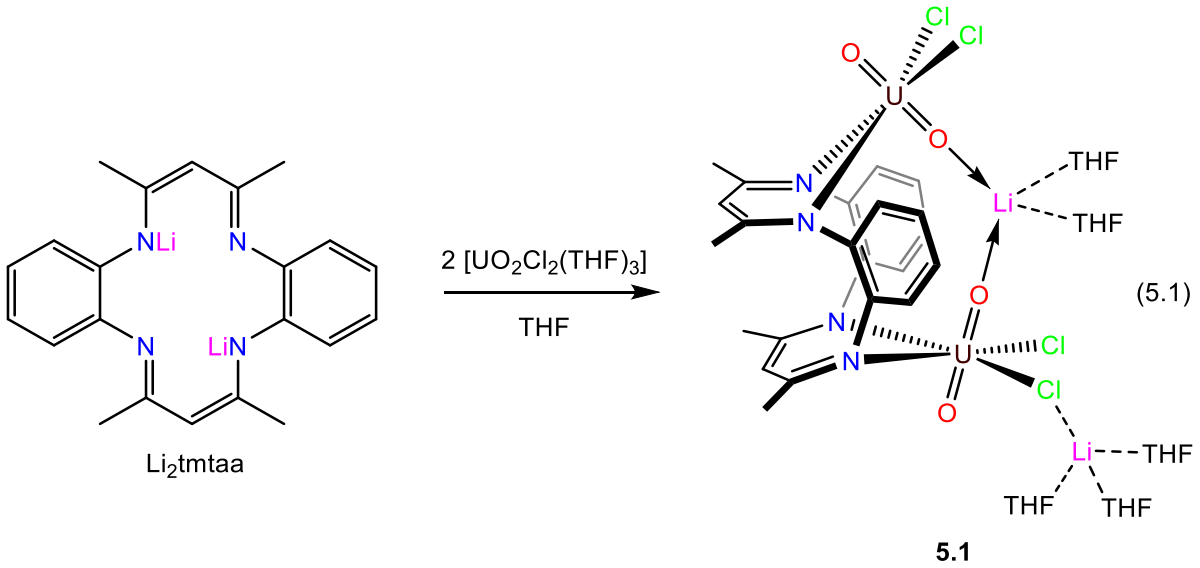

Complex **5.1** crystallizes in the monoclinic space group $P2_1/n$ (Figure 5.1). Its solid-state molecular structure reveals two $[UO_2Cl_2]$ fragments that are bridged via a highly puckered $(tmtaa)^{2-}$ ligand. A similar tmtaa binding mode is observed in $[(Rh(CO)_2)_2(tmtaa)]$.[17] Its structure also resembles that of the bis(uranyl) complex, $[\{UO_2(py)\}_2(L^A)]$ (L^A = anthracenyl-bridged polypyrrolic macrocycle), recently reported by Arnold and co-workers.[18] The two uranyl fragments in **5.1** are linear (O-U-O = 176.8(3)° and 178.0(3) °), while the U-O_{yl} bond lengths (1.764(6)-1.792(6) Å) are typical of the uranyl fragment.[19] The U-N_{tmtaa} bond lengths (2.383(7)-2.419(7) Å) in complex **5.1** are also comparable to the U-N bond lengths in other uranyl β-diketiminate complexes.[20-22] The most notable structural feature of **5.1** is the presence of a $[Li(THF)_2]^+$ cation that coordinates to both of the endo oxo ligands. The Li-O_{yl} distances 1.925(15) and 1.884(16) Å are within the reported range of U^{VI}=O---Li interactions.[7, 23-28] Interestingly, the U-O_{yl} distances for the endo oxo ligands are identical to those of the exo oxo ligands by the 3σ criterion, indicating that the Li-O dative interaction does not significantly

perturb the uranyl bonding framework. The structure of **5.1** also features a $[Li(THF)_3]^+$ cation, which is bound to a Cl^- ligand with Li-Cl distance of 2.364(16) Å.

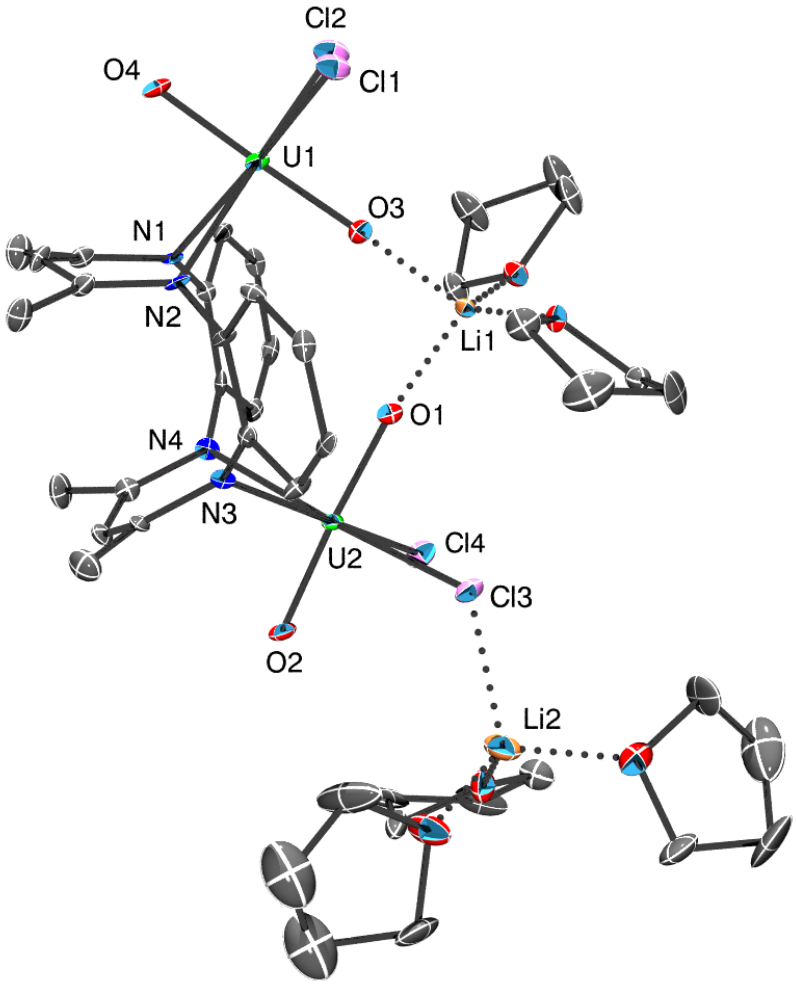

Figure 5.1. Solid-state molecular structure of $[Li(THF)_3][Li(THF)_2][(UO_2Cl_2)_2(tmtaa)]$ (**5.1**), with 50% probability ellipsoids. All hydrogen atoms have been removed for clarity. Selected bond lengths (Å) and angles (°) for **5.1**: U1-O3 = 1.786(6), U1-O4 = 1.764(6), U2-O1 = 1.792(6), U2-O2= 1.776(5), U1-N1 = 2.396(7), U1-N2 = 2.383(7), U2-N3 = 2.419(7), U2-N4 = 2.410(7), Li1-O1 = 1.925(15), Li1-O3 = 1.884(16), Li2-Cl3 = 2.364(16), U1-Cl1 = 2.714(2), U1-Cl2 = 2.658(2), U2-Cl3 = 2.659(2), U2-Cl4 = 2.679(2), O3-U1-O4 = 176.8(3), O1-U2-O2 = 178.0(3), U1-O3-Li1 = 171.8(6), U2-O1-Li1 = 168.4(6).

The ^{1}H NMR spectrum of **5.1** in THF-d_8 exhibits broad singlets at 8.11 and 7.22 ppm, which correspond to the two different aryl-CH environments (Figure A5.1). In addition, the spectrum features two sharp singlets at 4.49 and 1.94 ppm, which are assignable to the γ-CH and methyl environments, respectively. There are also resonances at 3.62 and 1.77 ppm, each integrating for 20 protons, in agreement with the incorporation of five THF molecules. Finally, its ^{7}Li{^{1}H} spectrum in THF-d_8 exhibits a single sharp resonance at -1.43 ppm (Figure A5.2), suggesting rapid exchange of the two different Li environments in this solvent.

5.2.2 Synthesis and Characterization of Three Isomers of $C_{22}H_{22}N_4$ (Compounds 5.2, 5.3 and 5.4)

The surprising ligation of two uranyl fragments to a single $(tmtaa)^{2-}$ ligand, along with the absence of LiCl salt elimination during the reaction, demonstrated that a new route for the synthesis of *cis*-[UO_2(tmtaa)] was needed. I hypothesized that the relatively Lewis acidic Li^+ cation may actually play a templating role during the formation of **5.1**. Accordingly, I sought a replacement for Li_2(tmtaa) and turned my attention to its potassium salt, K_2(tmtaa),[16] on the assumption that KCl elimination would offer sufficient thermodynamic driving force to promote *cis*-[UO_2(tmtaa)] formation. Additionally, $O_{yl}\cdots K^+$ dative interactions are much longer than $O_{yl}\cdots Li^+$ interactions,[3] suggesting that K^+ would not serve as an effective template for the unwanted 2:1 binding mode. Thus, reaction of [$UO_2Cl_2(THF)_3$] with 1 equiv of [K(DME)]$_2$[tmtaa] in pyridine resulted in formation of a dark brown solution, from which three isomers of $C_{22}H_{22}N_4$ (compounds **5.2**, **5.3**, and **5.4**) were isolated as a mixture of orange crystalline solids in 41% combined yield (Scheme 5.3). Also formed in the reaction is a small amount of tmtaaH_2 (see below). The identities of **5.2**, **5.3**, and **5.4** were confirmed by X-ray

diffraction and each is the product of the two electron oxidation of the {tmtaa)$^{2-}$ dianion. While tmtaa is a widely used macrocyclic ligand in transition metal chemistry,[17, 29-33] to my knowledge this is the first example where the products of its 2e$^-$ oxidation have been isolated and characterized, although the 1e$^-$ oxidation of the tmtaa ligand is known.[34-36]

Scheme 5.3. Synthesis of compounds **5.2**, **5.3**, and **5.4**.

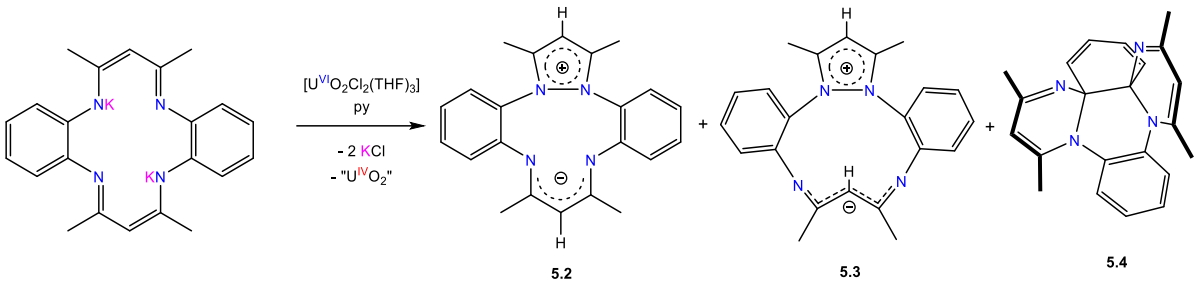

Compound **5.2** crystallizes in the monoclinic space group $P2_1/n$, while compound **5.3** crystallizes in the monoclinic space group $P2_1/c$, as the THF solvate **5.3**·C_4H_8O (Figure 5.2). Compounds **5.2** and **5.3** are zwitterionic isomers that differ by a change in the stereochemistry of their β-diketiminate fragments. They feature C_1 and C_s symmetry, respectively (see below). Both compounds contain a new pyrazolium ring, which is generated by N-N bond formation in the parent tmtaa fragment. The two isomers feature similar N-N bond lengths (**5.2**: 1.380(2) Å; **5.3**: 1.396(2) Å). The C-C (**5.2**: 1.376(3) and 1.385(3) Å; **5.3**: 1.388(3) and 1.376(3) Å) and C-N distances (**5.2**: 1.350(2) and 1.347(2) Å; **5.3**: 1.346(2) and 1.347(2) Å) of the pyrazolium fragments in **5.2** and **5.3** are also similar to each other, as well as with other structurally characterized pyrazolium cations.[37-41] The N-C (1.338(2) and 1.304(2) Å) and C-C (1.388(3) and 1.436(3) Å) distances within the β-diketiminate fragment of **5.2** are similar to those reported for the lithium β-diketiminate salt, 1,5-diphenyl-1,5-diaazapentadienyl lithium, which, like **5.2**, features Z stereochemistry.[42] In addition, the N-C (1.323(3) and 1.328(2) Å)

and C-C (1.404(3) and 1.403(3) Å) distances within the β-diketiminate fragment of **5.3** are similar to those reported for [K(HC{C(^{t}Bu)NDipp}{C(^{t}Bu)NHDipp})(THF)$_3$] (Dipp = 2,6-diisopropylphenyl), which, like **5.3**, exist as the *E*-isomer in the solid-state.[43]

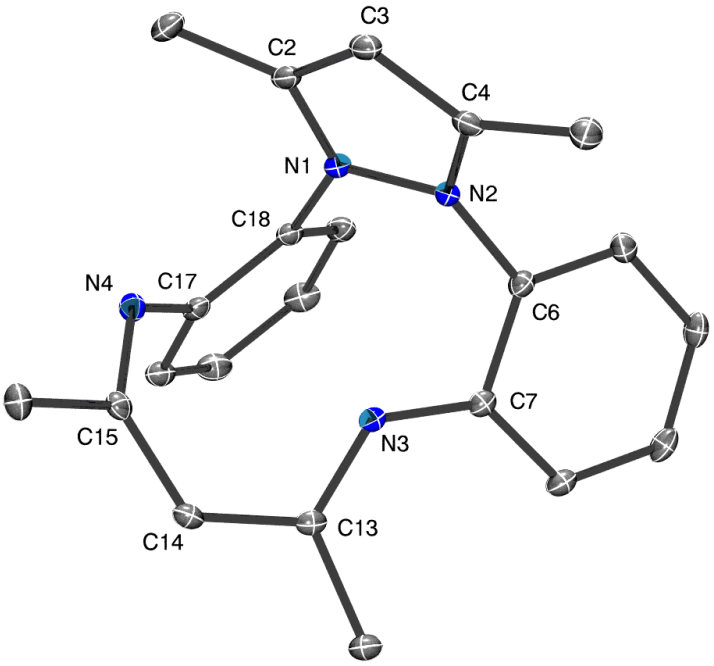

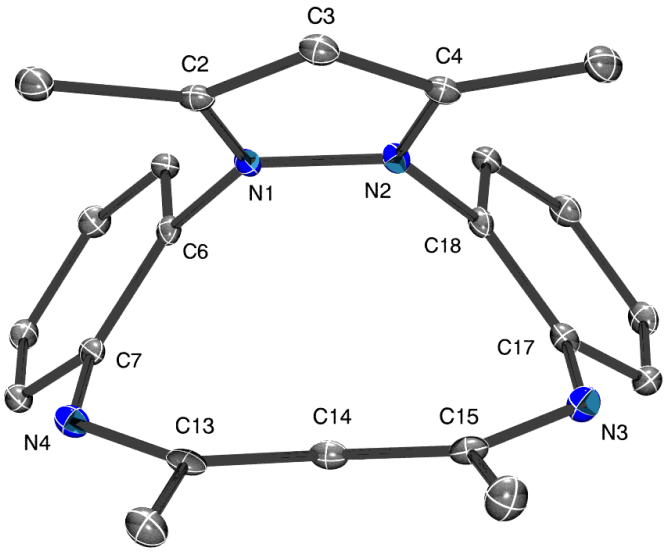

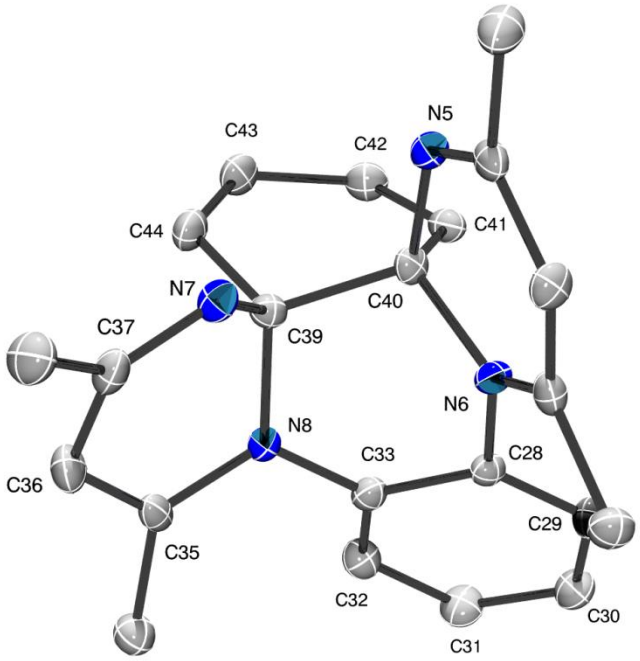

Figure 5.2. Solid-state molecular structures of **5.2** and **5.3**·C_4H_8O, and **5.4**, shown with 50% probability ellipsoids. All hydrogen atoms have been removed for clarity. Selected bond lengths (Å) for **5.2**: N1-N2 = 1.380(2), N1-C2 = 1.350(2), C2-C3 = 1.376(3), C3-C4 = 1.385(3), N2-C4 = 1.347(2), N3-C13 = 1.338(2), C13-C14 = 1.388(3), C14-C15 = 1.436(3), C15-N4 = 1.304(2), For **5.3**: N1-N2 = 1.396(2), N1-C2 = 1.346(2), C2-C3 = 1.388(3), C3-C4 = 1.376(3), N2-C4 = 1.347(2), N3-C15 = 1.323(3), C15-C14 = 1.404(3), C14-C13 = 1.403(3), C13-N4 = 1.328(2). For **5.4**: C28-C29 = 1.384(4), C28-C33 = 1.404(4), C29-C30 = 1.386(4), C30-C31 = 1.387(4), C31-C32 = 1.381(4), C32-C33 = 1.390(4), C28-N6 = 1.415(3), C33-N8 = 1.423(3), C35-N8 = 1.378(3), C35-C36 = 1.359(4), C36-C37 = 1.432(4), C37-N7 = 1.293(3), C39-N7 = 1.455(3), C39-N8 = 1.512(3), C39-C40 = 1.571(4), C39-C44 = 1.523(4), C40-C41 = 1.510(4), C41-C42 = 1.331(3), C42-C43 = 1.451(4), C43-C44 = 1.322(4), C40-N5 = 1.459(3), C40-N6 = 1.491(3).

Compound **5.4** crystallizes in the triclinic space group *P*-1, with two independent molecules in the asymmetric unit (Figure 5.2). Due to their similar metrical parameters, only one of the independent molecules will be discussed in detail. The C_1 symmetric structure of **5.4** contains two new N-C bonds within the tmtaa fragment (N8-C39 and N6-C40), which subsequently results in generation of a tetrahydropyrazine ring and two dihydropyrimidine rings. Consequently, this results in the de-aromatization of one aryl ring. The loss of aromaticity in this ring is evident in its C-C distances. In particular, the C41-C42 and C43-C44 distances (1.331(3) and 1.322(4) Å, respectively) are much shorter than those observed for C42-C43, C39-C44, C39-C40 and C40-C41 (1.451(4), 1.523(4), 1.571(4), and 1.510(4)Å, respectively). In addition, these distances are consistent with those previously reported for the 1,3 cyclohexadiene fragment within a fused ring framework.[44] The metrical parameters of the tetrahydropyrazine and dihydropyrimidine rings in **5.4** are also comparable to those reported for similar structures.[45-47]

Compounds **5.2** and **5.3** have similar solubility in THF, whereas **5.4** is slightly more soluble in this solvent. This difference in solubility permits a certain degree of separation, as **5.2** and **5.3** precipitate from THF solutions before **5.4**. Crystals of **5.2**, **5.3**, and **5.4** are nearly identical in color, and feature very similar morphologies, making their identification by eye very challenging. They are, however, easily distinguished by NMR spectroscopy. For example, a ^{1}H NMR spectrum of **5.2** and **5.3**, in a 1:4 ratio, in C_6D_6 exhibits two γ-CH resonances at 5.28 and 4.99 ppm, as well as 8 aryl CH resonances ranging from 7.05 to 6.33 ppm, which are all assignable to **5.2** (Figure A5.4). The number of peaks and their intensities are consistent with the C_1 symmetry observed for this material in the solid state. This same spectrum also features four aryl resonances at 7.24, 6.96, 6.87, and 6.52 ppm, and two methyl resonances at 2.26 and

1.87 ppm, which are assignable to **5.3**. The number of peaks and their intensities are consistent with the C_s symmetry observed for this material in the solid state. A ^{1}H NMR spectrum of **5.3** and **5.4**, in a 1:7 ratio, in C_6D_6 features two resonances at 5.52 and 5.86 ppm, which are assignable to two CH environments of the 1,3 cyclohexadiene fragment in **5.4** (Figure A5.5). This observation is not consistent with the C_1 symmetry observed for **5.4** in the solid state, and suggests that the tetrahydropyrazine ring in **5.4** can undergo a facile ring flip to give an overall C_s symmetric structure in solution. In addition, resonances at 1.64 and 2.09 ppm, which are present in a 6:6 ratio, are assignable to two methyl environments. This observation is also consistent with the proposed C_s symmetry in solution. Interestingly, it appears that **5.2** and **5.3** can convert to **5.4** upon heating. Thermolysis of a mixture **5.2**, **5.3**, and **5.4** (in a 1:4:2 ratio), in C_6D_6, at 50 °C for 24 h results in almost quantitative conversion to **5.4** (Scheme 5.4a), as revealed by ^{1}H NMR spectroscopy (Figure A5.9). Most likely, thermolysis of **5.2** and **5.3** generates a diradical intermediate via N-N bond homolysis, which rearranges to form the thermodynamically more stable isomer, **5.4**. Moreover, treatment of a mixture **5.2**, **5.3**, and **5.4** (in a 3:9:1 ratio) with 5 equiv of KC_8 in DME result in re-formation of $[K(DME)]_2$[tmtaa] after 48 h (Scheme 5.4b), which could be isolated in 26% yield after work-up of the reaction mixture (Figure A5.8). Intriguingly, the chemical reversibility of the tmtaa oxidation implies that $[tmtaa]^{2-}$ could be employed in a catalytic uranyl reduction process.

Scheme 5.4. Reactivity of the oxidized tmtaa products **5.2**, **5.3**, and **5.4**.

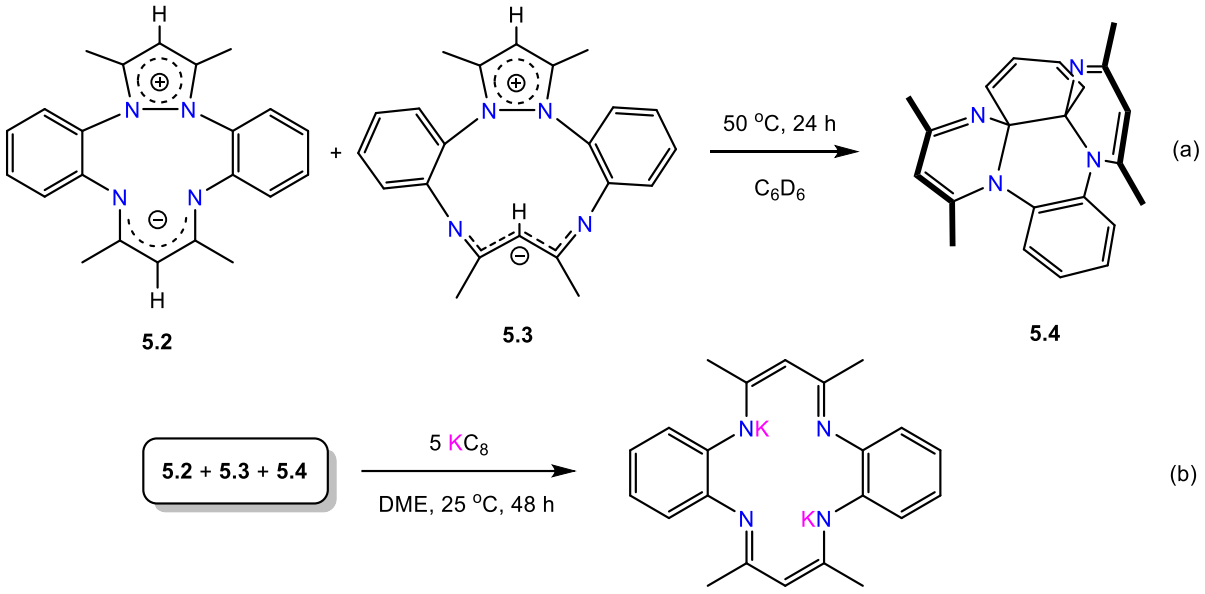

5.2.3 Mechanistic Considerations for the Formation of Compounds 5.2, 5.3 and 5.4

To rationalize the formation of **5.2**, **5.3** and **5.4**, I hypothesize that reaction of $[K(DME)]_2[tmtaa]$ with $[UO_2Cl_2(THF)_3]$ generates *cis*-$[UO_2(tmtaa)]$, which is unstable and rapidly decomposes via intramolecular electron transfer to form the $2e^-$ oxidation products, **5.2**, **5.3**, and **5.4**, along with uranium(IV) oxide. To test this hypothesis, I monitored the reaction of $[UO_2Cl_2(THF)_3]$ with $[K(DME)]_2[tmtaa]$ in py-d_5 by ^1H NMR spectroscopy. A ^1H NMR spectrum of the reaction mixture recorded after 1 min reveals the presence of compounds **5.2**, **5.3**, and **5.4**, as well as $tmtaaH_2$, in a 4:6:5:5 ratio, respectively (Figure A5.6). In addition, I observe two new γ-CH resonances at 5.34 and 4.29 ppm, in a 1:1 ratio, which are assignable to a new tmtaa environment. These resonances disappear rapidly on standing, and are not observed in the sample after 15 min (Figure 5.3). The observation of two γ-CH environments for a single tmtaa ligand suggests that tmtaa only coordinates to the uranium center through two of its N atoms, as previously observed for $[Li(THF)]_2[UO_2(N(SiMe_3)_2)_2(tmtaa)]$.[15] Given

the flexibility of tmtaa, this intermediate is unlikely to possess cis-oxo stereochemistry, but it could be a precursor to an unstable, and unobserved, cis-uranyl complex, which then decomposes to uranium oxide and **5.2**, **5.3**, and **5.4**, as I originally surmised.

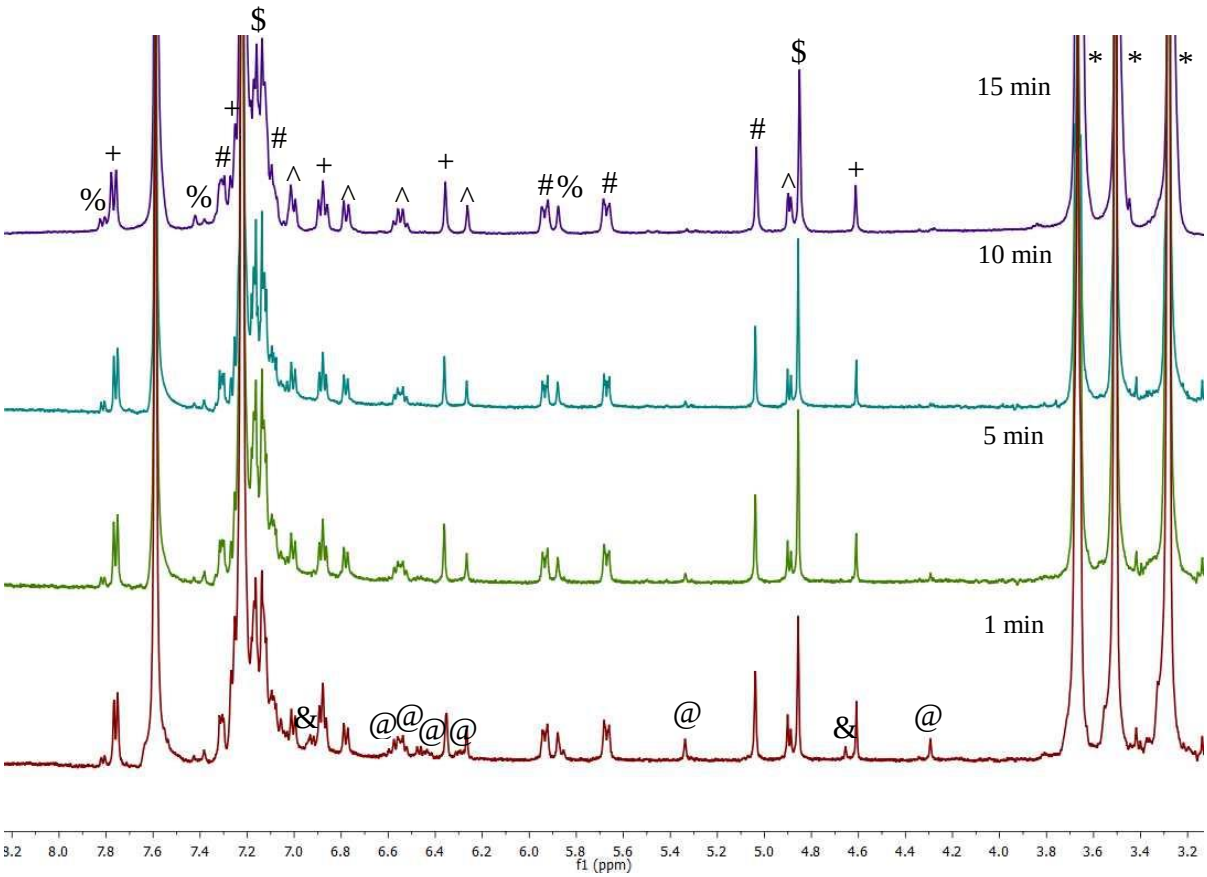

Figure 5.3. Partial *in situ* ^{1}H NMR spectra of a mixture of $[K(DME)]_2[tmtaa]$ and $[UO_2Cl_2(THF)_3]$ in py-d_5, recorded at room temperature. $ indicates resonances assignable to $tmtaaH_2$, ^ indicates resonances assignable to **5.2**, + indicates resonances assignable to **5.3**, # indicates resonances assignable to **5.4**, & indicates resonances assignable to $[K(DME)]_2[tmtaa]$, @ indicates resonances assignable to a new tmtaa environment, % indicates the presence of unidentified products, and asterisks indicate the presence of DME and THF.

I also observe the formation of a brown powder during the reaction work-up. An X-ray photoelectron spectrum (XPS) of this material reveals the presence of both uranium and oxygen (Figure 5.4), suggesting that the brown powder contains the expected uranium oxide by-product. Specifically, the spectrum features two prominent peaks at 392.6 and 381.8 eV, which are attributable to the U $4f_{5/2}$ and U $4f_{7/2}$ binding energies, respectively. These values are very similar to the binding energies reported for the mixed-valent uranium oxide, U_4O_9 (average U oxidation state = 4.5),[48] a finding which is broadly consistent with the reaction stoichiometry shown in Scheme 5.3. The XPS spectrum also reveals peaks assignable to potassium and chlorine, consistent with the presence of KCl. A small amount of carbon and nitrogen are also observed in this spectrum. Interestingly, this material is soluble in pyridine. Given this property, as well as the XPS data, this solid is unlikely to contain pure uranium(IV) oxide, but it could contain an oxide that has incorporated a small amount of tmtaa and pyridine. In this regard, Clark and co-workers also isolated a ligand-stabilized uranium oxide cluster, $Cp'_4(bipy)_2U_6O_{13}$, during a related attempt to make cis-uranyl.[8]

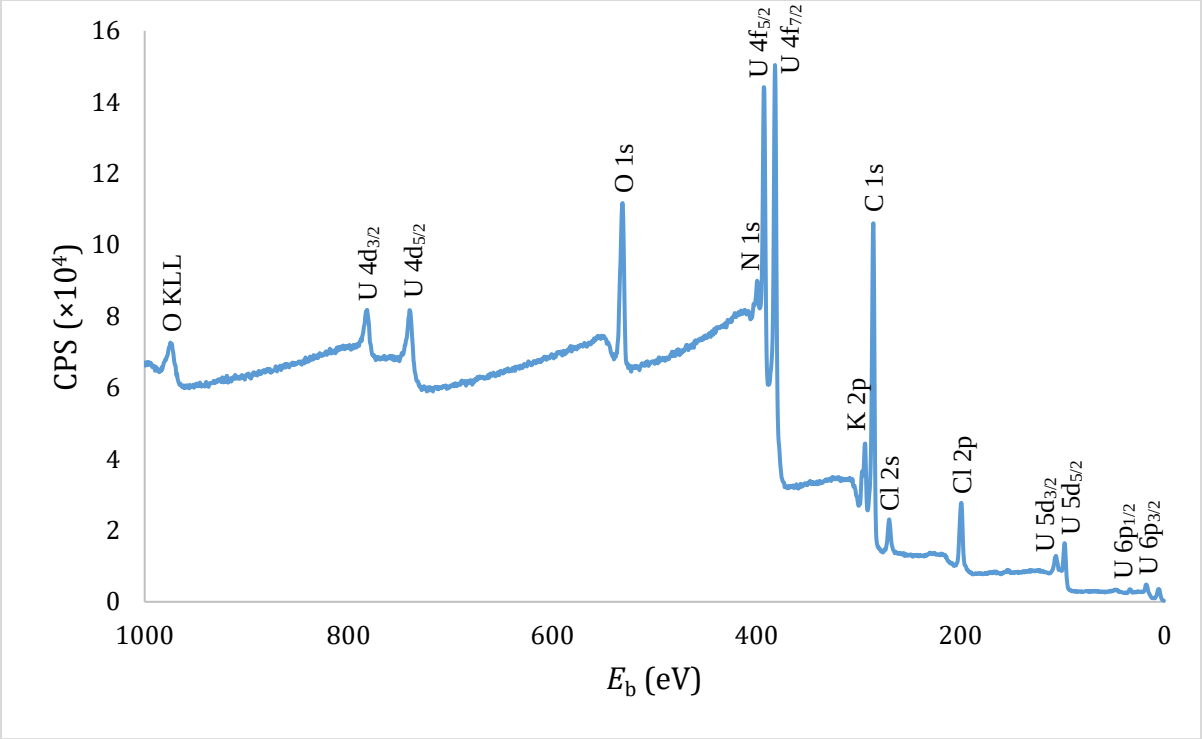

Figure 5.4. X-ray photoelectron spectrum of brown powder isolated from the reaction between $[UO_2Cl_2(THF)_3]$ and $[K(DME)]_2[tmtaa]$.

5.2.4 Electrochemistry

Several transition metal tmtaa complexes have been previously characterized by cyclic voltammetry. For example, Ni(tmtaa) features an irreversible oxidation wave at -0.01 V (vs. Fc/Fc^+) in acetonitrile,[49] while $[Rh(CO)_2]_2$(tmtaa) and $[Re(CO)_3]_2$(tmtaa) feature irreversible oxidation waves at 0.16 V and 0.35 V (vs. Fc/Fc^+) in DMF, respectively.[50] All three features are attributable to ligand-based oxidations. While the tmtaa oxidation potential is clearly dependent on the identity of its complexing ion, these data allow me to place a lower limit on the U(VI)/U(V) redox potential of the *cis*-uranyl fragment (i.e., -0.01 V vs. Fc/Fc^+), a value that is at least 0.34 V higher than that of *trans*-UO_2^{2+}(aq).[3] Overall, these results further

buttress the premise that the putative *cis*-uranyl ion is a strong oxidant, likely on account of diminished d and f orbital participation within its U-O bonding framework.

5.3 Summary

Reaction of Li_2tmtaa with 1 equiv of $[UO_2Cl_2(THF)_3]$ results in formation of $[Li(THF)_3][Li(THF)_2][(UO_2Cl_2)_2(tmtaa)]$ (**5.1**) in modest yield. Higher isolated yields can be achieved by reaction of Li_2tmtaa with 2 equiv of $[UO_2Cl_2(THF)_3]$. Under these conditions, **5.1** can be isolated in 44% yield. In contrast, reaction of $[K(DME)]_2$[tmtaa] with 1 equiv of $[UO_2Cl_2(THF)_3]$ does not result in the isolation of a uranyl-containing tmtaa complex. Instead, I observe the products of $2e^-$ ligand oxidation. These products can be isolated in 41% combined yield. I hypothesize that the ligand oxidation products are formed upon decomposition of unobserved cis uranyl intermediate, *cis*-$[UO_2(tmtaa)]$, which is unstable and undergoes a facile intramolecular redox reaction. While ultimately unsuccessful at generating a stable cis-uranyl complex, my results suggest that ligation of macrocyclic ligands to uranyl is a promising avenue for effecting a trans/cis isomerization. However, it is clear that successful isolation of *cis*-UO_2^{2+} will require the deployment of a highly robust and redox-inactive macrocyclic co-ligand, and efforts to identify promising candidates are currently ongoing.

5.4 Acknowledgments

I would like to thank my collaborators Dr. Elizabeth Owens and Megan E. Wakefield for optimizing the synthesis and X-ray crystallographic and spectroscopic characterization of compounds **5.2** and **5.3**. I also thank Dr. Thomas Mates for assistance with X-ray photoelectron spectroscopy measurements.

5.5 Experimental

5.5.1 General Procedures. All reactions and subsequent manipulations were performed under anaerobic and anhydrous conditions under an atmosphere of nitrogen. Hexanes, diethyl ether (Et_2O), and tetrahydrofuran (THF) were dried using a Vacuum Atmospheres DRI-SOLV solvent purification system, and stored over 3Å molecular sieves for 24 h prior to use. Pyridine was dried over activated 3Å molecular sieves for 24 h, degassed by bubbling dry N_2 into the solvent for 30 min, cannula transferred into a new vessel, and dried again over 3Å molecular sieves for 24 h prior to use. Dimethoxyethane (DME) was distilled over Na/benzophenone, and subsequently stored over 3Å molecular sieves for 24 h prior to use. C_6D_6, pyridine-d_5, and THF-d_8 were dried over activated 3Å molecular sieves for 24 h prior to use. $[UO_2Cl_2(THF)_3]$,[51] $tmtaaH_2$,[52] and $[K(DME)]_2[tmtaa]$[16] were prepared according to the reported literature procedures. All other reagents were purchased from commercial suppliers and used as received.

NMR spectra were recorded on a Varian UNITY INOVA 400 MHz spectrometer, a Varian unity INOVA 500 MHz spectrometer, or a Varian Unity Inova AS600 600 MHz spectrometer. ^1H and ^{13}C $\{^1H\}$ NMR spectra are referenced to external $SiMe_4$ using the residual protio solvent peaks as internal standards (^1H NMR experiments) or the characteristic resonances of the solvent nuclei (^{13}C NMR experiments). $^7Li\{^1H\}$ NMR spectra were referenced indirectly with the ^1H resonance of $SiMe_4$ at 0 ppm, according to IUPAC standard.[53, 54] IR spectra were recorded on a Mattson Genesis FTIR/Raman spectrometer with a NXR FT Raman Module. Elemental analyses were performed by the Microanalytical Laboratory at UC Berkeley.

X-ray Photoelectron Spectroscopy. XPS data were recorded using a Kratos Axis Ultra DLD spectrometer equipped with a monochromated Al-k alpha source (1486 eV). Survey and high-resolution scans were recorded at 160 eV and 20 eV pass energies, respectively. A low-energy electron flood was used for charge neutralization, and peak positions were calibrated against the aliphatic C1s peak (285.0 eV).

Caution! *Depleted uranium (isotope ^{238}U) is a weak alpha emitter with a half-life of 4.47×10^9 years. Manipulations and reactions should be carried out in a fume hood or inert atmosphere glovebox in a laboratory equipped with α- and β-counting equipment.*

5.5.2 Synthesis of Li_2(tmtaa). The preparation described below was modified slightly from the published procedure for Li_2(tmtaa).[55] To a stirring, yellow slurry of tmtaaH_2 (200.2 mg, 0.581 mmol) in Et_2O (8 mL), was added dropwise a hexanes solution of *n*-BuLi (0.47 mL, 1.175 mmol, 2.5 M), which was diluted with Et_2O (1 mL). This addition resulted in an immediate color change to deep red. The reaction mixture was allowed to stir at room temperature for 5 min, whereupon the solution was filtered through a Celite column supported on glass wool (0.5 cm × 2 cm). The resulting red filtrate was concentrated *in vacuo* (ca. 3 mL), which resulted in the deposition of red crystals (87.3 mg). These crystals were isolated by decanting away the supernatant and then dried *in vacuo*. The volume of the red supernatant was further reduced *in vacuo* (ca. 1.5 mL), and the solution was subsequently stored at -25 °C for 24 h, which resulted in the deposition of a second crop of red crystals (76.8 mg, 79% total yield). Spectral data of this material matched those previously reported for this material.[55]

5.5.3 Synthesis of [Li(THF)$_3$][Li(THF)$_2$][(UO_2Cl_2)$_2$(tmtaa)] (5.1). To a cold (-25 °C) stirring, yellow slurry of [UO_2Cl_2(THF)$_3$] (163.2 mg, 0.293 mmol) in THF (1 mL), was added dropwise a cold (-25 °C) red solution of Li_2(tmtaa) (52.0 mg, 0.146 mmol) in 1:1 Et_2O/hexanes

(3 mL). This addition resulted in immediate formation of a brown solution concomitant with deposition of a deep brown solid. The reaction mixture was allowed to stir for 1 min at room temperature, whereupon the solid was isolated by decanting away the mother liquor. The solid was then dissolved in THF (2 mL) and the resulting deep brown solution was filtered through a Celite column supported on glass wool (0.5 cm × 2 cm). The filtrate was very carefully layered with hexanes (1 mL) and subsequently stored at -25 °C for 48 h, which resulted in deposition of red-brown crystals (89.0 mg, 44% yield). A ^{1}H NMR spectrum of the isolated solid revealed the presence of **5.1** along with an unidentified impurity, in an approximately 5:1 ratio. Attempts to purify **5.1** by re-crystallization only led to an increase in amount of this impurity because of the thermal instability of **5.1**. As a result, I was unable to obtain an acceptable elemental analysis. X-ray quality crystals of **5.1** were grown from a concentrated THF solution, which was layered with hexanes and stored at -25 °C for 48 h. The normal timeframe for crystal growth was 48 h; however, in several instances crystal growth took much longer (1 week). ^{1}H NMR (THF-d_8, 25 °C, 400 MHz): δ 8.11 (br s, 4H, aryl CH), 7.22 (br s, 4H, aryl CH), 4.49 (s, 2H, γ-CH), 3.62 (br s, 20H, OCH_2), 1.77 (br s, 20H, OCH_2CH_2), 1.94 (s, 12H, CH_3). ^{7}Li{^{1}H} NMR (THF-d_8, 25 °C, 155 MHz): δ 1.93 (s). IR (KBr pellet, cm^{-1}): 2958 (m), 2927 (m), 2875 (m), 1622 (w), 1591 (vw), 1541 (m), 1471 (m), 1456 (m), 1446 (m), 1385 (s), 1367 (sh s), 1275 (w), 1180 (w), 1109 (w), 1039 (s), 1022 (sh s), 922 (br vs), 796 (w), 748 (w), 669 (w), 467 (br s).

5.5.4 Reaction of [K(DME)]$_2$[tmtaa] with [$UO_2Cl_2(THF)_3$]. To a stirring, yellow-green solution of [$UO_2Cl_2(THF)_3$] (77.0 mg, 0.138 mmol) in pyridine (1 mL) was added dropwise a deep red solution of [K(DME)]$_2$[tmtaa] (83.1 mg, 0.138 mmol) in pyridine (1 mL). This addition resulted in immediate color change to deep brown. The solution was stirred at room

temperature for 15 min, whereupon the volatiles were removed *in vacuo* and the resulting oil was triturated with Et_2O (2 × 1 mL) to yield a deep brown powder. The solid was then extracted into Et_2O (3 × 3 mL) and filtered through a Celite column supported on glass wool (0.5 cm × 2 cm) to yield an orange filtrate. A brown powder remained in the reaction vial after filtration (63.5 mg). The volatiles were removed from the filtrate *in vacuo* and the resulting yellow-orange powder was dissolved in THF (1 mL). The orange solution was then stored at -25 °C for 72 h, which resulted in deposition of bright orange crystals identified as a mixture of **5.2**, **5.3**, and **5.4** (in a 3:9:1 ratio) by X-ray crystallography and ^{1}H NMR spectroscopy (19.5 mg, 41% yield). X-ray quality crystals of **5.2** were obtained from a concentrated Et_2O solution stored at -25 °C for 24 h. X-ray quality crystals of **5.3** were obtained by recrystallization of a mixture of **5.2** and **5.3** from a 5:1 Et_2O/THF solution. X-ray quality crystals of **5.4** were obtained by recrystallization of a mixture of **5.3** and **5.4** from a concentrated Et_2O solution. Anal. Calcd $C_{22}H_{22}N_4$: C, 77.16; H, 6.48; N, 16.36. Found: C, 76.83; H, 6.38; N, 15.99. ^{1}H NMR of **5.2** (C_6D_6, 25 °C, 400 MHz): δ 7.05 (t, J_{HH} = 8 Hz, 1H, aryl CH), 7.01 (d, J_{HH} = 9 Hz, 1H, aryl CH), 6.99 (d, J_{HH} = 8 Hz, 1H, aryl CH), 6.72 (m, 2H, overlapping aryl CH), 6.61 (d, J_{HH} = 8 Hz, 1H, aryl CH), 6.42 (t, J_{HH} = 7 Hz, 1H, aryl CH), 6.33 (t, J_{HH} = 7 Hz, 1H, aryl CH), 5.28 (s, 1H, γ-CH), 4.99 (s, 1H, γ-CH), 2.31 (s, 3H, CH_3), 2.27 (s, 3H, CH_3), 2.06 (s, 3H, CH_3), 1.48 (s, 3H, CH_3). ^{13}C{^{1}H} NMR of **5.2** (C_6D_6, 25 °C, 100 MHz): δ 166.57 (s, 1C, N*C*CH$_3$), 157.09 (s, 1C, N*C*$_{aryl}$), 155.09 (s, 1C, N*C*CH$_3$) 150.34 (s, 1C, N*C*$_{aryl}$), 148.03 (s, 1C, N*C*$_{aryl}$), 145.23 (s, 1C, N*C*CH$_3$), 144.29 (s, 1C, N*C*CH$_3$), 132.25 (s, 1C, aryl *C*H), 131.62 (s, 1C, aryl *C*H), 126.40 (s, 1C, aryl *C*H), 125.84 (s, 1C, N*C*$_{aryl}$), 119.28 (s, 1C, aryl *C*H),, 117.93 (s, 1C, aryl *C*H), 111.61 (s, 1C, aryl *C*H), 105.90 (s, 1C, γ-*C*H), 99.70 (s, 1C, γ-*C*H), 29.03 (s, 1C, *C*H$_3$), 22.92 (s, 1C, *C*H$_3$) 13.10 (s, 1C, *C*H$_3$), 12.25 (s, 1C, *C*H$_3$). Two aryl *C*H resonances

are not observed possibly due to overlap with the benzene solvent resonances. ^{1}H NMR of **5.3** (C_6D_6, 25 °C, 400 MHz): δ 7.24 (d, J_{HH} = 7 Hz, 2H, aryl CH), 6.96 (t, J_{HH} = 6 Hz, 2H, aryl CH), 6.87 (d, J_{HH} = 6 Hz, 2H, aryl CH), 6.52 (t, J_{HH} = 5 Hz, 2H, aryl CH), 5.13 (s, 1H, γ-CH), 4.52 (s, 1H, γ-CH), 2.26 (s, 6H, CH_3), 1.87 (s, 6H, CH_3). ^{13}C{^{1}H} NMR of **5.3** (C_6D_6, 25 °C, 100 MHz): δ 160.91 (s, 2C, N*C*CH_3), 153.40 (s, 2C, N*C*$_{aryl}$), 147.16 (s, 2C, N*C*CH_3), 132.56 (s, 2C, aryl *C*H), 131.17 (s, 2C, aryl *C*H), 121.36 (s, 2C, N*C*$_{aryl}$), 116.84 (s, 2C, aryl *C*H), 106.44 (s, 1C, γ-*C*H), 88.19 (s, 1C, γ-*C*H), 25.18 (s, 2C, *C*H_3), 12.34 (s, 2C, *C*H_3). One aryl *C*H resonance is not observed possibly due to overlap with the benzene solvent resonances. ^{1}H NMR of **5.4** (C_6D_6, 25 °C, 400 MHz): δ 6.84 (m, 2H, aryl CH), 6.71 (m, 2H, aryl CH), 5.86 (m, 2H, C=CH), 5.52 (m, 2H, C=CH), 4.84 (s, 1H, γ-CH), 2.09 (s, 6H, CH_3), 1.64 (s, 6H, CH_3). ^{13}C{^{1}H} NMR of **5.4** (C_6D_6, 25 °C, 100 MHz): δ 162.94 (s, 2C, N*C*CH_3), 144.91 (s, 2C, N*C*CH_3), 138.60 (s, 2C, N*C*$_{aryl}$), 131.43 (s, 2C, aryl *C*H), 124.54 (s, 2C, aryl *C*H), 123.16 (s, 2C, aryl *C*H), 122.70 (s, 2C, aryl *C*H), 99.88 (s, 2C, γ-*C*H), 85.24 (s, 2C, N*C*), 25.04 (s, 2C, *C*H_3), 21.43 (s, 2C, *C*H_3). IR of **5.2** and **5.3** (KBr pellet, cm^{-1}): 1589(sh m), 1581(m), 1549(m), 1516(m), 1468(m), 1460(m), 1444(sh m), 1410(sh s), 1396(vs), 1385(sh m), 1367(m), 1309(sh w), 1299(m), 1272(sh w), 1265(m), 1207(m), 1173(w), 1155(w), 1103(w), 1029(w), 1024(w), 1007(m), 928(w), 850(w), 827(w), 810(m), 802(m), 771(w), 742(sh m), 744(s), 733(m), 719(s), 677(m), 627(m), 602(w), 543(w), 490(m). IR of **5.3** and **5.4** (KBr pellet, cm^{-1}): 1649 (m), 1614 (m), 1583 (w), 1558 (m), 1524 (m), 1497 (s), 1458 (m), 1419 (m), 1406 (m), 1362 (m), 1298 (s), 1281 (s), 1184 (w), 1163 (vw), 1107(vw), 1099 (m), 1065 (m), 1022 (m), 966

(w), 933 (w), 881 (w), 849 (m), 783 (m), 768 (s), 756 (s), 741 (w), 690 (vw), 667 (m), 644 (w), 590 (w), 586 (s), 534 (w), 526 (w), 428 (w), 399 (w).

5.5.5 X-ray Crystallography. Data collection for **5.1** – **5.4** was carried out on a Bruker KAPPA APEX II diffractometer equipped with an APEX II CCD detector using a TRIUMPH monochromater with a Mo Kα X-ray source (α = 0.71073 Å). Crystals were mounted on a cryoloop under Paratone-N oil and data were collected at 100(2) K, using an Oxford nitrogen gas cryostream system. A hemisphere of data was collected using ω scans with 0.5° frame widths. Frame exposures of 15, 10, 10, and 5 seconds were used for **5.1**, **5.2**, **5.3**, and **5.4**, respectively. Data collection and cell parameter determination were conducted using the SMART program.[56] Integration of the data frames and final cell parameter refinement were performed using SAINT software.[57] Absorption correction of the data was carried out using the multi-scan method SADABS.[58] Subsequent calculations were carried out using SHELXTL.[59] Structure determination was done using direct or Patterson methods and difference Fourier techniques. All hydrogen atom positions were idealized, and rode on the atom of attachment. Structure solution, refinement, graphics, and creation of publication materials were performed using SHELXTL.[59] Structures **5.1** – **5.4** have been deposited into the Cambridge Crystallographic Database (CCDC 1834597-1834600). Further crystallographic details can be found in Table 5.1.

Table 5.1. X-ray Crystallographic Information for **5.1**-**5.4**.

	5.1	**5.2**	**5.3·C_4H_8O**	**5.4**
empirical formula	$U_2O_9N_4Li_2Cl_4C_{42}H_{62}$	$N_4C_{22}H_{22}$	$N_4OC_{26}H_{30}$	$N_4C_{22}H_{22}$
Crystal habit, color	rod, red-brown	block, orange	hexagon, orange	rod, orange
crystal size (mm)	0.2 × 0.1 × 0.05	0.1 × 0.1 × 0.05	0.1 × 0.1 ×0.05	0.20 × 0.15 × 0.05
crystal system	monoclinic	monoclinic	monoclinic	triclinic
space group	$P2_1/n$	$P2_1/n$	$P2_1/c$	P-1
vol ($Å^3$)	5031.0(5)	1799.6(3)	2186.02(17)	1796.3(12)
a (Å)	17.5804(10)	12.2806(14)	8.9736(4)	9.861(4)
b (Å)	12.5497(7)	10.4045(12)	12.4407(6)	11.617(4)
c (Å)	22.8161(12)	14.8419(14)	19.6623(8)	16.019(6)
α (°)	90	90	90	98.494(12)
β (°)	91.943(3)	108.383(6)	95.202(3)	93.783(13)
γ (°)	90	90	90	96.653(13)
Z	4	4	4	4
fw (g/mol)	1398.69	342.43	414.54	342.43
density (calcd) (Mg/m^3)	1.847	1.264	1.260	1.266
abs coeff (mm^{-1})	6.695	0.077	0.078	0.077
F_{000}	2688	728	888	728
Total no. reflections	17271	10996	7282	11523
Unique reflections	7173	2589	3027	5136
final R indices [I > 2σ(I)]	R_1 = 0.0426 wR_2 = 0.0736	R_1 = 0.0368 wR_2 = 0.1038	R_1 = 0.0373 wR_2 = 0.0850	R_1 = 0.0488 wR_2 = 0.1028
largest diff peak and hole ($e^-Å^{-3}$)	1.290 and -1.188	0.294 and -0.235	0.231 and -0.246	0.251 and -0.266
GOF	1.063	0.783	0.999	0.994
Location of largest diff peak	0.18 Å from C42	0.54 Å from H14	0.54 Å from H14	0.63 Å from H36

5.6 Appendix

5.6.1 NMR Spectra

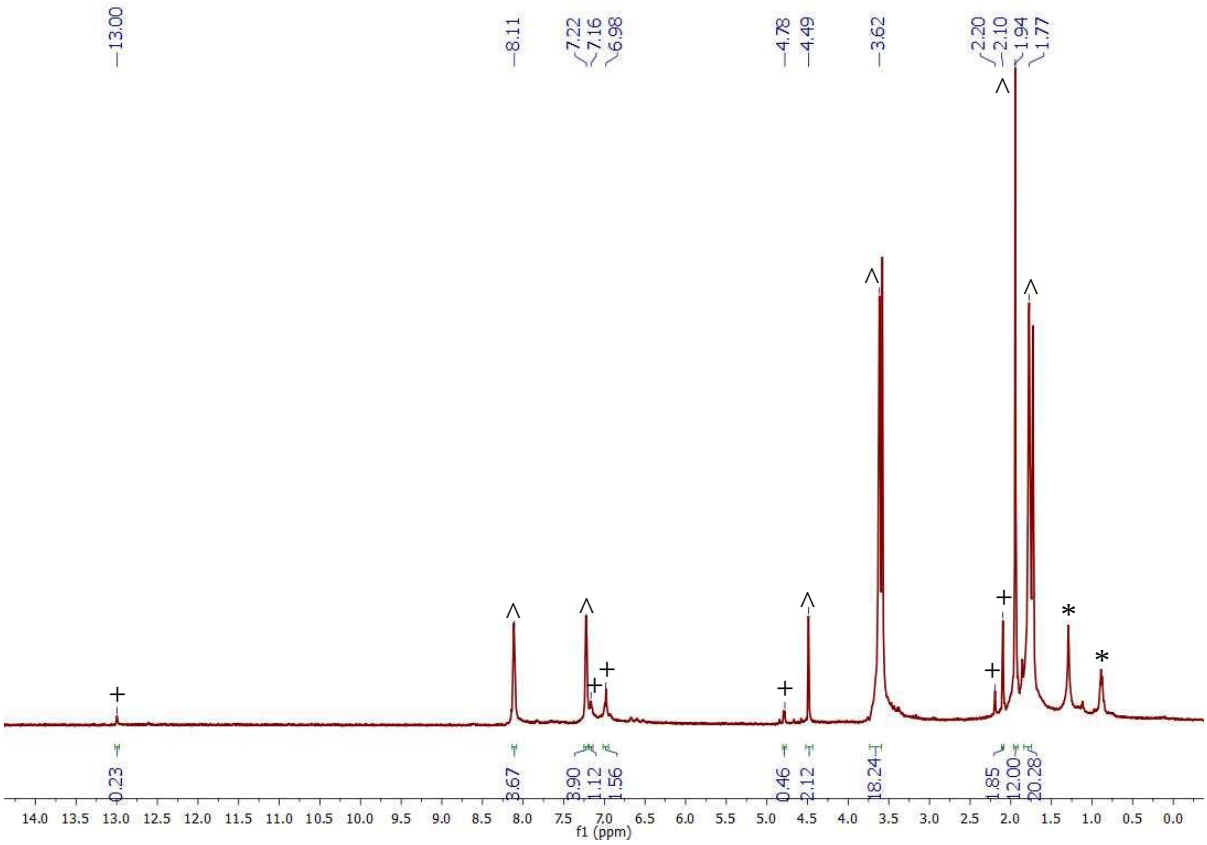

Figure A5.1. ^{1}H NMR spectrum of complex **5.1** in THF-d_8. ^ indicates resonances assignable to complex **5.1**, + indicates the presence of an unidentified impurity, and asterisks indicate the presence of hexanes.

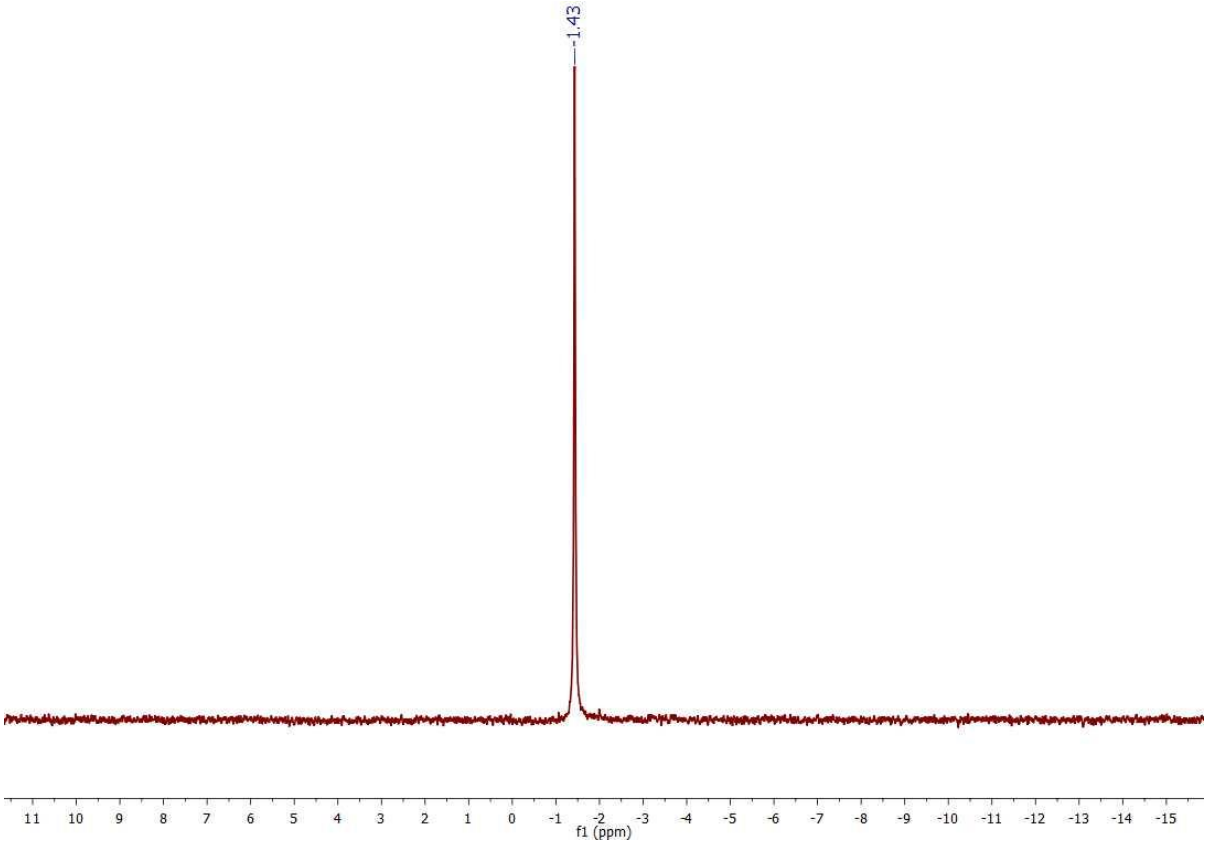

Figure A5.2. ^{7}Li {^{1}H} NMR spectrum of complex **5.1** in THF-d_8.

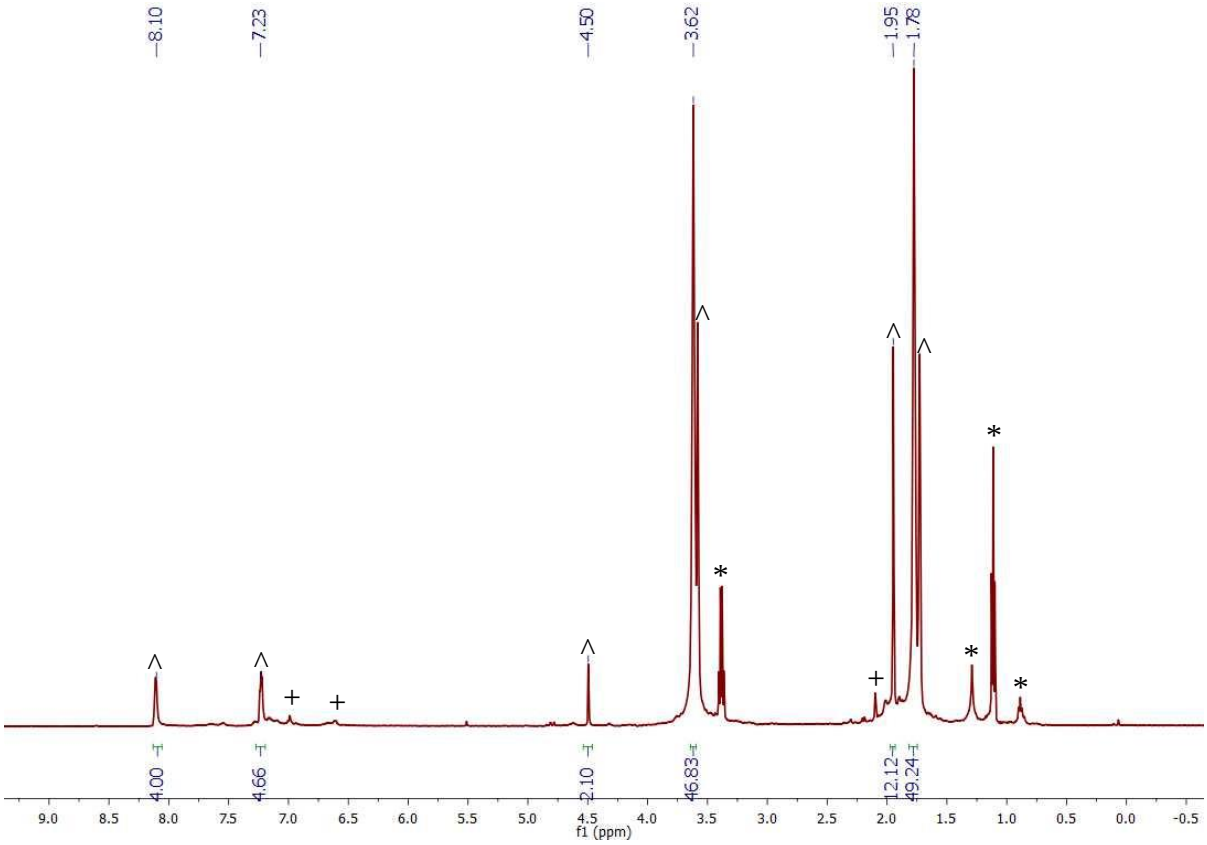

Figure A5.3. *In situ* ^{1}H NMR spectrum of the reaction of Li_2tmtaa with 2 equiv of $[UO_2Cl_2(THF)_3]$ in THF-d_8 after standing for 5 min. ^ indicates resonances assignable to complex **5.1**, + indicates the presence of an unidentified impurity, and asterisks indicate the presence of Et_2O and hexanes. **Experimental Details:** Li_2tmtaa (5.0 mg, 0.014 mmol) was dissolved in THF-d_8 (0.75 mL), which resulted in formation of a deep red solution. The solution was then transferred to an NMR tube equipped with a J-Young valve, removed from the glovebox, and its ^{1}H-NMR spectrum was recorded. The NMR tube was returned to the glovebox and $[UO_2Cl_2(THF)_3]$ (15.1 mg, 0.027 mmol) was added to the solution as a solid, and the mixture was allowed to stand for 5 min at room temperature. The NMR tube was removed from the glovebox and a ^{1}H NMR spectrum of the *in situ* reaction mixture was recorded.

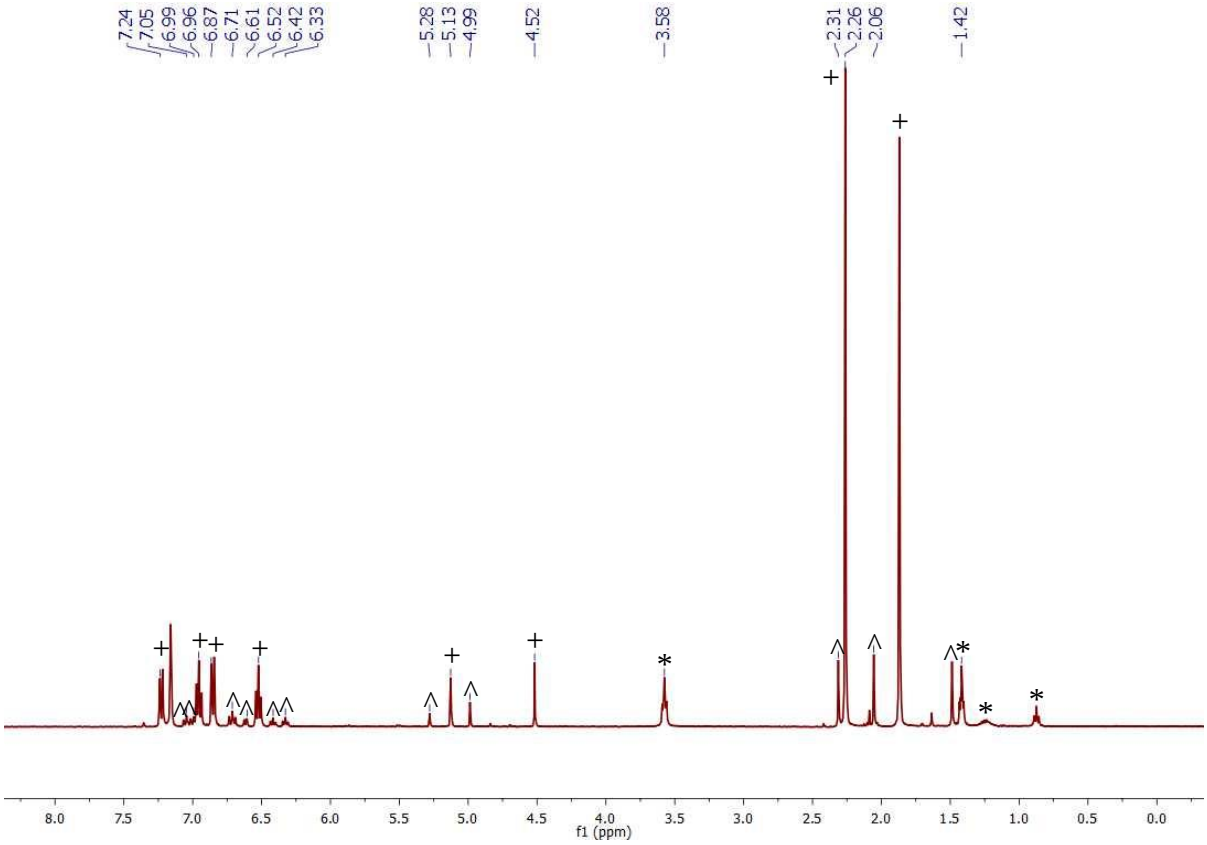

Figure A5.4. ^{1}H NMR spectrum of a mixture of **5.2** and **5.3** (in a 1:4 ratio) in C_6D_6. ^ indicates resonances assignable to **5.2**, + indicates resonances assignable to **5.3**, and asterisks indicate the presence of THF and hexanes.

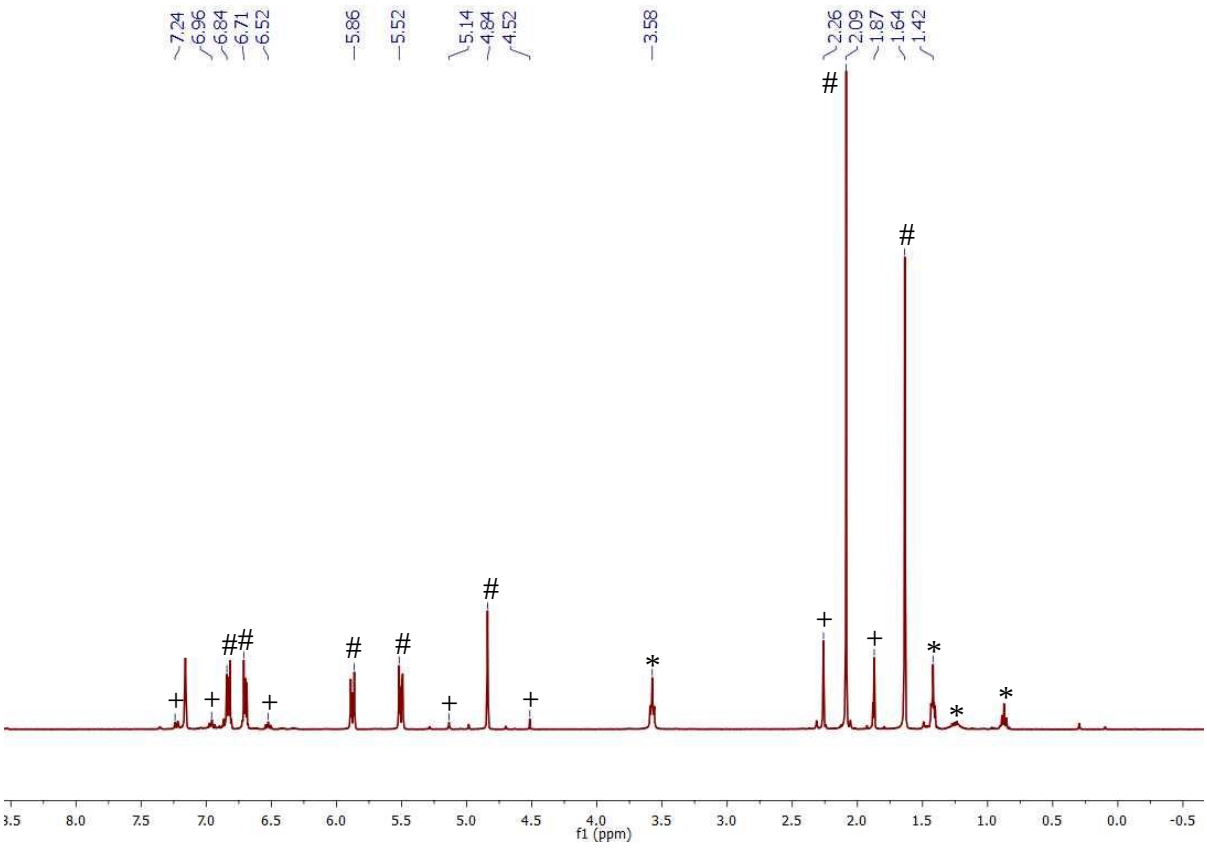

Figure A5.5. ^{1}H NMR spectrum of a mixture of **5.3** and **5.4** (in a 1:7 ratio) in C_6D_6. + indicates resonances assignable to **5.3**, # indicates resonances assignable to **5.4**, and asterisks indicate the presence of THF and hexanes.

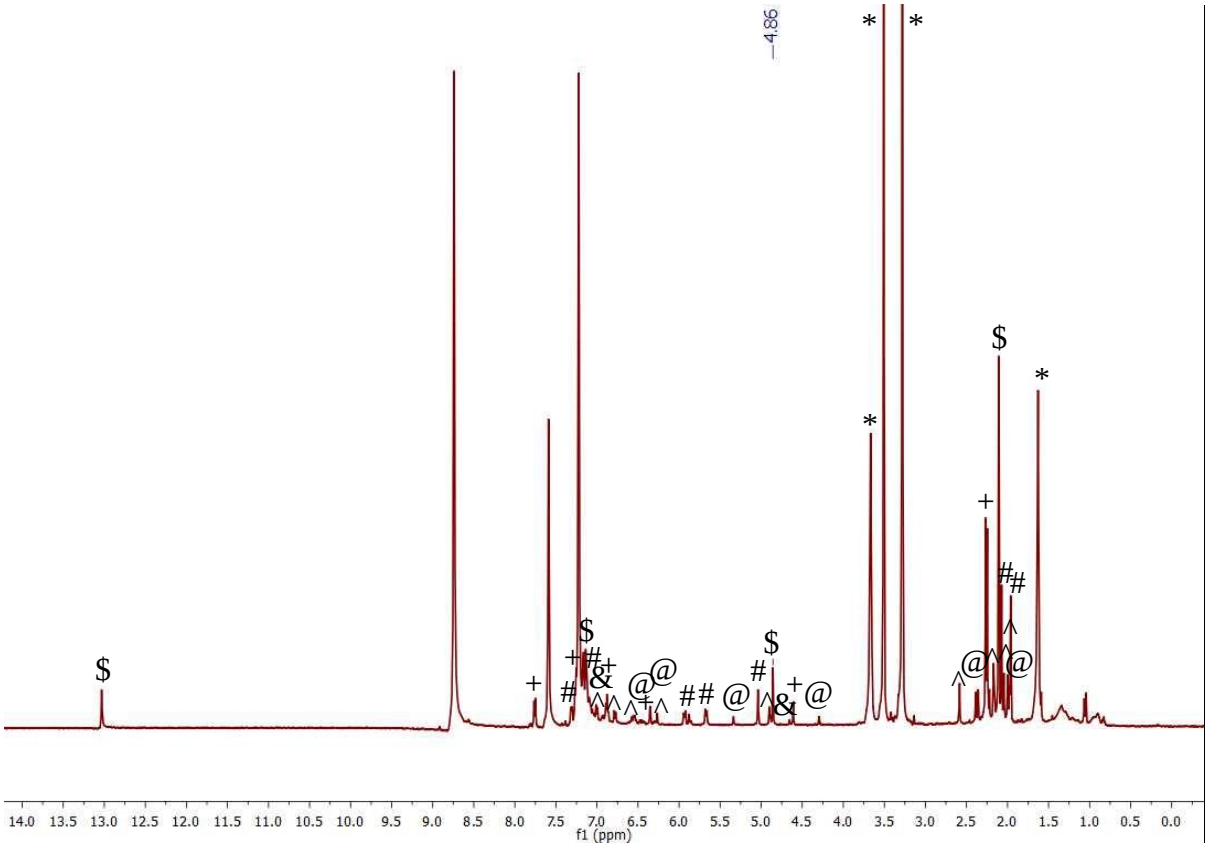

Figure A5.6. *In situ* ^{1}H NMR spectrum (in py-d_5) of a mixture of $[K(DME)]_2[tmtaa]$ and $[UO_2Cl_2(THF)_3]$ after standing for 1 min at room temperature. Compounds **5.2**, **5.3**, **5.4**, $tmtaaH_2$ and a new tmtaa product are present in a 4:6:5:5:4 relative ratio, respectively. ^ indicates resonances assignable to **5.2**, + indicates resonances assignable to **5.3**, # indicates resonances assignable to **5.4,** $ indicates resonances assignable to $tmtaaH_2$, & indicates resonances assignable to $[K(DME)]_2[tmtaa]$), @ indicates resonances assignable to a new tmtaa environment, and asterisks indicates the presence of DME and THF. ^{1}H NMR (py-d_5, 25 °C, 500 MHz): δ 13.03 (s, 2H, NH, $tmtaaH_2$), 7.76 (d, J_{HH} = 10 Hz, 2H, aryl CH, **5.3**), 7.32 (m, 2H, aryl CH, **5.4**), 7.25 (t, J_{HH} = 10 Hz, 2H, aryl CH, **5.3**), 7.16 (m, 4H, aryl CH, $tmtaaH_2$), 7.13 (m, 4H, aryl CH, $tmtaaH_2$), 7.09 (m, 2H, aryl CH, **5.4**), 7.01 (d, J_{HH} = 5 Hz, 2H, aryl CH, **5.2**), 6.93 (m, 4H, aryl CH, $[K(DME)]_2[tmtaa]$), 6.92 (m, 4H, aryl CH, $[K(DME)]_2[tmtaa]$), 6.88 (t, J_{HH} = 10 Hz, 2H, aryl CH, **5.3**), 6.78 (d, J_{HH} = 10Hz, 2H, aryl CH, **5.2**), 6.57 (t, J_{HH} = 15 Hz, 2H, aryl CH, new product), 6.54 (t, J_{HH} = 10 Hz, 2H, aryl CH, **5.2**), 6.47 (d, J_{HH} = 10 Hz, 2H, aryl CH, new product), 6.44 (t, J_{HH} = 10 Hz, 2H, aryl CH, new product), 6.35 (s, 1H, γ-CH, **5.3**), 6.29 (m, 2H, aryl CH, new product), 6.27 (s, 1H, γ-CH, **5.2**), 5.93 (m, 2H, C=CH,

5.4), 5.68 (m, 2H, C=CH, **5.4**), 5.34 (s, 1H, γ-CH, new product), 5.04 (s, 2H, γ-CH, **5.4**), 4.90 (s, 1H, γ-CH, **5.2**), 4.86 (s, 2H, γ-CH, tmtaaH_2), 4.66 (s, 2H, γ-CH, [K(DME)]$_2$[tmtaa]), 4.61 (s, 1H, γ-CH, **5.3**), 4.29 (s, 1H, γ-CH, new product), 3.67 (s, 4H, OCH_2, THF), 3.51 (s, 4H, OCH_2, DME), 3.28 (s, 6H, OCH_3, DME), 2.58 (s, 3H, CH_3, **5.2**), 2.39 (s, 6H, CH_3, new product), 2.26 (s, 6H, CH_3, **5.3**), 2.25 (s, 6H, CH_3, **5.3**), 2.17 (s, 3H, CH_3, **5.2**) 2.16 (s, 12H, CH_3, [K(DME)]$_2$[tmtaa]), 2.11 (s, 12H, CH_3, tmtaaH_2), 2.07 (s, 6H, CH_3, **5.4**), 2.04 (s, 3H, CH_3, **5.2**), 2.00 (s, 3H, CH_3, **5.2**), 1.98 (s, 6H, CH_3, new product) 1.96 (s, 6H, CH_3, **5.4**), 1.63 (s, 4H, CCH_2, THF).

Experimental Details: [K(DME)]$_2$[tmtaa] (10.9 mg, 0.018 mmol) was dissolved in py-d_5 (0.75 mL), which yielded a deep red solution. The mixture was transferred to an NMR tube equipped with J-Young valve, removed from the glovebox, and a ^{1}H NMR spectrum was recorded. The sample was then brought back into the glovebox and a yellow-green solution of [$UO_2Cl_2(THF)_3$](10.1 mg, 0.018 mmol) in py-d_5 (0.5 mL) was added. This addition resulted in a color change to dark brown. The tube was then quickly removed from the glovebox, and ^{1}H NMR spectra were recorded at 1, 5, 10, and 15 min. Compounds **5.2**, **5.3**, **5.4**, and tmtaaH_2 are present in a 4:8:6:8 relative ratio, respectively, in the 15 min spectrum.

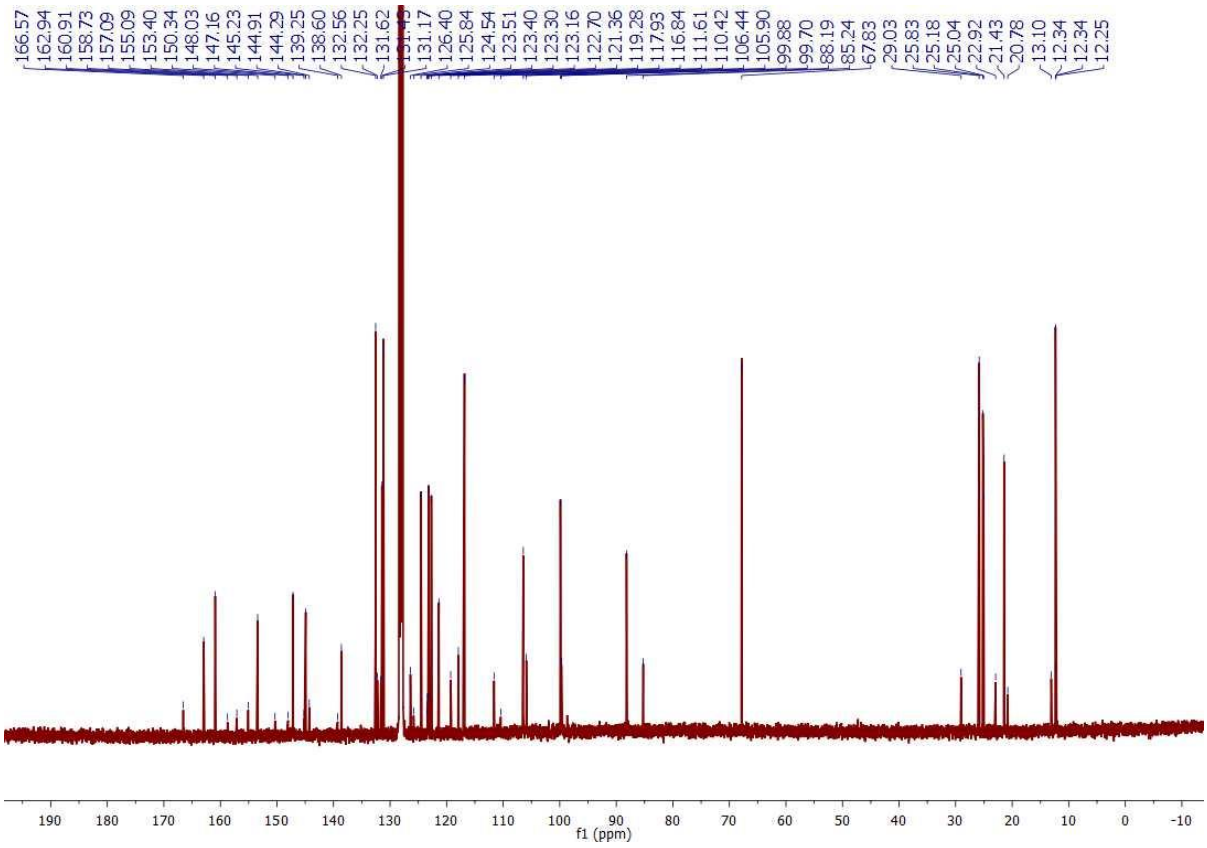

Figure A5.7. $^{13}C\{^{1}H\}$ NMR spectrum of a mixture of **5.2**, **5.3**, and **5.4** (in a 1:4:2 ratio) in C_6D_6.

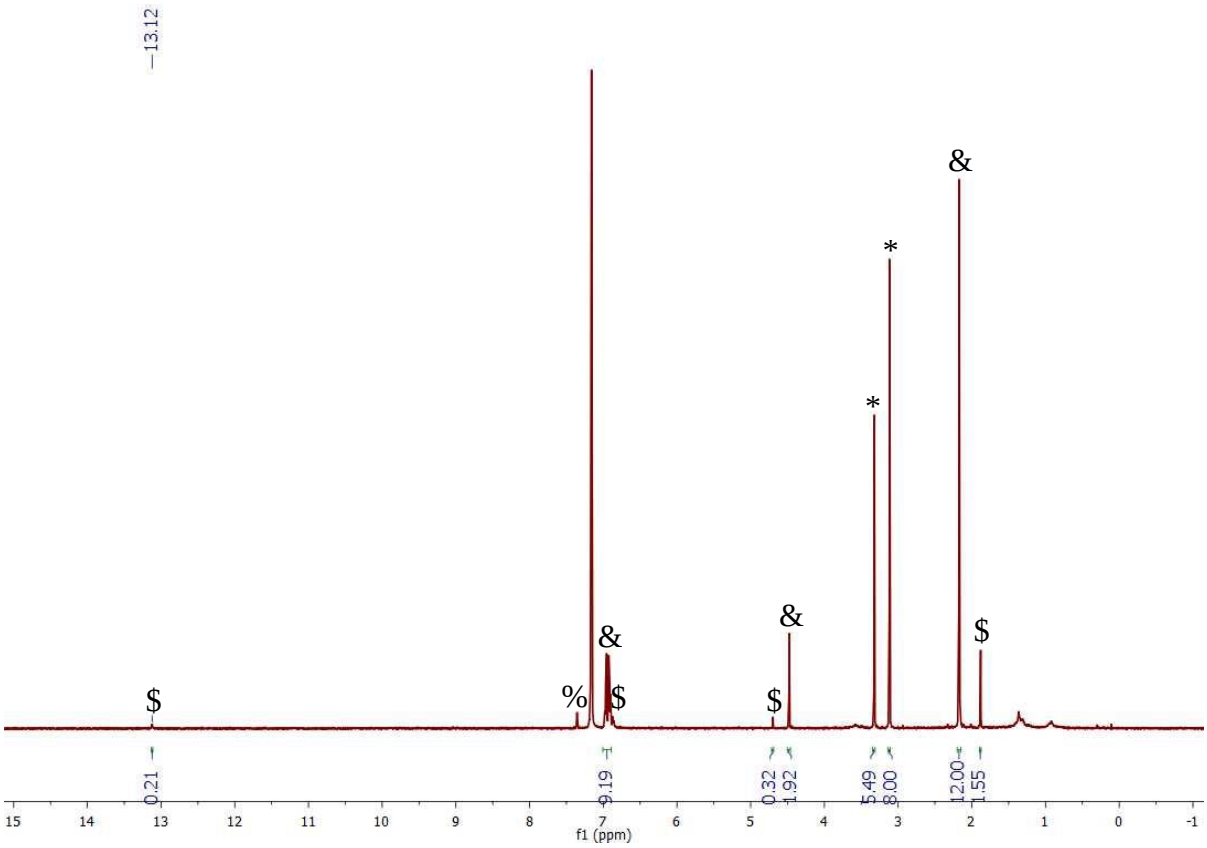

Figure A5.8. ^{1}H NMR spectrum (in C_6D_6) of an aliquot of the reaction of a mixture of **5.2**, **5.3**, and **5.4** (in a 3:9:1 ratio) with KC_8. & indicates resonances assignable to $[K(DME)]_2[tmtaa]$, $ indicates resonances assignable to $tmtaaH_2$, % indicates resonances assignable to unidentified products, and * indicates presence of DME.

Experimental Details: To a stirring orange solution of a mixture of **5.2**, **5.3**, and **5.4** in a 3:9:1 ratio (9.3 mg, 0.027 mmol) in DME (1 mL) was added a slurry of KC_8 (19.6 mg, 0.144 mmol, 5 equiv) in DME (2 mL). This addition resulted in an immediate color change to dark brown. The slurry was stirred for 48 h at room temperature, whereupon the resulting red-brown solution was filtered through a Celite column supported on glass wool (0.5 cm × 2 cm) to yield a deep red filtrate. A ^{1}H NMR spectrum of an aliquot of this solution was then recorded, which revealed presence of $[K(DME)]_2[tmtaa]$ and $tmtaaH_2$ in an 8:1 ratio, respectively. ^{1}H NMR (C_6D_6, 25 °C, 400 MHz): δ 13.12 (s, 2H, NH, $tmtaaH_2$), 6.95 (m, 4H, aryl CH, $[K(DME)]_2[tmtaa]$), 6.93 (m, 4H, aryl CH, $[K(DME)]_2[tmtaa]$), 6.87 (m, 4H, aryl CH, $tmtaaH_2$), 4.70 (s, 2H, γ-CH, $tmtaaH_2$), 4.48 (s, 2H, γ-CH, $[K(DME)]_2[tmtaa]$), 3.32 (s, 4H, OCH_2, DME), 3.12 (s, 6H, OCH_3, DME), 2.17(s, 12H, CH_3, $[K(DME)]_2[tmtaa]$), 1.88 (s, 12H,

CH_3, tmtaaH_2). One aryl resonance is not observed for tmtaaH_2 due to overlap with those of $[K(DME)]_2$[tmtaa]. The volume of the filtrate was reduced *in vacuo* (1 mL), and the solution was subsequently stored at -25 °C for 72 h, which resulted in deposition of red-brown crystals of $[K(DME)]_2$[tmtaa] (4.2 mg, 26% yield).

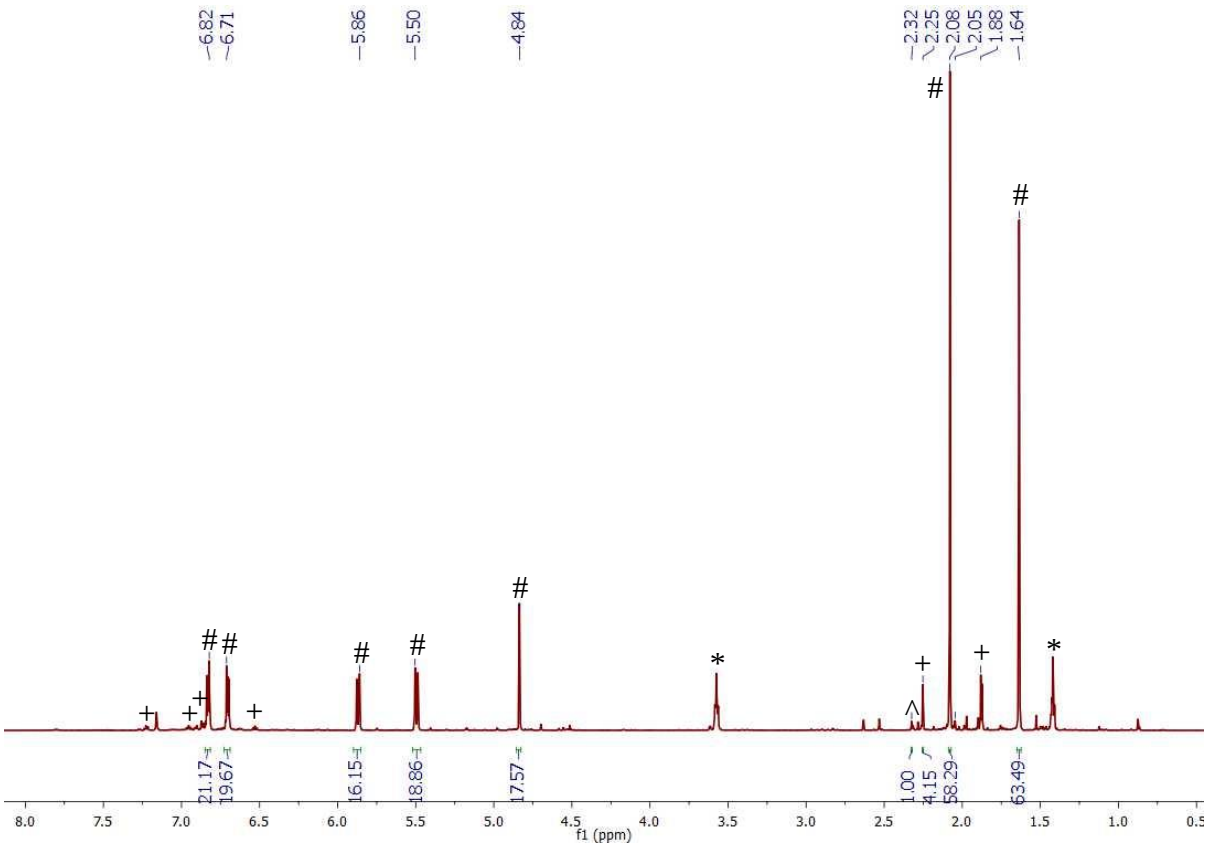

Figure A5.9. ^{1}H NMR spectrum of compounds **5.2**, **5.3**, and **5.4** (1:2:30 relative ratio) in C_6D_6 after heating at 50 °C for 24 h. ^ indicates resonances assignable to **5.2**, + indicates resonances assignable to **5.3**, # indicates resonances assignable to **5.4**, and asterisks indicate the presence of THF. **Experimental Details:** A mixture of compounds **5.2**, **5.3**, and **5.4** (21.2 mg) was dissolved in C_6D_6 (1 mL) to yield a deep orange solution. The solution was transferred to an NMR tube equipped with a J-Yound valve, removed from the glovebox, and a ^{1}H NMR spectrum was recorded. This spectrum revealed the presence of **5.2**, **5.3**, and **5.4**, in a 1:4:2 ratio, respectively. The sample was then heated at 50 °C for 24 h and its ^{1}H NMR spectrum was recorded again, which revealed the presence of **5.2**, **5.3**, and **5.4** in a 1:2:30 ratio, respectively.

5.6.2 X-ray Photoelectron Spectroscopy

Table A5.1. X-ray Photoelectron Spectroscopy Data

Assignment	E_b (eV)
O KLL	972.8
U $4d_{3/2}$	781.3
U $4d_{5/2}$	739.3
O 1s	531.8
N 1s	399.8
U $4f_{5/2}$	392.6
U $4f_{7/2}$	381.8
K 2p	293.8
C 1s	285.3
Cl 2s	269.3
Cl 2p	199.8
U $5d_{3/2}$	105.3
U $5d_{5/2}$	97.3
U $6p_{1/2}$	31.8
U $6p_{3/2}$	16.3

5.6.3 IR Spectra

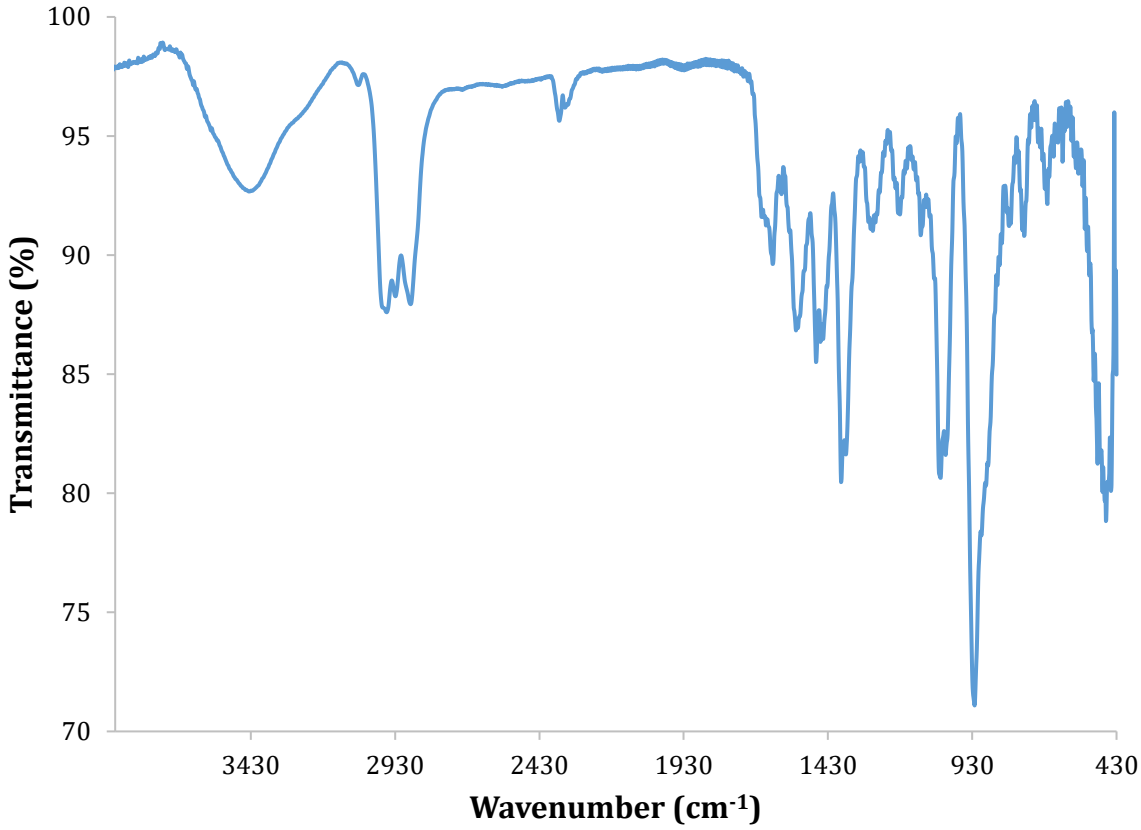

Figure A5.10. IR spectrum of **5.1** (as KBr pellet).

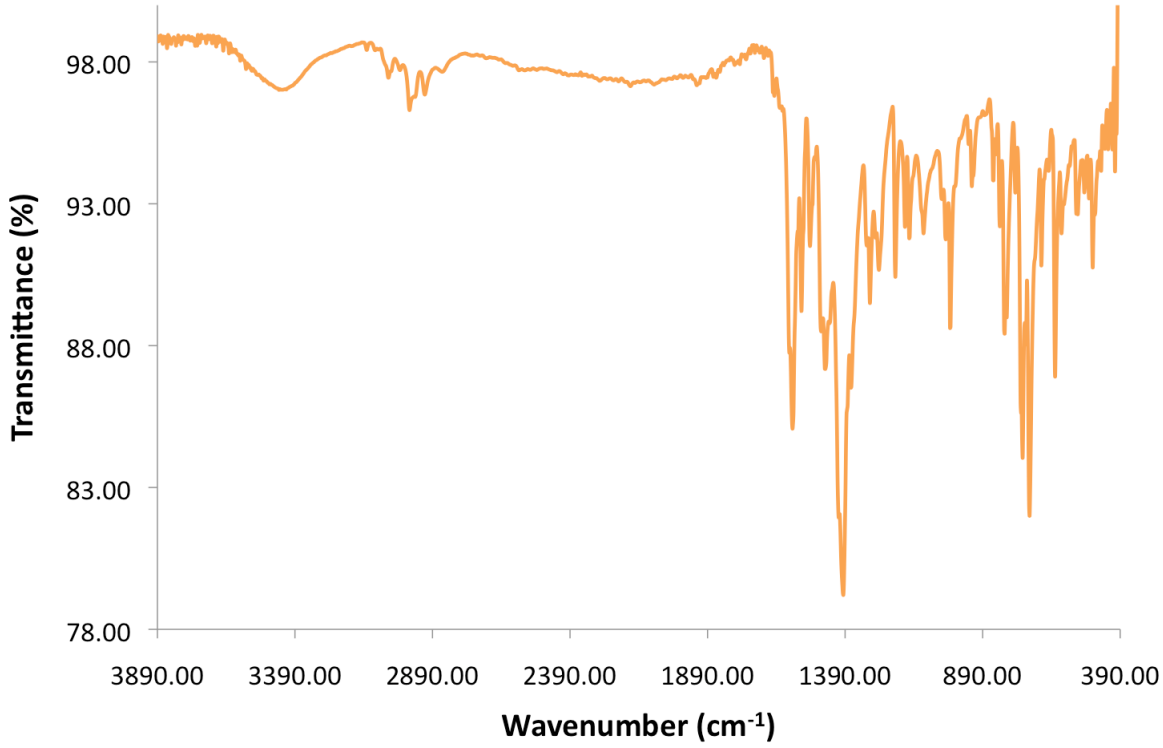

Figure A5.11. IR spectrum of a mixture of **5.2** and **5.3** in a 10:1 ratio (as KBr pellet).

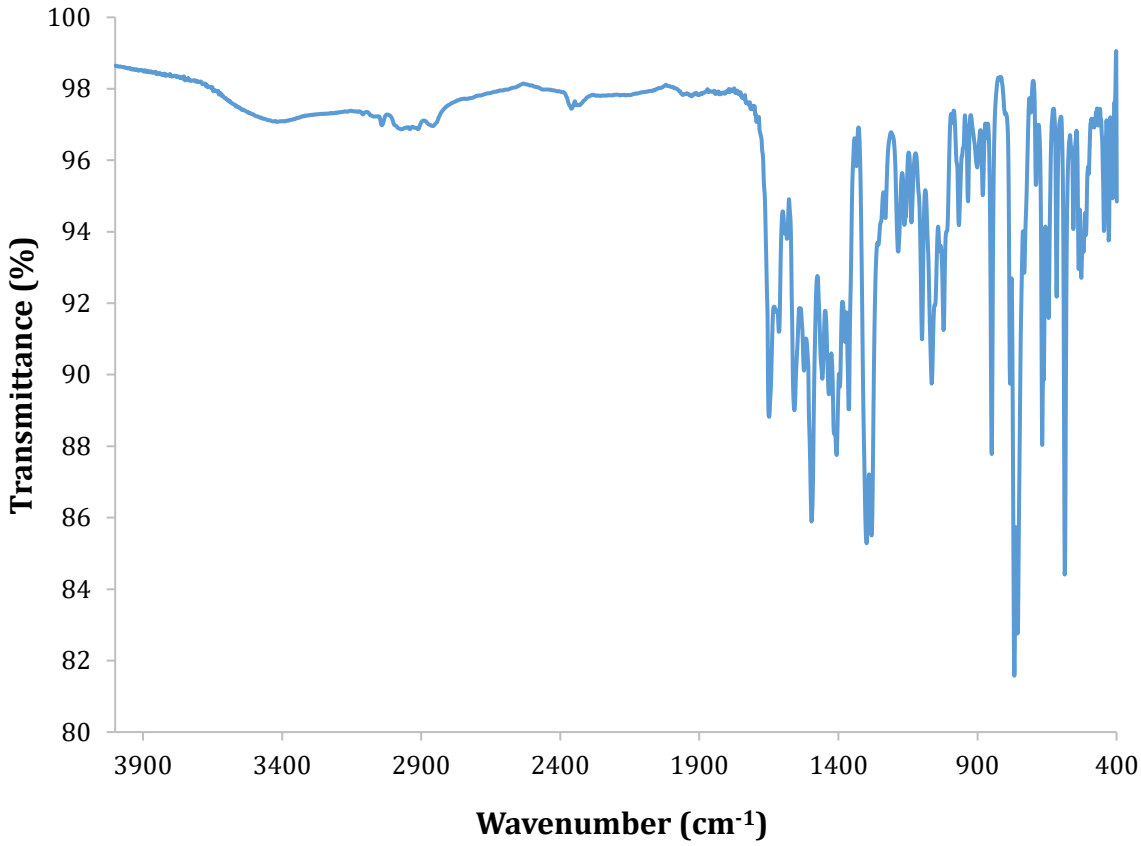

Figure A5.12. IR spectrum of a mixture of **5.3** and **5.4** in a 1:7 ratio (as KBr pellet).

5.7 References

1. Denning, R. G. Electronic Structure and Bonding in Actinyl Ions and their Analogs. *J. Phys. Chem. A* **2007,** 111, 4125-4143.

2. Cotton, S. *Lanthanide and Actinide Chemistry*. John Wiley & Sons, Ltd.: West Sussex, England, 2006.

3. Fortier, S.; Hayton, T. W. Oxo ligand functionalization in the uranyl ion (UO_2^{2+}). *Coord. Chem. Rev.* **2010,** 254, 197-214.

4. Bell, N. L.; Shaw, B.; Arnold, P. L.; Love, J. B. Uranyl to Uranium(IV) Conversion through Manipulation of Axial and Equatorial Ligands. *J. Am. Chem. Soc.* **2018,** 140, 3378-3384.

5. Schnaars, D. D.; Wu, G.; Hayton, T. W. Reduction of Pentavalent Uranyl to U(IV) Facilitated by Oxo Functionalization. *J. Am. Chem. Soc.* **2009,** 131, 17532-17533.

6. Hayton, T. W.; Wu, G. Exploring the Effects of Reduction or Lewis Acid Coordination on the U=O Bond of the Uranyl Moiety. *Inorg. Chem.* **2009,** 48, 3065-3072.

7. Lewis, A. J.; Yin, H.; Carroll, P. J.; Schelter, E. J. Uranyl-oxo coordination directed by non-covalent interactions. *Dalton Trans.* **2014,** 43, 10844-10851.

8. Duval, P. B.; Burns, C. J.; Clark, D. L.; Morris, D. E.; Scott, B. L.; Thompson, J. D.; Werkema, E. L.; Jia, L.; Andersen, R. A. Synthesis and Structural Characterization of the First Uranium Cluster Containing an Isopolyoxometalate Core. *Angew. Chem. Int. Ed.* **2001,** 40, 3357-3361.

9. Cantat, T.; Graves, C. R.; Scott, B. L.; Kiplinger, J. L. Challenging the Metallocene Dominance in Actinide Chemistry with a Soft PNP Pincer Ligand: New Uranium Structures and Reactivity Patterns. *Angew. Chem. Int. Ed.* **2009,** 48, 3681-3684.

10. La Pierre, H. S.; Meyer, K. Uranium–Ligand Multiple Bonding in Uranyl Analogues, $[L{=}U{=}L]^{n+}$, and the Inverse Trans Influence. *Inorg. Chem.* **2013,** 52, 529-539.

11. Kovács, A.; Konings, R. J. M. A Theoretical Study of the Structure and Bonding of UOX_4 (X=F, Cl, Br, I) Molecules: The Importance of Inverse *Trans* Influence. *Chem. Phys. Chem.* **2006,** 7, 455-462.

12. Lam, O. P.; Franke, S. M.; Nakai, H.; Heinemann, F. W.; Hieringer, W.; Meyer, K. Observation of the Inverse Trans Influence (ITI) in a Uranium(V) Imide Coordination Complex: An Experimental Study and Theoretical Evaluation. *Inorg. Chem.* **2012,** 51, 6190-6199.

13. Pedrick, E. A.; Wu, G.; Kaltsoyannis, N.; Hayton, T. W. Reductive Silylation of a Uranyl Dibenzoylmethanate Complex: An Example of Controlled Uranyl Oxo Ligand Cleavage. *Chem. Sci.* **2014,** 5, 3204-3213.

14. Pedrick, E. A.; Schultz, J. W.; Wu, G.; Mirica, L. M.; Hayton, T. W. Perturbation of the O–U–O Angle in Uranyl by Coordination to a 12-Membered Macrocycle. *Inorg. Chem.* **2016,** 55, 5693-5701.

15. Pedrick, E. A.; Assefa, M. K.; Wakefield, M. E.; Wu, G.; Hayton, T. W. Uranyl Coordination by the 14-Membered Macrocycle Dibenzotetramethyltetraaza[14]annulene. *Inorg. Chem.* **2017,** 56, 6638-6644.

16. Hohloch, S.; Garner, M. E.; Parker, B. F.; Arnold, J. New supporting ligands in actinide chemistry: tetramethyltetraazaannulene complexes with thorium and uranium. *Dalton Trans.* **2017,** 46, 13768-13782.

17. Fandos, R.; Walter, M. D.; Kazhdan, D.; Andersen, R. A. Selective Syntheses of Homo- and Hetero-dimetal Complexes with the Tetramethyltetraazaannulene Ligand of the Type [(ML,M‘L‘)(TMTAA)], Where M and M‘ Are Rh(I) or Ir(I) and L and L‘ Are COD or $(CO)_2$. *Organometallics* **2006,** 25, 3678-3687.

18. Cowie, B. E.; Nichol, G. S.; Love, J. B.; Arnold, P. L. Double uranium oxo cations derived from uranyl by borane or silane reduction. *ChemComm* **2018,** 54, 3839-3842.

19. The Chemistry of the Actinide and Transactinide Elements (3rd ed., Volumes 1-5). In 3 ed.; Morss, L. R., Edelstein, N., Fuger, J., Katz, J. J., Eds. Springer Netherlands: 2006; p 698.

20. Schettini, M. F.; Wu, G.; Hayton, T. W. Coordination of N-Donor Ligands to a Uranyl(V) b-Diketiminate Complex. *Inorg. Chem.* **2009,** 48, 11799-11808.

21. Hayton, T. W.; Wu, G. Synthesis, Characterization, and Reactivity of a Uranyl b-Diketiminate Complex. *J. Am. Chem. Soc.* **2008,** 130, 2005-2014.

22. Schettini, M. F.; Wu, G.; Hayton, T. W. Synthesis and reactivity of a uranyl-imidazolyl complex. *Chem. Commun.* **2012,** 48, 1484-1486.

23. Seaman, L. A.; Hrobárik, P.; Schettini, M. F.; Fortier, S.; Kaupp, M.; Hayton, T. W. A Rare Uranyl(VI)–Alkyl Ate Complex $[Li(DME)_{1.5}]_2[UO_2(CH_2SiMe_3)_4]$ and Its Comparison with a Homoleptic Uranium(VI)–Hexaalkyl. *Angew. Chem. Int. Ed.* **2013,** 52, 3259-3263.

24. Seaman, L. A.; Schnaars, D. D.; Wu, G.; Hayton, T. W. Isolation of a uranyl amide by "ate" complex formation. *Dalton Trans.* **2010,** 39, 6635-6637.

25. Arnold, P. L.; Pecharman, A.-F.; Hollis, E.; Yahia, A.; Maron, L.; Parsons, S.; Love, J. B. Uranyl oxo activation and functionalization by metal cation coordination. *Nat. Chem.* **2010,** 2, 1056-1061.

26. Thuery, P.; Masci, B. Synthesis and crystal structure of 1:2 mixed uranyl/alkali metal ions (Li^+, Na^+, K^+, Cs^+) complexes of p-tert-butyltetrahomodioxacalix[4]arene. *Dalton Trans.* **2003**, 2411-2417.

27. Danis, J. A.; Lin, M. R.; Scott, B. L.; Eichhorn, B. W.; Runde, W. H. Coordination Trends in Alkali Metal Crown Ether Uranyl Halide Complexes: The Series $[A(Crown)]_2[UO_2X_4]$ Where A = Li, Na, K and X = Cl, Br. *Inorg. Chem.* **2001,** 40, 3389-3394.

28. Seaman, L. A.; Pedrick, E. A.; Wu, G.; Hayton, T. W. Promoting oxo functionalization in the uranyl ion by ligation to ketimides. *J. Organomet. Chem.* **2018,** 857, 34-37.

29. De Angelis, S.; Solari, E.; Gallo, E.; Floriani, C.; Chiesi-Villa, A.; Rizzoli, C. Mono- and bis(dibenzotetramethyltetraaza[14]annulene) complexes of Group IV metals including the structure of the lithium derivative of the macrocyclic ligand. *Inorg. Chem.* **1992,** 31, 2520-2527.

30. Floriani, C.; Mazzanti, M.; Ciurli, S.; Chiesi-Villa, A.; Guastini, C. *cis*- and *trans*-Dichloro chelate complexes of niobium(IV): synthesis and structure of *trans*-dichloro[NN'-ethylenebis(acetylacetonylideneiminato)-(2-)]niobium(IV) and *cis*-dichloro{7,16-dihydro-6,8,15,17-tetramethyldibenzo-[b,i][1,4,8,11]tetra-azacyclotetradecinato(2-)}niobium(IV)-acetonitrile (1/2). *J. Chem. Soc., Dalton Trans.* **1988**, 1361-1365.

31. Goedken, V. L.; Weiss, M. C.; Place, D.; Dabrowiak, J. In *Inorg. Synth.*; 1980; Vol. 20, pp 115-119.

32. Willey, G. R.; Rudd, M. D. Group 14-tetraazamacrocycle complexes: Synthesis and characterization of $[Me_2M(tmtaa)]$ and $[Cl_2M(tmtaa)]$, where M = Si and Sn (H_2tmtaa = dibenzotetramethyltetraaza[14]annulene). *Polyhedron* **1992,** 11, 2805-2807.

33. Cotton, F. A.; Czuchajowska, J. Recent developments in the chemistry of mono- and dinuclear complexes of the macrocyclic dianion, 5,7,12,14-tetramethyldibenzo[b,i][1,4,8,11] tetraazac. *Polyhedron* **1990,** 9, 2553-2566.

34. Camp, C.; Arnold, J. On the non-innocence of "Nacnacs": ligand-based reactivity in b-diketiminate supported coordination compounds. *Dalton Trans.* **2016,** 45, 14462-14498.

35. Goedken, V. L.; Ladd, J. A. Deoxovanadium(IV) complexes of the dibenzotetramethyltetra-aza[14]-annulene ligand: formation of products containing thioxo-, m-nitrido-, and oxidatively coupled ligands. *J. Chem. Soc., Chem. Commun.* **1981**, 910-911.

36. McElroy, F. C.; Dabrowiak, J. C. Electrochemical generation of a dimeric macrocyclic complex. *J. Am. Chem. Soc.* **1976,** 98, 7112-7113.

37. Burschka, C.; Akgün, E.; Pindur, U. Zur Struktur von (Pyrazolinonyl)-(hydroxypyrazolium)methanperchloraten NMR-, IR-, spektroskopische Studien und Kristallstruktur. *Z. Naturforsch., B. Chem. Sci.* **1983,** 38, 373-377.

38. Han, Y.; Yuan, D.; Teng, Q.; Huynh, H. V. Reactivity Differences of Palladium(II) Dimers Bearing Heterocyclic Carbenes with Two, One, or No α-Nitrogen Atoms toward Isocyanides. *Organometallics* **2011,** 30, 1224-1230.

39. Esteruelas, M. A.; Gómez, A. V.; López, A. M.; Oñate, E. 1,2,3-Diheterocyclization Reactions on the Allenylidene Ligand of a Ruthenium Complex. *Organometallics* **1998,** 17, 3567-3573.

40. Han, Y.; Huynh, H. V. Preparation and characterization of the first pyrazole-based remote N-heterocyclic carbene complexes of palladium(ii). *Chem. Commun.* **2007**, 1089-1091.

41. Bertolasi, V.; Mantovani, N.; Marvelli, L.; Rossi, R.; Bianchini, C.; de los Rios, I.; Peruzzini, M.; Akbayeva, D. N. 1,3-Cycloaddition of pyrazole to the allenylidene ligand in $[Re\{C=C=CPh_2\}(CO)_2\{MeC(CH_2PPh_2)_3\}]^+$. *Inorg. Chim. Acta* **2003,** 344, 207-213.

42. Mair, F. S.; Scully, D.; Edwards, A. J.; Raithby, P. R.; Snaith, R. Synthetic, structural, spectroscopic and calculational studies of a lithium β-diketinimate complex. *Polyhedron* **1995,** 14, 2397-2401.

43. Wooles, A. J.; Lewis, W.; Blake, A. J.; Liddle, S. T. β-Diketiminate Derivatives of Alkali Metals and Uranium. *Organometallics* **2013,** 32, 5058-5070.

44. Fomenko, Y. S.; Gushchin, A. L.; Tkachev, A. V.; Vasilyev, E. S.; Abramov, P. A.; Nadolinny, V. A.; Syrokvashin, M. M.; Sokolov, M. N. Fist oxidovanadium complexes containing chiral derivatives of dihydrophenanthroline and diazafluorene. *Polyhedron* **2017,** 135, 96-100.

45. Gu, X.; Zhang, L.; Zhu, X.; Wang, S.; Zhou, S.; Wei, Y.; Zhang, G.; Mu, X.; Huang, Z.; Hong, D.; Zhang, F. Synthesis of Bis(NHC)-Based CNC-Pincer Rare-Earth-Metal Amido Complexes and Their Application for the Hydrophosphination of Heterocumulenes. *Organometallics* **2015,** 34, 4553-4559.

46. Karpov, V. M.; Platonov, V. E.; Rybalova, T. V.; Gatilov, Y. V.; Shakirov, M. M. The first synthesis and X-ray structures of polyfluorinated 1,2-, 2,3- and 2,4a-dihydro-1,3-diazafluorenes. *J. Fluor. Chem.* **2006,** 127, 936-942.

47. Wang, Y.; Chi, Y.; Zhang, W.-X.; Xi, Z. Regioselective Ring Expansion of 2,4-Diiminoazetidines via Cleavage of C–N and C(sp^3)–H Bonds: Efficient Construction of 2,3-Dihydropyrimidinesulfonamides. *J. Am. Chem. Soc.* **2012,** 134, 2926-2929.

48. Yurii, A. T.; Anton Yu, T. The structure of X-ray photoelectron spectra of light actinide compounds. *Russ. Chem. Rev.* **2004,** 73, 541.

49. Bailey, C. L.; Bereman, R. D.; Rillema, D. P.; Nowak, R. Redox and spectral properties of nickel(II) macrocycles containing dianionic, tetraazaannulene ligands. *Inorg. Chem.* **1984,** 23, 3956-3960.

50. Kadish, K. M.; Bottomley, L. A.; Schaeper, D.; Tsutsui, M.; Bobsein, R. L. Electron transfer reactivity of novel dirhenium and dirhodium tetraazaannulene complexes. *Inorg. Chim. Acta* **1979,** 36, 219-222.

51. Wilkerson, M. P.; Burns, C. J.; Paine, R. T.; Scott, B. L. Synthesis and Crystal Structure of $UO_2Cl_2(THF)_3$: A Simple Preparation of an Anhydrous Uranyl Reagent. *Inorg. Chem.* **1999,** 38, 4156-4158.

52. Niewahner, J. H.; Walters, K. A.; Wagner, A. Improved Synthesis of Geodken's Macrocycle through the Synthesis of the Dichloride Salt. *J. Chem. Educ.* **2007,** 84, 477.

53. Harris, R. K.; Becker, E. D.; Cabral De Menezes, S. M.; Goodfellow, R.; Granger, P. NMR Nomenclature. Nuclear Spin Properties and Conventions for Chemical Shifts. *Pure Appl. Chem.* **2001,** 73, 1795-1818.

54. Harris, R. K.; Becker, E. D.; Cabral De Menezes, S. M.; Granger, P.; Hoffman, R. E.; Zilm, K. W. Further Conventions for NMR Shielding and Chemical Shifts. *Pure Appl. Chem.* **2008,** 80, 59-84.

55. Black, D. G.; Swenson, D. C.; Jordan, R. F.; Rogers, R. D. Tetraaza Macrocycles as Ancillary Ligands in Early Metal Alkyl Chemistry. Synthesis and Characterization of Out-of-Plane $(Me_4taen)ZrX_2$ (X = alkyl, benzyl, NMe_2, Cl) and $(Me_4taen)ZrX_2(NHMe_2)$ (X = Cl, CCPh) Complexes. *Organometallics* **1995,** 14, 3539-3550.

56. *SMART Apex II*, Version 2.1; Bruker AXS Inc.: Madison, WI, 2005.

57. *SAINT Software User's Guide*, Version 7.34a; Bruker AXS Inc.: Madison, WI, 2005.

58. Sheldrick, G. M. *SADABS*, University of Gottingen, Germany: 2005.

59. *SHELXTL PC*, Version 6.12; Bruker AXS Inc.: Madison, WI, 2005.

Chapter 6. Uranyl Oxo Silylation Promoted by Silsesquioxane Coordination

Portions of this work were published in:

Assefa, M.K.; Wu, G.; Hayton, T.W. *J. Am. Chem. Soc*. **2020**, *142*, 8738-8747.

http://pubs.acs.org/articlesonrequest/AOR-MINYVIKJZDSPAZVHFGM8

6.1 Introduction

The chemical behavior of the actinyl ions, AnO_2^{2+} (An = U, Np, Pu, Am), has considerable practical importance. For example, it may be possible to co-extract uranium, neptunium, plutonium, and actinium during the processing of spent nuclear fuel.[1-3] This co-extraction would be accomplished by converting these actinides into their actinyl ions, which all have similar solvent extraction chemistry. Likewise, efforts are underway to design ligand systems that capture uranyl directly from sea water.[4-6] However, implementing these processes will require an improved understanding of actinyl reactivity to be successful, especially with respect to actinyl redox and oxo functionalization chemistry. Similarly, understanding the chemistry and bonding of the actinyl ions is crucial for developing models of actinyl speciation and transport at legacy waste sites.[7]

The best studied member of this class, uranyl (UO_2^{2+}), exhibits appreciable kinetic and thermodynamic stability.[8-9] For example, Ephritikhine and co-workers attempted the protonation of uranyl oxo (O_{yl}) ligands by treatment of UO_3 with anhydrous triflic acid at 110 °C.[10] However, this reaction only generated uranyl triflate, $UO_2(OTf)_2$, which proved resistant to further protonation. In contrast, attempts to functionalize uranyl using other electrophiles have proven more successful. For example, Arnold and co-workers reported the "reductive silylation" of $[U^{VI}O_2(THF)(H_2L)]$ (L = polypyrrolic macrocycle) by reaction with $KN(SiMe_3)_2$ and FeI_2, which results in formation of the U(V) silyloxide, $[U^{V}O(OSiMe_3)(THF)(Fe_2I_2L)]$ (Scheme 6.1).[11] Since this seminal example, several other research groups have reported examples of "reductive silylation".[11-27] Other electrophiles can also functionalize the uranyl oxo ligands, such as $(Bpin)_2$, $^{i}Bu_2AlH$, $[Cp_2TiCl]_2$, $[Sm\{N(SiMe_3)_2\}_2]$, but these reagents tend to be either strong electrophiles or strong reductants.[13, 28-29] There are also examples of oxo

functionalization that convert UO_2^{2+} to U(IV), either directly or through a U(V) intermediate.[19, 23, 29-32]

Scheme 6.1. Reductive silylation of uranyl[11]

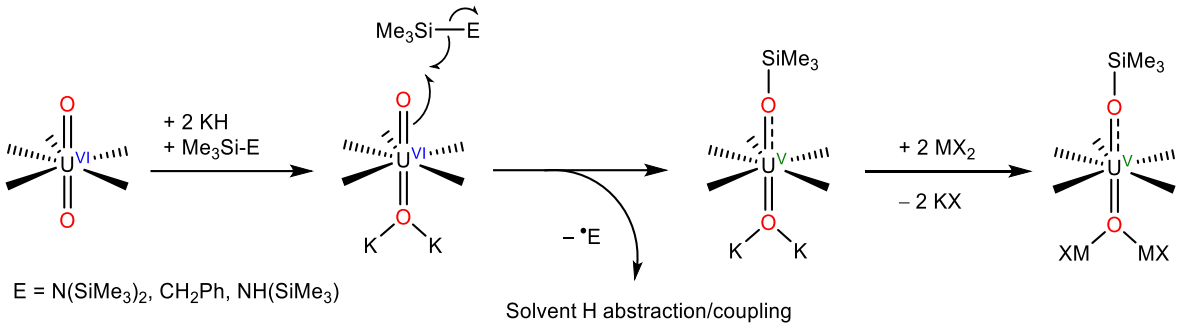

Formally, "reductive silylation" requires the silylation of one uranyl oxo ligand and reduction of the U^{6+} ion to U^{5+}.[11, 25, 33] A variety of silicon reagents can be used to effect this transformation. The most effective appear to be strong electrophiles, such as R_3SiOTf and R_3SiX (X = Cl, I), which can directly silylate even electron-poor uranyl fragments, such as those in cationic complexes.[12, 19, 21, 23, 31-32] In contrast, the use of weaker SiR_3 electrophiles, such as $N(SiMe_3)_3$, $HN(SiMe_3)_2$, or $PhCH_2SiMe_3$, requires the pre-activation of the uranyl fragment (Scheme 6.1). In the case of the Arnold example, this pre-activation is accomplished by the use the supramolecular Pacman macrocycle, which features a second metal binding site in close proximity to a uranyl oxo ligand.[11, 14, 24-25, 34-35] When this second site is occupied, the uranyl fragment is polarized sufficiently that its usual thermodynamic and kinetic stability is lost. Alternatively, the silylating agent itself can be activated by co-addition of Lewis acids, such as $B(C_6F_5)_3$.[26-27]

There has been recent progress in exploring the coordination of macrocyclic ligands to the uranyl ion, in an effort to effect O_{yl}-U-O_{yl} bending.[36-39] Examples include $^{H}N_4$ ($^{H}N_4$ = 2,11-diaza[3,3](2,6) pyridinophane), $^{Me}N_4$ ($^{Me}N_4$ = *N,N'*-dimethyl-2,11-diaza[3,3](2,6)

pyridinophane) and tmtaaH_2 (tmtaaH_2 = dibenzotetramethyltetraaza[14]annulene) (see chapter 5 for detailed discussion). The ligands investigated often feature ring sizes of less than 16 atoms, and are thus too small accommodate the uranyl fragment within their binding pockets. As a result, ligand coordination results in a "side-on"-type binding mode that perturbs the normally linear uranyl ion. Building on this work, I turned my attention to the silsequioxane ligand, $Cy_7Si_7O_9(OH)_3$ (Cy = cyclohexyl), which by virtue of its tripodal framework should not be able to ligate all three silyloxide arms to the equatorial plane of a single uranyl ion without any perturbation. Silsequioxanes were initially developed as models for silica surfaces, and have been widely used in mechanistic studies aimed at exploring the speciation of metal ions immobilized on silica.[40-42] They also display structural similarities with β-tridymite and β-crystobalite, as well as industrially important zeolites.[43] For example, Feher and Walzer reported the synthesis of the first vanadium silsesquioxanes, $[(Cy_7Si_7O_{12})VO]$ and $[(Cy_7Si_7O_{12})VO]_2$, which were used as models for monodisperse silica-supported vanadium catalysts.[42] Similarly, Edelmann *et al*. reported the synthesis of a novel Ce(IV) silsesquioxane, $[Ce(Cy_8Si_8O_{13})_2(py)_3]$,[44] a molecular analogue for silica-supported Ce(IV) oxidation catalysts. More recently, Edelmann and co-workers reported the synthesis of the first actinide silsesquioxane, $[U(Cy_7Si_7O_{12})_2]$, a rare example of a non-uranyl U(VI) complex. This species was made by reaction of UCl_4 with $Cy_7Si_7O_9(OH)_3$ in a mixture of THF and NEt_3.[45] To my knowledge, however, ligation of silsesquioxanes to the uranyl ion has not been explored. In this chapter, I describe the conversion of this ion into a U(VI) tris(silyloxide) upon coordination to $Cy_7Si_7O_9(OH)_3$, and present a detailed mechanistic proposal of the transformation. Ultimately, the results provide proof-of-concept that mineral surface mimics can be used to

manipulate and functionalize the actinyl ions, suggesting a new avenue for actinyl synthetic chemistry.

6.2 Results and Discussion

6.2.1 Synthesis and Characterization of $[K_3(THF)][(UO_2)_3(Cy_7Si_7O_{12})_3(Et_2O)_2(THF)]$ (6.1) and $[K(2,2,2\text{-cryptand})]_2[K_2UO_2(Cy_7Si_7O_{12})_2]$ (6.2)

Addition of $[K_3(DME)_2][Cy_7Si_7O_{12}]$ to 1 equiv of $[UO_2Cl_2(THF)_3]$ in THF affords $[K_3(THF)][(UO_2)_3(Cy_7Si_7O_{12})_3(Et_2O)_2(THF)]$ (**6.1**) as pale green plates in 30% yield after work-up (eq 6.1). Complex **6.1** crystallizes in the monoclinic space group $P2_1$, as the THF solvate **6.1**·THF (Figure 6.1). Its solid state molecular structure exhibits a trimeric $\{UO_2(Cy_7Si_7O_{12})\}_3$ cluster bridged by three potassium cations, wherein each uranyl unit is ligated by three silyloxide arms and an Et_2O or THF solvent molecule; i.e. all three uranium centers exhibit a distorted octahedral geometry. Curiously, the binding pocket of the tripodal silsesquioxane is occupied by the potassium cations, instead of the uranium centers. Each potassium cation is also involved in dative interactions with two O_{yl} ligands (range: 2.57(2) - 2.83(3) Å). Indeed, the potassium capped U-O_{yl} distances in **6.1** (1.80(2) - 1.92(2) Å) are somewhat longer than the terminal U-O_{yl} distances (1.66(2) - 1.73(2) Å). In addition, all uranyl fragments in **6.1** feature a linear O-U-O angle (174.3(12) - 178.2(13)°). Finally, the U-O(silsesquioxane) distances in **6.1** (2.11(3) - 2.28(2) Å) are comparable to those reported for $[U(Cy_7Si_7O_{12})_2]$ (2.085(2) - 2.268(2) Å).[45]

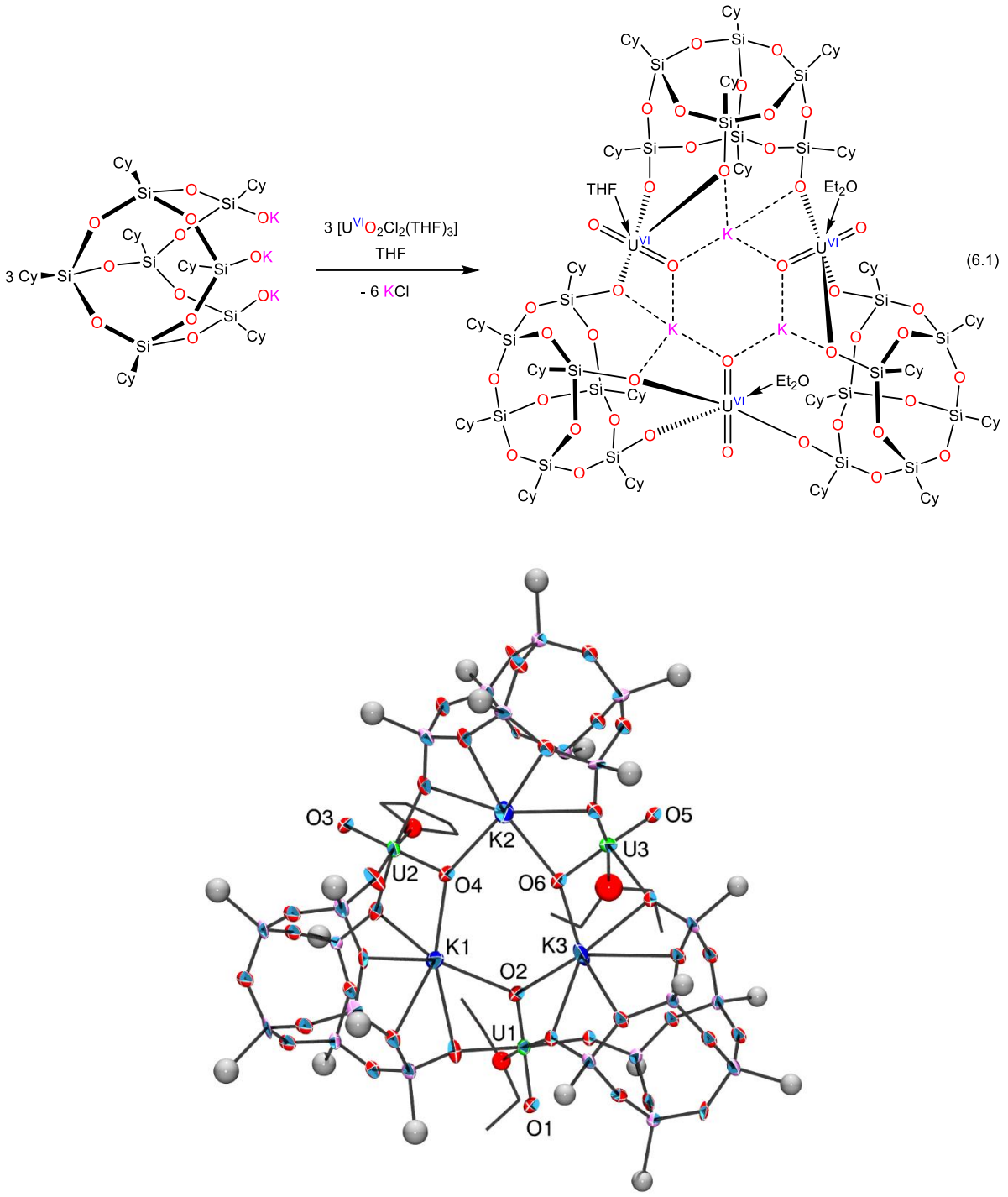

Figure 6.1. Solid-state molecular structure of **6.1**·THF shown with 50% probability ellipsoids. All hydrogen atoms and cyclohexyl groups (except the carbons directly attached to Si) have been omitted for clarity. Selected bond lengths (Å) and angles (°): U1-O1 = 1.78(2), U1-O2 =

1.65(2), U2-O3 = 1.70(2), U2-O4 = 1.83(2), U3-O5 = 1.69(2), U3-O6 = 1.92(2), K1-O4 = 2.70(3), K1-O2 = 2.82(3), K2-O6 = 2.71(2), K2-O4 = 2.72(3), K3-O6 = 2.59(3), K3-O2 = 2.85(3), O1-U1-O2 = 178.4(13), O3-U2-O4 = 173.7(13), O5-U3 -O6 = 178.7(11).

To circumvent the oligomerization observed for **6.1** and induce a κ^3 binding mode of the tripodal silsesquioxane, 2,2,2-cryptand was introduced during the synthesis of **6.1**. Thus, addition of 1 equiv of 2,2,2-cryptand to a 1:1 mixture of $[UO_2Cl_2(THF)_3]$ and $[K_3(DME)_2][Cy_7Si_7O_{12}]$ in THF, followed by work-up, results in isolation of a few colorless crystals which were identified as $[K(2,2,2\text{-cryptand})]_2[K_2UO_2(Cy_7Si_7O_{12})_2]$ (**6.2**) by X-ray crystallography (eq 6.2). Complex **6.2** crystallizes in the monoclinic space group $P2_1/n$ as the Et_2O solvate **6.2**·$2Et_2O$ (Figure 6.2). Its solid state molecular structure reveals an octahedral uranyl fragment that is ligated by two $\{Cy_7Si_7O_{12}\}^{3-}$ ligands that each bind the uranium through only two silyloxide arms. This partial coordination likely reflects the relative flexibility of the silsesquioxane backbone. The structure of **6.2** also features two $[K(2,2,2\text{-cryptand})]^+$ moieties, as well as two interstitial potassium cations that are each supported by dative interactions with an O_{yl} ligand, three silyloxide arms and two cryptand oxygen atoms. The U-O_{yl} (1.778(7) Å), U-O(silsesquioxane) (2.292(7) and 2.269(8) Å) and K-O (2.754(8) - 3.203(10) Å) distances in **6.2** are all comparable to those in **6.1**.

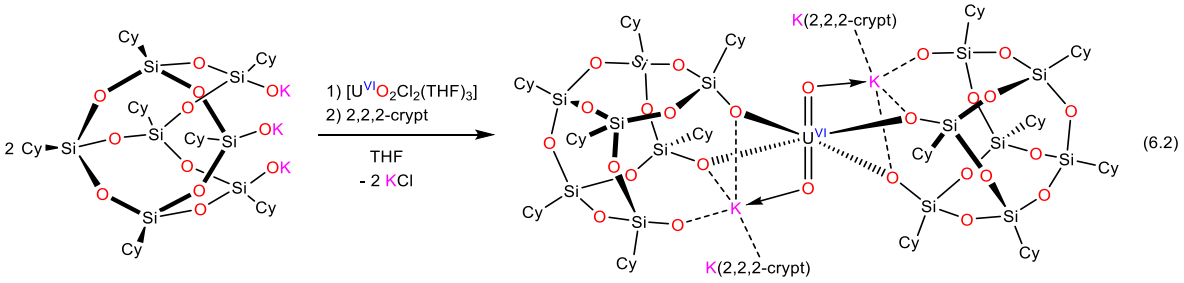

(6.2)

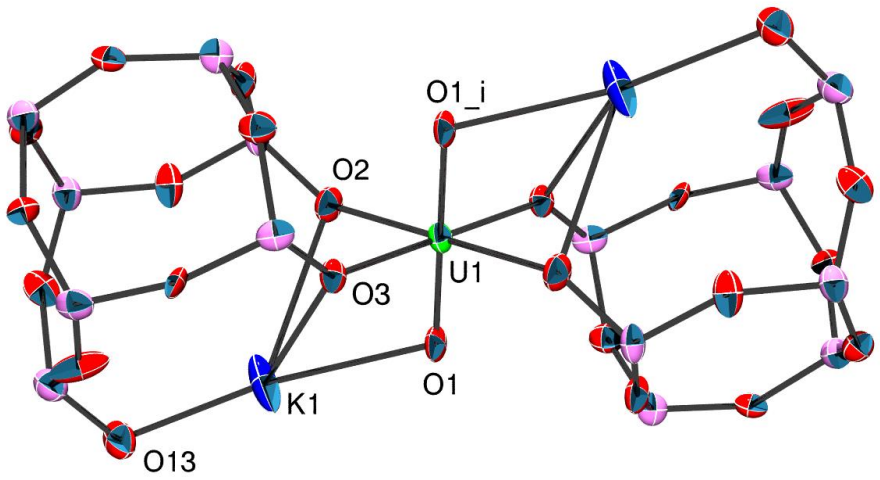

Figure 6.2. Solid-state molecular structure of **6.2**·2Et_2O shown with 50% probability ellipsoids. All hydrogen atoms and cyclohexyl groups and two [K(2,2,2-cryptand)] counterions have been omitted for clarity. Selected bond lengths (Å) and angles (°): U1-O1 = 1.800(7), U1-O2 = 2.257(7), U1-O3 = 2.244(7), K1-O1 = 2.751(8), K1-O2 = 3.067(8), K1-O3 = 2.873(7), K1-O13 = 2.570(8), O1-U1-O1_i = 180.0.

Given the unexpected 1:2 metal to ligand ratio observed for **6.2**, I sought an alternative route to induce κ^3 coordination of silsesquioxane to uranyl. I hypothesized that the presence of Lewis acidic alkali cations likely promotes the oligomerization and unwanted reaction stoichiometry observed for **6.1** and **6.2**. Hence, I modified my synthetic protocol from salt metathesis to protonolysis as outlined below.

6.2.2 Synthesis and Characterization of [U(OSiMe$_3$)$_3$(Cy$_7$Si$_7$O$_{12}$)] (6.3) and [(UO$_2$)$_3$(Cy$_7$Si$_7$O$_{12}$)$_2$(Et$_2$O)(MeCN)$_2$] (6.4)

Addition of $Cy_7Si_7O_9(OH)_3$ to 1 equiv of $[UO_2(N(SiMe_3)_2)_2(THF)_2]$ in THF results in rapid formation of an orange solution, concomitant with the deposition of a small amount of fine yellow precipitate. Work-up of this solution affords $[U(OSiMe_3)_3(Cy_7Si_7O_{12})]$ (**6.3**) as orange

plates in 24% isolated yield (based on uranium) (eq 6.3). Complex **6.3** is highly soluble in pentane, toluene, Et_2O and THF, but is insoluble in acetonitrile. It is also soluble, and stable, in both pyridine and dichloromethane at room temperature. Its ^{1}H NMR spectrum in C_6D_6 features a sharp resonance at 0.46 ppm attributable to the $OSiMe_3$ methyl groups. The spectrum also exhibits several broad resonances, ranging from 1.02 to 2.23 ppm, which correspond to the cyclohexyl CH and CH_2 protons. Additionally, the $^{13}C\{^{1}H\}$ NMR spectrum of **6.3** in C_6D_6 exhibits a sharp resonance at 3.79 ppm that is assignable to the $OSiMe_3$ methyl groups. There are also three resonances at 26.53, 24.01, and 23.93 ppm that are assignable to the three different HC-Si environments, as well as eight resonances between 27.31 and 28.23 ppm that are assignable to the cyclohexyl CH_2 environments. The more distinctive $^{29}Si\{^{1}H\}$ NMR spectrum features three resonances at -73.18, -69.06, and -68.12 ppm, in a 3:3:1 ratio, which are assignable to the three anticipated ^{29}Si environments of the silsesquioxane ligand in C_{3v} symmetry. In addition, there is a sharp resonance at 20.93 ppm assignable to the three equivalent $OSiMe_3$ ^{29}Si environments.

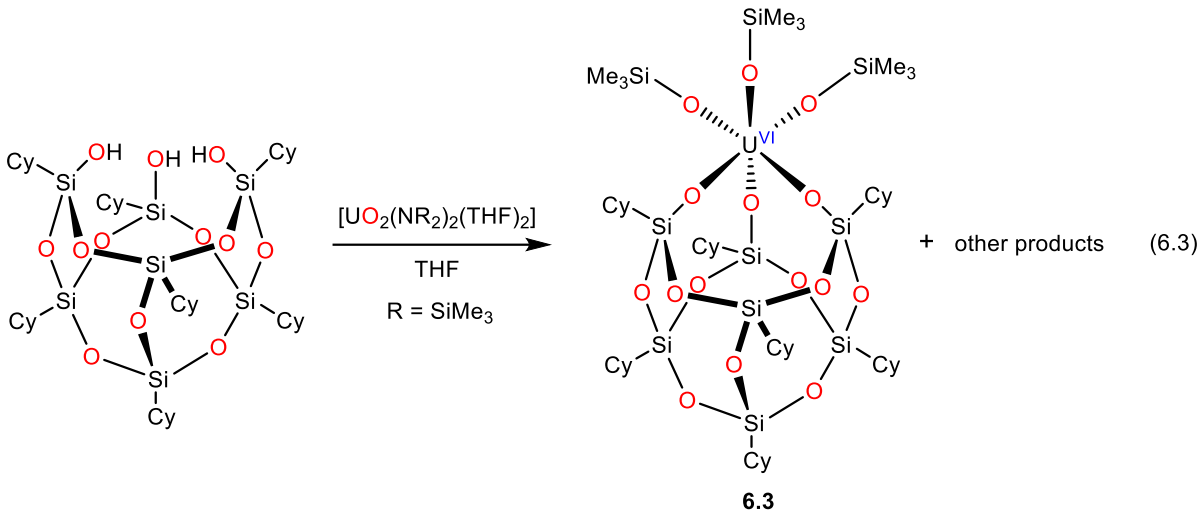

Complex **6.3** crystallizes in the monoclinic space group P2/c as the pentane solvate, **6.3**·0.5C_5H_{12} (Figure 6.3). Its solid-state molecular structure reveals an octahedral uranium center ligated by a tripodal $\{Cy_7Si_7O_{12}\}^{3-}$ ligand that coordinates via a κ^3 binding mode, along with three oxo-derived $OSiMe_3$ co-ligands. The $SiMe_3$ groups are evidently derived from the liberated $HN(SiMe_3)_2$. The average U-O(silsesquioxane) bond length is 2.056 Å (range = 2.047(6) - 2.066(6) Å), which is comparable to those reported for the only other known uranium silsesquioxane, namely, $[U(Cy_7Si_7O_{12})_2]$ (2.085(2) - 2.268(2) Å).[45] The average U-O($OSiMe_3$) bond length in **6.3** is 2.044 Å. This distance is much longer than those observed in the uranyl ion (1.78 Å), and slightly longer than the U(V)-$OSiMe_3$ bond distances reported for $[UO(OSiMe_3)(THF)(Fe_2I_2L)]$[11] and $[U(OSiMe_3)_2I_2(^{Ar}acnac)]$ (^{Ar}acnac = Ar*N*C(Ph)CHC(Ph)*O*, Ar = 3,5-^{t}Bu$_2$C$_6$H$_3$)[46] (1.993(4) and av. 1.911 Å, respectively). This lengthening may be a consequence of the strong σ-donor ability of the silsesquioxane ligand. However, this distance is very similar to those reported for the closely related octahedral U(VI) alkoxides, $[U(O^tBu)_6]$ (av. U-O = 2.039 Å)[47] and $[U(ONp)_6]$ (av. U-O = 2.002 Å; Np = CH_2CMe_3).[48] Finally, the U-O-$SiMe_3$ bond angles (145.2(4) - 149.8(4)°) are within the range reported for $[U\{Ph_2Si(OSiPh_2O)_2\}_2\{(Ph_2SiO)_2O\}]$ (136.17 – 169.64°),[49] and comparable to the U-O-C bond angles in $U(OCH_3)_6$ (av. 153.7°)[50] and $U(ONp)_6$ (145(2) and 147(3)°).[48]

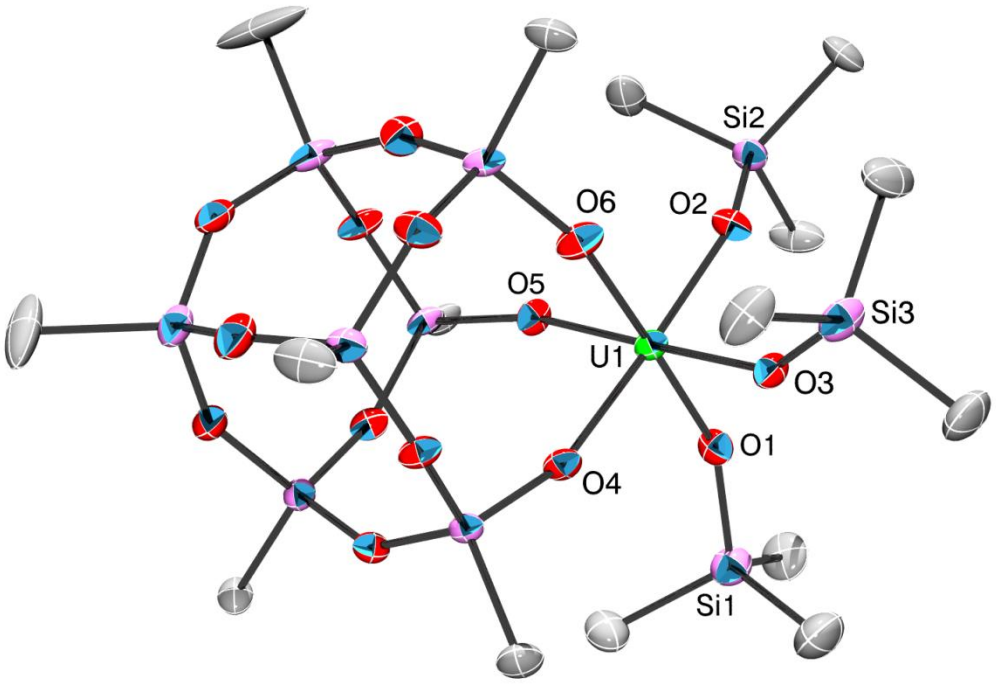

Figure 6.3. Solid-state molecular structure of **6.3**·0.5C_5H_{12} shown with 50% probability ellipsoids. All hydrogen atoms and cyclohexyl groups (except the carbons directly attached to Si) have been omitted for clarity. Selected bond lengths (Å) and angles (°): U1-O1 = 2.041(7), U1-O2 = 2.064(7), U1-O3 = 2.027(6), U1-O4 = 2.047(6), U1-O5 = 2.066(6), U1-O6 = 2.055(7), Si1-O1 = 1.676(7), Si2-O2 = 1.638(7), Si3-O3 = 1.666(7), U1-O1-Si1 = 147.7(4), U1-O2-Si2 = 149.8(4), U1-O3-Si3 = 145.2(4).

Curiously, reaction of $[UO_2(N(SiMe_3)_2)_2(THF)_2]$ with 1 equiv of $Cy_7Si_7O_9(OH)_3$ in neat hexanes only results in the formation of **6.3** as a minor product (Figure A6.21). The major product of this reaction, which can be isolated by crystallization from Et_2O/MeCN, is instead the trimetallic cluster, $[(UO_2)_3(Cy_7Si_7O_{12})_2(Et_2O)(MeCN)_2]$ (**6.4**). This complex can be made rationally by addition of 0.67 equiv of $Cy_7Si_7O_9(OH)_3$ to $[UO_2(N(SiMe_3)_2)_2(THF)_2]$ in hexanes (eq 6.4). Under these conditions, the number of acidic H^+ and basic $[NR_2]^-$ equivalents are balanced, and no acidic protons should remain attached to the silsesquioxane ligand. When the

reaction is performed in this fashion, **6.4** can be isolated as yellow rods in 42% isolated yield. Interestingly, I found that slow addition of a hexanes suspension of $Cy_7Si_7O_9(OH)_3$ to a solution of the uranyl bis(silyl)amide starting material in hexanes was critical to minimize formation of **6.3**. Utilization of the Et_2O/MeCN solvent combination for recrystallization of **6.4** was also important for the isolation of pure samples. Perhaps more importantly, the different reaction outcomes highlight the important roles that solvent and protons play in the silylation reaction required to form **6.3** (see below for more discussion).

Complex **6.4** is highly soluble in pentane, Et_2O, and THF, but is insoluble in acetonitrile. Its ^{1}H NMR spectrum in THF-d_8 features a series of broad and indistinct resonances that are attributable to the cyclohexyl CH and CH_2 environments. The spectrum also exhibits a sharp resonance at 1.94 ppm, and resonances at 1.11 and 3.37 ppm, that are assignable to the coordinated MeCN and Et_2O molecules, respectively. Its ^{29}Si NMR spectrum exhibits seven resonances, which is less than the 14 expected on the basis of its solid state molecular structure, suggesting that the solution phase structure of **6.4** is highly fluxional.

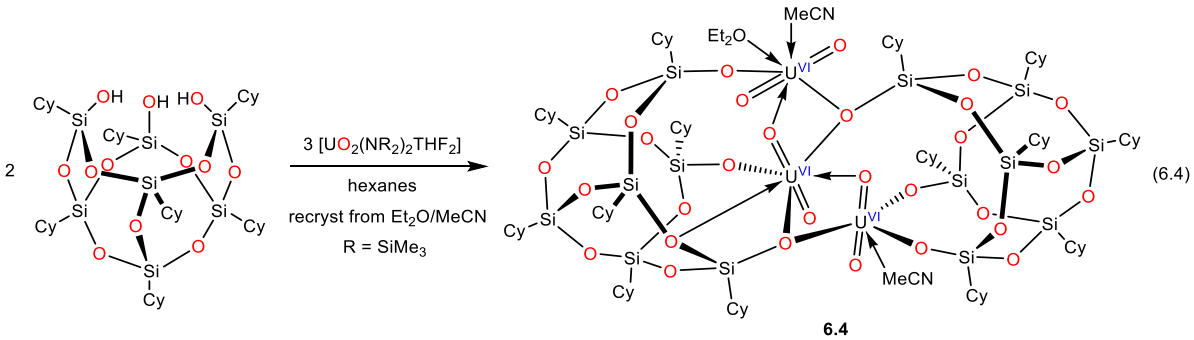

(6.4)

Complex **6.4** crystallizes in the monoclinic space group $P2_1/c$ as the Et_2O and MeCN solvate **6.4**·Et_2O·3MeCN (Figure 6.4). Its solid state molecular structure reveals two $[Cy_7Si_7O_{12}]^{3-}$ ligands bridged by three $[UO_2]^{2+}$ fragments, wherein two uranium centers are ligated by three

silyloxide arms and one uranium center is bound to two silyloxide arms. Two of the silyloxide arms are bridging, while the remaining four are terminal. There is also a uranium-silylether dative interaction with a bond length of 2.717(13) Å. Moreover, one of the $[UO_2]^{2+}$ fragments is supported by one MeCN and one Et_2O molecule, and another $[UO_2]^{2+}$ fragment is supported by one MeCN molecule, resulting in two uranium centers with pentagonal bipyramidal geometry and one uranium center with octahedral geometry. The UO_2^{2+} fragments in **6.4** exhibits metrical parameters typical of this ion, with short U-O_{yl} bond lengths (1.743(13) - 1.826(13) Å) and linear O-U-O angles (172.4(5) - 174.1(5)°). The terminal U-O(silsesquioxane) bond lengths (2.107(12) - 2.186(11) Å) are somewhat shorter than the bridging U-O(silsesquioxane) distances (2.279(12) - 2.415(12) Å), but similar to those reported for $[U(Cy_7Si_7O_{12})_2]$ (2.085(2) - 2.268(2) Å).[45] Lastly, the structure of **6.4** features two end-on $O_{yl}\cdots U$ dative interactions that serve to stabilize the trinuclear core of the cluster. The U-O distances in these "cation-cation interactions" (2.475(11) and 2.444(12) Å) are much longer than the U-O_{yl} distances, but comparable to other bridging $O_{yl}\cdots U$ dative interactions reported for similar interactions.[51-56]

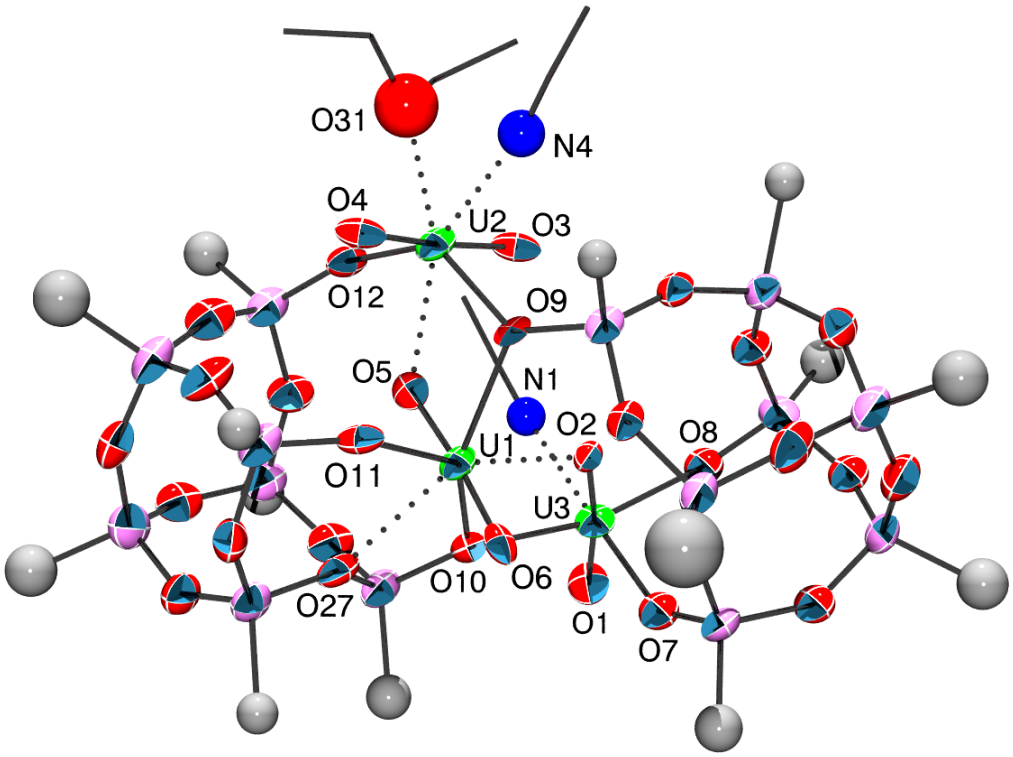

Figure 6.4. Solid-state molecular structures of **6.4**·Et_2O·3MeCN, shown with 50% probability ellipsoids. All hydrogen atoms and cyclohexyl groups (except the carbons directly attached to Si) have been removed for clarity. Selected bond lengths (Å) and angles (°): U1-O5 = 1.826(13), U1-O6 = 1.743(13), U2-O3 = 1.772(12), U2-O4 = 1.747(12), U3-O1 = 1.807(13), U3-O2 = 1.804(10), U1-O9 = 2.339(12), U1-O10 = 2.415(12), U1-O11 = 2.107(12), U2-O9 = 2.373(13), U2-O12 = 2.186(11), U3-O7 = 2.142(13), U3-O8 = 2.176(13), U3-O10 = 2.279(12), U1-O2 = 2.475(11), U2-O5 = 2.444(12), U1-O27 = 2.717(13), U2-O31 = 2.439(19), U2-N4 = 2.612(17), U3-N1 = 2.503(17), O5-U1-O6 = 173.2(5), O3-U2-O4 = 174.1(5), O1-U3-O2 = 172.4(5).

To better understand the formation of **6.3**, I followed the reaction of $[UO_2(N(SiMe_3)_2)_2(THF)_2]$ with 1 equiv of $Cy_7Si_7O_9(OH)_3$ in THF-d_8 by ^{29}Si NMR spectroscopy. A $^{29}Si\{^1H\}$ NMR spectrum of this sample reveals four resonances at -73.47, -

69.47, -68.57, and 20.91 ppm (Figure 6.5). These peaks integrate in a 3:3:1:3 relative ratio and are assignable to the silsesquioxane and trimethylsilyl ^{29}Si environments of **6.3**. The ^{29}Si{^{1}H} NMR spectrum also features three resonances at -74.54, -69.31, and -68.48 ppm, which I have tentatively assigned to the U(VI) bis(silsesquioxane) complex, [U($Cy_7Si_7O_{12})_2$] (**6.5**) (see below for synthetic and spectroscopic details).[45] Complexes **6.3** and **6.5** are found in a ca. 15:1 ratio in this sample. In addition, there is a sharp resonance at 1.44 ppm that is attributable to the ^{29}Si environment of $HN(SiMe_3)_2$. I also observe a minor resonance at -70.57 ppm assignable to the fully condensed octasilsesquioxane $Cy_8Si_8O_{12}$,[57] as well as minor resonances at -59.01 and -56.36 ppm that likely correspond to silsesquioxane decomposition products. Indeed, silsesquioxanes are known undergo cage rearrangement via Si-O cleavage under certain conditions.[58-61] Finally, I observe a very minor resonance at 7.05 ppm that is assignable to $(Me_3Si)_2O$, but I do not see a resonance assignable to Me_3SiOH. I also do not observe any signals that could be assigned to the free ligand, $Cy_7Si_7O_9(OH)_3$.

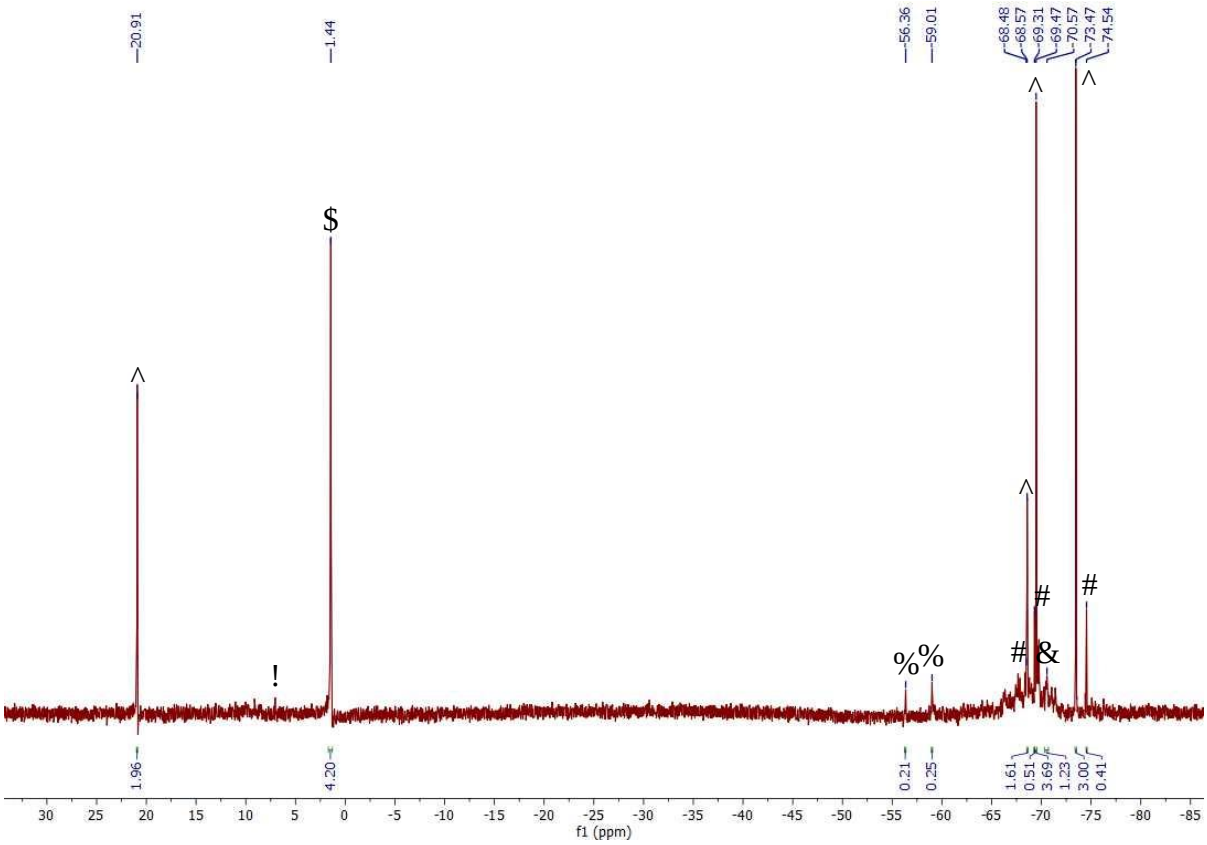

Figure 6.5. *In situ* $^{29}Si\{^{1}H\}$ NMR spectrum (in THF-d_8) of the reaction of $[UO_2(N(SiMe_3)_2)_2(THF)_2]$ and 1 equiv of $Cy_7Si_7O_9(OH)_3$. ^ indicates resonances assignable to **6.3**, # indicates resonances assignable to **6.5**, $ indicates resonances assignable to $HN(SiMe_3)_2$, & indicates resonances assignable to $Cy_8Si_8O_{12}$[11], ! indicates resonances assignable to $(Me_3Si)_2O$, and % indicates resonances assignable to unidentified ligand decomposition products.

6.2.3 Independent Synthesis of $[U(Cy_7Si_7O_{12})_2]$ (6.5)

To confirm the formation of **6.5** in the reaction of $[UO_2(N(SiMe_3)_2)_2(THF)_2]$ and $Cy_7Si_7O_9(OH)_3$, I sought to independently synthesize this material and investigate its NMR spectroscopic features; however, I was unable to prepare this complex using the reported literature procedure,[45] which prompted the design a new synthetic route that is outlined below.

Thus, addition of a THF solution of $[Li(THF)]_2[U(O^tBu)_6]$[47] to 2 equiv of $Cy_7Si_7O_9(OH)_3$ in THF, followed by storage at room temperature for 48 h resulted in deposition of $[Li(THF)_2]_2[U(Cy_7Si_7O_{12})_2]$ (**6.6**) as pale pink plates in 74% total yield (Scheme 6.2). Complex **6.6** is insoluble in hexanes, Et_2O, toluene, benzene, THF, MeCN, and DMSO at room temperature, which precluded its NMR spectroscopic characterization. It does, however, exhibit modest solubility in hot THF, which permitted the growth of X-ray quality crystals by allowing a hot THF solution of **6.6** to cool slowly to room temperature.

Scheme 6.2. Synthesis of complexes **6.5**, **6.6**, and **6.7**

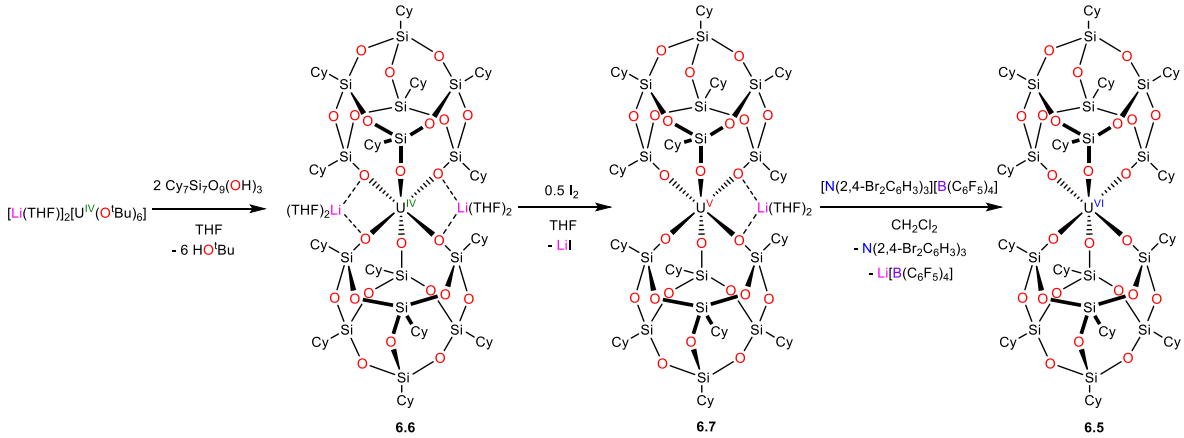

Complex **6.6** crystallizes in the monoclinic space group $P2_1/c$ as the THF solvate, **6.6**·4THF (Figure 6.6). Its solid state molecular structure reveals a hexa-coordinate uranium center ligated by two $\{Cy_7Si_7O_{12}\}^{3-}$ fragments in an octahedral fashion. The structure of **6.6** also features two Li counterions each supported by dative interactions with two THF molecules and one siloxide arm of each $\{Cy_7Si_7O_{12}\}^{3-}$ fragment. The U-O(terminal) bond lengths (2.159(9) and 2.137(9) Å) are slightly shorter than the Li-capped U-O distances (2.302(9) - 2.330(9) Å), but considerably longer than those in **6.3** (2.047(6) - 2.066(6) Å), consistent with the lower uranium oxidation state in **6.6**. Additionally, the Li-O distances (1.86(3) - 2.03(2) Å) are

comparable to those in the analogous Zr(IV) silsesquioxane, $[Li(O{=}CMe_2)]_2[Zr(Cy_7Si_7O_{12})_2]$ (1.895(8) – 2.066(9) Å).[62]

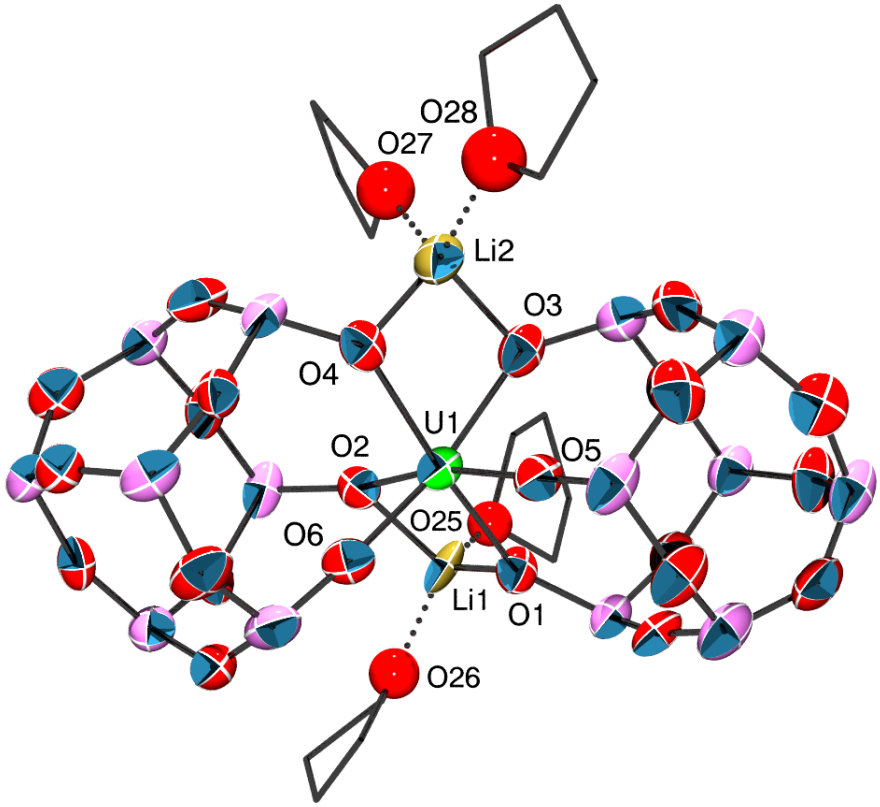

Figure 6.6. Solid-state molecular structure of **6.6** shown with 50% probability ellipsoids. All hydrogen atoms and cyclohexyl groups have been omitted for clarity. Selected bond lengths (Å): U1-O1 = 2.302(9), U1-O2 = 2.330(9), U1-O3 = 2.315(9), U1-O4 = 2.308(9), U1-O5 = 2.159(9), U1-O6 = 2.137(9), Li1-O1 = 1.95(3), Li1-O2 = 1.95(2), Li1-O25 = 1.90(3), Li-O26 = 1.96(3), Li2-O3 = 2.03(2), Li2-O4 = 1.96(3), Li2-O27 = 1.86(3), Li2-O28 = 2.00(3).

Treatment of **6.6** with 0.5 equiv of I_2 in THF results in formation of a pale yellow solution, from which the uranium(V) silsesquioxane, $[Li(THF)_2][U(Cy_7Si_7O_{12})_2]$ (**6.7**), can be isolated as a colorless microcrystalline solid in 89% yield after work-up (Scheme 6.2). Complex **6.7** is sparingly soluble in hexanes and Et_2O, but readily soluble in THF and CH_2Cl_2. Its ^1H NMR

spectrum in CD_2Cl_2 features a series of broad resonances from 0.60 to 1.87 ppm, attributable to overlapping CH and CH_2 cyclohexyl protons, as well as two singlets at 1.94 and 3.89 ppm, assignable to the coordinated THF molecules. The $^{29}Si\{^1H\}$ NMR spectrum of **6.7** in CD_2Cl_2 exhibits two singlets at -69.86 and -67.94 ppm in a 3:1 ratio that correspond to two of the three anticipated ^{29}Si environments of the silsesquioxane fragment. The resonance assignable to the three ^{29}Si environments nearest the uranium(V) center was not observed, likely due to paramagnetic broadening. Finally, the $^{7}Li\{^1H\}$ NMR spectrum of **6.7** in CD_2Cl_2 features a broad resonance at 1.52 ppm.

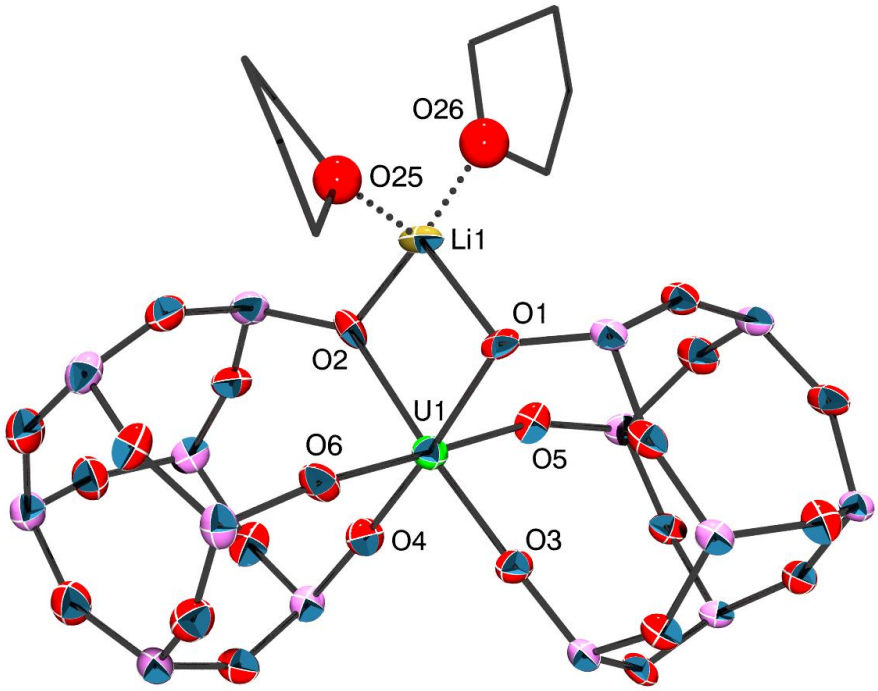

Figure 6.7. Solid-state molecular structure of **6.7** shown with 50% probability ellipsoids. All hydrogen atoms and cyclohexyl groups have been omitted for clarity. Selected bond lengths (Å): U1-O1 = 2.231(6), U1-O2 = 2.198(7), U1-O3 = 2.119(6), U1-O4 = 2.079(7), U1-O5 = 2.104(7), U1-O6 = 2.133(7), Li1-O1 = 1.988(17), Li1-O2 = 1.994(18), Li1-O25 = 1.955(17), Li-O26 = 1.933(18).

Crystals of **6.7** suitable for X-ray diffraction analysis were grown from a concentrated CH_2Cl_2 solution stored at -25 °C for 24 h. Complex **6.7** crystallizes in the triclinic space group P-1 as the CH_2Cl_2 solvate, **6.7**·0.5CH_2Cl_2, and its solid state molecular structure is shown in Figure 6.7. In the solid state, **6.7** adopts a distorted octahedral geometry about the uranium center, and features a single Li cation with an identical binding mode to those in **6.6**. The U-O(terminal) distances (2.079(7) – 2.133(7) Å) are slightly shorter than those in **6.6** (2.159(9) and 2.137(9) Å), but within the range reported for $[U(Cy_7Si_7O_{12})_2]$ (2.085(2) - 2.268(2) Å). Lastly, the Li-O distances (1.933(18) – 1.994(18) Å) in **6.7** are similar to those observed for **6.6** (1.86(3) - 2.03(2) Å) and $[Li(O{=}CMe_2)]_2[Zr(Cy_7Si_7O_{12})_2]$.[62]

To identify a suitable chemical oxidant for the $1e^-$ oxidation of **6.7**, I investigated its electrochemical properties by cyclic voltammetry. The cyclic voltammogram of **6.7** in THF, in the presence of 2 equiv of 12-crown-4, exhibits a U(V/VI) oxidation feature at 0.09 V (200 mV/s scan rate, vs. Fc/Fc^+) (Figure 6.8). Note that addition of 12-crown-4 was necessary to obtain well-defined redox features in the CV traces. This value is much more positive than those reported for the homoleptic $[U(O^tBu)_6]$[47] and $[Li][U(N{=}C^tBuPh)_6]$[63] complexes (-1.12 and -1.52 V, respectively, vs. Fc/Fc^+), which likely reflects the somewhat weaker σ- and π-donating ability of the silsesquioxane ligand. The highly anodic U(V/VI) couple also mandates that a relatively strong oxidant be used to effect the chemical oxidation of **6.7**.

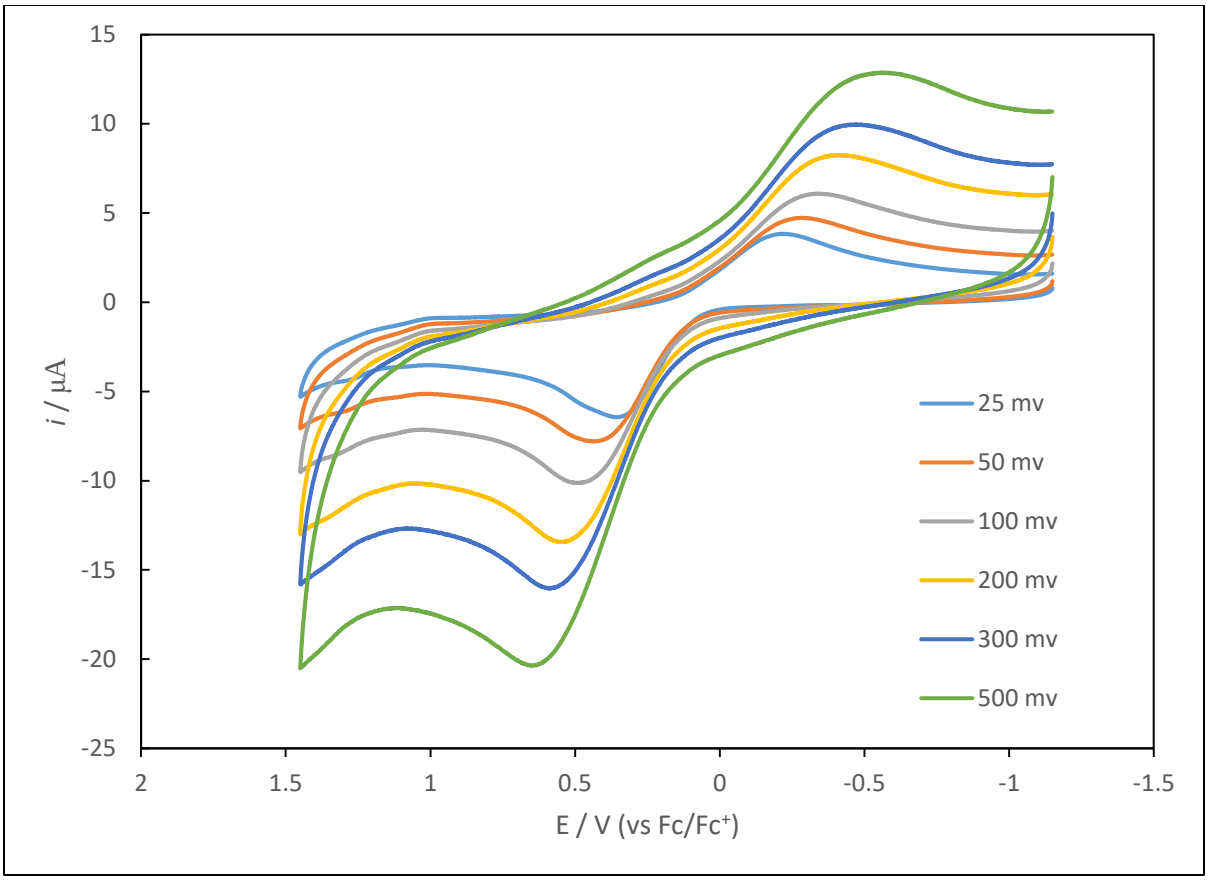

Figure 6.8. Partial cyclic voltammogram of the U(V/VI) oxidation event of **6.7** measured in CH_2Cl_2, in the presence of 2 equiv of 12-crown-4, with 0.1 M $[NBu_4][PF_6]$ as the supporting electrolyte (vs. Fc/Fc^+).

Surprisingly, reaction of **6.7** with either I_2 or AgOTf in THF or CH_2Cl_2 results in no reaction, despite their apparently favorable redox potentials. In contrast, reaction of **6.7** with 1.3 equiv of the powerful $1e^-$ oxidant $[N(2,4\text{-}C_6H_3Br_2)_3][B(C_6F_5)_4]$[64] in CH_2Cl_2 results in an immediate color change, first to pale yellow and then to green (Scheme 6.2). Analysis of the crude reaction mixture by $^{29}Si\{^1H\}$ NMR spectroscopy reveals new resonances at -74.40, -69.04, and -68.17 ppm in a 3:3:1 ratio, which I have assigned to $[U(Cy_7Si_7O_{12})_2]$ (**6.5**). Importantly, these three resonances are nearly identical to those assigned to **6.5** in the *in situ* $^{29}Si\{^1H\}$ NMR spectrum of the reaction between $[UO_2(N(SiMe_3)_2)_2(THF)_2]$ and $Cy_7Si_7O_9(OH)_3$ (Figure 6.5).

Unfortunately, however, pure samples of **6.5** could not be isolated from the reaction mixture due to its similar solubility with the $N(2,4\text{-}C_6H_3Br_2)_3$ by-product. Nonetheless, I was able to grow a few X-ray quality crystals of **6.5** from the reaction mixture (Figure 6.12), which provides further confirmation of its formation during the reaction.

6.2.4 X-ray Photoelectron Spectroscopy

To better understand the reaction stoichiometry, I characterized the yellow powder that was formed during the reaction of $[UO_2(N(SiMe_3)_2)_2(THF)_2]$ with 1 equiv of $Cy_7Si_7O_9(OH)_3$ in THF. This solid was insoluble in all aprotic solvents available, including pyridine, acetonitrile, and dichloromethane. An X-ray Photoelectron Spectrum (XPS) of this powder revealed presence of U, O, C, and Si in a 1:23:89:17 relative ratio (Figure A6.24), consistent with a U:silsesquioxane ratio of ca. 1:2. On the basis of this ratio and the isolated mass, the yellow powder was calculated to account for ~4% of the uranium present in the reaction mixture. Additionally, the insolubility of the material suggests that it is likely a uranium(VI) coordination polymer, i.e., $[UO_x\{Cy_7Si_7O_{12}\}_y]_z$. The high resolution XPS spectrum of this sample revealed two broad features at ca. 393 eV and 383 eV, attributable to $U4f_{5/2}$ and $U4f_{7/2}$ binding energies, respectively. These two features were fitted well using three components in a 3.3:2.8:1 ratio (Figure 6.9). Significantly, the values determined for the two major components (393.9 and 383.2 eV and 392.7 and 382.0 eV, respectively) are within the range of values reported for U(VI)-containing materials (e.g., UO_3 features $U4f_{5/2}$ and $U4f_{7/2}$ binding energies of 393.1 and 382.4 eV),[65] suggesting that the majority of the uranium in this solid is still in the 6+ oxidation state. Finally, the minor component (391.3 and 380.6 eV) is comparable to those energies reported for U_3O_8 (392.6 and 381.9 eV),[65] suggesting that some reduced uranium is also present in this sample.

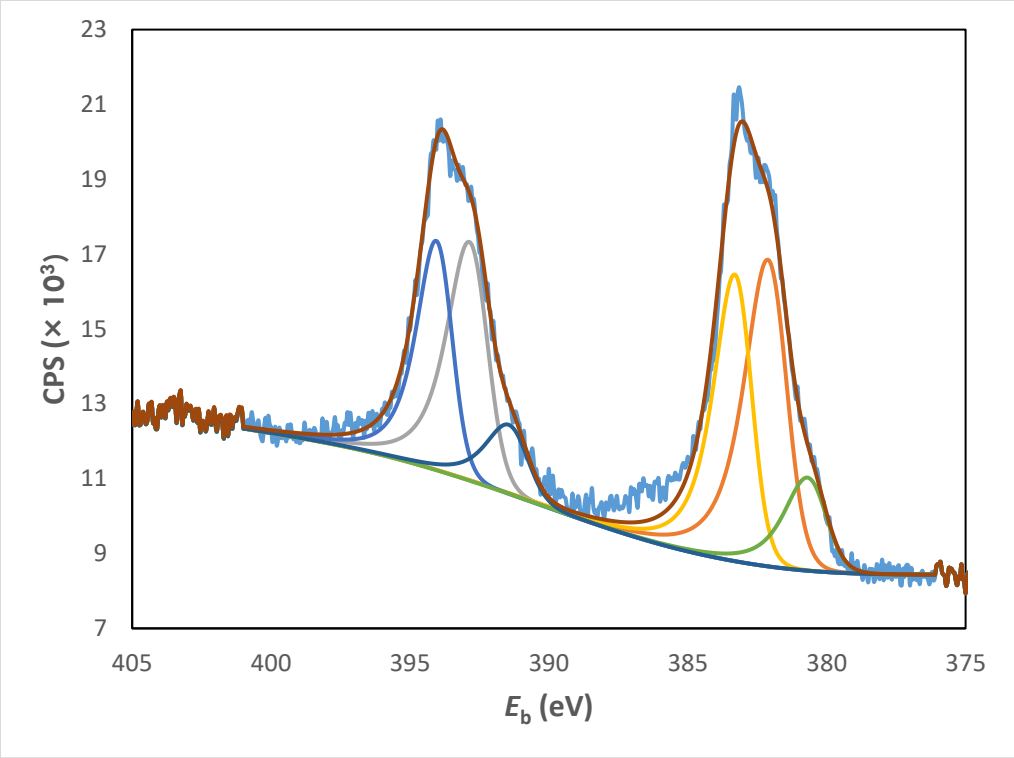

Figure 6.9. High resolution X-ray photoelectron spectrum of the yellow powder isolated from the reaction between $[UO_2(N(SiMe_3)_2)_2(THF)_2]$ and $Cy_7Si_7O_9(OH)_3$.

Table 6.1. X-ray Photoelectron Spectroscopy (XPS) Data

Component	Assignment	E_b (eV)
A	U $4f_{5/2}$	393.9
	U $4f_{7/2}$	383.2
B	U $4f_{5/2}$	392.7
	U $4f_{7/2}$	382.0
C	U $4f_{5/2}$	391.3
	U $4f_{7/2}$	380.6

6.2.5 Mechanistic Considerations for the Formation of 6.3

Given the available data, I hypothesize that the formation of **6.3** involves the initial reaction of $Cy_7Si_7O_9(OH)_3$ with $[UO_2(N(SiMe_3)_2)_2(THF)_2]$ to form the uranyl silsesquioxide complex, $[\{Cy_7Si_7O_{11}(OH)\}UO_2]$, and 2 equiv of $HN(SiMe_3)_2$ (Scheme 6.3). $[\{Cy_7Si_7O_{11}(OH)\}UO_2]$ then abstracts a $[SiMe_3]^+$ cation from $HN(SiMe_3)_2$, forming $[\{Cy_7Si_7O_{12}\}UO(OSiMe_3)]$ and H_2NSiMe_3. The latter is known to be unstable, disproportionating to $HN(SiMe_3)_2$ and NH_3.[66] $[\{Cy_7Si_7O_{12}\}UO(OSiMe_3)]$ subsequently undergoes oxo/silyloxy scrambling to form **6.3**, **6.5**, and a U(VI) oxo silsesquioxide oligomer, $[UO_x\{Cy_7Si_7O_{12}\}_y]_z$. To account for the relatively low isolated yield of the oligomeric product, I speculate that only a fraction of this material is insoluble, and that the majority remains in solution. Indeed, I do observe a number of minor unidentified resonances in the *in situ* $^{29}Si\{^1H\}$ NMR spectrum (Figure 6.5), which I attribute to the soluble component of this material.

Scheme 6.3. Proposed mechanism of formation of **6.3** and **6.5**.

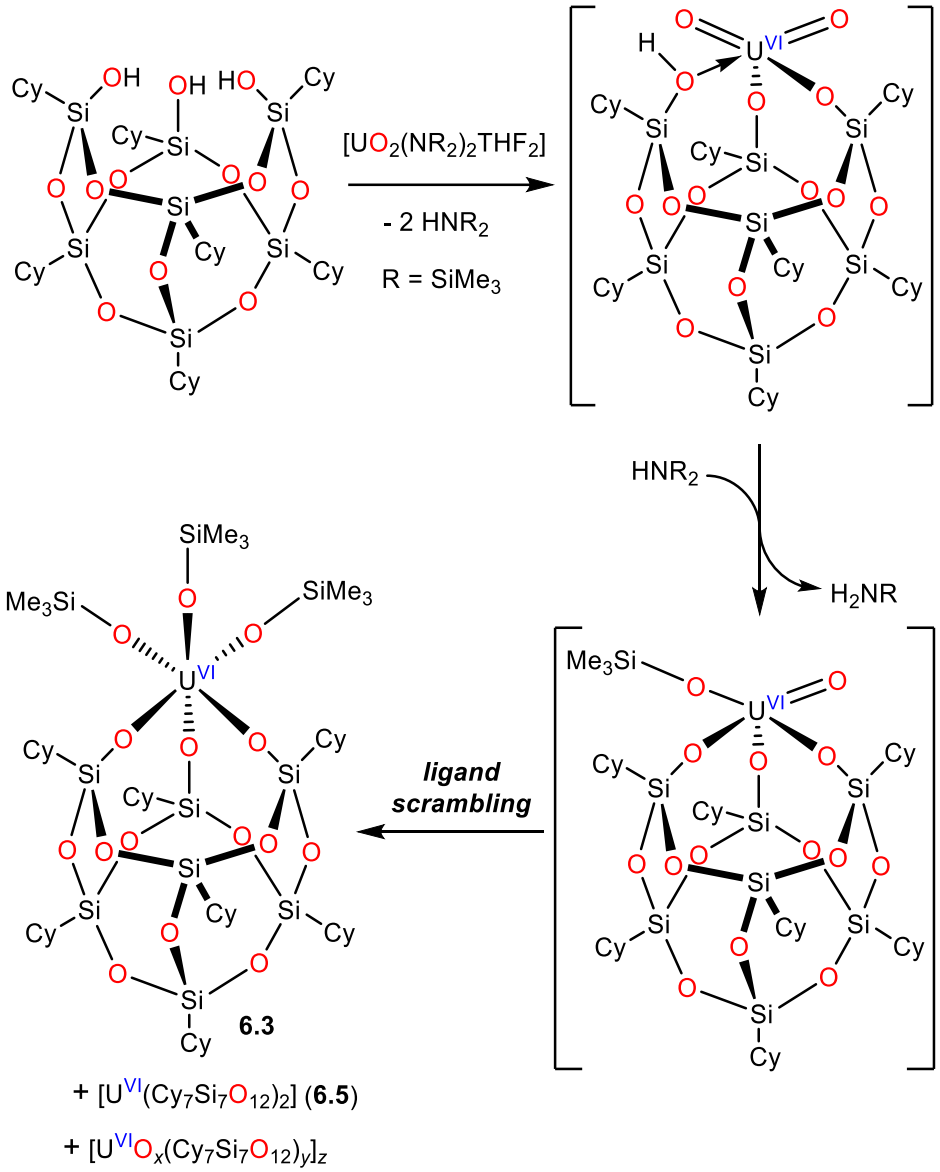

To validate my proposed mechanism and confirm the source of the $SiMe_3$ group in **6.3** as $HN(SiMe_3)_2$ (and not $[UO_2(N(SiMe_3)_2)_2(THF)_2]$), I monitored the reaction of **6.4** with $Cy_7Si_7O_9(OH)_3$ in THF-d_8, in the presence of excess $HN(SiMe_3)_2$, by ^{29}Si NMR spectroscopy (Figure 6.10). Addition of 5 equiv of $HN(SiMe_3)_2$ to a THF-d_8 solution of **6.4**, followed by addition of 1 equiv of $Cy_7Si_7O_9(OH)_3$, results in a rapid color change from yellow to orange, concomitant with deposition of a yellow precipitate. The ^{29}Si NMR spectrum of the resulting

mixture is essentially identical to that observed for the reaction between $[UO_2(N(SiMe_3)_2)_2(THF)_2]$ and $Cy_7Si_7O_9(OH)_3$ (eq 6.3). Specifically, the spectrum reveals complete consumption of **6.4**, and formation of **6.3** and **6.5** in an 8:1 ratio (Figure A6.19). I also observe minor resonances indicating formation of $Cy_8Si_8O_{12}$ and $(Me_3Si)_2O$. To rationalize these observations, I suggest that addition of $Cy_7Si_7O_9(OH)_3$ to **6.4** results in formation of $[\{Cy_7Si_7O_{11}(OH)\}UO_2]$, which subsequently undergoes silylation and silyloxy scrambling to form **6.3**, **6.5**, and $[UO_x\{Cy_7Si_7O_{12}\}_y]_z$. Importantly, these data conclusively identify $HN(SiMe_3)_2$ as the silylating agent, consistent with the mechanism outlined in Scheme 6.3. However, these data also suggest that the silyloxy protons in $Cy_7Si_7O_9(OH)_3$ play an important role in the silylation reaction, as conversion to **6.3** does not fully occur until they are introduced. To my knowledge, the ability of protons to mediate uranyl oxo silylation has not been previously recognized.[33] Curiously, though, after addition of $HN(SiMe_3)_2$ to **6.4**, but before addition of $Cy_7Si_7O_9(OH)_3$, I do see formation of minor amounts of **6.3** and **6.5** (in an approximately 1:3 ratio) in the reaction mixture, as revealed by the ^{29}Si NMR spectrum (Figure A6.17). However, the majority of the mixture still consists primarily of unreacted **6.4**. Thus, addition of $HN(SiMe_3)_2$ does result in some oxo silylation and ligand scrambling, and while I cannot fully explain this observation, given the intensity of the resonances assignable to **6.3** in this spectrum, almost no oxo silylation occurs until after the addition of $Cy_7Si_7O_9(OH)_3$, consistent with the mechanism outlined in Scheme 6.3. Interestingly, in the reaction of **6.4** with $Cy_7Si_7O_9(OH)_3$, in the presence of excess $N(SiMe_3)_3$, I observe no formation of **6.3**, even after heating, although I do observe formation of **6.5**. This result is rather surprising as it has been suggested that $N(SiMe_3)_3$ is a weaker base, and thus a better electrophile than $HN(SiMe_3)_2$.[67-70] Hence, the absence of **6.3** when utilizing $N(SiMe_3)_3$ suggests hydrogen

bonding may play a role in its formation (Scheme 6.4). Specifically, we hypothesize that hydrogen bonding between a coordinated alcohol and a hydrogen-bonded $HN(SiMe_3)_2$ can render the adjacent silyl group more susceptible to nucleophilic attack by the uranyl oxo ligand. Additionally, hydrogen bonding may stabilize the transition state of silyl transfer by anchoring the silyl group in close proximity to the uranyl oxo ligand. Presumably, some combination of these effects, which are absent in the case of $N(SiMe_3)_3$, could facilitate the oxo silylation to form **6.3**.

Scheme 6.4. Proposed role of hydrogen bonding in uranyl oxo silylation

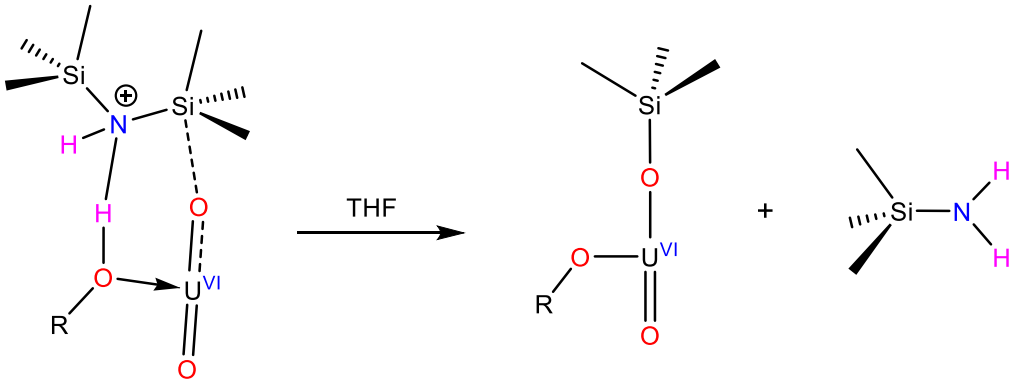

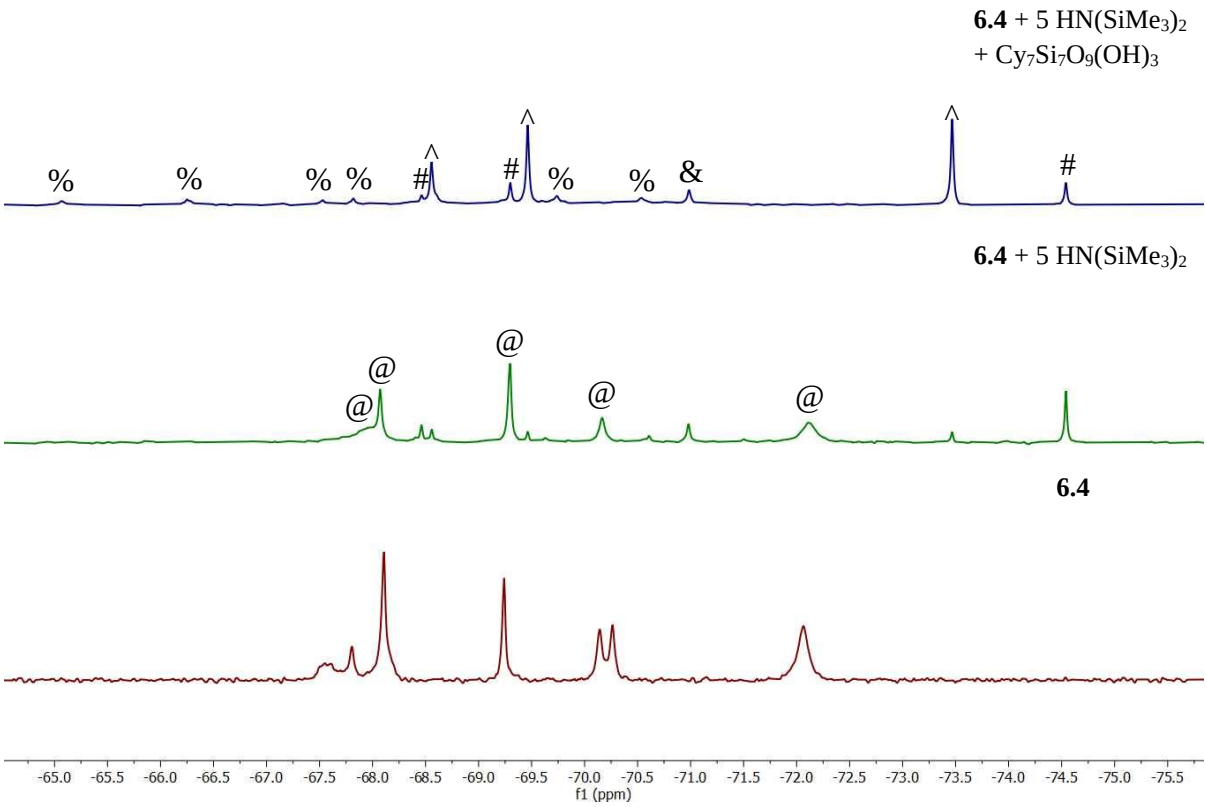

Figure 6.10. *In situ* $^{29}Si\{^{1}H\}$ NMR spectrum (in THF-d_8) of the reaction of $[(UO_2)_3(Cy_7Si_7O_{12})_2(MeCN)_2(Et_2O)]$ (**6.4**) with 5 equiv of $HN(SiMe_3)_2$ followed by 1 equiv of $Cy_7Si_7O_9(OH)_3$. ^ indicates resonances assignable to **6.3**, @ indicates resonances assignable to **6.4**, # indicates resonances assignable to **6.5**, & indicates resonances assignable to $Cy_8Si_8O_{12}$, and % indicates resonances assignable to unidentified products.

Scheme 6.5. Reaction of **6.4** with $HN(SiMe_3)_2$ and $Cy_7Si_7O_9(OH)_3$.

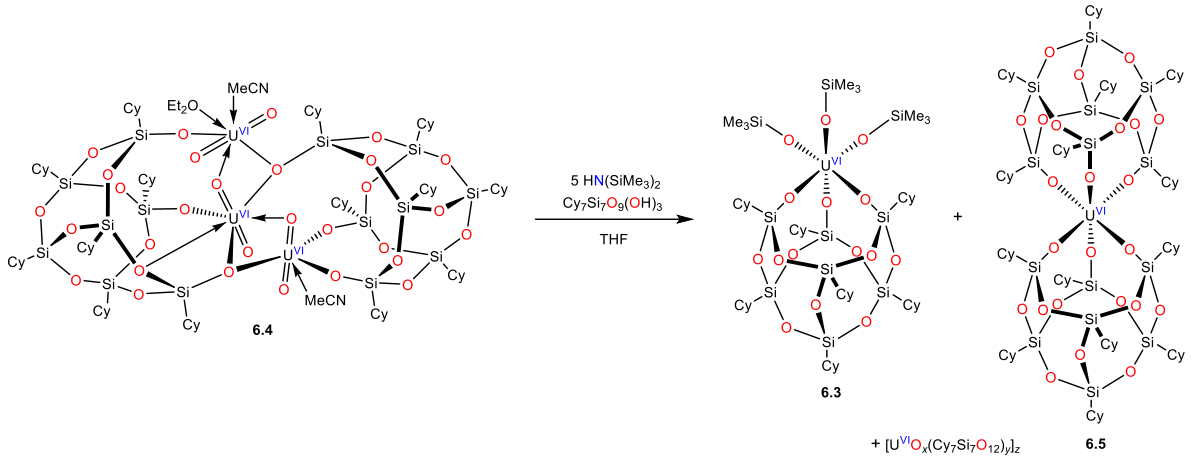

To further support my proposed mechanism, I note that oxo silylation is a well-established transformation.[71-79] Moreover, $HN(SiMe_3)_2$ is well known to act as a $[SiMe_3]^+$ source.[80-88] That said, un-activated uranyl is not known to undergo silylation with such a weakly electrophilic silyl source, suggesting that coordination of the tripodal silsesquioxane ligand to the uranyl ion is activating the uranyl ion toward oxo silylation. This activation may be a consequence of some O_{yl}-U-O_{yl} bending upon ligation of the silsesquioxane, which increases the O_{yl} nucleophilicity.[36-39] In this regard, reaction of the tripodal TREN ligand, $[Li]_3[N(CH_2CH_2NR)_3]$ (R = Si^tBuMe_2), with uranyl results in isolation of oxo-substitution product, $[\{UO(\mu\text{-}NCH_2CH_2N(CH_2CH_2NR)_2)\}_2]^-$, which was hypothesized to form via a reactive *cis*-uranyl intermediate.[89] In addition, I note that strongly basic alkoxide ligands are also known to increase O_{yl} nucleophilicity, which would render them more susceptible to both silylation and exchange.[9, 52, 90-91] For example, Wilkerson and co-workers have shown that the reaction between K(ONp) and $[UO_2Cl_2(THF)_2]_2$ in THF affords the $[U(ONp)_6]$ and UO_3 via scrambling of the oxo and neopentoxide ligands (Scheme 6.6).[48] Similarly, Burns and co-workers reported that reaction of UO_2Cl_2 with $K(O^tBu)$ resulted in formation $[UO_2][U(\mu\text{-}O)(\mu\text{-}$

$O^tBu)(O^tBu)_4]_2$ and UO_3.[52] In these example, it was suggested that the strongly donating alkoxide ligands render the uranyl oxo ligands more nucleophilic, which initiates a cascade of dimerization and ligand exchange reactions that eventually liberates UO_3 as a by-product.[48, 52] The comparably donating silesquioxide could promote oxo scrambling by a similar mechanism.

Scheme 6.6. Previous Example of Uranyl Oxo Ligand Scrambling. Taken from Ref. 48.

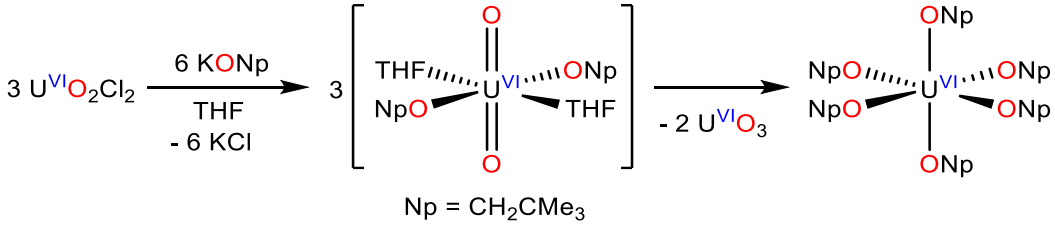

An alternative mechanism for oxo silylation might involve formation of a U(V) silyloxide intermediate via "reductive silylation", which then undergoes disproportionation and extensive ligand scrambling to generate **6.3** and **6.5**. Although I cannot definitely rule out this possibility, I note that "reductive silylation" followed by disproportionation would generate 0.5 equiv of U(IV), and I see no evidence for the presence of U(IV) in the reaction mixture in the quantities required. Moreover, past examples of "reductive silylation" required the use of strong electrophiles, such as R_3SiX (X = Cl, I, OTf),[19, 21, 23, 31-32, 46] utilized strong Lewis acids to activate the $[O=U=O]^{2+}$ fragment,[11, 24-25, 34-35] or required high temperatures,[14] to achieve oxo silylation. In contrast, my system lacks these features. Thus, on balance, I do not believe that "reductive silylation" is operative in my case, and I instead prefer the non-reductive silylation mechanism described in Scheme 6.3.

Finally, I note that the solvent-dependent formation of **6.3** is consistent with the previous silylation literature.[92-96] For example, Nagy *et al*. reported that the silylation of cellulose with

$HN(SiMe_3)_2$ in the presence of a Me_3SiCl catalyst proceeded smoothly in pyridine, DMSO, and DMF, while no reaction was observed in acetonitrile, nitromethane, or nitrobenzene.[94] Similarly, Zipse *et al*. reported that silylation of various primary and secondary alcohols with ^{t}BuMe$_2$SiCl was slow in $CHCl_3$ and CH_2Cl_2, but proceeded much faster in DMF.[95] Thus, the increased yield of **6.3** in THF can likely be attributed to a solvent-assisted transfer of the $[SiMe_3]^+$ electrophile.

6.2.6 Isolation of [{UO$_2$(THF)}{UO$_2$(Et$_2$O)}{UO$_2$(μ$_3$-O)(μ-O^{t}Bu)(O^{t}Bu)(Et$_2$O)}$_2${UO$_2$(O^{t}Bu)$_2$}$_2$] (6.8)

Interestingly, I found that oxo silylation of uranyl, when ligated by monodentate alkoxides, does not occur in the presence of a silyl source. Specifically, reaction of $[UO_2(N(SiMe_3)_2)_2(THF)_2]$ with 2 equiv of ^{t}BuOH in THF – in an effort to generate a mixture of $[UO_2(O^tBu)_2(THF)_2]$ and $HN(SiMe_3)_2$ that should be primed for oxo silylation – only results in isolation of Burns' $[UO_2][U(\mu\text{-}O)(\mu\text{-}O^tBu)(O^tBu)_4]_2$ complex[52] and a new hexa-uranyl cluster $[\{UO_2(THF)\}\{UO_2(Et_2O)\}\{UO_2(\mu_3\text{-}O)(\mu\text{-}O^tBu)(O^tBu)(Et_2O)\}_2\{UO_2(O^tBu)_2\}_2]$ (**6.8**) (Scheme 6.7). Unfortunately, I was unable to obtain pure samples of **6.8** in bulk for NMR spectroscopic characterization, which precluded analysis of its solution phase structure. However, I was able to confirm the connectivity of this cluster by single crystal X-ray crystallography, which I describe below.

Scheme 6.7. Synthesis of **6.8**

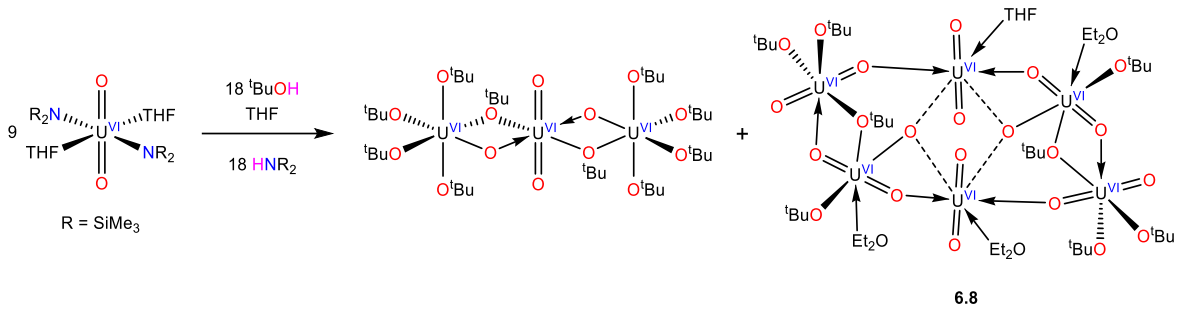

Complex **6.8** crystallizes in the tetragonal $P4_2/n$ space group and its solid state molecular structure is shown in Figure 6.11. The structure of **6.8** reveals a cluster composed of one $\{UO_2(THF)\}$, one $\{UO_2(Et_2O)\}$, two $\{UO_2(\mu_3\text{-}O)(\mu\text{-}O^tBu)(O^tBu)(Et_2O)\}$ and two $\{UO_2(O^tBu)_2\}$ units that are linked together via two μ_3-oxos, two bridging tert-butoxides, and six end-on O_{yl}-U cation-cation interactions. The uranyl fragments in $\{UO_2(THF)\}$ and $\{UO_2(Et_2O)\}$ are each coordinated by two μ_3-oxos and two neighboring O_{yl} ligands, in addition to the THF/Et_2O solvent molecules, resulting in a pentagonal bipyramidal geometry around these uranium centers. In contrast, the uranyl centers in both $\{UO_2(\mu_3\text{-}O)(\mu\text{-}O^tBu)(O^tBu)(Et_2O)\}$ units exhibit an octahedral geometry that is constructed by one terminal and one bridging tert-butoxide, a μ_3-oxo ligand and an Et_2O solvent molecule. Similarly, the uranyl fragments in both $\{UO_2(O^tBu)_2\}$ units are bound to a neighboring O_{yl} oxo and a bridging tert-butoxide, in addition to the two terminal tert-butoxides, resulting in an octahedral geometry about the uranium centers. The U-O_{yl} bond distances in **6.8** (1.735(19) -1.884(18) Å) are similar to that in Burn's $[UO_2][U(\mu\text{-}O)(\mu\text{-}O^tBu)(O^tBu)_4]_2$ complex (1.753(6) Å).[52] The terminal (2.054(17) -2.093(19) Å) and bridging (2.257(19) and 2.271(19) Å) U-O(tert-butoxide) bond lengths are also comparable to those in $[UO_2][U(\mu\text{-}O)(\mu\text{-}O^tBu)(O^tBu)_4]_2$ (2.015(6) - 2.055(6), and 2.295(6) Å, respectively).[52] However, the average U-(μ_3-O) distance

in the {UO_2(μ_3-O)(μ-O^{t}Bu)(O^{t}Bu)(Et_2O)} fragments (2.103 Å) is longer than the U-(μ-O) distance in [UO_2][U(μ-O)(μ-O^{t}Bu)(O^{t}Bu)$_4$] (1.923(6) Å),[52] presumably due to the different bridging modes. The {UO_2(THF)}-(μ_3-O) (2.320(16) and 2.327(16) Å) and {UO_2(Et_2O)}-(μ_3-O) (2.307(15) and 2.332(18) Å) bond lengths are also slightly longer than the uranyl-(μ-O) distance in [UO_2][U(μ-O)(μ-O^{t}Bu)(O^{t}Bu)$_4$] (2.301(6) Å).[52] Noteworthy, all uranyl fragments in **6.8** exhibit linear O-U-O angles (170.0(7) -177.3(9)°), suggesting the observed oligomerization does not significantly perturb the O-U-O bonding framework. Finally, the six cation-cation interactions in **6.8** (2.365(18) - 2.507(17) Å) are within the range of previously reported O_{yl}-U dative interactions.[51-56]

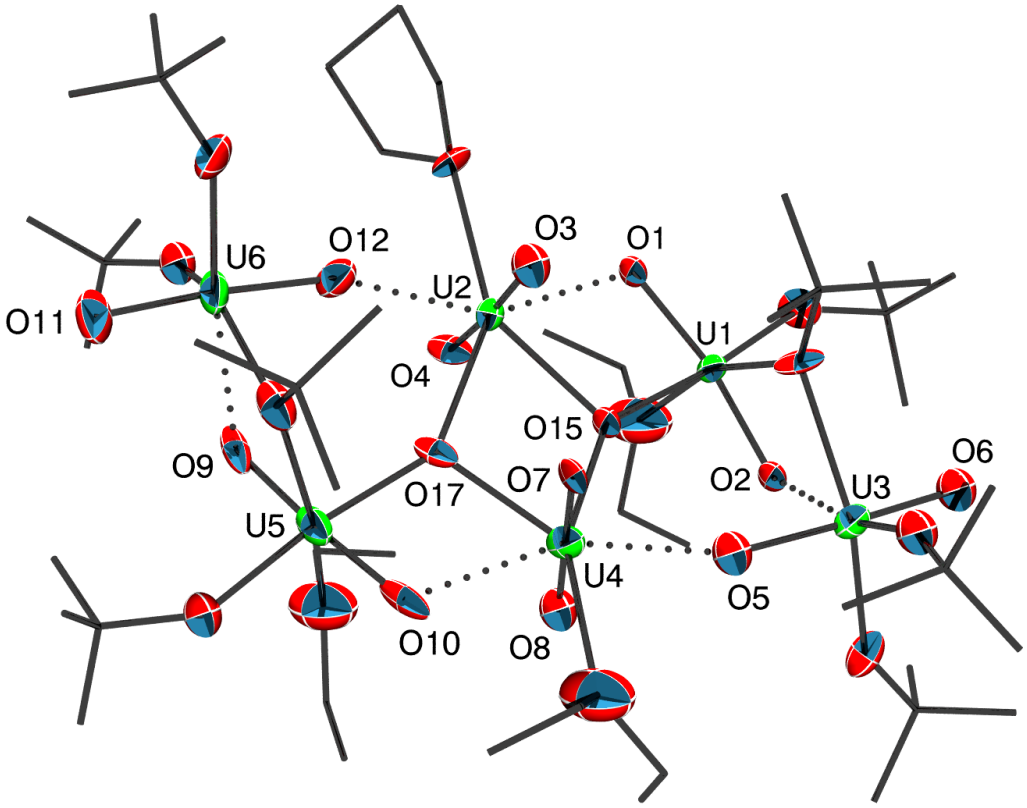

Figure 6.11 Solid-state molecular structure of **6.8** shown with 50% probability ellipsoids. All hydrogen atoms have been omitted for clarity. Selected bond lengths (Å) angles (°): U1-O1 =

1.864(16), U1-O2 = 1.852(16), U2-O3 = 1.75(2), U2-O4 = 1.771(18), U3-O5 = 1.884(18), U3-O6 = 1.769(18), U4-O7 = 1.735(19), U4-O8 = 1.74(2), U5-O9 = 1.85(2), U5-O10 = 1.82(2), U6-O11 = 1.79(2), U6-O12 = 1.817(17), U1-O15 = 2.113(15), U2-O15 = 2.327(16), U4-O15 = 2.307(15), U2-O17 = 2.320(16), U4-O17 = 2.332(18), U5-O17 = 2.093(16), U2-O12 = 2.405(17), U2-O1 = 2.471(15), U3-O2 = 2.404(16), U4-O5 = 2.365(18), U4-O10 = 2.507(17), U6-O9 = 2.425(18), O1-U1-O2 = 170.0(7), O3-U2-O4 = 174.1(8), O5-U3-O6 = 174.2(9), O7-U4-O8 = 177.3(9), O9-U5-O10 = 173.1(8), O11-U6-O12 = 175.0(9).

I hypothesize that the formation of **6.8** proceeds via an oxo/alkoxide ligand exchange mechanism similar to that observed for $[UO_2][U(\mu\text{-}O)(\mu\text{-}O^tBu)(O^tBu)_4]_2$.[52] An alternative reaction pathway might involve a heterolytic C-O cleavage in tert-butoxide followed by release of di-tert-butyl ether. Notably, the isolation of $[UO_2][U(\mu\text{-}O)(\mu\text{-}O^tBu)(O^tBu)_4]_2$ and **6.8**, rather than oxo silylation products, may be due to the absence of free acidic protons in the reaction mixture. Thus, future work will investigate the reaction of $[UO_2(N(SiMe_3)_2)_2(THF)_2]$ with excess ^{t}BuOH in THF to determine the possibility of simultaneous oxo silylation and oxo/alkoxide scrambling.

6.3 Summary

The U(VI) silyloxide complex, $[U(OSiMe_3)_3(Cy_7Si_7O_{12})]$ (**6.3**), was formed upon protonolysis of $[UO_2(N(SiMe_3)_2)_2(THF)_2]$ with 1 equiv of the silesesquioxane, $Cy_7Si_7O_9(OH)_3$, in THF, via a cascade of oxo silylation and silyloxide scrambling steps. Its formation is likely driven by an increase in O_{yl} nucleophilicity promoted by the strongly basic character of the silsesquioxane ligand or by some degree of O_{yl}-U-O_{yl} bending caused by silsesquioxane binding. Importantly, to my knowledge, this transformation is the first example of uranyl activation via simultaneous oxo silylation and oxo scrambling. Also formed in the

reaction is the U(VI) bis(silsequioxane), [U($Cy_7Si_7O_{12})_2$] (**6.5**). Its presence was confirmed by a $^{29}Si\{^1H\}$ NMR spectroscopic analysis of an independently synthesized sample, and comparison with the $^{29}Si\{^1H\}$ NMR spectrum of the *in situ* reaction mixture. While some uncertainty remains with respect to the exact reaction mechanism, I believe that "reductive silylation" of uranyl is not occurring in this transformation, as I have not isolated any U(IV)- or U(V)-containing complexes from the reaction mixture in the required quantities. Overall, given the structural similarities between silsesquioxanes and amorphous silica surfaces, my results highlight the utility of mineral surface mimics for the activation of actinyl ions, potentially paving way for the development of novel separation techniques for the reprocessing of nuclear fuel.

6.4 Acknowledgments

I would like to thank Dr. Thomas Mates for assistance with X-ray photoelectron spectroscopy measurements. I also thank Samuel Jacob for the gift of the [N(2,4-$C_6H_3Br_2)_3$][$B(C_6F_5)_4$].

6.5 Experimental

6.5.1 General Procedures. All reactions and subsequent manipulations were performed under anaerobic and anhydrous conditions in the glovebox or on the Schlenk line, under an atmosphere of dinitrogen. Hexanes, diethyl ether (Et_2O), and tetrahydrofuran (THF) were dried by passage over activated molecular sieves using a Vacuum Atmospheres solvent purification system. Pentane and CH_2Cl_2 were dried and degassed on an MBraun solvent purification system, and stored over activated 3Å molecular sieves for 24 h prior to use. Acetonitrile (MeCN) was dried over activated 3Å molecular sieves for 72 h, and then degassed by bubbling

dry N_2 into the solvent for 30 min, before being cannula transferred into a new vessel and again dried over 3Å molecular sieves for 24 h prior to use. C_6D_6, CD_2Cl_2, and THF-d_8 were dried over activated 3Å molecular sieves for 24 h prior to use. $[UO_2(N(SiMe_3)_2)_2(THF)_2]$,[97] $[Li(THF)]_2[U(O^tBu)_6]$,[47] and $[N(2,4\text{-}C_6H_3Br_2)_3][B(C_6F_5)_4]$[98] were prepared according to the reported literature procedures. All other reagents were purchased from commercial suppliers and used as received.

^1H, $^{13}C\{^1H\}$, $^7Li\{^1H\}$ and $^{29}Si\{^1H\}$ NMR spectra were recorded on an Agilent Technologies 400 MHz 400-MR DD2 spectrometer or a Bruker AVANCE NEO 500 MHz NMR spectrometer equipped with a Prodigy coldprobe. ^1H and $^{13}C\{^1H\}$ NMR spectra were referenced to external $SiMe_4$ using residual protio solvent resonances as internal standards. $^7Li\{^1H\}$ and $^{29}Si\{^1H\}$ NMR spectra were referenced indirectly with the ^1H chemical shift of $SiMe_4$ at 0 ppm, according to IUPAC standard.[99-100] IR spectra were recorded on a Nicolet 6700 FT-IR spectrometer. Elemental analyses were performed by the Microanalytical Laboratory at University of California (Berkeley, CA).

Cyclic Voltammetry Measurements. CV experiments were performed with a CH Instruments 600c Potentiostat, and the data were processed using CHI software (version 6.29). All experiments were performed in a glove box using a 20 mL glass vial as the cell. The working electrode was glassy carbon (3 mm diameter), the counter electrode was a platinum wire, and the reference electrode was a silver wire electroplated with silver chloride. Solutions employed for CV studies were typically 1 mM in analyte and 0.1 M in $[NBu_4][PF_6]$. All potentials are reported versus the $[Cp_2Fe]^{0/+}$ couple.

X-ray Photoelectron Spectroscopy. XPS data were recorded using a Thermo Fisher Escalab Xi+ spectrometer equipped with a monochromated Al-k alpha source (1486 eV). Survey and high-resolution scans were recorded at 100 eV and 20 eV pass energies, respectively. A low-energy electron flood was used for charge neutralization, and peak positions were calibrated against the aliphatic C1s peak (285.0 eV).

6.5.2 Synthesis of $[K_3(THF)][(UO_2)_3(Cy_7Si_7O_{12})_3(Et_2O)_2(THF)]$ (6.1): To a yellow-green solution of $[UO_2Cl_2(THF)_3]$ (19.1 mg, 0.034 mmol) in THF (1 mL) was added a white slurry of $[K_3(DME)_2][\ Cy_7Si_7O_{12}]$ (42.1mg, 0.033 mmol) in THF (1 mL). This addition resulted in an immediate color change to pale green, concomitant with formation of a fine white precipitate. The mixture was allowed to stir for 30 min at room temperature, whereupon the solvent was removed in vacuo to yield a pale green residue. The residue was extracted into Et_2O (1 mL) and filtered through a Celite column supported on glass wool (0.5 cm × 2 cm) to yield a pale green filtrate and a plug of white solid on the Celite. The filtrate was then transferred to a 4 mL vial, which was subsequently placed inside a 20 mL scintillation vial. Hexanes (1 mL) was added to the outer vial. Storage of the two-vial system at -25 °C for 4 d resulted in deposition of pale green plates, which were isolated by decanting off the supernatant (14.1 mg, 30 % yield).

6.5.3 Synthesis of $[K(2,2,2\text{-cryptand})]_2[K_2UO_2(Cy_7Si_7O_{12})_2]$ (6.2): To a yellow-green solution of $[UO_2Cl_2(THF)_3]$ (30.1 mg, 0.054 mmol) in THF (0.5 mL) was added a white slurry of $[K_3(DME)_2][\ Cy_7Si_7O_{12}]$ (70.2mg, 0.055 mmol) in THF (1 mL). This addition resulted in an immediate color change to pale green, concomitant with formation of a fine white precipitate. The mixture was allowed to stir for 30 min at room temperature, whereupon a colorless solution of 2,2,2-cryptand (62.0 mg, 0.165 mol) in THF (0.5 mL) was added. No

obvious color change was observed. The resulting mixture was stirred for 15 min at room temperature, whereupon the solvent was removed in vacuo to yield a pale green residue. The residue was triturated with pentane (2 × 1 ml) to yield a pale green solid, which was extracted into Et_2O (2 mL) and filtered through a Celite column supported on glass wool (0.5 cm × 2 cm). The resulting pale green filtrate was transferred to a 4 mL vial, which was subsequently placed inside a 20 mL scintillation vial. Hexanes (1 mL) was added to the outer vial. Storage of the two-vial system at -25 °C for 3 d resulted in deposition of few colorless plates of **6.2**, which were isolated by decanting off the supernatant.

6.5.4 Synthesis of [U(OSiMe$_3$)$_3$(Cy$_7$Si$_7$O$_{12}$)] (6.3): To a stirring orange solution of [UO_2(N(SiMe_3)$_2$)$_2$(THF)$_2$] (126.7 mg, 0.172 mmol) in THF (1 mL) was added dropwise a colorless solution of Cy$_7$Si$_7$O$_9$(OH)$_3$ (168.0 mg, 0.173 mmol) in THF (1 mL). This addition resulted in an immediate color change to bright orange, concomitant with the deposition of a small amount of a fine yellow precipitate. The reaction mixture was stirred for 15 min at room temperature, whereupon the volatiles were removed *in vacuo* and the resulting tacky solid was triturated with pentane (1 mL) to yield an orange powder. The powder was extracted into 2:1 Et_2O/MeCN (2 mL) and filtered through a Celite column supported on glass wool (0.5 cm × 2 cm) to yield an orange filtrate and a plug of yellow solid on the Celite. Storage of the filtrate at -25 °C for 24 h resulted in deposition of orange plates which were isolated by decanting off the supernatant (60.1 mg, 24 % yield). X-ray quality crystals of **6.3** were obtained from a concentrated pentane solution stored at -25 °C for 24 h. Anal. Calcd for $C_{51}H_{104}O_{15}Si_{10}U$: C, 41.49; H, 7.10. Found: C, 41.50; H, 7.06. ^{1}H NMR (C_6D_6, 25 °C, 400 MHz): δ 0.46 (s, 27H, Si-CH_3), 1.02 – 1.19 (m, 7H, overlapping Si-C*H*), 1.21– 1.44 (br m, 20H, overlapping CH_2), 1.56 – 1.82 (br m, 30H, overlapping CH_2), 1.92 (m, 6H, overlapping CH_2), 2.13 (m, 8H,

overlapping C*H*$_2$), 2.23 (m, 6H, overlapping C*H*$_2$). ^{13}C{^{1}H} NMR (C_6D_6, 25 °C, 100 MHz): δ 3.79 (OSi-*C*H$_3$), 23.93 (Si-*C*H), 24.01 (Si-*C*H), 26.53 (Si-*C*H), 27.31 (*C*H$_2$), 27.37 (*C*H$_2$), 27.40 (*C*H$_2$), 27.54 (*C*H$_2$), 27.79 (*C*H$_2$), 27.85 (*C*H$_2$), 27.91 (*C*H$_2$), 28.23 (*C*H$_2$). ^{29}Si{^{1}H} NMR (C_6D_6, 25 °C, 79 MHz): δ -73.18 (3Si, *Si*-CH), -69.06 (3Si, *Si*-CH), -68.12 (1Si, *Si*-CH), 20.93 (3Si, O*Si*-CH$_3$). IR (KBr pellet, cm^{-1}): 2922 (vs), 2850 (vs), 2667 (vw), 1448 (m, cyclohexyl H-C-H "scissor"), 1385 (vw), 1356 (vw), 1252 (m), 1248 (m), 1198 (m), 1122 (sh s, Si-O-Si stretch), 1078 (s, Si-O-Si stretch), 1026 (m), 997 (w), 847 (vs, Si-C stretch), 800 (m), 750 (w), 694 (vw), 640 (vw), 513 (s), 467 (m).

6.5.5 Synthesis of [(UO$_2$)$_3$(Cy$_7$Si$_7$O$_{12}$)$_2$(MeCN)$_2$(Et$_2$O)] (6.4): To a cold (-25 °C) stirring orange solution of [UO$_2$(N(SiMe$_3$)$_2$)$_2$(THF)$_2$] (169.3 mg, 0.230 mmol) in hexanes (3 mL) was added dropwise a cold (-25 °C) slurry of Cy$_7$Si$_7$O$_9$(OH)$_3$ (150.0 mg, 0.154 mmol) in hexanes (3 mL) over a course of 15 min. This addition resulted in an immediate color change to dark brown, and then gradually to bright yellow. The resulting slurry was stirred for 15 min at room temperature, whereupon the volatiles were removed *in vacuo* to yield a yellow powder. The powder was extracted into Et$_2$O (2 mL) and filtered through a Celite column supported on glass wool (0.5 cm × 2 cm) to yield a yellow filtrate. The filtrate was then transferred to a 4 mL vial, which was subsequently placed inside a 20 mL scintillation vial. Acetonitrile (1 mL) was added to the outer vial. Storage of the two-vial system at -25 °C for 48 h resulted in deposition of yellow plates which were isolated by decanting off the supernatant (94.3 mg, 42 % yield). Anal. Calcd for $C_{92}H_{170}N_2O_{31}Si_{14}U_3$: C, 38.00; H, 5.89; N, 0.96. Found: C, 38.39; H, 6.18; N, 0.88. ^{1}H NMR (THF-d_8, 25 °C, 500 MHz): δ 0.60 – 1.07 (br m, 20H, overlapping Si-C*H* and C*H*$_2$), 1.11 (t, 6H, OCH$_2$C*H*$_3$), 1.14 – 1.56 (br m, 68H, overlapping C*H*$_2$), 1.57 – 1.93 (br m, 66H, overlapping C*H*$_2$), 1.94 (s, 6H, C*H*$_3$CN), 3.37 (q, 4H, OC*H*$_2$). ^{29}Si{^{1}H} NMR (THF-d_8,

25 °C, 99 MHz): δ -72.07 (br), -70.27, -70.15, -69.24, -68.11, -67.81, -67.55 (br). IR (KBr pellet, cm^{-1}): 2920 (s), 2848 (s), 2665 (vw), 1618 (vw), 1448 (s, cyclohexyl H-C-H "scissor"), 1389 (vw), 1356 (vw), 1327 (vw), 1269 (m), 1196 (m), 1147 (br m, Si-O-Si stretch), 1026 (vw), 999 (vw), 978 (vw), 916 (sh w), 912 (sh w), 893 (w), 847 (s), 823 (m), 752 (m), 640 (w), 588 (vw), 582 (w), 513 (vs), 467 (m), 445 (m), 418 (s).

6.5.6 Synthesis of $[Li(THF)_2]_2[U(Cy_7Si_7O_{12})_2]$ (6.6): A pale blue solution of $[Li(THF)]_2[U(O^tBu)_6]$[2] (260.1 mg, 0.312 mmol) in THF (4 mL) was layered onto a colorless solution of $Cy_7Si_7O_9(OH)_3$ (604.2 mg, 0.621 mmol) in THF (3 mL). The resulting mixture was allowed to stand undisturbed for 48 h at room temperature, which resulted in deposition of pale pink plates. The crystals were isolated by decanting off the supernatant and dried *in vacuo* (445.4 mg). Concentration of the supernatant, followed by storage at -25 °C for 48 h, afforded a second crop of crystals (total yield: 568.2 mg, 74%). X-ray quality crystals of **6.6** were grown from a hot THF solution that was allowed to slowly cool to room temperature overnight. Anal. Calcd for $C_{100}H_{186}Li_2O_{28}Si_{14}U$: C, 48.39; H, 7.55; Found: C, 47.97; H, 7.34. IR (KBr pellet, cm^{-1}): 2920 (vs), 2848 (vs), 2665 (vw), 1618 (vw), 1460 (sh w), 1446 (vs, cyclohexyl H-C-H "scissor"), 1396 (w), 1346 (vw), 1300 (vw), 1282 (sh w), 1267 (m), 1196 (s, Si-O-Si stretch), 1134 (s, Si-O-Si stretch), 1076 (br s, Si-O-Si stretch), 1039 (m), 1026 (m), 997 (m), 945 (s), 922 (s), 893 (vs), 849 (s), 823 (m), 744 (w), 739 (m), 677 (br vw), 638 (w), 615 (vw), 567 (vw), 536 (m), 515 (s), 471 (m), 411 (m).

6.5.7 Synthesis of $[Li(THF)_2][U(Cy_7Si_7O_{12})_2]$ (6.7): To a stirring pink slurry of **6.6** (568.2. mg, 0.229 mmol) in THF (4 mL) was added an orange-brown solution of I_2 (29.1.2 mg, 0.115 mmol) in THF (2 mL). The resulting orange-brown mixture was allowed to stir for 1 h at room temperature, which resulted in dissolution of **6.6** and a color change to pale yellow,

concomitant with deposition of a pale yellow solid. The volume of the mixture was reduced to ~4 mL *in vacuo*, and the resulting solution was warmed until all the yellow solid dissolved. The resulting pale yellow solution was layered with Et_2O (4 mL) and stored at -25 °C for 24 h, which resulted in deposition a pale yellow microcrystalline solid (476.3 mg, 89% yield). X-ray quality crystals of **6.7** were obtained from a concentrated CH_2Cl_2 solution stored at -25 °C for 24 h. Anal. Calcd for $C_{92}H_{170}LiO_{26}Si_{14}U$: C, 47.41; H, 7.35. Found: C, 47.41; H, 7.21 ^{1}H NMR (CD_2Cl_2, 25 °C, 400 MHz): δ 0.60 – 1.12 (br m, 46H, overlapping Si-C*H* and CH_2), 1.13 – 1.50 (br m, 54H, overlapping CH_2), 1.51 – 1.87 (br m, 54H, overlapping CH_2), 1.94 (br m, 8H, OCH_2CH_2), 3.89 (br m, 8H, OCH_2CH_2). ^{13}C{^{1}H} NMR (CD_2Cl_2, 25 °C, 100 MHz): 24.66 (OCH_2CH_2), 26.18 (Si-*C*H), 27.25 (Si-*C*H), 27.39 (Si-*C*H), 27.48 (*C*H_2), 27.55 (*C*H_2), 28.21 (*C*H_2), 28.74 (*C*H_2), 69.65 (OCH_2CH_2). ^{7}Li{^{1}H} NMR (CD_2Cl_2, 25 °C, 155 MHz): 1.52 (br s, 1Li). ^{29}Si{^{1}H} NMR (CD_2Cl_2, 25 °C, 79 MHz): δ -69.86 (3Si), -67.94 (1Si). A resonance assignable to the three Si nuclei in the environment nearest to the U(V) center was not observed, likely due to paramagnetic broadening. IR (KBr pellet, cm^{-1}): 2922 (vs), 2848 (vs), 2665 (vw), 1637 (w), 1460 (sh w), 1446 (m, cyclohexyl H-C-H "scissor"), 1356 (vw), 1346 (vw), 1267 (m), 1196 (m), 1130 (s, Si-O-Si stretch), 1080 (s, Si-O-Si stretch), 1038 (w), 1026 (w), 997 (w), 922 (vs), 895 (vs), 849 (m), 825 (w), 756 (sh w), 741 (w), 640 (vw), 534 (vw), 513 (w), 471 (w), 411 (w).

6.5.8 Synthesis of [U(Cy$_7$Si$_7$O$_{12}$)$_2$] (6.5): To a stirring colorless solution of **6.7** (27.6 mg, 0.012 mmol) in CH_2Cl_2 (1 mL) was added a deep green solution of [N(2,4-$C_6H_3Br_2$)$_3$][B(C_6F_5)$_4$][3] (22.1 mg, 0.016 mmol, 1.3 equiv) in CH_2Cl_2 (1 mL). This addition resulted in an immediate color change, first to pale yellow and then to green. The resulting mixture was stirred for 5 min at room temperature, whereupon the volatiles were removed *in vacuo* to yield a mixture of

yellow and green solids. The residue was extracted into hexanes (2 × 2 mL) and filtered through a Celite column supported on glass wool (0.5 cm × 2 cm) to yield a pale yellow filtrate and a plug of green solid on the Celite. The volatiles were removed from the filtrate *in vacuo* to give a pale yellow solid. This solid was then dissolved in C_6D_6 (0.75 mL) and the ^{1}H and $^{29}Si\{^{1}H\}$ NMR spectra were recorded. X-ray quality crystals of **6.5** were obtained from slow evaporation of a concentrated pentane solution at room temperature. Unfortunately, pure samples of **6.5** could not be isolated due to its similar solubility with the $N(2,4\text{-}C_6H_3Br_2)_3$ by-product. ^{1}H NMR (C_6D_6, 25 °C, 400 MHz): δ 0.95 – 1.54 (m, 66H, overlapping Si-C*H* and C*H*$_2$, **6.5**), 1.55 – 1.88 (m, 54H, overlapping C*H*$_2$, **6.5**), 1.89 – 2.29 (m, 34H, overlapping C*H*$_2$, **6.5**), 6.16 (d, J_{HH} = 8 Hz, 3H, aryl C*H*, $N(2,4\text{-}C_6H_3Br_2)_3$), 6.96 (dd, J_{HH} = 8, 3 Hz, 3H, aryl C*H*, $N(2,4\text{-}C_6H_3Br_2)_3$), 7.55 (d, J_{HH} = 4 Hz, 3H, aryl C*H*, $N(2,4\text{-}C_6H_3Br_2)_3$). $^{29}Si\{^{1}H\}$ NMR (C_6D_6, 25 °C, 79 MHz): δ -74.40 (3Si), -69.04 (3Si), -68.17 (1Si).

6.5.9 Synthesis of [{UO$_2$(THF)}{UO$_2$(Et$_2$O)}{UO$_2$(μ$_3$-O)(μ-O^{t}Bu)(O^{t}Bu)(Et$_2$O)}$_2${UO$_2$(O^{t}Bu)$_2$}$_2$] (6.8): To a stirring orange solution of $[UO_2(N(SiMe_3)_2)_2(THF)_2]$ (102.1 mg, 0.139 mmol) in THF (2 mL) was added a colorless solution of ^{t}BuOH (28 μL, 0.295 mmol, 2 equiv). This addition resulted in an immediate color change to red-orange. The mixture was allowed to stir for 15 min at room temperature, whereupon the volatiles were removed *in vacuo* to yield a dark orange solid. This solid was extracted into hexanes (2 × 2 mL) and filtered over a Celite column supported on glass wool to yield a red orange filtrate. An aliquot was taken from this filtrate and dried *in vacuo*. The ^{1}H NMR spectra of the resulting residue was then recorded in C_6D_6. ^{1}H NMR (C_6D_6, 25 °C, 400 MHz): δ 1.56 (s, 18H, C*H*$_3$, μ-O^{t}Bu), 1.68 (br s, 36H, C*H*$_3$), 1.96 (br s, 18H, C*H*$_3$), 2.10 (s, 18H, C*H*$_3$). The filtrate was concentrated to 1 mL and stored at -25 °C for 24 hours, which

resulted in deposition of red crystals of $[UO_2][U(\mu\text{-}O)(\mu\text{-}O^tBu)(O^tBu)_4]_2$. A light orange powder remained undissolved after the hexanes extraction. This solid was dissolved in Et_2O (2 mL) and filtered over a Celite column supported on glass wool to yield a light orange filtrate. An aliquot was taken from this filtrate and dried *in vacuo*. The ^{1}H NMR spectra of the resulting residue was then recorded in C_6D_6. ^{1}H NMR (C_6D_6, 25 °C, 400 MHz): δ 1.24 – 2.35 (m, 72H, overlapping peaks for C*H*$_3$). The filtrate was concentrated to 1 mL and stored at -25 °C for 24 hours, which resulted in deposition of orange crystals of **6.8**.

6.5.10 X-ray Crystallography. Data for **6.1**-**6.8** were collected on a Bruker KAPPA APEX II diffractometer equipped with an APEX II CCD detector using a TRIUMPH monochromater with a Mo Kα X-ray source (α = 0.71073 Å). The crystals of **6.1**-**6.8** were mounted on a cryoloop under Paratone-N oil. Data for **6.1**-**6.4** were collected at 100(2) K, while data for **6.5**-**6.8** were collected at 110(2) K, using an Oxford nitrogen gas cryostream system. X-ray data for **6.3**, **6.4** and **6.8** were collected utilizing frame exposures of 5, 20 and 20 s, respectively, while **6.1**, **6.2**, **6.5**, **6.6** and **6.7** utilized frame exposures of 60 s. Data collection and cell parameter determination were conducted using the SMART program.[101] Integration of the data frames and final cell parameter refinement were performed using SAINT software.[102] Absorption corrections of the data were carried out using the multi-scan method SADABS.[103] Subsequent calculations were carried out using SHELXTL.[104] Structure determination was done using direct or Patterson methods and difference Fourier techniques. Unless stated otherwise, all hydrogen atom positions were idealized, and rode on the atom of attachment.

Structure solution, refinement, graphics, and creation of publication materials were performed using SHELXTL or OLEX2.[104-105]

Complex **6.1** contains seven cyclohexyl groups that exhibit positional disorder, which was addressing by constraining the affected atoms with the SADI, EADP and DFIX commands. One of these cyclohexyl groups was also modelled with two orientations in a 50:50 ratio. Additionally, two coordinated Et_2O molecules, a coordinated THF molecule and a THF solvate were constrained with the SADI and EADP commands. All cyclohexyl groups and solvent molecules were refined isotropically, and no hydrogen atoms were added to their carbon atoms.

Complex **6.2** contains three cyclohexyl groups that exhibit positional disorder, which was addressing by constraining the affected atoms with the EADP command. No hydrogens atoms were added to all cyclohexyl groups in **6.2**. Additionally, the Et_2O solvates were refined isotropically.

Complex **6.3** contains three cyclohexyl groups that exhibit positional disorder, which was resolved by modeling the affected atoms in two orientations in a 50:50 ratio using the PART command. Moreover, carbon atoms in the disordered cyclohexyl groups, and a disordered pentane solvate, were constrained with the SADI and EADP commands. Carbon atoms of the disordered pentane solvate were also refined isotropically.

Complex **6.4** contains five cyclohexyl groups, as well as three MeCN solvates and one Et_2O solvate that exhibit disorder. This disorder was addressed by constraining the affected atoms with the SADI, EADP, and DFIX commands. In addition, the carbon atoms of seven other cyclohexyl groups were constrained with the EADP command. The MeCN and Et_2O solvates were refined isotropically, and no hydrogen atoms were added to their carbon atoms.

Complex **6.5** contains five cyclohexyl groups in the asymmetric unit that exhibit disorder. This disorder was resolved by constraining the affected atoms with the SADI and EADP commands. In addition, two of the five disordered cyclohexyl groups were modelled in two orientations in a 50:50 ratio using the PART command. Finally, three cyclohexyl groups in the asymmetric unit were disordered over two symmetry related positions. No hydrogens atoms were added to these cyclohexyl groups.

All cyclohexyl groups and THF molecules in complex **6.6** exhibit positional disorder, which was addressed by constraining the affected atoms with the SADI and EADP commands. Additionally, THF solvates were refined isotropically, and no hydrogen atoms were added to their carbon atoms.

Complex **6.7** contains three cyclohexyl groups that exhibit positional disorder, which was resolved by modeling the affected atoms in two orientations in a 50:50 ratio using the PART and EADP commands. Additionally, the two coordinated THF molecules and three other cyclohexyl groups were constrained with the EADP command. The structure of **6.7** also contains a disordered CH_2Cl_2 solvate, which was modelled in two orientations in a 50:50 ratio using the SADI, DFIX, and EQIV commands. As in **6.6**, the CH_2Cl_2 solvate in **6.7** was refined isotropically, and no hydrogen atoms were added to its carbon atom.

All the *tert*-butyl groups, coordinated Et_2O and THF solvent molecules in the structure of **6.8** exhibited positional disorder, which was addressed by constraining the affected atoms with the SADI and EADP commands. Additionally, no hydrogen atoms were added to the three coordinated Et_2O solvent molecules.

Table 6.2. Crystallographic details for complexes **6.1** and **6.2**.

	6.1·THF	**6.2·2Et$_2$O**
Formula	$C_{146}H_{275}K_3O_{47}Si_{21}U_3$	$C_{128}H_{246}K_4N_4O_{40}Si_{14}U$
Crystal Habit, Color	Plate, Colorless	Plate, Colorless
Crystal Size (mm)	0.2 × 0.1 × 0.05	0.2 × 0.1 × 0.05
MW (g/mol)	4203.92	3268.96
crystal system	Monoclinic	Monoclinic
space group	$P2_1$	$P2_1/n$
a (Å)	15.635(4)	14.767(2)
b (Å)	36.800(10)	24.865(3)
c (Å)	17.842(5)	22.840(3)
α (°)	90	90.00
β (°)	106.661(4)	94.182(4)
γ (°)	90	90.00
V (Å^3)	9835(4)	8364.1(19)
Z	2	2
T (K)	100(2)	100(2)
λ (Å)	0.71073	0.71073
GOF	0.797	0.972
Density (calcd) (Mg/m^3)	1.420	1.298
Absorption coefficient (mm^{-1})	2.724	1.240
F_{000}	4308	3452
Total no Reflections	36116	37306
Unique Reflections	19149	17166
Final R indices*	R_1 = 0.0833	R_1 = 0.0922
	wR_2 = 0.1785	wR_2 = 0.2256
Largest Diff. peak and hole (e$^-$ A^{-3})	1.292, -1.522	2.152, -0.857

* For [I > 2σ(I)]

Table 6.3. Crystallographic details for complexes **6.3-6.5**.

	6.3·0.5C_5H_{12}	**6.4·Et_2O·3MeCN**	**6.5**
Formula	$C_{53.50}H_{110}O_{15}Si_{10}U$	$C_{102}H_{189}N_5O_{32}Si_{14}U_3$	$C_{84}H_{154}O_{24}Si_{14}U$
Crystal Habit, Color	Plate, Orange	Rod, Yellow	Plate, Yellow
Crystal Size (mm)	0.2 × 0.1 × 0.05	0.25 × 0.15 × 0.1	0.2 × 0.15 × 0.1
MW (g/mol)	1512.34	3104.92	2179.35
crystal system	Monoclinic	Monoclinic	Orthorhombic
space group	P2/c	$P2_1/c$	Cmca
a (Å)	25.785(3)	19.266(4)	18.9919(14)
b (Å)	13.9805(17)	31.423(6)	25.2308(18)
c (Å)	20.860(3)	24.877(5)	21.8579(16)
α (°)	90	90.00	90
β (°)	106.277(3)	92.053(3)	90
γ (°)	90	90.00	90
V ($Å^3$)	7218.2(16)	15051(5)	10473.9(13)
Z	4	4	4
T (K)	100(2)	100(2)	110(2)
λ (Å)	0.71073	0.71073	0.71073
GOF	1.020	1.009	1.047
Density (calcd) (Mg/m^3)	1.392	1.370	1.382
Absorption coefficient (mm^{-1})	2.470	3.393	1.775
F_{000}	3132	6256	4552
Total no Reflections	33272	55747	24395
Unique Reflections	15835	25090	5986
Final R indices*	$R_1 = 0.0785$	$R_1 = 0.0943$	$R_1 = 0.0714$
	$wR_2 = 0.1681$	$wR_2 = 0.2271$	$wR_2 = 0.1784$
Largest Diff. peak and hole ($e^- A^{-3}$)	3.066, -2.405	3.010, -2.911	1.954, -1.456

* For [$I > 2\sigma(I)$]

Table 6.4. Crystallographic details for complexes **6.6-6.8.**

	6.6·4THF	**6.7·0.5CH_2Cl_2**	**6.8**
Formula	$C_{116}H_{218}Li_2O_{32}Si_{14}U$	$C_{92.5}H_{171}ClLiO_{26}Si_{14}U$	$C_{48}H_{110}O_{26}U_6$
Crystal Habit, Color	Plate, Pink	Plate, Colorless	Plate, Orange
Crystal Size (mm)	0.2 × 0.15 × 0.1	0.15 × 0.15 × 0.1	0.2 × 0.15 × 0.1
MW (g/mol)	2770.06	2372.96	2531.53
crystal system	Monoclinic	Triclinic	Tetragonal
space group	$P2_1/c$	P -1	$P4_2/n$
a (Å)	18.8172(11)	14.417(4)	39.563(5)
b (Å)	28.943(2)	15.026(4)	39.563(5)
c (Å)	26.8419(16)	30.501(9)	10.4944(13)
α (°)	90	78.946(4)	90
β (°)	103.130(3)	77.534(3)	90
γ (°)	90	64.451(3)	90
V ($Å^3$)	14236.5(16)	5784(3)	16426(5)
Z	4	2	8
T (K)	110(2)	110(2)	110(2)
λ (Å)	0.71073	0.71073	0.71073
GOF	1.021	0.991	1.076
Density (calcd) (Mg/m^3)	1.292	1.362	2.047
Absorption coefficient (mm^{-1})	1.325	1.637	11.848
F_{000}	5856	2484	9264
Total no Reflections	57272	43951	36694
Unique Reflections	24492	22790	16166
Final R indices*	$R_1 = 0.1171$	$R_1 = 0.0826$	$R_1 = 0.1076$
	$wR_2 = 0.2980$	$wR_2 = 0.2139$	$wR_2 = 0.1982$
Largest Diff. peak and hole ($e^- A^{-3}$)	3.553, -0.982	3.905, -2.726	2.417, -2.638

* For [$I > 2\sigma(I)$]

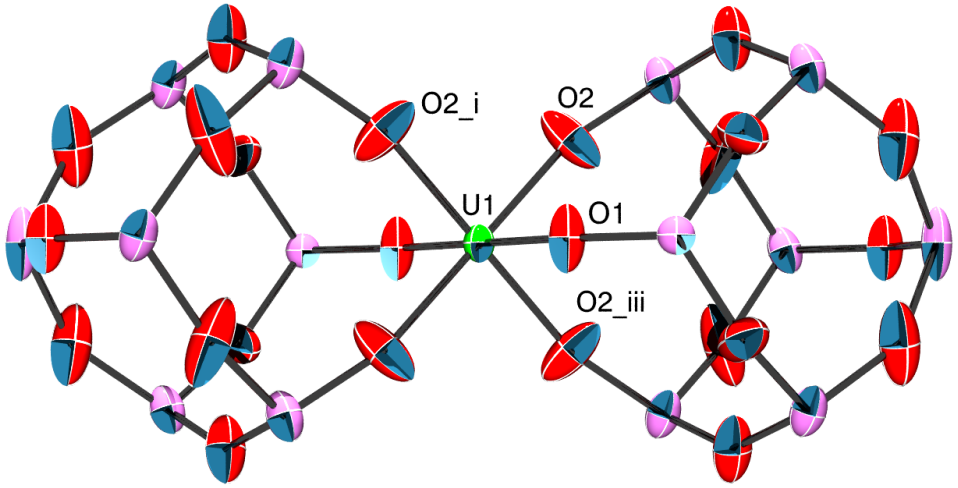

Figure 6.12. Solid-state molecular structure of **6.5** shown with 50% probability ellipsoids. All hydrogen atoms and cyclohexyl groups have been omitted for clarity. Selected bond lengths (Å) and angles (°): U1-O1 = 2.061(7), U1-O2 = 2.038(6), O1-U1-O2 = 89.6(2), O1-U1-O2_i = 90.4(2), O2-U1-O2_i = 91.0(4), O2-U1-O2_iii = 89.0(4).

6.6 Appendix

6.6.1 NMR Spectra

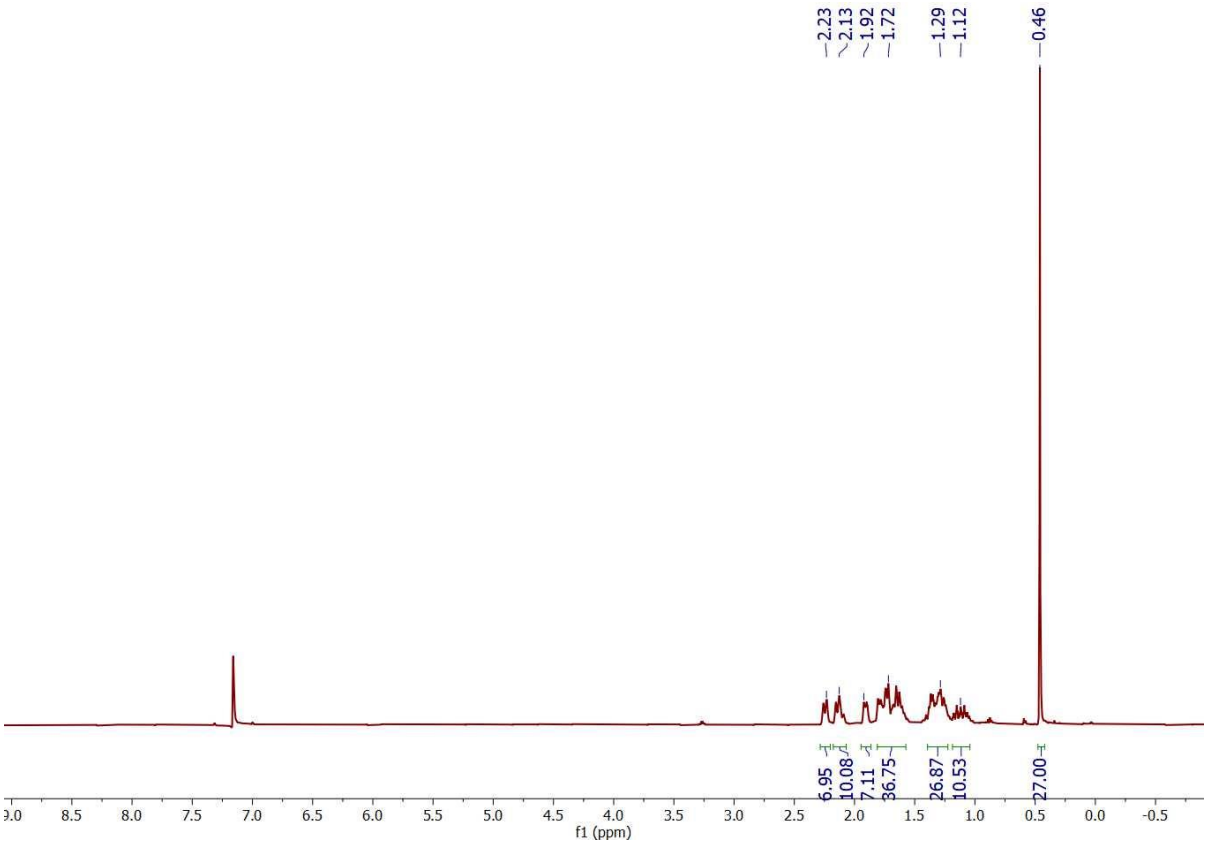

Figure A6.1. ^{1}H NMR spectrum of **6.3** in C_6D_6.

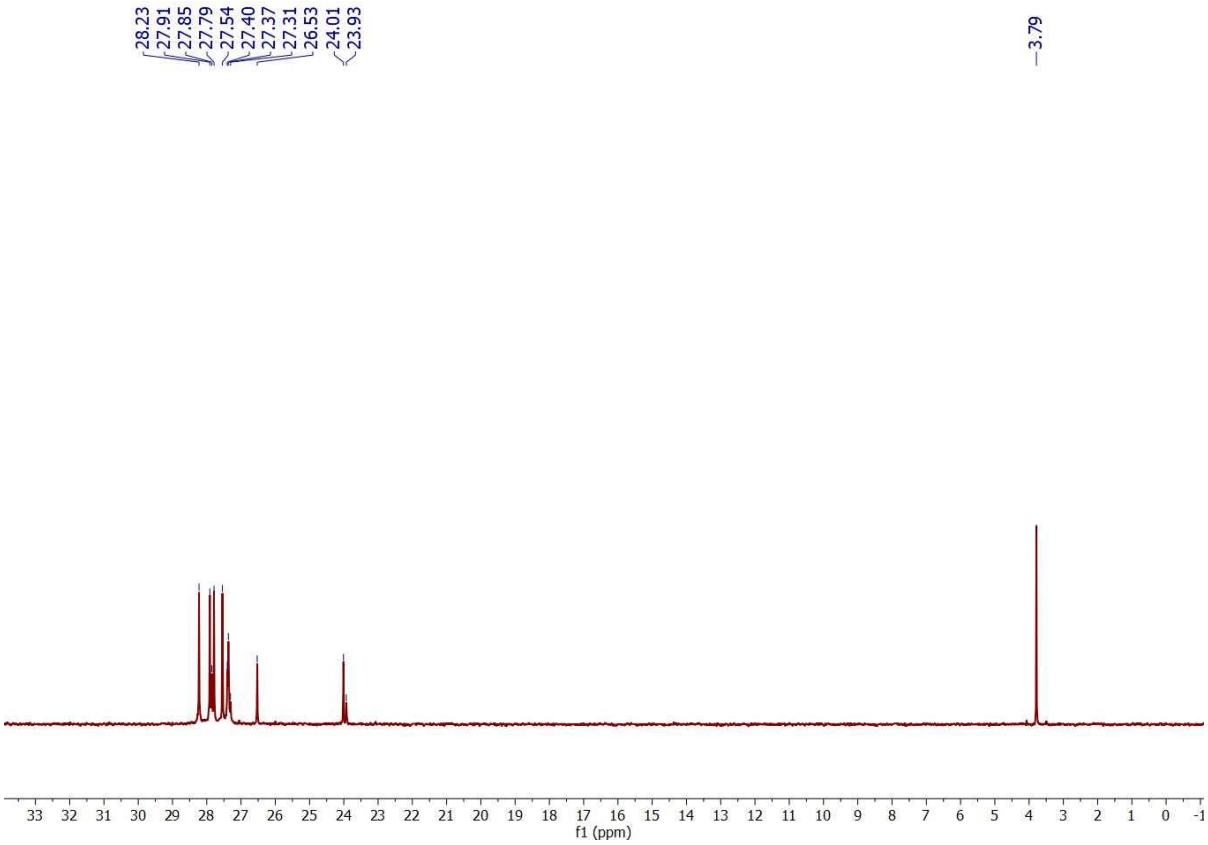

Figure A6.2. $^{13}C\{^{1}H\}$ NMR spectrum of **6.3** in C_6D_6.

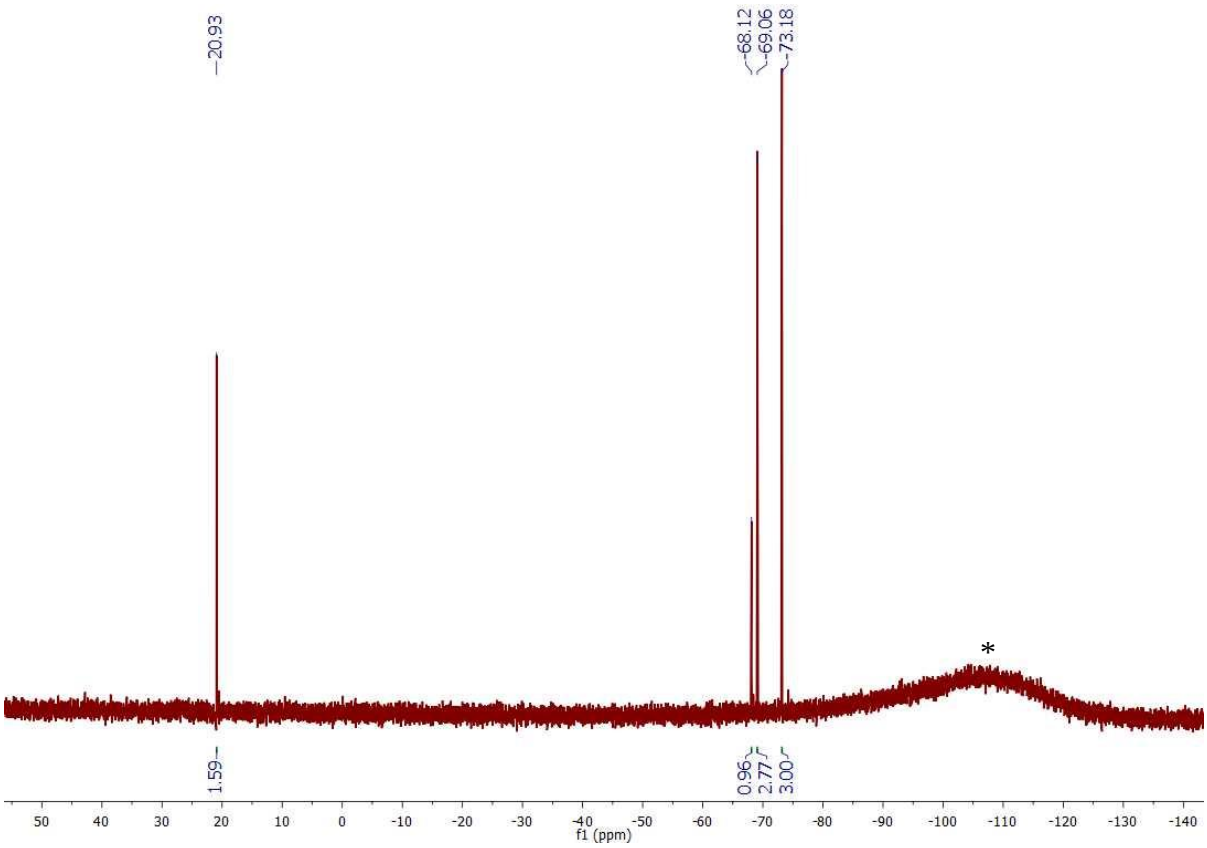

Figure A6.3. $^{29}Si\{^{1}H\}$ NMR spectrum of **6.3** in C_6D_6. * indicates resonances assignable to SiO_2 present in the NMR tube.

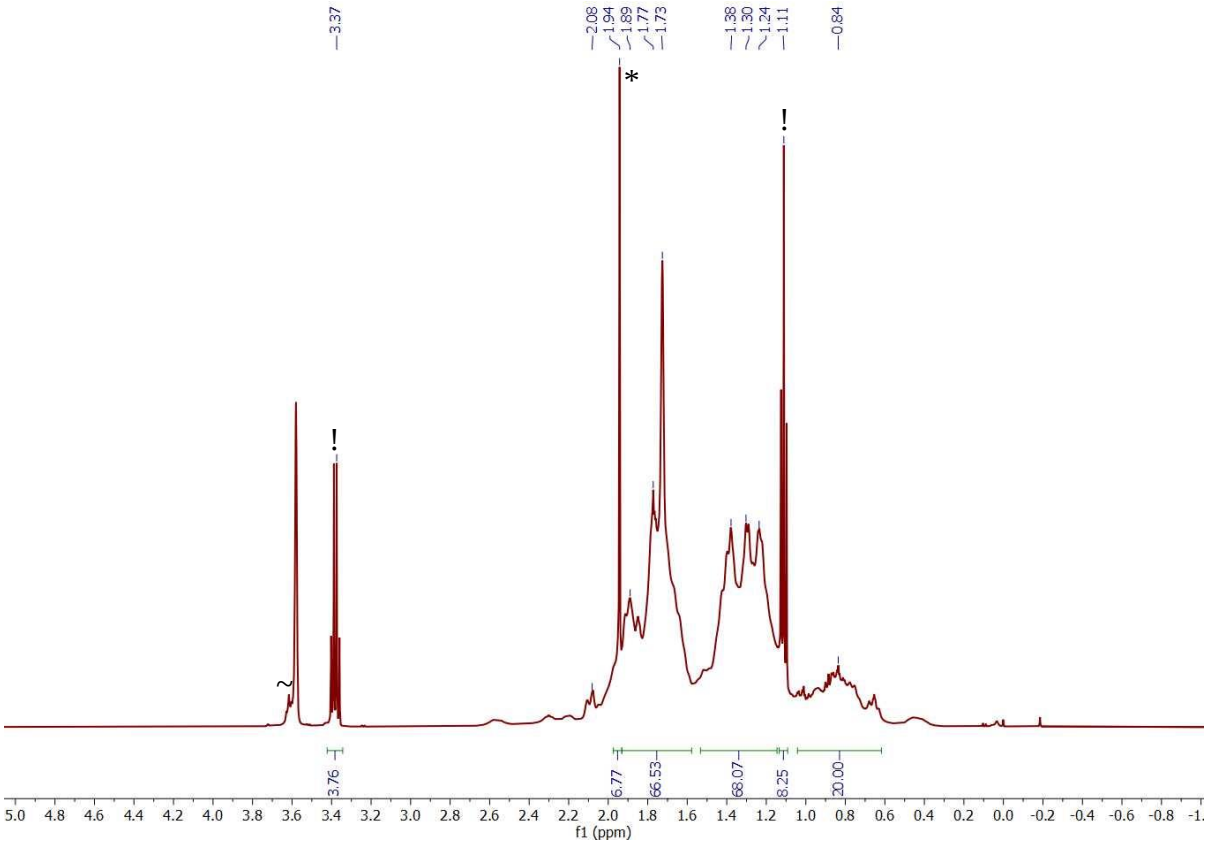

Figure A6.4. ^{1}H NMR spectrum of **6.4** in THF-d_8. (*) indicates resonances assignable to MeCN, (~) indicates resonances assignable to THF, and (!) indicates resonances assignable to Et_2O.

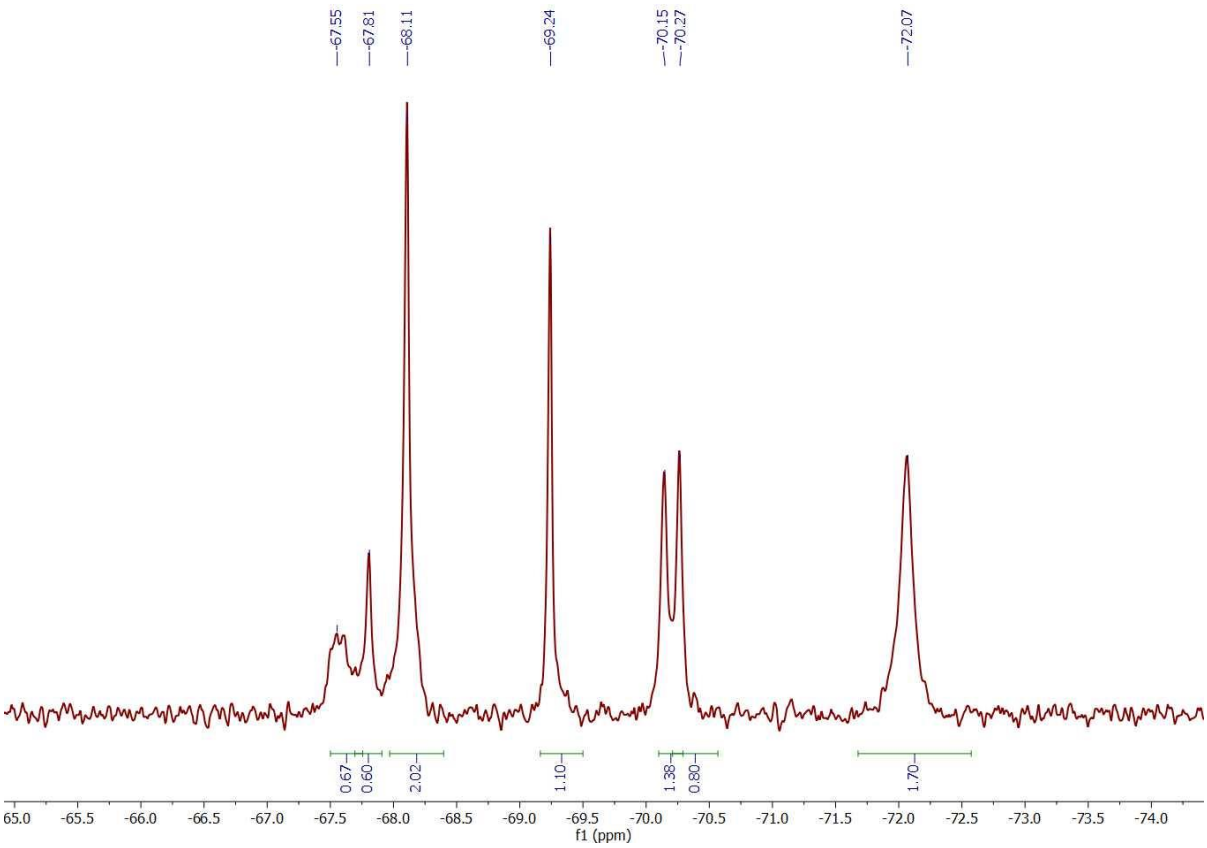

Figure A6.5. $^{29}Si\{^{1}H\}$ NMR spectrum of **6.4** in THF-d_8.

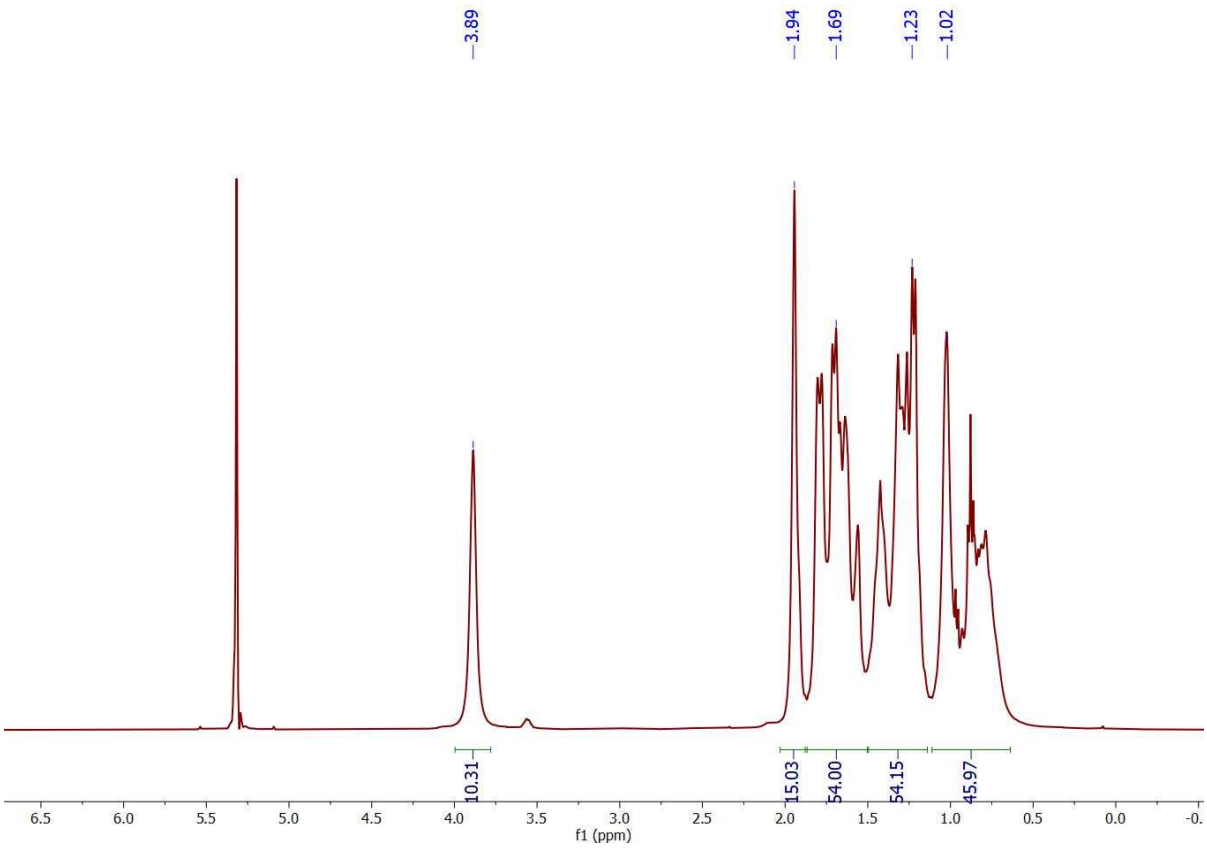

Figure A6.6. ^{1}H NMR spectrum of **6.7** in CD_2Cl_2.

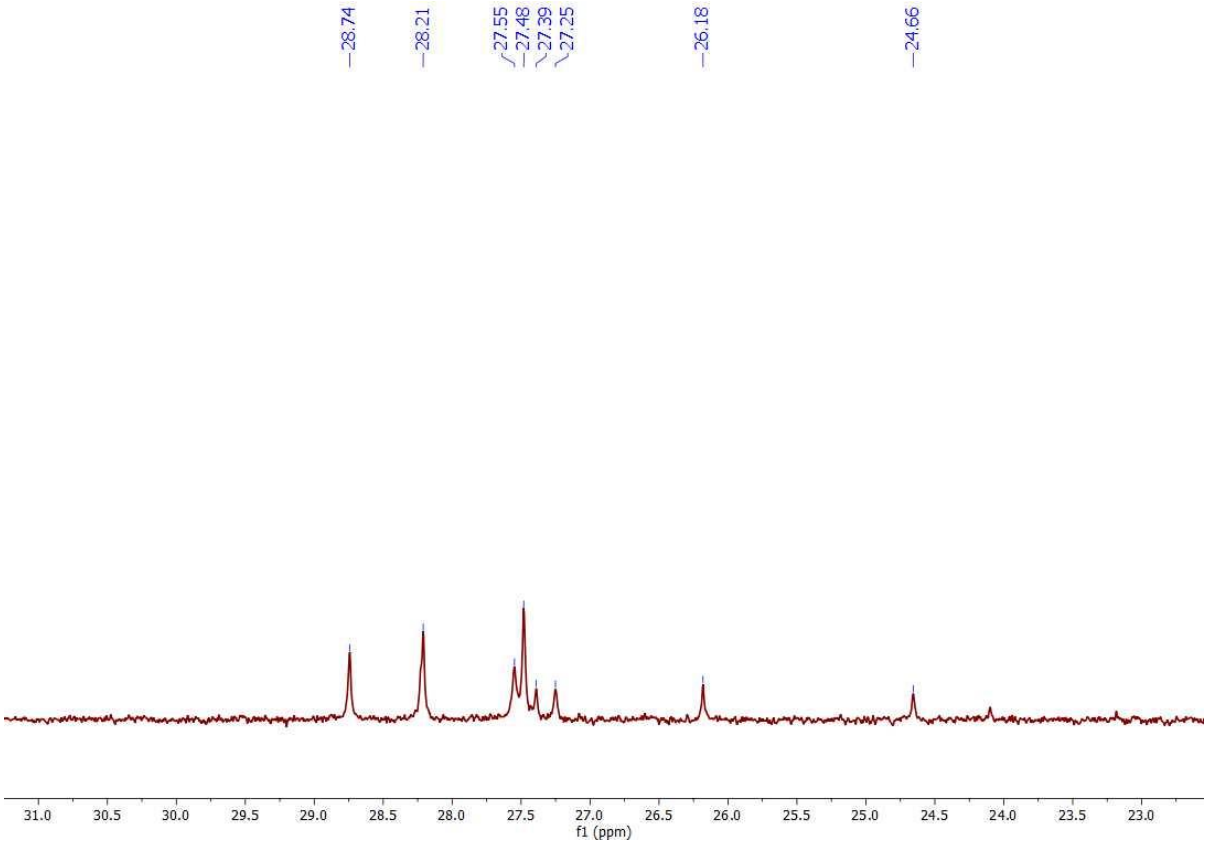

Figure A6.7. $^{13}C\{^{1}H\}$ NMR spectrum of **6.7** in CD_2Cl_2.

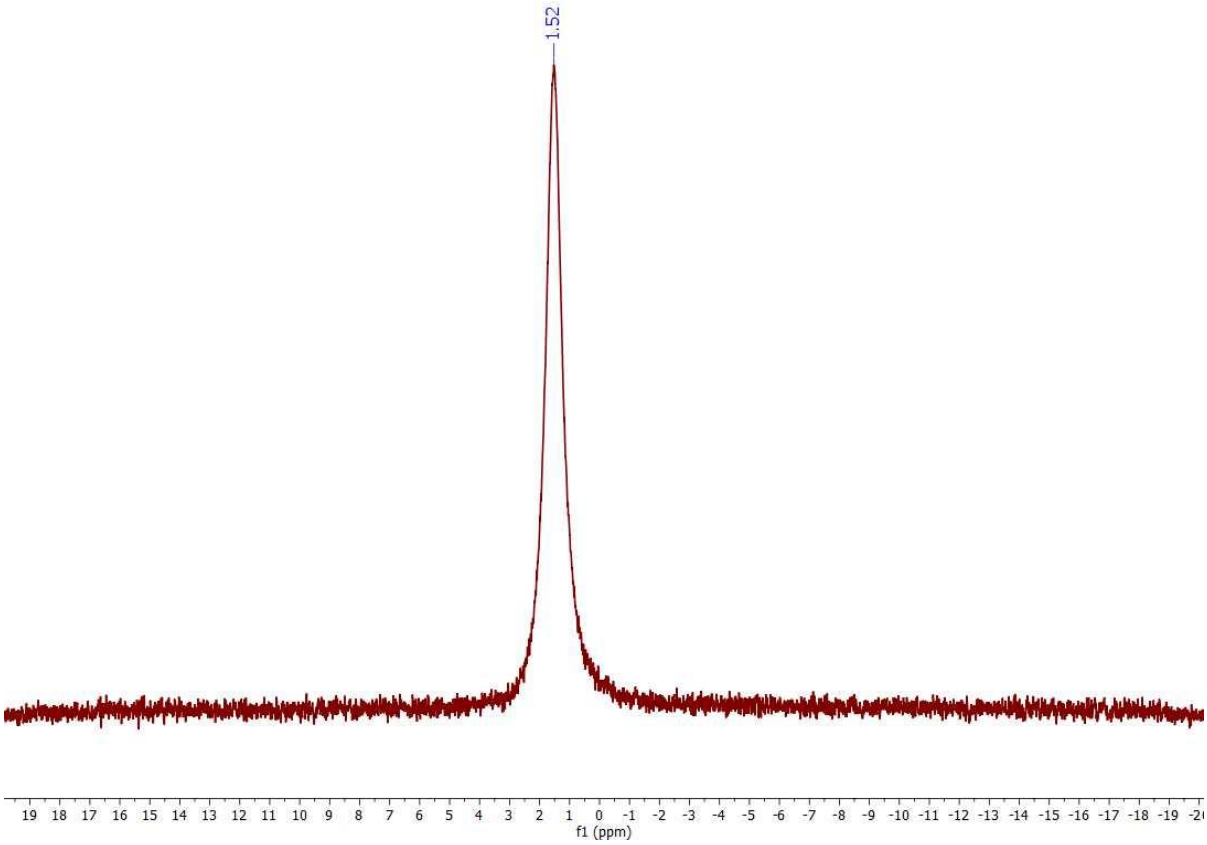

Figure A6.8. $^{7}Li\{^{1}H\}$ NMR spectrum of **6.7** in CD_2Cl_2.

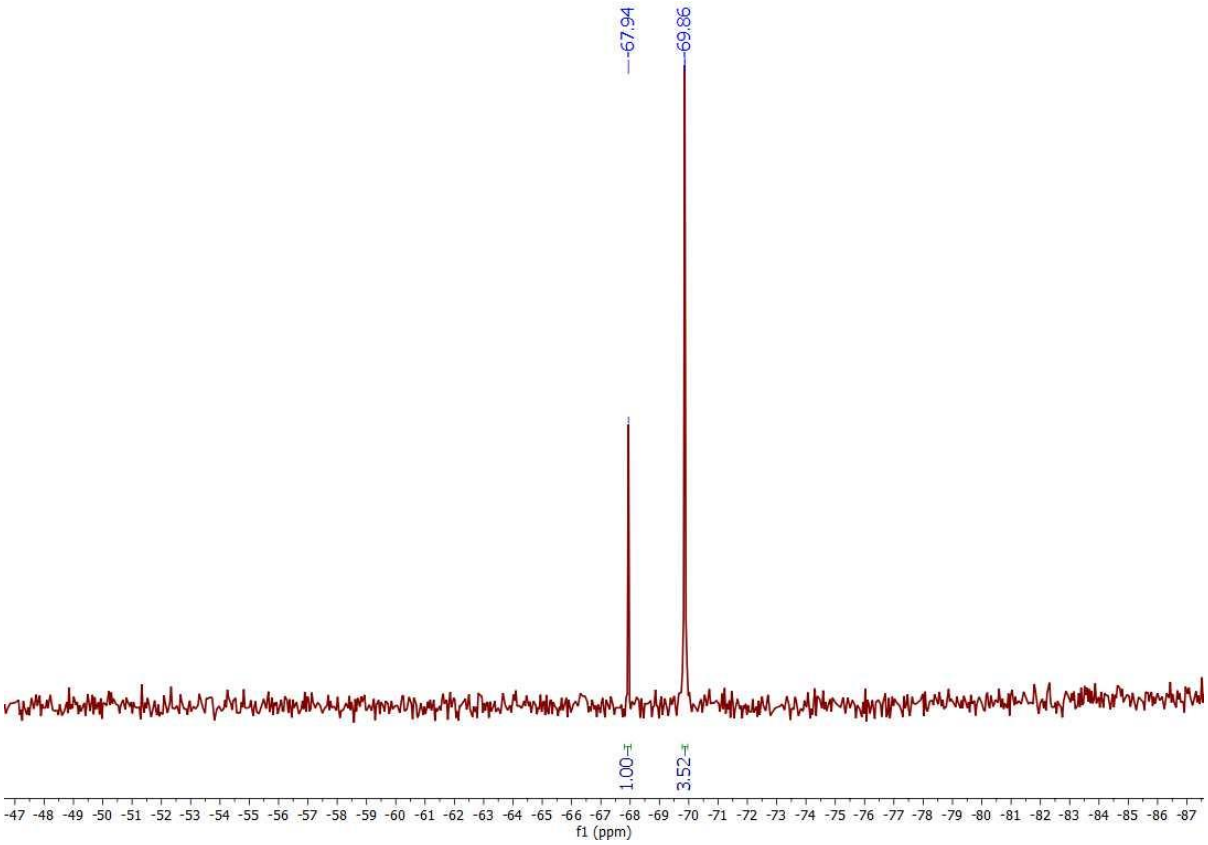

Figure A6.9. $^{29}Si\{^{1}H\}$ NMR spectrum of **6.7** in CD_2Cl_2.

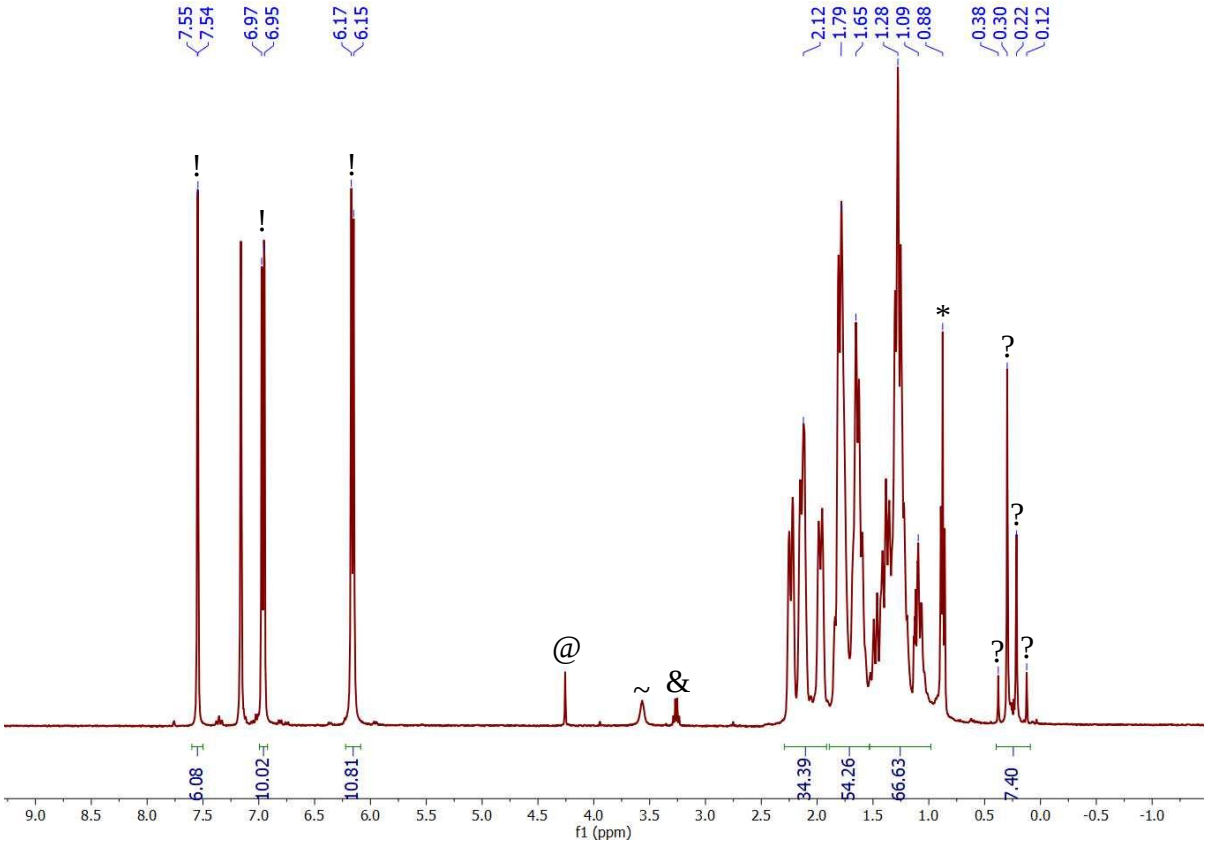

Figure A6.10. ^{1}H NMR spectrum (in C_6D_6) of a mixture of **6.5** and $N(2,4\text{-}C_6H_3Br_2)_3$. (!) indicates resonances assignable to $N(2,4\text{-}C_6H_3Br_2)_3$, * indicates resonances assignable to hexanes, @ indicates resonances assignable to CH_2Cl_2, & indicates resonances assignable to Et_2O, ~ indicates resonances assignable to THF, and (?) indicates resonances assignable to unidentified products.

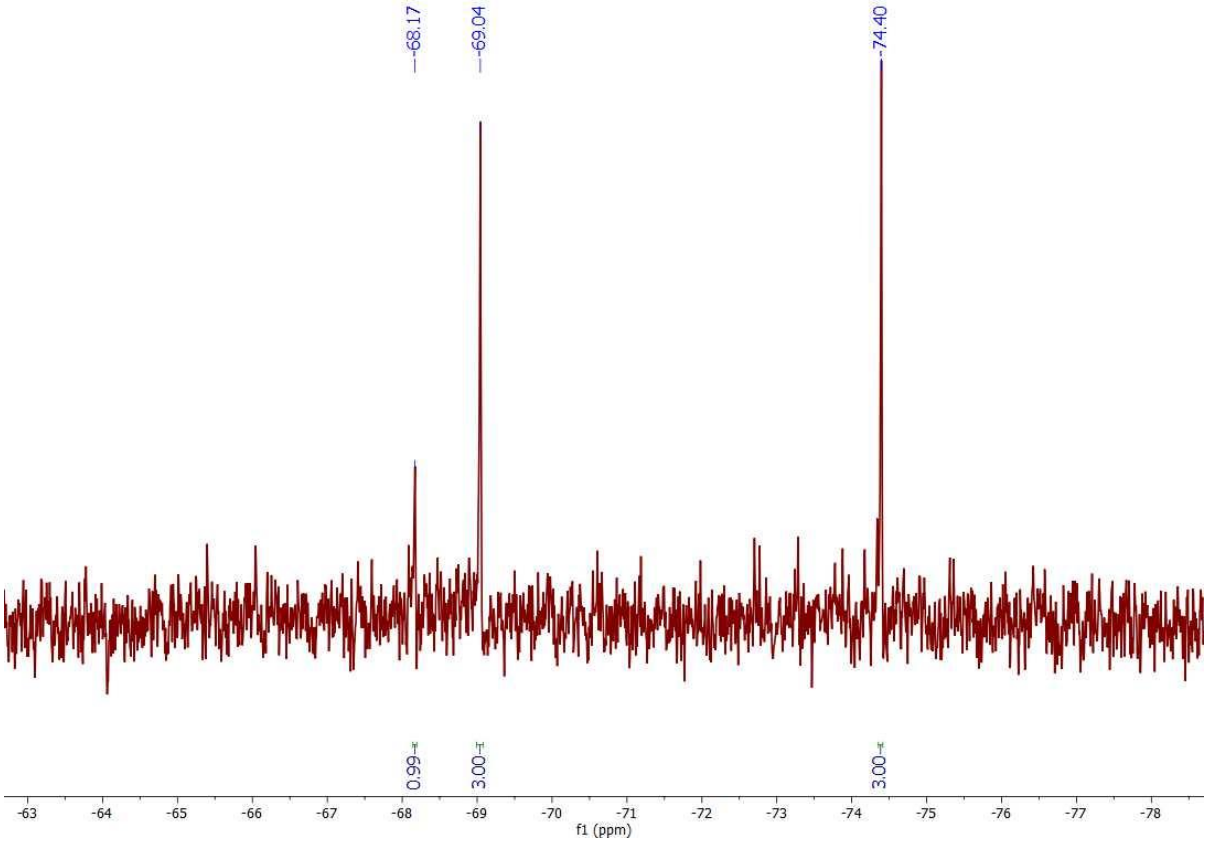

Figure A6.11. $^{29}Si\{^{1}H\}$ NMR spectrum (in C_6D_6) of a mixture of **6.5** and $N(2,4\text{-}C_6H_3Br_2)_3$.

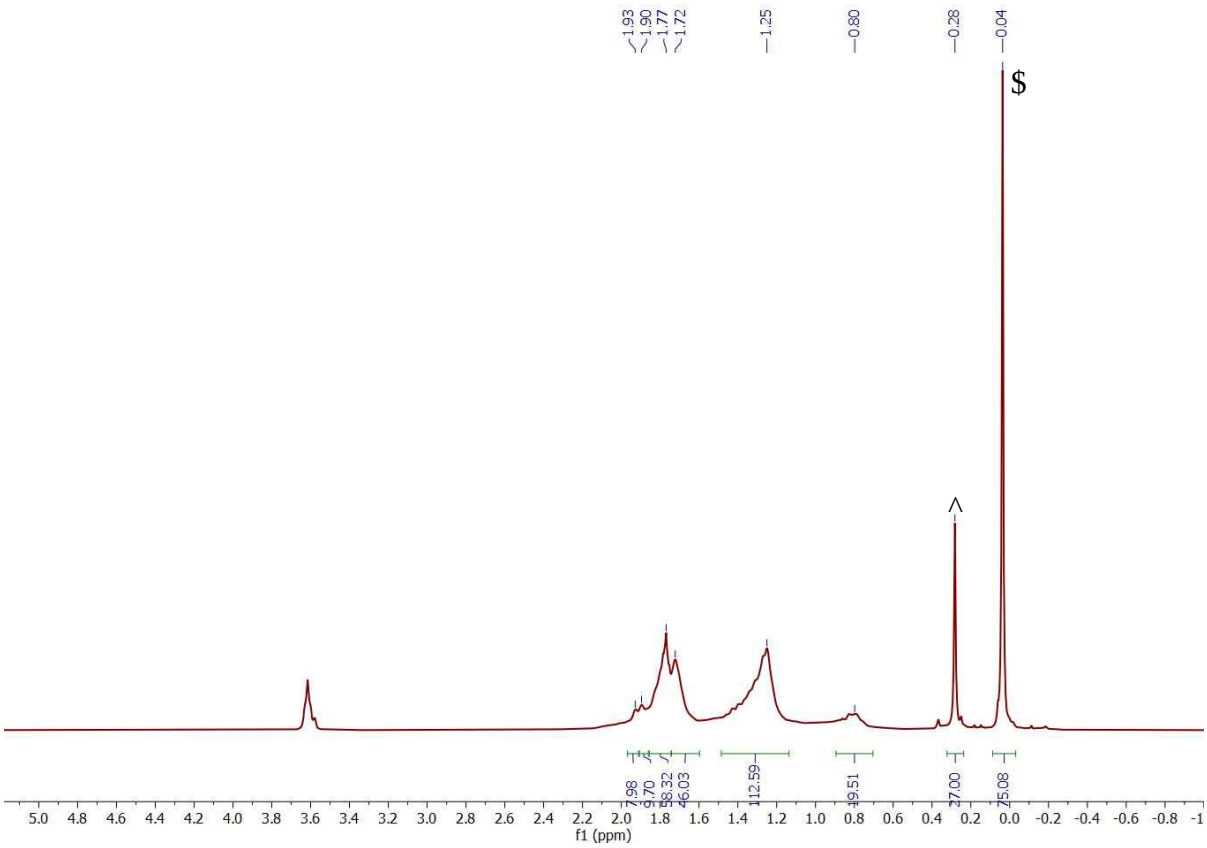

Figure A6.12. *In situ* ^{1}H NMR spectrum (in THF-d_8) of the reaction of $[UO_2(N(SiMe_3)_2)_2(THF)_2]$ and 1 equiv of $Cy_7Si_7O_9(OH)_3$. ^ indicates resonances assignable to **6.3**, and $ indicates resonances assignable to $HN(SiMe_3)_2$.

Experimental Details: $Cy_7Si_7O_9(OH)_3$ (119.1 mg, 0.122 mmol) was dissolved in THF-d_8 (0.75 mL) to yield a colorless solution. The solution was transferred to an NMR tube equipped with a J-Young valve and its ^{1}H and ^{29}Si{^{1}H} NMR spectra were recorded. The tube was brought back into the glovebox, and an orange solution of $[UO_2(N(SiMe_3)_2)_2(THF)_2]$ (88.3 mg, 0.120 mmol) in THF-d_8 (0.5 mL) was added. This addition resulted in an immediate color change to bright orange, concomitant with deposition of a small amount of fine yellow precipitate. The sample was then brought out of the glovebox and its ^{1}H and ^{29}Si{^{1}H} NMR spectra were recorded overnight. ^{1}H NMR (THF-d_8, 25 °C, 400 MHz): δ 0.04 (s, 18H,

$HN(SiMe_3)_2$), 0.28 (s, 27H, **6.3**). $^{29}Si\{^1H\}$ NMR (THF-d_8, 25 °C, 79 MHz): δ -74.54 (3Si, **6.5**), -73.47 (3Si, **6.3**), -70.57 (8Si, $Cy_8Si_8O_{12}$), -69.47 (3Si, **6.3**), -69.31 (3Si, **6.5**), -68.57 (1Si, **6.3**), -68.48 (1Si, **6.5**), 1.44 (2Si, $HN(SiMe_3)_2$), 20.91 (3Si, $OSiMe_3$, **6.3**). The mixture was brought back into the glovebox, and was filtered through a pre-weighed 0.2 μm PTFE membrane to yield an orange filtrate. A yellow powder remained inside the membrane, which was washed with THF (4 × 1 mL) and weighed after standing at room temperature for 5 d (9.8 mg). An XPS spectrum of this solid was then collected, which revealed an approximately 1:2 uranium to silsesquioxane ratio (Figure A6.24). Using this ratio, along with the isolated mass, the yellow powder was calculated to account for ~4% of the uranium in the reaction mixture. The volatiles were removed from the filtrate *in vacuo*, and the resulting orange solid was extracted into 2:1 Et_2O/MeCN (2 mL) and filtered through a Celite column supported on glass wool (0.5 cm × 2 cm) to yield an orange filtrate. Storage of this solution at -25 °C for 24 h resulted in deposition of orange plates of **6.3**, which were isolated by decanting off the supernatant (17.5 mg, 10% yield).

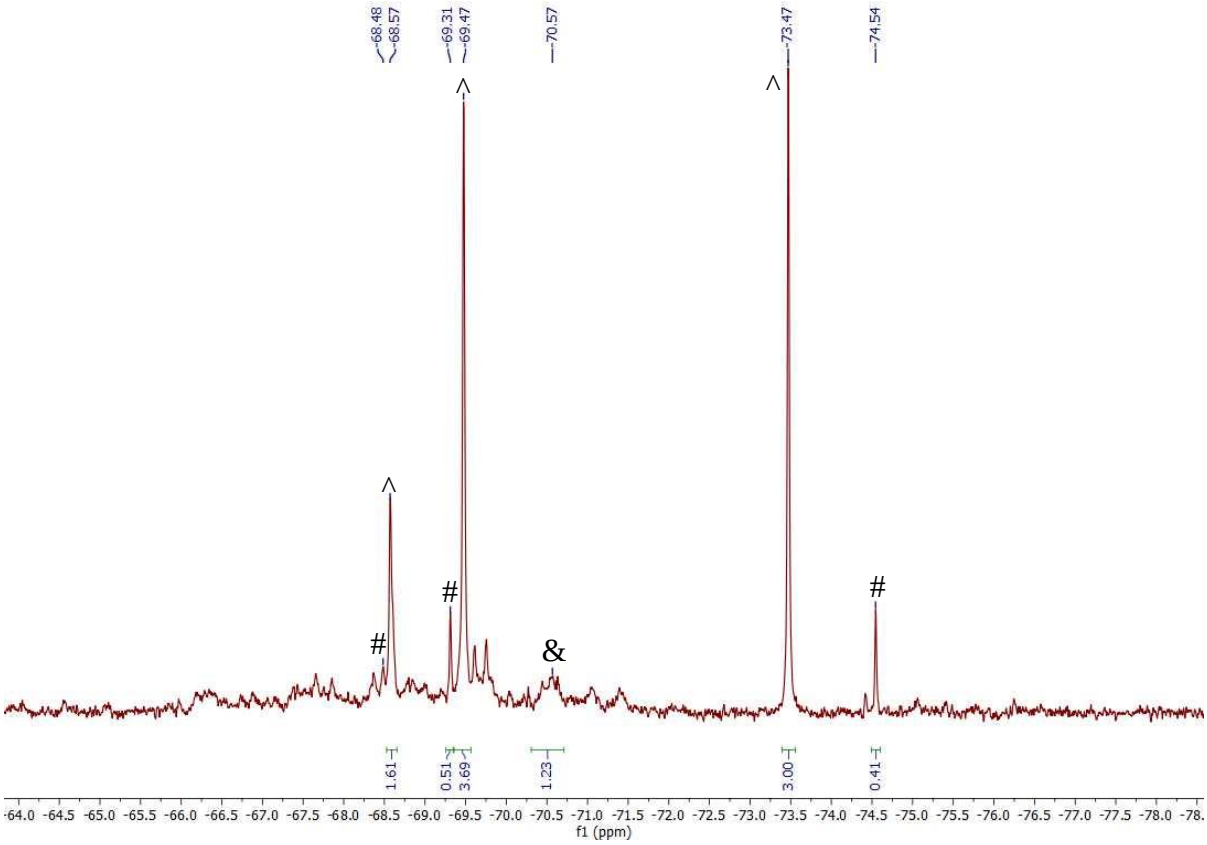

Figure A6.13. Partial $^{29}Si\{^{1}H\}$ NMR spectrum (in THF-d_8) of the reaction of $[UO_2(N(SiMe_3)_2)_2(THF)_2]$ and 1 equiv of $Cy_7Si_7O_9(OH)_3$. ^ indicates resonances assignable to **6.3**, # indicates resonances assignable to **6.5**, and & indicates resonances assignable to $Cy_8Si_8O_{12}$. **Experimental Details**: See details for Figure A6.12.

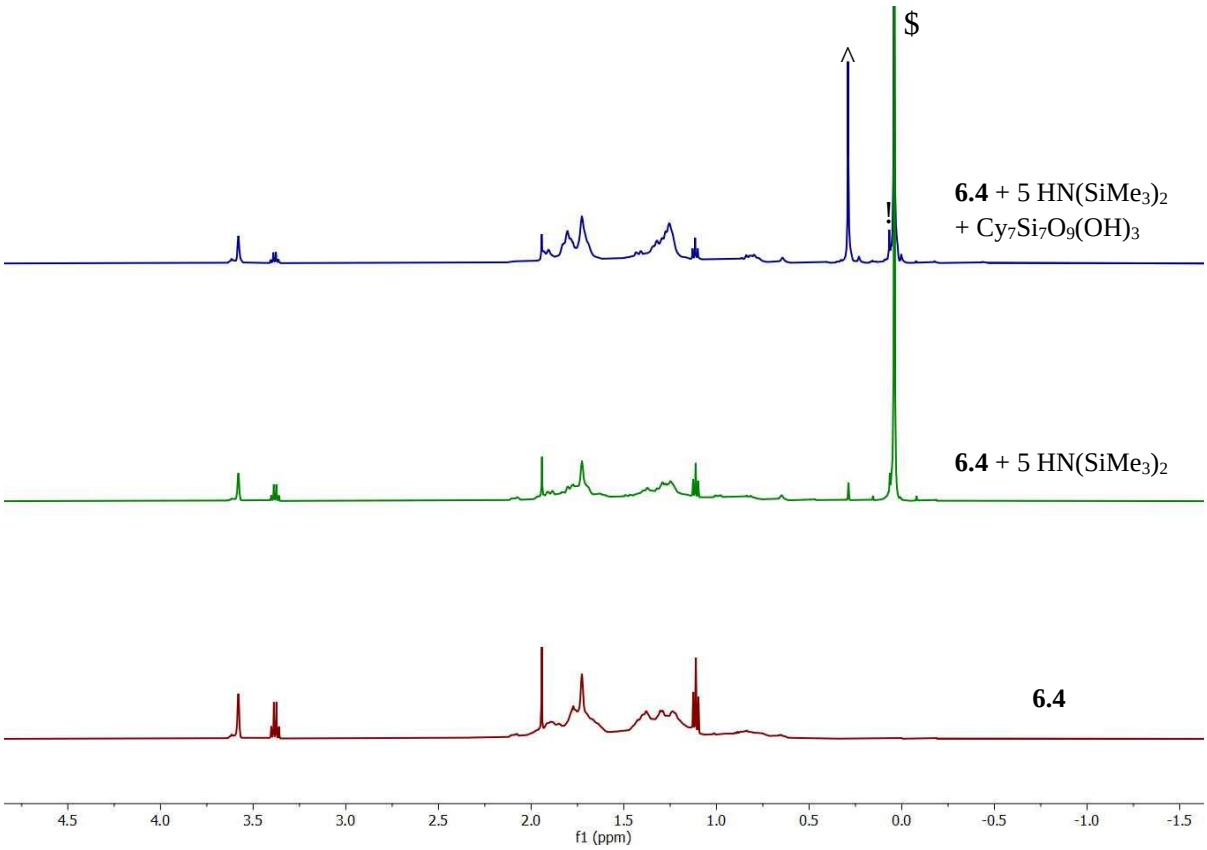

Figure A6.14. *In situ* ^{1}H NMR spectrum (in THF-d_8) of the reaction of $[(UO_2)_3(Cy_7Si_7O_{12})_2(MeCN)_2(Et_2O)]$ (**6.4**) with 5 equiv of $HN(SiMe_3)_2$ followed by 1 equiv of $Cy_7Si_7O_9(OH)_3$. ^ indicates resonances assignable to **6.3**, $ indicates resonances assignable to $HN(SiMe_3)_2$, and ! indicates resonances assignable to $(Me_3Si)_2O$.

Experimental Details: Crystals of **6.4** (38.8 mg, 0.013 mmol) were dissolved in 0.75 mL of THF-d_8 to yield a yellow solution. The solution was transferred to an NMR tube equipped with a J-Young valve and its ^{1}H and ^{29}Si{^{1}H} NMR spectra were recorded. The tube was brought back into the glovebox, and a colorless solution of $HN(SiMe_3)_2$ (14 µL, 0.067 mmol, 5 equiv) was added. The resulting solution was allowed to stand at room temperature for 30 min, whereupon a small amount of yellow precipitate formed. ^{1}H and ^{29}Si{^{1}H} NMR spectra of the resulting mixture were then recorded. ^{1}H NMR (THF-d_8, 25 °C, 500 MHz): δ 0.04 (s, 18H,

$HN(SiMe_3)_2$), 0.07 (s, 18H, $(Me_3Si)_2O$), 0.29 (s, 27H, **6.3**). $^{29}Si\{^1H\}$ NMR (THF-d_8, 25 °C, 99 MHz): δ -74.54 (3Si, **6.5**), -73.47 (3Si, **6.3**), -72.12 (**6.4**), -70.98 (8Si, $Cy_8Si_8O_{12}$), -70.17 (**6.4**), -69.46 (3Si, **6.3**), -69.29 (overlapping peaks for **6.4** and **6.5**), -68.56 (1Si, **6.3**), -68.46 (1Si, **6.5**), -68.07 (**6.4**), -67.79 (**6.4**), 1.45 (2Si, $HN(SiMe_3)_2$), 7.06 (2Si, $(Me_3Si)_2O$), 20.93 (3Si, $OSiMe_3$, **6.3**).The sample was brought back into the glove box and $Cy_7Si_7O_9(OH)_3$ (13.8 mg, 0.014 mmol, 1 equiv) was added as a solid. This addition resulted in an immediate color change to orange, concomitant with deposition of more fine yellow precipitate. The resulting mixture was allowed to stand at room temperature for 30 min, whereupon its ^1H and $^{29}Si\{^1H\}$ NMR spectra were re-recorded. ^1H NMR (THF-d_8, 25 °C, 500 MHz): δ 0.04 (s, 18H, $HN(SiMe_3)_2$), 0.07 (s, 18H, $(Me_3Si)_2O$), 0.29 (s, 27H, **6.3**). $^{29}Si\{^1H\}$ NMR (THF-d_8, 25 °C, 99 MHz): δ -74.54 (3Si, **6.5**), -73.47 (3Si, **6.3**), -70.99 (8Si, $Cy_8Si_8O_{12}$), -69.46 (3Si, **6.3**), -69.30 (3Si, **6.5**), -68.56 (1Si, **6.3**), -68.46 (1Si, **6.5**), 1.45 (2Si, $HN(SiMe_3)_2$), 7.06 (2Si, $(Me_3Si)_2O$), 20.93 (3Si, $OSiMe_3$, **6.3**).

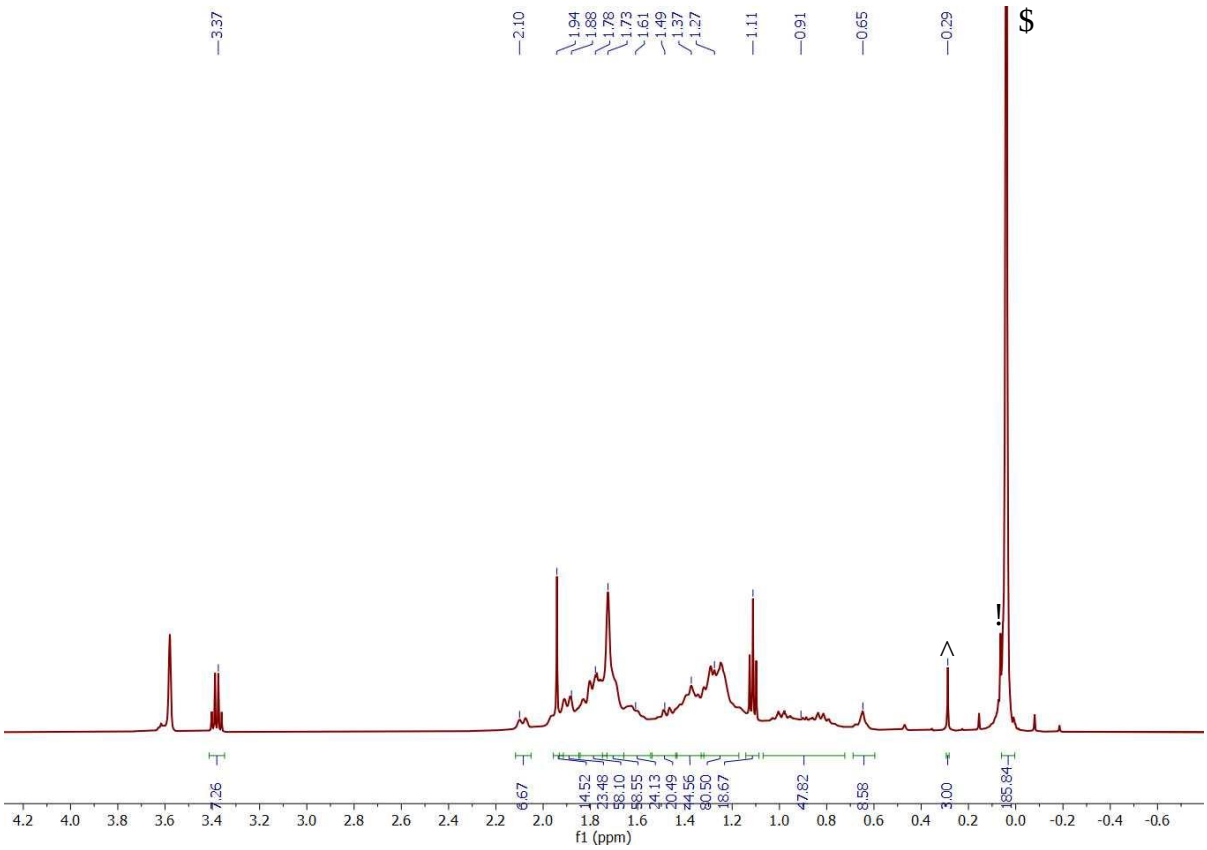

Figure A6.15. *In situ* ^{1}H NMR spectrum (in THF-d_8) of a mixture of $[(UO_2)_3(Cy_7Si_7O_{12})_2(MeCN)_2(Et_2O)]$ (**6.4**) and 5 equiv of $HN(SiMe_3)_2$. ^ indicates resonances assignable to **6.3**, $ indicates resonances assignable to $HN(SiMe_3)_2$, and ! indicates resonances assignable to $(Me_3Si)_2O$. **Experimental Details:** See figure caption for Figure A6.14.

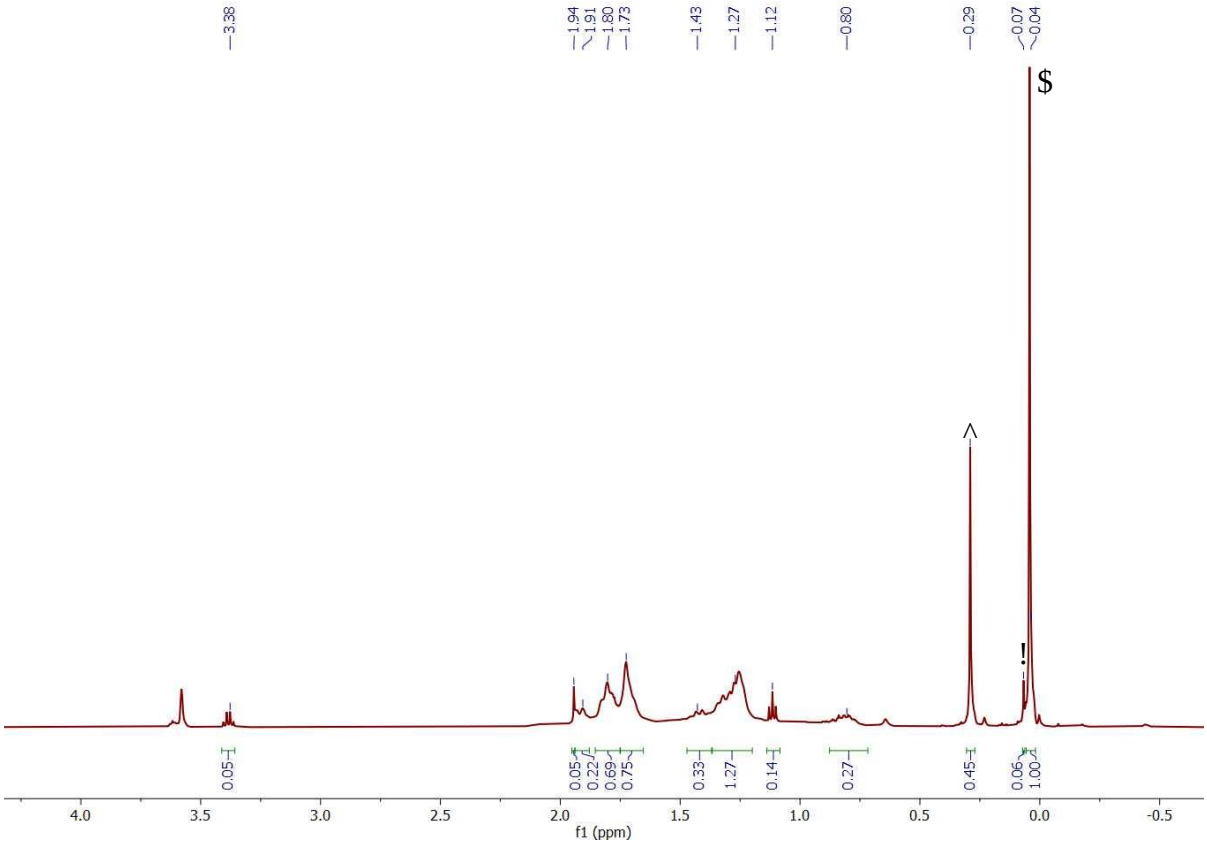

Figure A6.16. *In situ* ^{1}H NMR spectrum (in THF-d_8) of a mixture of $[(UO_2)_3(Cy_7Si_7O_{12})_2(MeCN)_2(Et_2O)]$ (**6.4**), 5 equiv of $HN(SiMe_3)_2$ and 1 equiv of $Cy_7Si_7O_9(OH)_3$. ^ indicates resonances assignable to **6.3**, $ indicates resonances assignable to $HN(SiMe_3)_2$, and ! indicates resonances assignable to $(Me_3Si)_2O$. **Experimental Details:** See figure caption for Figure A6.14.

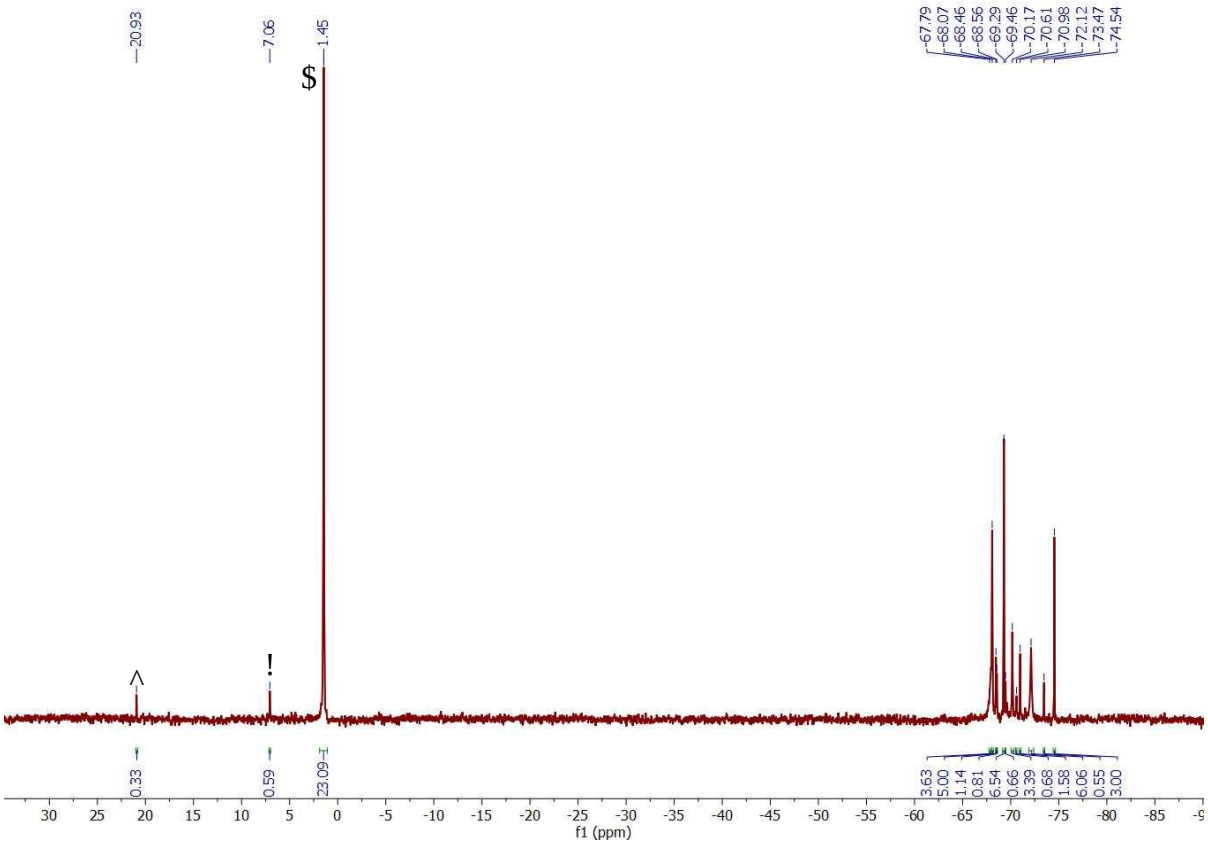

Figure A6.17. *In situ* $^{29}Si\{^{1}H\}$ NMR spectrum (in THF-d_8) of a mixture of $[(UO_2)_3(Cy_7Si_7O_{12})_2(MeCN)_2(Et_2O)]$ (**6.4**) and 5 equiv of $HN(SiMe_3)$. ^ indicates resonances assignable to **6.3**, $ indicates resonances assignable to $HN(SiMe_3)_2$, and ! indicates resonances assignable to $(Me_3Si)_2O$. **Experimental Details:** See figure caption for Figure A6.14.

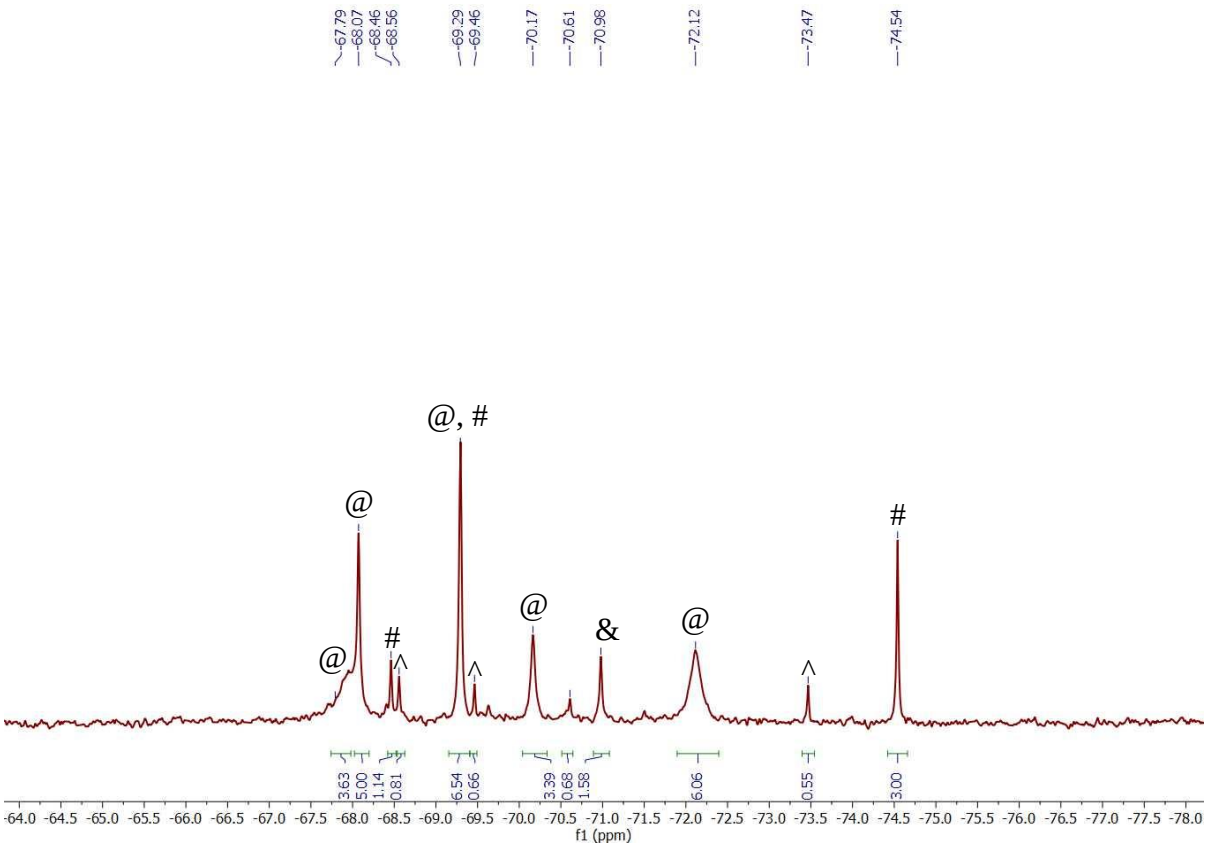

Figure A6.18. Partial *in situ* $^{29}Si\{^{1}H\}$ NMR spectrum (in THF-d_8) of a mixture of $[(UO_2)_3(Cy_7Si_7O_{12})_2(MeCN)_2(Et_2O)]$ (**6.4**) and 5 equiv of $HN(SiMe_3)_2$. ^ indicates resonances assignable to **6.3**, @ indicates resonances assignable to **6.4**, # indicates resonances assignable to **6.5**, and & indicates resonances assignable to $Cy_8Si_8O_{12}$. **Experimental Details:** See figure caption for Figure A6.14.

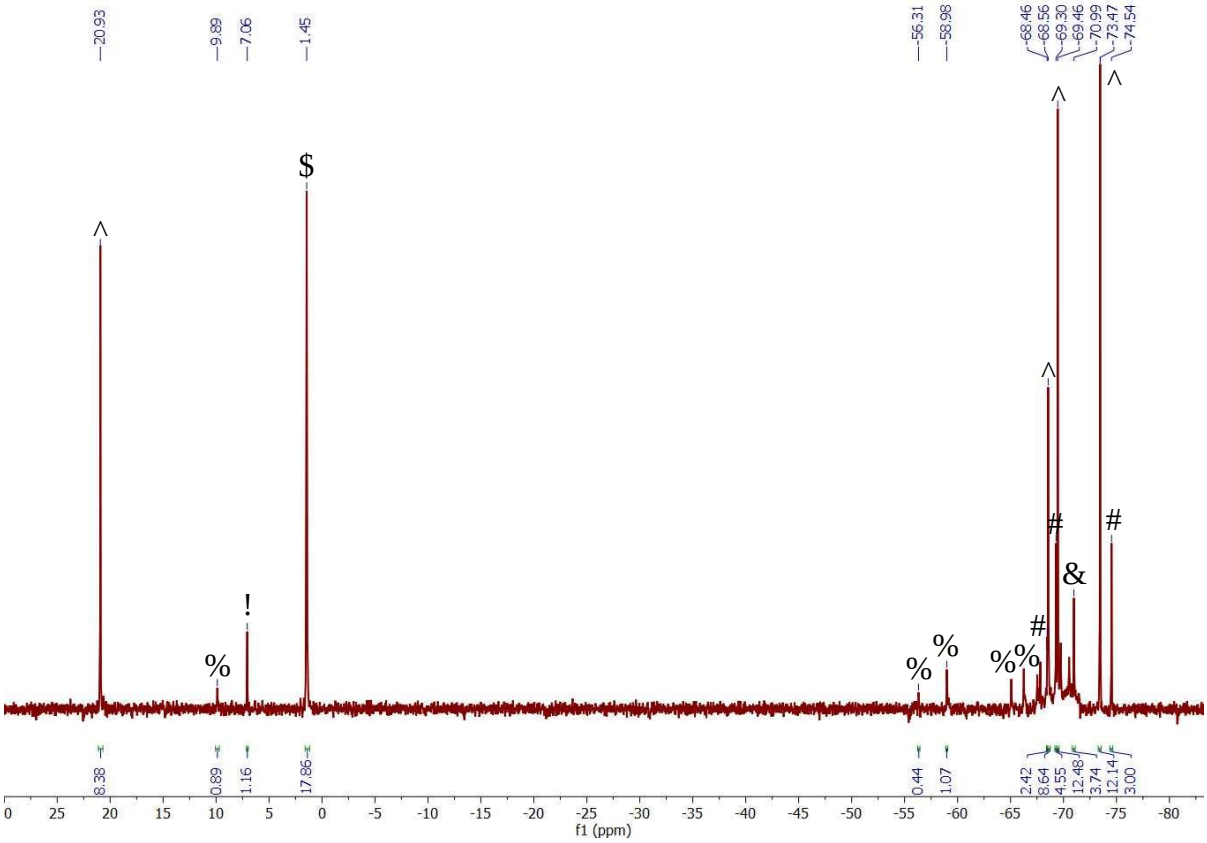

Figure A6.19. *In situ* $^{29}Si\{^{1}H\}$ NMR spectrum (in THF-d_8) of a mixture of $[(UO_2)_3(Cy_7Si_7O_{12})_2(MeCN)_2(Et_2O)]$ (**6.4**), 5 equiv of $HN(SiMe_3)_2$ and 1 equiv of $Cy_7Si_7O_9(OH)_3$. ^ indicates resonances assignable to **6.3**, # indicates resonances assignable to **6.5**, $ indicates resonances assignable to $HN(SiMe_3)_2$, & indicates resonances assignable to $Cy_8Si_8O_{12}$, ! indicates resonances assignable to $(Me_3Si)_2O$, % indicates resonances assignable to unidentified minor by-products. **Experimental Details:** See figure caption for Figure A6.14.

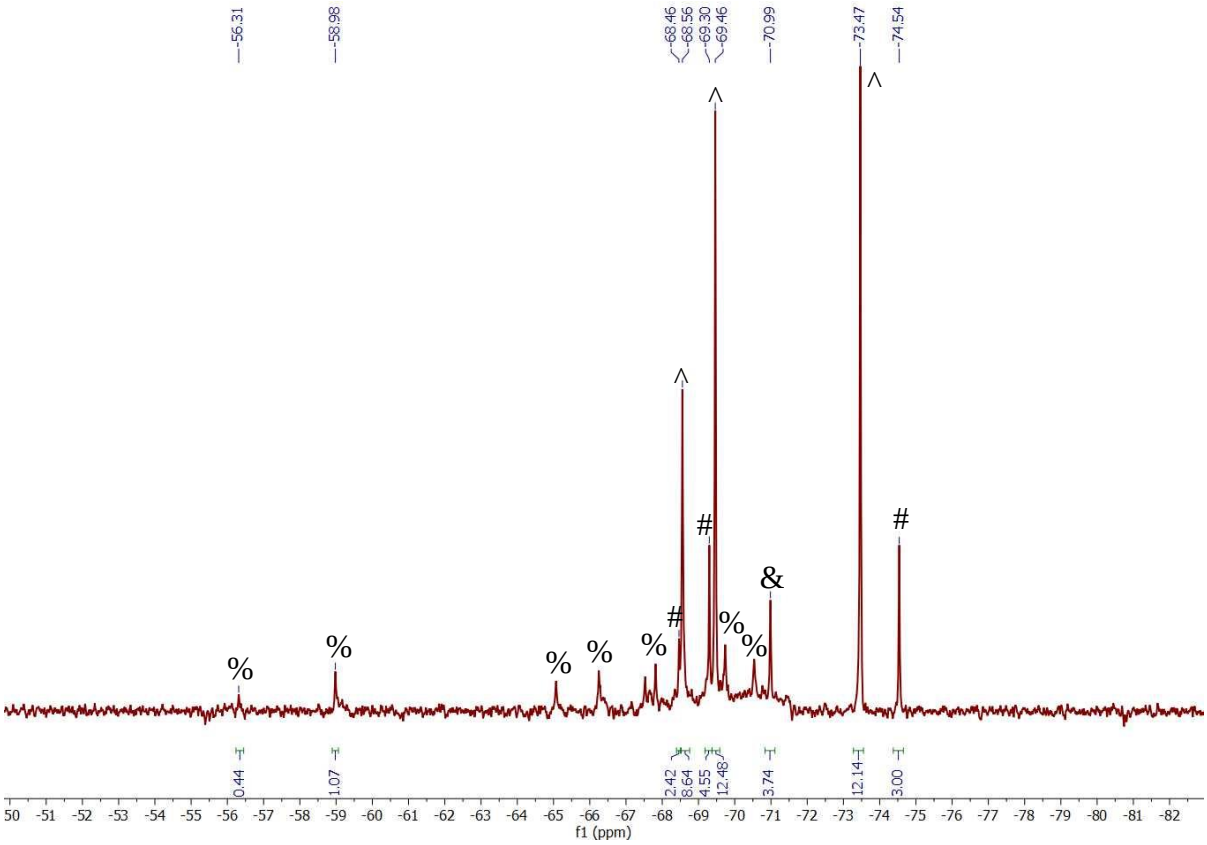

Figure A6.20. *In situ* $^{29}Si\{^{1}H\}$ NMR spectrum (in THF-d_8) of a mixture of $[(UO_2)_3(Cy_7Si_7O_{12})_2(MeCN)_2(Et_2O)]$ (**6.4**), 5 equiv of $HN(SiMe_3)_2$ and 1 equiv of $Cy_7Si_7O_9(OH)_3$. ^ indicates resonances assignable to **6.3**, # indicates resonances assignable to **6.5**, & indicates resonances assignable to $Cy_8Si_8O_{12}$, and % indicates resonances assignable to unidentified minor by-products. **Experimental Details:** See figure caption for Figure A6.14.

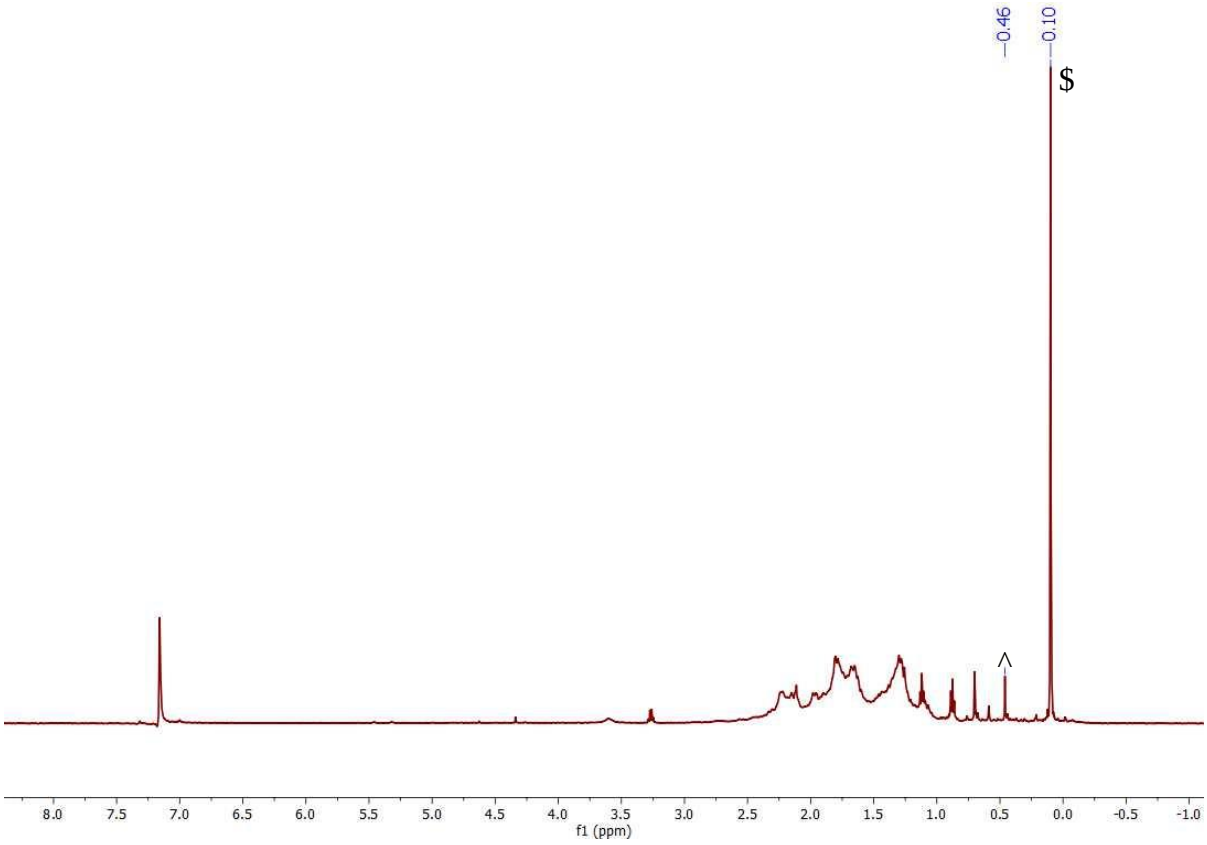

Figure A6.21. ^{1}H NMR spectrum (in C_6D_6) of an aliquot of the reaction between $[UO_2(N(SiMe_3)_2)_2(THF)_2]$ and 1 equiv of $Cy_7Si_7O_9(OH)_3$ in hexanes. ^ indicates resonances assignable to **6.3**, and $ indicates resonances assignable to $HN(SiMe_3)_2$. **Experimental Details:** To a stirring orange solution of $[UO_2(N(SiMe_3)_2)_2(THF)_2]$ (30.2 mg, 0.041 mmol) in hexanes (1 mL) was added dropwise, very slowly, a slurry of $Cy_7Si_7O_9(OH)_3$ (40.1 mg, 0.041 mmol) in hexanes (1 mL). This addition resulted in an immediate color change to dark brown, and then gradually to yellow-orange. The mixture was allowed to stir at room temperature for 15 min, whereupon the solution was filtered through a Celite column supported on glass wool (0.5 cm × 2 cm) to yield a yellow-orange filtrate. An aliquot of the reaction mixture was then dried *in vacuo*. The resulting yellow solid was dissolved in C_6D_6 (0.75 ml) and a ^{1}H NMR spectrum was recorded.

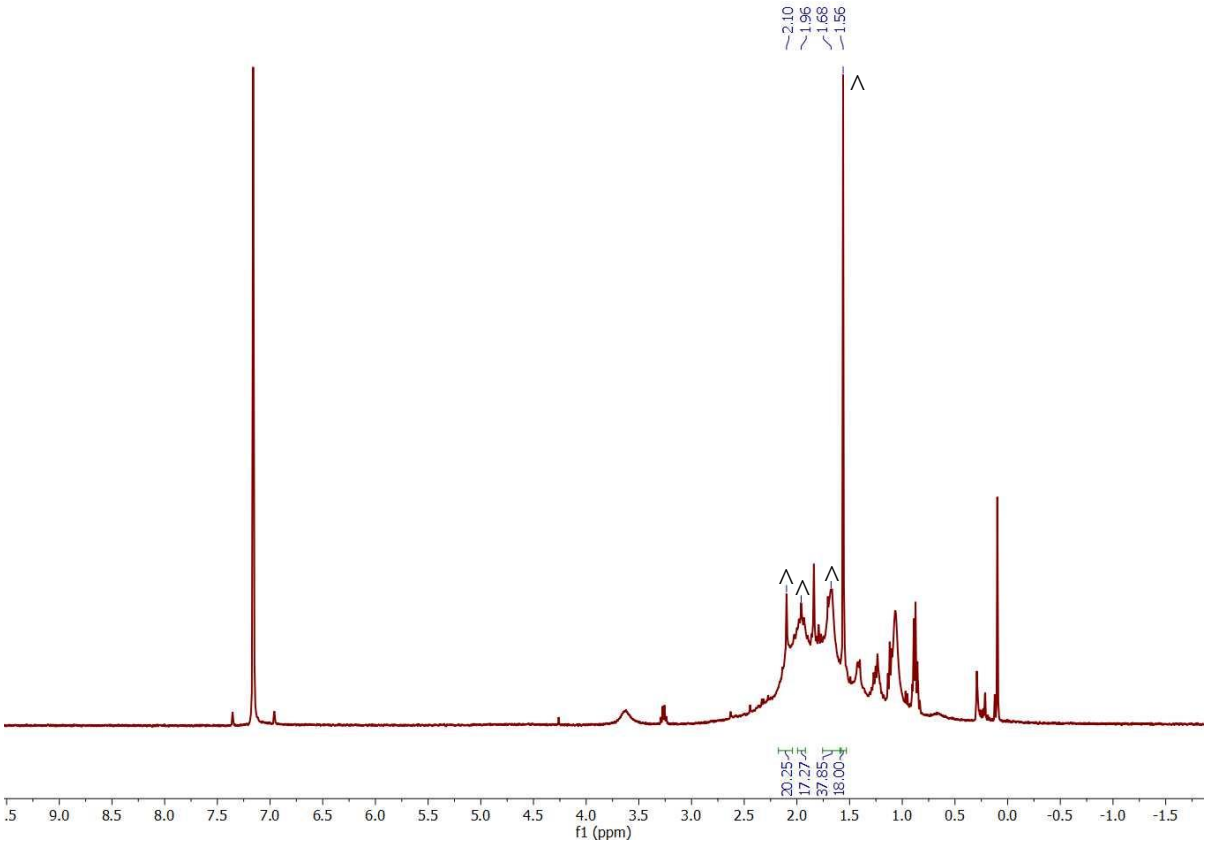

Figure A6.22. ^{1}H NMR spectrum (in C_6D_6) of an aliquot of the hexanes fraction obtained from the reaction between $[UO_2(N(SiMe_3)_2)_2(THF)_2]$ and 2 equiv of ^{t}BuOH in THF. ^ is assignable to $[UO_2][U(\mu\text{-}O)(\mu\text{-}O^{t}Bu)(O^{t}Bu)_4]_2$.

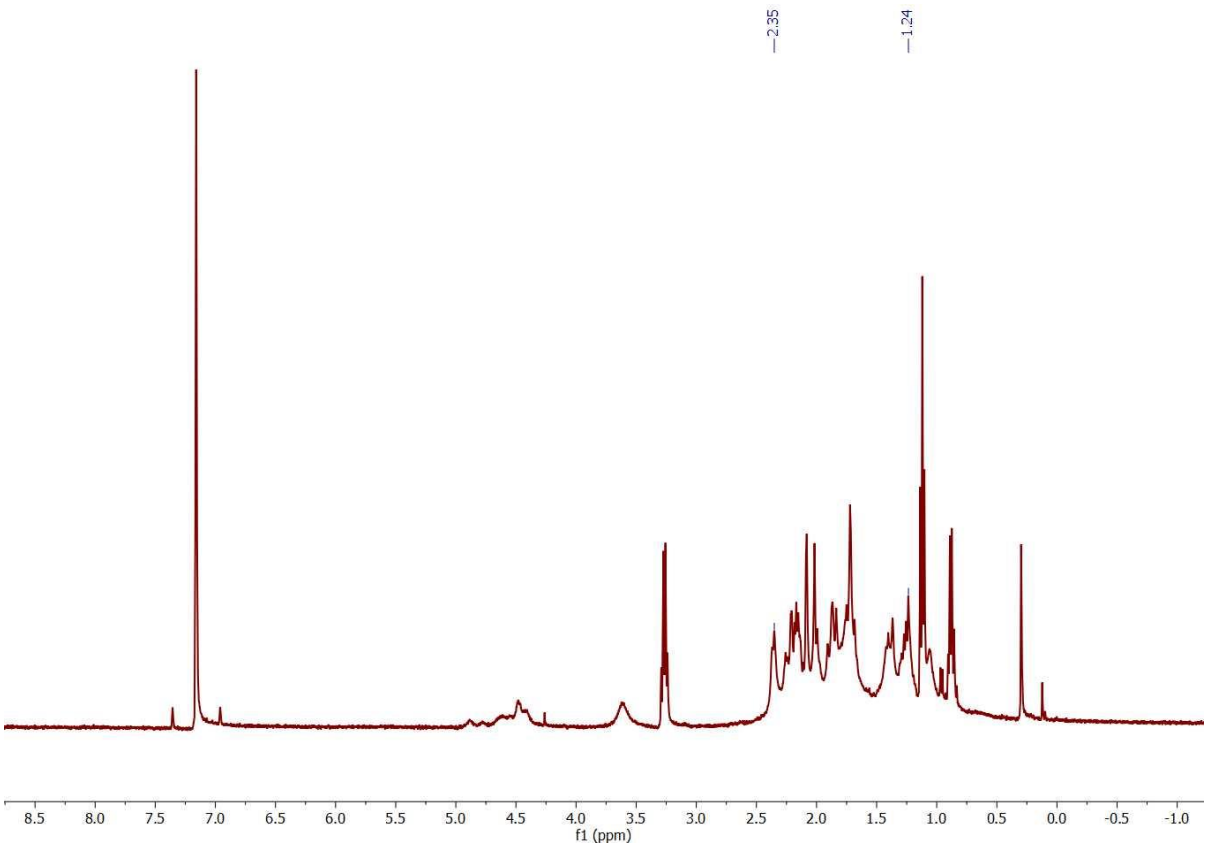

Figure A6.23. ^{1}H NMR spectrum (in C_6D_6) of an aliquot of the Et_2O fraction obtained from the reaction between $[UO_2(N(SiMe_3)_2)_2(THF)_2]$ and 2 equiv of ^{t}BuOH in THF.

6.6.2 Cyclic Voltammetry of $[Li(THF)_2][U(Cy_7Si_7O_{12})_2]$ (6.7)

Table A6.1. Electrochemical parameters for $[Li(THF)_2][U(Cy_7Si_7O_{12})_2]$ (**6.7**) in CH_2Cl_2, in the presence of 2 equiv of 12-crown-4 (vs. Fc/Fc^+, $[NBu_4][PF_6]$ as the supporting electrolyte).

Oxidation Feature	Scan Rate, V/s	$E_{p,a}$, V	$E_{p,c}$, V	$E_{1/2}$, V	ΔE_p, V	$i_{p,a}/i_{p,c}$
	0.025	0.347	-0.219	0.064	0.566	1.47
	0.050	0.424	-0.272	0.076	0.696	1.47
	0.100	0.477	-0.302	0.088	0.779	1.57
	0.200	0.535	-0.361	0.087	0.896	1.54
	0.300	0.578	-0.407	0.086	0.985	1.77
	0.500	0.637	-0.502	0.068	1.139	1.95

6.6.3 X-ray Photoelectron Spectroscopy

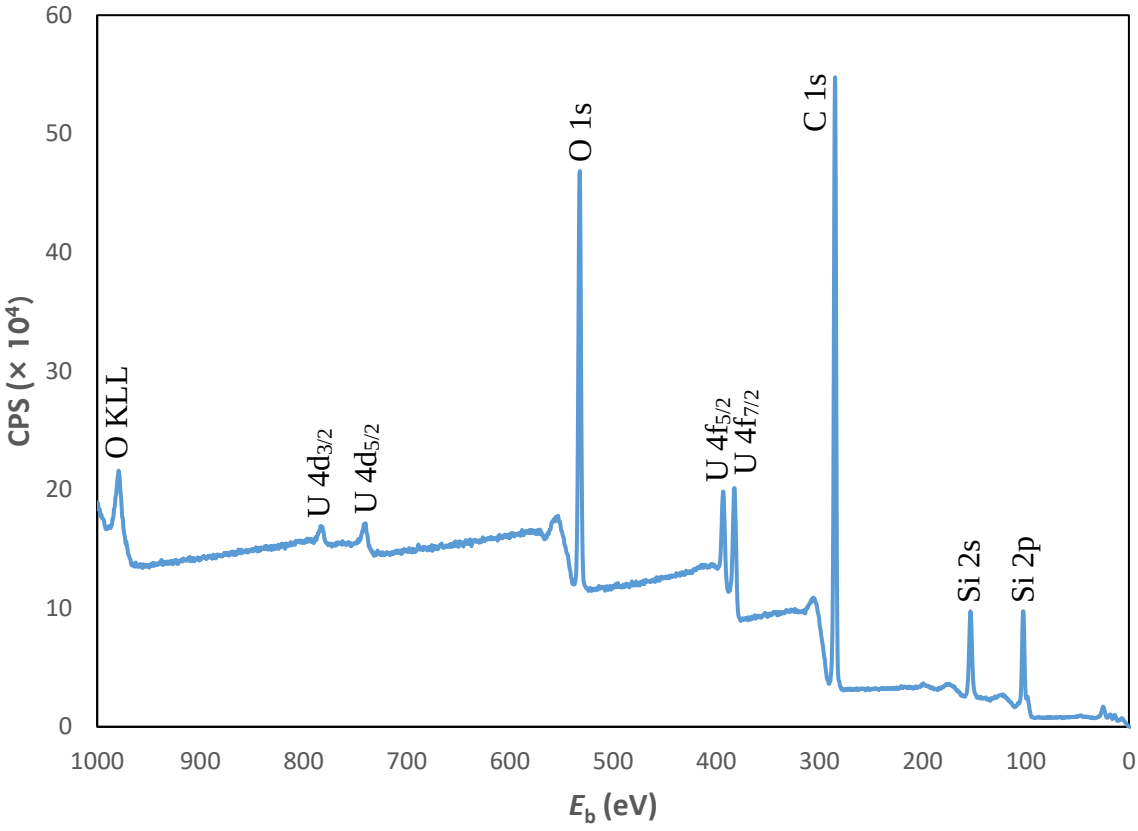

Figure A6.24. X-ray photoelectron spectrum of the yellow powder isolated from the reaction between $[UO_2(N(SiMe_3)_2)_2(THF)_2]$ and $Cy_7Si_7O_9(OH)_3$.

Table A6.2. X-ray Photoelectron Spectroscopy (XPS) Data

Assignment	E_b (eV)
O KLL	979.2
U $4d_{3/2}$	783.2
U $4d_{5/2}$	740.6
O 1s	532.0
U $4f_{5/2}$	393.9
U $4f_{7/2}$	383.2
U $4f_{5/2}$	392.7
U $4f_{7/2}$	382.0
U $4f_{5/2}$	391.3
U $4f_{7/2}$	380.6
C 1s	284.6
Si 2s	153.5
Si 2p	102.4

6.6.4 IR Spectra

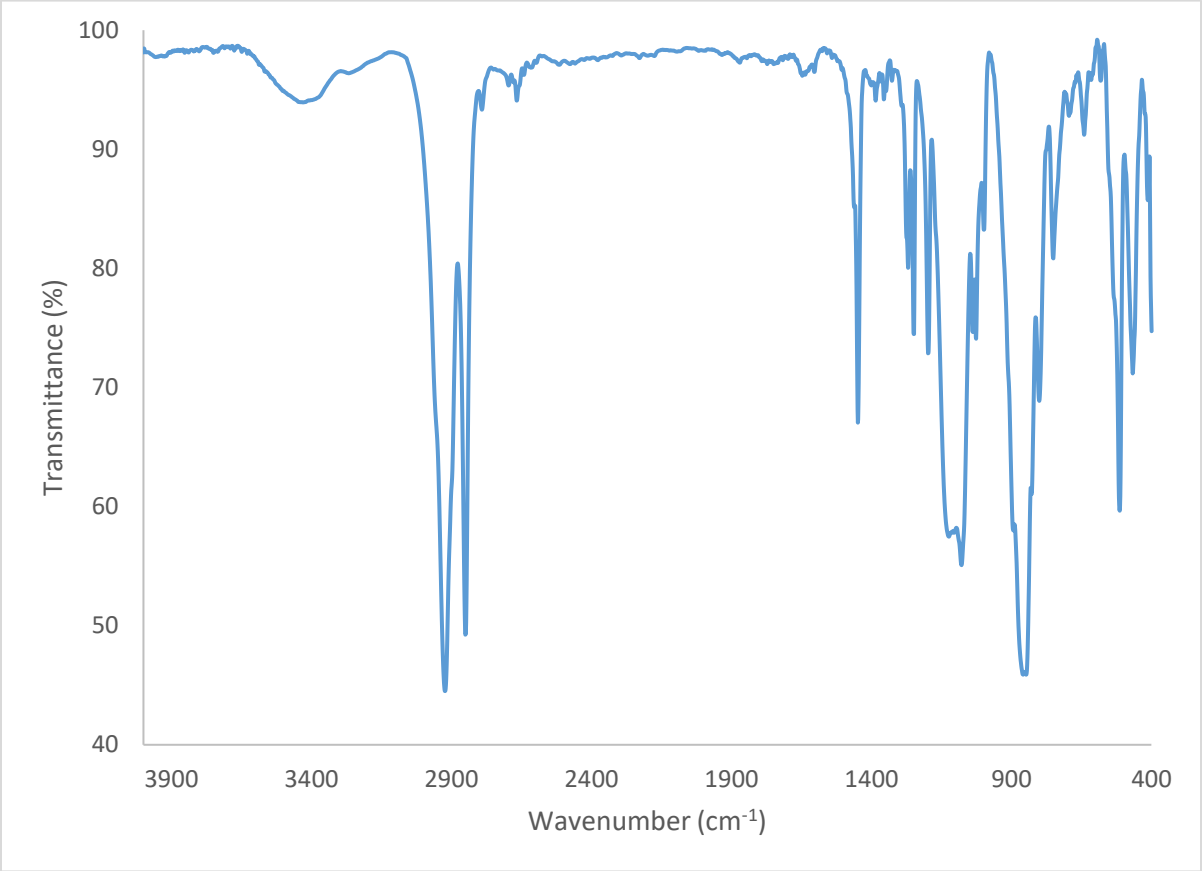

Figure A6.25. IR spectrum of **6.3** (KBr pellet).

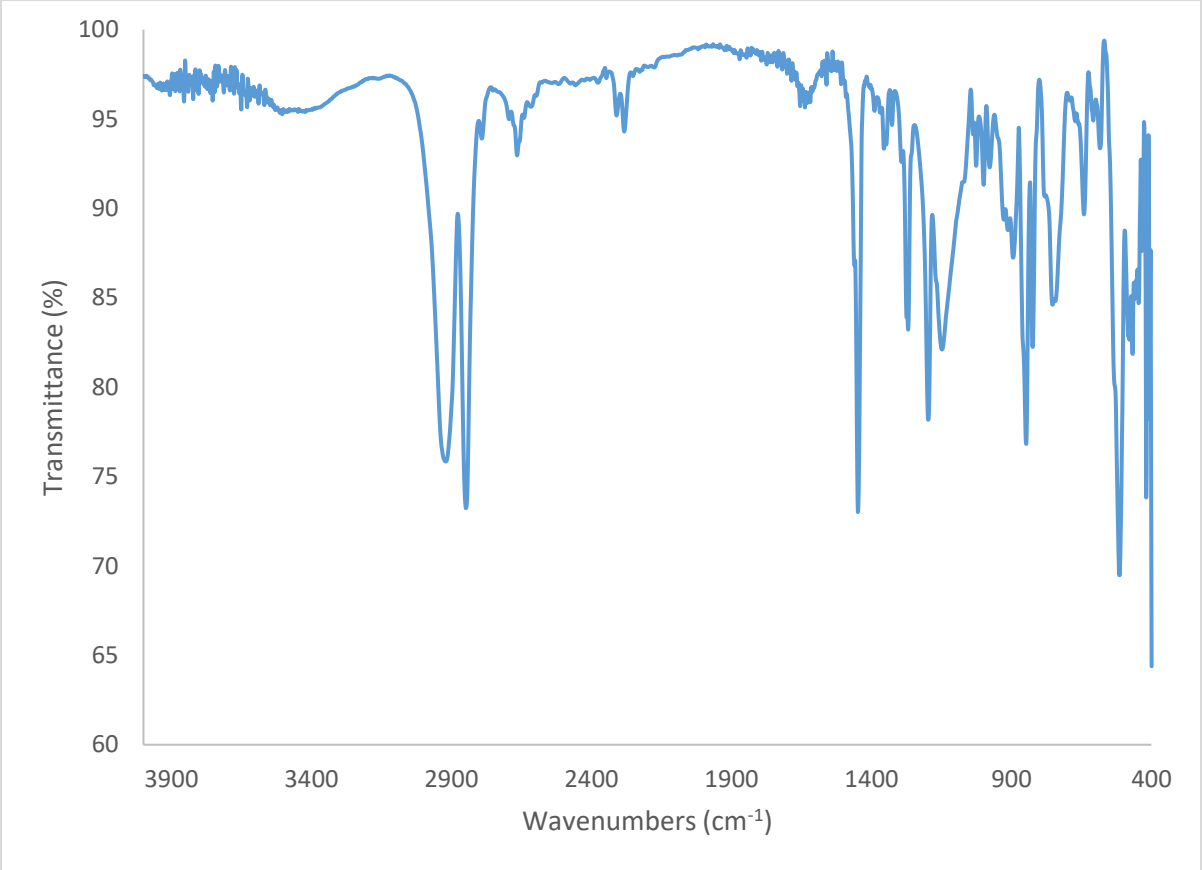

Figure A6.26. IR spectrum of **6.4** (KBr pellet).

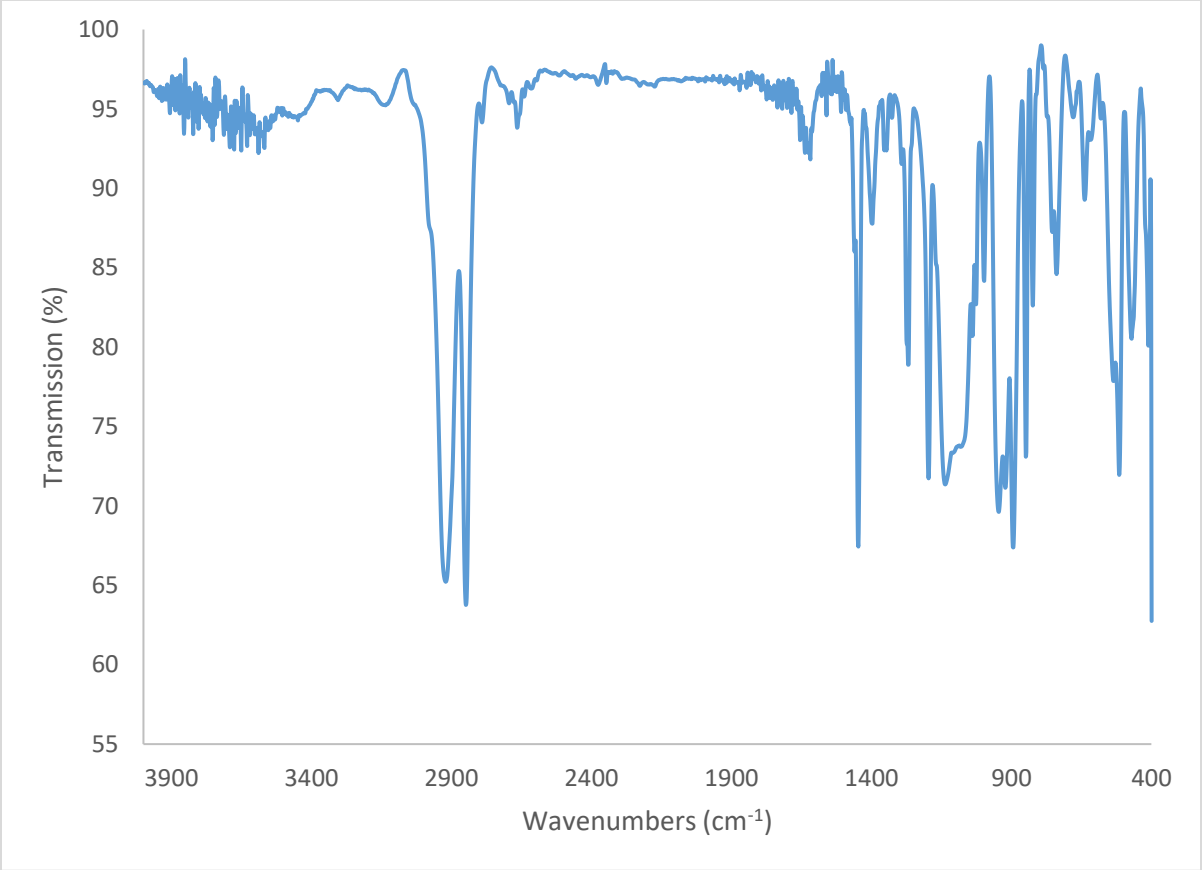

Figure A6.27. IR spectrum of **6.6** (KBr pellet).

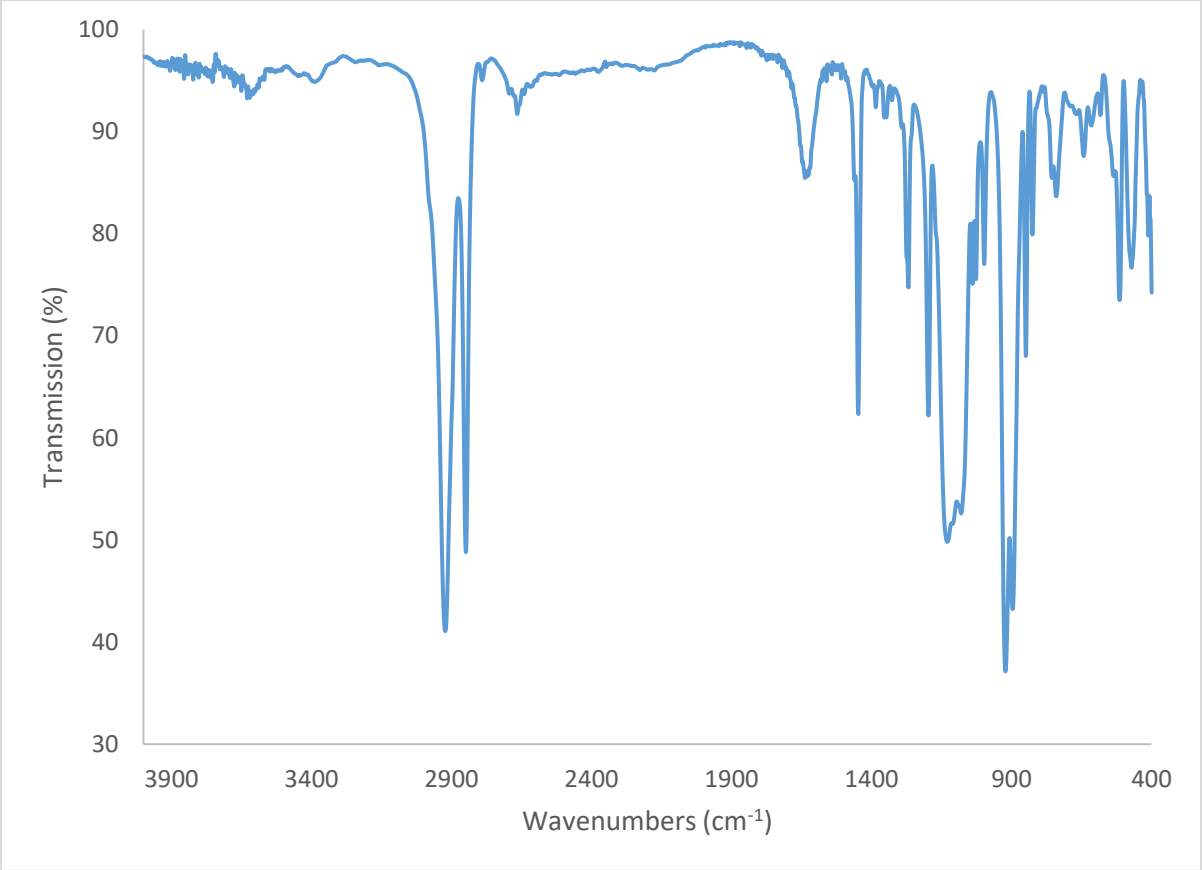

Figure A6.28. IR spectrum of **6.7** (KBr pellet).

6.7 References

1. McCann, K.; Mincher, B. J.; Schmitt, N. C.; Braley, J. C., Hexavalent Actinide Extraction Using *N*,*N*-Dialkyl Amides. *Ind. Eng. Chem. Res.* **2017,** *56* (22), 6515-6519.

2. McCann, K.; Brigham, D. M.; Morrison, S.; Braley, J. C., Hexavalent Americium Recovery Using Copper(III) Periodate. *Inorg. Chem.* **2016,** *55* (22), 11971-11978.

3. Runde, W. H.; Mincher, B. J., Higher Oxidation States of Americium: Preparation, Characterization and Use for Separations. *Chem. Rev.* **2011,** *111* (9), 5723-5741.

4. Keener, M.; Hunt, C.; Carroll, T. G.; Kampel, V.; Dobrovetsky, R.; Hayton, T. W.; Ménard, G., Redox-switchable carboranes for uranium capture and release. *Nature* **2020,** *577* (7792), 652-655.

5. Kim, J.; Tsouris, C.; Mayes, R. T.; Oyola, Y.; Saito, T.; Janke, C. J.; Dai, S.; Schneider, E.; Sachde, D., Recovery of Uranium from Seawater: A Review of Current Status and Future Research Needs. *Sep. Sci. Technol.* **2013,** *48* (3), 367-387.

6. Parker, B. F.; Zhang, Z.; Rao, L.; Arnold, J., An overview and recent progress in the chemistry of uranium extraction from seawater. *Dalton Trans.* **2018,** *47* (3), 639-644.

7. Geckeis, H.; Lützenkirchen, J.; Polly, R.; Rabung, T.; Schmidt, M., Mineral–Water Interface Reactions of Actinides. *Chem. Rev.* **2013,** *113* (2), 1016-1062.

8. Morss, L. R.; Edelstein, N. M.; Fuger, J.; Katz, J. J., *The Chemistry of the Actinide and Transactinide Elements*. Springer: 2006.

9. Fortier, S.; Hayton, T. W., Oxo ligand functionalization in the uranyl ion (UO_2^{2+}). *Coord. Chem. Rev.* **2010,** *254* (3), 197-214.

10. Berthet, J.-C.; Lance, M.; Nierlich, M.; Ephritikhine, M., Simple Preparations of the Anhydrous and Solvent-Free Uranyl and Cerium(IV) Triflates $UO_2(OTf)_2$ and $Ce(OTf)_4$ − Crystal Structures of $UO_2(OTf)_2(py)_3$ and $[\{UO_2(py)_4\}_2(\mu\text{-}O)][OTf]_2$. *Eur. J. Inorg. Chem.* **2000,** *2000* (9), 1969-1973.

11. Arnold, P. L.; Patel, D.; Wilson, C.; Love, J. B., Reduction and selective oxo group silylation of the uranyl dication. *Nature* **2008,** *451*, 315.

12. Berthet, J.-C.; Siffredi, G.; Thuéry, P.; Ephritikhine, M., Controlled Chemical Reduction of Uranyl Salts into $UX_4(MeCN)_4$ (X = Cl, Br, I) with Me_3SiX Reagents. *Eur. J. Inorg. Chem.* **2007,** *2007* (25), 4017-4020.

13. Arnold, P. L.; Hollis, E.; Nichol, G. S.; Love, J. B.; Griveau, J.-C.; Caciuffo, R.; Magnani, N.; Maron, L.; Castro, L.; Yahia, A.; Odoh, S. O.; Schreckenbach, G., Oxo-Functionalization and Reduction of the Uranyl Ion through Lanthanide-Element Bond Homolysis: Synthetic,

Structural, and Bonding Analysis of a Series of Singly Reduced Uranyl–Rare Earth $5f^1$-$4f^n$ Complexes. *J. Am. Chem. Soc.* **2013,** *135* (10), 3841-3854.

14. Arnold, P. L.; Jones, G. M.; Odoh, S. O.; Schreckenbach, G.; Magnani, N.; Love, J. B., Strongly coupled binuclear uranium–oxo complexes from uranyl oxo rearrangement and reductive silylation. *Nat. Chem.* **2012,** *4* (3), 221-227.

15. Arnold, P. L.; Pécharman, A.-F.; Love, J. B., Oxo Group Protonation and Silylation of Pentavalent Uranyl Pacman Complexes. *Angew. Chem. Int. Ed.* **2011,** *50* (40), 9456-9458.

16. Arnold, P. L.; Patel, D.; Blake, A. J.; Wilson, C.; Love, J. B., Selective Oxo Functionalization of the Uranyl Ion with 3d Metal Cations. *J. Am. Chem. Soc.* **2006,** *128* (30), 9610-9611.

17. Schnaars, D. D.; Wu, G.; Hayton, T. W., Reduction of Pentavalent Uranyl to U(IV) Facilitated by Oxo Functionalization. *J. Am. Chem. Soc.* **2009,** *131* (48), 17532-17533.

18. Hayton, T. W.; Wu, G., Exploring the Effects of Reduction or Lewis Acid Coordination on the U=O Bond of the Uranyl Moiety. *Inorg. Chem.* **2009,** *48* (7), 3065-3072.

19. Pedrick, E. A.; Wu, G.; Hayton, T. W., Oxo Ligand Substitution in a Cationic Uranyl Complex: Synergistic Interaction of an Electrophile and a Reductant. *Inorg. Chem.* **2015,** *54* (14), 7038-7044.

20. Pedrick, E. A.; Wu, G.; Kaltsoyannis, N.; Hayton, T. W., Reductive silylation of a uranyl dibenzoylmethanate complex: an example of controlled uranyl oxo ligand cleavage. *Chem. Sci.* **2014,** *5* (8), 3204-3213.

21. Pedrick, E. A.; Wu, G.; Hayton, T. W., Reductive Silylation of the Uranyl Ion with Ph_3SiOTf. *Inorg. Chem.* **2014,** *53* (23), 12237-12239.

22. Kiernicki, J. J.; Cladis, D. P.; Fanwick, P. E.; Zeller, M.; Bart, S. C., Synthesis, Characterization, and Stoichiometric U–O Bond Scission in Uranyl Species Supported by Pyridine(diimine) Ligand Radicals. *J. Am. Chem. Soc.* **2015,** *137* (34), 11115-11125.

23. Brown, J. L.; Mokhtarzadeh, C. C.; Lever, J. M.; Wu, G.; Hayton, T. W., Facile Reduction of a Uranyl(VI) β-Ketoiminate Complex to U(IV) Upon Oxo Silylation. *Inorg. Chem.* **2011,** *50* (11), 5105-5112.

24. Yahia, A.; Arnold, P. L.; Love, J. B.; Maron, L., The Effect of the Equatorial Environment on Oxo-Group Silylation of the Uranyl Dication: A Computational Study. *Chem.: Eur. J.* **2010,** *16* (16), 4881-4888.

25. Arnold, P. L.; Pécharman, A.-F.; Hollis, E.; Yahia, A.; Maron, L.; Parsons, S.; Love, J. B., Uranyl oxo activation and functionalization by metal cation coordination. *Nat. Chem.* **2010,** *2* (12), 1056-1061.

26. Schnaars, D. D.; Wu, G.; Hayton, T. W., Borane-Mediated Silylation of a Metal–Oxo Ligand. *Inorg. Chem.* **2011,** *50* (11), 4695-4697.

27. Schnaars, D. D.; Wu, G.; Hayton, T. W., Silylation of the Uranyl Ion Using $B(C_6F_5)_3$-Activated Et_3SiH. *Inorg. Chem.* **2011,** *50* (19), 9642-9649.

28. Arnold, P. L.; Hollis, E.; White, F. J.; Magnani, N.; Caciuffo, R.; Love, J. B., Single-Electron Uranyl Reduction by a Rare-Earth Cation. *Angew. Chem. Int. Ed.* **2011,** *50* (4), 887-890.

29. Faizova, R.; Fadaei-Tirani, F.; Bernier-Latmani, R.; Mazzanti, M., Ligand-Supported Facile Conversion of Uranyl(VI) into Uranium(IV) in Organic and Aqueous Media. *Angew. Chem. Int. Ed.* **2020,** *59*, 1-5.

30. Coughlin, E.; Bart, S. C., Reductive silylation of uranyl mediated by iminosemiquinone ligands. *Polyhedron* **2019,** *170*, 783-787.

31. Kiernicki, J. J.; Harwood, J. S.; Fanwick, P. E.; Bart, S. C., Reductive silylation of $Cp^*UO_2(^{Mes}PDI^{Me})$ promoted by Lewis bases. *Dalton Trans.* **2016,** *45* (7), 3111-3119.

32. Kiernicki, J. J.; Zeller, M.; Bart, S. C., Facile Reductive Silylation of UO_2^{2+} to Uranium(IV) Chloride. *Angew. Chem. Int. Ed.* **2017,** *56* (4), 1097-1100.

33. Cowie, B. E.; Purkis, J. M.; Austin, J.; Love, J. B.; Arnold, P. L., Thermal and Photochemical Reduction and Functionalization Chemistry of the Uranyl Dication, $[U^{VI}O_2]^{2+}$. *Chem. Rev.* **2019,** *119* (18), 10595-10637.

34. Arnold, P. L.; Pécharman, A.-F.; Lord, R. M.; Jones, G. M.; Hollis, E.; Nichol, G. S.; Maron, L.; Fang, J.; Davin, T.; Love, J. B., Control of Oxo-Group Functionalization and Reduction of the Uranyl Ion. *Inorg. Chem.* **2015,** *54* (7), 3702-3710.

35. Yahia, A.; Arnold, P. L.; Love, J. B.; Maron, L., A DFT study of the single electron reduction and silylation of the U–O bond of the uranyl dication in a macrocyclic environment. *Chem. Commun.* **2009,** (17), 2402-2404.

36. Assefa, M. K.; Pedrick, E. A.; Wakefield, M. E.; Wu, G.; Hayton, T. W., Oxidation of the 14-Membered Macrocycle Dibenzotetramethyltetraaza[14]annulene upon Ligation to the Uranyl Ion. *Inorg. Chem.* **2018,** *57* (14), 8317-8324.

37. Hayton, T. W., Understanding the origins of O_{yl}–U–O_{yl} bending in the uranyl (UO_2^{2+}) ion. *Dalton Trans.* **2018,** *47* (4), 1003-1009.

38. Pedrick, E. A.; Assefa, M. K.; Wakefield, M. E.; Wu, G.; Hayton, T. W., Uranyl Coordination by the 14-Membered Macrocycle Dibenzotetramethyltetraaza[14]annulene. *Inorg. Chem.* **2017,** *56* (11), 6638-6644.

39. Pedrick, E. A.; Schultz, J. W.; Wu, G.; Mirica, L. M.; Hayton, T. W., Perturbation of the O–U–O Angle in Uranyl by Coordination to a 12-Membered Macrocycle. *Inorg. Chem.* **2016,** *55* (11), 5693-5701.

40. Feher, F. J.; Newman, D. A., Enhanced silylation reactivity of a model for silica surfaces. *J. Am. Chem. Soc.* **1990,** *112* (5), 1931-1936.

41. Feher, F. J.; Newman, D. A.; Walzer, J. F., Silsesquioxanes as models for silica surfaces. *J. Am. Chem. Soc.* **1989,** *111* (5), 1741-1748.

42. Feher, F. J.; Walzer, J. F., Synthesis and characterization of vanadium-containing silsesquioxanes. *Inorg. Chem.* **1991,** *30* (8), 1689-1694.

43. Lorenz, V.; Blaurock, S.; Hrib, C. G.; Edelmann, F. T., Coupling of Silsesquioxane Cages in the Coordination Sphere of Erbium. *Eur. J. Inorg. Chem.* **2010,** *2010* (18), 2605-2608.

44. Gun'ko, Y. K.; Reilly, R.; Edelmann, F. T.; Schmidt, H.-G., The First Ce^{IV} Metallasilsesquioxane Complex: $[Ce\{(c\text{-}C_6H_{11})_8Si_8O_{13}\}_2(py)_3]$. *Angew. Chem.* **2001,** *113* (7), 1319-1321.

45. Gießmann, S.; Lorenz, V.; Liebing, P.; Hilfert, L.; Fischer, A.; Edelmann, F. T., Synthesis and structural study of new metallasilsesquioxanes of potassium and uranium. *Dalton Trans.* **2017,** *46* (8), 2415-2419.

46. Brown, J. L.; Wu, G.; Hayton, T. W., Oxo Ligand Silylation in a Uranyl β-Ketoiminate Complex. *J. Am. Chem. Soc.* **2010,** *132* (21), 7248-7249.

47. Fortier, S.; Wu, G.; Hayton, T. W., Synthesis and Characterization of Three Homoleptic Alkoxides of Uranium: $[Li(THF)]_2[U^{IV}(O^tBu)_6]$, $[Li(Et_2O)][U^{V}(O^tBu)_6]$, and $U^{VI}(O^tBu)_6$. *Inorg. Chem.* **2008,** *47* (11), 4752-4761.

48. Wilkerson, M. P.; Burns, C. J.; Dewey, H. J.; Martin, J. M.; Morris, D. E.; Paine, R. T.; Scott, B. L., Basicity of Uranyl Oxo Ligands upon Coordination of Alkoxides. *Inorg. Chem.* **2000,** *39* (23), 5277-5285.

49. Lorenz, V.; Fischer, A.; Brüser, W.; T. Edelmann, F.; Jacob, K.; Gelbrich, T.; G. Jones, P., Si–O–based inorganic ring systems containing f-elements: structural characterization of novel siloxanediolates of the lanthanides and actinides†. *Chem. Commun.* **1998,** (20), 2217-2218.

50. Bursten, B. E.; Casarin, M.; Ellis, D. E.; Fragala, I.; Marks, T. J., Combined helium I/helium II photoelectron spectroscopic and Hartree-Fock-Slater investigation of electronic structure and bonding in uranium hexamethoxide. *Inorg. Chem.* **1986,** *25* (8), 1257-1261.

51. Brandenburg, N. P.; Loopstra, B. O., β-Uranyl sulphate and uranyl selenate. *Acta Crystallogr. B* **1978,** *34* (12), 3734-3736.

52. Burns, C. J.; Sattelberger, A. P., Uranium(VI) oxo-alkoxide cluster synthesis via ligand redistribution. *Inorg. Chem.* **1988,** *27* (21), 3692-3693.

53. Taylor, J. C.; Ekstrom, A.; Randall, C. H., Crystal and molecular structure of trimeric bis(1,1,1,5,5,5-hexafluoropentane-2,4-dionato)dioxouranium(VI). *Inorg. Chem.* **1978,** *17* (11), 3285-3289.

54. Alekseev, E. V.; Krivovichev, S. V.; Depmeier, W.; Siidra, O. I.; Knorr, K.; Suleimanov, E. V.; Chuprunov, E. V., $Na_2Li_8[(UO_2)_{11}O_{12}(WO_5)_2]$: Three Different Uranyl-Ion Coordination Geometries and Cation–Cation Interactions. *Angew. Chem.* **2006,** *118* (43), 7391-7393.

55. Alekseev, E. V.; Krivovichev, S. V.; Malcherek, T.; Depmeier, W., One-Dimensional Array of Two- and Three-Center Cation−Cation Bonds in the Structure of $Li_4[(UO_2)_{10}O_{10}(Mo_2O_8)]$. *Inorg. Chem.* **2007,** *46* (21), 8442-8444.

56. Sullens, T. A.; Jensen, R. A.; Shvareva, T. Y.; Albrecht-Schmitt, T. E., Cation−Cation Interactions between Uranyl Cations in a Polar Open-Framework Uranyl Periodate. *J. Am. Chem. Soc.* **2004,** *126* (9), 2676-2677.

57. Unno, M.; Alias, S. B.; Arai, M.; Takada, K.; Tanaka, R.; Matsumoto, H., Synthesis and characterization of cage and bicyclic silsesquioxanes via dehydration of silanols. *Appl. Organomet. Chem.* **1999,** *13* (4), 303-310.

58. Feher, F. J., Controlled cleavage of $R_8Si_8O_{12}$ frameworks: a revolutionary new method for manufacturing precursors to hybrid inorganic–organic materials. *Chem. Commun.* **1998,** (3), 399-400.

59. Feher, F. J.; Soulivong, D.; Nguyen, F., Practical methods for synthesizing four incompletely condensed silsesquioxanes from a single $R_8Si_8O_{12}$ framework. *Chem. Commun.* **1998,** (12), 1279-1280.

60. Feher, F. J.; Terroba, R.; Ziller, J. W., A new route to incompletely-condensed silsesquioxanes: base-mediated cleavage of polyhedral oligosilsesquioxanes. *Chem. Commun.* **1999,** (22), 2309-2310.

61. Feher, F. J.; Terroba, R.; Ziller, J. W., Base-catalyzed cleavage and homologation of polyhedral oligosilsesquioxanes. *Chem. Commun.* **1999,** (21), 2153-2154.

62. Lorenz, V.; Gießmann, S.; Gun'ko, Y. K.; Fischer, A. K.; Gilje, J. W.; Edelmann, F. T., Fully Metalated Silsesquioxanes: Building Blocks for the Construction of Catalyst Models. *Angew. Chem. Int. Ed.* **2004,** *43* (35), 4603-4606.

63. Seaman, L. A.; Wu, G.; Edelstein, N.; Lukens, W. W.; Magnani, N.; Hayton, T. W., Probing the 5f Orbital Contribution to the Bonding in a U(V) Ketimide Complex. *J. Am. Chem. Soc.* **2012,** *134* (10), 4931-4940.

64. Connelly, N. G.; Geiger, W. E., Chemical Redox Agents for Organometallic Chemistry. *Chem. Rev.* **1996,** *96* (2), 877-910.

65. Teterin, Y. A.; Teterin, A. Y., The structure of X-ray photoelectron spectra of light actinide compounds. *Russ. Chem. Rev.* **2004,** *73* (6), 541.

66. Wiberg, N.; Uhlenbrock, W., Notiz zur Darstellung von Trimethylsilylamin. *Chem. Ber.* **1971,** *104* (8), 2643-2645.

67. Abel, E. W.; Armitage, D. A.; Brady, D. B., Relative basicities of organometallic ethers, amines and sulphides. *T. Faraday Soc.* **1966,** *62* (0), 3459-3462.

68. Abel, E. W.; Armitage, D. A.; Willey, G. R., Relative base strengths of some organosilicon amines. *T. Faraday Soc.* **1964,** *60* (0), 1257-1262.

69. Götze, H. J.; Garbe, W., Basizität und ν(CD)—Frequenzverschiebung von Organometallaminen im System Organometallamin/$CDCl_3$. *Spectrochim. Acta A-M* **1979,** *35* (8), 975-980.

70. Goubeau, J.; Jimenéz-Barberá, J., Tris-(trimethylsilyl)-amin. *Z. Anorg. Allg. Chem.* **1960,** *303* (5-6), 217-226.

71. Drees, M.; Strassner, T., Mechanism of the MoO_2Cl_2-Catalyzed Hydrosilylation: A DFT Study. *Inorg. Chem.* **2007,** *46* (25), 10850-10859.

72. Nolin, K. A.; Krumper, J. R.; Pluth, M. D.; Bergman, R. G.; Toste, F. D., Analysis of an Unprecedented Mechanism for the Catalytic Hydrosilylation of Carbonyl Compounds. *J. Am. Chem. Soc.* **2007,** *129* (47), 14684-14696.

73. Reis, P. M.; Romão, C. C.; Royo, B., Dioxomolybdenum(vi) complexes as catalysts for the hydrosilylation of aldehydes and ketones. *Dalton Trans.* **2006,** (15), 1842-1846.

74. Royo, B.; Romão, C. C., Reduction of carbonyl groups by high-valent rhenium oxides. *J. Mol. Catal. A Chem.* **2005,** *236* (1), 107-112.

75. Hasenaka, Y.; Okamura, T.-a.; Onitsuka, K., Efficient uptake of dimethyl sulfoxide by the desoxomolybdenum(iv) dithiolate complex containing bulky hydrophobic groups. *Dalton Trans.* **2015,** *44* (13), 6260-6267.

76. Ma, X.; Yang, Z.; Schulzke, C.; Ringe, A.; Magull, J., The Monomerization of a Binuclear Molybdenum(VI) Dioxo Complex by an Unusual Silylation Reaction. *Z. Anorg. Allg. Chem.* **2007,** *633* (9), 1320-1322.

77. Mazzotta, M. G.; Xiong, M.; Abu-Omar, M. M., Carbon Dioxide Reduction to Silyl-Protected Methanol Catalyzed by an Oxorhenium Pincer PNN Complex. *Organometallics* **2017,** *36* (9), 1688-1691.

78. Partyka, D. V.; Staples, R. J.; Holm, R. H., Nucleophilic Reactivity and Oxo/Sulfido Substitution Reactions of $M^{VI}O_3$ Groups (M = Mo, W). *Inorg. Chem.* **2003,** *42* (24), 7877-7886.

79. Reddy, K. R.; Domingos, Â.; Paulo, A.; Santos, I., Rhenium(V) Dioxo Complexes with Dihydrobis(pyrazolyl)borates: Synthesis and Reactivity toward Electrophilic Substrates. *Inorg. Chem.* **1999,** *38* (19), 4278-4282.

80. Fessenden, R.; Crowe, D. F., An Extension of and the Reversibility of the Silylamine-Amine Exchange Reaction[1,2]. *J. Org. Chem.* **1961,** *26* (11), 4638-4641.

81. Klebe, J. F., New Silyl Donors. *J. Am. Chem. Soc.* **1964,** *86* (16), 3399-3400.

82. Klebe, J. F., Silyl-proton exchange reactions. *Acc. Chem. Res.* **1970,** *3* (9), 299-305.

83. Langer, S. H.; Connell, S.; Wender, I., Preparation and Properties of Trimethylsilyl Ethers and Related Compounds. *J. Org. Chem.* **1958,** *23* (1), 50-58.

84. Anwander, R.; Eppinger, J.; Nagl, I.; Scherer, W.; Tafipolsky, M.; Sirsch, P., Yttrium Calix[4]arene Complexes. Silylation and Silylamine Elimination Reactions on Model Oxo Surfaces. *Inorg. Chem.* **2000,** *39* (21), 4713-4720.

85. Anwander, R.; Nagl, I.; Widenmeyer, M.; Engelhardt, G.; Groeger, O.; Palm, C.; Röser, T., Surface Characterization and Functionalization of MCM-41 Silicas via Silazane Silylation. *J. Phys. Chem. B* **2000,** *104* (15), 3532-3544.

86. Cauvel, A.; Renard, G.; Brunel, D., Monoglyceride Synthesis by Heterogeneous Catalysis Using MCM-41 Type Silicas Functionalized with Amino Groups. *J. Org. Chem.* **1997,** *62* (3), 749-751.

87. Hair, M. L.; Hertl, W., Reaction of hexamethyldisilazane with silica. *J. Phys. Chem.* **1971,** *75* (14), 2181-2185.

88. Lebedev, A. V.; Lebedeva, A. B.; Sheludyakov, V. D.; Ovcharuk, S. N.; Kovaleva, E. A.; Ustinova, O. L., Organosilicon synthesis of thiophene analogs of isatoic acid anhydride. *Russ J. Gen. Chem.* **2007,** *77* (2), 321-322.

89. Duval, P. B.; Burns, C. J.; Buschmann, W. E.; Clark, D. L.; Morris, D. E.; Scott, B. L., Reaction of the Uranyl(VI) Ion (UO_2^{2+}) with a Triamidoamine Ligand: Preparation and Structural Characterization of a Mixed-Valent Uranium(V/VI) Oxo−Imido Dimer. *Inorg. Chem.* **2001,** *40* (22), 5491-5496.

90. Leverd, P. C.; Rinaldo, D.; Nierlich, M., Crystal structure determination of 4f–5f heterometallic complexes. *J. Chem. Soc., Dalton Trans.* **2002,** (6), 829-831.

91. Bradley, D. C.; Chatterjee, A. K.; Chatterjee, A. K., Sexavalent compounds of uranium—I: Uranyl alkoxides and uranium hexa-alkoxides. *J. Inorg. Nucl. Chem.* **1959,** *12* (1), 71-78.

92. Adams, C.; Riviere, P.; Riviere-Baudet, M.; Morales-Verdejo, C.; Dahrouch, M.; Morales, V.; Castel, A.; Delpech, F.; Manríquez, J. M.; Chávez, I., Catalytic study of heterobimetallic rhodium complexes derived from partially alkylated *s*-indacene in dehydrogenative silylation of olefins. *J. Organomet. Chem.* **2014,** *749*, 266-274.

93. Beagan, D. M.; Huerfano, I. J.; Polezhaev, A. V.; Caulton, K. G., Reductive Silylation Using a Bis-silylated Diaza-2,5-cyclohexadiene. *Chem.: Eur. J.* **2019,** *25* (34), 8105-8111.

94. Nagy, J.; Borbély-Kuszmann, A.; Becker-Pálossy, K.; Zimonyi-Hegedüs, E., Über den lösungsmitteleffekt bei der silylierung von cellulose mit hexamethyl-disilazan. *Makromolekul. Chem.* **1973,** *165* (1), 335-338.

95. Patschinski, P.; Zhang, C.; Zipse, H., The Lewis Base-Catalyzed Silylation of Alcohols—A Mechanistic Analysis. *J. Org. Chem.* **2014,** *79* (17), 8348-8357.

96. W. Gehrke, C.; Leimer, K., Trimethylsilylation of amino acids: Effect of solvents on derivatization using bis(trimethylsilyl)trifluoroacetamide. *J. Chromatogr. A* **1970,** *53* (2), 201-208.

97. Barnhart, D. M.; Burns, C. J.; Sauer, N. N.; Watkin, J. G., Synthesis of Neutral and Anionic Uranyl Aryloxide Complexes from Uranyl Amide Precursors: X-ray Crystal Structures of UO_2(O-2,6-*i*-$Pr_2C_6H_3)_2(py)_3$ and $[Na(THF)_3]_2[UO_2$(O-2,6-$Me_2C_6H_3)_4]$. *Inorg. Chem.* **1995,** *34* (16), 4079-4084.

98. Lam, K.; Geiger, W. E., Anodic Oxidation of Disulfides: Detection and Reactions of Disulfide Radical Cations. *J. Org. Chem.* **2013,** *78* (16), 8020-8027.

99. Harris, R. K.; Becker, E. D.; Menezes, S. M. C. d.; Goodfellow, R.; Granger, P., NMR nomenclature. Nuclear spin properties and conventions for chemical shifts (IUPAC Recommendations 2001). *Pure Appl. Chem.* **2001,** *73* (11), 1795-1818.

100. Harris, R. K.; Becker, E. D.; Menezes, S. M. C. d.; Granger, P.; Hoffman, R. E.; Zilm, K. W., Further conventions for NMR shielding and chemical shifts (IUPAC Recommendations 2008). *Pure Appl. Chem.* **2008,** *80* (1), 59-84.

101. *SMART Apex II*, 2.1; Bruker AXS Inc.: Madison, WI, 2005.

102. *SAINT Software User's Guide*, 7.34a; Bruker AXS Inc.: Madison, WI, 2005.

103. Sheldrick, G. M. *SADABS*, University of Gottingen: Germany, 2005.

104. *SHELXTL PC*, 6.12; Bruker AXS Inc.: Madison, WI, 2005.

105. Dolomanov, O. V.; Bourhis, L. J.; Gildea, R. J.; Howard, J. A. K.; Puschmann, H., OLEX2: a complete structure solution, refinement and analysis program. *J. Appl. Cryst.* **2009,** *42* (2), 339-341.